MAFIC DYKES OF THE EAST ANTARCTIC SHIELD: EXPERIMENTAL, GEOCHEMICAL AND PETROLOGICAL STUDIES FOCUSING ON THE PROTEROZOIC EVOLUTION OF THE CRUST AND MANTLE

Milton
Scott M. Kuehner

B.A. (Minnesota), M.Sc. (Univ. Western Ontario)

Submitted in partial fulfilment of the requirements
of the degree of Doctor of Philosophy
at the University of Tasmania.

September 1986

graduating
1987

This thesis contains no material which has been accepted for the award of any other degree or diploma in any University and, to the best of my knowledge and belief, contains no copy or paraphrase of material previously published or written by another person, except where due reference is made in the text of this thesis.

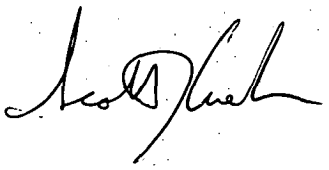

Scott M. Kuehner
September, 1986.

This thesis is dedicated to the memory of my father,
who passed away during the course of my study.

MILTON LESTER KUEHNER

May 3, 1923 - September 21, 1983

For as long as I can remember, he worked six,
and sometimes seven days a week, but still managed to
find time to watch me participate in various
High School athletic programs.

CONTENTS

LIST OF FIGURES

LIST OF TABLES

ACKNOWLEDGEMENTS

I wish first to thank Professor D.H. Green, my supervisor, for patient instruction and guidance through all stages of this thesis. I am also indebted to Prof. Green for offering me an innovative research topic, and for giving me two opportunities to visit Antarctica during the course of my study. I also want to acknowledge the friendship extended to me, and all Ph.D. students of the department, by the Green family, which has enhanced the enjoyable memories of my stay in Tasmania.

Dr David Ellis (now of A.N.U.) provided a great deal of assistance in acquainting me with Antarctic geology at the onset of this study. Dr Ellis also attempted to educate me in the methods of geothermometry-barometry, as well as in the interpretation of Schreinemaker's diagrams. I thank David, and his wife Chris, for their friendship, and for the opportunity to experience an Australian Christmas.

A very important addition to the ranks of Ph.D. students, with respect to my thesis, was Bob Tingey. Bob's extensive experience in Antarctic geology, connections with the Bureau of Mineral Resources, and his willingness to "lend an ear" were valuable resources during the writing-up of this thesis. Similarly, discussions with Drs Tony Crawford, Mark Barsdell and Joe Stolz helped in interpreting the geochemistry of the dykes. Dr Ramsay Ford provided me with information on mineralogical topics throughout this study. Dr John Sheraton (B.M.R.) gave me access to the Bureau of Mineral Resources' collection of mafic dykes from Enderby Land and also to unpublished (in press) manuscripts.

The most important person, outside of the author, in the production of this thesis was my typist - Ms June Pongratz, who did a remarkable job in transforming near-illegible, hand-written text filled with "Americanisms", into a thesis written in the Queen's English, that at least looks good. I would also like to thank June for helping with many of the figures in Chapter 6, and her overall cheery disposition, even when I was caught making alterations to her thesis.

I would like to thank Steve Eggins, John Adam and Sharon Adrichem for assistance in finalizing diagrams in Chapters 5 and 6. The major portion of the diagrams used in this thesis were constructed using a computer program written by Dr Graeme Wheller. As the reader will find, this program was invaluable. An enormous debt of graditude is owed to Dave Huston, Sharon Adrichem and Richard Wedekind for photocopying the final draft.

The technical staff of the Geology Department and the Central Science Laboratory played very important roles in acquiring data for this thesis. Keith Harris gave detailed instructions in the use of the piston cylinder apparatus and manufactured most of the components used in high pressure assemblages. Phil Robinson instructed me in the use of the departmental XRF, and kept the instrument producing high quality data despite its age. Similarly, Wierslaw Jablonski kept an aging, and over used microprobe operational, and instructed me in its use.

Keith (Skygod) Harris, Dr Wayne Taylor, Bob Tingey and Dr Tony Crawford each read and commented on portions of this thesis which improved both the content and presentation of the results.

Finally, it is pleasure to acknowledge the companionship of Dr Simon Harley (Davis Base) and G. Clark, Steve Foley and David Young (Mawson Base) with whom I shared the occasional blizz, and plum pudding with custard, while holidaying in the Antarctic.

The Antarctic Division of the Department of Science and Technology was responsible for all logistic support on each of these expeditions, and I thank them for their assistance.

ABSTRACT

The Vestfold Hills block of the East Antarctic Shield is an Archean granulite facies complex crossed by hundreds of mafic dykes. The dykes compose five chemically distinct suites emplaced in three separate magmatic episodes during the Early-Middle Proterozoic. Sampling of chilled margins coupled with detailed documentation of cross-cutting relationships form the basis for studying the chemical and temporal evolution of each dyke suite as well as providing insight into the chemical evolution of the subcontinental mantle during the Proterozoic. Furthermore, the emplacement of the swarms is bracketed by tectonothermal metamorphic events at ca.2500 Ma and ca.1100 Ma. Previous studies of the metamorphic assemblages which developed during these events have provided constraints on the P,T,time path of the Shield. A principal purpose of the present study has been to determine emplacement depths of the dyke suites in order to further restrict the possible uplift path of the shield during the ~1400 Ma interval separating the final two major deformations.

High pressure experimental techniques were used to determine the load pressure at the emplacement depth of two samples representing dyke suites intruded at ca.2400 Ma and ca.1360 Ma. This was accomplished by experimentally reproducing the chilled margin phenocryst assemblage and the phase compositions after first rigorously evaluating crystal/liquid K_D's to ensure the studied material represented liquid compositions. The results of the experimental studies were also applied to compositionally similar dykes from the Napier Complex of Enderby Land. The studies indicate the Napier Complex and the Vestfold Hills are characterized by ~2000 Ma of crustal stability following the peak metamorphic event at ca.3100 Ma. Both terrains followed identical isobaric cooling paths to ca.2500 Ma, after which the Napier Complex remained at deep crustal levels (~28 km) until ca.1000 Ma, while the Vestfold Hills was exhumed at a rate of ~1cm/1000 a until ca.1100 Ma. This long period of crustal stability experienced by both terrains was terminated by a Himalayan-style tectonic event which resulted in isothermal decompression at a minimum net rate of 11cm/1000 a in the Napier Complex, while crustal loading depressed the Vestfold Hills from depths of ~16 km to ~22 km resulting in the formation of garnet in the mafic dykes. In the absence of more recent deformational events, it is assumed that these terrains experienced slow, erosion controlled uplift since ca.1000 Ma.

The oldest undeformed mafic dyke swarm in the Vestfold Hills was emplaced at ca.2400 Ma and is composed of two contemporaneous suites, a SiO_2-rich, high-Mg tholeiite suite and a Fe-rich tholeiite suite, which compare favourably to basaltic komatiite-Fe tholeiite associations of Archean greenstone belts. Normalized plots of incompatible trace elements, phase compositions, and major element ratios divide the high-Mg suite into three distinct subgroups. The trace element characteristics and isotopic studies prohibit these subgroups from being related by crystal fractionation and previous isotopic studies preclude crustal contamination as a source of chemical variations. Major and trace element evaluation also indicates that two of the chemically distinct subgroups were derived from a primitive liquid extracted from "chondritic" mantle sources leaving an olivine + orthopyroxene residue. Superimposed upon the chondritic characteristics is evidence for selective trace element contamination through a "wall-rock" reaction-type process, possibly with a plagioclase-bearing lherzolite. Comparison of an estimated parental liquid composition with experimental melting studies indicates magma extraction took place at pressures of ~10 kbar (35 km), consistent with the geochemical signature indicating partial melting with a plagioclase-bearing mantle. The more differentiated Fe-rich tholeiites are depleted in LIL elements compared to the high-Mg tholeiites which excludes any simple relationship between the suites by a fractional crystallization process.

Three petrographically and chemically distinct groups can be identified within the Fe-rich suite. Two groups can be related in both major and trace element variations by crystal fractionation, but field relationships preclude this simple interpretation. All the groups have REE patterns indicating derivation from an unfractionated mantle, which precludes a relationship with the high-Mg suite by polybaric melt extraction of a single source. The two closely related groups display enrichment in P and Zr in excess of that due to crystal fractionation. This may represent a relatively deep level wall-rock reaction process as the third group displays elemental enrichments identical to that of the high-Mg tholeiites (formed at ~10 kbar).

The youngest and volumetrically largest dyke swarm was emplaced in the Vestfold Hills at ca.1360 Ma and is dominated by Fe-rich tholeiites with subsidiary, though widespread alkaline dykes. The major and trace element diversity of the Fe-rich suite can be accounted for by a crystal fractionation dominated process. However, the geochemical trends are defined by clusters of analyses which in themselves define differentiation trends that cannot be related to fractionation of the phenocryst phases.

Furthermore, the ordering of the groups does not relate to a simple, monotonic emplacement sequence. The nature of the small-scale geochemical trends and the complex emplacement style may be the result of "open system" magma chamber processes. Rare earth element profiles, as well as the incompatible element plots indicate the parental liquids to this suite were derived from a primitive source which had not experienced previous melting events.

PART 1

EXPERIMENTAL AND METAMORPHIC STUDIES OF MAFIC DYKES APPLIED TO THE CRUSTAL HISTORY OF THE EAST ANTARCTIC SHIELD

Introduction
Regional geological history of the East Antarctic Shield
Mafic dyke swarms
Purpose of study

Chapter 1 The emplacement depths of two Vestfold Hills mafic dykes determined by duplicating natural phenocryst assemblages through the application of high pressure experimental petrology.

Chapter 2 The emplacement depths of several East Antarctic dyke suites predicted from the experimental results of 060 and 206.

Chapter 3 Garnet development within mafic dykes of the Vestfold Hills: evaluation and implications.

Chapter 4 Conclusions: Integration of mafic dyke studies with the previously described crustal history of the Vestfold Hills and Enderby Land - implications for Archean-Proterozoic uplift paths in the East Antarctic Shield.

INTRODUCTION

High pressure experimental studies of basaltic compositions have focussed largely on samples which possess geochemical characteristics that suggest they may be partial melts derived directly from a peridotitic mantle. These investigations seek to characterize the pressure, temperature and volatile conditions at which multiple saturation occurs in these compositions particularly in the phases olivine, orthopyroxene and clinopyroxene. The experimentally determined conditions at multiple saturation are then regarded as those which prevailed during partial melting within the mantle (see Basaltic Volcanism on the Terrestrial Planets, 1981, Chapter 3, for general discussion and references to this approach).

A second approach has been to use high pressure studies to investigate the P-T history of a specific rock type in order to evaluate problems such as the origin of "megacrysts" (whether or not they are cognate or xenocrystic) or the relationship between contemporaneous liquid compositions found within a single basalt province. For example, Green & Hibberson (1970a) studied an olivine basalt containing partially resorbed "xenocrysts" of orthopyroxene, clinopyroxene and amphibole, and demonstrated the cognate origin of these phases by reproducing the assemblage and phase compositions near the 16 kbar olivine basalt liquidus. Similarly, Cox & Jamieson (1974) found that polybaric crystal fractionation was required to explain the observed phenocryst assemblage of the Nuanetsi basalts. Furthermore, Thompson (1975) used high pressure studies to evaluate the possible genetic relationship between a flood basalt and associated tholeiitic andesite from the Snake River Plain and found the andesite could be derived by limited fractionation of the 8 kbar liquidus assemblage of the basalt.

An extension of the "crystal-matching" approach used in the experimental studies of volcanic rocks described above, is applied in Chapter 1 to account for the phenocryst assemblages found in the chilled margins of mafic dykes. It is well known that increasing pressure commonly favours the precipitation of pyroxene from basaltic liquids over that of plagioclase and olivine. Furthermore, the compositions of these phases, and the order of their appearance are also pressure dependent. These pressure-sensitive characteristics offer the possibility to determine the load pressure at the time of dyke emplacement by experimentally reproducing the chilled margin phenocryst assemblage and the phase compositions.

Applied to the East Antarctic Shield, determination of the emplacement pressures of mafic dikes of known age constitutes an independent approach to previous investigations which have sought to determine the pressure-temperature-time (P-T-t) path of the Shield by studying metamorphic mineral assemblages of the host granulites.

At locations where the mafic dykes have been recrystallized during a subsequent metamorphism, the resulting garnet-bearing mineral assemblages provide additional information which can be applied to the crustal history of the Shield. This topic is discussed in Chapter 3.

At least six suites of mafic dykes were emplaced within the East Antarctic Shield during the Early-Mid Proterozoic, samples from two of these were studied experimentally. In Chapter 2, the emplacement pressures of the additional suites are estimated by applying the experimental results of Chapter 1, through the use of projections into the "basalt tetrahedron".

REGIONAL GEOLOGICAL HISTORY OF THE EAST ANTARCTIC SHIELD

Combined structural, geochemical and petrological studies of Enderby Land rocks have focussed on understanding the thermal and tectonic history of the Archean Napier Complex and its relationship to the adjacent Late Proterozoic Rayner Complex (Fig. I1.1; see also James & Tingey, 1983). These studies have yielded evidence for an extensive history of repeated ductile deformation in conjunction with high metamorphic temperatures within a crust containing zircon ages of 3950 Ma (Williams et al., 1984). The first metamorphic episode recognized within the Napier Complex has been dated at 3072^{+35}_{-33} Ma (James & Black, 1981). This event produced the rare metamorphic assemblages sapphirine + quartz, orthopyroxene + sillimanite and osumilite, which taken in conjunction with other mineralogical studies indicates unusually dry metamorphic conditions at pressures of 8-10 kbar and temperatures of 900-1000°C (Ellis, 1980, Ellis et al., 1980; Harley, 1983; Sandiford, 1985). A second localized and less well defined deformation occurred at ca.2900 Ma under continuing high-grade granulite facies conditions (Black & James, 1983; Harley, 1985b).

At ca.2500 Ma, the Napier Complex again experienced a widespread, though only locally intensive tectono-thermal metamorphism (Black et al., 1983a). Mineral assemblages attributed to this granulite facies event record a significantly lower temperature than earlier events (630-700°C) but only marginally (and localized) lower pressures (5-9 kbar; Ellis, 1980; Harley, 1983, 1985b; Sandiford & Wilson, 1983; Ellis & Green, 1985). Taken

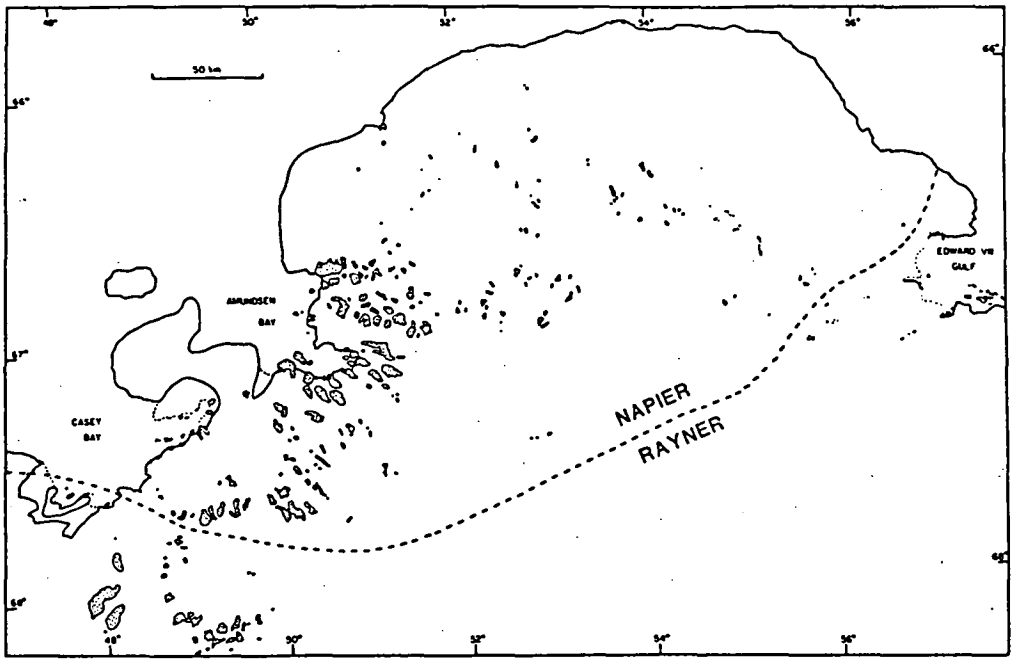

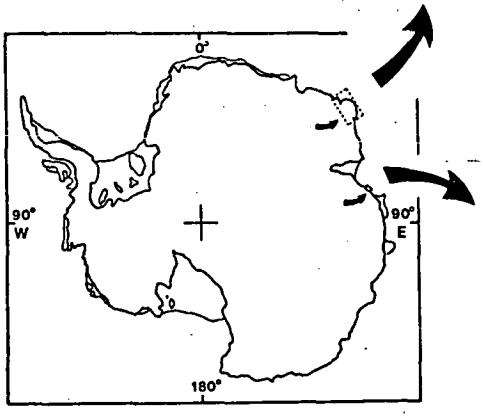

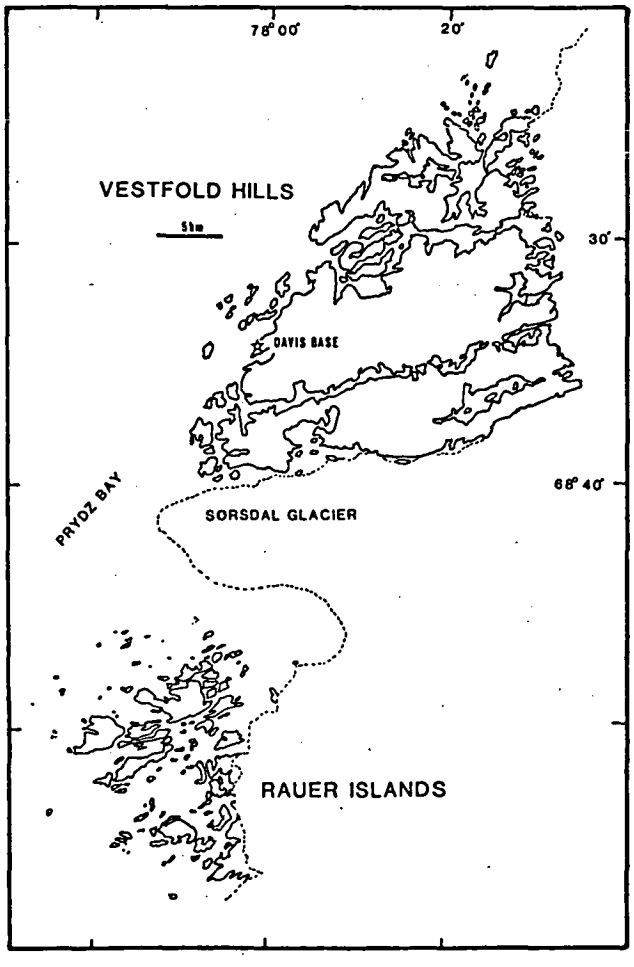

Figure I1.1
The Archean Napier and Proterozoic Rayner Complexes of Enderby and Kemp Lands. (Top)

The Archean Vestfold Hills and Proterozoic Rauer Islands, Princess Elizabeth Land. (Right)

together, these studies indicate regional crustal stability with similar depths of burial for Napier Complex rocks (25-30 km) during a generalized isobaric cooling history from 900-1000°C at ca.3100 Ma to 630-700°C at ca.2500 Ma.

Ellis (1980) pointed out that an isobaric cooling path is inconsistent with any theory which would invoke crustal thickening during continental collision-type tectonism as being responsible for the ca.3100 Ma granulite facies metamorphism. Instead, it was suggested that a disturbed crustal geotherm was produced in response to the ponding of mantle-derived mafic liquids at the crust-mantle boundary. The conductive transfer of heat from the crystallizing liquids was thought to provide a transient thermal pulse without requiring the crust to sink isostatically to deeper, hotter levels of the lithosphere.

The Rayner Complex can be distinguished from the Napier basal on differences in metamorphic grade, and on the occurrence of undeformed Proterozoic mafic dikes in the Napier Complex, while their metamorphosed equivalents outcrop in the Rayner Complex. These field relations signify that the Rayner Complex is composed of, in part, Napier material which experienced a pervasive metamorphism at ca.1000 Ma (1073^{+31}_{-36} Ma, Black & James, 1983; 1022±62 Ma, Grew, 1978, adjusted to Rb decay constant of $1.42 \times 10^{-11} yr^{-1}$). In marked contrast to the isobaric cooling path deduced for the Archean Napier Complex mineral assemblages, the Late Proterozoic Rayner Complex records an isothermal decompression path. Harley (1985a), Sandiford & Wilson (1983) and Ellis (1983) report Napier Complex metamorphic conditions (8 kbar, 720°C) preserved in rocks variably affected by the ca.1000 Ma metamorphism, while corona assemblages and chemical zoning within phases attributed to the Rayner metamorphism indicate conditions of 3-5 kbar pressure and temperatures of 570-650°C. The formation of hydrous minerals in Napier Complex areas affected by the Rayner metamorphism has been used as evidence to indicate the Rayner metamorphism and associated isothermal uplift was the result of underplating and subsequent partial dehydration of continental crust beneath the margins of the Napier Complex during a continental collision-type tectonic event (Ellis, 1983; Harley, 1985a).

Detailed metamorphic-geochronological studies of the Vestfold Hills-Rauer Islands terrains have yet to be reported (Harley, in prep.). However, previous reconnaissance work indicates a similar crustal history to that described from Enderby Land. Isotopic studies of Vestfold Hills granulites have defined Archean metamorphic events at ca.3000-2800 Ma and ca.2500-2400 Ma, and a Proterozoic event in the adjacent Rauer Islands (ca.1100 Ma; Collerson et al., 1983a). Peak metamorphic conditions of ~1000°C and 8-10 kbar can be correlated with the oldest metamorphic episode (Collerson et al., 1983b). However estimated P-T conditions for the younger two events in the Vestfold Hills-Rauer Islands region are at present too unconstrained to be useful.

MAFIC DYKE SWARMS

Mafic dykes occur in great abundance within the Vestfold Hills and are commonly found throughout the much larger area of Enderby Land. The dykes can be subdivided into chemically distinct swarms which are largely confined to the Archean terrains of these areas but can also be identified as metamorphosed relics within the Proterozoic Rauer Islands and Rayner Complex (Fig. I1.1; Sheraton et al., 1980; Sheraton & Collerson, 1983). Chemically identical mostly quartz normative high-Mg tholeiites (Mg# 70-54) were emplaced in both the Vestfold Hills and Enderby Land at ca.2400 Ma and were accompanied by an Fe-rich tholeiite suite in the Vestfold Hills (Sheraton & Collerson, 1983; see also Chapter 5). All the high-Mg tholeiites contain orthopyroxene phenocrysts and a second olivine-bearing subgroup is recognised in the Vestfold Hills. The contemporaneous Fe-rich tholeiite suite ranges in Mg# from 47-36. Dykes composing this suite are often retrogressively altered to green amphibole-quartz-iron oxide assemblages with relic phenocrysts of plagioclase + clinopyroxene $\pm$ orthopyroxene. At ca.1800 Ma a second Fe-rich tholeiite suite was emplaced within the Vestfold Hills, but has not been identified in Enderby Land. These dykes differ from younger tholeiites in the Vestfold Hills only in their incompatible trace element characteristics (Collerson and Sheraton, in press), but differ significantly from the ca.2400 Ma Fe-tholeiite in both mineralogy and chemistry.

The most abundant suite(s) of tholeiite dykes were emplaced in both the Vestfold Hills and Enderby Land over the period 1200-1400 Ma. In Enderby Land, considerable chemical diversity exists among these dykes. Group 1 tholeiites (Sheraton & Black, 1981) are Fe-rich (Mg# 47-40) quartz normative rocks which contain phenocrysts of plagioclase + clinopyroxene + orthopyroxene and are dated at 1190$\pm$200 Ma. Group 2 dykes are olivine normative tholeiites with phenocrysts of plagioclase + clinopyroxene $\pm$ olivine. Samples belonging to this suite do not form an isochron. In contrast, the Vestfold Hills suite forms a generally coherent group dated at 1362$\pm$108 Ma (Chapter 6; Sheraton & Collerson, in press). Dykes which compose this suite are olivine normative to slightly quartz normative over a range of Mg#'s of 56-30. Phenocryst assemblages are plagioclase + clinopyroxene $\pm$ olivine. Orthopyroxene phenocrysts were observed in only one sample.

Intersecting relationships documented in this study, indicate a suite of alkaline dykes located in the Vestfold Hills, previously thought to be Phanerozoic in age (Sheraton & Collerson, 1983), was emplaced

contemporaneously with the ca.1360 Ma tholeiites. The sampled dykes are strongly undersaturated with phenocrysts of olivine, clinopyroxene and often mica, and range in Mg# from 74-51.

PURPOSE OF STUDY

We chose to undertake an experimental study of selected mafic dyke samples to further constrain the uplift history of the East Antarctic Shield. Detailed metamorphic studies (see above) have defined the pressure and temperature conditions which prevailed in the Napier Complex, and to a lesser extent the Vestfold Hills, during the ca.2500 Ma and ca.1000 Ma metamorphisms. However, these studies cannot directly evaluate the P-T-t trajectory which the Shield followed between these two episodes. As the emplacement ages of the mafic dykes are bracketed by these two metamorphic events, determination of emplacement depths of each swarm can restrict possible uplift and cooling path interpretations.

CHAPTER 1

THE EMPLACEMENT DEPTHS OF TWO VESTFOLD HILLS MAFIC DYKES DETERMINED BY DUPLICATING NATURAL PHENOCRYST ASSEMBLAGES THROUGH THE APPLICATION OF HIGH PRESSURE EXPERIMENTAL PETROLOGY

INTRODUCTION

In order to evaluate the depth at which the selected dyke samples crystallized, we have sought to reproduce the phenocryst assemblages observed within the chilled margins through high pressure experimental studies. Central to this approach is the assumption that the phenocrysts have not been transported from significantly much greater depths, and that each of the whole rock analyses can be equated with a liquid composition. The validity of these assumptions can be critically examined by studying the textures and phases contained in the chilled margins of the sampled dykes in conjunction with evaluating the extent of crystal/liquid equilibrium using previously determined crystal/liquid $K_D^{Fe/Mg}$'s. The samples which were finally selected are those which show crystal/liquid equilibrium, or near equilibrium in addition to containing mineral assemblages which give independent estimates on emplacement pressures and/or temperatures using geothermometry-barometry methods.

The water content of the magma is one variable which can strongly influence liquidus phase relationships. The role of water dissolved in mafic magmas at high pressure is to depolymerize the melt structure, which enhances the stability of olivine at the expense of pyroxene. Thus, incorrectly establishing the water content of the natural magma can lead to an erroneous experimentally determined phase geometry, and a misinterpretation of the dyke emplacement pressure. High pressure crystallization of hydrous basaltic liquids should produce an amphibole $\pm$ biotite-bearing assemblage. Additionally, the expulsion of vapour during crystallization of a water-bearing magma may lead to hydration of the marginal granulitic facies wall rocks. The absence of these features from all the tholeiitic dykes sampled indicates these magmas contained little dissolved H_2O, and therefore may be closely characterized by anhydrous experimental studies.

1.1 SAMPLE EVALUATION

1.1.1 SAMPLE DESCRIPTIONS

Sample 060

This sample belongs to the 2420 Ma high-Mg tholeiite suite defined by Sheraton & Collerson (1983), and was collected from a 10 km long by 30 m wide, roughly east-west trending dyke located 1-2 km south of, and generally paralleling Long Fjord (Fig. 1.1). The dyke was sampled approximately 1 m from the chilled margin, consequently the studied material contains a relatively coarser grained groundmass (Fig. 1.2A).

Petrographically, sample 060 contains 6% orthopyroxene and 4% olivine phenocrysts in a mesh work of columnar clinopyroxene crystals (Mg# = 100 Mg/Mg+Fe = 80-69; calculated on four cations) and granular to intersertal orthopyroxene with minor quartz. Plagioclase (An_{64-50}) is restricted to the groundmass and forms elongate laths with subophitic margins. The colourless orthopyroxene phenocrysts are zoned from Mg# 88-72, and may reach 2 mm in length but are generally ~1 mm long. Groundmass orthopyroxene and phenocryst rims are strongly pleochroic from a deep chestnut brown to pale pinkish brown, and differ chemically from the orthopyroxene phenocryst cores in having higher TiO_2, MnO and Fe_2O_3 as well as lower Mg# (Table 1.1, Fig. 1.3A).

Many of the olivine phenocrysts have experienced secondary oxidation and are now composed of orthopyroxene (Wo < 1%)-magnetite symplectites. Cores of several olivine crystals have been preserved and exhibit a range of compositions from Mg# 78.5-68.1.

Sample 206

This sample was collected from the margin of a 10 m by 0.5 m dyke located along the southern shore of an unnamed lake which lies between Ace Lake and Lake Abnaxas in the Northern Peninsula region of the Vestfold Hills (Fig. 1.1). The dyke is an iron-rich (Mg# 42.6) member of the 1360 Ma chemically-defined suite of Sheraton & Collerson (1983) and contains phenocrysts of olivine, plagioclase, clinopyroxene and orthopyroxene (Table 1.2, Fig. 1.2B).

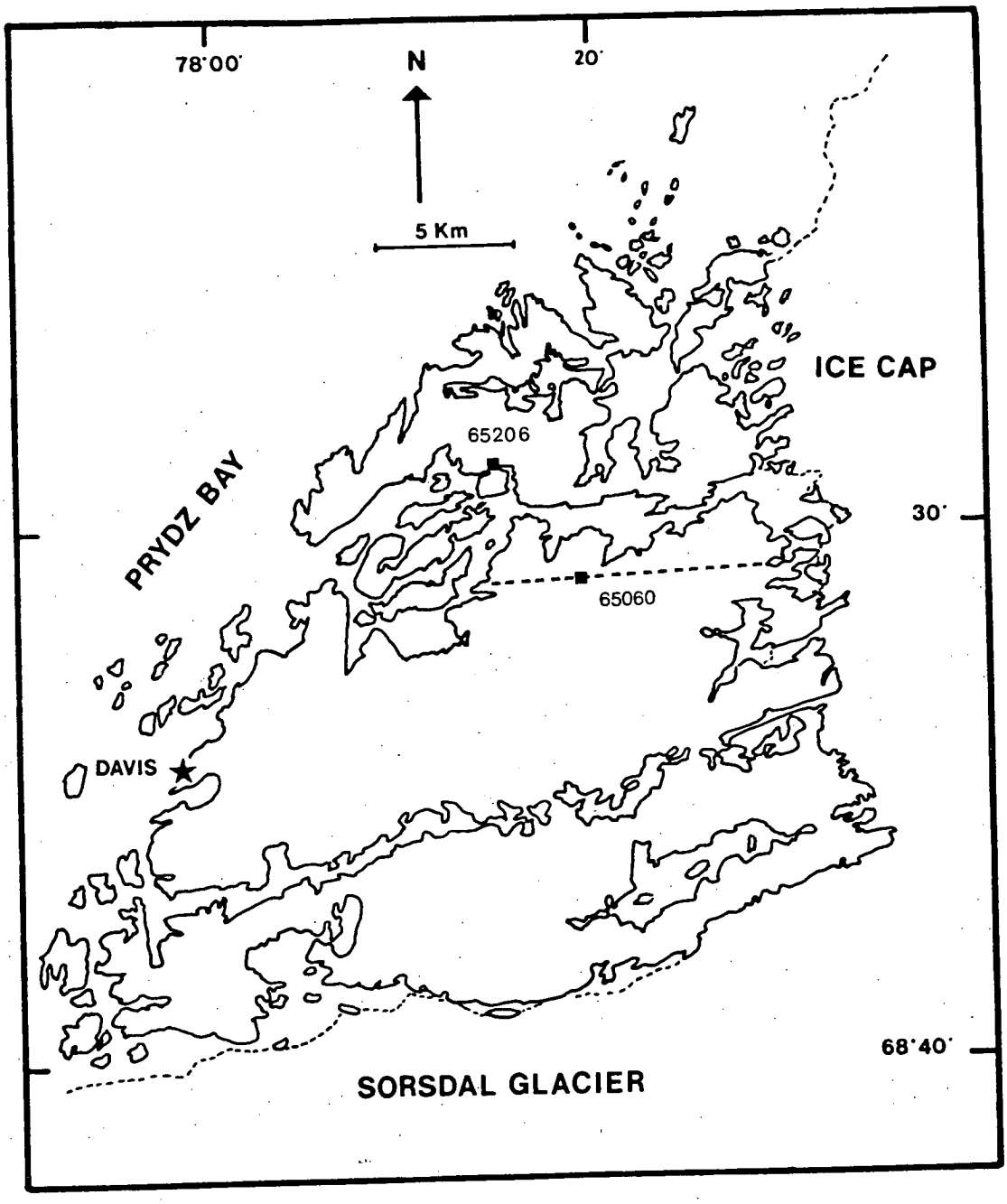

Figure 1.1
Location of dykes from the Vestfold Hills selected for experimental studies.

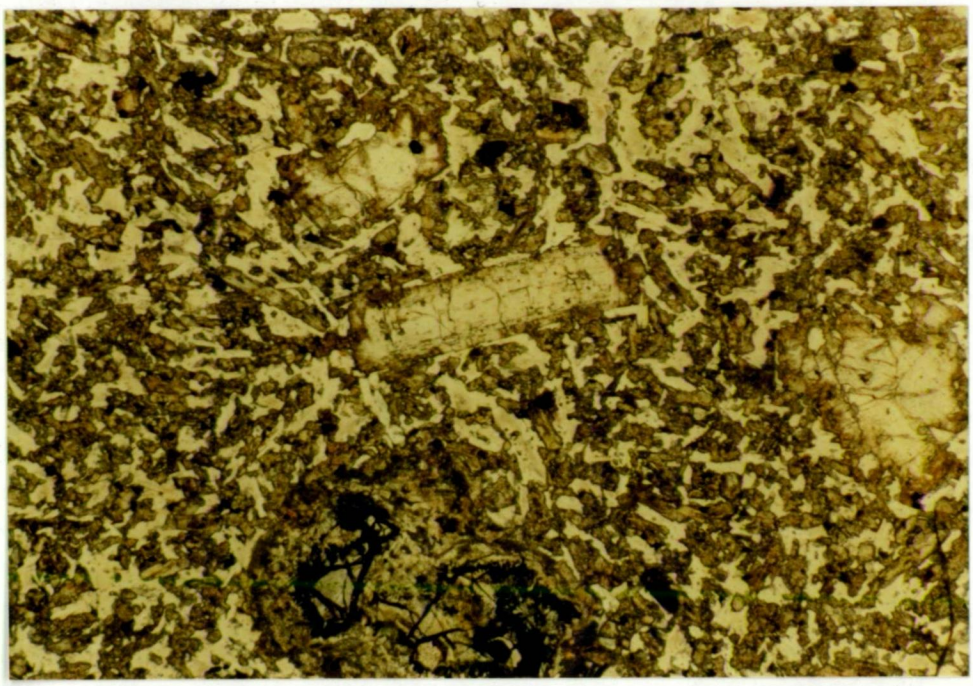

Figure 1.2A

Sample 65060. Red-rimmed orthopyroxene and olivine phenocryst (resorbed) with microphenocrysts of Ca-clinopyroxene (left of centre) in a medium grained plagioclase-pyroxene groundmass. Length of frame = 3.5 mm.

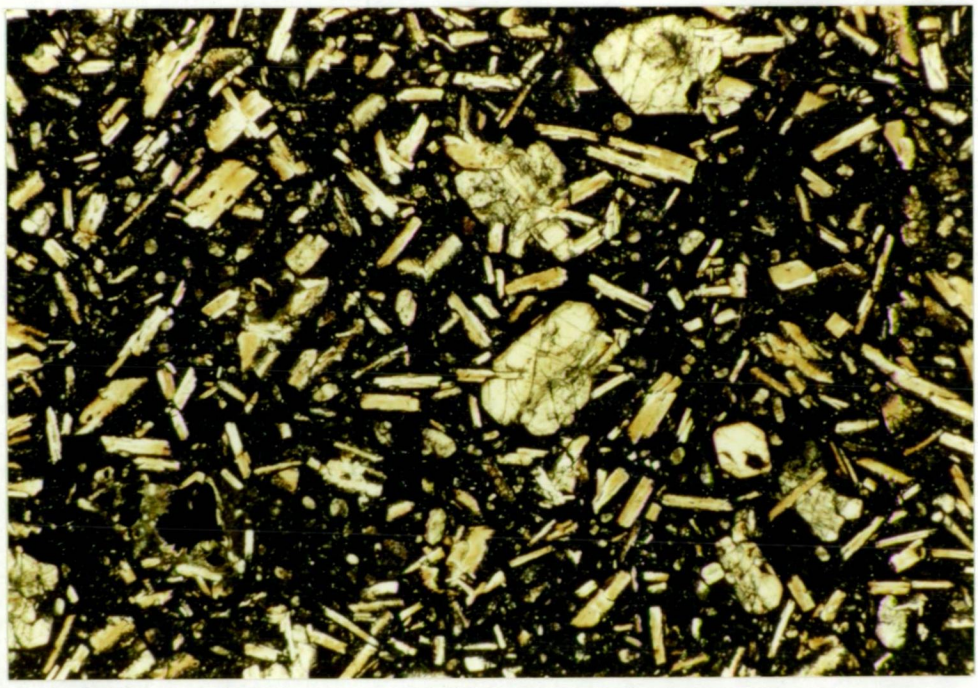

Figure 1.2B

Phenocrysts and crystal clots of clinopyroxene and plagioclase in fine grained opaque-rich groundmass. The large opaque grain is composed of orthopyroxene-magnetite symplectite after olivine. The pinkish euhedral phenocryst is orthopyroxene. Length of frame = 4.0 mm. Sample 65206.

TABLE 1.1
MINERAL ANALYSES FROM SAMPLE 65060

	ORTHOPYROXENE PHENOCRYSTS			ORTHOPYROXENE RIMS ON PHENOCRYSTS			CLINOPYROXENE LATHS			OLIVINE PHENOCRYSTS	
SIO2	55.57	54.99	53.50	50.70	51.92	51.39	51.91	51.65	51.95	37.18	39.04
TIO2				0.35	-	0.63	-	0.21	-		
AL2O3	1.31	1.39	1.60	1.27	1.83	1.47	2.04	2.63	2.07		
CR2O3	0.59	0.41	-	-	0.19	-	0.61	0.75	0.54		
FE2O3*	1.27	0.63	2.12	3.92	1.99	2.13	0.50	0.50	0.32		
FEO	7.60	11.44	14.14	20.25	19.44	20.34	12.16	10.91	12.95	25.54	20.02
MNO				0.41	0.29	0.34	-	-	-	0.23	
MGO	31.34	28.78	26.33	21.30	22.28	21.89	15.71	16.36	15.75	36.92	40.93
CAO	2.32	2.36	2.27	1.81	2.06	1.89	17.08	16.98	16.43	0.13	
SI	1.9482	1.9568	1.9360	1.9065	1.9292	1.9199	1.9392	1.9232	1.9415	0.9843	1.1021
TI				0.0098	-	0.0177	-	0.0059	-		
AL	0.0541	0.0582	0.0702	0.0563	0.0801	0.0649	0.0898	0.1156	0.0910		
CR	0.0162	0.0114	-	-	0.0057	-	0.0180	0.0220	0.0161		
FE3+	0.0334	0.0169	0.0577	0.1111	0.0558	0.0599	0.0140	0.0070	0.0096		
FE2+	0.2229	0.3405	0.4280	0.6369	0.6040	0.6354	0.3798	0.3399	0.4048	0.5655	0.4297
MN				0.0129	0.0093	0.0102	-	-	-	0.0053	
MG	1.6382	1.5261	1.4201	1.1937	1.2339	1.2189	0.8752	0.9090	0.8773	1.4570	1.5660
CA	0.0871	0.0902	0.0879	0.0728	0.0821	0.0732	0.6839	0.6776	0.6578	0.0037	
MG#	88.0	81.8	76.8	65.2	67.1	65.7	69.7	72.8	68.4	72.0	78.5
CA#	4.5	4.6	4.5	3.8	4.3	3.8	35.3	35.2	33.9		
a_{en}				0.3511	0.3763	0.3669	0.1442	0.1585	0.1508		
CaTs							0.0469	0.0594	0.0488		

* CALCULATED BASED ON 4.000 CATIONS. MG# =100 MG/(MG+FE). CA# =100 CA/(CA+MG+FE).

TABLE 1.2
MINERAL ANALYSES FROM SAMPLE 65206

	PHENOCRYSTS								GROUNDMASS		
	CLINOPYROXENE			ORTHOPYROXENE			PLAGIOCLASE		OPX	CPX	PLAG
SIO2	52.31	51.10	49.18	52.72	51.91	50.00	52.23	52.45	50.16	47.91	56.96
TIO2	0.57	0.72	1.08	0.26	0.44	0.22		0.27	0.68	1.82	
AL2O3	2.12	2.91	3.69	1.17	2.25	1.68	29.97	29.80	0.88	4.69	27.68
CR2O3	-	0.31	0.30	-	-	-					
FE2O3*	1.22	1.02	3.09	3.18	2.79	2.59			1.56	1.88	
FEO	7.32	11.17	8.88	14.67	15.51	17.80	0.51	0.85	27.41	10.98	
MNO	-	-	-	0.29	0.34	0.24			0.90	0.26	
MGO	18.04	17.12	15.17	25.58	24.53	23.39	0.17		17.31	12.18	
CAO	18.41	15.66	18.61	2.11	2.25	2.07	13.27	12.13	1.10	20.28	9.57
NA2O							3.66	4.11			5.59
K2O							0.19	0.38			0.20
SI	1.9213	1.8976	1.8404	1.9239	1.9011	1.9212	2.3741	2.3851	1.9377	1.8165	2.5507
TI	0.0158	0.0201	0.0303	0.0073	0.0120	0.0062		0.0092	0.0197	0.0520	
AL	0.0919	0.1272	0.1627	0.0503	0.0971	0.0732	1.6052	1.5972	0.0399	0.2094	1.4607
CR	-	0.0090	0.0088	-	-	-			-	-	
FE3+	0.0338	0.0284	0.0870	0.0874	0.0768	0.0721			0.0454	0.0535	
FE2+	0.2247	0.3468	0.2780	0.4479	0.4750	0.5498	0.0193	0.0324	0.8854	0.3482	
MN	-	-	-	0.0091	0.0104	0.0075			0.0295	0.0084	
MG	0.9877	0.9477	0.8465	1.3916	1.3393	1.2882	0.0117		0.9968	0.6883	
CA	0.7247	0.6233	0.7464	0.0826	0.0882	0.0818	0.6460	0.5907	0.0456	0.8238	0.4591
NA							0.3226	0.3627			0.4857
K							0.0112	0.0220			0.0112
TOTAL							4.9901	4.9993			4.9674
MG#	81.5	73.2	75.3	75.7	73.8	70.1			53.0	66.4	
CA#	37.4	32.5	39.9	4.3	4.1	4.3	65.9	60.6	2.4	44.3	48.0
a_{CaTs}^{en}	0.1714	0.1852	0.1252	0.4799	0.4431	0.4117			0.2407	0.0636 0.0260	

* CALCULATED BASED ON 4.000 CATIONS. MG# = 100 MG/(MG+FE). CA# = 100 CA/(CA+NA+K) or 100 CA/(CA+MG+FE).

Texturally the phenocryst assemblage is dominated by seriate plagioclase (27%*; An_{60-66}) which occurs as individual dusty laths up to 1 mm in length, or in glomeroporphyritic clots with clinopyroxene (10%) and/or olivine (5%). Similarly, the clinopyroxene may form individual idiomorphic crystals (~0.7 mm) or complexly intergrown aggregates.

All the olivine grains in this sample are oxidized and form irregularly shaped masses of orthopyroxene-magnetite symplectites which have green fibrous amphibole coronas when adjacent to plagioclase crystals. Orthopyroxene (<1%) is not observed in any of the glomeroporphyritic clots; it occurs as slightly pleochroic idiomorphic single crystals (~0.7 mm). The groundmass is composed of abundant fine grained opaque oxides with plagioclase and minor quartz. A three-phase pyroxene assemblage may also be present (see Fig. 1.3B) though the scattered analyses could be due to rapid disequilibrium crystallization following emplacement.

1.1.2 APPRAISAL OF LIQUID COMPOSITIONS

The extent to which the studied samples represent liquid composition (i.e. not a phenocryst or xenocryst enriched sample) can be evaluated by making use of previously determined crystal/liquid $K_D^{Fe/Mg}$ relationships. To a certain extent, the degree to which these relationships can be applied to natural systems depends in part on the role of Fe^{3+} in the phases considered, and how it is handled during the calculations. For the purpose of this exercise it is assumed that all iron exists as Fe^{2+}. This assumption is incorrect, but necessary because the Fe_2O_3/FeO ratio of the samples is not known, and even if the ratio had been determined it may not represent the fO_2 conditions which existed during crystallization of the phenocrysts, even disregarding secondary alteration (Mathez, 1984). Also, the calculation of Fe_2O_3 of minerals analysed by microprobe is strongly dependent on the accuracy of the SiO_2 determination, which can consequently produce erroneous Fe^{2+}/Mg ratios. The wide range of calculated Fe_2O_3 values in orthopyroxene phenocrysts from 060 (0.40-2.20%) may partly reflect this problem.

---

* A maximum value considering the seriate texture.

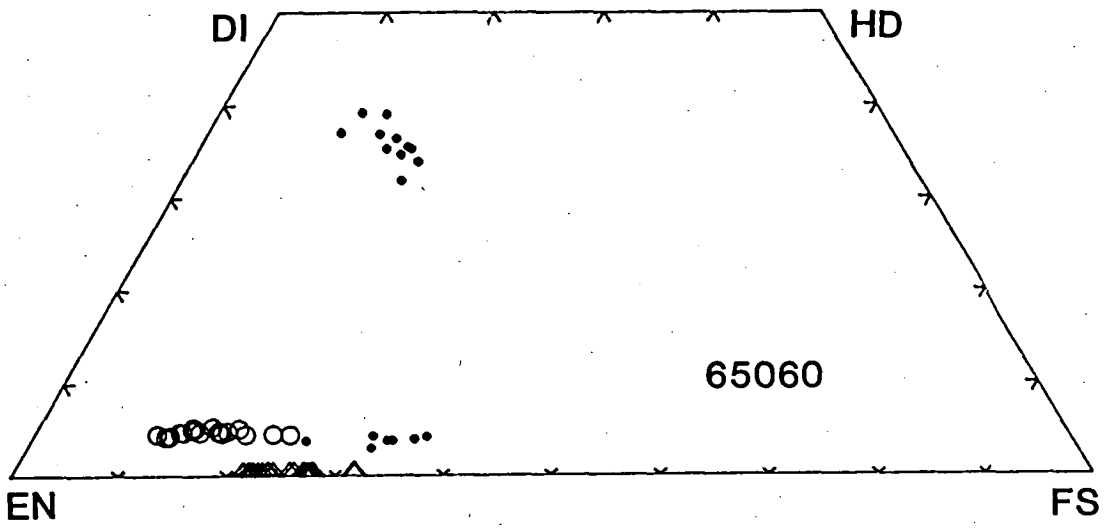

Figure 1.3

A. Composition of orthopyroxene (open circles) and olivine (triangles) phenocrysts of the natural phase assemblage. Dots represent compositions of the coloured orthopyroxene phenocryst rims, and clinopyroxene microphenocrysts. (Mole %)

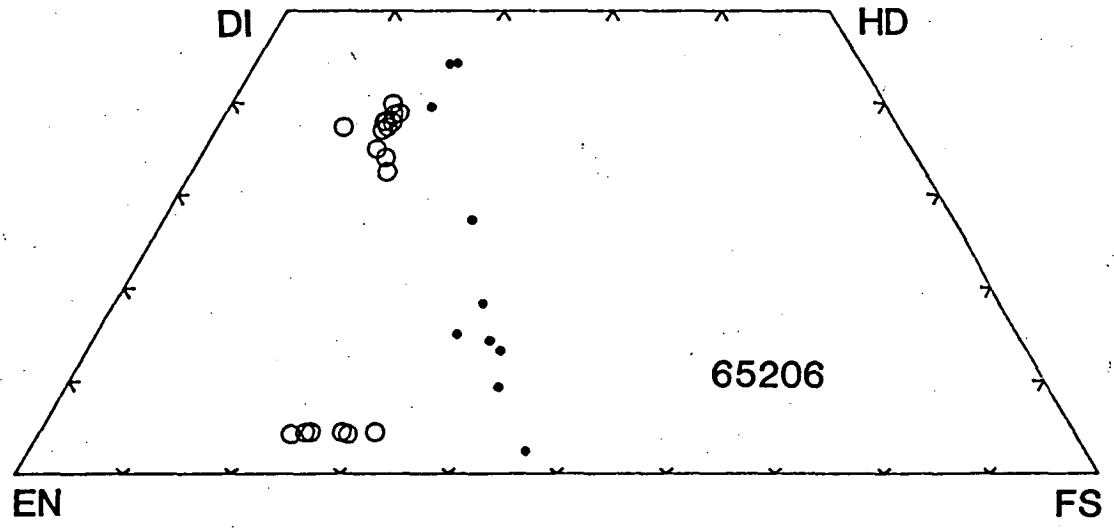

Figure 1.3

B. Compositions of orthopyroxene and clinopyroxene phenocrysts (open circles) of the natural phase assemblages. Dots represent pyroxene analyses from the fine grained groundmass. (Mole %)

Sample 060

If this sample represents a liquid composition (Mg# 65.0), then an equilibrium orthopyroxene of Mg# 86.1 is predicted by applying $K_D^{Fe/Mg}{}_{opx/liq}$ = 0.30 (Jaques & Green, 1979). This expected orthopyroxene composition is nearly identical to the most Mg-rich orthopyroxene in the natural rock (86.5)* and provides a sound basis for considering the bulk rock as a liquid composition. The most Mg-rich olivine (Mg# 78.5) is predicted to be in equlibrium with an orthopyroxene of Mg# 80.1 using $K_D^{Fe/Mg}{}_{ol/opx}$ = 1.1 (Matsui & Nishazawa, 1974; Mori & Green, 1978; Jaques & Green, 1979). This predicted equilibrium value is significantly lower than the most Mg-rich orthopyroxene observed, but falls within the range of orthopyroxene compositions (Mg# 86.5-70.0)*. The latter calculation suggests orthopyroxene may be the liquidus phase in sample 060 which is then joined by olivine at lower temperatures.

Sample 206

Unfortunately, crystal-liquid equilibria are more difficult to assess in this sample than in 060 as the olivine phenocrysts are completely altered, in addition to which considerable variation exists in published $K_D^{Fe/Mg}{}_{cpx/liq}$ values (0.23-0.33; Thompson, 1974; Green et al., 1979; Grove and Bryan, 1983). However, some conclusions can be drawn. Assuming $Fe^T = Fe^{2+}$, the most Mg-rich clinopyroxene has a Mg# = 79.2 while the bulk rock Mg# = 42.6, resulting in a $K_D^{Fe/Mg}{}_{cpx/liq}$ = 0.20. This value is outside the range of reported K_D values and requires the crystallization of this pyroxene composition from a more Mg-rich liquid than that represented by the bulk rock. However, the exclusion of this single Mg-rich analysis (Fig. 1.3B) reduces the observed range of clinopyroxene Mg#'s (75.7-69.9) and a minimum K_D = 0.24 is obtained. This value lies just within the observed range of reported K_D values which implies the clinopyroxene phenocrysts could be in equilibrium with a liquid represented by the whole rock composition, though evidence for descent from a more magnesiun liquid may still be found in the cores of some grains.

---

* Calculated on the basis of $Fe^T = Fe^{2+}$, values reported in Table 1.1 were calculated after the removal of Fe^{3+} based on 4.000 cations.

Similarly, the orthopyroxene phenocryst ranges in Mg# from 72.2-64.5, with the most Mg-rich value giving a $K_{D_{opx/liq}}^{Fe/Mg} = 0.28$. This value compares well with the generally used value of $K_D = 0.30$, though it may also indicate that a history of slightly more Mg-rich compositions is preserved in the orthopyroxene cores. As both the ortho- and clinopyroxenes appear to be nearly equilibrated with the bulk rock composition, it implies that the two pyroxenes have co-precipitated. In addition, these phases must have also crystallized with the olivine phenocrysts as early crystallization of olivine would create Fe-rich liquids resulting in crystal/liquid $K_D^{Fe/Mg}$ values higher, not lower, than the previously determined K_D values of the pyroxenes.

The above discussion has assumed the liquid did not contain Fe^{3+}, though certainly small amounts of Fe^{3+} did exist in the magma. Considering a small amount of Fe^{3+} in the liquid, the resulting Mg-value of the bulk rock would increase slightly and result in crystal/liquid K_D's more appropriate to equilibrium values.

1.1.3 DETERMINATION OF EMPLACEMENT PRESSURES AND TEMPERATURES BY APPLYING GEOTHERMOMETRY AND BAROMETRY TO NATURAL PHASE ASSEMBLAGES

Nearly all of the samples belonging to the high-Mg tholeiite suite were collected from chilled margins, and consequently contain fine grained and sometimes quench textured groundmasses. The reasons for choosing sample 060 for experimental studies were that it not only satisfied the critical requirement of being a liquid composition (determined by opx/Liq K_D's) but also that its somewhat coarser grained groundmass facilitated the application of "two pyroxene" thermometry, as well as being suitable for pressure determinations using the clinopyroxene-plagioclase-quartz assemblage. Similarly, coexisting ortho- and clinopyroxene phenocrysts in sample 206 provide a basis for temperature calculations, a characteristic not shared with other members of the 1360 Ma suite. In addition, crystallization pressures can also be calculated from sample 206 by applying the clinopyroxene-plagioclase-quartz barometer to the groundmass assemblage.

Numerous studies have been undertaken to calibrate a thermometer which can be applied to the compositions of coexisting pyroxenes (see review in Stephenson, 1984). Most of these studies have met with only limited acceptability among petrologists due to a broad range of underlying approximations which result in a narrow range of application or questionable reliability.

The Wells (1977) thermometer is probably the most widely used thermodynamically-based two-pyroxene thermometer and is essentially an updated version of the Wood & Banno (1973) formulation. Despite its thermodynamic simplicity, the Wells thermometer has been shown to give good results when applied to pyroxene pairs equilibrated at temperatures >900°C (Nickel & Brey, 1984; Essene, 1982; Lindsley & Anderson, 1983).

Lindsley & Anderson (1983) and Lindsley (1983) developed a pressure-corrected two-pyroxene graphical thermometer based on reversed experimental studies within the iron-bearing Di-En-Hd-Fs system over a temperature range of 800-1200°C. Natural pyroxene compositions are plotted onto the quadrilateral following a projection scheme to account for "other" components. The thermometer gives independent temperature estimates based on each of the coexisting pyroxene compositions and includes temperature relationships for pigeonite.

Kretz (1982) combined experimental and natural pyroxene data on igneous and metamorphic assemblages to develop two thermometers. The first is based on the clinopyroxene limb of the En-Di solvus, and consists of two expressions to account for the change of slope in the solvus curve at ~1080°C. The second expression is based on the temperature-dependence of the Mg-Fe exchange between coexisting pyroxenes. Lindsley (1983) reported good agreement between his graphical thermometer and the solvus temperature method of Kretz, but suggests the exchange thermometer may over-estimate temperature by several hundred degrees. No specific allowance is made for non-quadrilateral components in either Kretz formulation. Errors for all of the above thermometers are reported to be in the order of ±50°C.

The only geobarometer applicable to these igneous assemblages is the clinopyroxene-plagioclase-quartz equilibrium of Ellis (1980) which models the exchange:

Anorthite	=	Ca Tschermaks molecule	+	Quartz
$CaAl_2Si_2O_8$		$CaAl_2SiO_6$		SiO_2

This reaction was not studied directly, but was created by combining the appropriate thermodynamic parameters of the individual components. The resulting expression exhibits minor temperature dependence under crustal conditions and has a reported error of ±1 kbar (Ellis, 1980; Ellis & Green, 1985).

The activity-composition relations used for clinopyroxene restricts the application of this barometer to pyroxene assemblages with <0.35 mole%

CaTs; this maximum value is an order of magnitude greater than that observed in the clinopyroxenes of the present study.

Sample 060: geothermometry

The temperature derived from the application of the previously discussed thermometers to the coloured orthopyroxene rims and clinopyroxene groundmass laths are listed in Table 1.3. Data and calculated temperatures are presented in two groups: that calculated assuming all iron in the pyroxenes exists as Fe^{2+}, and with Fe^{3+} calculated based on 4.000 cations. Note the only difference between the latter calculation and the charge balance equation of Papike et al. (1974) used in the Lindsley projection is in the normalization procedure. As cation totals of the raw pyroxene analyses obtained in this study rarely exceed 4.02, the normalization step (a change of 0.5%) creates an insignificant difference in the calculated temperatures. With the exception of the temperatures determined using the Lindsley thermometer, the calculated temperatures are based on averaged data values. This was a necessary procedure as chemical zoning, though limited in extent, is observed in both the ortho- and clinopyroxenes. Simply applying the thermometer to the most Fe-rich compositions was considered improper because of the possible effects of local chemical disequilibrium between these phases during the final stages of crystallization.

Essentially identical temperatures are obtained from four of the five thermometers (av. 1168°C) after the extraction of Fe^{3+} from the pyroxene data. The calculated Wells, Kretz (solvus and exchange) temperatures differ from one another by a maximum of 22°C, and fall within the 1150-1200°C temperature range obtained from the cpx limb of the Lindsley graphical thermometer (Fig. 1.4A). In contrast, the temperature obtained from the opx limb of the Lindsley thermometer is 50-100°C lower than that from the cpx limb. A disparity between the temperatures obtained from the separate limbs of the Lindsley thermometer was also noted by Lindsley (1983), Stevenson (1984) and Ellis & Green (1985). In these cases, the thermometers were applied to pyroxenes equilibrated under granulite facies conditions. Lindlsey (1983) suggested two possibilities for the discrepancy: either the orthopyroxene experienced some unspecified retrograde reaction that did not affect the clinopyroxene (perhaps a lower blocking temperature) or it reflects imprecision in either the projection method or placement of the geotherm.

Analyses of the orthopyroxene phenocrysts plot in a tight grouping along the 1300°C, 10 kbar isotherm of Lindsley's quadrilateral. Because

TABLE 1.3
TEMPERATURE CALCULATIONS ON SAMPLE 65060 MINERAL ASSEMBLAGES

	a_{En}^{cpx}	a_{En}^{opx}	X_{Mg}^{cpx}	X_{Mg}^{opx}	X_{Ca}^{cpx}	METHOD	T^{o} C
	0.1263	0.3410	0.745	0.631	0.390		
	0.1497	0.3970	0.748	0.671	0.369	WELLS	1171
	0.1571	0.3272	0.709	0.620	0.348		
	0.1399	0.3669	0.722	0.657	0.375	KRETZ (solv)	1174
	0.1454	0.3511	0.702	0.652	0.355		
Fe^{3+}	0.1444	0.4613	0.722	0.736	0.364	KRETZ (exch)	1152
	0.1442	0.3763	0.697	0.671	0.353		
	0.1585		0.728		0.352	LINDSLEY	
	0.1508		0.684		0.339	(cpx limb)	1150-1200
	0.1745		0.700		0.319		
	0.1735		0.806		0.370	(opx limb)	1100-1150
AVG.	0.1513	0.3744	0.724	0.663	0.358		
	0.1263	0.3346	0.745	0.619	0.390		
	0.1497	0.3913	0.748	0.662	0.369	WELLS	1163
	0.1571	0.3206	0.709	0.608	0.348		
	0.1399	0.3561	0.722	0.637	0.375	KRETZ (solv)	1176
	0.1454	0.3316	0.702	0.615	0.355		
Fe^{tot}	0.1444	0.4471	0.701	0.714	0.357	KRETZ (exch)	1069
	0.1424	0.3661	0.690	0.652	0.350		
	0.1574		0.724		0.351	LINDSLEY*	
	0.1493		0.679		0.337		
	0.1732		0.696		0.315		
	0.1620		0.766		0.359		
AVG.	0.1497	0.3639	0.717	0.644	0.355		

* Not applicable to this situation, recommended for use only with ferric iron calculated.
ref: Wells (1977) ,Kretz (1982), Lindsley (1983)
Activity of enstatite (a_{En}) calculated following Wood-Banno (1973).
X_{Mg}= Mg/(Mg+Fe), X_{Ca}= Ca/(Ca+Mg+Fe).

the orthopyroxene does not coexist with a clinopyroxene, 1300°C is a minimum temperature for the crystallization of the phenocrysts (Lindsley, 1983).

Temperatures calculated using the Wells and Kretz (solvus) thermometer under conditions of $Fe^T = Fe^{2+}$, differ insignificantly from the Fe^{2+} determined temperature (av. 1170°C). However, the Kretz (exchange) expression results in a calculated temperature 80° lower than the Fe^{3+} exchange temperature despite only minor changes in the Mg# of the averaged ortho- and clinopyroxene (opx, 66.3 —> 64.4; cpx, 72.4 —> 71.7). The apparent sensitivity of the Kretz (exchange) thermometer makes it very susceptible to variations in calculated Fe^{3+}, and ultimately on the accuracy of SiO_2 determinations.

The similarity between the Kretz exchange temperature and the Kretz solvus, Wells and Lindsley temperatures, where Fe^{3+} has been calculated, may be purely fortuitous or may indicate the Fe^{3+} calculation procedure and the thermometers are well calibrated.

Sample 060: geobarometry

Crystallization pressures were calculated from the average Ca-tschermaks content of the groundmass clinopyroxene (following Kushiro, 1962) which is assumed to be in chemical equilibrium with the average plagioclase compositions. Textural relationships indicate these phases coprecipitated from a siliceous liquid shown by the common occurrence of small intersertal quartz grains. The calculated pressures range from 8.0-8.1 kbar (Table 1.4 below).

TABLE 1.4
PRESSURE CALCULATION ON SAMPLE 65060

	CaTs (Fe3+)	X_{Ab}	T (°C)	P (kbar)
	0.0302	0.427		
	0.0539	0.487		
	0.0512	0.343	1171	8.0
	0.0543	0.388		
	0.0404		1174	8.0
	0.0387			
	0.0469		1152	8.1
	0.0594			
	0.0488			
	0.0622			
	0.0370			
AVG.	0.0480	0.411		

Ref. CaTs calculated after Kushiro(1962), X_{Ab} = Na/(Na+Ca), pressure calculated after Ellis (1980), see text for temperature details.

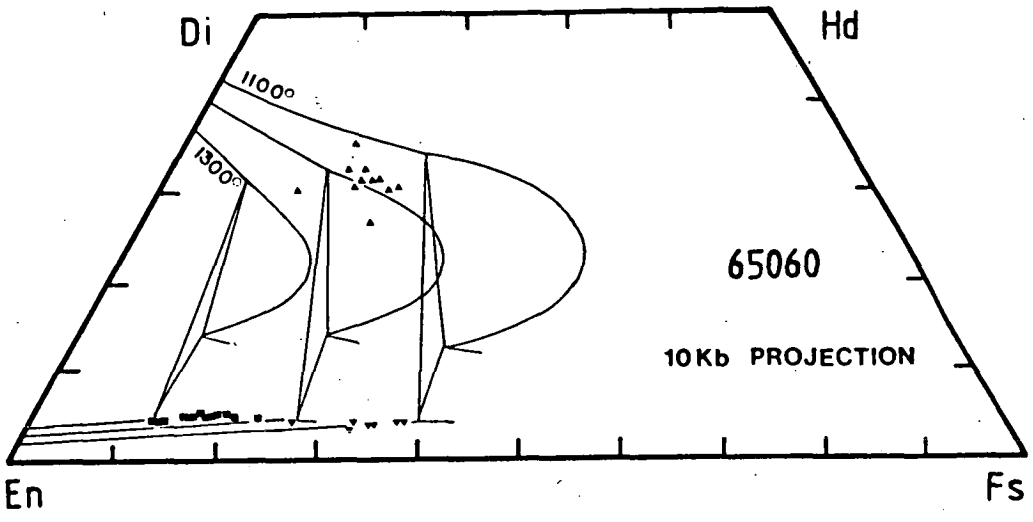

Figure 1.4A
Lindsley's graphical thermometer applied to natural pyroxene compositions of 060: squares - orthopyroxene phenocrysts; inverted triangles - coloured phenocryst rims; triangles - clinopyroxene microphenocrysts.

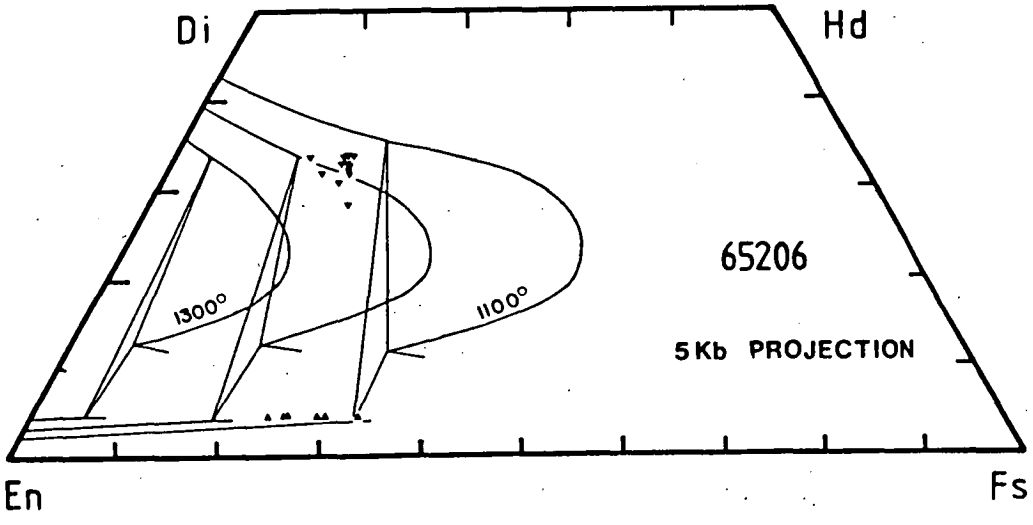

Figure 1.4B
Lindsley's graphical thermometer applied to the natural phenocryst assemblage of 206: triangles - orthopyroxene; inverted triangles - clinopyroxene.

Sample 206: geothermometry

The occurrence of coexisting pyroxenes as phenocrysts and groundmass phases in sample 206 permits temperature estimates to be made on both assemblages. Temperatures calculated using the compositions of the coexisting orth- and clinopyroxene phenocryst pairs are given in Table 1.5, and follow the same format for the calculation of Fe^{3+} as in the previous example. The temperatures were calculated by averaging the required parameters for each of the individual phases, which, considering the observed chemical zoning in the orthopyroxene is a necessary over-simplification.

The temperatures calculated from the Wells, Kretz (solvus) and Lindsley (cpx limb) thermometers, after extraction of Fe^{3+}, are identical within error and average 1165°C. A slightly wider range of temperatures, though still within the uncertainty of the individual thermometers is calculated assuming $Fe^{2+} = Fe^{T}$, with only a marginally lower average temperature of 1155°C. Temperatures calculated using the Kretz (exchange) expression gives excessively high temperatures for both Fe^{2+} and Fe^{T} situations (1414° and 1357°C). The sensitivity of this thermometer to even slight shifts in Mg/Fe (see previous section) probably indicates the averaged opx/cpx compositions equated in the temperature calculations do not represent equilibrium values. This possibility may also be indicated from the >1200°C temperatures obtained from the Lindsley (opx limb) thermometer which is more than 50° higher than the cpx limb temperatures (Fig. 1.4B). In contrast, apparent equilibrium pyroxene compositions from granulite terranes (and sample 060) indicate the reverse is true: the opx limb gives the lower temperature.

The data used to calculate temperatures from the coexisting groundmass pyroxenes are listed in Table 1.5. Only Wells and Kretz (solvus) thermometers, which exhibit good correspondence in the previous examples, were applied. The resulting temperatures (985° and 957°C respectively) indicate some subsolidus re-equilibration has occurred.

TABLE 1.5
TEMPERATURE CALCULATIONS ON SAMPLE 65206 MINERAL ASSEMBLAGES

	a_{En}^{cpx}	a_{En}^{opx}	X_{Mg}^{cpx}	X_{Mg}^{opx}	X_{Ca}^{cpx}	METHOD	T^{o} C
	PHENOCRYSTS						
	0.1714	0.4182	0.815	0.707	0.374		
	0.1698	0.3781	0.725	0.675	0.341	WELLS	1162
	0.1453	0.4117	0.732	0.701	0.374		
	0.1413	0.4799	0.754	0.757	0.380	KRETZ (solv)	1157
	0.1429	0.4534	0.757	0.743	0.380		
Fe^{3+}	0.1489	0.4431	0.756	0.738	0.371	KRETZ (exch)	1414
	0.1282		0.739		0.389		
	0.1722		0.756		0.350	LINDSLEY (cpx limb)	1150-1200
	0.1331		0.745		0.387		
	0.1391		0.744		0.379		
	0.1252		0.753		0.399	(opx limb)	>1200
AVG.	0.1470	0.4307	0.752	0.720	0.375		
	0.1650	0.4004	0.792	0.678	0.368		
	0.1651	0.3615	0.725	0.645	0.332	WELLS	1147
	0.1409	0.3960	0.732	0.674	0.369		
	0.1376	0.4573	0.738	0.722	0.374	KRETZ (solv)	1163
	0.1363	0.4345	0.731	0.712	0.371		
Fe^{tot}	0.1374	0.4027	0.712	0.689	0.357	KRETZ (exch)	1357
	0.1204		0.706		0.378		
	0.1651		0.733		0.343	LINDSLEY*	
	0.1228		0.702		0.373		
	0.1324		0.717		0.371		
	0.1132		0.699		0.381		
AVG.	0.1397	0.4087	0.726	0.687	0.365		
	GROUNDMASS						
	0.636	0.2407	0.664	0.530	0.443	WELLS	985
Fe^{3+}	0.631		0.678		0.442	KRETZ(solv)	954
AVG.	0.634	0.2407	0.671	0.530	0.442		

* Not applicable to this situation: recommended for use only with ferric iron calculated. Ref: Wells (1977), Kretz (1982), Lindsley (1983). Activity of enstatite (a_{En}) calculated following Wood and Banno (1973). X_{Mg}= Mg/(Mg+Fe), X_{Ca}= Ca/(Ca+Mg+Fe).

Sample 206: geobarometry

Emplacement pressures were calculated on the data derived from two groundmass clinopyroxene-plagioclase pairs (+ quartz; Table 1.6 below) while the temperature used in the calculation is the average of the Wells (985°C) and Kretz solvus (954°C) methods applied to groundmass pyroxenes (Table 1.5). As this barometer has a slight -(dP/dT), the averaged temperature (970°C) gives a maximum emplacement pressure of 5.3 kbar.

TABLE 1.6
PRESSURE CALCULATION ON SAMPLE 65206

	CaTs(Fe3+)	X_{Ab}	T (°C)	P (kbar)
	0.0260	0.508		
	0.0258	0.501		
AVG	0.0259	0.505	970	5.3

Ref. CaTs calculated following Kushiro(1962), X_{Ab}=Na/(Na+Ca), temperature is average of Wells and Kretz(solv), pressure calculated following Ellis (1980).

1.2 TECHNICAL CONSIDERATIONS

1.2.1 EXPERIMENTAL METHODS

Starting compositions were prepared by mixing AR GRADE oxide or carbonate reagents (except iron and phosphorus) in the proportions appropriate to produce 1 gram of the desired composition. The resulting mixture was ground under acetone in an agate mortar, pelletized, and then sintered for 12 hours at 1000°C. Iron and a fraction of the silica were added to the sintered oxide mix in the form of previously synthesized "stock" fayalite. Similarly, phosphorus and a fraction of the calcium was added as $Ca_2P_2O_7$. The resulting mixture was reground three times to dryness under acetone. To ensure the final mixture was completely anhydrous, a Pt bucket containing the powder mix was placed within a 1 atmosphere furnace and dried for 2 hours at 450°C in an argon atmosphere. The final compositions were checked by microprobe analysis of Ir-strip glasses made from each mixture. These are compared with the XRF analyses of the selected samples in Table 1.7.

TABLE 1.7
SYNTHETIC STARTING COMPOSITIONS COMPARED WITH NATURAL ROCK VALUES

	65060		65206	
	SYN	NAT	SYN	NAT
SiO2	52.68	52.47	49.45	49.30
TiO2	0.61	0.62	2.25	2.39
Al2O3	11.76	11.98	13.91	13.89
Cr2O3	0.14*	0.14	-	-
FeO	10.73	10.85	14.89	15.13
MnO	0.18*	0.18	0.26*	0.26
NiO	0.02*	0.02	-	-
MgO	11.45	11.26	6.55	6.29
CaO	10.26	10.00	10.03	9.87
Na2O	1.52	1.79	1.95	2.10
K2O	0.55	0.60	0.45	0.51
P2O5	0.10*	0.10	0.26	0.25
Mg#	65.5	65.0	44.0	42.6

* Oxides added to synthetic composition but not detected during microanalyses.

One atmosphere experiments were performed in a Pt-wound vertical quenching furnace using Spec-pure Fe capsules and lids sealed in evacuated silica tubes. Run temperatures were calibrated at the onset of each experiment using a Digical II model AN6520 (Analogic Corp.) digital thermometer (accurate to $\pm 1^{o}C$) fitted with a $Pt/Pt_{90}Rh_{10}$ thermocouple. The internal furnace controller indicated that the temperature remained essentially constant ($\pm 1^{o}C$) during the course of each experiment (up to 40 hours). Runs were terminated by quenching the capsule-bearing silica tube in a beaker of deionized water. Quench crystallization products were not observed in any 1 atmosphere experiments.

High pressure experiments were carried out in a solid media 1/2 inch piston cylinder apparatus using the "piston in" technique. Talc sleeves were used in all runs with pyrex inserts adjacent to the graphite furnace. Temperature was measured using the Digical II controller with $Pt/Pt_{90}Rh_{10}$ thermocouple, and was controlled to $\pm 5^{o}C$ of the set point. Accuracy in the pressure determination is considered to be ± 0.5 kbar, which includes a -10% pressure correction.

Sample containers were predominantly spec-pure Fe, although several runs were made using Pt or C capsules. Design of the capsule assemblage allowed 10-15 mg of mix to be used. Platinum capsules were sealed under argon using a graphite arc welder, while the graphite and iron capsules were covered by snug-fitting lids. Runs were quenched at pressure by terminating the power to the graphite furnace. Very minor quench crystallization was observed in some runs (see Fig. 1.7D).

A fraction of each charge was examined optically using RI oils. The phases olivine, low-Ca pyroxene and plagioclase could easily be identified on the basis of crystal habit and relief. The presence of clinopyroxene was best determined by electron microprobe analysis using a JEOL JX-50A electron microprobe-scanning electron microscope fitted with an energy dispersive analytical system. Back scattered and secondary electron imagery provided adequate phase discrimination up to 2000x magnification. Run conditions were always 15 kV and 0.7 nA standardized on pure Cu with 60 second counting times. A beam diameter of ~0.5 μm was used, resulting in an analysed volume of ~4 μm^3. Data processing followed the methods of Reed & Ware (1973, 1975) and Griffin (1979).

1.2.2 THE IRON EXCHANGE PROBLEM

Background

The problems associated with the interaction between the capsule composition and the experimental mix have been summarized in Basaltic Volcanism on the Terrestrial Planets (1981, pp.517-519). Despite a variety of capsule compositions and techniques, it seems inevitable that low pressure (<10 kbar) studies of basalts will be hampered by the loss of iron to noble metal capsules, or the addition of iron from pure iron capsules. Above 10 kbar, graphite capsules, used in short duration runs, can eliminate iron exchange problems. However, at pressures less than ~10 kbar the high solidus temperatures of anhydrous basaltic compositions essentially restrict capsule compositions to iron or platinum as opposed to gold or silver-palladium alloys. With either iron or platinum capsules, the effects of iron exchange on the position of the determined phase boundaries must be evaluated before the results of the experimental program can be properly interpreted.

Several studies have sought to document the scope of iron exchange between the experimental mix and the enclosing container (Merril & Wyllie, 1973; Nehru & Wyllie, 1975; Stern & Wyllie, 1975; O'Hara & Humphries, 1977; Jaques & Green, 1979). These authors have shown that the rate of iron exchange between the container and charge (particularly iron loss to noble metals) increases with increasing temperature, and run duration. In addition to these variables, the volume ratio between the sample and container also plays a major role in determining the extent of iron exchange.

These studies have also shown that phases crystallizing from the charge will adjust to the changing liquid compositions at unequal rates. Jaques & Green (1979) using iron doped Pt-capsules, found orthopyroxene remained unaffected by iron loss during run times of up to 2 hours (10 kbar, 1300^{o}C). The co-existing olivine experienced detectable iron exchange after the first hour, while the liquid began losing iron from the onset of the experiment.

There appears to be no complementary study detailing the effects of iron addition on individual phases. However, since volume diffusion depends, in part, on the type of crystal lattice and not on the direction of element exchange, one can confidently assume that the liquid, olivine, and orthopyroxene will respond to iron addition at the same relative rates as those determined under conditions of iron loss.

In addition to altering the Mg#'s of the precipitating phases, the exchange of iron will also influence the position of the phase boundaries. Iron gain has the effect of reducing the degree of silica saturation in the charge, and expanding the stability field of olivine to higher pressure at the expense of orthopyroxene, as well as depressing the liquidus temperature of the composition (O'Hara & Humphries, 1977).

Evaluation of the effects of iron exchange on the experimental results from samples 060 and 206

Near-liquidus phase diagrams constructed from the experimental studies of two mafic dykes from the Vestfold Hills are illustrated in Figs 1.6 and 1.13. Run details are reported in Table 1.8. The phase proportions and extent of iron exchange in each run was determined by using a least-squares mixing program which follows the method of Reid et al. (1973); the results are listed in Table 1.8. The calculated direction of iron exchange is entirely consistent with the predicted results: iron gain occurred in Fe-capsule runs and iron loss in Pt-capsules. In addition, short duration runs in C-capsules (max. 1.5 hours) resulted in no calculated iron exchange while during longer runs (5 hours) the calculations indicate FeO was reduced to Fe metal, and therefore iron loss.

The effect of temperature and run duration on the diffusion of iron is evident in these experiments when the 1 atmosphere runs of the two experimental systems are compared. The Mg-rich composition, 060, has a 1 atmosphere liquidus temperature 120^{o}C higher than that of 206, and experienced twice the amount of iron addition than did 206 despite half the run time. Run AT181 experienced the most iron gain (7%)* of the 1 atmosphere runs on 206 despite being the lowest temperature experiment (1100^{o}C). However, in this case the long run time (40 hours) evidently became the critical factor in controlling the iron gain as only 3% iron addition occurred after 24 hours at 1124^{o}C (AT178). Because of its higher liquidus temperature, sample 060 is prone to more extensive iron exchange and subsequent phase boundary modifications than is 206. Thus, in order to determine the extent to which iron addition affected the positions of the phase boundaries, three experiments in Pt-capsules were conducted on sample 060.

---

* 7% iron addition =

$$[(FeO_{final} - FeO_{starting}) / (FeO_{starting})] \times 100$$

TABLE 1.8
EXPERIMENTAL CONDITIONS AND RESULTS

RUN	PRESSURE (kbar)	TEMPERATURE (°C)	CAPSULE	DURATION (HR.)	Fe EXCHANGE (**)	RESULTS
SAMPLE 65060						
AT-169	0	1300	Fe	1.67	+ 7	Liq
AT-173	0	1280	Fe	1	+11	<1% OL
AT-171	0	1250	Fe	1	+ 4	3% OL
AT-170	0	1200	Fe	2.33	+ 5	10% OL
AT-183	0	1180	Fe	4	+ 5	12% OL
AT-175	0	1150	Fe	4	+ 0	5% OL, 9% PIG, 20% CPX*, 1% PLAG, 3% SP
AT-176	0	1100	Fe	22	+ 5	10% OL, 6% PIG, 35% CPX, 27% PLAG, 3% SP
T-1593	5	1300	Fe	1	+ 4	Liq
T-1594	5	1280	Fe	1	+15	Liq
T-1643	5	1280	Pt	1	- 8	<1% OL
T-1595	5	1250	Fe	1	+ 7	2% OL
T-1720	5	1220	Fe	1	0	8% OL, <1% PIG
T-1649	7.5	1300	Pt	1	-10	LIQ
T-1650	7.5	1280	Pt	1	- 7	<1% PIG
T-1600	7.5	1270	Fe	1	+14	1% OPX, 1% OL
T-1598	10	1290	Fe	1	+11	6% PIG
T-1596	10	1270	Fe	1	+11	13% PIG
T-1602	12	1340	C	0.75	0	LIQ
T-1601	12	1310	C	1	0	5% PIG
T-1604	12	1270	C	1.5	0	16% PIG
SAMPLE 65206						
AT-180	0	1174	Fe	7	+ 4	LIQ
AT-182	0	1162	Fe	9.5	+ 5	<1% Ol
AT-179	0	1149	Fe	20	+ 3	3% OL, 4% PLAG
AT-178	0	1124	Fe	24	+ 3	8% OL, 14% PLAG
AT-181	0	1100	Fe	40	+ 7	11% OL, 22% PLAG, 7%CPX
T-1734	2.5	1090	Fe	9	+ 3	8% OL, 3% CPX, 14% PLAG
T-1730	4	1130	Fe	8	+ 1	6% OL, 2% CPX, 12% PLAG
T-1845	4	1110	Fe	12	***	OL, OPX, CPX, PLAG, SP
T-1665	5	1180	Fe	1	+12	LIQ
T-1693	5	1170	Fe	1	+ 7	<1% OL
T-1668	5	1160	Fe	1	+ 2	1% OL
T-1669	5	1140	Fe	2	***	OL, OPX, CPX, PLAG
T-1699	7.5	1180	Fe	1	+ 9	<1% OL
T-1694	7.5	1170	Fe	1	+ 2#	1% OL, 2% OPX, 4% CPX, 4% PLAG, 1% SP
T-1664	10	1220	Fe	1	+10	LIQ
T-1662	10	1200	Fe	2	+ 8#	1% OPX, 3% CPX
T-1689	10	1200	C	5	- 2#	<1% OPX, 1% CPX
T-1660	10	1180	Fe	2	+ 7#	15% PLAG, 7% OPX, 12% CPX
T-1690	10	1180	C	5	- 7#	2% OPX, 3% CPX 3% PLAG

* CPX refers to calcic clinopyroxene
** % of initial FeO
*** phase proportions and Fe exchange could not be calculated, due to crystallization of metastable pigeonite, see text
\# run contains metastable pigeonite, phase proportions based on opx and cpx compositions estimated from Lindsley (1983)

The 1 atmosphere liquidus of sample 060 was determined at 1280°C from a run which experienced iron addition of 11% of the original FeO concentration and resulted in the crystallization of <1% olivine. At 5 kbar, 1280°C, the charge experienced 15% iron gain which had the effect of suppressing the liquidus, and if not taken into consideration would indicate an unrealistic negative liquidus slope. Reproducing the 5 kbar, 1280°C run in a Pt-capsule resulted in 7% iron loss and the crystallization of <1% olivine.

Experiments in Fe-capsules resulted in olivine and orthopyroxene as liquidus phases at 7.5 kbar, 1270°C. A Pt-capsule experiment at these conditions crystallized only orthopyroxene (<1%) with the loss of 7% iron, consistent with the anticipated contraction of the olivine field with iron loss. The phase geometry determined by including a hyperliquidus Pt-capsule run at 7.5 kbar, 1300°C indicates the olivine + orthopyroxene two-phase point shifted from 7.5 kbar, 1275°C in Fe-capsules to 7 kbar, 1285°C in Pt-capsules, an adjustment which is within the experimental error of the pressure-temperature determinations.

The calculated composition of the bulk charge resulting from the 7.5 kbar experiments in Fe and Pt capsules are compared with the starting composition in Table 1.9. A difference of 5.5 Mg-units and 3.1% normative olivine was produced between T1600 (Fe-capsule) and T1650 (Pt-capsules) due to Fe-exchange. Although these would seem to be marked deviations from the starting compositions, the differences in the interpreted phase boundaries of these two compositions are small as indicated above. The resulting variation in the compositions are displayed graphically in Fig. 1.5, where the compositions of T1600, T1650 and sample 060 are projected into the basalt tetrahedron following Green (1970). The projected positions of the resulting Fe-exchanged compositions are nearly identical to the starting composition and is consistent with the minimal modification of the phase boundaries deduced from the P-T diagram.

It is clear from the observations discussed above that the techniques used in the study of 060 resulted in an amount of Fe-exchange which had a trivial effect on the positions of the experimentally determined phase boundaries. It follows then that the iron gain which occurred during the lower temperature experiments on sample 206 will also play a negligible role in controlling the phase geometry. As such, monitoring the positions of the phase boundaries by using Pt-capsules in conjunction with Fe-capsules was not considered necessary during the experimental study of 206.

TABLE 1.9
COMPARISON OF CHARGE COMPOSITIONS FROM FE AND PT CAPSULE RUNS AT 7.5 KBAR

RUN CAPSULE	T1650 PT	T1600 FE	SAMPLE 65060
SIO2	53.09	52.07	52.63
TIO2	0.57	0.57	0.62
Al2O3	12.04	11.76	11.97
FEO	10.01	12.15	10.88
MNO	-	-	0.18
MGO	11.75	11.21	11.29
CAO	10.27	10.07	10.03
NA2O	1.72	1.63	1.80
K2O	0.56	0.53	0.60
MG#	67.7	62.2	64.9
WT % CIPW NORM:			
QTZ	-	-	-
OR	3.31	3.13	3.55
AB	14.55	13.79	15.23
AN	23.48	23.21	22.81
DI	22.35	21.94	22.03
HYP	33.68	32.21	31.36
OLIV	1.55	4.62	3.85
IL	1.08	1.08	1.18
JD+CATS*	23.5	23.1	23.9
QTZ	49.2	47.6	48.0
OLIV	27.3	29.3	28.1

* PROJECTION COORDINATES (MOLE %) FOLLOWING GREEN (1970).

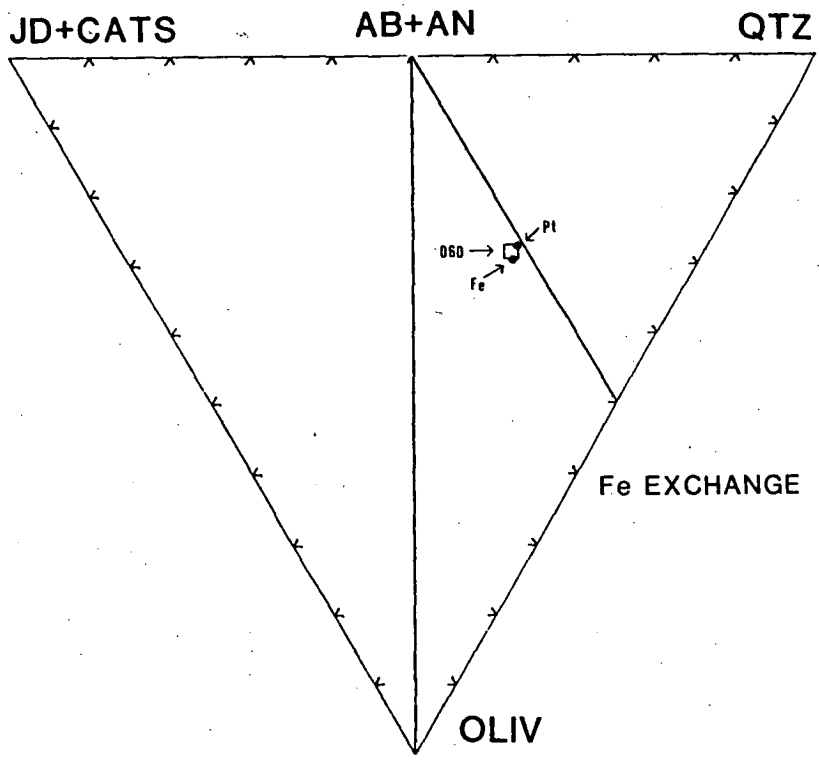

Figure 1.5
Comparison of the compositional change of the bulk experimental charge due to Fe exchange with Fe or Pt capsules compared to the starting composition (sample 060). Composition projected from Di following Green (1970). Fe = run T1600, 7.5 kbar, 1270°C; Pt = run T1694, 7.5 kbar, 1300°C.

1.3 EXPERIMENTAL RESULTS

1.3.1 RESULTS OF THE EXPERIMENTAL STUDY OF SAMPLE 060 AND COMPARISON WITH THE NATURAL PHASE ASSEMBLAGE

The experimentally determined phase relations of sample 060 are shown in Fig. 1.6. Separate fields delimiting the stability range of pigeonite vs orthopyroxene are not indicated, but are grouped together and labelled Lpx (low calcium pyroxene). Olivine is the sole crystallizing phase at 1 atmosphere from the 1280°C liquidus to 1180°C. Between 1180° and 1150°C pigeonite, clinopyroxene, plagioclase and Fe-Mg spinel join olivine as precipitating phases and dramatically increase the percentage of crystals from 12% at 1180°, 39% at 1150°, and 82% at 1100°C (Table 1.8).

Orthopyroxene co-precipitates with olivine on the liquidus at 7.5 kbar, 1270°C, while at higher pressures pigeonite is the liquidus phase. A pigeonite + olivine phase field exists at 5 kbar, approximately 40° below the liquidus. SEM photographs of selected run products are shown in Fig. 1.7.

In the section which follows, the results of the experimental studies will be discussed, and the phase chemistry compared to the natural phenocryst assemblage and composition in order to estimate the load pressure at the time of dyke emplacement.

Sample 060: pyroxene - 1 atmosphere

Calcic clinopyroxene and pigeonite precipitated in two 1 atmosphere experiments, both over 100° below the liquidus of 060. The compositions of these phases are plotted on the pyroxene quadrilateral in Fig. 1.8, averaged analyses are listed in Table 1.10. The calcic clinopyroxene analyses show considerable scatter among the quadrilateral components and suggest that despite (or due to) its extremely rapid growth rate (Kirkpatrick, 1981) it is slow to attain equilibrium, even after 22 hours. Some of the compositional scatter could be the result of iron exchange with the container, but this would not account for the variation in CaO. In addition, no iron exchange was calculated to have occurred in AT175 (Table 1.8).

Fig. 1.19 illustrates plots of TiO_2 and Al_2O_3 vs Wo for the coexisting pyroxene of AT175 and AT176. Although pigeonite shows negligible compositional variation in terms of the quadrilateral components, scatter is observed in both TiO_2 and Al_2O_3. The range over which the TiO_2 and Al_2O_3 vary in the pigeonite of AT176 is nearly identical

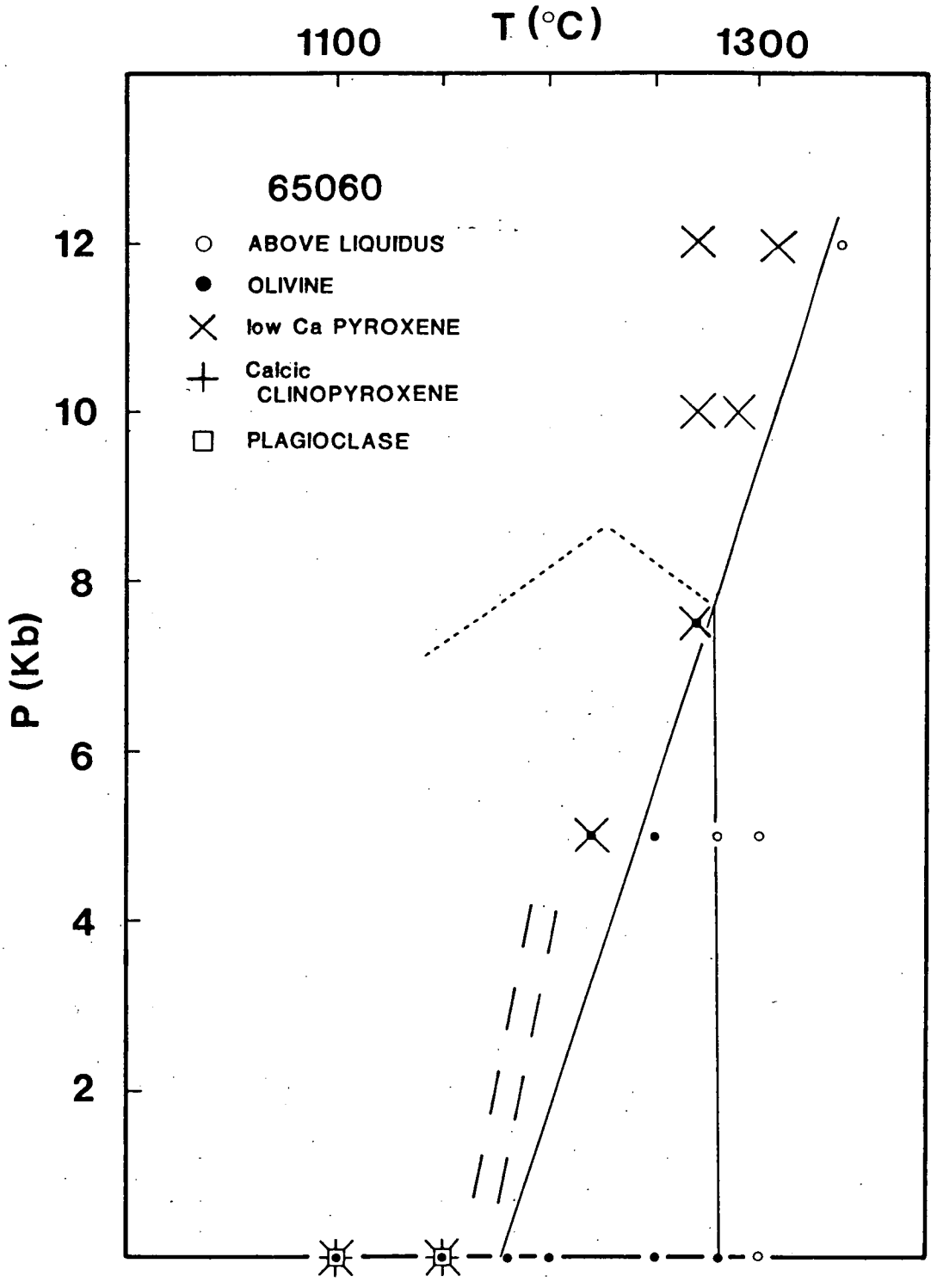

Figure 1.6
Experimentally determined near-liquidus phase relations of sample 65060. Low-Ca pyroxene includes pigeonite and orthopyroxene (see text).

Figure 1.7A
Experiment AT175 (Table 1.8). Large equi-dimensional olivine crystals (bright grey) with blocky Ca-clinopyroxene (medium grey, upper left of centre) pigeonite laths (lower left of centre) and plagioclase (dark, right margin) in glass. Bright white material is surficial contamination. Bar scale at bottom, 2.02×10^3 magnification.

Figure 1.7B
Experiment T1720. Long laths of pigeonite with larger equidimensional olivines (top).

Figure 1.7C
Experiment T1600. Large orthopyroxene crystals with slightly smaller olivine (bright grey). Bright white circles left of centre probably Fe-metal from capsule wall, other bright white material is contamination.

Figure 1.7D
Experiment T1601. Large crystals of pigeonite with well developed calcic clinopyroxene quench evident as projections from the crystal corners into the surrounding liquid.


A
10µm25.0kV 2.02E3 0002/00 AT175

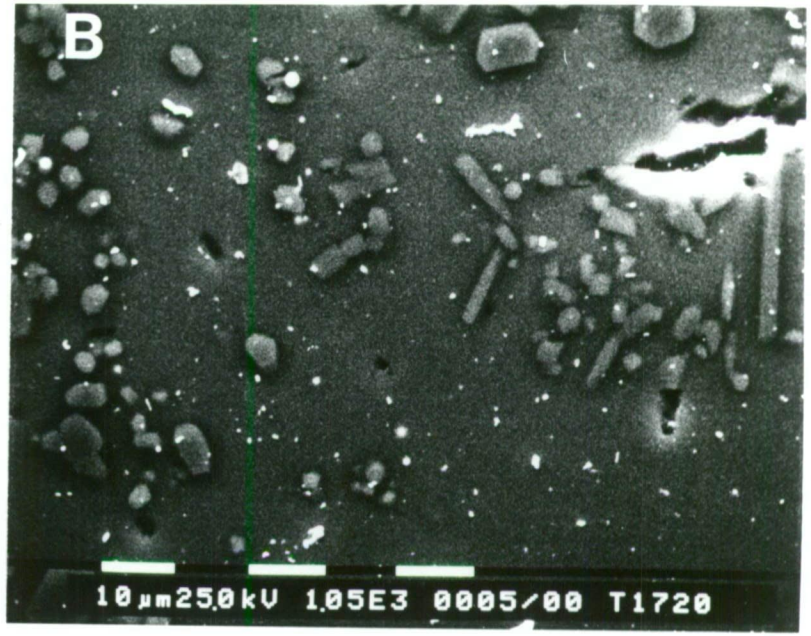
B
10µm25.0kV 1.05E3 0005/00 T1720

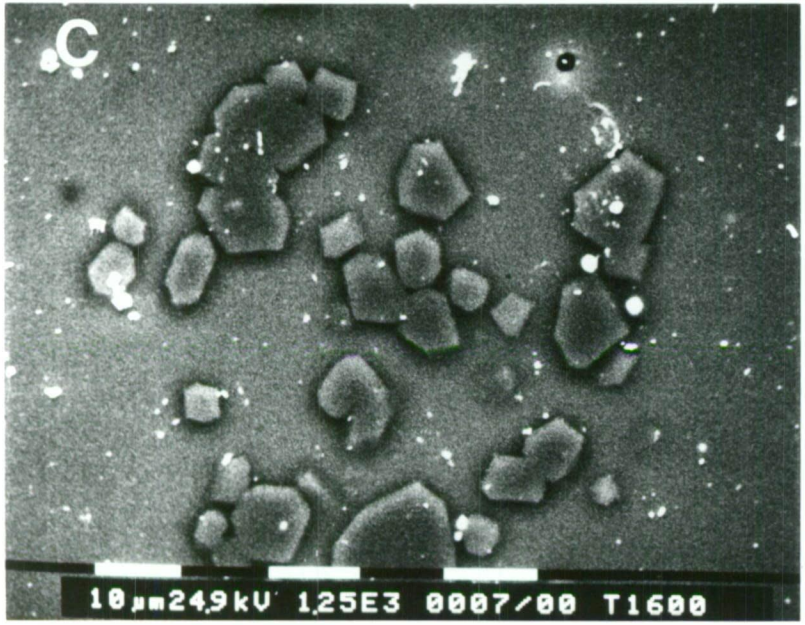
C
10µm24.9kV 1.25E3 0007/00 T1600

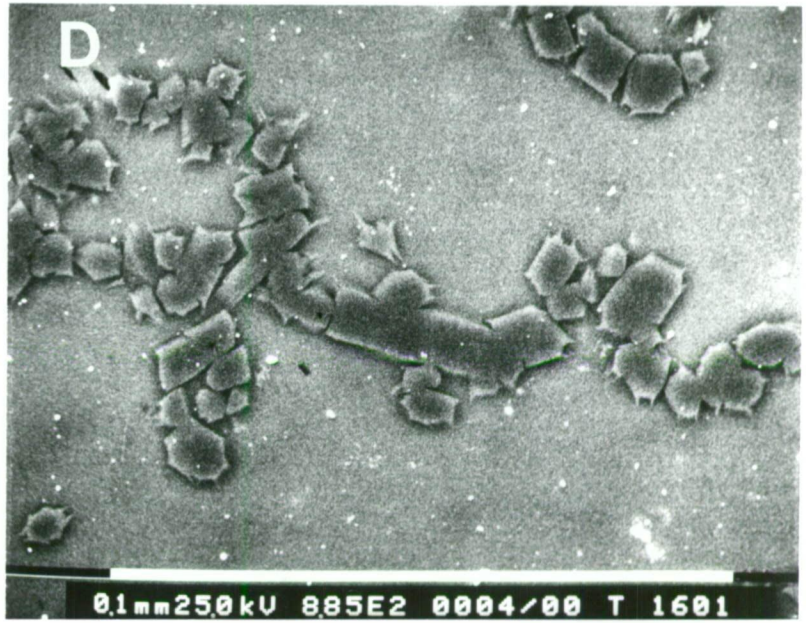
D
0.1mm25.0kV 8.85E2 0004/00 T 1601

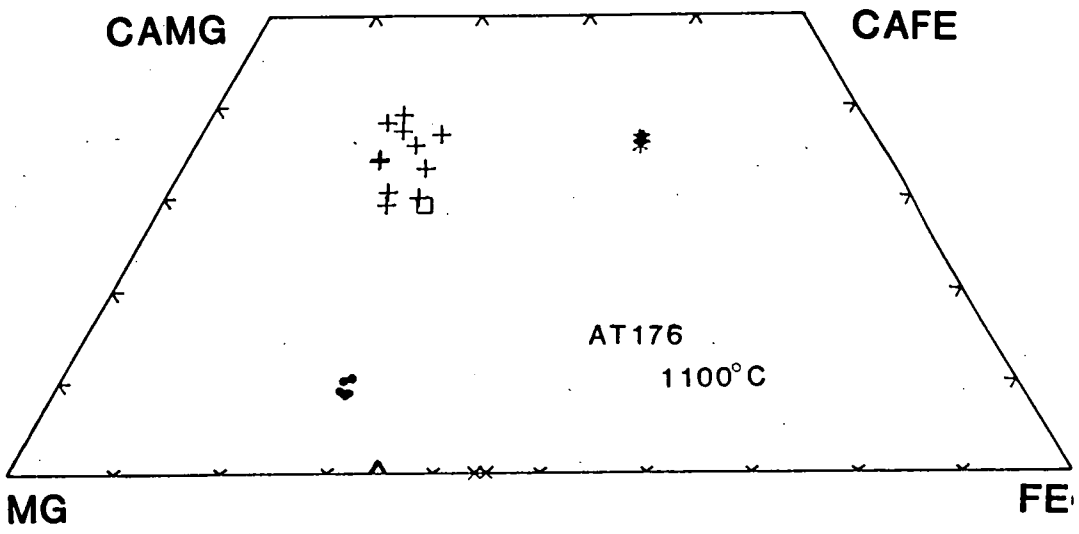

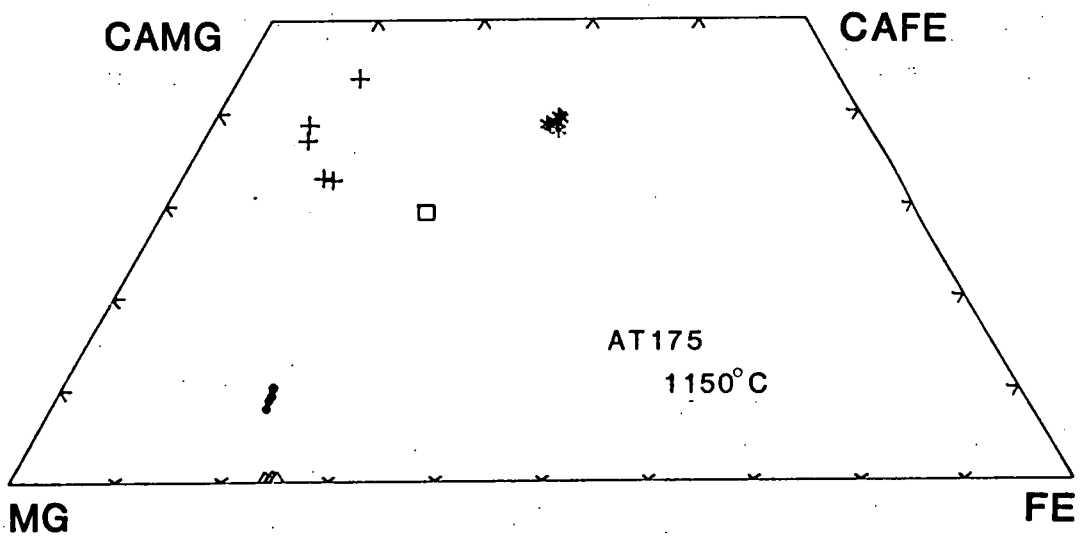

Figure 1.8
Phase compositions of pyroxene-bearing 1 atmosphere experiments. Square symbol - starting composition; cross - calcic clinopyroxene; dot - pigeonite; triangle - olivine; X - spinel; asterisk - liquid. (Mole %)

TABLE 1.10
AVERAGE EXPERIMENTAL PYROXENE COMPOSTIONS : SAMPLE 65060

RUN NO.	AT-176	AT-176	AT-175	AT-175	T-1720	T-1600	T-1596	T-1598	T-1604	T-1601
PRESS.(kbar)	0	0	0	0	5	7.5	10	10	12	12
TEMP.(°C)	1100	1100	1150	1150	1220	1270	1270	1290	1270	1310
PHASE	PIG	CPX	PIG	CPX	PIG	OPX	PIG	PIG	PIG	PIG
SIO2	53.37	52.44	54.80	53.64	55.87	56.03	54.98	55.66	55.02	55.14
TIO2	0.58	0.52		0.40						
AL2O3	0.97	1.12	0.77	1.09	0.58	0.92	1.39	1.39	1.84	1.80
CR2O3			0.12	0.26	0.21	0.13	0.17	0.12	0.15	0.22
FEO	17.40	12.77	13.29	7.45	10.14	9.98	10.94	10.40	9.78	9.56
MNO										
MGO	22.84	16.11	26.36	18.58	29.40	30.18	27.00	28.66	26.90	28.71
CAO	4.70	16.96	4.68	18.56	3.81	2.78	5.52	3.73	6.31	4.58
SI	1.9650	1.9603	1.9744	1.9630	1.9788	1.9757	1.9644	1.9722	1.9590	1.9527
TI	0.0161	0.0146		0.0110						
AL	0.0421	0.0493	0.0327	0.0470	0.0242	0.0382	0.0585	0.0581	0.0772	0.0751
CR			0.0034	0.0075	0.0059	0.0036	0.0048	0.0034	0.0042	0.0062
FE	0.5358	0.3992	0.4005	0.2280	0.3004	0.2943	0.3269	0.3082	0.2912	0.2831
MN										
MG	1.2536	0.8977	1.4158	1.0136	1.5523	1.5864	1.4380	1.5138	1.4278	1.5156
CA	0.1854	0.6793	0.1807	0.7286	0.1446	0.1050	0.2113	0.1416	0.2407	0.1738
TOT	3.9979	4.0005	4.0041	3.9987	4.0061	4.0033	4.0040	3.9971	4.0002	4.0065
MG#	70.1	69.2	78.0	81.6	83.8	84.4	81.5	83.1	83.1	84.3
range	70.6-69.6	72.7-65.9	78.0-77.9	85.2-79.7	82.9-82.4	85.0-83.9	81.7-81.5	84.7-82.5	83.7-82.6	84.8-83.2
CA*	9.4	34.4	9.1	37.0	7.2	5.3	10.5	7.2	12.3	8.8

100MG/(MG+FE)
* 100CA/(CA+MG+FE)

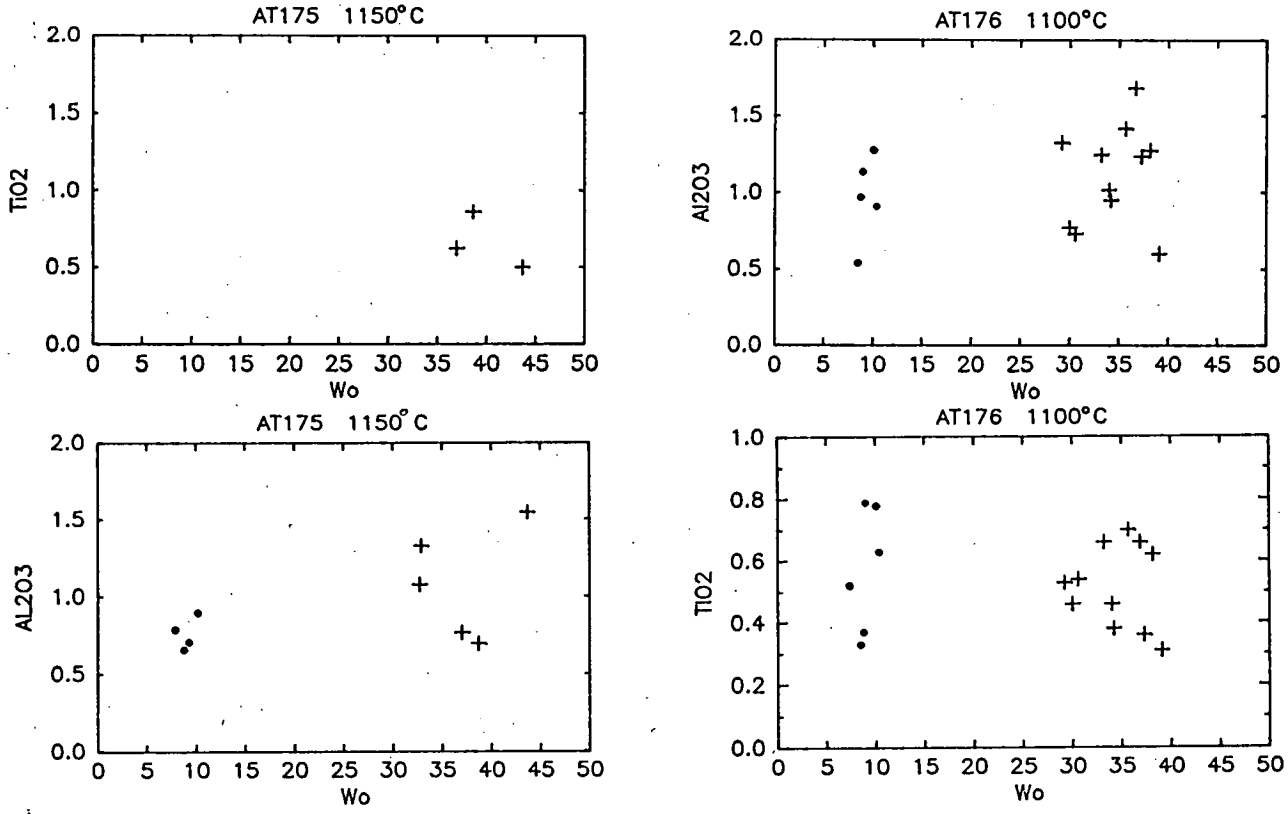

Figure 1.9
Variations in TiO_2 and Al_2O_3 versus Wo content (Ca/(Ca+Mg+Fe)) of pyroxenes from 1 atmosphere experiments.

to that of the coexisting calcic clinopyroxene despite the much more heterogeneous nature of the calcic clinopyroxene analyses in terms of the quadrilateral components. Note that TiO_2 is absent from the pigeonite of AT175 (0.82% TiO_2 in the liquid) but ranges up to 0.8% in AT176 (1.5% TiO_2 in the liquid). TiO_2 is present in the calcic clinopyroxenes of both experiments. It should also be noted that there is no tendency for the calcic clinopyroxene and pigeonite analyses to form a continuous spread of compositions across the solvus, a problem which will be discussed with regards to the experimental results from sample 206.

In spite of the compositional scatter in the calcic clinopyroxene analyses, temperatures obtained by applying the Lindsley (1983) graphical thermometer to the averaged pyroxene analyses of AT175 and AT176 are within error of the actual run conditions (Fig. 1.10). Lindsley & Anderson (1983) indicated the equilibrium three-phase fields at 1100° and 1200°C may be shifted a few mole percent towards the Fs-Hd join due to the effect of non-quadrilateral components enhancing the stability of natural pyroxenes as compared to the CMFS system used in the calibration of these temperatures. However, the coexisting pyroxenes from AT176 would suggest the 1100°C three-phase triangle would better fit the experimental data if it was rotated clockwise about the augite-pigeonite consolute line by ~2 mole percent. As published, the pigeonite analyses from AT176 plot within the 1100°C three-phase field, while the average clinopyroxene analyses falls on the iron-rich side of the augite-pigeonite join. Rotation of the triangle would have the effect of moving these compositions onto the augite-pigeonite tie line. The resulting $K_D^{Fe/Mg}$ of the rotated triangle would remain intermediate to the 1000° and 1200°C values.

Both the average pigeonite and calcic clinopyroxene analyses from AT175 (1150°C) fall on the Mg-rich side of an interpolated 1150° three-phase triangle (Fig. 1.10). Except for the low Wo content of the pigeonite, repositioning the 1200°C three-phase triangle to a position 4 mole % nearer to the En-Di join would result in the analyses of both phases plotting on the pigeonite-augite solidus curve.

Pyroxene - High pressure

Low Ca pyroxene in crushed mounts of high pressure experimental charges was easily identified by its tendency to form elongate euhedral prisms (Fig. 1.7). However distinguishing optically the types of low Ca pyroxene, pigeonite or orthopyroxene, was hindered by the crystallization of quench calcic clinopyroxene. The quench pyroxene occurs as a thin envelope wrapping each pyroxene lath and having cone-like terminations

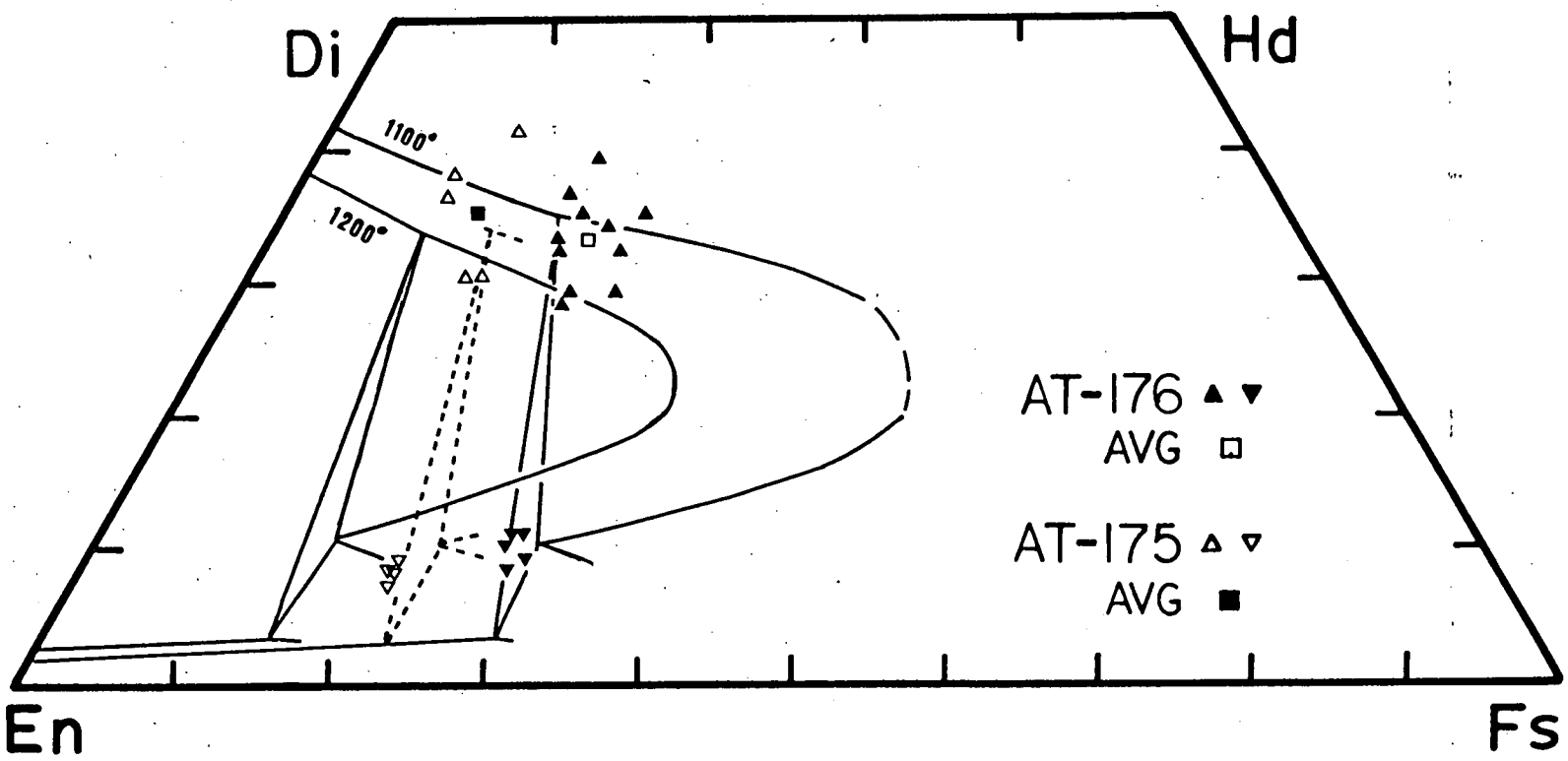

Figure 1.10
Analyses of coexisting pigeonite and calcic clinopyroxene from 1 atmosphere experiments projected onto the Lindsley graphical thermometer. Dashed three-phase 1150°C triangle interpolated. See text for discussion.

extending from the crystal corners into the liquid (Fig. 1.7D). The higher birefringence of the quench pyroxene masks the low birefringence of orthopyroxene crystals such that the extinction position of the grain is dominated by the quench calcic clinopyroxene. This was a feature of all pyroxene-bearing runs above 1 atmosphere, and was expecially well developed in the 10 and 12 kbar runs where the low Ca-pyroxene was the only crystallizing phase. Microprobe analyses indicate that only at 7.5 kbar is the low Ca pyroxene an orthopyroxene, with pigeonite occurring at higher and lower pressures. In retrospect, a few pyroxene laths can be found in T1600 (7.5 kbar, 1270°C) which have a darkened central region with bright narrow rims when the crystals are oriented parallel to a polarizing direction. Upon rotation of the microscope stage a dark narrow band paralleling the length of the crystal traverses the grain suggestive of alternating extinctions in a simply twinned crystal. However, the twinning is only apparent, and the result of lengths of the quench pyroxene rim moving through an extinction position over the width of the orthopyroxene crystal.

As with the 1 atmosphere pigeonites, the high pressure low Ca-pyroxenes plot within a restricted compositional range in terms of quadrilateral components (Fig. 1.11A). With the exception of run T1600, the low Ca-pyroxenes are pigeonites, and plot within the pyroxene quadrilateral at compositions slightly more magnesian than the "magnesian pigeonite" field of Poltervaart & Hess (1951). Pyroxenes from T1600 plot directly on the orthopyroxene-pigeonite chemically defined boundary of Poltervaart & Hess (1951), and cannot be discriminated as an orthopyroxene or pigeonite on this basis alone.

Cr_2O_3 and Al_2O_3 are the only non-quadrilateral components found in the high pressure pyroxenes (Table 1.10). The average Cr_2O_3 in the orthopyroxene phenocrysts of sample 060 (0.38%) is twice the averaged value of the experimental pyroxenes. One possible explanation for the difference may be that the low experimental values are due to slight errors in weighing the small amount of required Cr_2O_3 during preparation of the starting mix. Chromium was not detected during microprobe analyses of the starting composition. It is important to note that the available Cr readily enters the experimental pyroxenes, which crystallized under fO_2 conditions buffered by the run assemblage near iron-wustite. Cr_2O_3 can exceed 1% in some orthopyroxene phenocrysts found in samples belonging to the high-Mg tholeiite suite, and coupled with the extreme rarity of chromites, may indicate that low fO_2 conditions prevailed during the crystallization of the natural pyroxenes. Note that the spinels found in

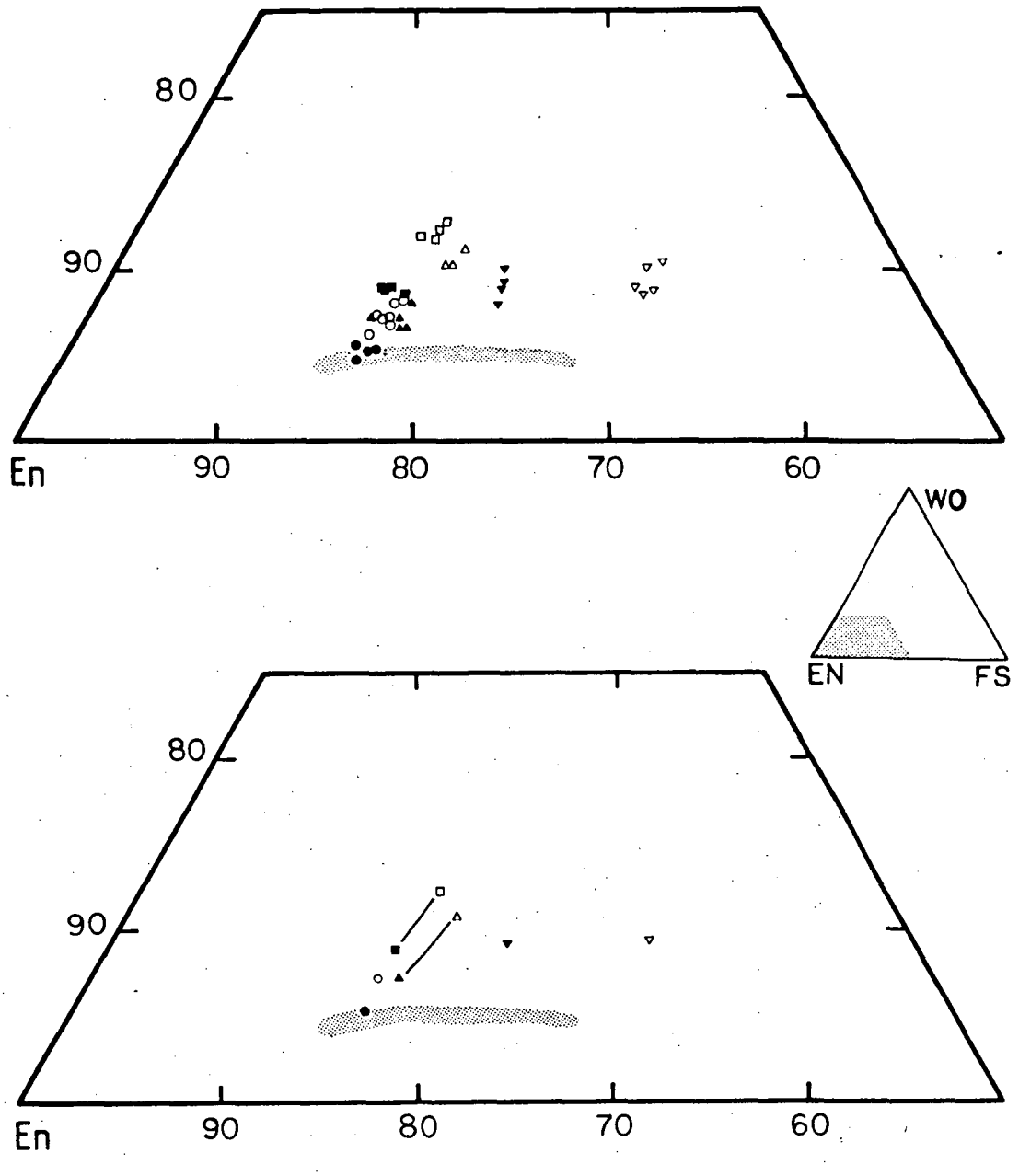

Figure 1.11

A. Low-Ca pyroxene analyses plotted onto a portion of the pyroxene quadrilateral (see inset). Shaded field covers range of natural orthopyroxene phenocryst compositions.

B. Averaged pyroxene compositions. Tie lines connect compositions from constant pressure experiments.

Figure 1.12A

Al_2O_3 contents of high pressure pyroxenes plotted against Wo (Ca/(Ca+Mg+Fe)). Key as in Fig. 1.12B. Note decrease in Wo with decrease in temperature at constant pressure.

Figure 1.12B

Averaged Al_2O_3 contents of pyroxenes from individual experiments plotted against pressure. Note differences in experimental temperature has had no effect on the Al_2O_3 content of pyroxene at a constant 10 or 12 kbar pressure. Exclusion of the high Al_2O_3 analysis from the 5 kbar experiment (Fig. 1.12A) results in a correlation coefficient (R) of 0.99.

Figure 1.12C

As in B (above) but with range of pyroxene analyses for each experiment shown. Dashed lines are Al_2O_3 contents of natural orthopyroxene phenocrysts, nine analyses (several overlap) fall between 1.0 and 1.4% Al_2O_3.

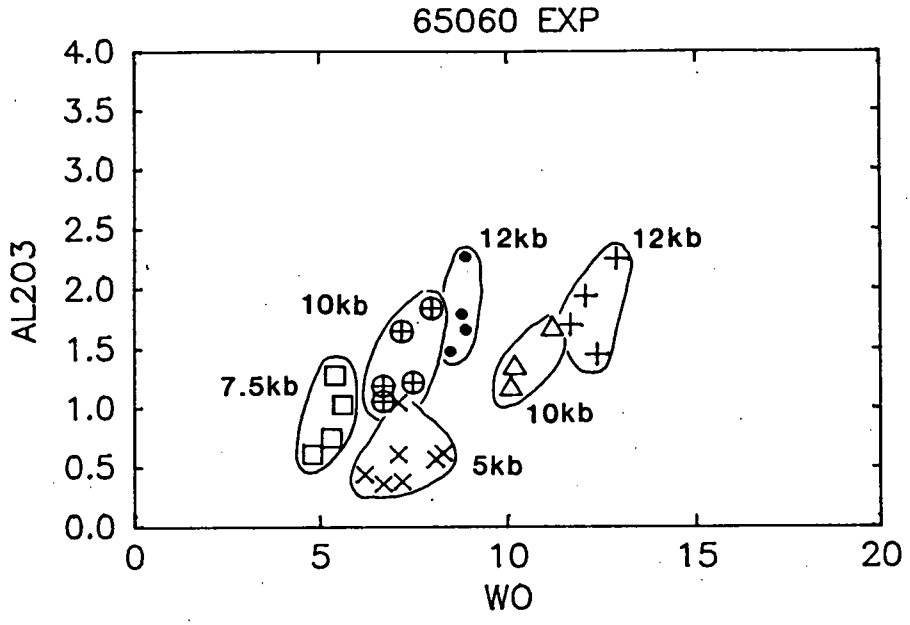
65060 EXP
AL203
WO
12kb
12kb
10kb
7.5kb
10kb
5kb

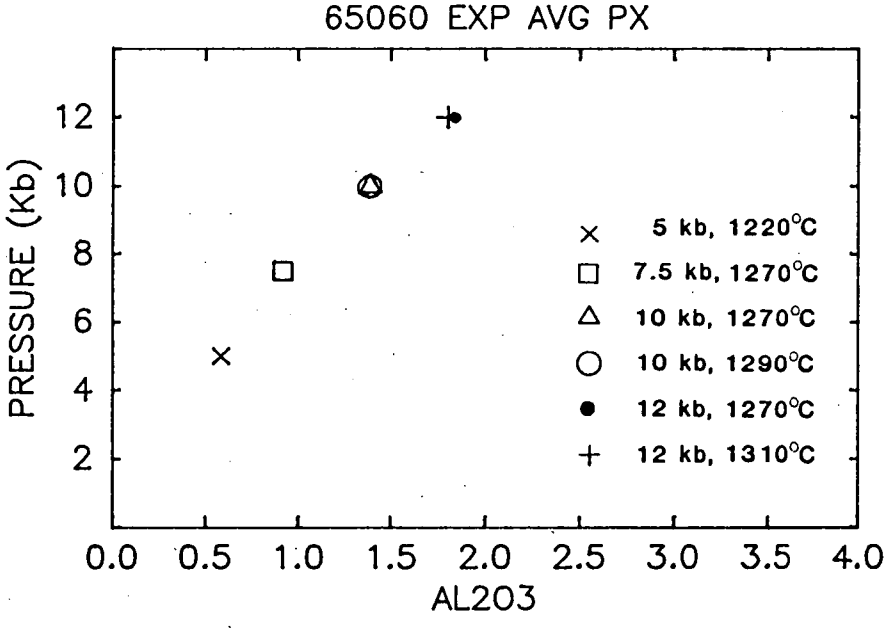
65060 EXP AVG PX
PRESSURE (Kb)
AL203
5 kb, 1220°C
7.5 kb, 1270°C
10 kb, 1270°C
10 kb, 1290°C
12 kb, 1270°C
12 kb, 1310°C

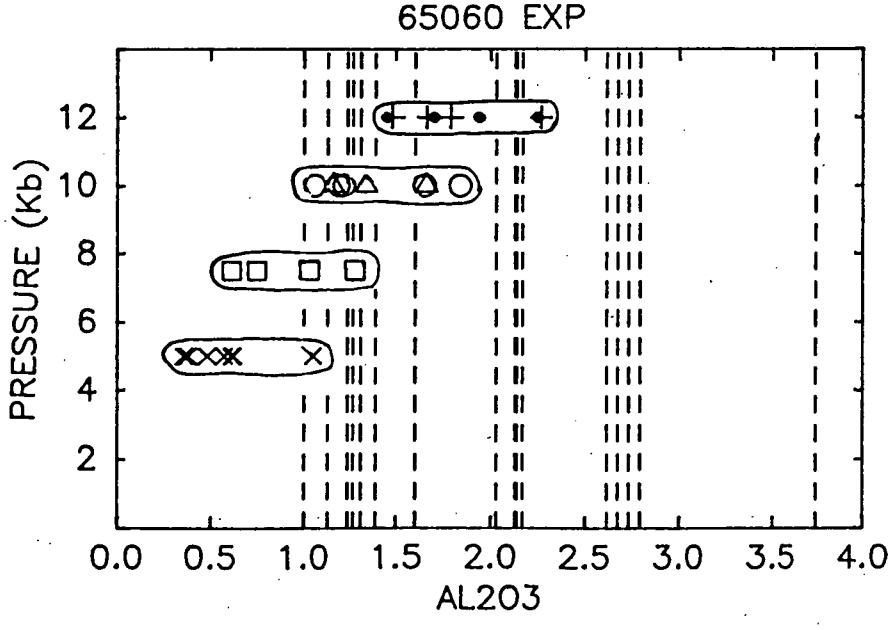
65060 EXP
PRESSURE (Kb)
AL203

the 1 atmosphere experiments are spinel-hercynite solid solutions, not chromites.

The Al_2O_3 contents of the averaged high-pressure pyroxenes from individual experiments range from 0.38% (5 kbar, 1220°C) to 2.27% (12 kbar, 1310°C). Within a single experiment, regardless of run conditions, the Al_2O_3 contents scatter over a range of not more than 0.8% (Fig. 1.12A). The averaged Al_2O_3 is strongly dependent on the pressure of the experiment ($R = 0.995$) and independent of temperature ($R = 0$; Fig. 1.12B). Ideally, applying this relationship to the Al_2O_3 contents of the natural orthopyroxene phenocrysts could provide evidence constraining the possible pressures at which the phenocrysts precipitated. In Fig. 1.12C, the Al_2O_3 contents of the experimental low Ca-pyroxenes are plotted versus pressure, along with the Al_2O_3 from analyses of the natural phenocrysts. The Al_2O_3 contents of the phenocrysts vary from 1.0-3.75%, overlapping the range in Al_2O_3 of the experimental pyroxenes at all studied pressures.

The scatter to higher Al_2O_3, and perhaps Cr_2O_3 in the natural orthopyroxene phenocrysts, compared to the values from the equilibrium experiments can be explained in terms of a difference in cooling history during the crystallization of the two systems. The limited chemical variation within the synthetic pyroxenes represent the extent to which equilibrium was attained under the constant physical conditions of the experiment. In the natural system, temperature is not a constant, and the rate at which a system cools has been shown by Grove & Bence (1977) to be a critical factor in controlling minor element concentrations in pyroxenes. These authors conducted controlled cooling rate experiments (1 atmosphere) and found the partitioning of major elements between low-Ca pyroxenes and liquid is independent of cooling rate. However Al_2O_3, Cr_2O_3 and TiO_2 were found to increase in concentration with increased rates of cooling compared to values obtained from equilibrium experiments.

Assuming that the cooling rate of the natural system was the only factor responsible for producing the variance from chemical equilibrium, the lowest Al_2O_3 contents of the orthopyroxene phenocrysts should more closely represent equilibrium values. Of the twenty phenocryst analyses, nine fall between 1.0-1.4 % Al_2O_3. Excluding the one anomalously high experimental Al_2O_3 datum at 5 kbar, the suggested equilibrium Al_2O_3 values restrict crystallization of the phenocrysts in sample 060 to pressures in the order of 7.5-10 kbar.

As the liquid compositions studied at high pressure are saturated in only a single pyroxene, the Ca-Mg-Fe proportions of the precipitating pyroxene is not constrained to follow a temperature-composition surface as

do co-existing pyroxenes. The effect of pressure and temperature on the pyroxene chemistry can be evaluated for the composition studied by considering the 10 and 12 kbar experiments. At each of these pressure, two experiments at separate temperatures were conducted, the resulting averaged pyroxene compositions are connected by tie lines in Fig. 1.11B. Decreasing temperature at a constant 10 or 12 kbar increases the Ca and Fe/Mg of the pyroxene, while decreasing pressure at a constant temperature (1270^{o}C) lowers both the Ca content and the Fe/Mg of the precipitating pigeonite. Reduction in the amount of Ca-solid solution in the liquidus pigeonite will continue with decreasing pressure until orthopyroxene becomes the stable phase. This occurs at ~7.5 kbar in sample 060 (Fig. 1.12A).

The re-appearance of pigeonite at pressures <7.5 kbar is a result of olivine becoming the liquidus phase (Fig. 1.6). The crystallization of olivine enhances the concentration of CaO in the co-existing liquid, and stabilizes the more calcic pyroxene, pigeonite, over orthopyroxene. As the olivine phase field expands to lower pressure, the pigeonite will become increasingly calcic, until calcic clinopyroxene and pigeonite become the stable pyroxene assemblage. This occurs between 0-5 kbar in sample 060.

Also plotted in Fig. 1.11 is a field representing the range of orthopyroxene phenocryst compositions sample 060. It is clear from the comparison that the natural orthopyroxene phenocrysts are nearly identical to the orthopyroxenes from T1600; 7.5 kbar and 1270^{o}C. The most Mg-rich experimental pyroxene is Mg# 85, which compares with Mg# 86.5 (Fe^{T}) in the natural phenocrysts.

Sample 060: Olivine

Olivine crystallized from all runs at, and below 7.5 kbar; the composition of the most Mg-rich olivine from each run is listed in Table 1.11. Although Jaques & Green (1979) have shown that olivine readily adjusts to the effects of iron exchange, only minor modifications are observed in the 1 atmosphere experiments of this study. The predicted equilibrium olivine composition of the starting mix is Mg# 85.2 (K_D = 0.33) compared to the most Mg-rich, 1 atmosphere liquidus olivine of Mg# 84.8. As AT173 experienced the most Fe-addition of this series of experiments (13%), the most Mg-rich olivine compositions from lower temperature experiments should closely represent ideal compositions.

The exact form of the subliquidus olivine boundary was not determined experimentally. However intersection of the olivine boundary with the extrapolated "plagioclase-in" curve should generate the reaction

TABLE 1.11
EXPERIMENTAL OLIVINE AND SPINEL (AVG.) ANALYSES : SAMPLE 65060

RUN NO.	AT-173	AT-171	AT-170	AT-183	AT-175	AT-176	T-1595	T-1720	T-1600	AT-176
PRESS.(kbar)	0	0	0	0	0	0	5	5	7.5	0
TEMP.(^{o}C)	1280	1250	1200	1180	1150	1100	1250	1220	1270	1100
PHASE	OLIV	OLIV	OLIV	OLIV	OLIV	OLIV	OLIV	OLIV	OLIV	SPINEL
SIO2	39.55	39.43	39.48	38.59	38.44	36.52	39.52	39.28	39.18	
TIO2										0.62
AL2O3										64.17
CR2O3										0.70
FEO	14.50	15.10	17.33	18.14	22.05	30.50	14.61	16.21	16.03	20.29
MNO						0.24				
MGO	45.62	45.13	42.60	42.76	39.09	32.37	45.61	44.17	44.48	14.23
CAO	0.33	0.33	0.59	0.50	0.41	0.37	0.26	0.35	0.31	
SI	0.9914	0.9912	1.0022	0.9856	0.9982	0.9910	0.9911	0.9923	0.9895	
TI										0.0121
AL										1.9722
CR										0.0144
FE	0.3038	0.3175	0.3679	0.3874	0.4790	0.6923	0.3064	0.3425	0.3386	0.4425
MN						0.0054				
MG	1.7045	1.6910	1.6118	1.6277	1.5131	1.3094	1.7045	1.6634	1.6741	0.5533
CA	0.0088	0.0090	0.0160	0.0137	0.0115	0.0108	0.0070	0.0095	0.0083	
TOT	3.0086	3.0088	2.9978	3.0144	3.0018	3.0090	3.0089	3.0076	3.0105	2.9946
MG#	84.9	84.2	81.4	80.8	76.0	65.4	84.8	82.9	83.2	55.6
range	84.9-84.6	84.2-83.7	81.4-81.2	80.8-79.4	76.0-74.9	65.4-65.2	84.8-84.2	82.9-82.4	83.2-82.7	56.1-55.0
K_D*	0.31	0.32	0.31	0.32	0.30	0.28	0.31	0.32	0.33	

100MG/(MG+FE)
* CALCULATED FROM MOST FE-RICH OLIVINE COMPOSITION AND AVERAGE GLASS ANALYSES (LISTED IN APPENDIX 1)

$$\text{oliv} + \text{plag} = \text{Al-cpx} + \text{Al-opx} \pm \text{spinel}$$

(Green & Ringwood, 1967a)

and is shown in Fig. 1.6 as a backbend in the olivine boundary. This reaction is seen petrographically in sample 060 as irregularly-shaped olivine phenocrysts which have rims composed of a shapeless mat of pleochroic orthopyroxene, occasionally the olivine is partially enclosed by an orthopyroxene phenocryst.

A difficult problem to interpret is the iron-rich nature of the olivine phenocrysts. It was suggested in Section 1.1.2 that olivine may have crystallized from a fractionated liquid due to earlier precipitation of orthopyroxene. Although the suggested subliquidus topology of sample 060 (Fig. 1.6) is an accordance with such an interpretation, there are insurmountable obstacles with the explanation. In order to precipitate an olivine of Mg# 78.5, equilibrium crystallization of ~13% orthopyroxene is required to modify the liquid to Mg# 54.5. Point counting indicates only 6% orthopyroxene phenocrysts occur in 060; loss of any additional crystals from the system could not have occurred as discussed in Section 1.1.2. Additionally, multiple broad beam area scans of the matrix give an average composition of Mg# 62.4; far too Mg-rich to be in equilibrium with the observed olivines.

There is also little latitude for crystallization of sample 060 at pressures above ~7.5 kbar as required for olivine to crystallize from a strongly fractionated liquid. As shown in Fig. 1.12A, orthopyroxene is stable only over a very narrow range of pressures near ~7.5 kbar. Therefore, it is unlikely that a long interval of orthopyroxene crystallization could occur prior to the onset of olivine precipitation, even assuming a nearly flat subliquidus olivine boundary. In addition, the nearly exact reproduction of the natural orthopyroxene phenocryst compositions at 7.5 kbar weighs heavily against possible crystallization at higher pressure.

In Section 1.1.2, a previously determined $K_D^{Fe/Mg}$ was used to show that the most Mg-rich orthopyroxene phenocryst could be in equilibrium with a liquid having a composition represented by sample 060. The experimental study showed this to be true. Therefore, the olivines cannot be xenocrystic in origin.

As other olivine-bearing high-Mg dykes do contain olivines that have equilibrium K_D's with orthopyroxene (see Chapter 5) it is possible that similar olivines in sample 060 exist, but were not analysed during the microprobe study. Once this problem was recognized, twelve separate olivine crystals were examined in detail from three thin sections,

specifically to obtain Mg-rich olivine analyses. The results of the re-examination differed little from the initial study of three olivine crystals.

The only clear, distinctive difference between sample 060 and other olivine-bearing high-Mg tholeiites is that sample 060 is not a chilled margin sample, and therefore has a relatively coarser grained texture compared to other samples in the suite. This difference may be significant in that intracrystalline diffusion of Fe-Mg readily occurs in olivine in response to a changing liquid composition, relative to the sluggish adjustment by orthopyroxene (Jaques & Green, 1979). The unexpected Fe-rich nature of the olivine phenocrysts may be reflecting the somewhat slower cooling conditions experienced by the sample, resulting in the continuous readjustment of olivine to the changing liquid composition. This seems to be the most likely explanation. One other possibility is that the subsolidus alteration of olivine to orthopyroxene-magnetite assemblages was somehow selective toward Mg-rich olivines, but this study lies outside the context of the discussion.

Sample 060: Plagioclase

Plagioclase occurs only in the 1 atmosphere runs at temperatures more than 100°C below the liquidus. It forms very small individual rhombohedral plates, or aggregates, which are too thin for quantitative microprobe analysis. The compositions used in the mass balance calculations (Table 1.8) were obtained by subtracting the averaged glass composition from the overlapped plagioclase-glass analyses assuming the plagioclase is MgO-free. As plagioclase is not a phenocryst phase in the natural rock it will not be discussed further.

Sample 060: Spinel

Because experiments in Fe-capsules produce relatively low fO_2 (near the I-W buffer), Cr-spinels (chromite-magnetite-spinel solid solution) will not precipitate despite high Cr contents in the liquid. The near absence of Cr-spinels from 060 (one inclusion in orthopyroxene phenocryst) may imply that a low fO_2 prevailed during the formation of the high-Mg tholeiite suite, although other interpretations are possible (Irvine, 1977).

Although Cr-rich spinels are absent from the experiments, Mg-Fe spinels have been identified as run products in At175 and AT176. In all observed occurrences, the spinel forms the core to crystal clots of plagioclase (Fig. 1.6). Their very small size hampered quantitative

analysis; the average of two analyses is listed in Table 1.11. The paragenesis of these spinels is not understood. Their restriction to the cores of crystal clots indicates they have crystallized very early within the charge and acted as nucleation sites for the other phases. Their absence as individual grains within the liquid suggests the spinel crystallized metastably and was preserved from reaction with the liquid only when surrounded by an armour of stable phases. Spinel-pyroxene partition coefficients for chromium are very high (Irving, 1978) and as complete solid solution exists between Al^{3+} and Cr^{3+}, any spinel coexisting with the Cr-rich pyroxenes should also be very Cr-rich; the observed spinel has <1% Cr_2O_3. These observations could indicate that the spinel resulted from contamination during the preparation procedure, however mass balance calculations require the spinel to be a precipitating phase from the charge. These observations will not be discussed further as they have no bearing on the emplacement of mafic dykes.

1.3.2 RESULTS OF THE EXPERIMENTAL STUDY OF SAMPLE 206 AND COMPARISON WITH THE NATURAL PHASE ASSEMBLAGE

The experimentally determined phase relations of sample 206 are illustrated in Fig. 1.13. Olivine precipitates alone from the 1 atmosphere liquidus at 1165°C to ~1155°C where it is joined by plagioclase, followed by clinopyroxene* at ~1100°C. The olivine + plagioclase + clinopyroxene field persists to a maximum of 5-6 kbar, above which a five-phase field exists with the onset of orthopyroxene precipitation. Olivine remains at the liquidus up to 8 kbar and is replaced by a two-pyroxene assemblage at higher pressures. SEM photographs of selected run products are shown in Fig. 1.14.

Similar problems were encountered in optically identifying pyroxene in crushed mounts of these experimental charges as was discussed previously with regards to sample 060. Tentative phase fields distinguished by the presence or absence of low-Ca pyroxene laths (Fig. 1.14B,D) could be constructed from optical examination of the run products while microprobe studies were necessary to confirm the presence of clinopyroxene. Microprobe analyses of the pyroxene laths revealed extensive chemical inhomogeneity and will be discussed in detail in a later section.

---

* Unless otherwise noted, clinopyroxene refers to calcic clinopyroxene, low-Ca clinopyroxene will be referred to as pigeonite.

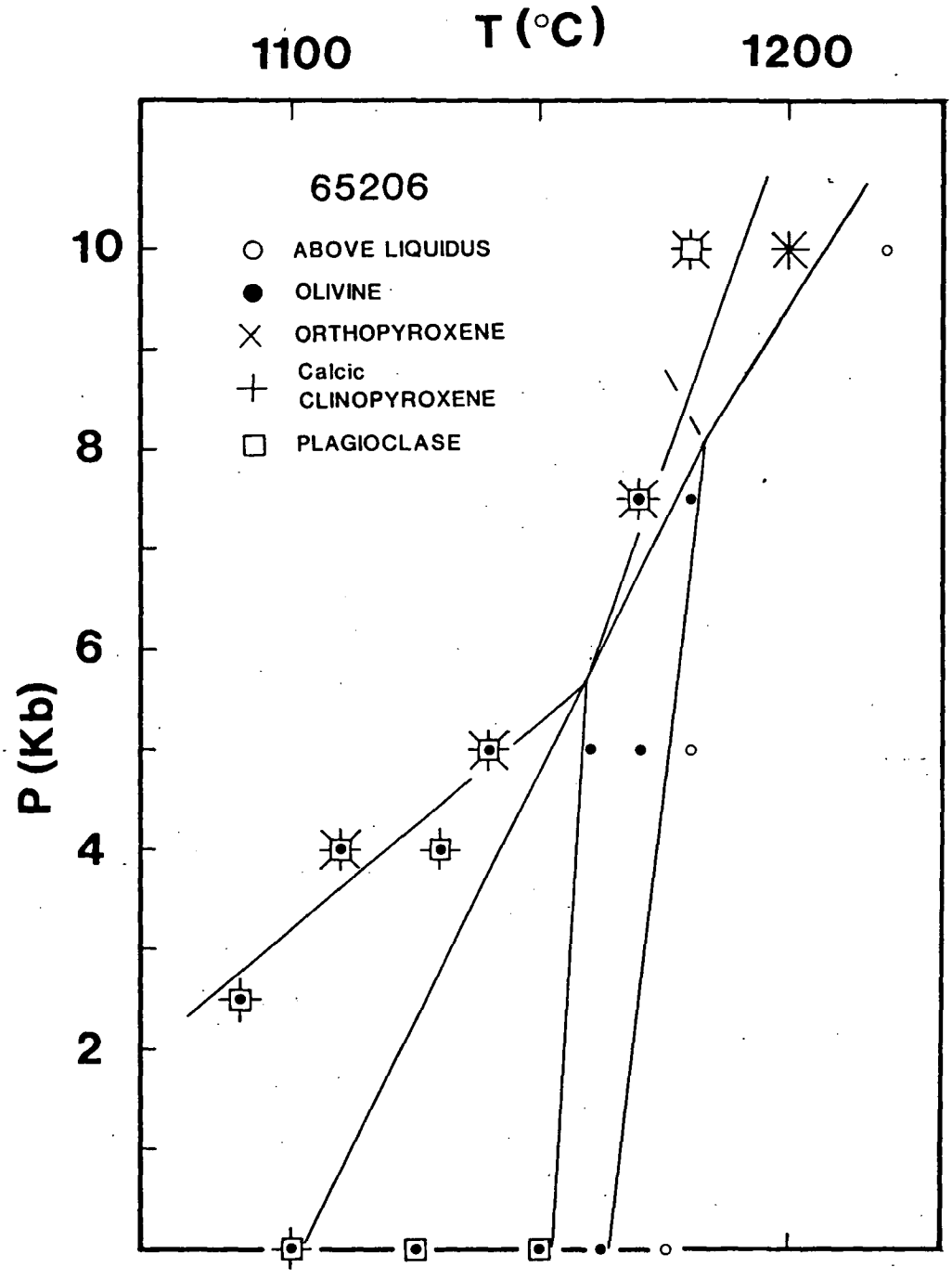

Figure 1.13
Experimentally determined near-liquidus phase relationships for sample 65206.

Figure 1.14A

Experiment AT181 (Table 1.8). Large olivine crystals (bright), blocky Ca-clinopyroxene (medium grey) and plagioclase crystals (dark) in glass. Bar scale at bottom, magnification 1.69×10^3. White specks are surficial contamination.

Figure 1.14B

Experiment T1669. Large olivine crystals (bright) with dark laths of plagioclase. Pyroxenes (medium grey) are metastable pigeonites (see text).

Figure 1.14C

Experiment T1730. Poorly formed crystals of olivine (bright) with abundant plagioclase (dark). Plagioclase cluster in upper right corner is cored by fine granular spinel. Medium grey Ca-clinopyroxene forms clusters and intergrowths with plagioclase and olivine. Compare with Fig. 1.2B.

Figure 1.14D

Experiment T1694. Abundant laths of metastable pigeonite (medium grey) with small, euhedral olivines (slightly brighter than pigeonite). Note the clots of euhedral plagioclase crystals (dark).

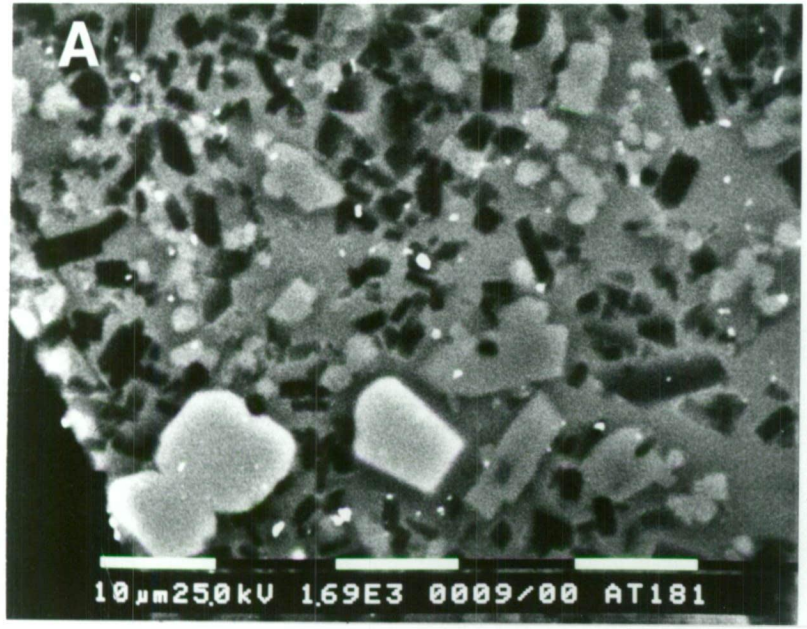
A
10µm25.0kV 1.69E3 0009/00 AT181

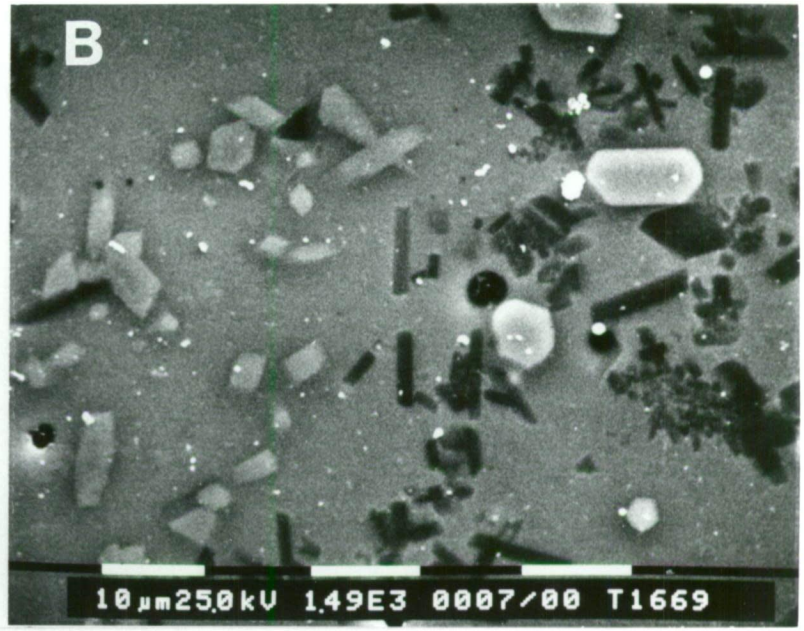
B
10µm25.0kV 1.49E3 0007/00 T1669

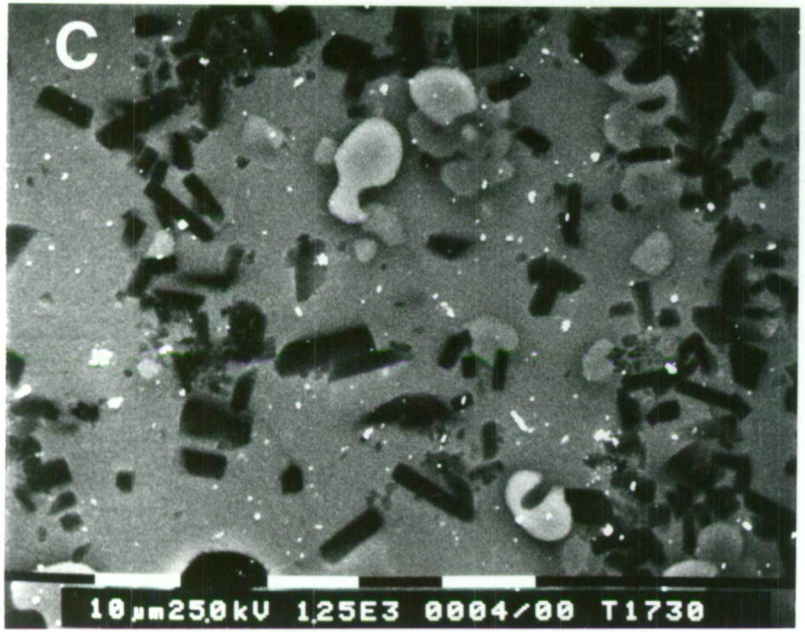
C
10µm25.0kV 1.25E3 0004/00 T1730

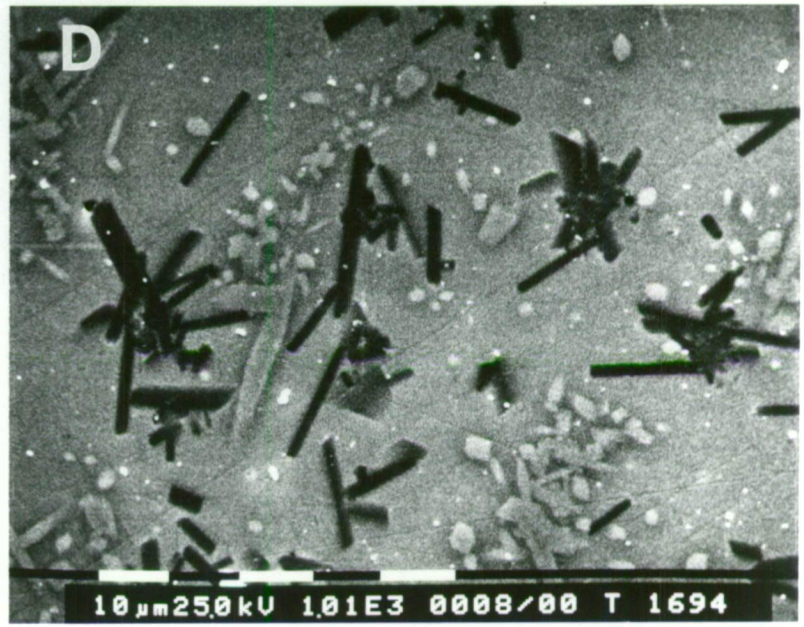
D
10µm25.0kV 1.01E3 0008/00 T 1694

Sample 206: Olivine

Olivine compositions from individual experiments are reported in Table 1.12. Olivine analyses from T1699 (7.5 kbar, 1180°C) were not obtained due to the rarity of olivine in the charge: no crystals were found in the chips prepared for microanalysis.

Iron addition had an insignificant effect on the composition of the liquidus olivine at 1 atmosphere, illustrated by the restricted range of olivine compositions (Table 1.12). In addition, the most Mg-rich liquidus olivine (Mg# 70.5) is identical to that predicted to be in equilibrium with the starting composition (K_D = 0.33). The calculated crystal/liquid K_D (0.31) suggests that the 1 atmosphere olivines, once precipitated, react sluggishly to the continued addition of iron to the coexisting liquid. At 5 kbar, the most Mg-rich liquidus olivine is Mg# 68.1 (T1693), well below the predicted value, while olivine which crystallized at a temperature 10°C lower (T1668) is more Mg-rich at Mg# 69.4. This apparent contradiction is due to the addition of 7% Fe in the liquidus run, but only 2% in the lower temperature experiment. The most Mg-rich olivines of both assemblages have calculated $K_D^{Fe/Mg}$ = 0.33 indicating the olivine crystals adjusted readily to the changing liquid composition at this pressure. Mass balance calculations indicate 1% olivine crystallized from the lower temperature run T1668 (Table 1.8). Ideally, following 1% crystallization of olivine the starting composition should be in equilibrium with a Mg# 69.6 olivine. This compares closely with the observed value of 69.4. On this basis, the olivine compositions determined in lower temperature experiments with comparable amounts of Fe-gain should be unaffected (or nearly so) by iron addition. Run T1694 (7.5 kbar, 1170°C) though at a higher pressure and temperature than T1668 experienced only 2% iron addition suggesting the most Mg-rich olivine, based on the above obsevations, should be very near the equilibrium composition.

As olivine crystals in sample 206 are altered to orthopyroxene + magnetite symplectites, the compositions of the experimental olivine cannot be used as a guide in determining the emplacement depths of the studied dyke. However, textural relationships in sample 206, as well as other members of the Fe-rich tholeiite suite, indicate olivine is the liquidus phase which implies a maximum emplacement pressure of 8 kbar for this composition.

TABLE 1.12
EXPERIMENTAL OLIVINE ANALYSES : SAMPLE 65206

RUN NO.	AT-182	AT-179	AT-178	AT-181	T-1734	T-1730	T-1845	T-1693	T-1668	T-1669	T-1694
PRESS.(kbar)	0	0	0	0	2.5	4	4	5	5	5	7.5
TEMP.(°C)	1162	1149	1124	1100	1090	1130	1110	1170	1160	1140	1170
PHASE	OLIV	OLIV	OLIV	OLIV	OLIV	OLIV	OLIV	OLIV	OLIV	OLIV	OLIV
SIO2	36.69	36.33	35.77	35.01	35.50	36.41	35.97	36.79	36.59	36.47	36.80
TIO2											
AL2O3											
CR2O3											
FEO	26.88	28.80	32.18	37.07	33.09	31.47	32.96	28.50	27.69	29.68	28.50
MNO											
MGO	36.07	34.52	31.64	27.45	30.98	31.79	30.68	34.06	35.31	33.41	34.26
CAO	0.37	0.34	0.41	0.46	0.43	0.33	0.39	0.65	0.41	0.44	0.45
SI	0.9784	0.9782	0.9797	0.9832	0.9771	0.9917	0.9879	0.9885	0.9796	0.9855	0.9879
TI											
AL											
CR											
FE	0.5993	0.6485	0.7370	0.8707	0.7617	0.7166	0.7569	0.6404	0.6201	0.6706	0.6399
MN											
MG	1.4334	1.3851	1.2915	1.1491	1.2712	1.2904	1.2558	1.3639	1.4091	1.3456	1.3713
CA	0.0104	0.0099	0.0121	0.0138	0.0128	0.0097	0.0115	0.0187	0.0117	0.0128	0.0129
TOT	3.0215	3.0217	3.0202	3.0168	3.0228	3.0083	3.0121	3.0115	3.0204	3.0145	3.0120
MG#	70.5	68.1	63.7	56.9	62.5	64.3	62.4	68.1	69.4	66.7	68.2
range	70.5-70.2	68.1-67.8	63.7-63.0	56.9-56.3	62.5-61.5	64.3-63.9	62.4-61.8	68.1-64.7	69.4-68.7	66.7-65.4	68.2-67.4
K_D*	0.31	0.31	0.32	0.31	0.33	0.32	0.30	0.38	0.34	0.33	0.31

100MG/(MG+FE)
* CALCULATED FROM MOST FE-RICH OLIVINE COMPOSITION AND AVERAGE GLASS ANALYSES (LISTED IN APPENDIX 1)

Sample 206: Plagioclase

Plagioclase is the second phase to appear at 1 atmosphere to 5-6 kbar, and precipitates near the liquidus to at least 10 kbar. In crushed mounts the plagioclase can be seen as thin, idiomorphic rhombohedral plates occurring as individual crystals or aggregates (Fig. 1.14). In all cases, the plagioclase crystals were too narrow to obtain microprobe analyses free of glass overlaps. The compositions reported in Table 1.13 were calculated by subtracting the averaged glass composition from the plagioclase assuming all TiO_2, FeO and MgO were components from the glass overlap. This assumption may slightly over-estimate the amount of glass overlap as small amounts of MgO and especially FeO may be structurally included in plagioclase. SiO_2 and Al_2O_3 contents of the calculated plagioclase will be the components most affected by any over-estimation in the proportions of glass overlap. This is probably partly responsible for the low cation totals in the structural formulae of the calculated plagioclase compositions (Table 1.13). Slight changes in the proportion of glass subtracted have negligible effect on the Ca/Na/K ratios. Additionally, replicate analyses of a Lakeside Plagioclase standard (An_{68}) produced structural totals which ranged from 4.974-4.985 (based on 8 oxygens). These low totals (compared to the recommended value of 4.992 of the standard) were found to be due entirely to slight deviations in the calibration of SiO_2. No difference from the quoted Ca/Na/K ratios were observed. The calculated plagioclase compositions vary up to a maximum of 7 mole % An in any one experiment but in general range only by ~3 mole % An.

Plots of individual plagioclase analyses versus pressure are illustrated in Figs 1.15A,B with the averaged compositions from runs which define the "plagioclase-in" boundary connected by tie lines. Of particular importance to this study is the prominent trend of decreasing An content with increasing pressure, a feature previously identified from other experimental studies of basaltic compositions (Green et al., 1979; Duncan & Green, submitted). However, this general statement concerning the composition of plagioclase in response to changing pressure must be tempered by the fact that in the Duncan & Green study, plagioclase (An_{89}, 0 kbar; An_{85}, 5 kbar) crystallizes at temperatures below the onset of clinopyroxene crystallization. As the stability of clinopyroxene expands with pressure and incorporates a greater proportions of $CaAl_2SiO_6$ (CaTs) in solid solution, the Ca/Na ratio of the coexisting liquid decreases with pressure. Plagioclase crystallizing subsequent to clinopyroxene will then become increasingly Ab-rich with pressure.

TABLE 1.13
AVERAGED EXPERIMENTAL PLAGIOCLASE ANALYSES: SAMPLE 65206

RUN NO.	AT-179	AT-178	AT-181	T-1734	T-1730	T-1845	T-1669	T-1694	T-1660
PRESS.(kbar)	0	0	0	2.5	4	4	5	7.5	10
TEMP °C	1149	1124	1100	1090	1130	1110	1140	1170	1180
PHASE	PLAG	PLAG	PLAG	PLAG	PLAG	PLAG	PLAG	PLAG	PLAG
SIO2	50.93	51.16	53.38	51.91	52.26	53.56	53.41	53.31	53.93
AL2O3	31.24	30.51	29.58	30.79	30.70	29.59	29.80	29.83	29.44
CAO	15.10	13.98	13.17	13.86	13.48	13.15	12.33	13.09	12.33
NA2O	2.62	3.20	3.67	3.31	3.41	3.52	4.23	3.59	4.07
K2O	0.12	0.12	0.20	0.13	0.17	0.18	0.25	0.18	0.23
SI	2.3164	2.3652	2.4146	2.3542	2.3666	2.4203	2.4143	2.4032	2.4345
AL	1.6748	1.6307	1.5771	1.6459	1.6387	1.5756	1.5878	1.5932	1.5665
CA	0.7359	0.6793	0.6383	0.6735	0.6541	0.6366	0.5972	0.6356	0.5964
NA	0.2311	0.2814	0.3219	0.2911	0.2994	0.3084	0.3708	0.3154	0.3563
K	0.0070	0.0069	0.0115	0.0075	0.0098	0.0104	0.0144	0.0208	0.0132
TOTAL	4.9652	4.9635	4.9634	4.9722	4.9687	4.9513	4.9845	4.9682	4.9669
CA#	75.6	70.1	65.7	69.3	67.9	66.6	60.8	65.4	61.8
RANGE	80.1-73.0	71.2-68.4	67.6-63.2	70.3-68.5	70.0-65.7	68.4-64.4	61.8-58.9	67.0-64.0	63.0-60.7

CA# = 100 CA/(CA+NA+K).

Figure 1.15A

Plagioclase compositions from individual experiments plotted against pressure. Differences in symbols separate plagioclase analyses from experiments at the same pressure but differing temperatures. Tie line connects possible compositions along the "plagioclase-in" boundary (see Fig. 1.13, and text).

Figure 1.15B

The heavy line marks the maximum anorthite content of plagioclase coexisting with Ca-clinopyroxene defined by the average plagioclase compositions of the pertinent experiments (square symbols, see Fig. 1.13). Narrow line marks the maximum anorthite content of plagioclase coexisting only with olivine. Dashed lines are analyses from the most calcic plagioclase phenocryst in 206.

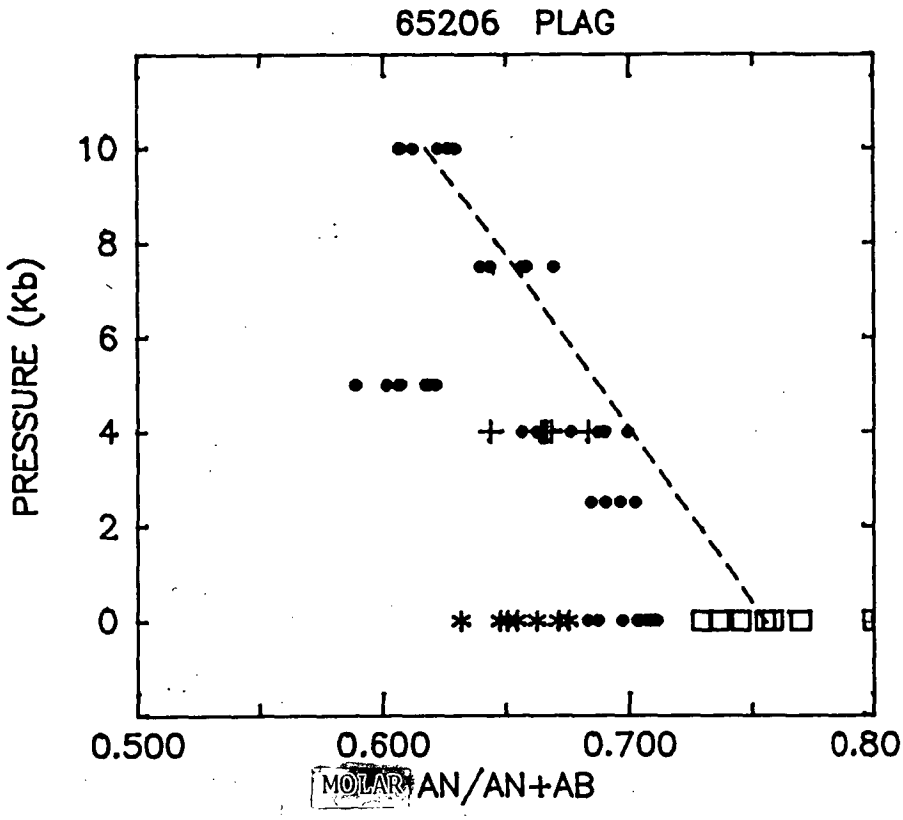
65206 PLAG
PRESSURE (Kb)
10
8
6
4
2
0
0.500
0.600
0.700
0.80
MOLAR AN/AN+AB

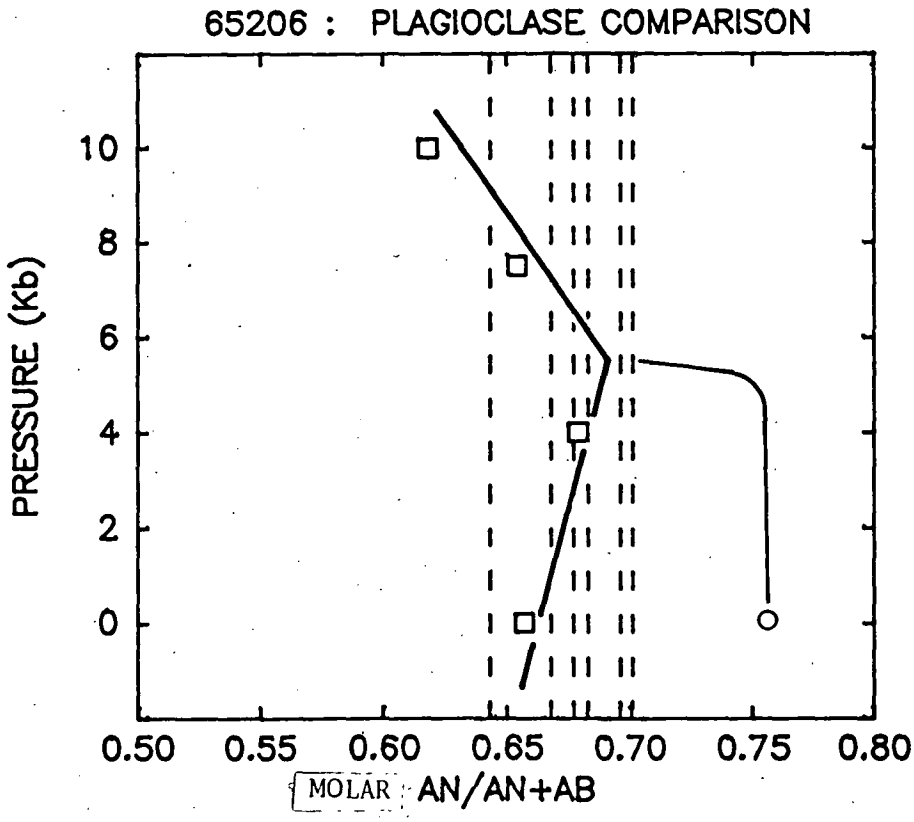
65206 : PLAGIOCLASE COMPARISON
PRESSURE (Kb)
10
8
6
4
2
0
0.50
0.55
0.60
0.65
0.70
0.75
0.80
MOLAR AN/AN+AB

The effect of clinopyroxene precipitation on the composition of plagioclase, as discussed above, applies to pressures >5-6 kbar in sample 206. At lower pressures, the first formed plagioclase coexists with olivine, and as only one experiment was conducted along the "plagioclase-in" boundary at these pressures the effect of pressure on the composition of plagioclase coexisting with olivine cannot be determined directly from this study. It is possible that pressure-induced modifications of the melt structure could affect plagioclase/liquid Ca/Na partitioning, but Drake (1975) concluded that the composition of plagioclase in H_2O-free systems is insensitive to pressure to at least 10 kbar. This is in accord with the data of Green et al. (1979) where plagioclase co-precipitating with olivine changed in composition from An_{78} at 0 kbar, to An_{77} at 5 kbar. Not until the incoming of clinopyroxene at 10 kbar did the plagioclase composition change significantly (An_{73}). It is expected from these observations that the first-formed plagioclase at pressures <5-6 kbar in sample 206 will vary little from the 0 kbar composition of $An_{75.6}$.

A solid line marking the maximum An content of plagioclase coexisting with clinopyroxene in sample 206 is shown as a function of pressure in Fig. 1.15B. This boundary is defined by the average plagioclase composition of the relevant experiments, also shown. The increase in An content of plagioclase coexisting with clinopyroxene from 0-5.5 kbar appears contrary to the previous discussions, but is simply the result of the narrowing in the plagioclase + olivine phase field which causes the liquid at pyroxene saturation to have increasingly higher Ca/Na ratios. A narrow line marks the maximum An content of plagioclase coexisting only with olivine. This latter curve seems quite irregular, though the form is consistent with the data of Green et al. (1979) as discussed above. Note however, that the rather wide range of An contents in the 0 kbar data may have resulted in an averaged plagioclase composition that over-emphasizes the back-bend in the "plagioclase-in" boundary.

The most calcic plagioclase phenocryst from sample 206 has an $An_{70.1}$ core, and is zoned normally to $An_{64.3}$. Fig. 1.15B indicates the core is too calcic to have crystallized at any pressure greater than the multiple saturation point at 5-6 kbar, and is consistent with the plagioclase cores having nucleated with olivine at a pressure <5-6 kbar. The rimward zoning to less calcic compositions indicates a cooling path into the olivine + clinopyroxene + plagioclase stability field.

Sample 206: Pyroxene laths

The interpretation of phase equilibria in experiments which produced lath-shaped pyroxene crystals (Fig. 1.14) was complicated considerably by pyroxene/liquid disequilibria. The range of pyroxene analyses from individual experiments in terms of the quadrilateral pyroxene components is illustrated in Figs 1.16, 1.17 & 1.18. In all but perhaps run T1660, the pyroxenes have apparently reached equilibrium with regards to Fe/Mg. However the Wo content of pyroxenes from individual runs may range over 20%, with much of that variation being obtainable through multiple analyses of a single crystal. (Note that all plotted analyses have structural totals which lie between 4.01 and 3.99.) The non-quadrilateral components, TiO_2 and Al_2O_3, also increase regularly with Wo.

The initial interpretation of these data was that they represented an intimate mixture of co-precipitating Ca-rich and Ca-poor pyroxenes. It was noted that the low-Ca end of these trends was consistently ~10% Wo, which raised the question of whether or nor the low-Ca component was pigeonite and not orthopyroxene. However, the 10% Wo value lies below the Wo content of pigeonite predicted to be in equilibrium with Ca-rich pyroxene (Lindsley, 1983) while the consistency of this composition between different experiments raised doubts about the positioning of the pigeonite-augite solvus used by Lindsley.

Pyroxene analyses from the 10 kbar, 1180° and 1200°C experiments in Fe capsules tend to form two separate groups: one within the pigeonite-augite immiscibility field and the other clustered within the orthopyroxene-pigeonite immiscibility field (Figs 1.17, 1.18). These analyses suggested that three pyroxenes may coexist under the 10 kbar run conditions, which if true, would contribute additional complexities to the lower pressure pyroxene data.

A further complication is that the trends produced by the data in the pyroxene quadrilateral do not parallel tie lines connecting equilibrium orthopyroxene-augite or orthopyroxene-pigeonite pairs, as would be expected if the analyses were the result of simple binary mixing between a high- and low-Ca pyroxene. Instead, the resulting trends are considerably oblique to either tie line, with the more Ca-rich compositions being more Fe-rich than expected.

In order to resolve these inconsistencies it was thought that experiments of longer duration would act to separate the mixed crystals into their Ca-rich and Ca-poor endmember components. To test this proposal, the 10 kbar, 1180° and 1200°C runs (both 2 hours duration) were repeated with run times of 5 hours. Graphite capsules were used to

Figure 1.16 A-F

The compositions of pyroxene laths from experiments at 4, 5 and 7.5 kbar are illustrated on the following two pages. The analyses display a wide range of Al_2O_3 and TiO_2 contents, and span the miscibility gap between high- and low-Ca pyroxenes as shown in the pyroxene quadrilateral diagrams. The coexisting phases are: open circle - olivine; solid square - spinel; open square - starting composition; triangle - glass. Figs. B, D, F are mole % plots; Figs. A, C, E are WT% TiO_2, Al_2O_3 vs Molor Wo.

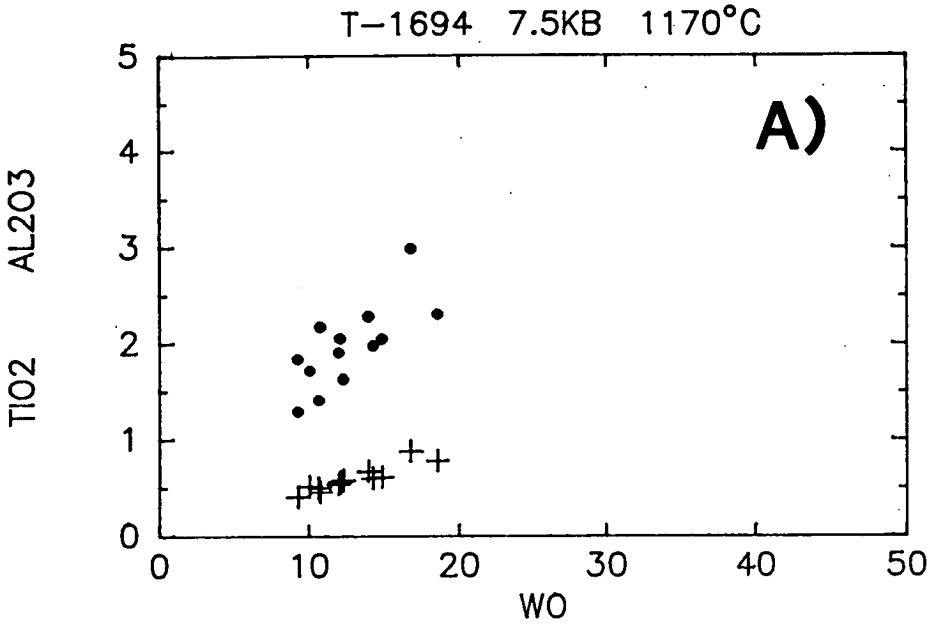
T−1694 7.5KB 1170°C
A)
TIO2 AL2O3
WO
0
10
20
30
40
50
1
2
3
4
5

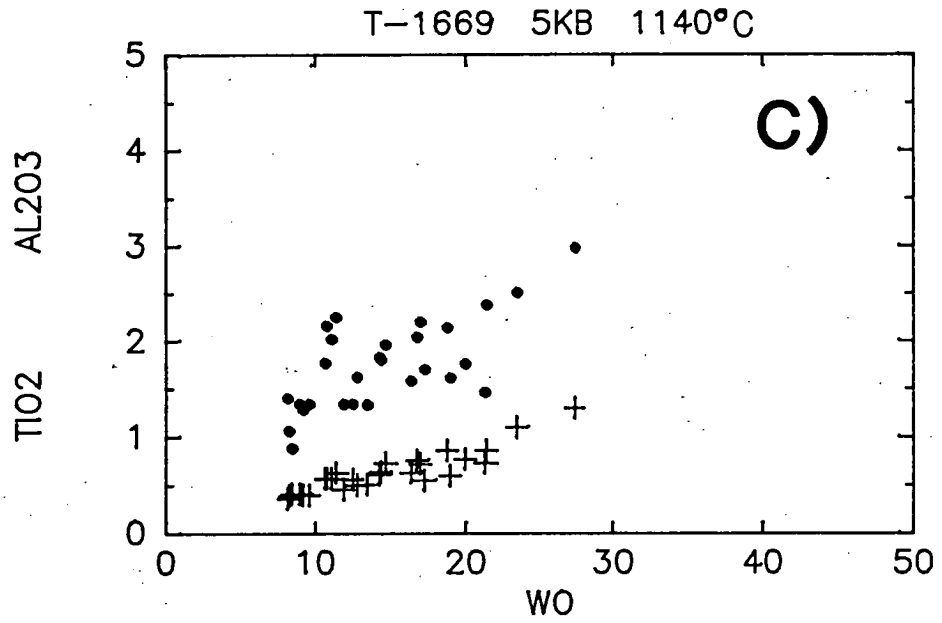
T−1669 5KB 1140°C
C)
TIO2 AL2O3
WO
0
10
20
30
40
50
1
2
3
4
5

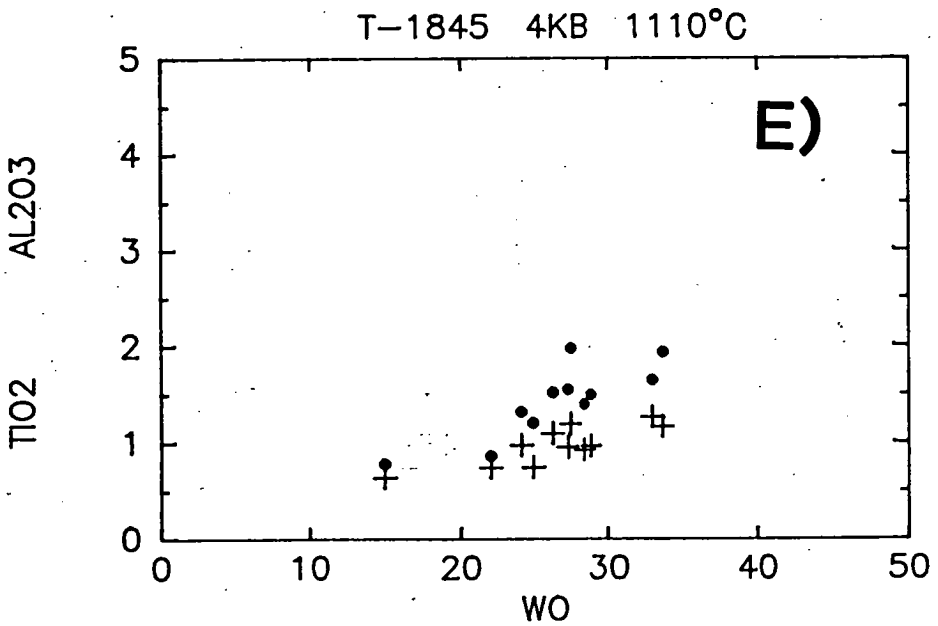
T−1845 4KB 1110°C
E)
TIO2 AL2O3
WO
0
10
20
30
40
50
1
2
3
4
5

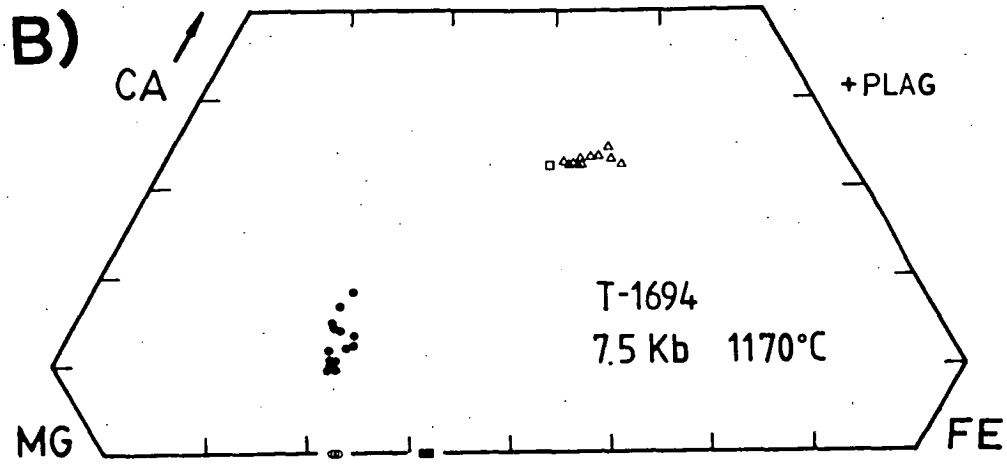
B)
CA
+PLAG
T-1694
7.5 Kb 1170°C
MG
FE

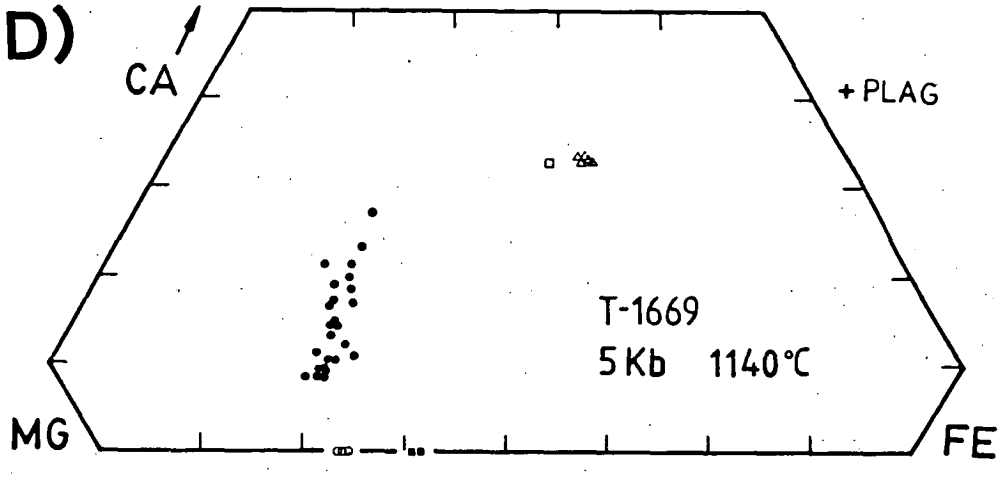
D)
CA
+PLAG
T-1669
5 Kb 1140°C
MG
FE

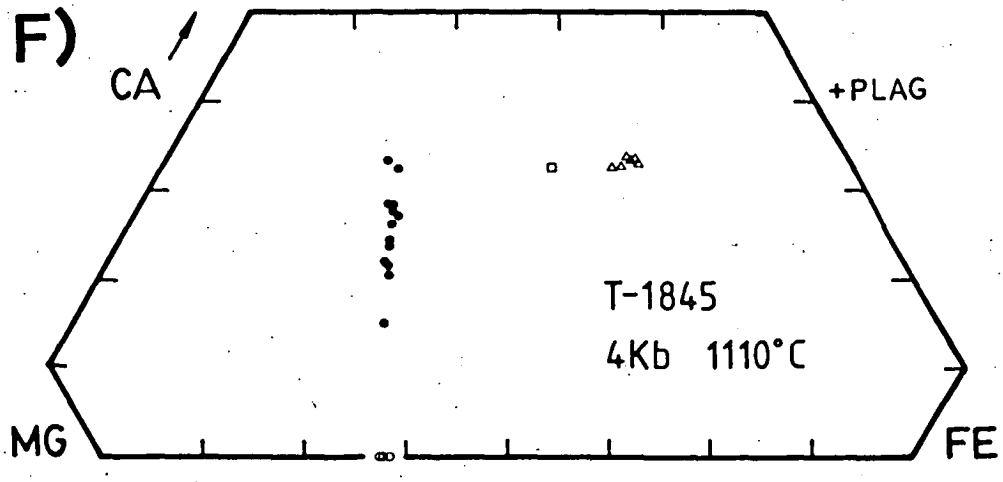
F)
CA
+PLAG
T-1845
4Kb 1110°C
MG
FE

minimize the effects of iron exchange over the extended run time. The data resulting from the 5 hour experiments are compared with the 2 hour runs in Figs 1.17, 1.18. Plots of Al_2O_3 and TiO_2 versus Wo readily illustrate that the effect of increased run time was to reduce the range of the Wo component, but did not act to separate the phases into Ca-rich and Ca-poor endmembers. The minimum Wo content of both the 1180° and 1200°C runs did not vary according to run duration though more Ca-poor analyses were obtained from the 5 hour run products. Note also that there is a tendency for the Al_2O_3 contents of the pyroxene from both the 2 and 5 hour runs to form a curved trend from high Al_2O_3 at high Wo values to low and intermediate Al_2O_3 at low Wo values (Figs 1.17, 1.18).

The results of the graphite capsule experiments are interpreted to indicate that the scatter to high Wo values, especially evident in the 2 hour runs, is a disequilibrium feature, and under longer duration run times pigeonite of ~Wo_{10} would be the sole crystallizing pyroxene. The range of ~1.5-2% Al_2O_3 at the lowest Wo values probably indicates the limit to which the pigeonite component has reached "equilibrium" in terms of the minor components, similar to the scatter observed in the Al_2O_3 contents of the experimental pyroxenes of sample 060 (Fig. 1.8). This conclusion also explains why the pyroxene analyses do not parallel tie-line trends when plotted onto the pyroxene quadrilateral: the high-Ca component is not an equilibrium pyroxene and is not constrained to form at solvus limb compositions. This conclusion is believed applicable to all the experiments which crystallized lath-shaped pyroxenes.

A feature of the experimental pyroxene data which is not explained by this conclusion is that the minimum Wo value (~Wo_{10}) is essentially constant over the range of run conditions (4 kbar, 1110°C-10 kbar, 1200°C). It was noted previously in the discussion of the experimental results from sample 060 that pigeonite compositions changed along a regular and predictable path in response to variations in pressure and temperature. This is not observed in the presumed pigeonites of sample 206. Two complementary explanations can be advanced and are developed below.

In a previous section, the effect of iron exchange on the composition of the liquidus olivine was considered. It was concluded that at pressures above 1 atmosphere, olivines which crystallized at and below the boundary marking the incoming of the second liquidus phase were little affected by iron addition. In the case of the subliquidus "pigeonite-bearing" experiments the coexisting olivines should closely approach equilibrium compositions. With this conclusion as a starting point, the $K_D^{Fe/Mg}{}_{ol/pig}$ of the

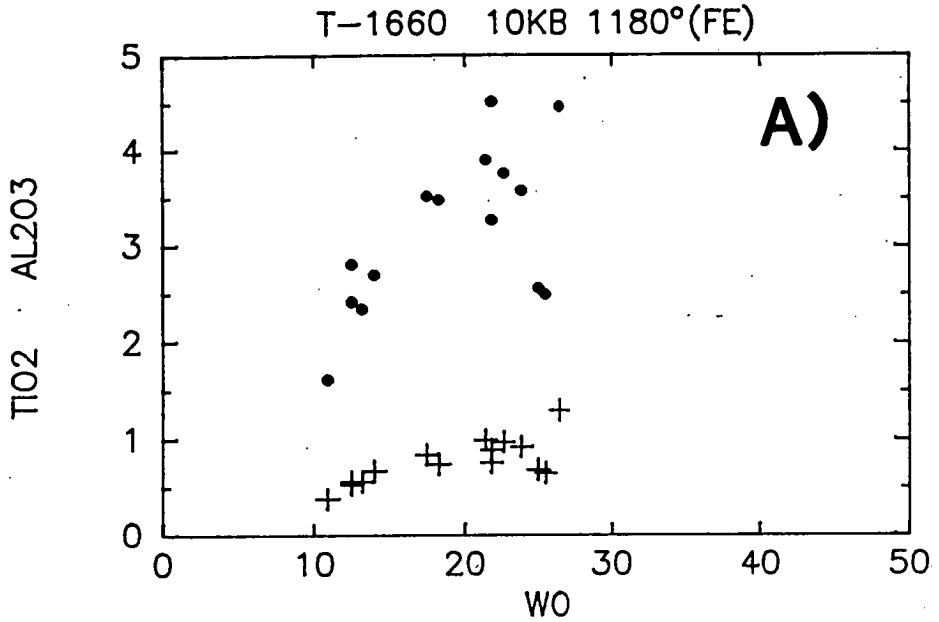
T-1660 10KB 1180°(FE)
A)
TI02 AL203
WO
0
10
20
30
40
50
1
2
3
4
5

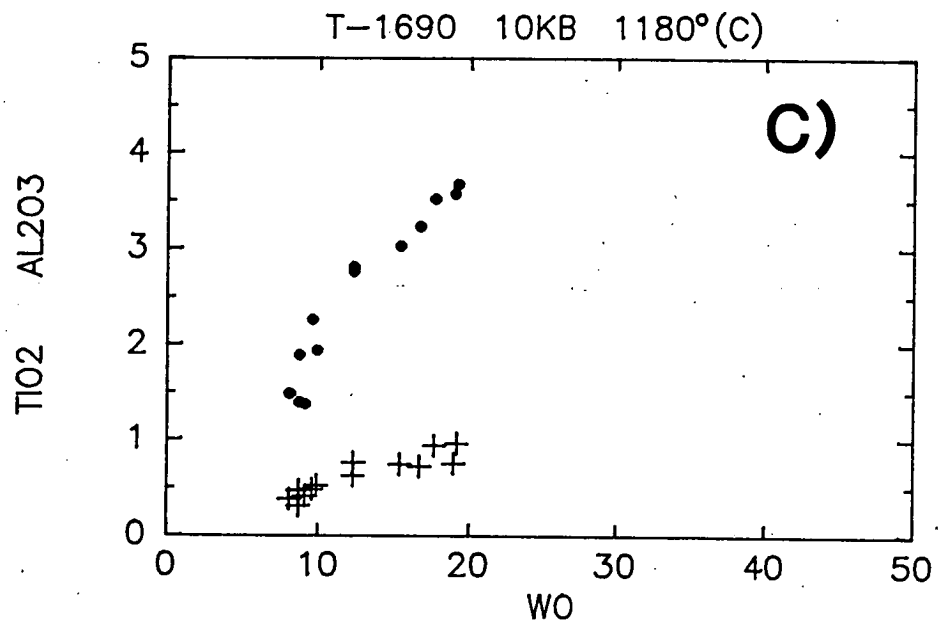
T-1690 10KB 1180°(C)
C)
TI02 AL203
WO
0
10
20
30
40
50
1
2
3
4
5

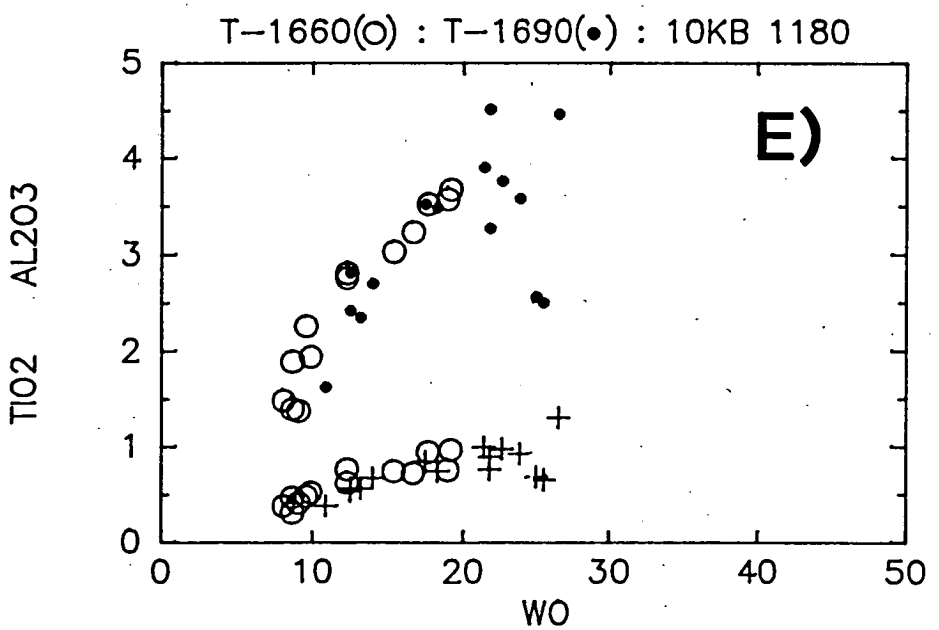
T-1660(O) : T-1690(•) : 10KB 1180
E)
TI02 AL203
WO
0
10
20
30
40
50
1
2
3
4
5

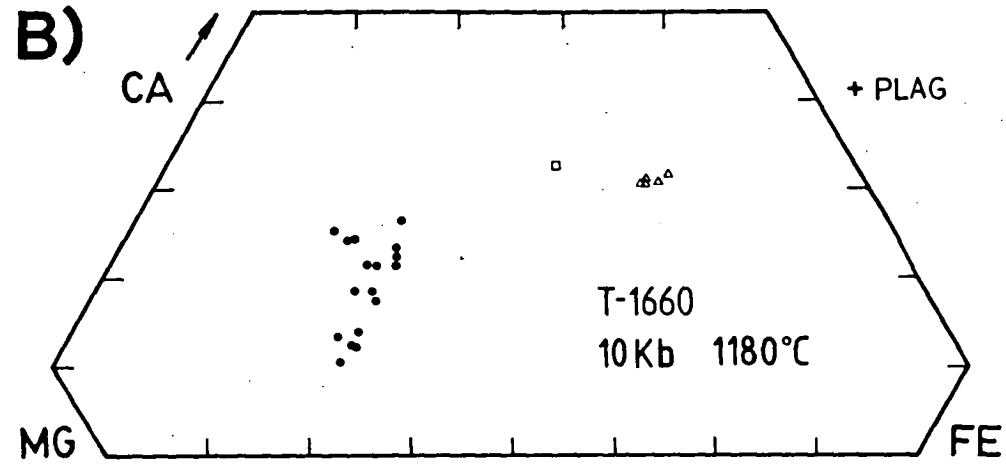

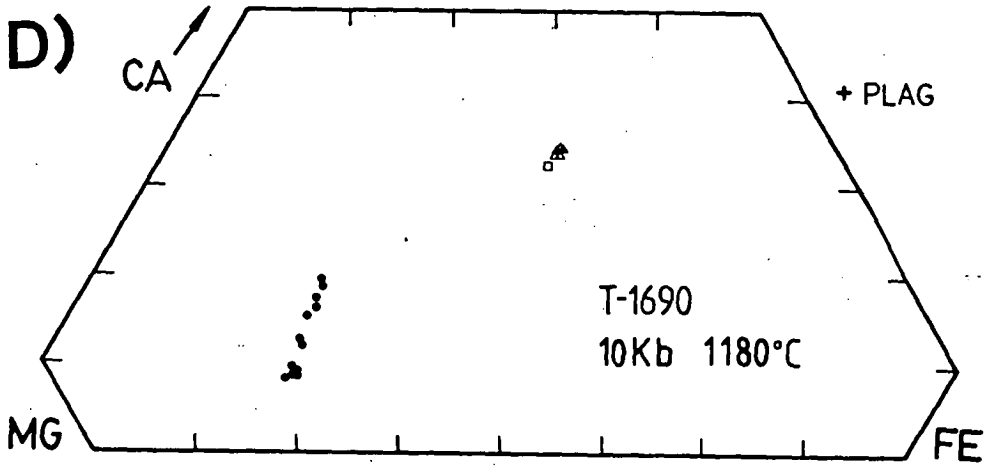

Figure 1.17

Variation in the composition of lath shaped pyroxenes from experiments at 10 kbar, 1180°C with Fe and C capsules.
Dots - pyroxene analyses; square - starting composition (206); triangles - coexisting glass.

A-B: iron capsule
C-D: graphite capsule
E: combined plot emphasizing the reduction in Wo, TiO_2 and Al_2O_3 in pyroxenes from the graphite capsule experiments compared to the iron capsule runs.

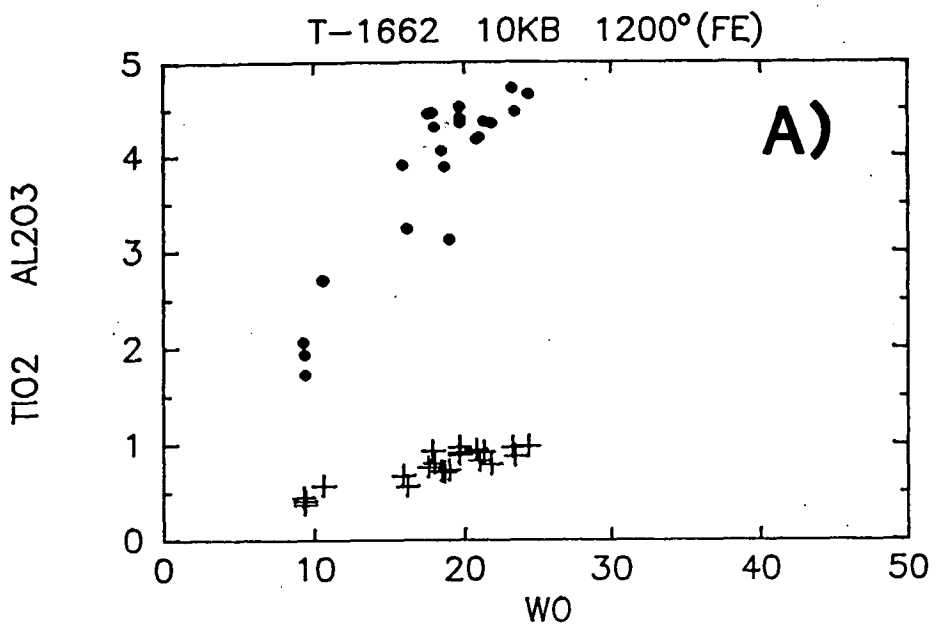
T−1662 10KB 1200°(FE)
A)
TIO2 AL2O3
WO
0
10
20
30
40
50
1
2
3
4
5

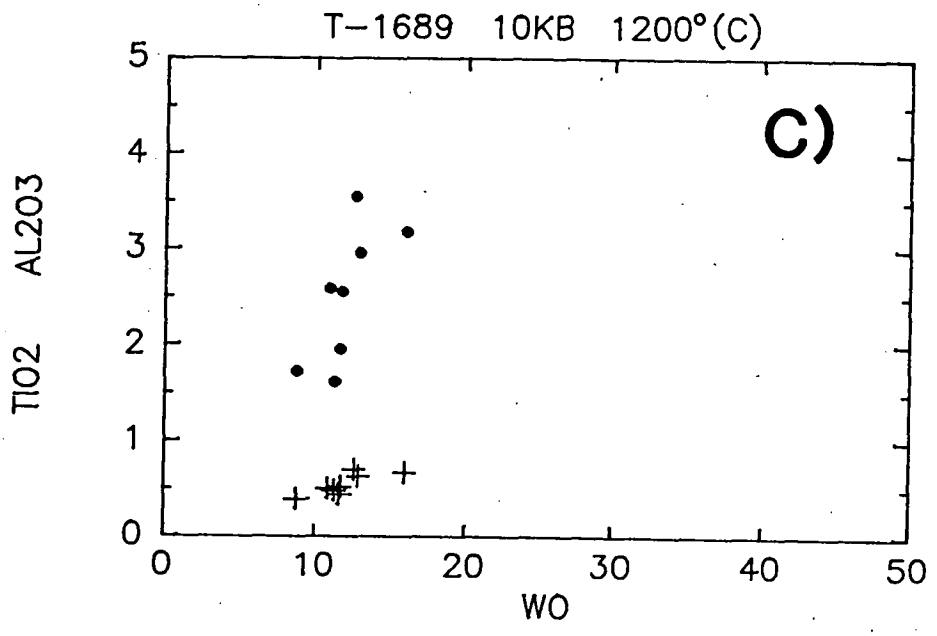
T−1689 10KB 1200°(C)
C)
TIO2 AL2O3
WO
0
10
20
30
40
50
1
2
3
4
5

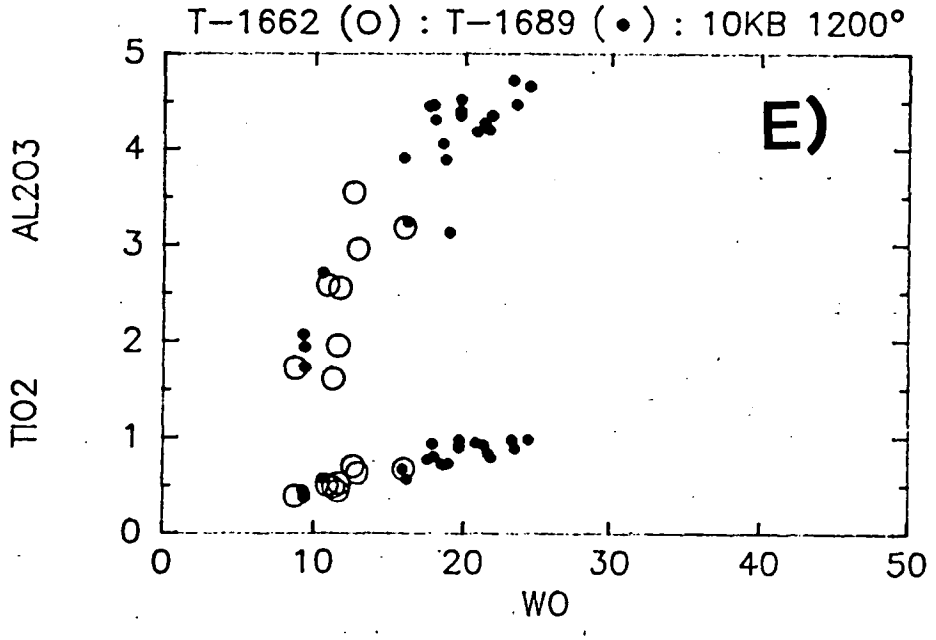
T−1662 (O) : T−1689 (•) : 10KB 1200°
E)
TIO2 AL2O3
WO
0
10
20
30
40
50
1
2
3
4
5

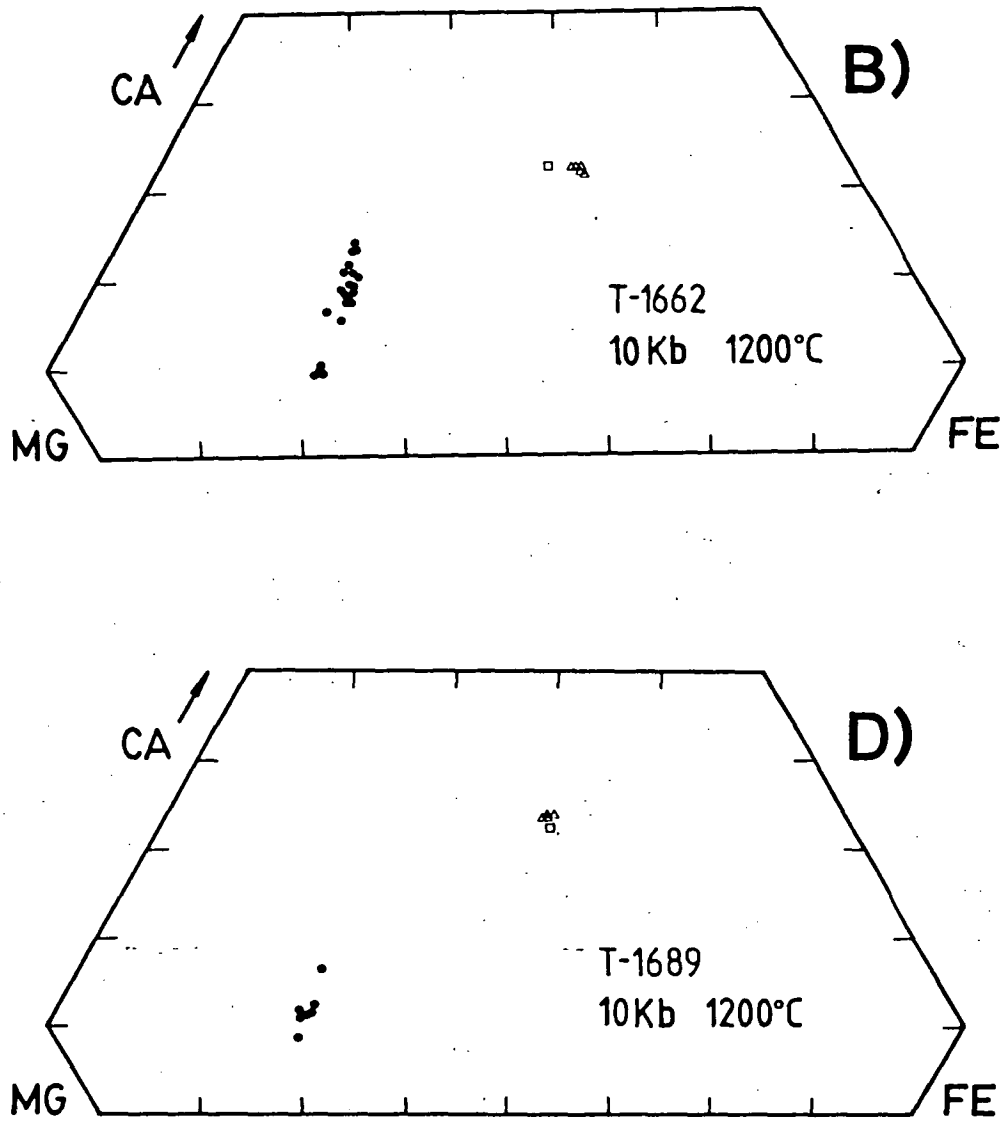

Figure 1.18

Variation in the composition of lath shaped pyroxenes from experiments at 10 kbar, 1200°C with Fe and C capsules.
Dots - pyroxene analyses; square - starting composition (206); triangles - coexisting glass.

A-B: iron capsule
C-D: graphite capsule
E: combined plot emphasizing the reduction in Wo, TiO_2 and Al_2O_3 in pyroxenes from the graphite capsule experiments compared to the iron capsule run.

experimental phases can be critically examined by applying a $K_D^{Fe/Mg}_{ol/pig}$ calculated from the pressure and temperature dependent $K_D^{Fe/Mg}_{opx/pig}$ determined from Lindsley's diagrams, and the value $K_D^{Fe/Mg}_{ol/opx} = 1.1$. The calculated and observed values are compared in Table 1.14 below.

TABLE 1.14
COMPARISON OF OBSERVED AND CALCULATED OLIVINE / PIGEONITE K_D'S

RUN	T1845	T1669	T1694
P (kbar)	4	5	7.5
T (°C)	1110	1140	1170
CALC.	0.96	1.00	0.99
OBS.	1.07	1.16	1.06

The calculated K_D's indicate pigeonite in equilibrium with olivine should have an equivalent or slightly lower Mg value. However, the K_D's observed in the experimental assemblages indicate the pigeonites are too Mg-rich to be in equilibrium with the coexisting olivines. Assuming Lindsley's diagrams to be correct, this contradiction can be rationalized only by considering the pigeonite to be metastable, a conclusion for which the following experimental evidence exists.

High pressure studies of several lunar basalts (Green et al., 1975) were found to crystallize two clinopyroxenes along their high pressure liquidus (Wo_{13} and Wo_{19}; compare with T1662, Fig. 1.18). Further experimentation on the stability of the coexisting lunar clinopyroxenes (Green, 1976a) found that after "long run times" the initial clinopyroxene pair was metastable, forming instead an orthopyroxene (Wo_5) and a Ca-rich clinopyroxene (Wo_{30}). Furthermore, when plotted onto the pyroxene quadrilateral the equilibrium compositions do not fall along a line passing through the metastable points. Instead, the tie line connecting the equilibrium pair is rotated such that the orthopyroxene is slightly more Fe-rich and the clinopyroxene more Mg-rich than anticipated from the metastable compositions. Similar contents of non-quadrilateral components were found in the Ca-rich pyroxene as in the metastable phases while the orthopyroxene contained lower comparative amounts, the difference forming a small amount of spinel. Another study which documents the difficulties in precipitating equilibrium Ca-rich and Ca-poor pyroxenes can be found in Green et al. (1979).

It is concluded from the above observations and discussion that pyroxene laths from the olivine-bearing experiments are metastable pigeonites crystallizing instead of an orthopyroxene and Ca-rich clinopyroxene pair. The wide range of Wo contents is itself an effect of disequilibrium crystallization which overprints the composition of the metastable pigeonite. The olivine compositions were used as a "set point" to evaluate the possible equilibrium nature of the pigeonite. In the absence of olivine in the 10 kbar runs, the identification of the pyroxene as a metastable pigeonite forming in place of Ca-rich and Ca-poor pyroxene pairs can only be inferred from the similarities to the chemical trends observed in runs at the lower pressures.

It is clear that the analytical data obtained from the metastable pigeonite cannot be applied directly to the interpretation of pyroxenes crystallized in the natural rocks. The Fe/Mg of the orthopyroxene and clinopyroxene pair which should have crystallized in the place of the metastable pigeonite can be calculated from the Fe/Mg of the coexisting olivines. This was accomplished by first calculating the theoretical orthopyroxene Fe/Mg using $K_{D_{ol/opx}}^{Fe/Mg} = 1.1$, and the resulting value plotted onto Lindsley's graphical thermometer at the appropriate pressure and temperature. The equilibrium clinopyroxene Fe/Mg was obtained by interpolating the slope of a tie line from adjacent pairs defined on the diagrams. The predicted compositions are listed in Table 1.15.

TABLE 1.15
CALCULATED COEXISTING PYROXENE COMPOSITIONS : 65206

RUN	T1845	T1669	T1694	T1662
P (kbar)	4	5	7.5	10
T (^{o}C)	1110	1140	1170	1200
OLIV: MG#	62.4	66.1	67.7	-
OPX : MG#	64.6	68.2	69.7	73.0
WO	4	4	4	4
CPX : MG#	66	72	74	77
WO	34	34	33	32

MG# = 100 MG/(MG+FE) WO = 100 CA/(CA+MG+FE)

In the absence of olivine, the compositions of the coexisting pyroxenes at 10 kbar, 1200°C were obtained directly from Lindsley's diagram. The compositions listed in Table 1.15 are the minimum possible Mg-values for the run conditions, but in the case of the orthopyroxene this value (Mg# 73.2) agrees well with Mg# 72.0 calculated using a crystal/liquid K_D = 0.30. The calculated coexisting pyroxene compositions will be applied to the phenocrysts of sample 206 in the following section.

Sample 206: Clinopyroxene

Clinopyroxene* coexisting with plagioclase ± olivine is the dominant phenocryst assemblages in nearly all members of the 1360 Ma tholeiite suite, including sample 206. Experimental liquids saturated in this assemblage exist only within a restricted pressure-temperature region which has a maximum stability of 5-6 kbar in the studied sample (Fig. 1.13). The quadrilateral components of the pyroxenes from the three experiments which define the boundaries of this field are plotted in Fig. 1.19. The clinopyroxene (and glass) analyses from the 1 atmosphere and 4 kbar runs fall within a relatively tight grouping in terms of the quadrilateral pyroxene components, while a considerable amount of chemical scatter exists in the 2.5 kbar run (1090°C). The averaged clinopyroxene composition from each experiment is listed in Table 1.16.

The Al_2O_3 content of clinopyroxene in equilibrium with plagioclase is known to be pressure-sensitive, and increases with pressure. Although this is an important relationship in the context of the present study, it is difficult to apply here due to the wide range of Al_2O_3 contents in both the experimental and natural clinopyroxenes. The concentration of Al_2O_3 in the clinopyroxene analyses of the 2.5 and 4.0 kbar runs varies by more than 1%. Similarly, a range of over 2% Al_2O_3 exists in the natural clinopyroxene phenocrysts, with no tendency to cluster about a particular concentration. If it is assumed that the average of the clinopyroxene analyses of each experiment is representative of the pressure effect on the Al_2O_3 concentration, then this effect is small over the 4 kbar range as Al_2O_3 increases by only 0.5%. This insensitivity and the wide range of Al_2O_3 in the natural phenocrysts limit the usefulness of the Al_2O_3 content of the pyroxenes as a pressure indicator.

---

* Clinopyroxene refers to calcic clinopyroxene.

Figure 1.19

Phase composition of Ca-rich clinopyroxene-bearing experiments plotted onto the pyroxene quadrilateral. Solid circle - clinopyroxene; open circle - olivine; square - starting composition; triangle - glass.

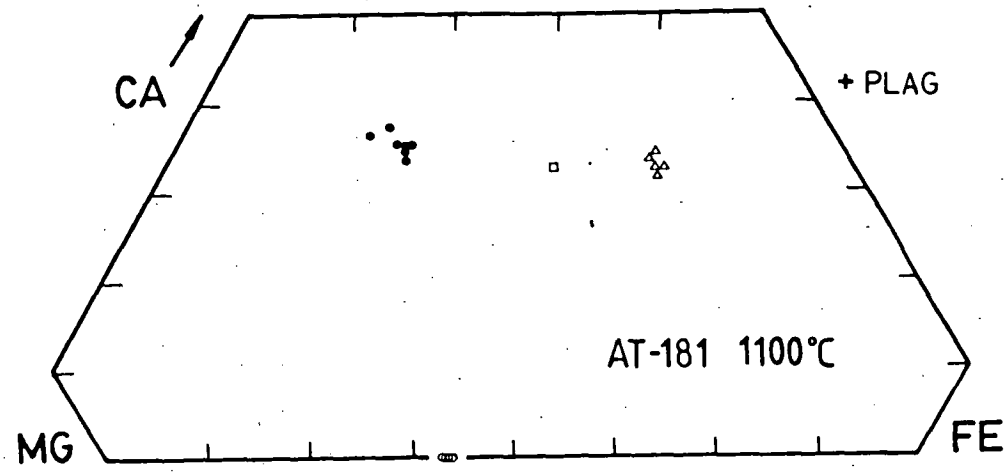
CA
+ PLAG
AT-181 1100°C
MG
FE

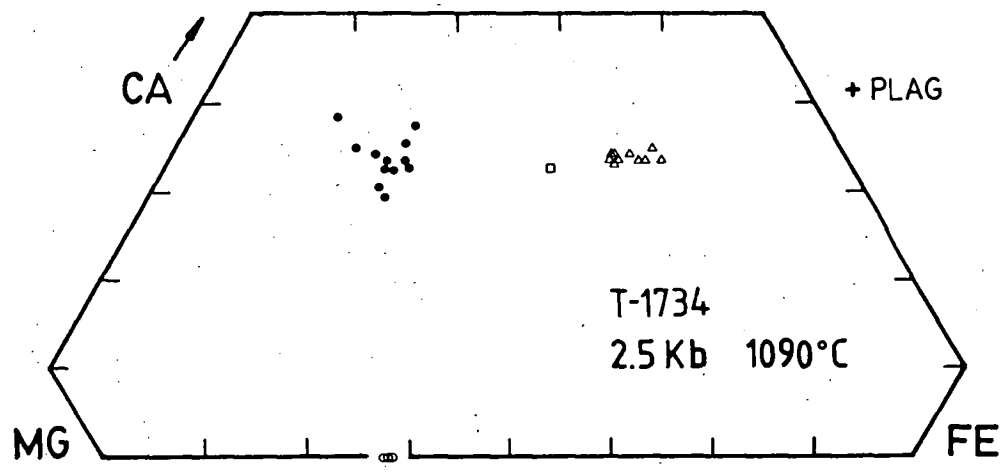
CA
+ PLAG
T-1734
2.5 Kb 1090°C
MG
FE

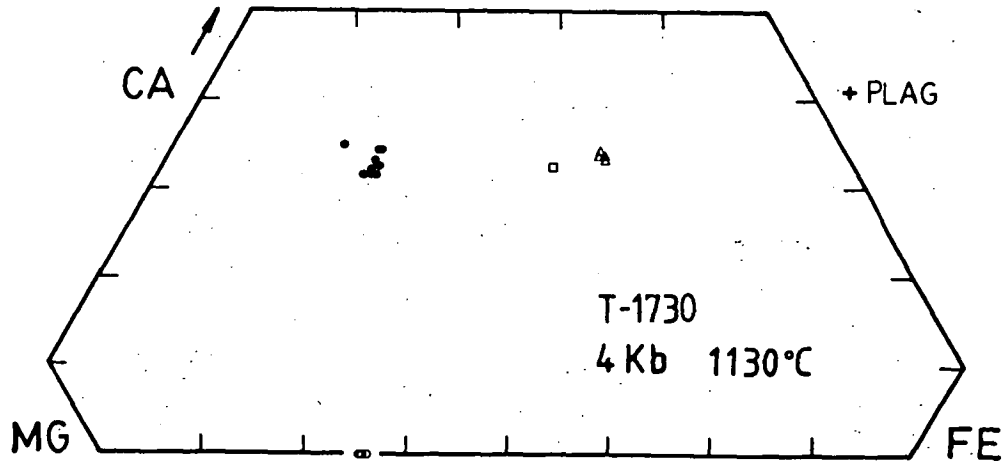
CA
+ PLAG
T-1730
4 Kb 1130°C
MG
FE

TABLE 1.16

AVERAGED HIGH CALCIUM CLINOPYROXENES : SAMPLE 65206

RUN NO.	AT-181	T-1734	T-1730
PRESS.(kbar)	0	2.5	4.0
TEMP.(°C)	1100	1090	1130
PHASE	CPX	CPX	CPX
SIO2	51.56	51.30	51.66
TIO2	1.19	1.20	1.22
AL2O3	1.64	1.96	2.05
FEO	13.17	13.14	12.51
MNO	Nd	Nd	Nd
MGO	15.16	15.90	16.49
CAO	17.28	16.50	16.07
SI	1.9342	1.9208	1.9246
TI	0.0336	0.0338	0.0343
AL	0.0725	0.0865	0.0900
FE	0.4132	0.4115	0.3897
MN			
MG	0.8480	0.8877	0.9161
CA	0.6946	0.6620	0.6416
TOT	3.9961	4.0022	3.9963
MG#	67.2	68.3	70.2
range	71.8-65.3	77.9-64.8	75.3-67.8
CA*	35.5	33.8	32.9
range	37.4-33.3	38.9-29.4	35.0-31.4

100MG/(MG+FE)

* 100CA/(CA+MG+FE)

Nd = Not detected

A comparison between natural and experimental clinopyroxene Mg-values with respect to pressure is illustrated in Fig. 1.20B. As in the plagioclase comparison (Fig. 1.15B) the boundaries of the phase fields have been superimposed onto the diagram. The square symbols represent the calculated compositions obtained in the previous section, while the triangles are averaged experimental analyses. Note that in this diagram, the averaged clinopyroxene values differ slightly from those reported in Table 1.16 as clearly anomalous analyses have been omitted here.

With one exception, the Mg-value distribution of the phenocrysts falls within the range of compositions predicted to co-precipitate with olivine and plagioclase at pressure ~4-5 kbar. This observation, coupled with the dominant clinopyroxene + plagioclase ± olivine assemblage in the 1360 Ma suite in general provides strong evidence that the pressure prevailing during the emplacement and crystallization of the studied dyke was less than the multiple saturation point at 5-6 kbar.

This conclusion is not entirely definitive as equivalent compositions could be produced at higher pressure, but at temperatures well below the "clinopyroxene-in" boundary. The single $Mg_{79.2}$ analysis is evidence for at least some crystallization of clinopyroxene at pressures above 5-6 kbar from either this composition or a more Mg-rich liquid. However, the absence of extensive chemical zoning within the natural clinopyroxene phenocrysts suggests they precipitated under a narrower range of temperatures. Also, crystallization of the studied composition at pressures above 5-6 kbar must be accompanied by co-precipitation of orthopyroxene. The rarity of orthopyroxene phenocrysts in sample 206 implies extensive crystallization of clinopyroxene did not occur at pressures above 5-6 kbar.

Sample 206: Orthopyroxene

Calculated experimental orthopyroxene compositions are plotted in Fig. 1.20A, and define a boundary representing the most Mg-rich orthopyroxene composition that can crystallize at pressures less than 10 kbar. The precise location of the boundary is somewhat arbitrary in that the boundary is not bracketed by coupled experiments. Consequently, the most Mg-rich orthopyroxene phenocryst composition ($Mg_{72.2}$) may lie below, or above the multiple saturation point at 5-6 kbar depending on the selected geometry. However, at least four of the phenocryst analyses (N = 5) can be interpreted to have crystallized at pressures less than the

Figure 1.20A

Variation in the calculated orthopyroxene compositions (see text) with pressure. Heavy line marks the maximum Mg/(Mg+Fe) content of orthopyroxene to crystallize from sample 206 interpreted from the average orthopyroxene compositions and Fig. 1.13. Dashed lines represent analyses from the single orthopyroxene phenocryst of 206 (Fig. 1.2B).

Figure 1.20B

Variation in the Mg/(Mg+Fe) content of clinopyroxene with pressure. Square symbols are calculated compositions (see text) in equilibrium with orthopyroxene. Triangles are averaged compositions from clinopyroxenes in equilibrium with olivine and plagioclase. Dashed lines mark compositions of the natural clinopyroxene phenocrysts.

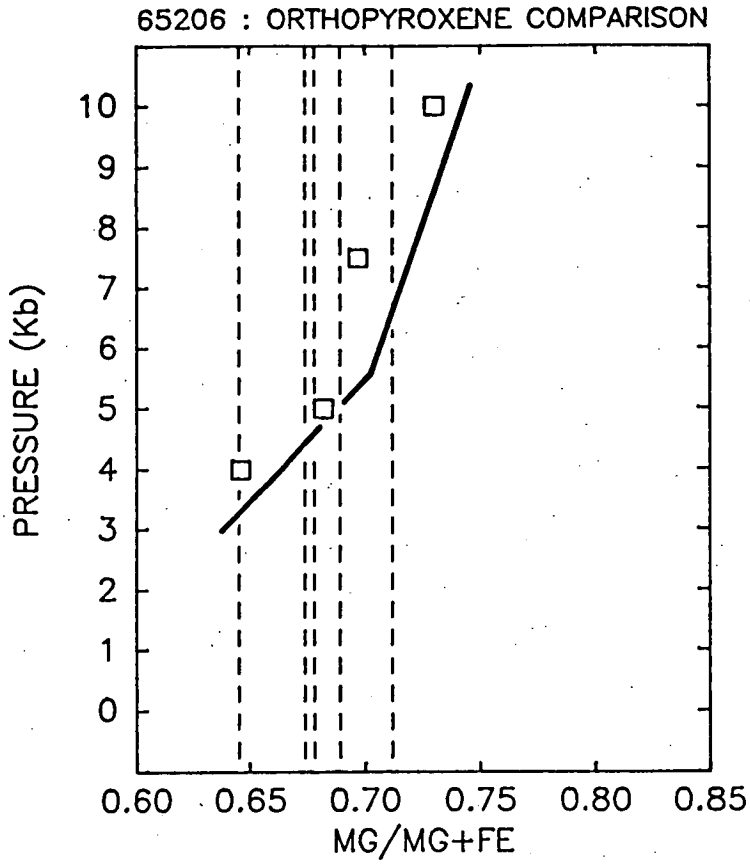
65206 : ORTHOPYROXENE COMPARISON
PRESSURE (Kb)
10
9
8
7
6
5
4
3
2
1
0
0.60
0.65
0.70
0.75
0.80
0.85
MG/MG+FE

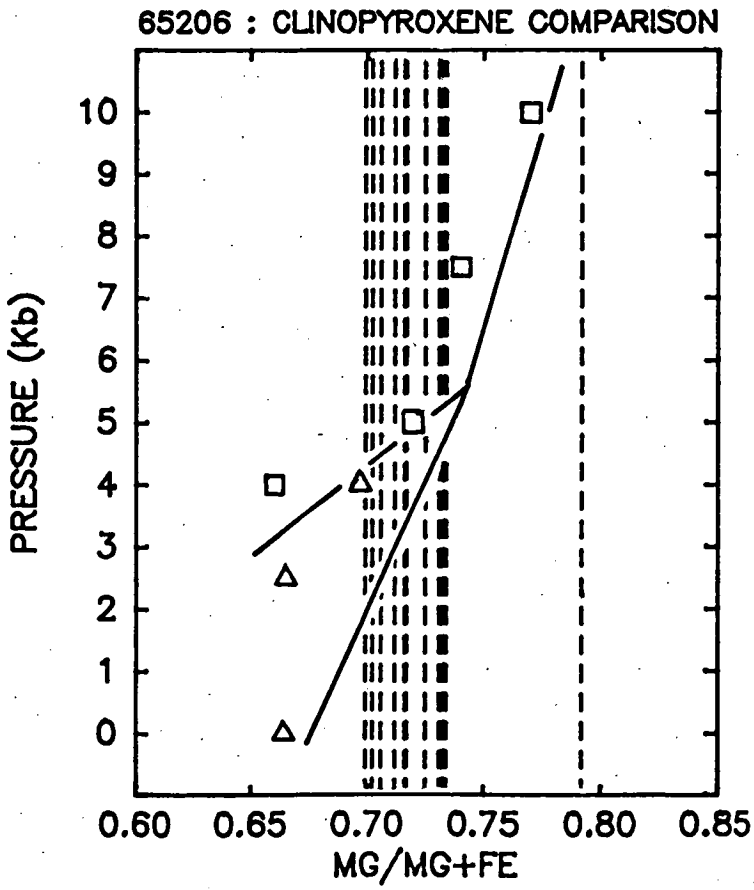
65206 : CLINOPYROXENE COMPARISON
PRESSURE (Kb)
10
9
8
7
6
5
4
3
2
1
0
0.60
0.65
0.70
0.75
0.80
0.85
MG/MG+FE

multiple saturation point at 5-6 kbar. It follows then that the most Mg-rich phenocryst composition records an early stage of crystallization at higher pressures.

Based solely on the comparison of Fig. 1.20A, it is not possible to place any limits on the pressures at which the orthopyroxene phenocrysts crystallized. The Al_2O_3 content of the experimental orthopyroxene, as well as the coexisting clinopyroxene, would be very useful in this respect, but the method by which the Mg-values of these phases were obtained does not permit the Al_2O_3 contents of either phase to be predicted.

Sample 206: Spinel

Fe-Mg spinels have been found in the run products of three experiments: T1669, T1694 and T1845. In all observations, the spinels formed the core to plagioclase aggregates, as in sample 060. Analyses of two grains are given below, but will not be discussed further.

Table 1.17
SPINEL ANALYSES: SAMPLE 206

RUN	T1694	T1669
P (kbar)	7.5	5
T (°C)	1170	1140
TIO2	0.58	
AL2O3	64.19	66.13
FEO	19.78	18.71
MGO	15.45	15.16

1.4 CONCLUSIONS

1.4.1 METHODOLOGY

The most difficult problem encountered in this study was the precipitation of metastable pigeonite in the place of coexisting orthopyroxene and clinopyroxene in sample 206. To some extent this was circumvented by calculating the Fe/Mg of the potential orthopyroxene-clinopyroxene pair from the coexisting olivine, once the metastable nature of the pigeonite was recognized. The lack of pressure-sensitive Al_2O_3 data from the calculated equilibrium pair is a handicap, and could have been useful particularly in the orthopyroxene comparison. If detailed reproduction of a two-pyroxene natural assemblage is required in any future studies, additional steps in the experimental procedure will be required to force the precipitation of coexisting orthopyroxene and clinopyroxene. This would probably involve the addition of pyroxene "seed" crystals as part of the starting composition. Additional problems that may appear as the result of this step include the incomplete reaction of the seeds resulting in a modification of the starting composition, and difficulties in forming equilibrium crystals, or rims on seeds, large enough to distinguish from any incompletely reacted seed compositions.

A range of ~0.8-1.0% Al_2O_3 does occur within the pyroxene analyses from individual experiments as well as some scatter of Fe/Mg. Calculating the "average pyroxene" for each experiment seems to be a legitimate method to circumvent the minor disequilibrium features as a near-perfect correlation between experimental pressure and Al_2O_3 content of the averaged pyroxenes can be obtained through this procedure. Additionally, averaged clinopyroxene and pigeonite analyses from the 1 atmosphere experiments of sample 060 reproduce the experimental temperatures when applied to the Lindsley graphical thermometer whereas individual analyses scatter over several hundred degrees.

Even though the experimental pyroxene compositions suffer from minor disequilibrium effects of the Al_2O_3 content, this effect is minor compared with the range of Al_2O_3 from the natural phenocrysts. This difference was considered the result of an essentially static experimental system being compared with the dynamic natural system where the physical parameters which influence the phase chemistry are not constant. In this respect, the minimum Al_2O_3 contents of the natural pyroxene were considered the closest approach to equilibrium values.

The effects of iron addition were found to be negligible as applied to the positioning of the phase boundaries, and the compositions of the

precipitating phases. In the higher temperature system of sample 060, the movement of the liquidus and phase geometry was monitored by reproducing selected Fe-capsule experiments (Fe-gain) with Pt-capsule (Fe-loss). The resulting difference in the positioning of the phase boundaries was found to be within the range of experimental error of the pressure-temperature determinations of the experimental apparatus. Iron gain did not affect the most Mg-rich olivine compositions in the 1 atmosphere experiments, although high pressure liquidus olivines did adjust to slightly higher Fe/Mg ratios. Subliquidus high pressure olivine experienced negligible exchange.

1.4.2 EMPLACEMENT PRESSURE OF SAMPLE 060

The liquidus phase relations determined by high pressure experimental studies indicate that the dyke from which sample 060 was collected was emplaced at pressures of 7-8 kbar. Several lines of evidence point to this conclusion. The experimental assemblage produced at 7.5 kbar, 1270°C matches the phenocryst assemblage of the natural rock: orthopyroxene and olivine. More importantly, the CaO and Fe/Mg ratio of the liquidus orthopyroxene at 7.5 kbar is essentially identical to the phenocryst pyroxene composition, while at lower pressure the pyroxene which coexists with olivine is a pigeonite. A comparison of the Al_2O_3 contents of the orthopyroxene phenocrysts with the pressure-dependent Al_2O_3 content of the experimental low-Ca pyroxenes is not definitive, but clearly indicates pressures of >5 kbar.

The experimental liquidus orthopyroxene crystallized at ~1270°C. This is identical, within experimental error, to the predicted crystallization temperatures of the natural orthopyroxene phenocrysts (1300°C) using the Lindsley thermometer (Table 1.3). The pressure calculated from the groundmass mineralogy of sample 060 (8 kbar; Table 1.4) also agrees readily with the experimental determinations of emplacement conditions (7-8 kbar).

1.4.3 EMPLACEMENT PRESSURE OF SAMPLE 206

It is concluded from the experimental study of sample 206 that the dyke from which this sample was collected crystallized at pressures of 4-5 kbar. This estimate was derived from the following observations. As the natural phenocryst assemblage is olivine-bearing, the maximum emplacement pressure is the upper limit of olivine stability: 8 kbar. The dominant

mineralogy of the Fe-tholeiite suite, in general, is olivine-clinopyroxene-plagioclase, only sample 206 contains orthopyroxene which is rare. Based on the experimentally determined phase relations of sample 206, the general petrography of the suite suggest emplacement at pressures <5-6 kbar.

The most calcic plagioclase phenocryst compositions are inconsistent with having crystallized at pressures above 5-6 kbar. Nucleation in the olivine + plagioclase stability field is indicated, with normal zoning produced during cooling. The slightly more sodic rim compositions are consistent with crystallizing in the olivine + plagioclase + clinopyroxene field.

With one exception, the range of Mg-values of the clinopyroxene phenocrysts in the natural rock falls directly within the experimentally-defined field of clinopyroxene compositions which coexists with olivine and plagioclase in the absence of orthopyroxene and suggests emplacement pressures of 4-5 kbar. The narrow range of clinopyroxene Mg-values is inconsistent with extensive subliquidus crystallization at higher pressures.

Little detailed information could be gained from the comparison of natural and synthetic orthopyroxene as the experimental composition was calculated from coexisting olivines. However, the calculated Mg-values are not inconsistent with crystallization at pressures <5-6 kbar.

Crystallization of sample 206 into the orthopyroxene stability field at 4-5 kbar indicates temperatures in the range of 1120-1140^{o}C (Fig. 1.13). This compares well with the temperature of 1160^{o}C calculated on the average orthopyroxene-clinopyroxene phenocryst compositions (Section 1.1.3). Additionally, the calculated emplacement pressure based on the groundmass mineralogy of sample 206 (5 kbar, Table 1.6) is also consistent with the emplacement conditions determined through the high pressure studies (4-5 kbar).

CHAPTER 2

THE EMPLACEMENT PRESSURES OF SEVERAL EAST ANTARCTIC DYKE SUITES ESTIMATED FROM THE EXPERIMENTAL STUDIES OF VESTFOLD HILLS DYKE COMPOSITIONS

INTRODUCTION

One reason petrologists continue to conduct high pressure studies on mafic rocks is that liquidus phase geometries and compositions of precipitating phases cannot as yet be confidently predicted from previously studied samples. This is due to the complex interplay of major variables such as FeO + MgO and silica saturation as well as the minor components H_2O, K_2O, Na_2O and TiO_2, CO_2, P_2O_5. The oxides composing the latter two groups play major, but opposing, roles in modifying melt structure which in turn affects the relative stability of olivine and orthopyroxene liquidus phase fields (Kushiro, 1975).

In the discussion which follows, results from the experimental studies of the Vestfold Hills samples 060 and 206 will be applied to selected samples from Napier Complex dyke swarms in order to estimate their emplacement conditions. In order to minimize the effect of compositional variation on phase relations, only representative samples which closely resemble the studied compositions are interpreted. An estimate of the emplacement pressure for the 1800 Ma suite in the Vestfold Hills is also discussed. The projection methods used in this chapter are applied only to the estimation of emplacement pressures of selected dyke compositions, petrogenetic implications will be discussed in Part 2.

2.1. ESTIMATION OF EMPLACEMENT PRESSURES

2.1.1 HIGH-Mg THOLEIITES (ca.2400 Ma) - NAPIER COMPLEX

Of particular importance in predicting the emplacement pressures of samples belonging to the high-Mg tholeiite suite is the location of the olivine/orthopyroxene liquidus phase boundary. For the olivine + orthopyroxene phyric sample 060, this boundary was experimentally located at 7-8 kbar. Olivine is not observed in any Napier Complex high-Mg tholeiite samples (see also Sheraton & Black, 1981) suggesting that these dykes were emplaced at pressures greater than the olivine/orthopyroxene saturation point for their compositions. However, the Vestfold Hills and Napier Complex suites may not be directly comparable as Napier Complex samples which have similar Mg-values to sample 060 are quartz normative, a feature which would have the effect of expanding the orthopyroxene stability field to lower pressure. The one Napier Complex sample which does have a similar degree of silica saturation to sample 060 has a higher Mg-value (72 vs 65). Fortunately, several experimental studies on rocks similar in composition to sample 060 have been reported, and can assist in estimating the emplacement pressure of the Napier Complex high-Mg tholeiite suite.

Listed in Table 2.1 are the compositions of Mg-rich basalts which have been studied under high pressure conditions, and the pressure at which liquidus two-phase saturation was determined for each sample. These compositions have been projected into the basalt tetrahedron (Fig. 2.1) following the method of Green (1970). Jaques & Green (1980) used this projection method to illustrate the trend of liquid compositions produced by increasing degrees of partial melting from selected peridotitic sources.

Melts produced at constant pressure in equilibrium with olivine and orthopyroxene were found to roughly parallel the (An + Ab) - Hyp join and move towards more siliceous compositions at lower pressure. In keeping with this trend, olivine/orthopyroxene cotectics, defined by the two-phase saturation pressures of the individual Mg-rich basalt compositions, have been drawn slightly oblique to the (An + Ab)- Hyp tie line (Fig. 2.1). In the same manner, the Mg-rich basalt compositions projected from plagioclase* onto the face olivine-diopside-quartz illustrate the relative

---

* Projection method calculated from molecular norm. Qtz = Qtz + Hyp; Cpx = Diop; Oliv = Oliv + Hyp. (Falloon, pers. comm.)

TABLE 2.1
COMPARISON OF MG-RICH BASALT COMPOSITIONS

LOCATION	VESTFOLD	TROODOS[1]	PILBARA[2]	BUSHVELD[3]	NAPIER
NUMBER	65060			4	3793[4]
SIO2	52.59	52.27	55.72	55.67	51.91
TIO2	0.62	0.30	0.43	0.36	0.43
AL2O3	11.95	11.67	11.82	12.73	12.05
FE2O3	0.00	0.00	0.00	0.00	0.00
FEO	10.87	8.38	9.32	8.70	10.04
MNO	0.18	0.15	0.22	0.09	0.20
MGO	11.28	15.76	12.23	12.44	14.51
CAO	10.02	10.67	7.82	6.96	9.51
NA2O	1.79	0.70	1.92	2.02	0.90
K2O	0.60	0.10	0.48	1.03	0.40
P2O5	0.10		0.04		0.05
TOTAL	100.00	100.00	100.00	100.00	100.00
MG#	64.9	77.0	70.1	71.8	72.0
WT% CIPW NORMATIVE MINERALS					
QTZ			3.70	2.01	
OR	3.55	0.59	2.84	6.09	2.36
AB	15.15	5.92	16.25	17.09	7.62
AN	22.80	28.41	22.22	22.62	27.66
CPX	21.46	19.72	13.25	9.64	15.54
OPX	32.27	44.36	40.84	41.86	43.71
OL	3.36	0.42			2.18
IL	1.18	0.57	0.82	0.68	0.82
AP	0.24		0.09		0.12
PROJECTION COORDINATES-MOLE%					
JD+CATS	23.9	18.8	19.8	20.6	19.1
QTZ	48.1	49.8	54.3	52.4	49.0
OLIV	28.0	31.4	25.9	27.0	31.9
QTZ	35.2	41.0	50.3	49.0	41.4
CPX	24.0	17.5	11.9	9.3	14.3
OLIV	40.8	41.5	37.8	41.7	44.3
OLIV/OPX SATURATION (kbar)	7-8	7-8	~6	6-8	

1-DUNCAN AND GREEN (1980), AND SUBMITTED; 2-GREEN (1981); 3-CAWTHORN AND DAVIS (1983); 4-AUSTRALIAN BUREAU OF MINERAL RESOURCES SAMPLE NUMBER: PREFIXED BY 7728- (SHERATON 1981)

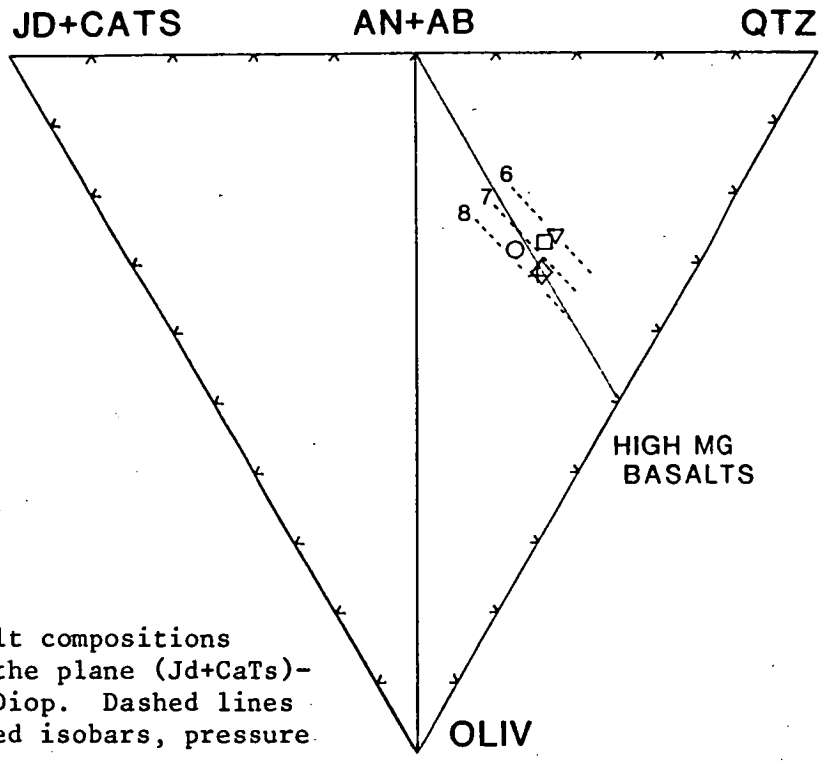

Figure 2.1
High-Mg basalt compositions projected onto the plane (Jd+CaTs)-Oliv.-Qtz from Diop. Dashed lines indicate proposed isobars, pressure in kbar.

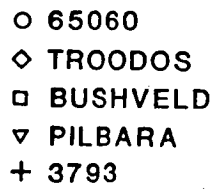

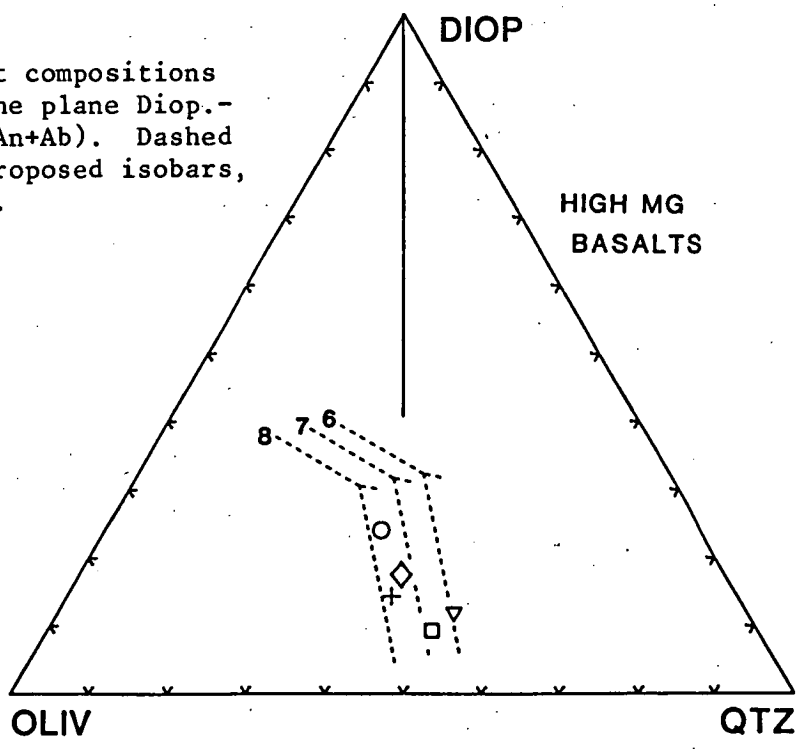

Figure 2.2
High-Mg basalt compositions projected onto the plane Diop.-Oliv.-Qtz from (An+Ab). Dashed lines indicate proposed isobars, pressure in kbar.

positions of these compositions in the third dimension of the basalt tetrahedron, that is, towards the clinopyroxene apex. (Fig. 2.2).

Olivine/orthopyroxene cotectics interpreted as being subparallel to the Hyp-Diop tie line are also indicated, and are consistent with the positions shown in Fig. 2.1. Both of these constructions result in pressure predictive grids at which liquids, compositionally similar to those employed in the diagrams, will be saturated in both olivine and orthopyroxene. The olivine normative high-Mg sample from the Napier Complex (3793) is assessed in this context.

Sample 3793 is a chilled margin which has experienced static recrystallization though the fine grained metamorphic assemblages has not disturbed the original igneous texture. The sample is dominated by a meshwork of "quench" pyroxene crystals, with some grains still preserving hollow cross sections and swallowtail terminations, set in a very fine grained intersertal matrix (Fig. 2.5). Many of the orthopyroxene phenocrysts are recrystallized, though some may retain castellated terminations. The phenocrysts account for <2% of the sample (estimated).

The petrography indicates sample 3793 should closely approach a liquid composition which, based on the projected position in Figs 2.1 and 2.2, will be saturated in olivine and orthopyroxene at pressures of 7-8 kbar. As this sample lacks olivine, 7-8 kbar is the minimum emplacement depth of the dyke.

2.1.2 Fe-RICH THOLEIITES (ca.1200 Ma) - NAPIER COMPLEX

The method used to compare the Fe-rich tholeiites of Enderby Land to sample 206 was intended to be the same as that used for the high-Mg tholeiites. However, unlike the comparison between the high-Mg tholeiites where several experimental studies on compositionally similar samples were available, very few studies of Fe-rich tholeiites (anhydrous conditions) have been published. Six studies, including three lunar samples were found, but these compositions exhibit a broad range of silica saturation (18% Ol - 3% Qtz) and total alkalies (0.28% - 3.40%). When projected into the basalt tetrahedron, inconsistencies in the configuration of the olivine/pyroxene cotectics resulted. For example, both samples 206 and 395A (Table 2.2) are saturated in olivine-orthopyroxene-clinopyroxene at ~8 kbar. Although multiple saturation occurs at similar pressures these compositions plot at widely different coordinates in the clinopyroxene and especially the plagioclase projections, and in positions which would suggest multiple saturation at quite different pressures (Fig. 2.3 & 2.4).

TABLE 2.2
COMPARISON OF FE-RICH THOLEIITE COMPOSITIONS

LOCATION	VESTFOLD	NAPIER[1]	NAPIER[2]	NAPIER[2]	NAPIER[1]	MORB[3]
NUMBER	65206	49590	4079	4659	49520	395A
SUITE		GP 1	GP 1	GP 2	GP 2	
SIO2	49.45	50.17	50.03	52.07	52.44	50.06
TIO2	2.25	2.35	2.19	1.18	0.97	1.64
AL2O3	13.91	13.43	14.47	13.68	12.27	15.02
FE2O3	0.00	0.00	0.00	0.00	0.00	0.00
FEO	14.89	14.08	13.50	13.27	16.81	11.21
MNO	0.26	0.19	0.20	0.21	0.23	0.22
MGO	6.55	6.45	5.91	6.08	4.86	8.41
CAO	10.03	10.10	9.83	10.31	9.88	10.61
NA2O	1.95	2.14	2.79	2.52	2.17	2.70
K2O	0.45	0.81	0.81	0.56	0.30	0.13
P2O5	0.26	0.27	0.26	0.12	0.07	0.00
TOTAL	100.00	100.00	100.00	100.00	100.00	100.00
MG#	44.0	45.0	43.8	45.0	34.0	57.2
WT% CIPW NORMATIVE MINERALS						
QTZ					2.46	
OR	2.66	4.79	4.79	3.31	1.77	0.77
AB	16.50	18.11	23.61	21.33	18.36	22.85
AN	27.87	24.65	24.57	24.36	22.86	28.48
CPX	16.92	19.82	18.86	21.81	21.90	19.89
OPX	28.95	24.82	13.54	25.69	30.63	12.38
OL	2.21	2.71	9.86	0.98		12.51
IL	4.27	4.46	4.16	2.24	1.84	3.11
AP	0.62	0.64	0.62	0.28	0.17	
PROJECTION COORDINATES-MOLE%						
JD+CATS	27.8	29.0	33.7	30.1	25.5	33.6
QTZ	48.9	48.5	44.6	49.5	53.4	43.3
OLIV	23.2	22.5	21.7	20.5	21.2	23.1
QTZ	37.2	33.8	22.7	34.4	43.3	20.1
CPX	21.8	27.2	32.0	29.4	24.0	32.0
OLIV	41.0	39.0	45.3	36.2	32.8	47.9

1-UNIVERSITY OF TASMANIA SAMPLE NUMBERS
2-AUSTRALIAN BUREAU OF MINERAL RESOURCES SAMPLE NUMBERS:
PREFIXED BY 7728- (SHERATON 1981)
3-FUJII AND KUSHIRO (1977)

The most important chemical difference responsible for this variation is the higher Al_2O_3 and $Na_2O + K_2O$ in sample 395A. These features result in higher normative olivine as well as a greater proportion of total feldspar than sample 206. Variations in Fe/Mg do not affect the relative positions of the projected points as the norm calculation combines Fe+Mg (contrast the saturation pressures of 060 and Troodos versus Fe/Mg). The grossly different positions of these Fe-rich tholeiite compositions in the Di-Ol-Qtz diagram is due largely to the method of projection. Because plagioclase is not at an apex of the basalt tetrahedron, an orthogonal relationship does not exist between a projection from plagioclase to the centre of the Di-Oliv-Qtz plane. Additionally, both 206 and 395A plot nearer plagioclase than the Di-Oliv-Qtz plane. These factors result in the compositional differences between 206 and 395A, particularly the variation in the normative olivine, to be greatly exaggerated in the plagioclase projection. Thus, projected positions of multiple saturation points from a spectrum of Fe-rich basalt compositions are difficult to assess in terms of predicting emplacement pressures of Fe-rich basalts from the East Antarctic Shield.

Fortunately, compositions exist in both the group 1 and group 2 tholeiite suites of the Napier Complex (Sheraton & Black, 1981) which closely resemble sample 206, and allow a direct comparison with the experimental results of sample 206.

Group 1 tholeiites

The projected position of the group 1 sample 49590 (Table 2.2) onto the Qtz-Oliv-(Jd+CaTs) diagram (Fig. 2.3) is nearly identical to that of sample 206, suggesting liquidus olivine/orthopyroxene saturation should occur at a pressure comparable to that of sample 206. But the slightly lower Al_2O_3 in sample 49590 results in a higher proportion of normative diopside than sample 206, as illustrated in the plagioclase projection (Fig. 2.4). It is difficult to decide exactly what significance this has on the positioning of multiple saturation boundaries in the plagioclase projection considering the discussion of sample 395A. However, judging from the remarkable overall similarity in composition between samples 206 and 49590 (Table 2.2) a significant difference in the pressure of olivine/pyroxene saturation is not expected.

Although samples 206 and 49590 are very similar chemically, there is a dramatic petrographic difference between these two samples (Figs 2.6 and 2.7). Sample 206 is dominated by phenocrysts of olivine-clinopyroxene-plagioclase whereas sample 49590, which is also a chilled margin, contains

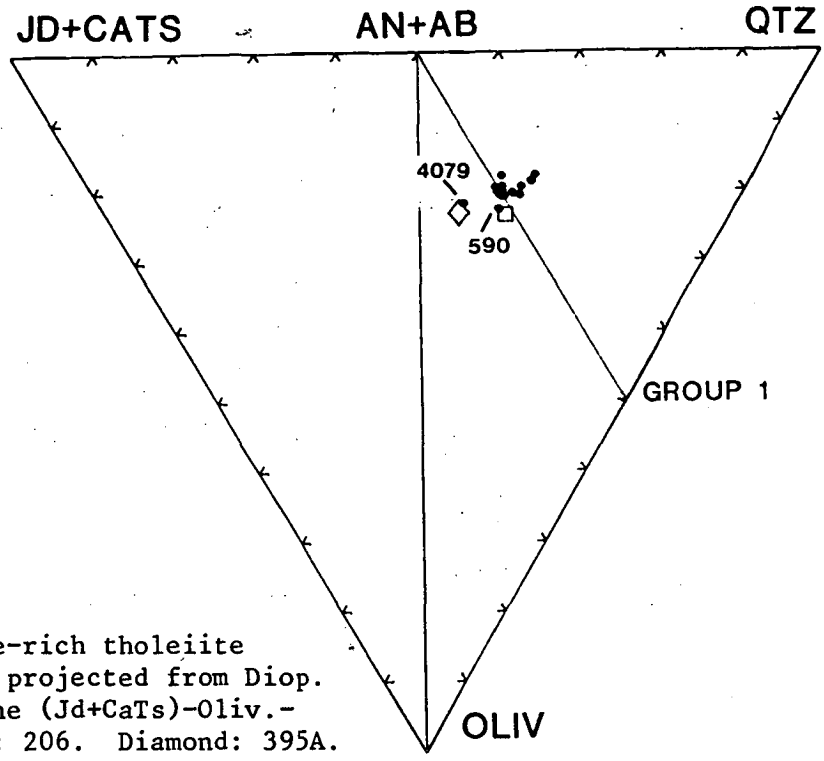

Figure 2.3
Group 1 Fe-rich tholeiite compositions projected from Diop. onto the plane (Jd+CaTs)-Oliv.-Qtz. Square: 206. Diamond: 395A.

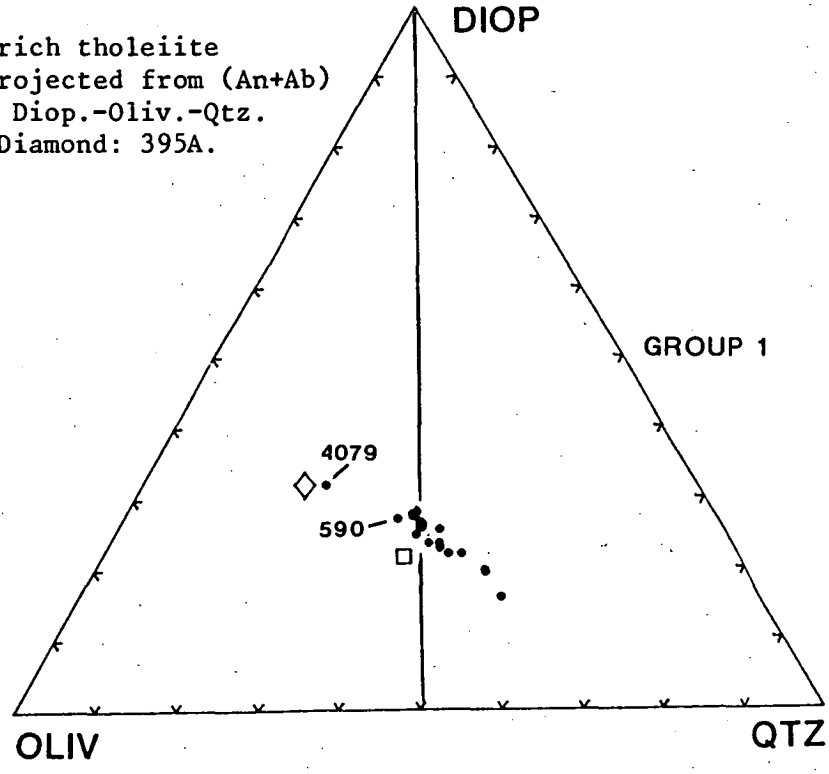

Figure 2.4
Group 1 Fe-rich tholeiite compositions projected from (An+Ab) onto the plane Diop.-Oliv.-Qtz. Square: 206. Diamond: 395A.

Figure 2.5
Napier Complex high-Mg tholeiite 3793. Two orthopyroxene phenocrysts (centre) in mat of recrystallized quench pyroxene. Note hollow cross-sections. Red material is secondary biotite. Long dimension: 3.5 mm.

Figure 2.6
Napier Complex group 1 tholeiite 49590. Intergrown clots of co-precipitating orthopyroxene (brown), clinopyroxene (dusty) and plagioclase (colourless). Compare with Fig. 2.7 below. Long dimension: 4.0 mm.

Figure 2.7
Vestfold Hills sample 206. Chemically similar to 49590 (above) but has phenocrysts of olivine (altered, upper left) intergrown clinopyroxene and plagioclase, and one orthopyroxene (lower left). Long dimension: 4.0 mm.

individual and glomerocrysts of clinopyroxene, orthopyroxene and plagioclase. Importantly, there is no evidence of olivine in sample 49590. This phenocryst assemblage is consistent with sample 49590 having crystallized at pressures above the upper stability limit of liquidus olivine, and implies emplacement pressures $\geq$8 kbar, based on the phase relations of sample 206.

Another group 1 sample, 4079 (Table 2.2), contains higher Al_2O_3 and total alkalies than sample 49590 and accordingly has higher normative olivine. Significantly, this sample lacks orthopyroxene, and is clinopyroxene + plagioclase phyric. Small, altered relics of olivine can be located as inclusions in clinopyroxene crystals. Assuming all group 1 dikes were emplaced under similar load pressures, the phenocryst assemblage of this group 1 sample indicates the high pressure limit of the olivine + clinopyroxene + plagioclase phase field has expanded to ~8 kbar in this composition compared to 5.5 kbar in the less saturated sample 206 (Fig. 1.13). In support of this prediction, it is relevant to note that the major element composition (excluding Fe/Mg) and normative mineralogy of 4079 closely resembles that of sample 395A (Table 2.2) which was shown to be multiply saturated in olivine + orthopyroxene + plagioclase at ~8 kbar (see Figs 2.3 & 2.4; Fujii & Kushiro, 1977).

Group 2 tholeiites

The group 2 sample, 4659 (Table 2.2), has higher SiO_2 than sample 206 (52.06 vs 49.45) though the effect of this on silica saturation is offset by sample 4659 also having higher total alkalies. Consequently, the resulting coordinates are only marginally different from sample 206 in the clinopyroxene projection (Fig. 2.8), while the slightly higher alkalies and CaO in sample 4659 result in higher normative diopside in the plagioclase projection (Fig. 2.9). Unfortunately, sample 4659 is not a chilled margin sample, but instead has a medium grained doleritic texture and therefore may not represent a liquid composition. Even if this sample had accumulated a small amount of clinopyroxene (olivine is rare), the plagioclase projection indicates the unmodified liquid composition would plot closer to that of sample 206. Petrographically all olivine normative members of the group 2 suite contain the assemblage clinopyroxene + plagioclase $\pm$ olivine and are free of orthopyroxene. These chemical and petrographic similarities with the 1360 Ma Fe-rich tholeiite suite of the Vestfold Hills (which includes sample 206) suggests maximum emplacement pressures of 5-6 kbar. Interestingly, the quartz normative group 2 sample (49520, Table 2.2) contains the olivine-free assemblage clinopyroxene + pigeonite (inverted) + plagioclase indicating the emplacement pressure was greater than that for olivine saturation in this composition. When sample 49520 is compared

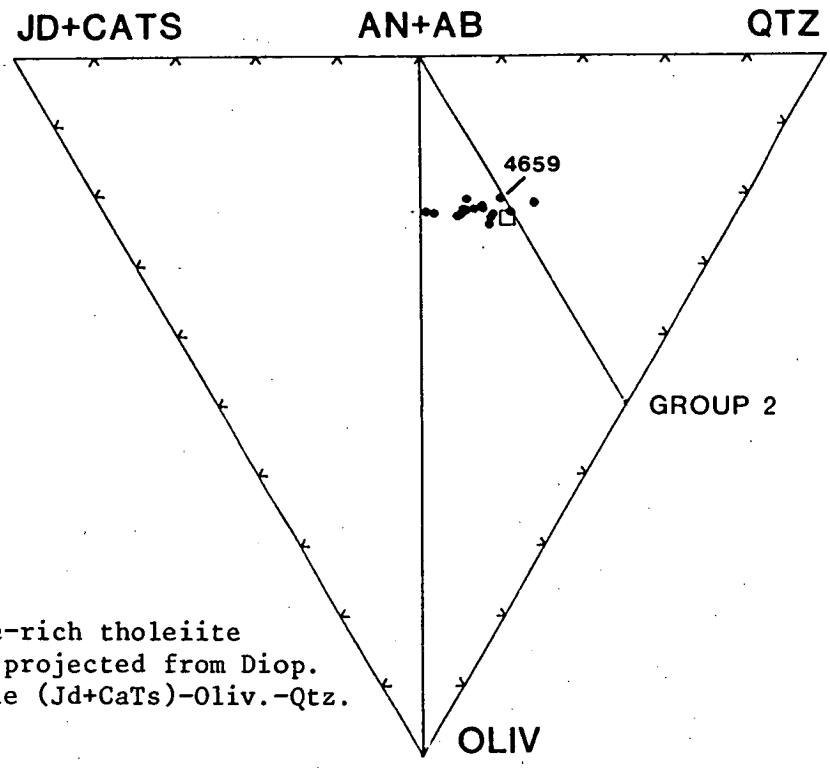

Figure 2.8
Group 2 Fe-rich tholeiite compositions projected from Diop. onto the plane (Jd+CaTs)-Oliv.-Qtz. Square: 206.

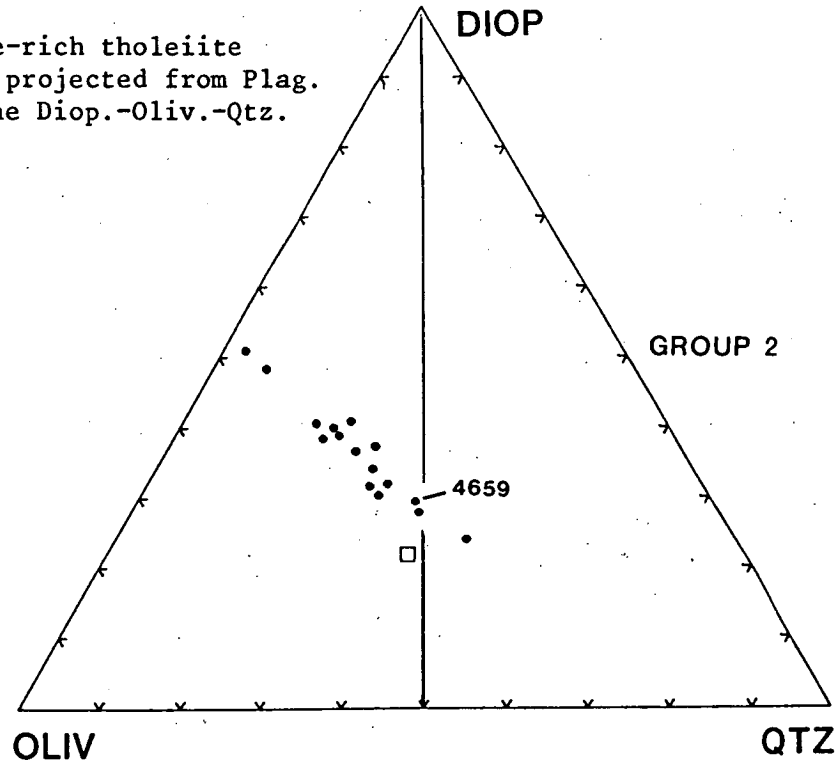

Figure 2.9
Group 2 Fe-rich tholeiite compositions projected from Plag. onto the plane Diop.-Oliv.-Qtz. Square: 206.

directly to the projections of Jaques & Green (1980) and Duncan & Green (submitted), olivine saturation is estimated at ~5 kbar.

According to Sheraton & Black (1981), a reliable estimate of the emplacement age of the group 2 suite is not possible due to isotopic heterogeneity of the source. With regard to the relative age of the group 2 suite, these authors state that "... the field relations suggest a generally similar age to that of the group 1 tholeiites". It is significant then, that the estimated emplacement pressure of group 2 is ~3 kbar lower than that of the 1190 ± 200 Ma group 1 tholeiites. Considering the difference in emplacement pressure there are two possibilities relating their relative ages:

(i) the group 2 suite is older than group 1, implying uplift of the Napier Complex prior to ca.1190 Ma, emplacement of the group 2 suite followed by depression of the crust and emplacement of group 1 at ca.1190 Ma, with uplift again at ca.1000 Ma; or

(ii) the group 2 suite is younger than group 1, and was emplaced in conjunction with the uplift at ca.1000 Ma.

Possibility (ii) is clearly the simplest explanation and is supported the studies of D3 metamorphic assemblages in pelitic granulites (ca.2500 Ma) which have single stage coronas attributed to the ca.1000 Ma metamorphism (Harley, 1985b).

It is concluded then that the group 2 suite is younger than group 1, and was emplaced in conjunction with the Rayner metamorphism and associated uplift at ca.1000 Ma. The only other known example of mantle-derived melts accompanying the Late Proterozoic tectonic event in the East Antarctic Shield is from the Mawson Coast where a small number of mafic dykes were emplaced within the syn-orogenic Mawson Charnockite (Kuehner, in press).

2.1.3 Fe-RICH THOLEIITES (ca.1800 Ma) - VESTFOLD HILLS

Sheraton & Collerson (1983) identified a small suite of tholeiite dykes (seven samples) in the Vestfold Hills which have been dated at 1791 ± 62 Ma. However, the trace element characteristics which distinguish this suite from the 1360 Ma tholeiites have not been identified in the samples collected by the author for this study. As such, the limited compositional range (Sheraton, 1981) permits only a broad generalization to be made concerning the emplacement pressure of the suite.

The projected positions of the analyses of the ca.1800 Ma tholeiites (compiled in Sheraton, 1981) into the basalt tetrahedron are shown in Figs 2.10 and 2.11. All the compositions are quartz normative (FeO^T) which will

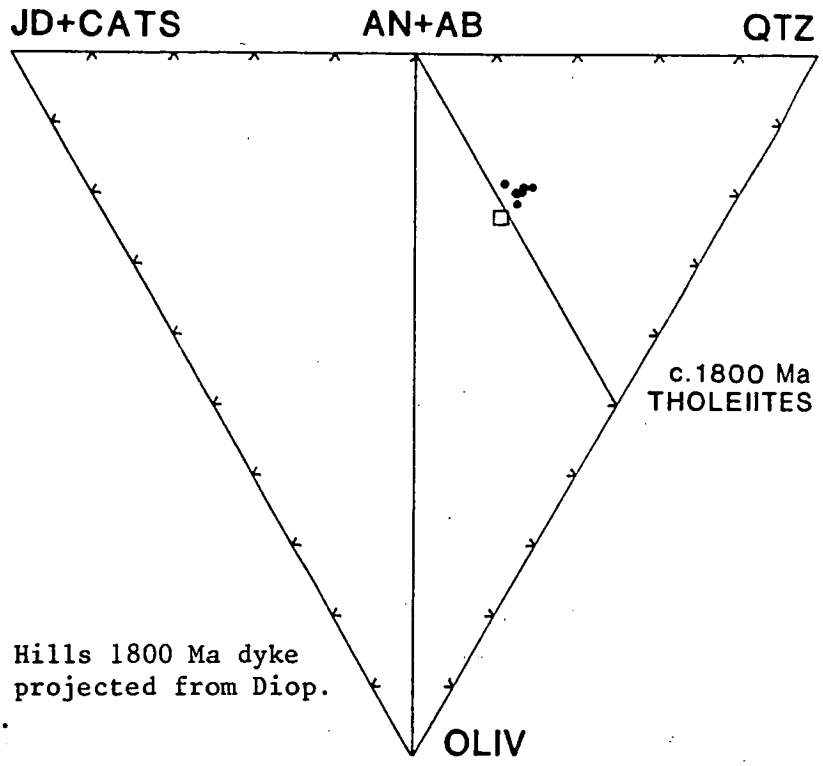

Figure 2.10
Vestfold Hills 1800 Ma dyke composition projected from Diop. Square: 206.

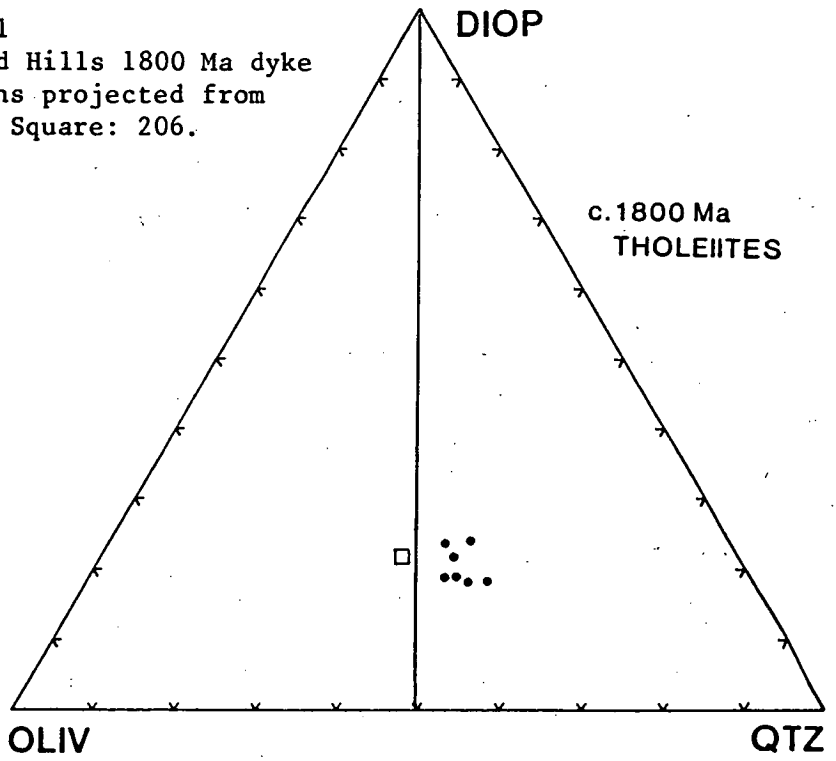

Figure 2.11
Vestfold Hills 1800 Ma dyke compositions projected from (An+Ab). Square: 206.

have the effect of reducing the pressure of liquidus olivine-orthopyroxene saturation compared with the olivine normative sample 206 (see cotectic trends in Figs 2.1 and 2.2).

Petrographic descriptions of the samples comprising this group have not been detailed. Sheraton et al. (in press) report only that these samples have subophitic textures which implies the phases clinopyroxene and plagioclase. Sheraton & Collerson (1983) grouped the petrographic descriptions of the 1800 Ma dykes with the younger 1360 Ma suite and commented that only a single sample, a 1360 Ma tholeiite, had phenocrysts of orthopyroxene. It is assumed from these brief descriptions that the 1800 Ma suite contains plagioclase + clinopyroxene $\pm$ olivine, and apparently does not have phenocrysts of orthopyroxene. This assemblage indicates precipitation, and emplacement, at pressures less than that of the olivine-orthopyroxene cotectic, which for the projected compositions implies pressures <8 kbar, and could be as low as 5 kbar based on the Jaques & Green (1980) projection.

2.2 DISCUSSION OF THE IMPORTANCE OF A REGIONAL PRESSURE GRADIENT IN THE NAPIER COMPLEX

It may be reasonably assumed that the 400 km^2 Vestfold block acted as a structurally coherent unit during uplift such that the estimated emplacement depths of individual dykes (060, 206) will reflect the load pressure acting on the entire terrain at the time of dyke emplacement. However, the Enderby Land dykes were collected from a much larger area (~100,000 km^2) and it cannot be assumed that this region acted as a single tectonic unit, nor that the emplacement pressure estimated from a single dyke representing a widely distributed swarm would also apply to exposures ~250 km distant (Fig. 2.12) In the following paragraphs, the question of a regional variation in the level of exhumation presently observed in the Napier Complex is examined.

Harley (1985b) applied geothermometry-barometry methods to orthopyroxene-bearing assemblages collected from a wide area of the Napier Complex and found evidence for a regional gradient in metamorphic pressures. The inferred pressures were generally higher in the Casey Bay-Scott Mt region than in the North Tula Mts (Fig. 2.12), however, due to the errors inherent in the pressure calibration and mineral analyses, there is considerable overlap in the calculated pressures from these areas. Additionally, the North Tula Mts, as well as the Casey Bay region contain aluminous metapelites with the assemblage sapphirine + quartz, spinel + quartz, and osumilite. Based on the phase equilibrium studies of Ellis (1980) these assemblages indicate somewhat higher pressures of 8-10 kbar during the ~3100 Ma metamorphism, than the 6-8 kbar indicated by the garnet-orthopyroxene geobarometry of Harley (1985b). The presence of cordierite rather than the higher pressure assemblage sapphirine + quartz in the Napier Mts (Sheraton et al., 1980) does suggest a regional pressure gradient but the pressure difference implied by these two assemblages need not be great as they may coexist along a univariant boundary in the system $FeO-MgO-Al_2O_3-SiO_2$ (Henson & Essene, 1971; Hensen, 1971).

As discussed above, the strong chemical similarities between the Enderby Land high-Mg tholeiite 3793 and group 1 tholeiite 590 when compared to the experimentally studied samples from the Vestfold Hills (Chapter 1), provides the basis for very confident estimates of their emplacement pressures. The widely separated locations of these dykes, both considered to have been emplaced at pressures not less than 7-8 kbar, is shown in Fig. 2.12. A generalized northeasterly trend of significantly decreasing

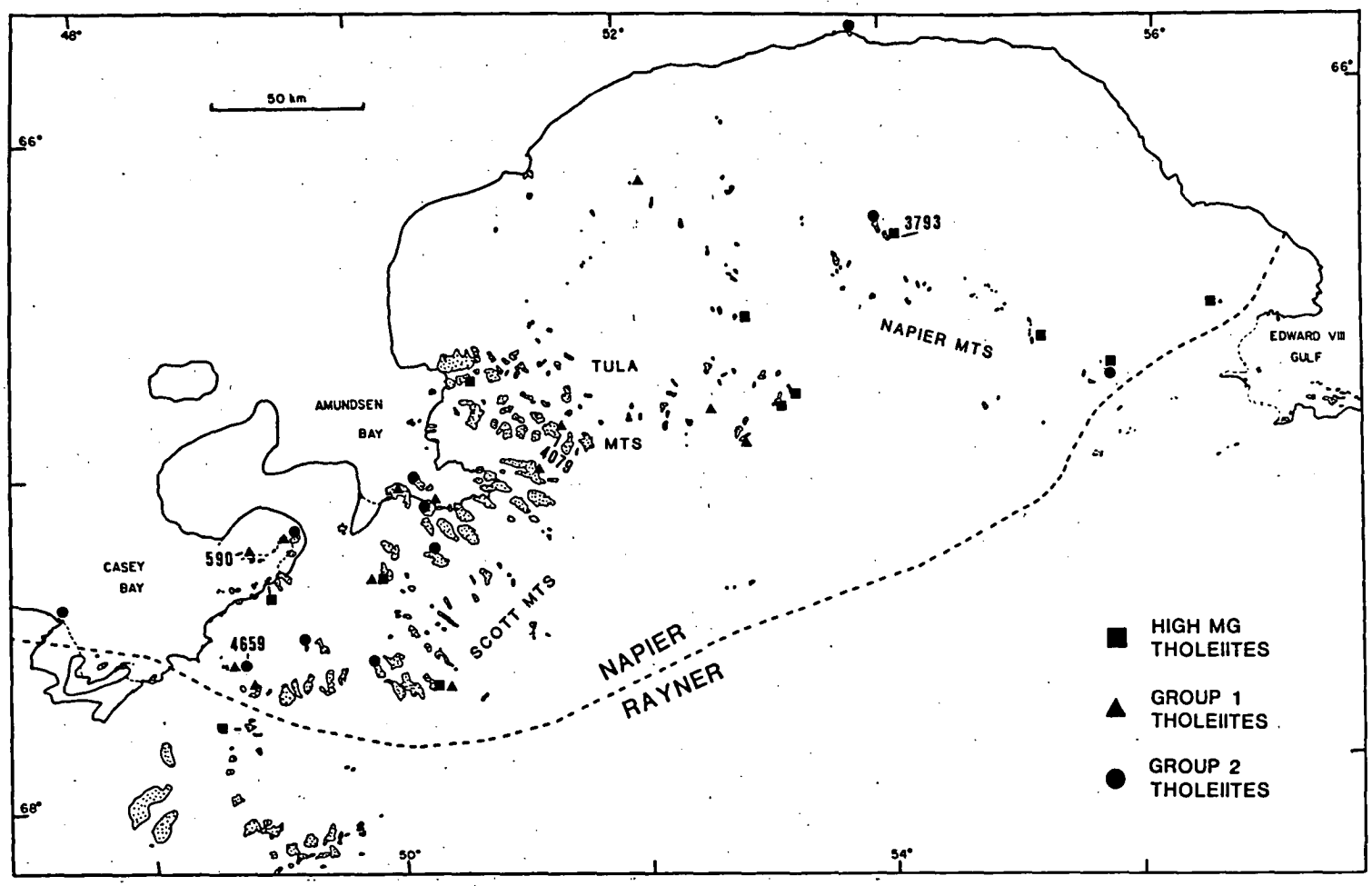

Figure 2.12 Enderby Land dyke localities. Samples discribed in text are indicated.

pressure throughout the Napier Complex is not supported by the occurrence of 3793 in the Napier Mts. Instead, the emplacement pressures of this sample suggest that high load pressure existed over the whole of the exposed Napier Complex during the ca.2500 Ma metamorphism, and was not restricted to locations south and southwest of Amundsen Bay (Harley, 1985b).

High pressures are also indicated in the Tula Mts at ca.1200 Ma by the group 1 sample 4079, though this pressure estimate is not confidently determined and slightly lower pressures may be interpreted.

Although evidence from metamorphic studies suggests somewhat shallower crustal levels may be exposed in the North Tula and Napier Mts than in the Casey Bay region, the evidence cannot be interpreted as signifying greatly different levels of exposure. It is considered then, that the individual dykes composing a single suite were emplaced throughout the presently exposed level of the Napier Complex under approximately the same load pressures. Inferences based on the emplacement pressures of samples 590 and 3973 can then be extended to all of the Napier Complex.

2.3. CONCLUSIONS

2.3.1 NAPIER COMPLEX HIGH-Mg THOLEIITES (ca.2400 Ma)

The experimentally determined olivine/orthopyroxene saturation points of several Mg-rich tholeiites were used to construct isobaric multiple saturation contours within the basalt tetrahedron. Projection of the single Napier Complex olivine normative high-Mg tholeiite into the tetrahedron predicts olivine saturation for this sample at pressures of 7-8 kbar. As olivine is absent from all high-Mg tholeiites sampled from the Napier Complex the minimum emplacement pressure of the suite is 7-8 kbar.

2.3.2 NAPIER COMPLEX Fe-RICH THOLEIITES (ca.1190 Ma)

Compositions exist in both the group 1 and group 2 tholeiite suites which can be compared directly with sample 206. The group 1 sample 49590 contains phenocrysts of orthopyroxene + clinopyroxene + plagioclase which require crystallization at pressures $\geq$8 kbar. A more undersaturated group 1 sample (4079) contains phenocrysts of clinopyroxene + plagioclase and compares closely to a MORB composition which exhibits multiple saturation at ~8 kbar. The constrasting phenocryst assemblages of samples 49590 and 4079, which represent crystallization above and below the multiple saturation point of their respective compositions, could be used to "bracket" the actual emplacement pressure if the multiple saturation pressure of sample 4079 could be determined precisely. These samples indicate emplacement of the group 1 suite at pressures $\geq$8 kbar.

The group 2 sample 4659 is compositionally and petrographically (clinopyroxene + plagioclase + olivine) similar to sample 206, implying emplacement of the group 2 tholeiite suite at pressures $\leq$5-6 kbar. A quartz normative and olivine-free group 2 sample contains pigeonite + clinopyroxene + plagioclase phenocrysts and, as in the group 1 suite, "brackets" the actual emplacement depths. The lower emplacement pressures of this suite compared to group 1 requires emplacement to be contemporaneous with uplift produced by the Rayner metamorphism, a fact previously unrecognized.

The limited amount of information of the 1800 Ma tholeiite suite in the Vestfold Hills suggests these dykes were emplaced at pressures <8 kbar, and possibly ~5 kbar.

CHAPTER 3

GARNET DEVELOPMENT WITHIN MAFIC DYKES OF THE VESTFOLD HILLS: EVALUATION AND IMPLICATIONS

INTRODUCTION

The southwest portion of the Vestfold Hills is interpreted to have been affected by a Late Proterozoic (ca. 1100 Ma) metamorphism (Sheraton & Collerson, 1983), an event which played a major role in the geological history of the Rauer Islands 20 km to the southwest. With the exception of localized shearing, the mafic dykes outcropping in this section of the Vestfold Hills have not been deformed during the metamorphic event, although they have been variably hydrated and recrystallized to garnet-amphibole assemblages and therefore differ significantly from the otherwise igneous textured dykes typical of elsewhere in the region.

In this chapter, geothermometric-barometric methods will be applied to the garnet-bearing assemblages in order to determine the pressure and temperature conditions of their formation. Petrographic features of the metamorphic assemblage will also be examined in the light of experimental and theoretically-determined phase relations. In the absence of any previous detailed evaluation of the P-T conditions during the Late Proterozoic metamorphism in the Vestfold Hills region, the information described here is important in constraining the crustal position of the Vestfold Block during the youngest tectonothermal event recognized in the area.

3.1 FIELD OBSERVATIONS ON THE OCCURRENCE OF GARNET

The sample locations of garnet-bearing dykes studied in detail within this chapter are shown in Fig. 3.1. Also indicated is an approximate garnet isograd defined by both field and petrographic observations. The development of garnet within the northernmost occurrence (sample 233B) is somewhat anomalous, and is restricted to narrow, carbonated mylonitic zones which cross the dyke. Garnet was not observed in dykes between the garnet isograd and 233B.

Field observations resulted in the characterization of the garnet occurrences into three paragenesis:

1) garnet development associated with localized deformation,

2) garnet associated with sulfide-carbonate veinlets, and

3) garnet growth under conditions of static recrystallization.

Most commonly, garnet forms lenticular, flame-like aggregates up to 5 cm in length paralleling the foliation developed within sheared dyke margins. In these occurrences, garnet development is entirely restricted to the sheared margins while the structurally isotropic dyke centre may remain garnet-free. In addition, the occurrence of garnet is not always continuous along the length of the dyke, but is sporadic in location and intensity of development.

An additional garnet occurrence which resulted from, or was concurrent with brittle deformation is illustrated in Fig. 3.2A. Here, garnet forms planar, evenly spaced thin sheets orientated in trellis-like patterns which are developed along the dyke margins and extend up to ~0.5 m inwards towards the dyke centre. These features do not continue into the country rock.

In outcrop, the spatial orientation of the garnet sheets is very similar to fracture cleavages described by Foster & Hudleston (1986) which occur in troctolitic rocks of the Duluth Gabbro. The cleavages were interpreted to have formed in semi-brittle rocks under the influence of a shear stress prior to breakage and shear movement. The conjugate fracture planes which developed under relatively low confining pressures (<2 kbar) in this example, are lined with a narrow coating of serpentine minerals, indicating the existence of fluid mobility during the formation of the fractures. The Vestfold Hills occurrences differ in this respect as there

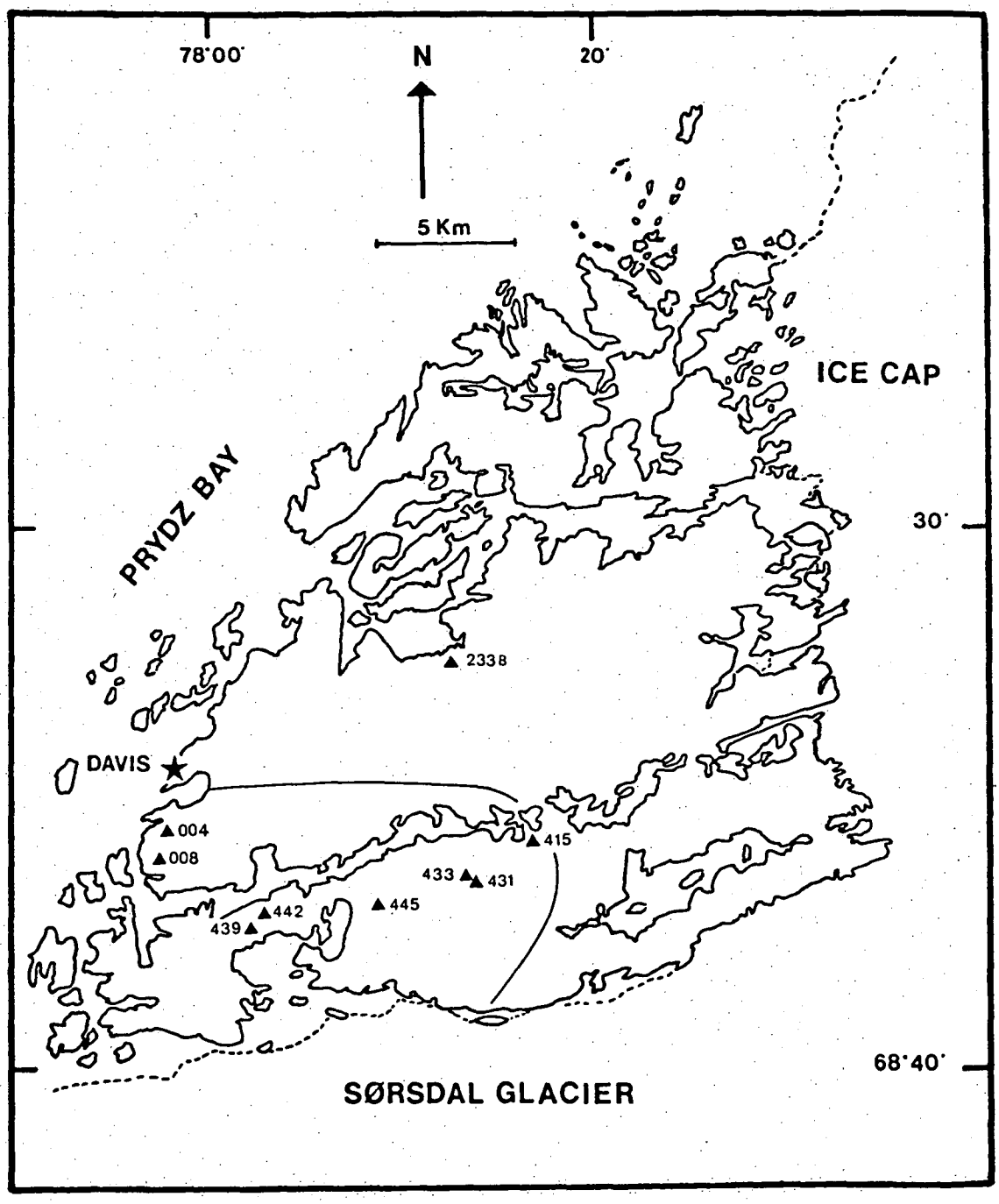

Figure 3.1

Sample locations of garnet-bearing dykes examined in detail within this chapter. Also shown is the field defined boundary (narrow line) marking the limit of garnet occurrences in mafic dykes.

Figure 3.2A
Trellis-like pattern of intersecting planes of garnet.
Sample 65443.

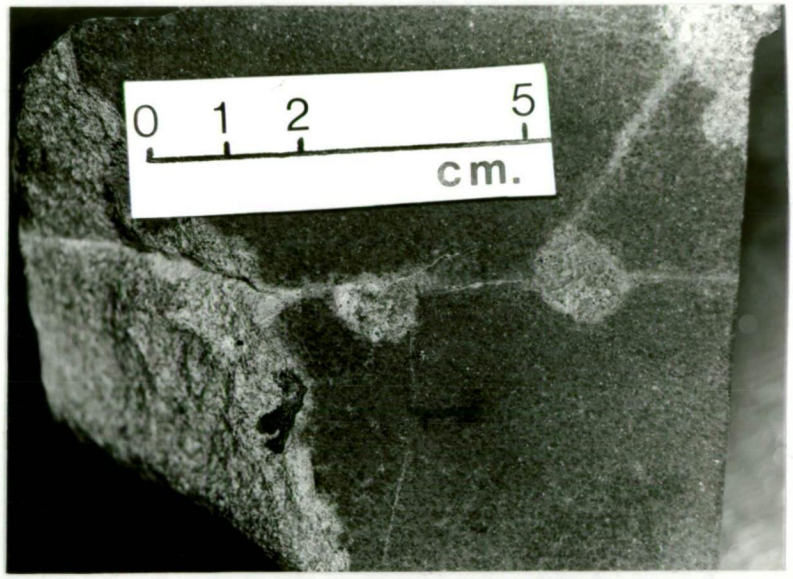

Figure 3.2B
Large aggregates of garnet forming within carbonate-sulphide veinlets.
Sample 65421.

Figure 3.2C
Snowflake-like aggregates of garnet formed in an unfoliated dyke, crossed by a carbonate-sulphide veinlet (note bright sulphides in veinlet).
Sample 65445.

is no petrographic indication that the features presently defined by the garnet sheets ever acted as fluid pathways, although as discussed later, the garnet may have entirely replaced an original hydrous phase such as hornblende.

Alternatively, it is possible that under the high pressure environment envisaged for the Vestfold Hills at the time of metamorphism, dilatancy within the fracture cleavage may not have occurred (Foster & Hudleston, 1986). If this is the case, the stresses directed along potential planes of shear fracture would be entirely absorbed through the development of site defects within the affected phases, and as an increase in surface energy along grain boundaries (Wintsh, 1985). Both of these features are known to enhance reaction kinetics and importantly, nucleation rates.

It is well known to experimental petrologists that garnet is a difficult phase to produce in experimental charges without the use of seed crystals, particularly under fluid absent conditions. Similarly, Buddington (1965) and Whitney (1978) have discussed the problem of kinetics with regard to the erratic occurrence of garnet in the amphibolite-granulite facies rocks of the Adirondack region, and stressed, among other factors, the importance of deformation in the nucleation of garnet. The association of garnet with deformation is obvious within the sheared margins of the Vestfold Hills dykes. It seems reasonable then, that the strain developed within phases along potential shear fractures has also acted as a nucleation catalyst for garnet. Once garnet has nucleated, the presence of fluids, in part derived by the dehydration of amphibole, would aid in rapid diffusion and continued garnet growth.

The second, and more spectacular occurrence of garnet is as individual aggregates or clots up to 2 cm in diameter located along narrow (~1 mm) sulphide-carbonate-bearing veinlets (Fig. 3.2B). The development of garnet is quite sporadic along an individual fracture as two or three garnet clots can be developed over an interval of 20 cm, while a further 3 m of veinlet may be garnet-free. Unlike the previously discussed paragenesis where garnet formation defined a "fracture", poorly developed crystals of garnet associated with the sulphide-carbonate veinlets nucleate at the veinlet-dyke interface, with continued garnet growth directed into the mafic dyke. In general, the veinlets occur singly, without any preferred orientation within the dykes and post-date the foliation developed in the sheared dyke margins.

Finally, garnet may occur as undeformed snowflake-like masses which have nucleated without any apparent structural catalyst (Fig. 3.2C). This

type of garnet development was not commonly observed in the field but may be more widespread as it was only recognized on surfaces where the contrasting resistance of the metamorphic mineral assemblage to weathering enhanced the garnet clots. Thin section examination of several dykes recorded as "garnet-free" in the field has revealed this type of garnet development.

It is particularly important to emphasize the strong structural control on the extent to which a dyke has undergone secondary hydration, in addition to the structural effect on the development of garnet, as noted above. Dyke margins, which are commonly sheared, have allowed ready access by fluids resulting in the extensive development of hornblende. Strongly foliated and hydrated samples are composed largely of granular to lath-shaped, dark green hornblende, plagioclase, quartz and ilmenite. Biotite and clinopyroxene are minor accessory minerals. Samples collected from dyke centres may retain igneous textures, or may be extensively recrystallized. In the latter case, the resulting textures are granoblastic, with little hornblende development. The occurrence of garnet in sheared dyke margins and the absence of garnet and hornblende from the dyke interiors highlight the role of deformation in contributing to the metamorphic facies concept in that rocks belonging to the almandine amphibolite facies and the granulite facies may be collected from the same dyke.

These observations are not unique to the Vestfold Hills area. In a similar manner, Buddington (1963, 1965), noting the unsystematic occurrence of garnet in the Adirondack amphibolite and mafic granulites discussed the role of kinetics in the appearance of garnet. In addition to pressure, temperature and bulk rock composition, variations in grain size, intensity of deformation and the existence of a fluid phase were all recognized as factors which require consideration in order to understand the distribution of garnet. Similarly, Glassley & Sørensen (1980) described mafic dykes from West Greenland which are zoned from amphibolite facies at the margin to garnet granulites in the core. These features were considered to be the result of prograde metamorphism of dykes compositionally zoned in secondary hydrous phases.

3.2 PETROGRAPHIC OBSERVATIONS ON AMPHIBOLE AND GARNET FORMING REACTIONS

Although the mafic dykes investigated in this study were not sampled in such a way as to permit a detailed examination of possible mineralogical variations across a single dyke, the petrographic features of the collected samples can still furnish information on possible garnet-forming reactions which in turn provide evidence for evaluating the crustal history at ca.1000 Ma in terms of P-T-a_{H_2O}.

It is clear from the examination of poorly foliated samples that the groundmass assemblage is much more readily hydrated and recrystallized than are the phenocrysts. This observation simply reflects the larger surface area provided by the smaller groundmass grains accessible to react with any available fluids, a feature which also enhances the kinetics of recrystallization. When hydration reactions are incomplete, clinopyroxene remains as an accessory phase. Relict groundmass orthopyroxene is not observed, even in quartz normative samples though it is a common phase in nearly all unmetamorphosed dykes. This may indicate that orthopyroxene reacts to hornblende more readily than clinopyroxene, or simply that the modal abundance of orthopyroxene is subordinate to clinopyroxene.

Relict clinopyroxene and orthopyroxene phenocrysts have nearly opaque cores composed of a dense population of exsolved ilmenite needles (Fig.3.3). A narrow ilmenite-free pyroxene rim often exists adjacent to a crude corona of dark green granular or slightly lath-shaped hornblende and blocky ilmenite. Pyroxene phenocrysts lacking hornblende coronas are entirely filled with exsolved ilmenite providing evidence that the opaque-free rims developed as a result of outward diffusion of Fe and Ti from the pyroxene during reaction with plagioclase to produce the hornblende coronas. Precipitation of excess Fe and Ti above that required in the hornblende forms the blocky ilmenite crystals. These textures indicate the following reactions:

$$\text{Cpx} + \text{Plag} + H_2O \longrightarrow \text{Hbd} + \text{Qtz} + \text{Ilm}$$

$$\text{Opx} + \text{Plag} + H_2O \longrightarrow \text{Hbd} + \text{Qtz} + \text{Ilm}.$$

It should be noted that microprobe studies have identified quartz in all samples examined, even those with up to 20% normative olivine (FeO^T).

Garnet not associated with the carbonate - sulfide veinlets usually takes the form of xenomorphic poikiloblasts which in detail are found to be composed of fine aggregates of vermicular granules. In unfoliated, but slightly recrystallized samples such as 003, many of the poikiloblasts have

coalesced into masses over 1 cm in diameter. The matrix surrounding the garnet is composed of randomly orientated laths of plagioclase, small laths of hornblende, granular clinopyroxene and ilmenite. This texture is continuous, as inclusions, through the garnet porphyroblasts although in many instances the original igneous plagioclase laths are completely pseudomorphed by garnet (Fig. 3.4). Hornblende only rarely occurs as inclusions in garnet. Where hornblende is found, the grains are smaller than those in the matrix, and elliptical in outline. This is interpreted to indicate that the hornblende is in an arrested state of reaction to produce garnet.

Where the garnet has enclosed relict phenocrysts of orthopyroxene the crystals retain their primary igneous form and display no tendency to participate in garnet-forming reactions. Furthermore, the hornblende coronas which encompass the matrix pyroxenes are absent from the pyroxenes enclosed by garnet, though the previous existence of the coronas may be inferred from narrow ilmenite-free rims on otherwise opaque filled pyroxene crystals (Fig.3.5).

The petrographic features described above indicate the following generalized reaction has occurred:

$$\text{Amph} + (\text{Ca} - \text{plag}) + \text{Qtz} \longrightarrow \text{Gt} + \text{Cpx} + (\text{Na} - \text{plag}) + H_2O.$$

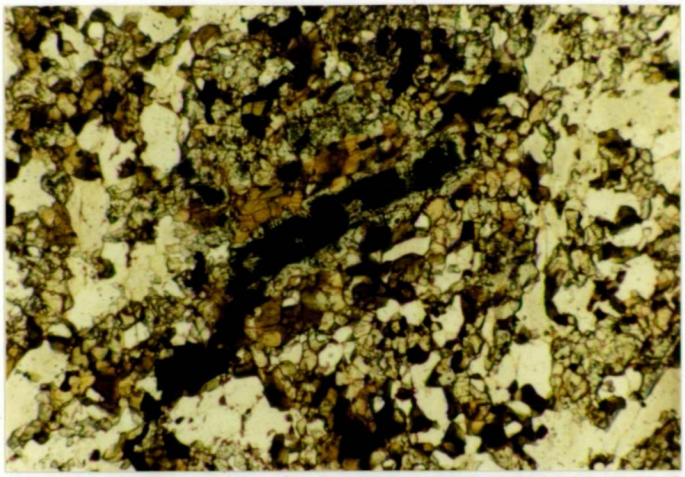

Figure 3.3
Opaque filled relict clinopyroxene phenocryst rimmed by amphibole. Sample 65004. Long dimension of photo = 1 mm.

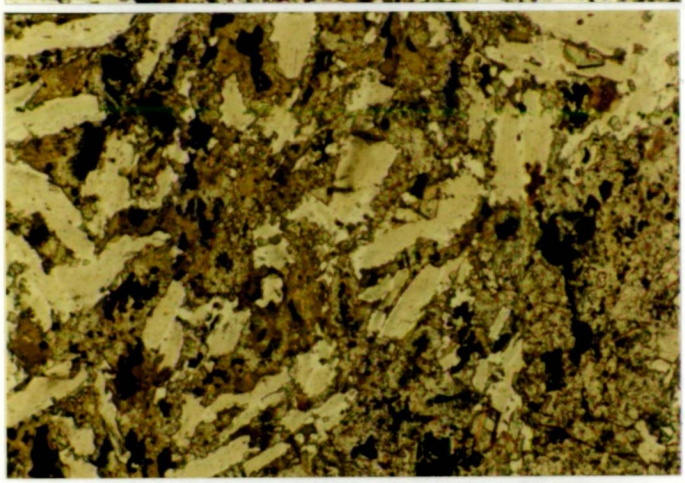

Figure 3.4
Garnet (colourless, high relief) replacing amphibole-plagioclase assemblage. Note narrow corona of garnet between amphibole and plagioclase - bottom centre, and non-reactant opaques. Sample 65002. Long dimension of photo = 2 mm.

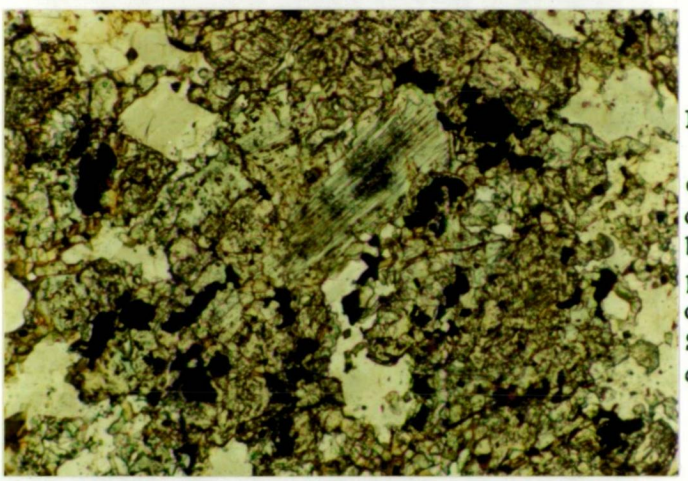

Figure 3.5
Opaque-filled relict clinopyroxene with partial rim of ilmenite separated by narrow band of garnet. Garnet interpreted to have replaced original amphibole corona. Sample 65004. Long dimension of photo = 1 mm.

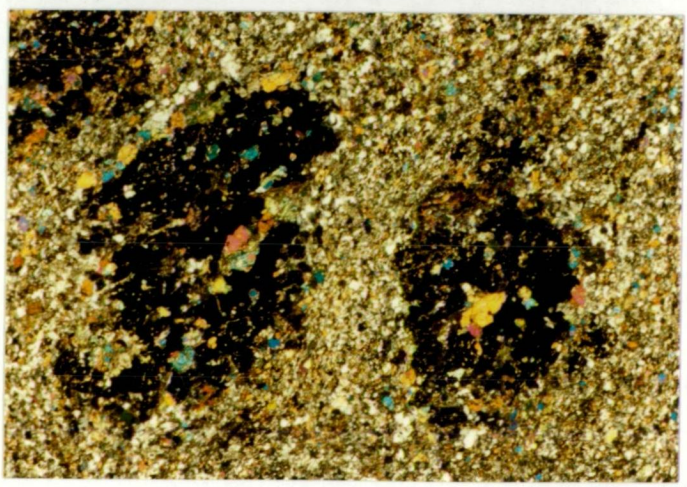

Figure 3.6
Garnet development in narrow sheared zone of sample 65442. Note inclusions of large clinopyroxenes compared to fine groundmass. Long dimension of photo = 5.5 mm.

3.3 PETROGENETIC IMPLICATIONS

The petrographic characteristics discussed above have been drawn from studying samples of the ca.1360 Ma and ca.2420 Ma Fe-tholeiites which range in Mg-value from 30-45 (FeO^T). In the view of the importance of the Fe/Mg ratio in determining the pressure which corresponds to the incoming of garnet in rocks of basaltic composition (Green & Ringwood, 1967b, 1972; also Hensen, 1976; Bohlen et al., 1983) the absence of garnet, outside of narrow carbonated shears, in a more magnesian tholeiite (65442; Mg-value = 55.2) collected from well within the garnet isograd (Fig. 3.1) is worth noting. Sample 442 has a fine grained granoblastic equigranular polygonal texture composed of orthopyroxene + clinopyroxene + plagioclase with minor hornblende + quartz. The development of localized shears post-dates the static recrystallization and has provided access to C-O-H fluids as indicated by the development of carbonate and amphibole. Large, elongated porphyroblasts of garnet have developed within, and are restricted to, the sheared zones and are associated with minor amounts of scapolite (Fig.3.6). The most important petrographic observation is that orthopyroxene and plagioclase stably coexist in the fine grained recrystallized groundmass. Furthermore, there is no evidence for disequilibrium between the equigranular hornblende and plagioclase.

The upper pressure limit of coexisting plagioclase + orthopyroxene is temperature-dependent, but more importantly, the reaction occurs at lower pressure (at a given level of silica saturation) with increasing Fe/Mg in the reacting assemblage. The clear implication derived from the mineral assemblage in sample 442 is that the P-T conditions of metamorphism experienced by the southwest portion of the Vestfold Hills were below that required to destabilize orthopyroxene + plagioclase in a Mg_{55} basaltic composition.

The contrasting metamorphic mineral assemblage found in the Fe-rich and Mg-rich tholeiites can be viewed by making use of the theoretical phase relations within the simplified system Na-CMASH (Glassley & Sørensen, 1980). This is illustrated in a P-T diagram (Fig. 3.7) where the model amphibole-absent reaction:

$$En + An \longrightarrow Py + Di + Qtz$$

is depicted as existing at a higher pressure for the Mg-tholeiite composition (8% normative olivine) than the most magnesian garnet-bearing sample (6% normative olivine). The relative locations of the reaction boundaries are schematic, but the topology indicates the garnet-forming reaction determined petrographically in the Fe-tholeiites occurs at

pressures above the amphibole-absent reaction for those compositions, while the equilibrium phase assemblage in the Mg-tholeiite is stable at pressures below the En + An reaction boundary. The equilibrium assemblage within these examples bracket the actual metamorphic conditions in that the pressure at which the observed mineral assemblages formed was less than that required to produce garnet in a Mg_{55} dyke, but above En + An stability in the Mg_{45} sample (445).

With respect to the Mg-tholeiite, the phase relations of Fig. 3.7 allow an isobaric interpretation for the conditions of hydration and recrystallization. However, the petrographic evidence clearly indicates that the formation of hornblende in the Fe-tholeiites followed the modal reaction:

$$En + Di + An + H_2O \longrightarrow Amph + Qtz.$$

This reaction requires hydration at pressures within the En + An stability region of the Fe-tholeiites. In order for garnet to subsequently form via the model reaction:

$$Amph + An + Qtz \longrightarrow Py + Di + Ab + H_2O$$

depression of the terrain to higher pressures is required.

The actual P-T positions of the reactions drawn in Fig. 3.7 have not been determined, but as depicted it is possible for the dehydration boundary to have been reached isothermally. More likely, movement of the terrain to higher pressures was also accompanied by a temperature rise; shown as a positive dP/dT path in Fig. 3.7. As the equilibrium hydrated assemblage in the Fe-tholeiite is orthopyroxene-free, the hornblende + plagioclase $\pm$ clinopyroxene stability field will exist both above and below the En + An reaction boundary. Thus it is possible for the terrain to follow a positive dP/dT path without an accompanying change in mineralogy until the amphibole dehydration reaction is reached.

Reduction in the activity of H_2O has an effect similar to an increase in temperature on the equilibrium assemblages of Fig. 3.7. Amphibole dehydration could then result from a reduction in a_{H_2O} at high pressure, with or without a concomitant temperature increase. There is, unfortunately, no evidence to support or refute this possibility as a process operating on a regional scale within the Vestfold Hills. The concept of regional dehydration resulting from "CO_2-flushing" is commonly advocated as a method to produce charnockites and granulite terrains in general from hydrous granitoid precursors. Evidence for the latter suggestion has come from fluid inclusion studies which have found CO_2 to be

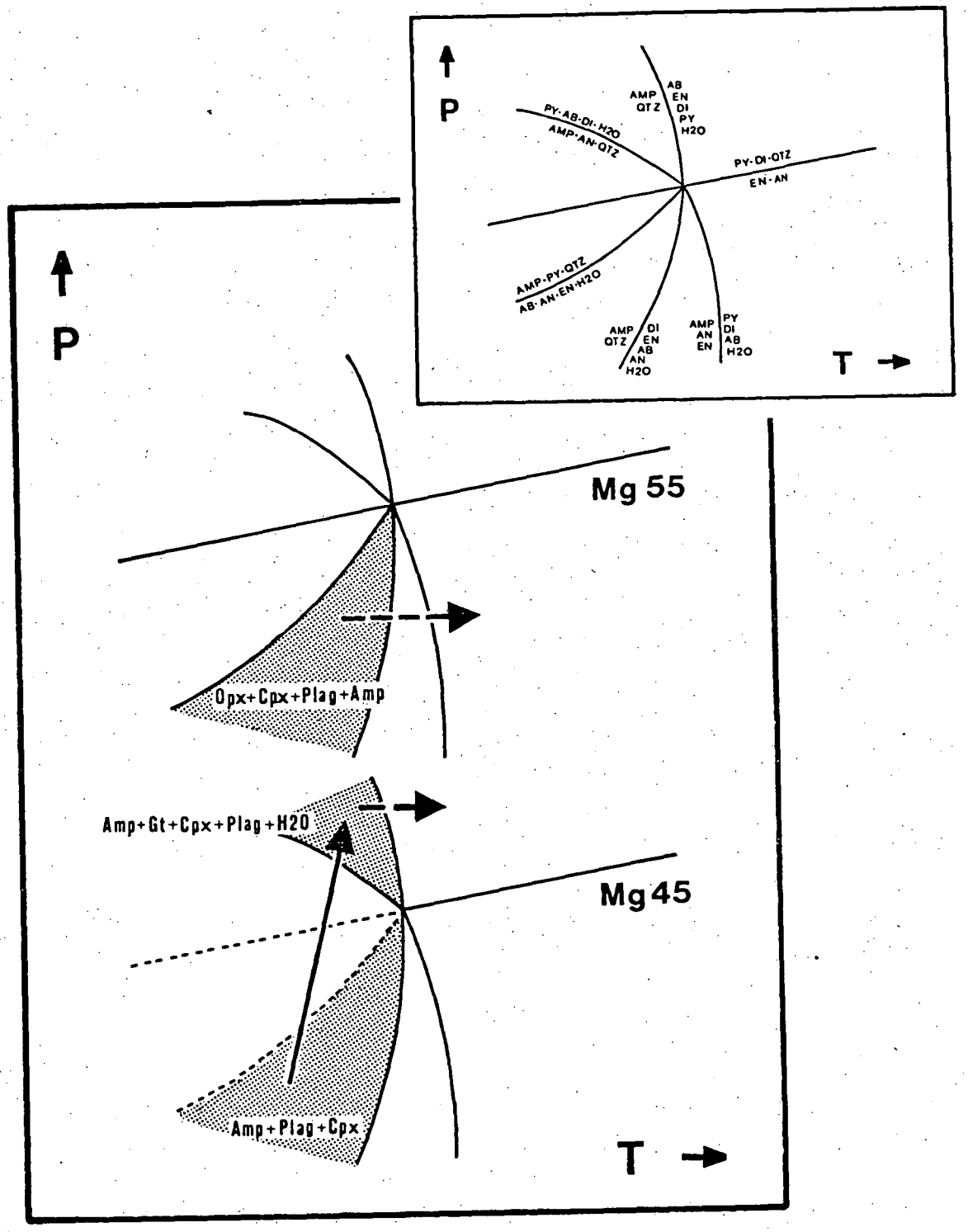

Figure 3.7

Schematic phase relations in the simple system Na-CMASH (inset) applied to the metamorphic mineral assemblages of sample 442 (garnet-free, Mg_{55}) and 445 (garnet-bearing, Mg_{45}). Solid arrow marks relative P-T path followed by the Vestfold Hills terrain deduced from petrographic observations. Dashed arrows illustrate localized dehydration reactions in carbonate-bearing veinlets. The equilibrium metamorphic assemblage observed in the mafic dykes (+ quartz) is indicated.

the dominant volatile species within granulites (see Ferry & Burt (1982) and Newton & Hansen (1983) for discussion and references on this topic).

Although there is no evidence to substantiate a regional dehydration process resulting from changes in a_{H_2O}, there is evidence for this process occurring on a localized scale. Restricted to the narrow shears crossing sample 442 are large laths of hornblende associated with carbonate. Garnet porphyroblasts, intergrown with large crystals of clinopyroxene are also confined to the shears (Fig.3.6). The textural relationships indicate hornblende and garnet are incompatible phases, implying the quartz-absent reaction:

$$\text{Amph} + \text{An} + \text{En} \longrightarrow \text{Gt} + \text{Cpx} + \text{Ab} + H_2O$$

with the orthopyroxene and plagioclase derived from the equigranular matrix. Quartz is an accessory phase in the matrix, but within the localized environment of the sheared zone the minor quartz must have been initially consumed by reaction with the modally dominant amphibole which in turn produced garnet in the restricted quartz-free environment. The appearance of garnet and not olivine requires the P-T conditions of dehydration to be at pressures above the reaction:

$$\text{Oliv} + \text{Plag} \longrightarrow \text{Gt} + \text{Cpx}$$

for the localized bulk composition of the undersaturated sheared zone. At temperatures of 600-650°C (see next section) this reaction takes place at 4-5 kbar in a Mg_{60} olivine normative basalt (Green & Ringwood, 1967).

Because amphibole + plagioclase + orthopyroxene are part of the stable assemblage of sample 442 outside of the sheared areas and have not reacted to form garnet, the development of garnet in the shears cannot be attributed to an overall temperature increase within the terrain. The occurrence of carbonate within the shears suggests the equilibrium fluid was CO_2-rich compared to the fluid composition which equilibrated with the host rock. On a localized scale, the lower a_{H_2O} within the shears would have the effect of modifying the equilibrium phases from a hornblende + orthopyroxene assemblage to a garnet-bearing assemblage. This is illustrated by a dashed line in Fig. 3.7.

The development of garnet clots within the sulphide-carbonate veinlets can also be related to a lower a_{H_2O} in the veinlets as compared to the host rock. In sample 415, a large garnet crystal (~5 mm in length) has grown from a sulphide-carbonate vein <1 mm wide. The garnet has deformed the foliation on both sides of the veinlet, and produced pressure shadows adjacent to each of its margins. The pressure shadows contain large crystals of clinopyroxene and plagioclase, with minor orthopyroxene

accompanied by calcite, dolomite (ss) and siderite (ss). The development of two pyroxenes and garnet, based on Fig. 3.7 indicates that the conditions for the hornblende dehydration reaction were locally exceeded. This is shown as a dashed arrow in Fig. 3.7.

3.4 P-T DETERMINATIONS

The metamorphic P-T conditions recorded in the garnet-bearing assemblages of the mafic dykes were estimated by applying the Ellis & Green (1979) garnet-clinopyroxene geothermometer, the Newton & Perkins (1982) garnet-clinopyroxene-plagioclase-quartz geobarometer, and the Ellis (1980) clinopyroxene-plagioclase-quartz geobarometer. Although a number of other garnet-clinopyroxene thermometers are available (Raheim & Green, 1974; Mori & Green, 1978; Ganguly, 1979; Saxena, 1979; Dahl, 1980), the Ellis & Green method has been recommended for use in both granulite and mantle nodule studies following the evaluations of Finnerty & Boyd (1984), Griffin et al. (1984) and Johnson et al. (1983).

As the garnet-clinopyroxene thermometer is based on Fe/Mg exchange, the accuracy of the thermometer is particularly dependent on the determination of ferric iron. The mineral analyses used in these calculations were derived via electron microprobe methods, and as such estimates of Fe^{3+} are necessarily based on assumptions. For clinopyroxene, Fe^{3+} was calculated using the charge balance equation:

$$Fe^{3+} = 4 - 2Si - 2Ti - Al - Cr + Na$$

following normalization to 4.000 cations. Ellis & Green (1985) showed that the difference between this recalculation procedure and wet chemical determinations of Fe^{3+} in clinopyroxenes from mafic granulites resulted in a difference of <1% in the calculated Mg-values.

Ryburn et al. (1975) suggested a similar charge balance equation for determining Fe^{3+} in garnet, but this method over-estimates the amount of Fe^{3+} in the octahedral site after allocation of Al^{IV}. Ferric iron has thus been calculated based on 8.000 cations, such that the octahedral site cations total 2.000 (Ghent et al., 1983). These calculations are cosmetic in that only eleven of the sixty garnet and clinopyroxene analyses have >1% calculated Fe_2O_3, and only one analysis (clinopyroxene) has >1.5% Fe_2O_3.

Microprobe analyses of all the data used in the P-T determinations are plotted in Figs 3.8 and the calculation parameters listed in Table 3.1. Note that the garnet and clinopyroxene are plotted within the "pyroxene" quadrilateral while plagioclase compositions are plotted in the upper Ca-Na-K triangle. Tie lines connect analyses obtained from phases in mutual contact; the analyses collected near the grain junctions. Quartz is an "excess" phase in each sample, but its occurrence adjacent to the analysed garnet-clinopyroxene-plagioclase assemblage was not thought critical to prove an equilibrium relationship with the analysed assemblage.

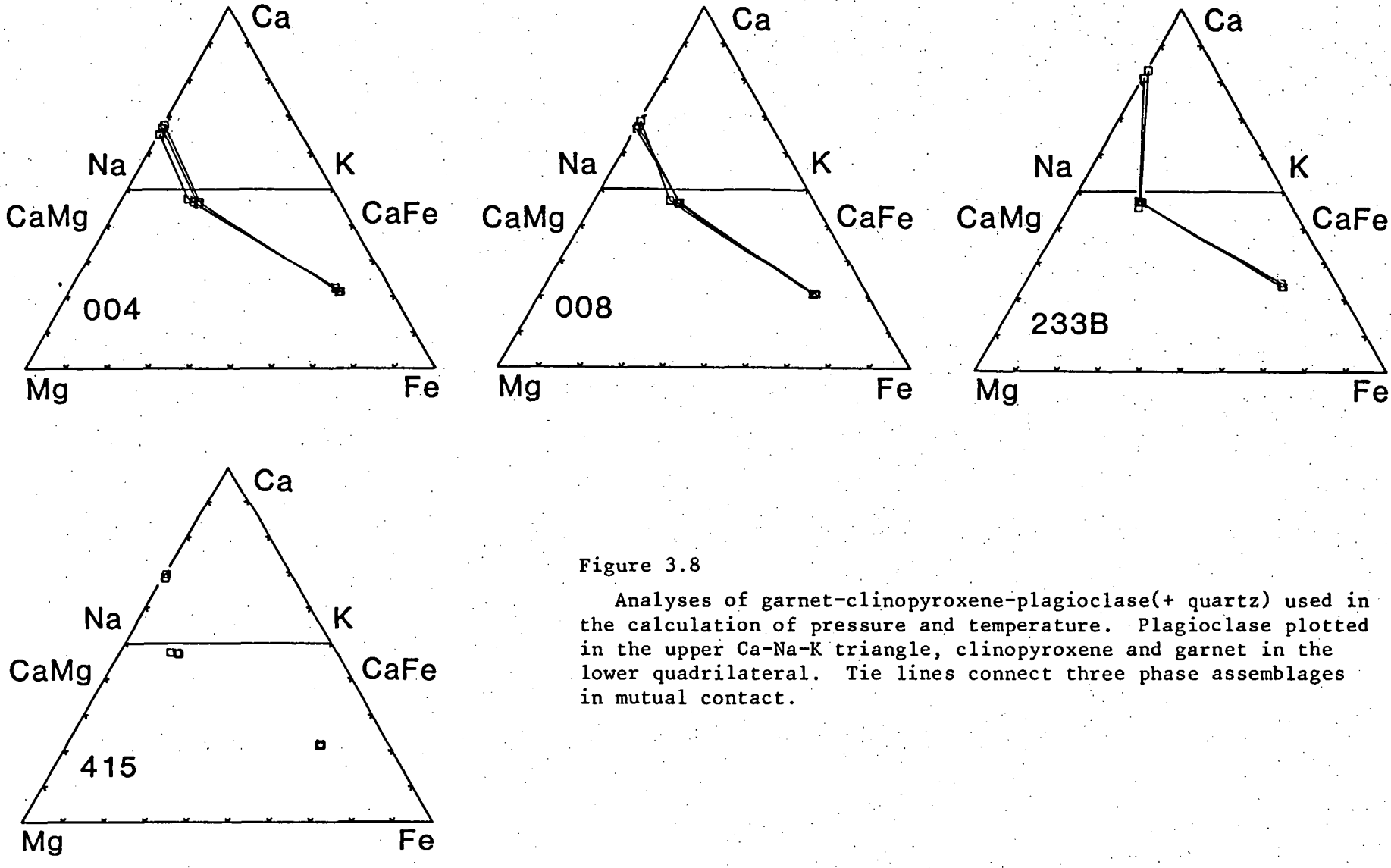

Figure 3.8

Analyses of garnet-clinopyroxene-plagioclase(+ quartz) used in the calculation of pressure and temperature. Plagioclase plotted in the upper Ca-Na-K triangle, clinopyroxene and garnet in the lower quadrilateral. Tie lines connect three phase assemblages in mutual contact.

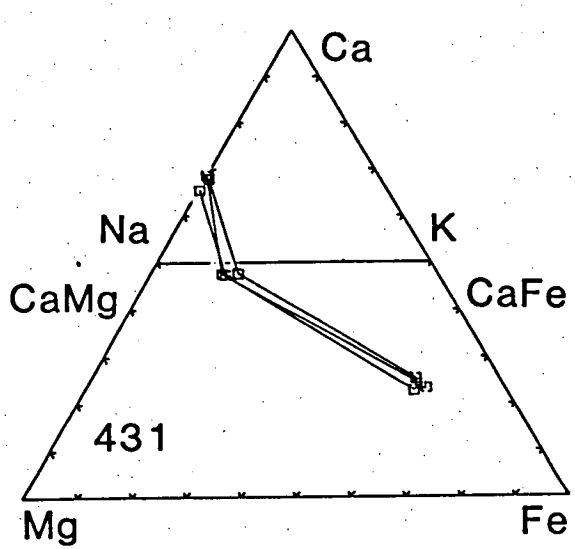
Ca
Na
K
CaMg
CaFe
431
Mg
Fe

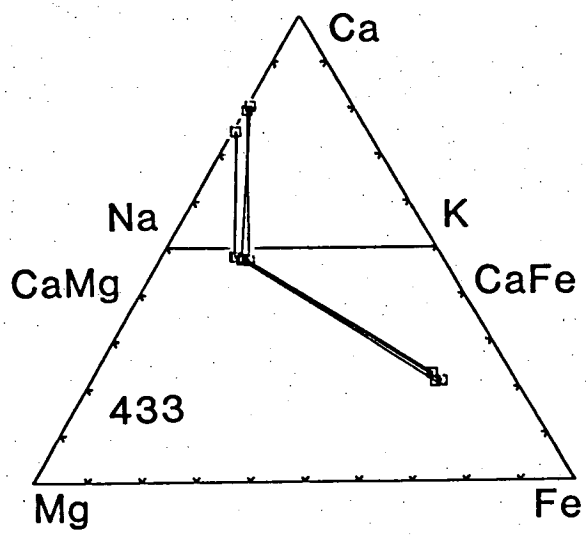
Ca
Na
K
CaMg
CaFe
433
Mg
Fe

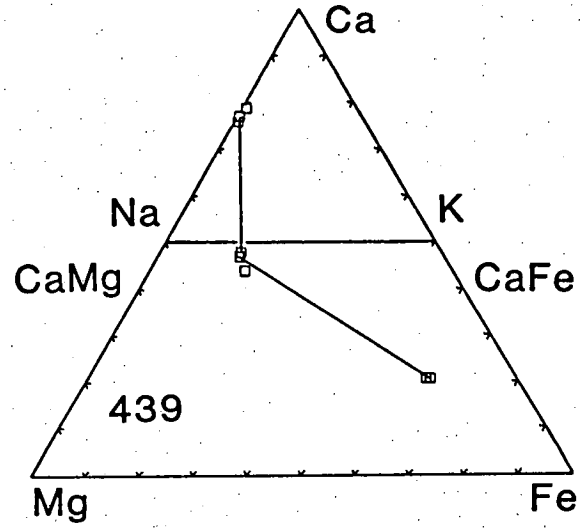
Ca
Na
K
CaMg
CaFe
439
Mg
Fe

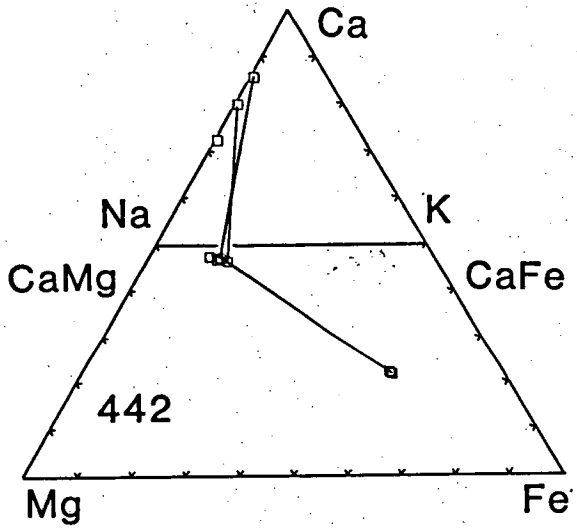
Ca
Na
K
CaMg
CaFe
442
Mg
Fe

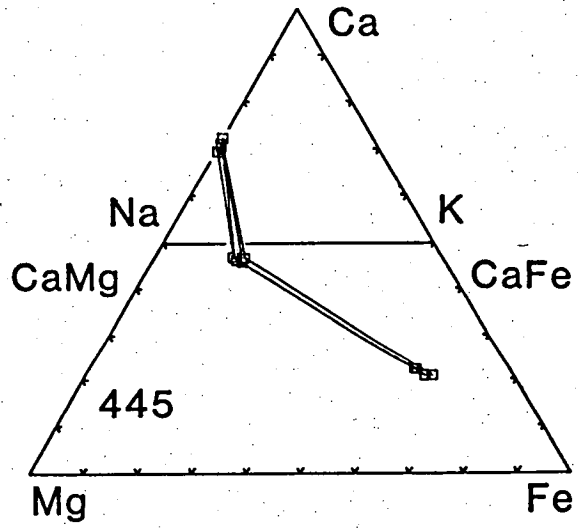
Ca
Na
K
CaMg
CaFe
445
Mg
Fe

Very little compositional zoning is observed within the phases of a particular sample indicating that equilibrium, on a local scale, has been approached. Plagioclase compositions are generally in the range of An_{35-40}. These albite-rich compositions are consistent with the Ca-rich igneous plagioclase components being incorporated into the garnet (Green & Ringwood, 1967b). Samples which contain more calcic plagioclase compositions or slightly scattered analyses (442, 233B, 433) may suggest disequilibrium, although, with the exception of the pressure calculated by the method of Ellis (1980) from sample 233B, they do not result in significantly different pressures or temperatures. These samples contain minor amounts of amphibole, indicating only a small volume of fluid may have been available to aid diffusion at these low temperatures, unlike the well equilibrated amphibole-rich samples noted above.

3.4.1 GARNET-CLINOPYROXENE GEOTHERMOMETRY

The average pressure (Gt-Cpx-Plag-Qtz) and temperature determined from each sample is plotted in Fig. 3.9. The temperatures calculated on the garnet-clinopyroxene assemblages range from 602-660°C for all samples; regional trends in the calculated temperatures are not apparent. For the sake of discussion, the temperatures from all the localities have been averaged (634°C), although there is no scientific basis for this as any (or none) of the calculated temperatures could represent a "peak" metamorphic value. Ellis & Green (1979) reported a ±5% error in calculated temperatures when the thermometer is checked against the experimental data of other workers. This percentage results in ±30°C for the temperatures obtained in this study, which essentially incorporates all calculated temperatures on either side of the mean.

3.4.2 GARNET-CLINOPYROXENE-PLAGIOCLASE-QUARTZ GEOBAROMETRY

Calculated pressures using the Gt-Cpx-Plag-Qtz assemblage range from 4.0-5.9 kbar, averaging 4.8 kbar. Experimental error is reported as 1.6 kbar. According to Newton & Perkins (1982) their clinopyroxene barometer results in pressures somewhat lower than the analogous garnet-orthopyroxene-plagioclase-quartz barometer when applied to samples collected from closely spaced localities. The possibility that this discrepancy was the result of staggered closure times with respect to equilibrium in the respective assemblages was discounted as the disparity was also found to include "quenched" lower crustal granulites entrained

TABLE 3.1
DATA USED IN GEOTHERMOMETRY-BAROMETRY CALCULATIONS

	$MG\#_{Cpx}$	$MG\#_{Gt}$	X^{Gt}_{Ca}	X^{Gt}_{Mg}	X^{Gt}_{Fe}	a^{Cpx}_{Diop}	X^{Plag}_{An}	X^{Cpx}_{CaTs}	$T^{o}C$	P(kbar) N-P	P(kbar) Ellis
65004	0.642	0.170	0.222	0.132	0.646	0.570	0.338	0.0188	653	5.4	
	0.691	0.159	0.213	0.125	0.662	0.597	0.302	0.0110	583	4.5	
	0.635	0.164	0.211	0.130	0.659	0.567	0.353	0.0234	642	4.8	
	0.665	0.171	0.224	0.132	0.643	0.593		0.0233	634		
Avg.*	0.658	0.166	0.218	0.130	0.653	0.582	0.331	0.0191	628	4.7(6.5)**	8.3
65008	0.657	0.170	0.209	0.134	0.657	0.562	0.370	0.0239	629	4.5	
	0.609	0.162	0.211	0.128	0.661	0.544	0.327	0.0201	664	5.1	
	0.617	0.159	0.208	0.126	0.667	0.538	0.340	0.0132	649	4.7	
Avg.	0.628	0.164	0.209	0.129	0.662	0.548	0.346	0.0191	647	4.7(6.3)	8.4
65233B	0.689	0.176	0.236	0.134	0.630	0.616	0.622		627	4.1	
	0.696	0.180	0.236	0.137	0.627	0.620	0.663		624	4.2	
	0.667	0.178	0.247	0.134	0.619	0.609		0.0105	650		
	0.688					0.565		0.0166			
	0.683					0.610		0.0129			
Avg.	0.687	0.178	0.240	0.135	0.625	0.604	0.643	0.0134	635	4.4(6.0)	3.2
65415	0.724	0.210	0.216	0.165	0.619	0.660	0.360	0.0154	622	nic	
	0.722	0.212	0.219	0.165	0.616	0.657	0.389	0.0153	630	nic	
	0.735	0.218	0.213	0.171	0.615	0.659	0.369	0.0089	619	nic	
	0.763					0.695	0.389	0.0159			
Avg.	0.736	0.213	0.216	0.167	0.617	0.668	0.377	0.0139	613	4.9(6.5)	6.0
65431	0.693	0.205	0.225	0.153	0.593	0.631	0.359	0.0251	679	6.5	
	0.735	0.219	0.229	0.169	0.602	0.633	0.309	0.0301	632	6.2	
	0.749	0.198	0.243	0.150	0.607	0.640	0.372	0.0186	600	5.4	
	0.693					0.605		0.0245			
		0.189	0.235	0.144	0.621						
Avg.	0.718	0.203	0.241	0.154	0.606	0.627	0.347	0.0246	639	5.9(7.5)	9.5
65433	0.740	0.174	0.214	0.136	0.650	0.629	0.500	0.0071	559	3.4	
	0.712	0.189	0.212	0.149	0.640	0.614	0.610	0.0270	604	3.8	
	0.706	0.188	0.230	0.145	0.625	0.606	0.590	0.0	622	4.3	
	0.686	0.189	0.230	0.146	0.625	0.617		0.0271	644		
	0.736							0.0051			
Avg.	0.716	0.185	0.222	0.144	0.635	0.616	0.567	0.0153	602	4.0(5.6)	4.8
65439	0.710	0.198	0.207	0.157	0.636	0.609	0.542		615	4.0	
	0.708	0.225	0.206	0.179	0.615	0.609	0.576		nic	nic	
	0.681	0.207	0.207	0.164	0.628	0.601	0.520		nic	nic	
Avg.	0.700	0.210	0.207	0.167	0.626	0.606	0.546		641	4.3(5.9)	8.6
65442	0.785	0.263	0.216	0.207	0.578	0.690	0.448	0.0229	615	5.3	
	0.757	0.267	0.220	0.209	0.571	0.686	0.710	0.0190	657	5.2	
	0.746					0.665		0.0367			
	0.718					0.641		0.0223			
Avg.	0.752	0.265	0.218	0.208	0.575	0.671	0.585	0.0252	660	5.4(7.0)	6.9
65445	0.714	0.223	0.222	0.173	0.605	0.637	0.423	0.0161	654	5.3	
	0.693	0.203	0.208	0.165	0.627	0.596	0.447	0.0150	640	4.7	
	0.687	0.191	0.208	0.151	0.640	0.608	0.411	0.0095	629	4.4	
	0.727	0.226	0.224	0.176	0.601	0.637	0.389	0.0173	646	5.6	
Avg.	0.705	0.211	0.216	0.166	0.618	0.619	0.418	0.0145	644	5.0(6.6)	5.4

$Mg\# = Mg/(Mg+Fe)$. $X^{Gt}_{B} = B/(Ca+Mg+Fe)$.

* Raw data were numerically averaged- the average temperature and pressure were calculated from the averaged data.
** These pressure determinations contain the 1.6 kbar adjustment recommended by Newton & Perkins, see text.
Temperature calculated from Ellis & Green (1979) (@ 5 kbar).
Pressure calculated from Newton & Perkins (1982), Ellis (1980).
CaTs calculated following Kushiro (1962).
nic = phases were not in contact.

within kimberlite diatremes. It was concluded that the most probable source of the disagreement was in the thermodynamic data, and the barometers will coincide, on average, if 1.6 kbar is added to the cpx-barometer, and 0.6 kbar subtracted from the opx-barometer. According to the authors "... such adjustments are empirical and necessarily subjective and are left to the reader's discretion." However, the adjusted pressures in the examples used by Newton & Perkins properly predicted kyanite vs sillimanite-bearing granulites. Similarly, Ghent et al. (1983) found the adjusted clinopyroxene barometer reproduced to within 0.4 kbar, pressure estimated from the garnet-plagioclase-Al_2O_3-quartz barometer, and also the kyanite-sillimanite transition. In view of these consistencies with other barometric indicators, the metamorphic conditions indicated by the garnet-bearing assemblages in the Vestfold Hills are considered to be 630 $\pm$ 30°C and 6.4 $\pm$ 1.6 kbar.

3.4.3 CLINOPYROXENE-PLAGIOCLASE-QUARTZ GEOBAROMETRY

The averaged pressure calculated from individual samples based on the clinopyroxene-plagioclase-quartz assemblage varies widely (3.2-9.5 kbar; Table 3.1). Perhaps fortuitously, the average pressure (6.7 kbar) is nearly identical to that calculated from the garnet assemblage. The lowest pressure estimate (3.2 kbar, sample 233B) is from an igneous textured rock with garnet and clinopyroxene developed in localized shears. The relatively high X_{An} used in the calculation may indicate igneous compositions, and not plagioclase compositions which are in equilibrium with the garnet assemblage. The pressure calculated using the garnet assemblage of 233B is generally consistent with the pressures estimated from other samples, thus the difference between the pressures calculated from each barometer is probably due to the relative weightings given to the plagioclase composition. Excluding sample 233B, the average metamorphic pressure based on the Cpx + Plag + Qtz assemblage of the garnet bearing dykes is 7.2 kbar. This value is within error of the 6.4 kbar calculated from the garnet-clinopyroxene-plagioclase-quartz barometer and tends to substantiate the 1.6 kbar adjustment to the Newton & Perkins cpx-barometer.

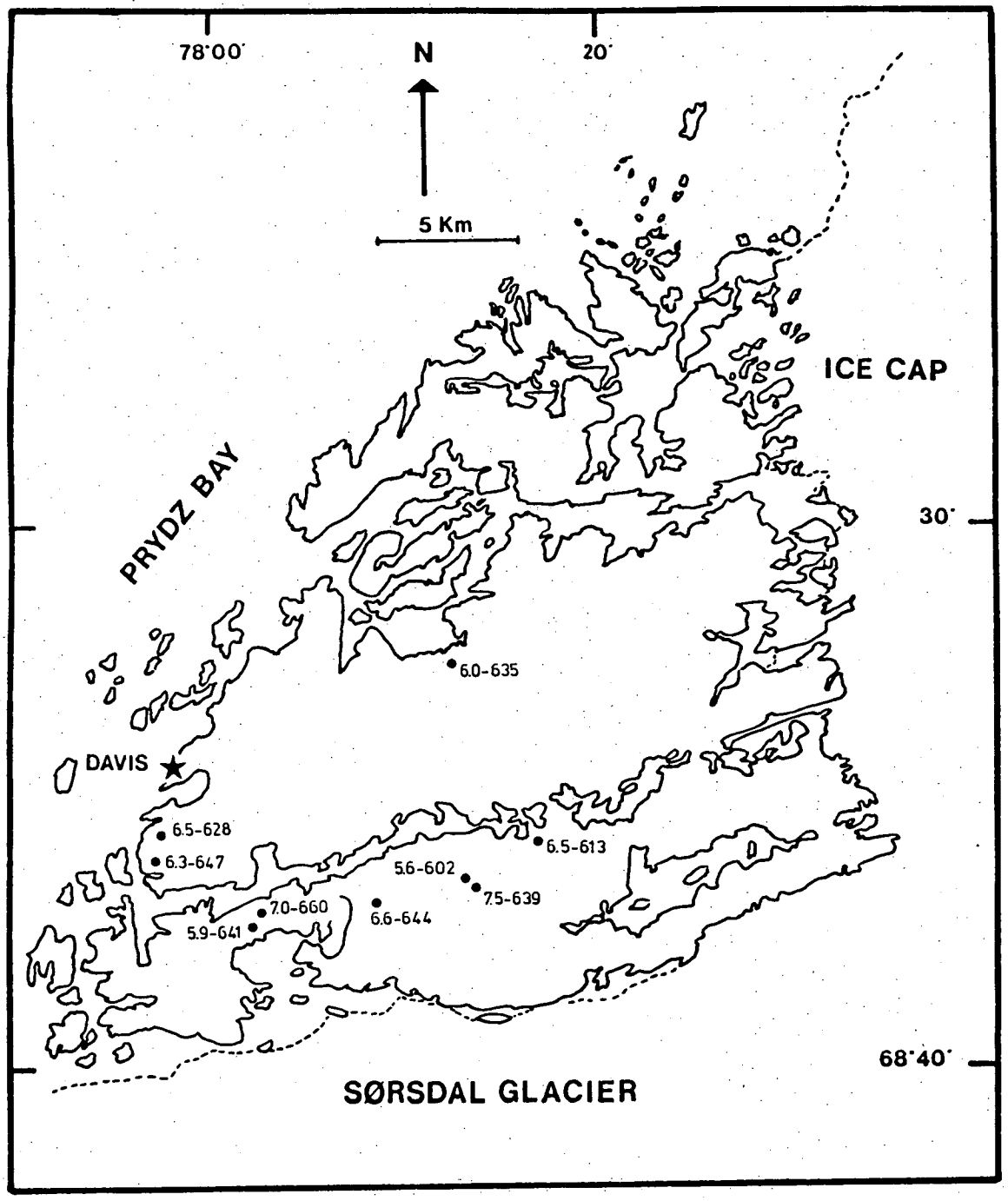

Figure 3.9

Results of P-T calculations on samples indicated in Fig. 3.1 First number refers to pressure calculated from garnet assemblage in kbar, second number is garnet-clinopyroxene temperature in °C.

3.5 CONCLUSIONS

In terms of the crustal history of the Vestfold Hills, the most important conclusion obtained from studying the petrographic relationships of the metamorphic mineral assemblages in the Fe-rich tholeiite dykes is that garnet development occurred through the dehydration of a secondary hornblende-bearing assemblage. Interpretation of the disequilibrium textures indicates that hydration of the original igneous assemblage was by the reaction:

$$Opx + Cpx + Plag + H_2O \longrightarrow Hbd + Qtz$$

followed by the development of garnet via the reaction:

$$Hbd + Qtz + (Ca\text{-}Plag) \longrightarrow Gt + Cpx + (Na\text{-}Plag) + H_2O.$$

The topological arrangement of equilibrium assemblages in the simple system Na-CMASH indicates that the observed sequence of metamorphic reactions in the Vestfold Hills dykes resulted from an increase in pressure and temperature. A pressure increase is clearly required to produce the textural relationships, although this may have been accompanied by either a temperature increase and/or a reduction in a_{H_2O}. There is no evidence for, or against, lowering of a_{H_2O} on a regional scale. However, garnet is found in carbonated shears and veinlets suggesting that in localized instances, garnet development was promoted by a reduction in a_{H_2O}. The garnet assemblages record metamorphic conditions of 6.4 kbar, 630°C which then imply that hydration of the igneous assemblage occurred at pressures <6.4 kbar.

CHAPTER 4

CONCLUSIONS:
INTEGRATION OF MAFIC DYKE STUDIES WITH THE PREVIOUSLY DESCRIBED CRUSTAL HISTORY OF THE VESTFOLD HILLS AND ENDERBY LAND - IMPLICATIONS FOR ARCHEAN-PROTEROZOIC UPLIFT PATHS IN THE EAST ANTARCTIC SHIELD

CHAPTER 4

CONCLUSIONS:
INTEGRATION OF MAFIC DYKE STUDIES WITH THE PREVIOUSLY DESCRIBED CRUSTAL HISTORY OF THE VESTFOLD HILLS AND ENDERBY LAND - IMPLICATIONS FOR ARCHEAN-PROTEROZOIC UPLIFT PATHS IN THE EAST ANTARCTIC SHIELD

The three preceding chapters have focused on the crustal history of the East Antarctic Shield as recorded in the chemistry and mineralogy of the mafic dykes in the Vestfold Hills and Enderby Land. In Chapter 1, the emplacement pressures of two Vestfold Hills dykes of known age were determined by applying high pressure experimental techniques to reproduce their chilled margin phenocryst assemblages. The liquidus phase relationships of these two samples were then used to estimate the emplacement pressures of other dyke suites in the Vestfold Hills and Enderby Land (Chapter 2). In Chapter 3, the P-T conditions of metamorphism at ca.1100 Ma were deduced from petrographic and geothermometric-barometric studies of recrystallized garnet bearing assemblages of dykes in the southwest portion of the Vestfold Hills.

In this the concluding chapter of Part 1, the P-T information obtained from the mafic dyke studies is combined with previous metamorphic and chronological studies to further constrain the pressure (depth) versus time path followed by the East Antarctic Shield from the Late Archean through the Proterozoic.

4.1 THE UPLIFT PATH OF THE NAPIER COMPLEX

The pressure versus time diagram illustrating the uplift history of the Napier Complex over a time period of ~2000 Ma is shown in Fig. 4.1. The retention of the Napier Complex at deep crustal levels until at least ca.1190 Ma has been inferred in the work of Ellis (1983), Sandiford & Wilson (1983), Harley (1985a), and Black et al. (1983a), but could not be proven by their methods of study which contrasted the metamorphic conditions of M1-M3 with those at M4/5 (Fig. 4.1). These authors examined metamorphic rocks from areas of the Napier Complex which were inferred to have been reworked by the Rayner metamorphism at ca.1000 Ma, and found that near-isothermal decompression paths were recorded in the textures and phase chemistry. Cores of mineral assemblages were shown to retain evidence of pressures up to 8.5 kbar, while symplectic rims and core-rim zoning patterns record pressures of 3-5 kbar.

The overprinting by lower pressure metamorphic mineral assemblages and the retention of relict high pressure cores do not preclude the possibility of slow uplift between ca.2500 Ma (M3) - ca.1000 Ma (M4/5) with recrystallization of the metastable M1-M3 assemblages proceeding only where deformation associated with M4/5 catalyzed reaction rates. The alternative possibility, that high pressure conditions prevailed up to ca.1000 Ma is equally consistent with the metamorphic petrology studies.

The emplacement of the group 1 tholeiites at ca.1190 Ma and at pressures $\geq$8 kbar is only consistent with, and independently confirms the second model, i.e. rapid decompression at ca.1000 Ma.

Isotopic age determinations for the Rayner metamorphism have been reported from synorogenic intrusives as 1022 $\pm$ 62 Ma (Grew, 1978, adjusted to $\lambda_{Rb} = 1.42 \times 10^{-11}\ a^{-1}$) and a monazite age of $1073\ ^{+31}_{-36}$ (Black & James, 1983). If it is assumed that these dates (mid point of error overlap = 1061 Ma) correspond to a post-peak metamorphic age, an estimate of the uplift rate representing the dominant tectonic event can be calculated by combining the emplacement age (1190 Ma) and pressure (~8 kbar) of the group 1 suite with the minimum load pressure for the Rayner metamorphism (~4 kbar). This results in an estimated uplift rate of 11 cm/1000 a.

This value is very low compared to present day uplift rates measured in the collision zones of the Himalayas (80 cm/1000 a, reported in Sharma et al., 1980, p.148; 500 cm/1000 a, Gansser, 1979) and Alps (100 cm/1000 a, reported in Ollier, 1981, p.249). However, the calculated uplift rate for the Napier Complex represents a net decompression path averaged over 129 Ma., and as such, may give an oversimplified impression of what may

Figure 4.1

Pressure versus time plot incorporating previous metamorphic and geochronological studies with the emplacement pressures of Napier Complex dyke suites as determined in Chapter 2. Note absolute age of group 2 tholeiites has not been determined, see text. Metamorphic events (M1-M5) after Harley (1985a). Diagonal pattern: Scott Mts-Casey Bay region. Dotted pattern: North Tula Mts. No pattern: mafic dyke determinations.

Data sources: Black & James (1983), Black et al. (submitted), Ellis (1980, 1983), Grew (1981), Harley (1985a, 1985b), Sandiford (1985), Sandiford & Wilson (1983), Sheraton & Black (1981).

a - ca.2400 Ma High-Mg tholeiites; b - ca.1190 Ma Fe-rich group 1 tholeiites; c - undated group 2 tholeiites.

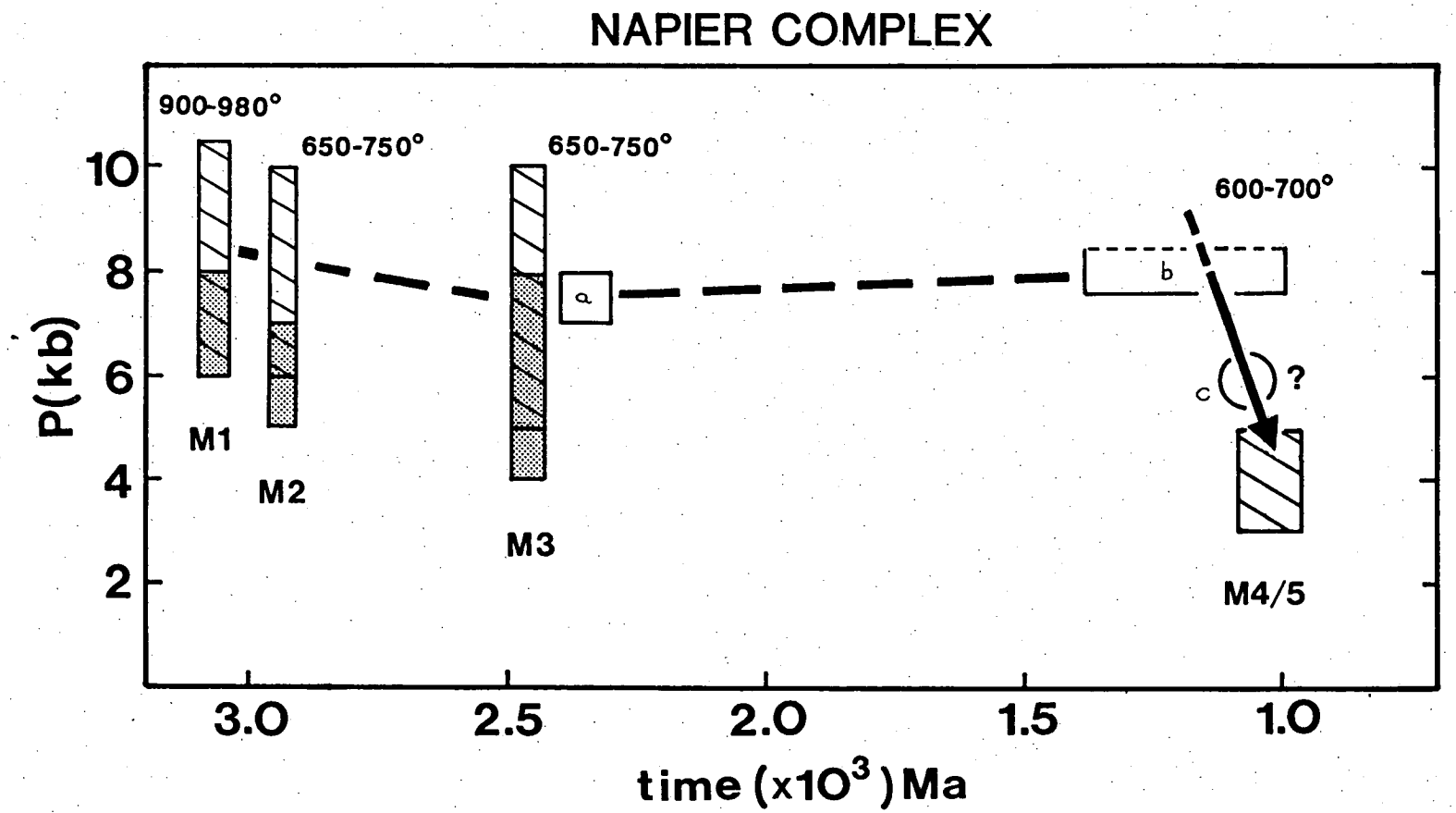
NAPIER COMPLEX
900-980°
650-750°
650-750°
600-700°
M1
M2
M3
M4/5
a
b
c
?
P(kb)
10
8
6
4
2
3.0
2.5
2.0
1.5
1.0
time (x10³) Ma

have been a very complicated uplift trajectory which perhaps included periods of rapid decompression, crustal stability, and possibly subsidence (Tingey, 1985). As the onset of uplift may not have been contemporaneous with the emplacement of the group 1 dykes, the 129 Ma time span would be a maximum and the uplift rate a minimum.

Considering the limitations inherent to net uplift rates and the difficulty in comparing these values with those obtained from modern environments, it is worth noting the similarity between the uplift rate calculated for the Napier Complex during the Rayner metamorphism and that calculated for the Cretaceous granulites found in the northwest Himalayas (9 cm/1000 a) over a comparable time period (94 Ma, Ollier, 1981, Zeilter, 1985). It is well established that the Himalayas are the result of the Indian subcontinent colliding with Eurasia, a process that has produced crustal thicknesses of up to 80 km, double that of modern 'stable' cratons. If it is assumed that by ca.1000 Ma the physical properties of the upper mantle, in terms of crust-mantle buoyancy relationships, were much as they are today (Goodwin, 1981; Thompson, 1984), then, it can be inferred from the similar rate of uplift during the Rayner metamorphism and the formation of the Himalayas, that Napier Complex crustal thickness must also have been doubled during the Rayner metamorphism. As the group 1 dykes were emplaced at ~8 kbar, the minimum crustal thickness prior to underthrusting would have been ~28 km, giving a minimum crustal thickness of ~56 km during the Rayner metamorphism.

Prior to this study, the only evidence for uplift during the Rayner metamorphism was restricted to areas of the Napier Complex transected by shear zones assumed to have been produced during the ca.1000 Ma event. The shear zones acted as conduits for the introduction of fluids and were also sites of recrystallization catalyzed by deformation which recorded the change to lower pressure conditions. Outside of these shear zones there is no metamorphic evidence for significant post-D3 uplift in the Napier Complex. It is possible then that only the reworked (M4/5) areas were uplifted at ca.1000 Ma with the greater part of the Napier Complex remaining at deep crustal levels. However, in Chapter 2, the emplacement pressure of the group 2 tholeiite suite was discussed and it was concluded that the phenocryst assemblage indicated emplacement at pressures <8 kbar, and possibly ~5-6 kbar. As the group 2 suite crops out throughout the entire Napier Complex (Fig. 2.12) the emplacement of the suite at pressures less than group 1 (~8 kbar) provides direct evidence for uplift of the entire Napier Complex in conjunction with the Rayner metamorphism.

4.2 THE UPLIFT PATH OF THE VESTFOLD HILLS

The results of preliminary metamorphic and geochronological studies of the Vestfold Hills define the first Archean deformation at 3062 ± 212 Ma, 8-10 kbar and ~1000°C, with a second event at 2411 ± 212 Ma, 5-8.5 kbar, ~700°C (Collerson et al., 1983a (abstract only), 1983b). These data are incorporated into a P-t diagram for the Vestfold Hills shown in Fig. 4.2. Collerson et al. (1983a) thought that metamorphic pressures during the later event were ~5 kbar, but the post-kinematic emplacement of the high-Mg tholeiite suite at pressures of 7-8 kbar (Section 1.3.1) clearly indicates that this assumption is incorrect. Cooling from ~1000°C at ca.3100 Ma to ~700°C at ca.2500 Ma with only a minor decrease in pressure is the same evidence used by Ellis (1980) to suggest that a magmatic-derived heat flux at the base of the Napier Complex was responsible for the high metamorphic geotherm (~1000°C at ~9 kbar) at ca.3100 Ma.

Following emplacement of the high-Mg tholeiite suite at ca.2400 Ma, the uplift history of the Vestfold Hills markedly diverged from that of the Napier Complex. Experimental studies (Section 1.3.2) defined the emplacement pressure of the ca.1360 Ma tholeiites at 4-5 kbar, signifying an uplift of ~10 km following the emplacement of the high-Mg suite.

No evidence presently exists which can directly clarify the uplift path between ca.2400 and 1360 Ma. The ca.1800 Ma tholeiites are known only to have been emplaced at pressures <8 kbar, though the phenocryst assemblage may indicate pressures as low as 5-6 kbar (Section 2.1.3). The latter pressure range would be consistent with the slow uplift path (~1 cm/1000 a) shown in Fig. 4.2. The absence of recognizable tectonic events over this time span also argues against significant changes in the uplift rate prior to ca.1360 Ma.

The development of garnet in the mafic dykes of the southwest portion of the Vestfold Hills is believed to be the result of the ca.1100 Ma metamorphism (Sheraton & Collerson, 1983). Geobarometric methods applied to the garnet-bearing assemblages (Chapter 3) record pressures of 6-7 kbar. Furthermore, a comparison with simple system phase topology indicates that a pressure increase is required to explain the reaction relationships observed petrographically. The petrographic interpretation and estimated pressure of metamorphism are in agreement with the independently determined, slightly higher crustal level of the Vestfold Hills terrain at ca.1360 Ma (~14-17 km). Subsequent depression of the terrain at ca.1100 Ma to 21-24 km resulted in dehydration of the secondary hornblende assemblage and reaction to garnet.

Figure 4.2

Pressure versus time plot incorporating previous metamorphic and geochronological studies with the emplacement pressures of the Vestfold Hills dyke suites as determined in Chapters 1 and 2. Diagonal pattern: pressures determined from metamorphic assemblages. No pattern: mafic dyke determinations. Error in the isotopic data for the ca. 2500 Ma metamorphism exceeds 200 Ma, only that portion of the error range which exceeds the emplacement age of the high-Mg suite is shown.

Data sources: Collerson et al. (1983a), Collerson et al. (1983b), Collerson & Sheraton (in press), Sheraton & Black (1981), Sheraton et al. (1984).

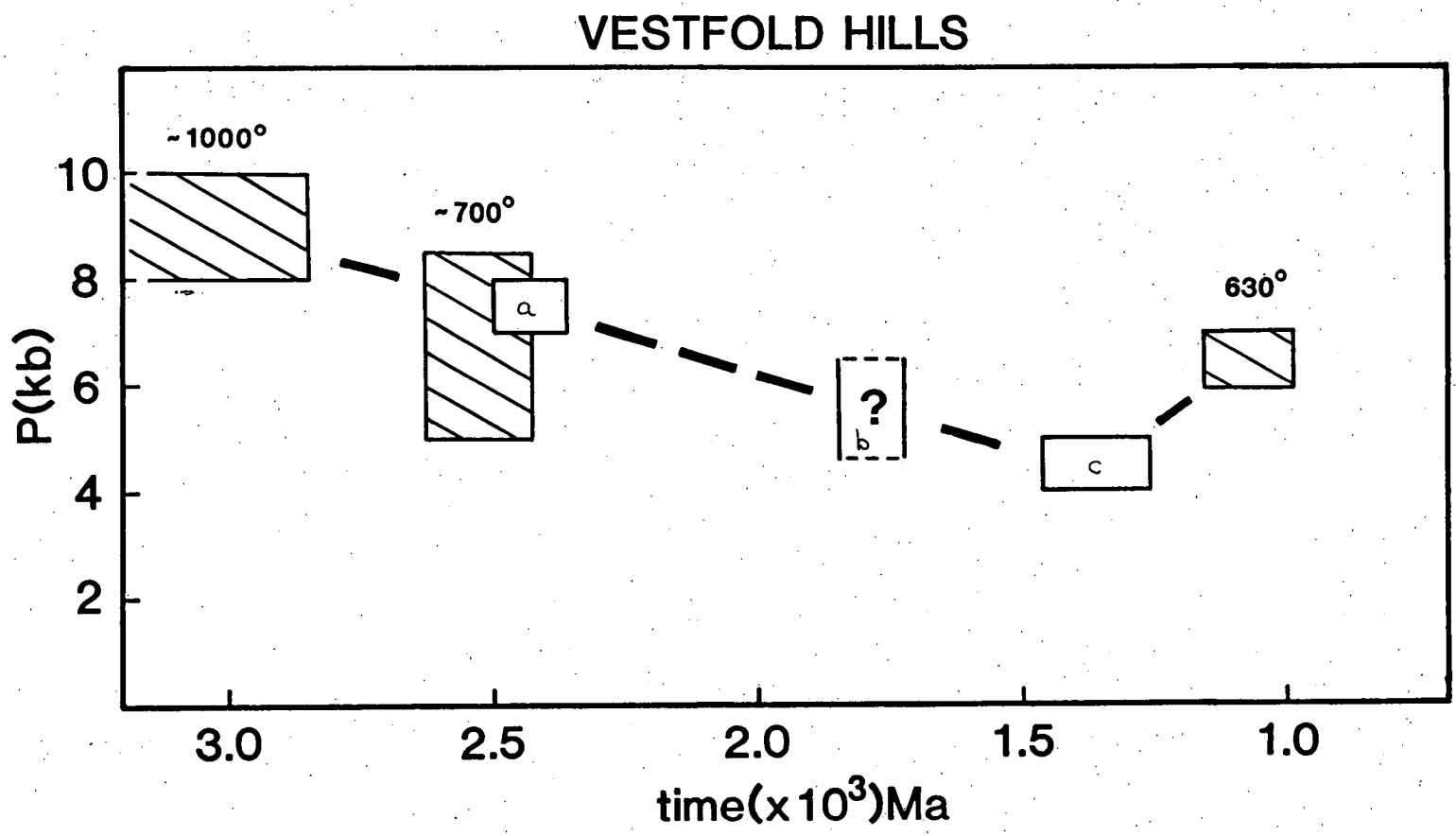
VESTFOLD HILLS
~1000°
~700°
630°
a
?
b
c
10
8
6
4
2
P(kb)
3.0
2.5
2.0
1.5
1.0
time(x10³)Ma

Sheraton & Black (1981), Sheraton et al. (1984). a - ca.2400 Ma High-Mg tholeiites; b - ca.1800 Ma Fe-rich tholeiites; c - ca.1360 Ma Fe-rich tholeiites.

4.3 DISCUSSION

Ellis (1980), Ellis & Green (1985) and Harley (1985b) have inferred unusually stable crustal conditions following the peak Archean metamorphic event in the Napier Complex, and emphasized that the complex experienced near-isobaric cooling for at least 500 Ma. A similar Archean history has now been identified in the Vestfold Hills following the recognition that the post-kinematic high-Mg tholeiite suite was emplaced at a ca.2400 Ma under load pressures only slightly lower than those of the peak metamorphism at ca.3100 Ma. As the Napier Complex and Vestfold Hills are separated by ~1000 km, it is evident that the tectonic style responsible for the Archean metamorphism was not a localized or unique event, but was operative on an extensive scale.

Many models have been proposed to explain the geological features of high grade Archean gneiss terrains throughout the world (see review in Kröner, 1985). A major problem is to reconcile the high temperatures required to produce granulite facies mineral assemblages with the cool crustal geotherms implied by the formation of diamonds in the Archean (Richardson et al. 1984). Granulites are presently being formed in Alpine-Himalayan and Andean-Cordilleran type collision zones and these styles of tectonism have been proposed on a uniformitarian basis to explain the geothermal gradients required to produce Archean granulites. This line of reasoning has been advanced specifically by De Paolo et al. (1982) to explain the Napier Complex granulites.

A characteristic of both the Himalayan and Andean tectonic models is the formation of greatly thickened crust (up to ~80 km). It is recognized that exposed Archean granulite terrains metamorphosed at 8-10 kbar (28-35 km) are now underlain by 30-40 km of crust, which could indicate Archean crustal thicknesses of ~60-70 km, comparable to modern collisional environments (Wells, 1981). As a result of the thickened crust, modern-day collision zones experience massive isostatic disequilibrium with the mantle, producing rapid rates of exhumation and near-isothermal decompression paths (England & Richardson, 1977; Hollister, 1982).

Based on the above characteristics, there appears to be no evidence from the Napier Complex or the Vestfold Hills to suggest that collisional tectonics, in the sense of a modern-day Wilson cycle, operated before ca.1100 Ma. The recognition in this study of the high pressure, post-kinematic emplacement of the high-Mg suites, and the evidence documented by Ellis (1980), Ellis & Green (1985) and Harley (1985), excludes any style of tectonism which would require large scale crustal thickening to produce the

granulite facies metamorphisms from ca.3100-2500 Ma. The absence of rapid uplift during, or even directly following these metamorphic events, is inconsistent with collisional tectonic models. In addition, it will be argued in Chapter 5 that the high-Mg tholeiites were derived by partial melting of a peridotitic mantle at ~10 kbar pressure. Thus the maximum crustal thickness at ca.2400 Ma was ~35 km, and ~42 km at ca.3100 Ma. These crustal thicknesses are also inconsistent with modern collisional environments.

Ellis (1980) proposed that the temperatures responsible for the ca.3100 Ma granulite facies metamorphism in the Napier Complex resulted from the conductive transfer of heat from the crystallization of mantle-derived liquids coalescing at the base of the crust. This model could produce granulites within a stable crustal segment without crustal thickening, which would subsequently cool isobarically following the cessation of the heating event. An identical model was advocated by Herzberg et al. (1983) after considering magma densities and the often transitional seismic nature of the crust-mantle boundary. These authors considered Archean granulite terrains to be a "... vast 'contact aureole' due to magma underplating." The existence of a large positive modified free-air gravity anomaly beneath the Napier Mts (Wellman & Tingey, 1982) was put forward by Ellis (1980) as corroborating evidence for this type of model. Conversely however, Grew (1980) concluded that the distribution of the mineral assemblages sapphirine + quartz and osumilite, which are coincident with a large negative gravity anomaly in the Casey Bay region, corresponds to a large thermal aureole developed around a subsurface anorthosite complex comparable to the association found on a smaller scale in the Grenville Province. A large positive anomaly has also been identified beneath the Vestfold Hills (Wellman & Williams, 1982).

A more efficient method of transporting heat into the lower crust is through convection, by way of emplacement and crystallization of the synorogenic tonalite and granodiorite intrusives described from both the Napier Complex and Vestfold Hills (Sheraton & Collerson, 1983; James & Black, 1981). The geochemistry of these orthogneisses has been studied by Sheraton & Black (1983) and Sheraton & Collerson (1984) who defined Y-depleted and Y-undepleted suites which were considered to be the result of melting garnet-bearing amphibolites or eclogite and felsic crustal material respectively. Partial melts derived from the base of the crust would be anticipated from the accumulation of high temperature possibly picritic or komatiitic liquids at the crust/mantle boundary. Movement of the anatectic melts into slightly higher crustal levels, and their crystallization as

sheets would pre-heat an extensive portion of the tectonically active lower crust and reduce the amount of conducted heat necessary to produce the high grade metamorphic terrain. An implication from the existence of the undepleted suite is that the crustal thickness at ca.3100 Ma was probably nearer 42 km than 35 km.

If both geochemical orthogneiss suites had their source in the extant crust there would be no net crustal growth. However, Sheraton & Collerson (1984) and Sheraton & Black (1983) favour a model where depleted melts are derived from "subducted" or "down-sagging" eclogitic mafic crust. If this is the case, a substantial amount of crustal thickening may have occurred with the emplacement of the felsic melts. Structural studies have produced more definitive evidence for crustal thickening during D1. Black & James (1983) and James & Black (1981) reported stacked nappe structures and reclined folds, indicative of tectonic thickening, though it has been argued repeatedly (see above) that the isobaric cooling path deduced from metamorphic studies of the Napier Complex and the Vestfold Hills is not consistent with a style of tectonism producing large scale crustal thickening.

Harley (1985b) appears to have been the only researcher to recognize this contradiction, and explained it by relying on the thermal event to play the dominant role in the evolution of the P-T-t path. This is probably a justified conclusion, especially considering that the result of the tectonism was a crust <42 km thick. Furthermore, the ~7 km of uplift which took place between M1 and M3 may not have been linear as shown in Fig. 4.1, but could have taken place directly after the crustal thickening associated with the peak metamorphism.

Neither the Vestfold Hills nor the Napier Complex experienced any pronounced tectonic events in the ~1400 Ma following the deformation at ca.2500 Ma. Both terrains were apparently part of a very stable continental mass well away from tectonically active continental margins, and in the case of the Napier Complex unaffectd even by erosion induced isostatic processes. Comparable examples to the Proterozoic stability of the Napier Complex and hence a possible indication of the prevailing style of tectonism, can presently be found on the South African Precambrian cratons, where sediments of ca.1700 Ma are undeformed and have experienced <2 km of net uplift since their deposition (Shackleton, 1970). Similarly, Podghan (1981) reported that <1 km of material has been eroded from the Slave Province of Northern Canada in the last ~1700 Ma.

Even though the Vestfold Hills experienced ~10 km of uplift over the ~1400 Ma period, the net uplift rate was very slow: ~1 cm/1000 a. This

rate of exhumation may be accounted for simply by invoking erosional processes, but the emplacement of two suites of mafic dykes, unaccompanied by deformational events, may have enhanced the uplift. McKenzie (1984) and Stolper & Walker (1980) suggested that primary mantle-derived liquids of density ~2.9 g/cc may pond at the crust/mantle boundary and fractionate to evolved liquids having densities of ~2.7 g/cc. The addition of this new material to the crust will result in permanent uplift. McKenzie (1984) calculated that 2.7 km of uplift will result from the addition of a magma body 15 km thick within or at the base of the crust. The large amount of material required to produce a small uplift indicates that this may not be a major process but the mechanism must have occurred at least on a small scale in the Vestfold Hills, as evidenced by the emplacement of dykes having evolved compositions at ca.1800 Ma and ca.1360 Ma. In addition, the emplacement of the swarms would have heated the lower crust resulting in thermally-induced though transitory uplift.

Neither the Vestfold Hills nor the Napier Complex has experienced major deformational events since ca.1000 Ma. Intrusion of granitic pegmatites and an ultrapotassic dyke in the Napier Complex and a granitic body about 250 km west of the Vestfold Hills have been related to a thermal event at ca.500 Ma (James & Tingey, 1983) and may have been caused minor, transitory uplift. Minor thermally-induced uplift would also be expected to be associated with the rifting of Gondwanaland at ca.100 Ma though this would also only have been temporary. In the absence of evidence for more recent deformational events, it is assumed that these terrains have experienced slow, erosion-controlled uplift since ca.1000 Ma.

PART 2

PETROLOGY AND GEOCHEMISTRY OF VESTFOLD HILLS PROTEROZOIC DYKE SUITES

INTRODUCTION

The Vestfold Hills comprise a low lying, ice-free area in Antarctica of approximately 400 km^2, interspersed with lakes and fjords. The near-continuous exposure makes the Vestfold Hills an ideal locality for not only sampling the hundreds of Proterozoic mafic dykes outcropping throughout the region, but also for determining the relative age relationships of dykes that form a chemically or petrographically coherent group, through the detailed documentation of intersecting relationships. The purpose of this aspect of the sampling program was to use the intersections to establish a time and spatial framework for the chemical evolution within and between suites, in much the same manner as stratigraphy is used in subaereal volcanic terrains (Francis et al., 1981; Faure et al., 1974). The mafic dyke samples collected during the regional reconnaissance by Sheraton & Collerson (1983) and Collerson & Sheraton (in press) were invaluable in this respect, as these authors provided the geochemical and isotopic studies which related the emplacement of specific geochemical suites with absolute time. This formed the basis from which the intra-suite chemical variations could be examined.

Critical to the experimental approach used to determine the emplacement pressures of samples 060 and 206 (Chapter 1) was the ability to first show that these samples had not accumulated phenocrysts, and could be considered as liquid compositions. Crystal settling and therefore liquid modification will readily occur within slowly cooled dyke interiors. Thus in order to minimize the possibility of obtaining phenocryst-enriched samples, as dictated by the experimental program, sampling of the dykes emphasized the collection of "quenched" margin samples. To the extent that these chilled margins are aphanitic, they are believed to closely approach the composition of the liquid at the time of dyke emplacement, and not to have experienced subsequent crystal accumulation or fractionation. This was demonstrated for both 060 and 206 (Chapter 1). Due to circumstances such as relative weathering profiles between the dykes and the country rock, or sheared dyke margins, chilled margins could not always be obtained. However, of the 144 samples analysed (248 collected) the vast majority of samples were collected from chilled margins and have <10% phenocryst contents. Thus the compositional trends described in the following chapters are largely those of liquid variations.

A convenient first-order discriminant used to subdivide the 144 analyses into chemically-defined suites is a plot of FeO/MgO versus TiO_2 (Fig. I2.1). Based on this diagram, five relatively well defined suites

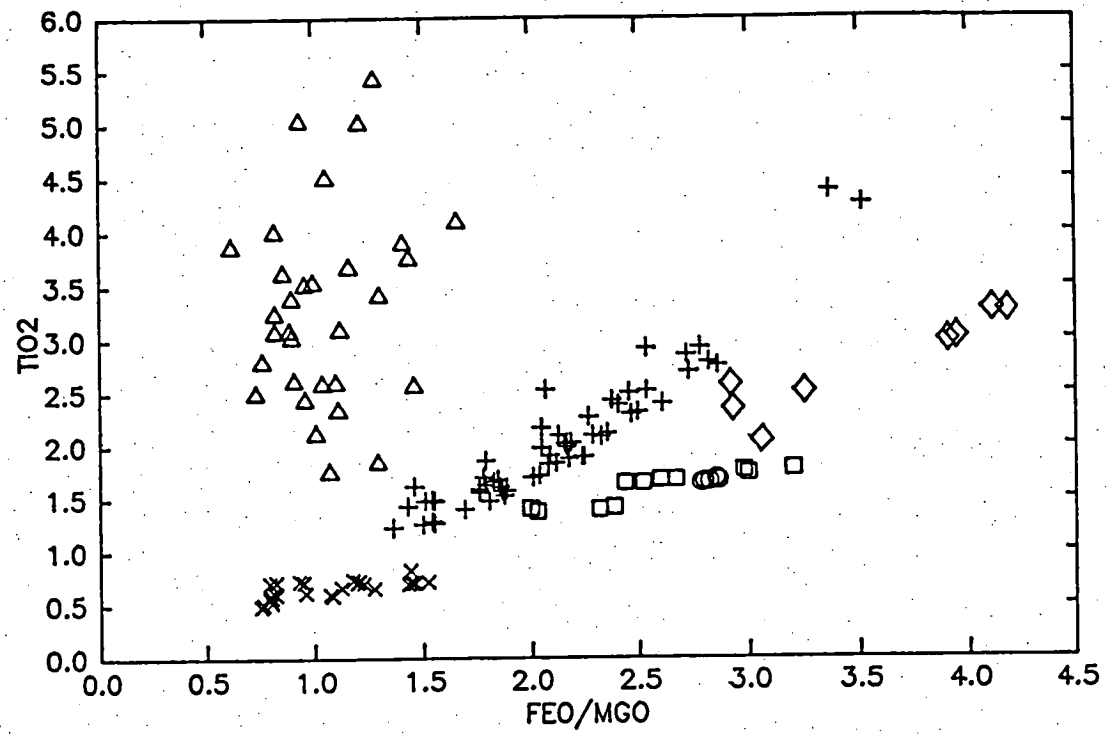

Figure 12.1

TiO_2 versus FeO/MgO of the Vestfold Hills mafic dyke samples collected for this study: high-Mg tholeiite (x) ca.2420 Ma; Fe-rich tholeiites (□,o) ca.2420 Ma; Fe-tholeiites (+) ca.1360 Ma; alkaline dykes (Δ) ca.1360 Ma; Fe-rich tholeiites (◇) ca.1800 Ma?, see text.

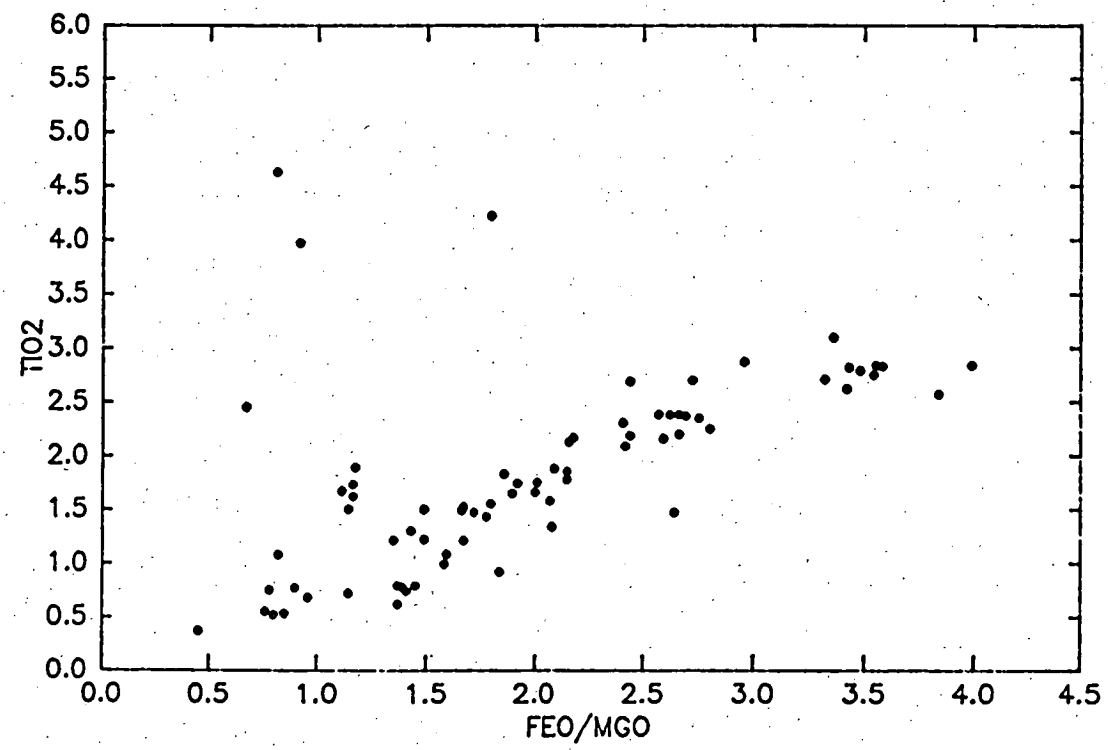

Figure I2.2

TiO_2 versus FeO/MgO of mafic dyke samples collected during the regional geological survey of the Vestfold Hills (Sheraton, 1985).

can be distinguished from the data collected in this study. Plotted on Fig. I2.2 are 74 mafic dyke compositions which are the result of the regional geological survey (tabulated in Sheraton, 1985), which did not specifically address the study of mafic dykes, nor focus on sampling chilled margins (R. Tingey, pers. comm., 1986). Aside from the fact that the regional survey did not recognize one of the suites reported in this study, the chemical trends are similar between the two sets of data, as would be expected. There is, however, a tendency for the chilled margin analyses to define tighter, more well defined groups than the data in Fig. I2.2. This is particularly evident in the ca.1360 Ma tholeiites (+ symbol) where the chilled margin analyses tend to define clusters of analyses at specific FeO/MgO ratios, this is not readily apparent in Fig. I2.2. It is considered that some of the observed scatter shown in the data of Fig. I2.2 is due to the analysing samples which are not "liquid compositions", but instead represent modified liquids resulting from the accumulation and/or fractionation of phenocryst phases within the cooling dykes. Based on this comparison it is concluded that the sampling program followed in this study, which emphasized the collection of chilled dyke margins, has resulted in a data set which closely records evolving liquid compositions in the dyke suites, and has removed much of the post-emplacement "blurring" of the chemical record. Furthermore, recognition of phenocryst phases and possible fractionating assemblages are unequivocal in chilled margin samples. This is not always the case in coarser grained, slowly cooled rocks where growth rates, crystal-liquid reactions and re-equilibration of precipitating phases may obscure liquidus assemblages and compositions.

The studies of Sheraton & Collerson (1983) and Collerson & Sheraton (in press) have documented the emplacement of a high-Mg dyke suite at ca.2420 Ma. With reference to Fig. I2.1, samples collected in this study which correspond to the high-Mg suite are shown by an **x**. Field and geochemical work undertaken for this thesis has also defined a Fe-rich tholeiite suite which was emplaced contemporaneously with the high-Mg dykes. These samples are shown in Fig. I2.1 with squares and circle symbols. The petrology and geochemistry of these two suites, and their relationship to one another are discussed in Chapter 5.

The largest suite of dykes was emplaced within the Vestfold Hills at ca.1360 Ma (Collerson & Sheraton, in press). This is an Fe-rich suite defined on Fig. I2.1 with **+** symbols Field work undertaken for this study found that at least some of a suite of alkaline dykes (triangular symbols, Fig. I2.1) were emplaced contemporaneously with the tholeiites. Prior to this study, the alkaline dykes were thought to be Mesozoic in age. Major

and trace element compositions of the alkaline dykes are documented in Appendix 2, but are not discussed in the text. The major and trace element concentrations coupled with documented dyke intersections of the ca.1360 Ma tholeiites are discussed in Chapter 6.

Collerson & Sheraton (in press) have also documented the emplacement of a small number of mafic dykes at ca.1800 Ma; these are some of the very Fe-rich compositions in Fig. I2.2. Dykes which do not fall into any of the previously discussed geochemical groups were collected in this study (diamonds, Fig. I2.1) and in general, correspond to the ca.1800 Ma dykes on the basis of TiO_2-Feo/MgO. However, trace element ratios differ significantly between the two data sets. As such, the age of the Fe-rich dykes (diamond symbols) collected in this study is uncertain. Consequently, these few dykes are not further discussed in this thesis, but their analyses are tabulated in Appendix 2.

CHAPTER 5

GENESIS OF THE ca.2420 Ma DYKE SUITES

A: THE HIGH-Mg THOLEIITES

B. THE Fe-THOLEIITES

CHAPTER 5

GENESIS OF THE 2420 Ma DYKE SUITES

A: THE HIGH-Mg THOLEIITES

INTRODUCTION

High-Mg tholeiite dykes are readily identified in the field by smooth, blocky outcrops and slightly red-brown surface colour, compared with the grey and brown tones of the Fe-rich tholeiites. The high-Mg dykes usually do not have a distinctive chilled margin but instead vary continuously from a very fine grained, dense, almost glassy margin (with conchoidal fracture) to a coarse grained noritic interior which may contain honey-coloured orthopyroxene phenocrysts up to 1 cm in length. This suite is petrographically distinct from Fe-rich suites in being plagioclase-free and orthopyroxene $\pm$ olivine phyric. Recalling that the majority of the studied samples were collected from chilled margins and therefore should closely approach liquid compositions, the geochemical characteristics of high-SiO_2 (51-57%), MgO (7-14%) and low-TiO_2 (<0.7%) are also distinguishing features of this suite.

In addition to the 28 high-Mg dykes analysed in this study, two coarse grained norites were also examined. These samples were collected from an intrusion interpreted as a ring dyke outcropping in the Northern Peninsula region of the Vestfold Hills. Airphoto interpretation by previous researchers (Reid, pers. comm., 1982; Collerson et al., 1983a) categorized a part of this structure as belonging to the oldest recognized lithology in the area, the Archean Tryne Metavolcanics, and the curvature was thought to define a macroscopic D2 fold. Field work carried out for this thesis traced the structure through a ~180^{o} arc, and includes the "gabbro dyke" of Collerson et al. (1983). The whole-rock and phenocryst geochemical characteristics of the norites are consistent with a genetic relationship with the high-Mg dykes, and the relatively young age compared to the Tryne Metavolcanics is indicated by their unrecrystallized, igneous texture.

Geochemical studies of the high-Mg suite have delineated distinct subgroups based on trace element concentrations and major element ratios. In order to facilitate the petrogenetic discussion of the suite, the chemical basis for the subdivisions will be presented in the following section. Further discussion will focus on petrographic and chemical contrasts and similarities between these groupings.

5.1 INITIAL CHEMICAL CHARACTERIZATION OF SUBGROUPS

The most convenient method for visualizing the chemical differences between the subgroups is by comparing their incompatible element concentrations on spiderplots. In this case, the data are normalized to model primordial mantle values following Wood et al. (1979). This plot subdivides the high-Mg suite into two distinctive groups based on the presence or absence of a negative $(Sr)_N$ anomaly (Sr_N depletion; Figs 5.1 and 5.2), and distinguishes samples that cannot be related to one another through the fractionation of olivine, orthopyroxene, or clinopyroxene. It is also observed that samples with the negative anomaly normally have $(Rb/Ba)_N > 1$, while in samples having no $(Sr)_N$ anomaly this ratio is generally <1. These chemical distinctions coincide with petrographic differences in that the "normal $(Sr)_N$" subgroup is olivine + orthopyroxene phyric, while the "$(Sr)_N$ depleted" subgroup is dominated by olivine-free dykes.

It is clear from Figs 5.1 and 5.2 that there are several exceptions to these subgroup definitions. Samples 229, 214 and 034, while each having a large $(Sr)_N$ depletion have $(Rb/Ba)_N < 1$. These three samples are also olivine-bearing. Two samples, 069 and 209 (Fig. 5.1), have trace element patterns entirely consistent with the "normal $(Sr)_N$" subgroup except for their $(Rb/Ba)_N$ ratio. Furthermore, 069 does not contain olivine. Sample 413 has a highly irregular trace element pattern exhibiting relative depletion in Ba, Rb, K and Sr but is otherwise similar to the other members of the subgroup (compare $(Ti/Y)_N$).

By making use of the Ol-Qtz-(Jd+CaTs) projection following Green (1970), a further division of the high-Mg suite can be identified (Fig. 5.3; the petrogenic implication of this diagram will be discussed in a later section). All the olivine-bearing samples from each trace element defined subgroup, plot along the Plag-Opx join, whereas the olivine-absent, orthopyroxene phyric samples (including 069) are subdivided into two distinct groupings. Comparison of the data plotted in Figs 5.2 and 5.3 shows that the lower $(Rb)_N$ cluster, excluding the two most enriched analyses, correspond to the normative olivine-poor subgroup in the Ol-Qtz-(Jd+CaTs) projection. Note also that the norite samples 584 and 302 project outside of all subgroup trends in Fig. 5.3. The discussions which follow will be based on these three subgroups, summarized below:

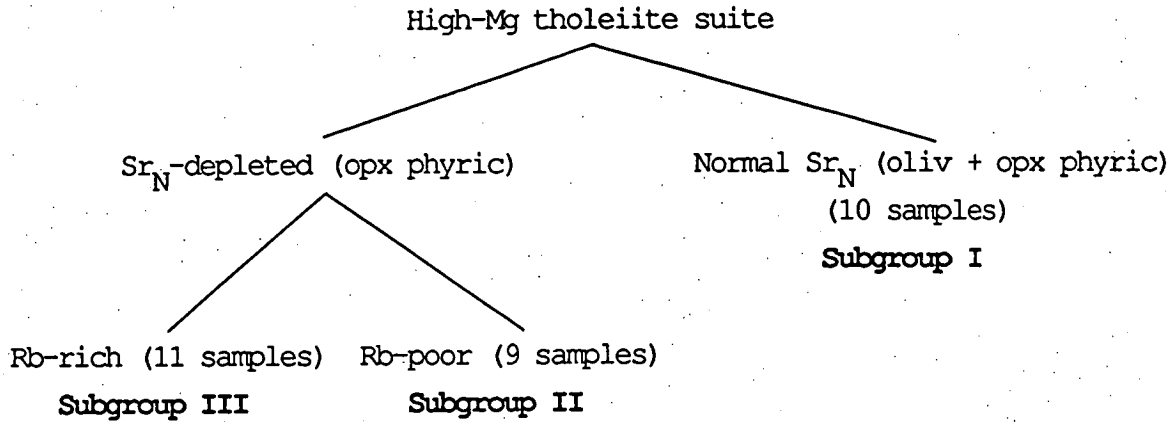
High-Mg tholeiite suite
Sr_N-depleted (opx phyric)
Normal Sr_N (oliv + opx phyric)
(10 samples)
Subgroup I
Rb-rich (11 samples)
Subgroup III
Rb-poor (9 samples)
Subgroup II

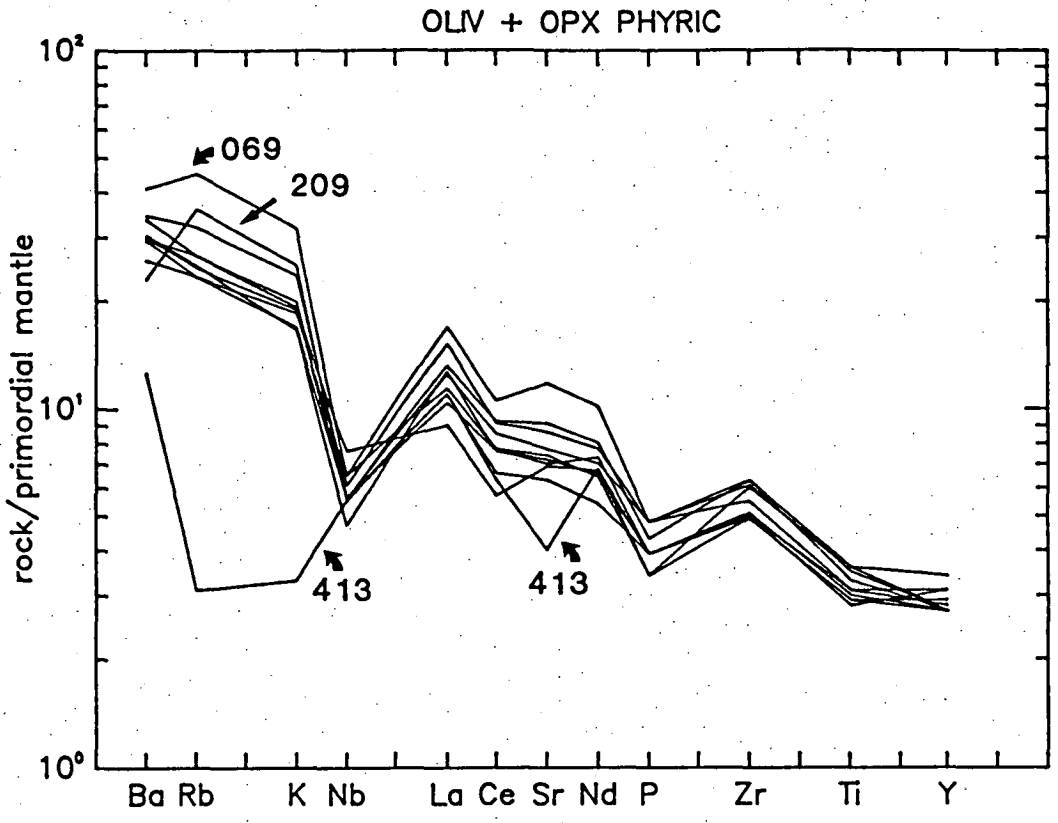

Figure 5.1
'Spiderplot' of incompatible element abundances from olivine+ orthopyroxene phyric high-Mg samples.

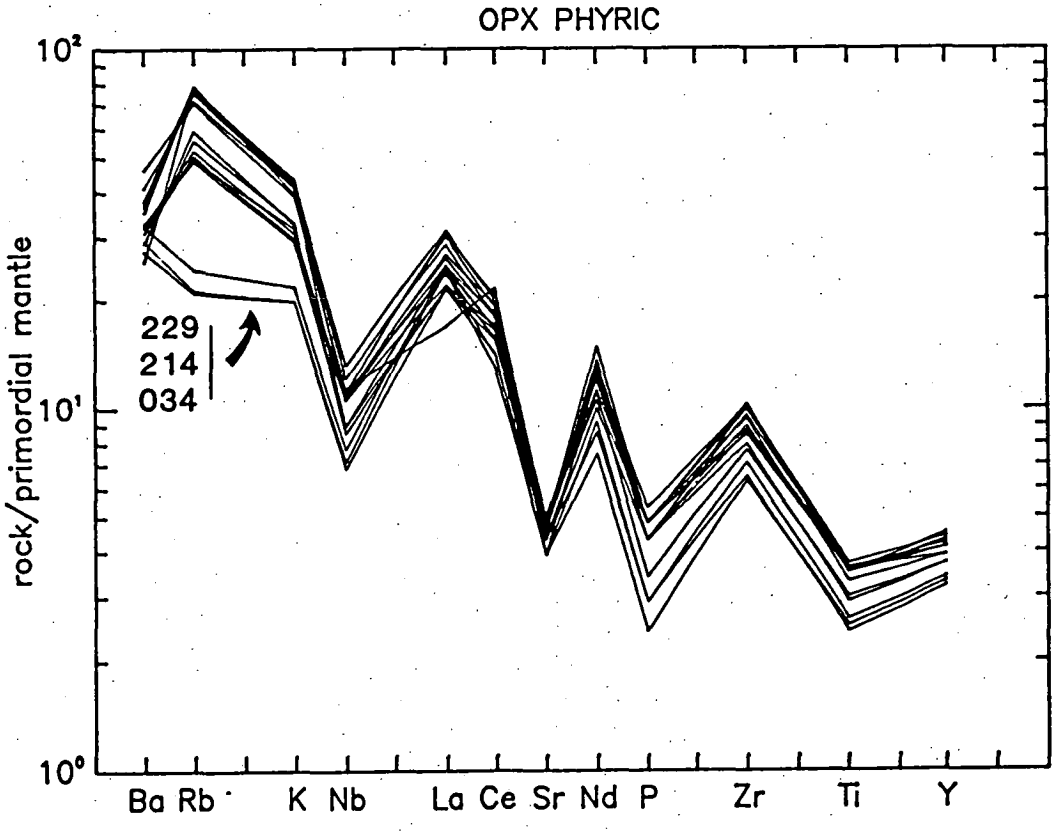

Figure 5.2
'Spiderplot' of incompatible element abundances characteristic of olivine-free, orthopyroxene phyric high-Mg dykes. Olivine-bearing samples 229, 214, 034 are indicated, see text for discussions.

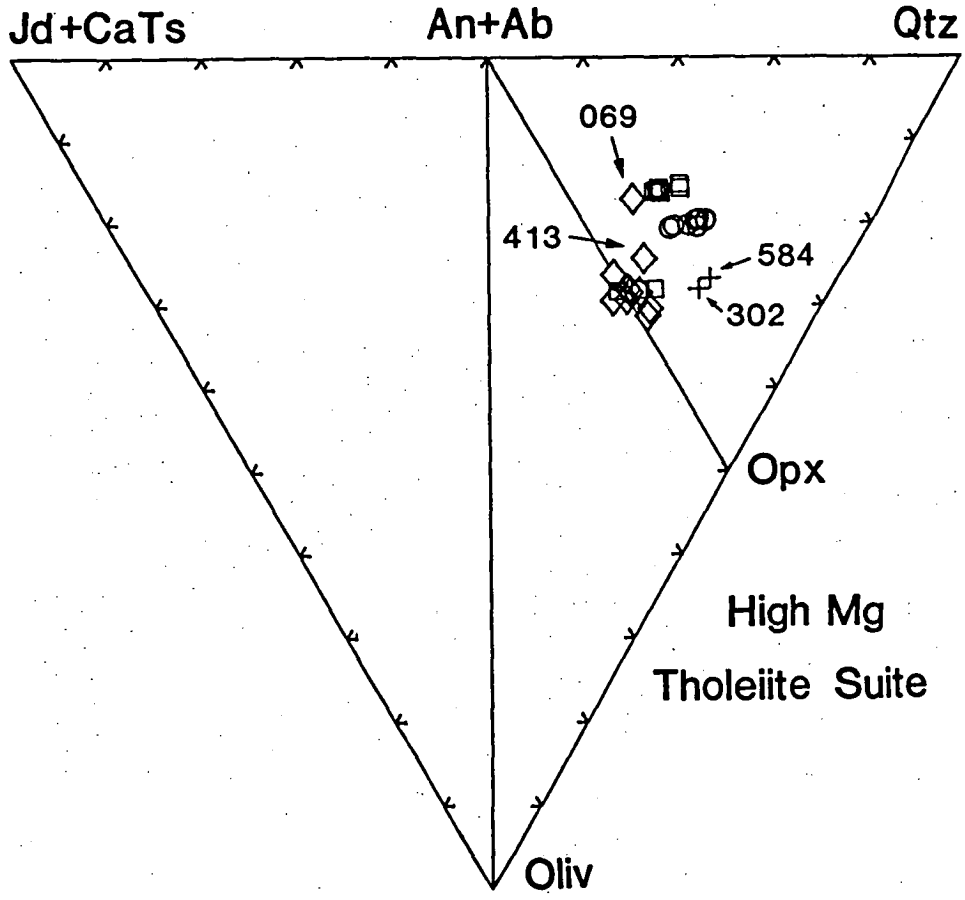

Figure 5.3

Projection of high-Mg dyke compositions from diopside onto the plane (Jd+CaTs)-Oliv-Qtz following Green (1970). The projection separates the high-Mg dykes into three groups complimentary to the incompatible element relationships of Figs 5.1 and 5.2. See text for discussion of numbered samples. $Fe_2O_3/FeO = 0.10$. Diamonds: subgroup I; squares: subgroup II; circles: subgroup III; crosses: norites.

5.2 PETROGRAPHY AND CRYSTAL CHEMISTRY

It has already been noted that the two trace element defined groupings of the high Mg suite can be categorized, in general, on the basis of their phenocryst assemblages. In detail, the olivine-free samples (Sr_N depleted) can also be subdivided texturally, a distinction which is consistent with the Rb-rich (subgroup III) and Rb-poor (subgroup II) divisions observed in Fig. 5.3. The petrography and crystal chemistry of each of the three subgroups is outlined below. In addition, three samples which are inconsistent with the subgroup designations will be discussed separately, along with a pyroxenite nodule collected from one of the norite localities.

5.2.1 SUBGROUP I

Petrography

The orthopyroxene phenocrysts in the samples comprising this subgroup occur as stout, colourless, euhedral crystals rarely exceeding 1 mm in length (i.e. "microphenocrysts" rather than "phenocrysts; Fig. 5.4a). They occur singly, or occasionally in clots of 2-3 generally euhedral crystals and comprise no more than 14% of any sample. Because of the very small grainsize, none of these samples are believed to have accumulated crystals (Clague and Frey, 1982).

Olivine phenocrysts form isolated crystals in all samples comprising this subgroup except 069, and do not exceed 5% of the mode. The crystals have a highly irregular form and are typically rimmed by a fine grained mosaic of groundmass pyroxene or occasionally, orthopyroxene phenocrysts. These textural features are indicative of a reaction relationship between olivine phenocrysts and the coexisting liquid. Many olivine crystals have experienced subsolidus oxidation and have been replaced by orthopyroxene (<1% CaO)-magnetite symplectites.

The matrix to the phenocrysts of the chilled margin samples contains lath-shaped "microphenocrysts" of calcic clinopyroxene and pigeonite enclosed within a much finer grained groundmass of brown pyroxene with randomly orientated needles of plagioclase (Fig. 5.4A). In coarse grained samples (see example 060) the plagioclase post-dates the crystallization of groundmass pyroxene (Fig. 1.2).

Chrome-rich spinels are very uncommon in the high-Mg suite and are confined to olivine-bearing samples; in subgroup I only five crystals were observed. The opaque grains are idiomorphic in form when included in olivine or rarely orthopyroxene, but when the host olivine has been resorbed through reaction with the liquid exposing the spinel, it too is rounded and apparently in reaction relationship with the coexisting liquid. Spinel phenocrysts were not observed in the matrix. These textures are consistent with the reaction

olivine + chromite + liquid$_{(1)}$ —> orthopyroxene + liquid$_{(2)}$

described from the simple system (MgO-SiO_2-Cr_2O_3) by Irvine (1977).

The most evolved sample of subgroup I, based on Mg-value and enrichment of incompatible trace elements (Fig. 5.1) is 069. The earliest formed crystals in this sample are orthopyroxene and pigeonite which are ragged and resorbed, and form the cores to most calcic clinopyroxene phenocrysts (<0.5 mm in length). Similar textures are observed in 207 and 067 where large resorbed orthopyroxene and pigeonite (~2 mm long) have broad rims of calcic clinopyroxene. Sample 067 (not a chilled margin) also contains abundant blocky phenocrysts of twinned calcic clinopyroxene.

Mineral Chemistry: Pyroxene

Pyroxene phenocrysts and matrix lath compositions are plotted onto the pyroxene quadrilateral in Fig. 5.5, and selected analyses listed in Table 5.1. The colourless orthopyroxene phenocrysts are zoned normally from a maximum of Mg_{88} (calculated on 4.000 cations) to Mg_{68}, with the majority of the analyses having Mg-values $\geq$81. The Al_2O_3 contents vary widely (3.75-1.2%) and do not correlate with Fe/Mg.

The lath-shaped calcic clinopyroxene microphenocrysts reach Mg_{80}, and in general have a more restricted range in Al_2O_3 than the phenocrysts. Analyses from well formed microphenocrysts of Mg-pigeonite (sample 062) initially parallel the Fe-enrichment trend of the orthopyroxene phenocrysts but the Fe-rich compositions zone across the two pyroxene miscibility gap reflecting rapid disequilibrium growth resulting from undercooling following emplacement (Grove & Bence, 1977).

Pyroxene compositions from the olivine-free sample 069 are plotted in Fig. 5.6, which shows that those orthopyroxene phenocrysts resorbed and rimmed by calcic clinopyroxene are Fe-rich compared to the predominant phenocryst compositions in the olivine + orthopyroxene-bearing samples. Similarly, pigeonite microphenocrysts in olivine-bearing sample 062 are Mg-rich compared to the clinopyroxene-rimmed pigeonites of sample 069. These features, as well as the overall enriched nature of the trace elements

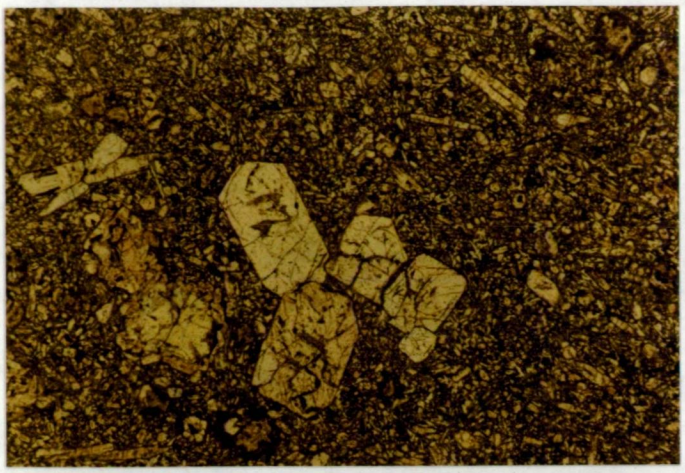

Figure 5.4A
Euhedral orthopyroxene phenocrysts with resorbed pyroxene rimmed olivine. Several well formed Ca-clinopyroxene laths also visible. Sample 054A. Long dimension of photo = 5.5 mm.

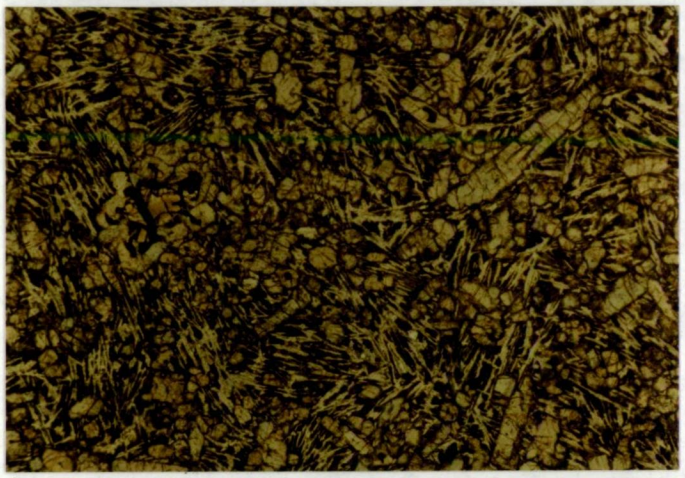

Figure 5.4B
Laths of orthopyroxene phenocrysts and resorbed pyroxene-rimmed olivine in comb textured groundmass. Sample 214. Long dimension of photo = 3.0 mm.

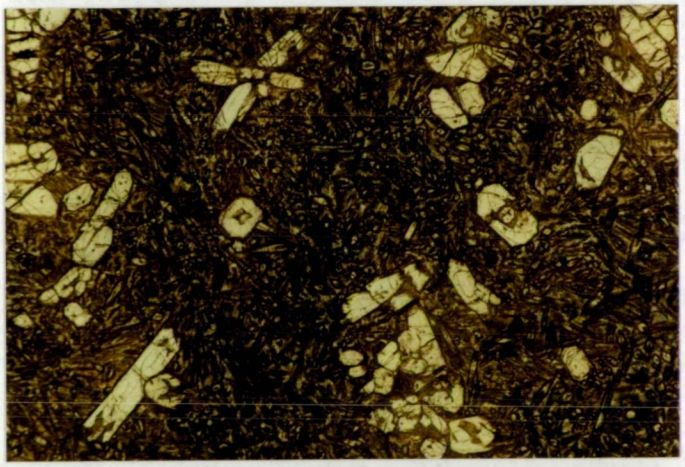

Figure 5.4C
Quench textured ortho-pyroxene phenocrysts with hollow cross-sections and castellated terminations in a groundmass of swallow-tailed hollow pigeonite and calcic clinopyroxene. Sample 027. Long dimension of photo = 3.0 mm.

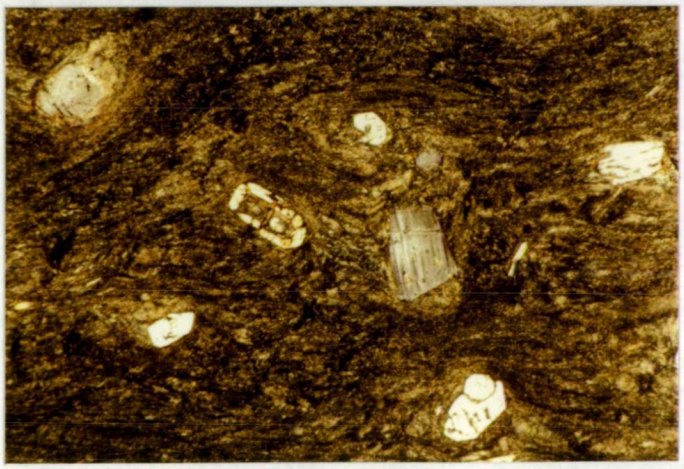

Figure 5.4D
Flow-banded sample with quench orthopyroxene phenocrysts, X-nichols. Sample 088. Long dimension of photo = 2.5 mm.

TABLE 5.1
PYROXENE COMPOSITIONS FROM SUBGROUP I

SAMPLE	054A	054A	054A	054A	054A	060	060	060	060	060
TYPE	OPX	OPX	CA-CPX	CA-CPX	CA-CPX	OPX	OPX	OPX	CA-CPX	CA-CPX
SIO2	55.55	54.44	52.40	52.22	52.57	55.57	53.59	54.99	51.91	51.53
TIO2										
AL2O3	1.14	2.61	2.43	2.49	2.12	1.31	1.00	1.39	2.04	2.55
CR2O3	0.40	0.39	1.26	1.08	0.63	0.59	-	0.41	0.61	0.83
FE2O3*	0.76	0.66	0.79	0.68	0.20	1.27	2.19	0.63	0.50	2.20
FEO	9.63	10.52	6.25	7.92	10.67	7.60	15.19	11.44	12.16	7.55
MNO										
MGO	30.18	28.68	18.30	17.75	17.73	31.34	25.87	28.78	15.71	17.54
CAO	2.34	2.70	18.57	17.86	16.08	2.34	2.18	2.36	17.08	17.80
SI	1.9606	1.9311	1.9184	1.9209	1.9419	1.9482	1.9487	1.9568	1.9392	1.9018
TI										
AL	0.0474	0.1093	0.1050	0.1081	0.0921	0.0541	0.0428	0.0582	0.0898	0.1109
CR	0.0113	0.0109	0.0365	0.0313	0.0184	0.0162		0.0114	0.0180	0.0243
FE3+	0.0201	0.0175	0.0217	0.0187	0.0056	0.0334	0.0598	0.0169	0.0140	0.0612
FE2+	0.2842	0.3122	0.1913	0.2437	0.3295	0.2229	0.4618	0.3405	0.3798	0.2329
MN										
MG	1.5879	1.5162	0.9988	0.9733	0.9763	1.6382	1.4020	1.5261	0.8752	0.9651
CA	0.0886	0.1028	0.7283	0.7039	0.6362	0.0871	0.0849	0.0902	0.6839	0.7039
MG#	84.8	82.9	83.9	80.0	74.8	88.0	75.2	81.8	69.7	80.6
CA#	4.8	5.3	38.0	36.6	32.8	4.5	4.4	4.6	35.3	37.0

SAMPLE	062	062	062	062	062	069	069	069	069	069	069
TYPE	OPX	OPX	PIG	QUENCH	QUENCH	PIG	PIG	OPX	OPX	CPX	CPX
SIO2	56.12	53.93	54.83	52.59	52.72	54.96	55.02	54.44	53.78	53.12	53.19
TIO2											
AL2O3	1.24	2.02	1.86	2.99	2.63	1.50	1.33	1.49	1.14	2.19	2.20
CR2O3	0.51	-	0.21	0.57	0.50	0.55	0.51	0.65	0.48	0.97	0.82
FE2O3	0.23	0.80	1.27	-	-	-	-	0.59	0.53	0.07	-
FEO	8.55	14.78	8.53	7.26	15.63	10.94	12.10	12.76	16.78	6.35	9.44
MNO											
MGO	31.58	26.37	28.67	16.53	21.21	27.25	26.17	27.56	25.06	18.72	19.97
CAO	1.77	2.14	4.64	20.06	7.31	4.80	4.86	2.51	2.24	18.57	14.38
SI	1.9645	1.9462	1.9413	1.9318	1.9382	1.9612	1.9727	1.9514	1.9613	1.9379	1.9422
TI											
AL	0.0510	0.0858	0.0777	0.1295	0.1138	0.0631	0.0562	0.0631	0.0490	0.0942	0.0947
CR	0.0141		0.0058	0.0165	0.0145	0.0155	0.0145	0.0184	0.0137	0.0281	0.0237
FE3+	0.0060	0.0217	0.0338					0.0158	0.0146	0.0019	-
FE2+	0.2502	0.4453	0.2525	0.2230	0.4807	0.3266	0.3629	0.3826	0.5117	0.1938	0.2882
MN											
MG	1.6478	1.4183	1.5130	0.9047	1.1624	1.4494	1.3987	1.4723	1.3622	1.0181	1.0870
CA	0.0664	0.0826	0.1759	0.7897	0.2881	0.1837	0.1869	0.0965	0.0875	0.7260	0.5627
MG#	86.8	76.1	85.7	80.2	70.7	81.6	79.4	79.4	72.7	84.0	79.0
CA#	3.4	4.2	9.1	41.2	14.9	9.4	9.6	4.9	4.5	37.5	29.0

* CALCULATED BASED ON 4.000 CATIONS. MG# = 100MG/(MG+FE). CA# = 100CA/(CA+MG+FE).

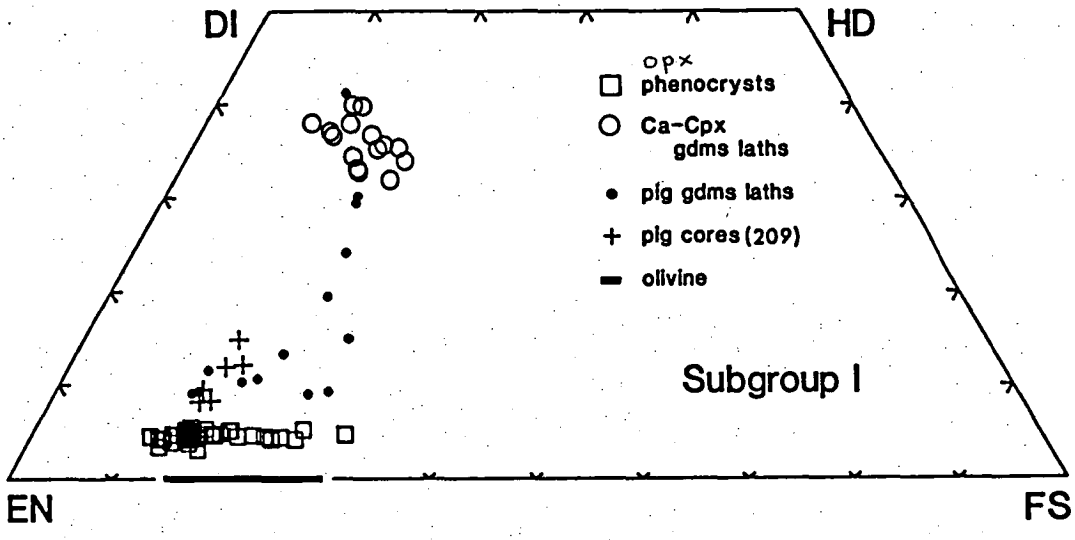

Figure 5.5
Pyroxene and olivine compositions from subgroup I dykes. Selected analyses listed in Tables 5.1 and 5.2.

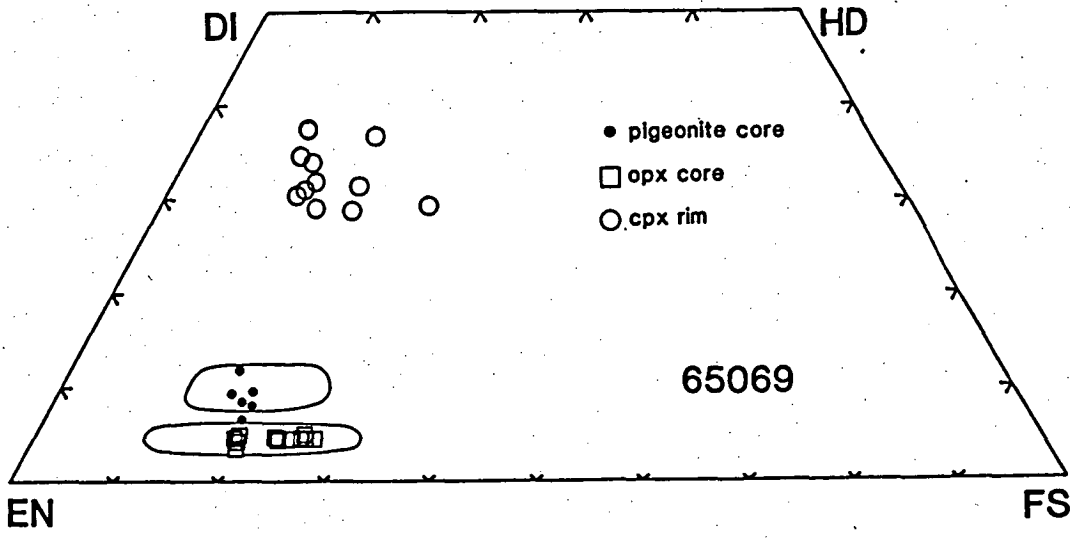

Figure 5.6
Pyroxene compositions from the olivine-free subgroup I sample 069. Encircled areas cover range of pyroxene compositions found in the more mafic olivine-bearing samples (Fig. 5.5).

(Fig. 5.1) suggest that 069 is related to the olivine-bearing members of this subgroup through the fractionation of orthopyroxene ± olivine.

Mineral Chemistry: Olivine

Olivine compositions are listed in Table 5.2, and plotted in Fig. 5.5. Except for sample 060, microprobe studies of these samples have not been exhaustive in the sense of searching for the most Mg-rich olivine (or orthopyroxene) compositions. Therefore, the olivine/orthopyroxene $K_D^{Fe/Mg}$'s calculated from the most Mg-rich compositions from each chilled margin sample, which range from 1.2-1.3, are considered to be in good agreement with the experimentally determined equilibrium value of 1.1 (Jaques & Green, 1979) and imply equilibrium crystallization of olivine and orthopyroxene. Olivine does however, always tend to be slightly more Fe-rich compared to the orthopyroxene which could imply that orthopyroxene was the liquidus phase (see Section 1.3.1), though the Fe-rich nature of the olivine could also be related to the subsolidus oxidation and development of orthopyroxene-magnetite intergrowths observed in some crystals.

The calculated olivine/orthopyroxene K_D from coarse grained sample 060 (K_D = 2.0) differs greatly from the experimental value. An identical relationship occurs in the Bushveld Complex, where chilled margin samples retain equilibrium olivine-orthopyroxene compositions, but slowly cooled samples do not (Sharp & Halbert, 1985). A reasonable explanation presented by these authors and applicable here, relies on the elemental diffusion data of Freer (1981). Freer calculated that an originally zoned olivine crystal 2 mm in diameter will become completely homogenized with respect to Fe/Mg in the very short period of 130 years if at an average temperature of 1100°C. This effect could account for the contrasting olivine/orthopyroxene compositions in 060 considering the near 1300°C liquidus temperature and cooling to the 7-8 kbar ambient temperature of 600-700°C over an extended period of time.

Mineral Chemistry: Chromite

The most Cr-rich spinel compositions of subgroups I and II are listed in Table 5.3, and all analyses are plotted in Fig. 5.7A and 5.7B. Although the Vestfold Hills chromites have a much lower Mg# [$Mg/(Mg+Fe^{2+})$] than chromites occurring in komatiite flows, western Pacific boninites and the lava flows of the Troodos Ophiolite, they overlap the compositional fields of these localities in terms of their Cr# [Cr/(Cr+Al)]. Chromites from subgroup I are significantly enriched in Cr compared to MORB chromites, while some low-Cr analyses were obtained from subgroup II. Also shown in

TABLE 5.2
OLIVINE COMPOSITIONS FROM SUBGROUP I

SAMPLE	054A	054A	060	060	062	062
PHASE	OLIV	OLIV	OLIV	OLIV	OLIV*	OLIV
SIO2	39.14	39.84	39.04	36.55	39.19	38.94
FEO	16.75	17.47	20.02	28.86	15.85	17.97
MGO	43.95	42.52	40.93	34.59	44.59	42.96
CAO	0.17	0.17				0.13
SI	0.9910	1.0095	1.0021	0.9825	0.9898	0.9915
FE	0.3546	0.3702	0.4297	0.6488	0.3343	0.3827
MG	1.6588	1.6060	1.5660	1.3861	1.6783	1.6305
CAO	0.0045	0.0047				0.0036
TOTAL	3.0089	2.9904	2.9978	3.0161	3.0102	3.0084
MG#	82.4	81.3	78.5	68.1	83.4	81.0

MG# = 100 MG/(MG+FE).
* INCLUDES 0.39% NIO, 0.0078 CATIONS NI.

TABLE 5.3
CHROMITE ANALYSES FROM HIGH-MG THOLEIITES

SAMPLE	060	060	054A	054A	053	229	239
subgroup	I	I	I	I	I	II	II
TIO2	0.43	0.39	0.24	0.35	0.23	-	-
AL2O3	12.34	12.09	9.84	10.49	13.14	13.29	10.62
CR2O3	48.95	48.98	51.56	52.20	47.01	42.75	51.94
FE2O3*	6.86	7.21	6.22	3.88	8.26	10.92	5.15
FEO	25.43	25.38	29.06	31.32	29.59	31.15	29.62
MNO	0.47	0.47			0.45		
MGO	5.51	5.49	3.08	1.76	1.34	1.89	2.67
TI	0.0111	0.0099	0.0062	0.0093	0.0061		
AL	0.4922	0.4830	0.4038	0.4330	0.5395	0.5431	0.4355
CR	1.3103	1.3128	1.4201	1.4457	1.2942	1.1715	1.4291
FE3+	0.1749	0.1839	0.1632	0.1023	0.2165	0.2849	0.1349
FE	0.7201	0.7195	0.8466	0.9177	0.8610	0.9028	0.8621
MN	0.0135	0.0135			0.0135		
MG	0.2780	0.2773	0.1601	0.0921	0.0692	0.0973	0.1385
MG#	27.9	27.8	15.9	9.1	7.4	9.7	13.8
CR#	72.7	73.1	77.9	77.0	70.6	68.3	76.6
FE3+#	8.8	9.3	8.2	5.2	10.6	14.2	6.7

* CALCULATED BASED ON 3.000 CATIONS.
MG# = 100MG/(MG+FE).
CR# = 100 CR/(CR+MG+FE).
FE3+# = 100FE3+/(FE3+CR+AL).

Fig. 5.7A are chromite analyses from quench textured micropyroxenites of the Bushveld (Sharp & Halbert, 1985) which are very similar in terms of both Mg# and Cr# to the chromites of subgroup I.

The compositions of liquidus chromite crystallizing from melts of basaltic composition depend on several variables including Si/Al and Cr contents of the liquid, as well as fO_2. Irvine (1976) and Dick & Bullen (1984) have shown that chromite precipitating from melts of equal Al content will have a greater Cr# in the more siliceous liquid. This relationship is shown in Fig. 5.7B, and illustrates the similarity in bulk rock-chromite composition of the Vestfold Hills high-Mg suite with the MgO-SiO_2-rich compositions of the Troodos and western Pacific boninites.

The low Mg# of the chromites from the Vestfold Hills and Bushveld are intuitively inconsistent with their occurrence in $>Mg_{65}$ bulk rock compositions. In quantitative terms, the Fe and Mg partition coefficient data of Maurel & Maurel (1984) predicts a liquidus spinel composition of Mg_{77} from sample 054A (see Appendix 2) compared with the analysed value of Mg_{9-17}.

It is well known that Fe/Mg exchange between mafic silicate and chromite continues to temperatures well below the solidus of basic melts (Irvine, 1967; Roeder et al., 1979; Ozawa, 1983). Thus the low Mg# of the Vestfold Hills and Bushveld chromites may be the result of subsolidus re-equilibration. As the Vestfold Hills dykes and the Bushveld micropyroxenites were both emplaced in a plutonic environment, their chromites no doubt cooled more slowly than chromites of equivalent Cr# found in boninites and Troodos lavas. In Section 1.3.1, it was suggested that the disequilibrium $K_D^{Fe/Mg}$ between olivine and orthopyroxene was due to more extensive subsolidus re-equilibration of olivine. If subsolidus exchange was responsible for the low Fe/Mg in the chromites it would be expected that chromite included in olivine would have a greater opportunity for continued subsolidus Fe/Mg exchange than chromite inclusions in orthopyroxene. This relationship is exactly what is depicted in Fig. 5.7A, and is identical to the observations of Hatton & Van Gruenewaldt (1985) and Irvine (1967): chromite inclusions in olivine have a higher Fe/Mg than chromite included in orthopyroxene. These observations suggest the unusually low Fe/Mg of the chromites in the high-Mg dykes is a result of subsolidus re-equilibration, and magmatic compositions may have been more similar in Fe/Mg to Troodos spinels. Most chromites appear to have retained their high Cr# during subsolidous re-equilibration, though the somewhat low Cr# in some subgroup II samples may indicate moderate Cr exchange accompanied the Fe/Mg redistibution (Roeder et al., 1979).

Figure 5.7A

Chromite compositions from subgroups I and II compared to chromites of other high-Mg rock types: Troodos (Cameron, 1985; Duncan & Green, submitted); Boninites (Cameron et al., 1980; Cameron, 1985); Komatiites (Cameron & Nesbitt, 1982); Bushveld micropyroxenites (Sharp & Hulbert, 1985); MORB (Frey et al., 1974; Sigurdsson & Schilling, 1976).

Figure 5.7B

Chromite composition of subgroups I and II versus whole-rock (liquid) Si/Al, and compared with relations from other localities. MORB (Dungan et al., 1978); Troodos (Cameron, 1985); Bushveld (Sharp & Hulbert, 1985); Cape Vogel (Jenner, 1982).

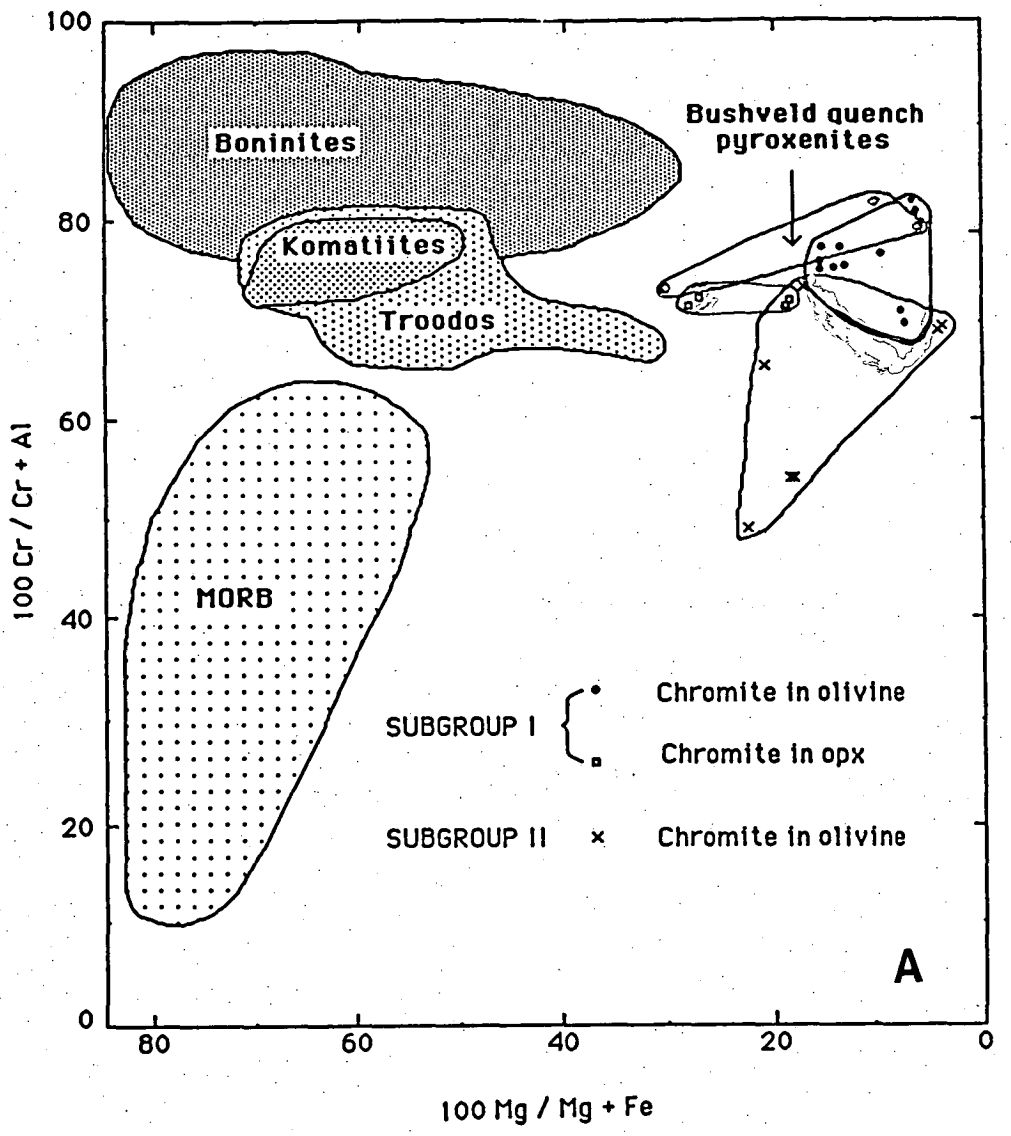
Boninites
Komatiites
Troodos
Bushveld quench pyroxenites
MORB
SUBGROUP I
Chromite in olivine
Chromite in opx
SUBGROUP II
Chromite in olivine
A
100 Cr / Cr + Al
100 Mg / Mg + Fe
100
80
60
40
20
0

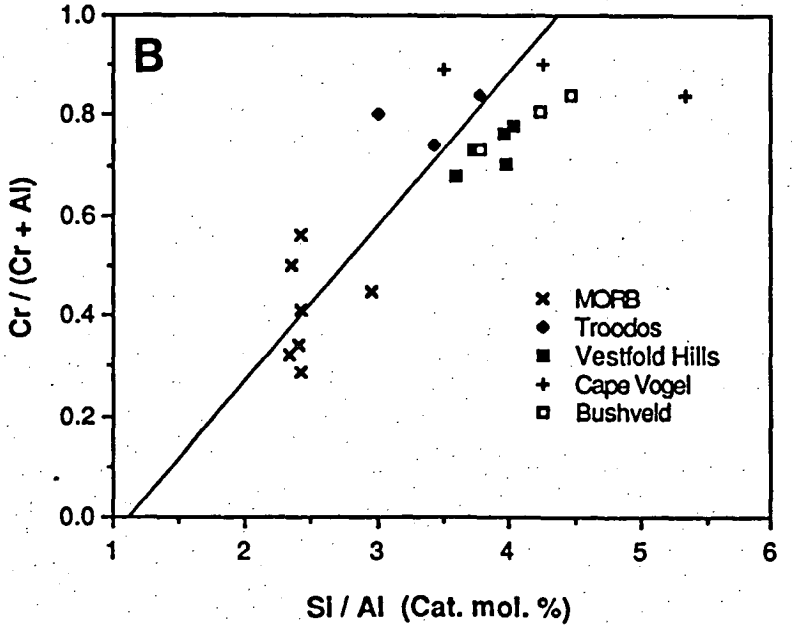
B
MORB
Troodos
Vestfold Hills
Cape Vogel
Bushveld
Cr / (Cr + Al)
Si / Al (Cat. mol. %)
1.0
0.8
0.6
0.4
0.2
0.0
1
2
3
4
5
6

Schrieber & Haskin (1976) and Hill & Roedder (1974) have shown that while Cr^{3+} and Cr^{2+} will both readily substitute into pyroxenes, Cr^{3+} has a much greater preference for spinel. Furthermore, the volume of chromite that precipitates from a basic liquid is proportional to the $Cr^{3+}/(Cr^{3+}+Cr^{2+})$ ratio, and not the absolute abundance of Cr in the liquid. Chromite saturation occurs in basaltic liquids at levels of ~200-300 ppm Cr (Hill & Roedder, 1974; Sigurdsson & Schilling, 1976). The restriction of chromite to inclusion within the phenocryst phases of the high-Mg suite while the bulk rock contains ~900-1600 ppm Cr suggests low concentrations of Cr^{3+}, which implies low fO_2 conditions.

Unfortunately, a suitable phase assemblage does not exist in the high-Mg suite from which a quantitative estimate of the magmatic fO_2 could be obtained. The cumulate textured norites contain large titanomagnetites, but are unaccompanied by magmatic ilmenite. The titanomagnetites have exsolved trellis textured ilmenite and fO_2 determinations on this subsolidus assemblage result in oxygen fugacities that fall between QFM and CoCoO at 500-550°C. Extrapolating these buffer curves to magmatic temperatures (~1300°C) represents a maximum oxygen fugacity (~10^{-9} bars) as the intercumulus titanomagnetite crystallized from a highly fractionated, Fe^{3+}-enriched liquid and may also have experienced some subsolidus fluid interaction and oxidation.

5.2.2 SUBGROUP II

Petrography

The orthopyroxene microphenocrysts in this subgroup are poorly formed, faintly pleochroic crystals rarely exceeding 0.5 mm in length. They have slightly tapered to rounded terminations, and some crystals may enclose irregularly shaped voids suggesting rapid crystallization. An important distinguishing petrographic characteristic of this subgroup is that, even in the finest grained quenched margin, small laths of plagioclase have crystallized. In coarser grained samples, plagioclase is comb textured with intersertal granular pyroxene, and thus differs in the crystallization order of the groundmass phases from the olivine + orthopyroxene subgroup described above.

The three olivine-bearing samples 214, 034 and 229 are included in this petrographic subdivision of the orthopyroxene phyric subgroup because they exhibit well formed comb textured plagioclase (Fig. 5.4B). Although the three samples are olivine-bearing, olivine composes <<1% of each

sample. The olivine grains are always highly irregular in shape and are enclosed by orthopyroxene. Three grains contain small opaque cubes of Cr-rich spinels.

Mineral Chemistry

The compositions of the olivine and orthopyroxene phenocrysts are plotted in Fig. 5.8, and selected analyses listed in Table 5.4. The most magnesian orthopyroxenes, up to $Mg_{87.7}$ (compared to Mg_{88} of subgroup I), are found in the olivine-bearing samples of this subgroup, and the Fe-rich rim compositions of these phenocrysts overlap the Mg-rich phenocryst core compositions of the olivine-free samples. The Mg-rich orthopyroxene analyses contain appreciable Cr_2O_3, while the Fe-rich compositions lack Cr_2O_3 and contain MnO. The Al_2O_3 contents range from~1.0-2.5% and on average are slightly lower than the Al_2O_3 content of orthopyroxenes in subgroup I.

Olivine crystals are rare, resorbed, and were not extensively analysed. However, the most Mg-rich olivine and orthopyroxene (Table 5.4) result in a $K_D^{Fe/Mg} = 1.2$, suggesting co-precipitation. It is noted that the olivine is again slightly more Fe-rich than predicted, as discussed previously.

The chemical features of the orthopyroxene phenocrysts, as well as the fact that the olivine-bearing samples have lower concentrations of incompatible trace elements than the olivine-free samples (Fig. 5.2), suggests crystal fractionation may play an important role in relating the samples of this trace element defined subgroup.

5.2.3 SUBGROUP III

Petrography

The orthopyroxene phenocrysts in this subgroup form narrow, quench textured, colourless laths ~2 mm in length. Longitudinal sections of the phenocrysts display irregularly shaped internal voids and many of the crystals have castellated terminations, while skeletal crystal shapes are observed when the phenocrysts are sectioned parallel to (001) (Fig. 5.4C). In samples 088 (Fig. 5.4D), 090 and 215, the groundmass is dark brown and contains no discernible crystals. Fine wisps of slightly lighter coloured groundmass material, can be observed wrapping about the phenocrysts defining flow lines. The groundmass in these samples probably quenched directly to a glass. Other samples in the subgroup have swallow-tailed,

TABLE 5.4
PYROXENE AND OLIVINE COMPOSITIONS FROM SUBGROUP II

SAMPLE	034	214	234	265	265	214	214	034
PHASE	OPX	OPX	OPX	OPX	OPX	OLIV	OLIV	OLIV**
SIO2	56.16	55.13	54.98	51.59	50.89	40.05	39.93	38.97
TIO2								
AL2O3	1.29	1.36	1.05	1.26	2.55			
CR2O3	0.59	0.60						
FE2O3*	0.32	0.57	0.85	1.50	0.07			
FEO	8.04	11.01	12.90	23.33	26.24	14.26	15.16	16.59
MNO				0.54	0.56			
MGO	32.02	29.45	28.21	19.76	17.59	45.69	44.92	44.10
CAO	1.59	1.89	2.01	2.02	2.10			
SI	1.9612	1.9556	1.9663	1.9505	1.9417	1.0006	1.0014	0.9878
TI								
AL	0.0529	0.0568	0.0444	0.0562	0.1145			
CR	0.0163	0.0168						
FE3+	0.0083	0.0152	0.0229	0.0427	0.0020			
FE2+	0.2347	0.3266	0.3859	0.7377	0.8372	0.2979	0.3179	0.3517
MN				0.0174	0.0182			
MG	1.6670	1.5572	1.5035	1.1138	1.0004	1.7010	1.6791	1.6658
CA	0.0596	0.0719	0.0769	0.0817	0.0860			
MG#	87.7	82.7	79.6	60.2	54.4	85.1	84.1	82.6
CA#	3.0	3.7	3.9	4.2	4.5			

* CALCULATED BASED ON 4.000 CATIONS.
** INCLUDES 0.34% NIO AND 0.0069 CATIONS NI.
MG# = 100 MG/(MG+FE).
CA# = 100 CA/(CA+MG+FE).

TABLE 5.5
PYROXENE COMPOSITIONS FROM SUBGROUP III

SAMPLE	215	215	088	088	027	027	027	027	027
PHASE	OPX	OPX	OPX	OPX	OPX	PIG	PIG	CPX	CPX
SIO2	56.13	54.96	55.87	52.90	53.58	50.80	50.24	51.34	52.02
TIO2							0.18	0.21	0.19
AL2O3	0.80	1.32	0.88	0.92	1.20	1.69	1.82	2.66	2.38
CR2O3	0.55	0.56	0.46	0.33	0.41		0.26		0.24
FE2O3*	0.41	0.89	0.80	0.84	0.65	0.99	1.31		
FEO	9.51	11.44	9.54	20.56	17.84	25.09	25.39	15.25	14.61
MNO		0.13		0.33		0.37	0.49		
MGO	31.61	29.32	31.35	22.87	24.99	16.42	16.64	13.73	16.19
CAO	1.01	1.48	1.08	1.25	1.31	4.65	3.67	16.73	14.37
SI	1.9702	1.9539	1.9647	1.9633	1.9592	1.9475	1.9306	1.9381	1.9440
TI							0.0053	0.0060	0.0054
AL	0.0331	0.0555	0.0365	0.0403	0.0518	0.0763	0.0823	0.1184	0.1048
CR	0.0153	0.0129	0.0128	0.0097	0.0119		0.0079		0.0070
FE3+	0.0108	0.0237	0.0213	0.0235	0.0180	0.0285	0.0380		
FE2+	0.2789	0.3402	0.2806	0.6380	0.5456	0.8060	0.8160	0.4814	0.4565
MN		0.0040		0.0104		0.0120	0.0159		
MG	1.6539	1.5535	1.6433	1.2652	1.3621	0.9388	0.9529	0.7728	0.9016
CA	0.0380	0.0563	0.0408	0.0497	0.0514	0.1909	0.1512	0.6801	0.5754
MG#	85.6	82.0	85.4	66.5	71.4	53.81	53.9	61.6	66.4
CA#	1.9	2.9	2.1	2.5	2.6	9.9	7.9	35.2	29.8

* CALCULATED BASED ON 4.000 CATIONS.
MG# = 100 MG/(MG+FE).
CA# = 100 CA/(CA+MG+FE).

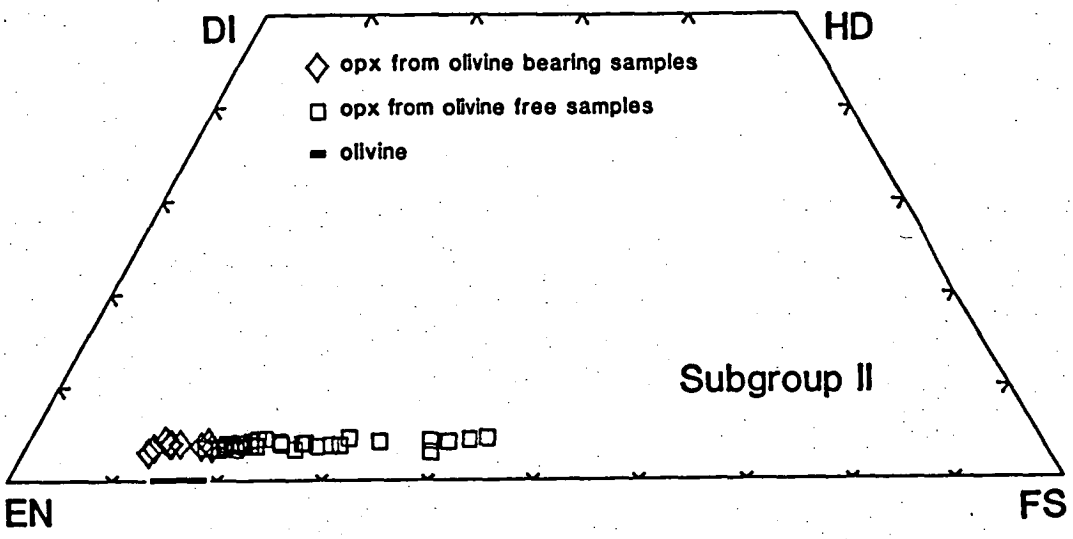

Figure 5.8
Compositions of olivine and orthopyroxene phenocrysts from subgroup II samples. Selected analyses listed in Table 5.4.

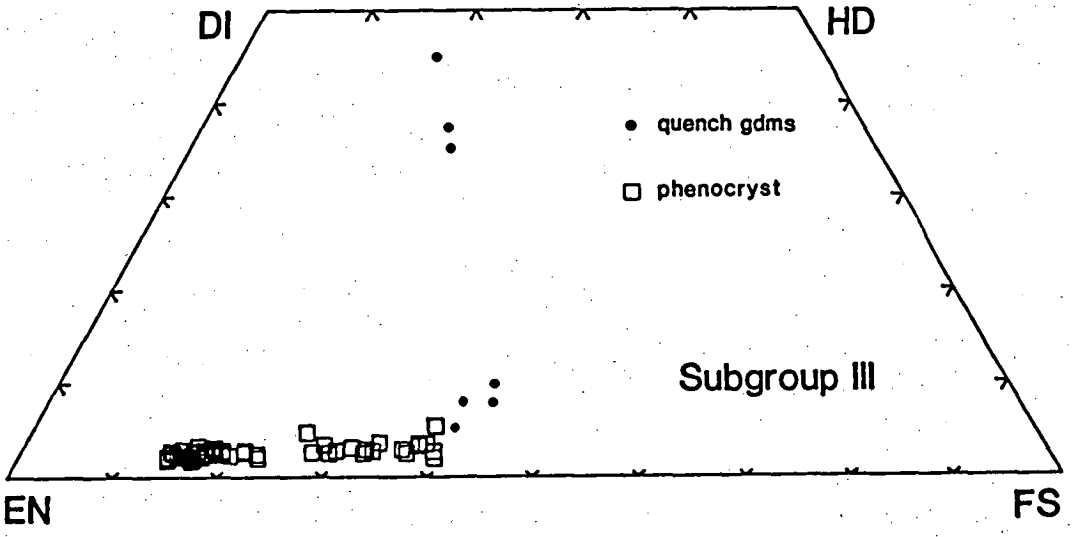

Figure 5.9
Pyroxene compositions from subgroup III samples. Selected compositions listed in Table 5.5.

hollow pigeonite and calcic clinopyroxene quench crystals in the groundmass, which may be enveloped by fine, comb-textured plagioclase (Fig. 5.4C). The orthopyroxene phenocrysts commonly have very narrow birefringent rims identical to the textures observed in the experimental charges described from the study of sample 060 (Section 1.3.1). In both cases, the rims are believed to be the result of clinopyroxene nucleation and growth during quenching.

Mineral Chemistry

Pyroxene compositions are plotted in Fig. 5.9, and selected analyses listed in Table 5.5. The majority of the analyses are Mg-rich (up to $Mg_{85.6}$), with Fe-rich rims ($Mg_{56.3}$). The Al_2O_3 contents tend to increase slightly with Fe/Mg, and in general average ~1.25%. A compositional gap in the pyroxene analyses between ~Mg_{70}-Mg_{75} is shown in Fig. 5.9. Although the location of individual analyses cannot be categorized as core or rim crystal compositions because of the random orientation of the crystals exposed in the thin section, the textures suggest the compositional gap is due to quenching of the liquid and the rapid disequilibrium crystallization of the outer portions of the pyroxene phenocrysts.

5.2.4 DISCUSSIONS OF SAMPLES WITH DISTINCTIVE CHARACTERISTICS

Samples 584 and 302

Both of these samples were field classified as norites, and were collected from the ring dyke outcropping in the Northern Peninsula of the Vestfold Hills. Microscopic examination reveals that both samples are orthocumulates and have accumulated only orthopyroxene primocrysts. The orthopyroxenes are often rimmed, and in several occurrences have nearly completely reacted with the intercumulus liquid to form pigeonite (now inverted, Fig. 5.10A). Large blocky and slightly dusty plagioclase crystals and granophyre compose the major portion of the intercumulus matrix. Trellis textured Fe-Ti oxides, as well as pyroxene, may be partially rimmed by late-stage brown biotite or light green chlorite (Fig. 5.10A). Globules of Cu, Fe, Ni, Zn sulphides have also accumulated, and are especially common in the unanalysed sample 185.

Two orthopyroxene crystals were analysed from 584, and found to be zoned from $Mg_{85.9}$ to $Mg_{76.1}$, accompanied by increasing CaO (Fig. 5.11, Table 5.6). Thus, the phases contained in the norites retain their primary igneous compositions and have not experienced extensive subsolidus

TABLE 5.6
PYROXENE COMPOSITIONS FROM NORITE AND PYROXENITE NODULE

SAMPLE	584	584	584	584	584	189	189	189	189
PHASE	OPX	OPX	PIG	EXSOL	HOST	OPX	OPX	CPX**	CPX**
SIO2	54.89	54.04	52.14	52.01	52.56	57.70	57.70	52.30	52.72
TIO2			0.20	0.34				0.25	0.28
AL2O3	1.21	1.05	1.70	1.77	1.05	0.46		3.04	2.84
CR2O3	0.44	0.28		0.27				1.23	1.16
FE2O3*	1.91	1.36	1.26	1.68	2.09	0.21	0.75	0.19	
FEO	9.90	14.94	17.88	9.04	19.92	6.37	6.45	4.97	5.03
MNO			0.38		0.27				
MGO	30.31	26.73	20.74	17.48	22.95	34.85	35.09	18.12	17.22
CAO	1.34	1.60	5.70	17.41	1.28	0.40		19.90	20.26
SI	1.9432	1.9551	1.9395	1.9247	1.9478	1.9879	1.9903	1.9073	1.9222
TI			0.0055	0.0094				0.0070	0.0076
AL	0.0503	0.0446	0.0746	0.0771	0.0460	0.0189	-	0.1308	0.1218
CR	0.0123	0.0081		0.0079				0.0354	0.0334
FE3+	0.0510	0.0371	0.0354	0.0468	0.0583	0.0054	0.0194	0.0052	
FE2+	0.2931	0.4519	0.5563	0.2798	0.6185	0.1834	0.1861	0.1515	0.1535
MN			0.0118		0.0083				
MG	1.5992	1.4411	1.1498	0.9640	1.2701	1.7895	1.8041	0.9851	0.9628
CA	0.0509	0.0621	0.2271	0.6903	0.0510	0.0149	-	0.7778	0.7913
MG#	84.5	76.1	67.4	77.5	67.2	90.7	90.6	86.7	86.3
CA#	2.6	3.2	11.7	35.7	2.6	0.8	0.0	40.7	41.5

* CALCULATED BASED ON 4.000 CATIONS.
** INTERCUMULUS.
MG# = 100 MG/(MG+FE).
CA# = 100 CA/(CA+MG+FE).

Figure 5.10A
Cumulate textured norite collected from ring dyke. Photograph shows orthopyroxene primocrysts with rims of inverted pigeonite. 'Dusty' patches are intercumulus plagioclase crystals enclosed by quartz-K feldspar granophyre. Biotite rimmed by late stage green chlorite, magnetite also present. Sample 584. Long dimension of photo = 3.0 mm.

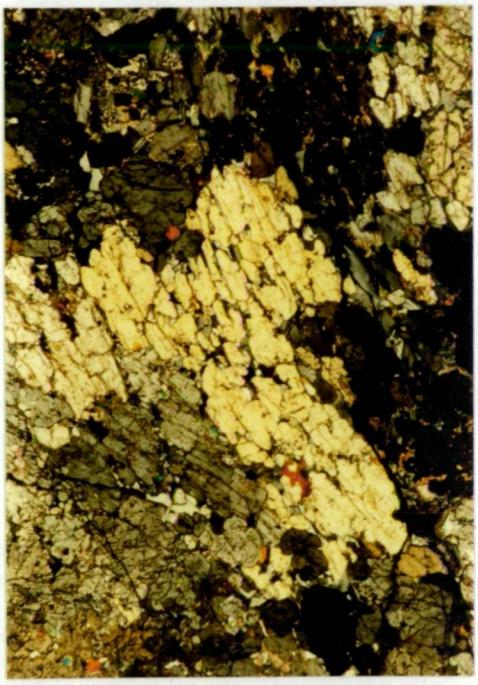

Figure 5.10B
Pyroxenite nodule collected from cumulate textured noritic ring dyke displaying irregularly shaped clusters of orthopyroxene. The orthopyroxenes of each cluster have parallel alignment, but different to that of adjacent clusters. High birefringent grains are intercumulus Ca-clinopyroxene or phlogopite. Minor quartz-K feldspar granophyre can be seen in the upper left. Sample 109. Long dimension of photo = 5.5 mm.

Figure 5.10C
Two orthopyroxene phenocrysts viewed normal to (010) displaying patchy extinction and crossed by high birefringent lamellae. Sample 054A. Long dimension of photo = 2.0 mm.

homogenization as is commonly found in cumulates (Wager et al., 1960). Also shown in Fig. 5.11 is the composition of the intercumulus inverted pigeonite obtained from wide-beam rapid area scans, tie lines connect the composition of the exsolutions and the directly adjacent host pyroxene. Temperatures calculated from these pairs are discussed in a later section.

Both 302 and 584 have trace element patterns which characterize subgroup III yet their projected compositions do not plot with this subgroup in Fig. 5.3. The difference is simply explained by noting the samples contain accumulated orthopyroxene and thus project between the chilled margin liquid compositions and the orthopyroxene compositional point.

Sample 189

Of particular importance to this study (discussed later) is an orthopyroxenite nodule collected from the margin of the norite ring dyke. The sample is composed of irregular masses of orthopyroxene which in detail are composed of aggregates of stocky orthopyroxene laths, all sharing the same crystallographic orientation, and differing in orientation to that of the adjacent aggregates (Fig. 5.10B). A very small amount of intercumulus plagioclase and granophyre is present, accompanied by colourless to pale brown mica. Rare crystals of intercumulus calcic clinopyroxene have been observed replacing the margins of some orthopyroxene cumulate crystals.

The pyroxene compositions from this sample are plotted in Fig. 5.11, and selected analyses listed in Table 5.6. The orthopyroxenes reach $Mg_{91.2}$ (enstatite) and have very low contents of CaO and Al_2O_3, one analysis is CaO- and Al_2O_3-free. There is an excellent correlation between Fe/Mg and CaO indicating that these phases have not experienced subsolidus re-equilibration and the low CaO contents are an igneous characteristic. The smooth transition in orthopyroxene compositions between the nodule and the cumulate host is strong evidence for a cognate origin for the nodule (Figs 5.11 and 5.12).

The high MgO and especially the very low CaO content of these pyroxenes are consistent with these crystals being clinoenstatite. However, they lack its polysynthetic twinning and characteristic cracks due to the volume change accompanying the proto-clino inversion, and have evidently crystallized above the upper pressure limit of clinoenstatite. This structural inversion boundary follows a shallow dP/dT, and at 1300-1400^{o}C protoenstatite is stable only at pressures <6-8 kbar (Jenner, 1982).

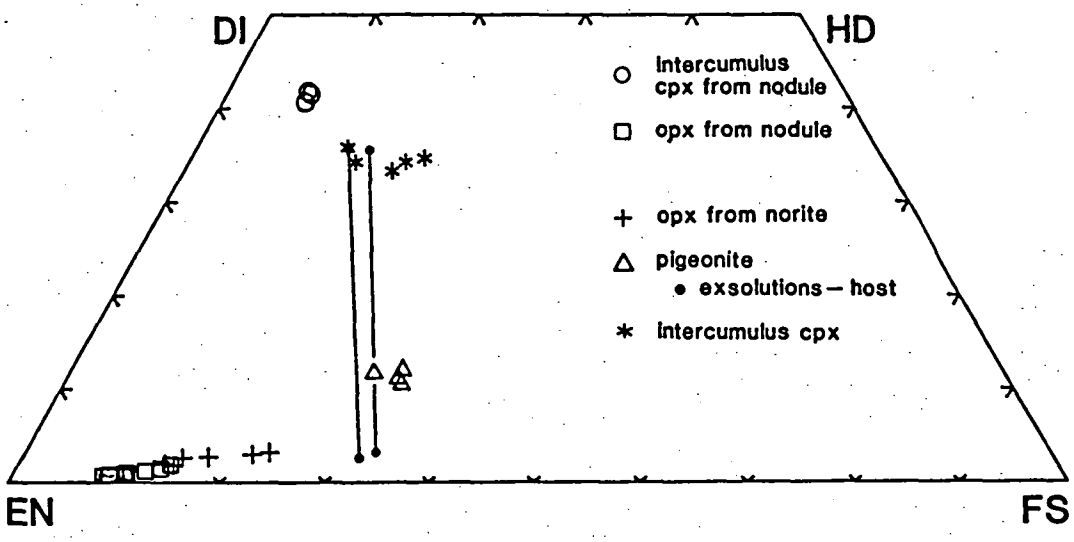

Figure 5.11
Pyroxene compositions from cumulate textured norite (584) and cognate pyroxenite nodule (189). Note continuum of orthopyroxene compositions between these two samples. Tie lines connect exsolutions and directly adjacent host pyroxene from intercumulus inverted pigeonite. Selected compositions listed in Table 5.6.

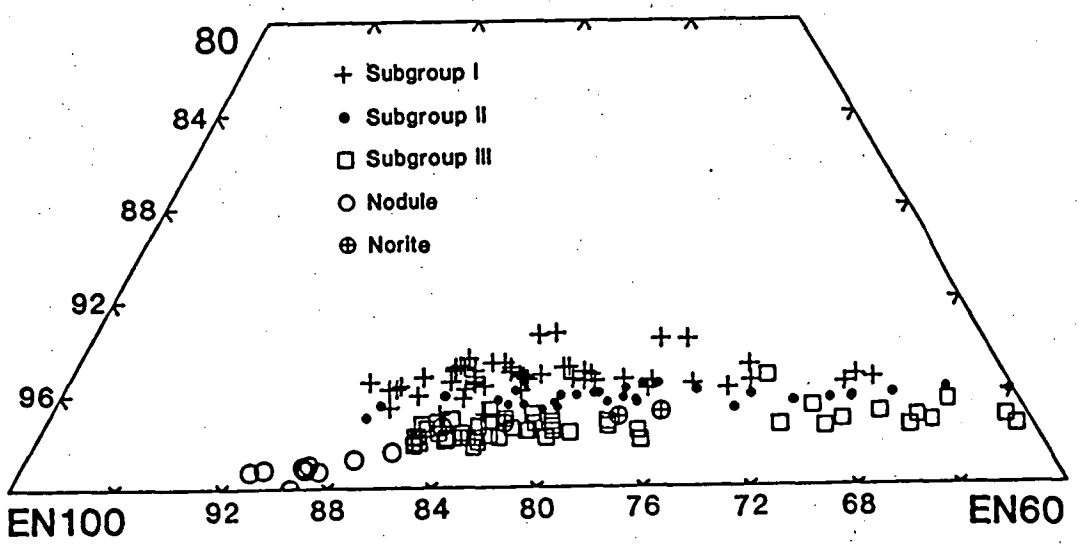

Figure 5.12
Comparison of orthopyroxene phenocryst compositions between subgroups, including analyses from the norite and pyroxenite nodule. Note the diagram covers only the Mg-rich section of the pyroxene quadrilateral.

Sample 413

It was noted in the introduction to this chapter that sample 413 has a highly anomalous trace element pattern compared to other olivine-orthopyroxene phyric samples, and although 413 exhibits a "$(Sr)_N$ depletion" it was categorized into subgroup I based on its Ti/Y ratio.

This sample was collected from within the garnet isograd shown in Fig. 3.1, near the location of sample 415. Petrographically, sample 413 is strongly recrystallized, and contains relict orthopyroxene phenocrysts which display undulose extinction and subgrain development. The groundmass is composed of very fine grained, granular pyroxene with blades of deformed plagioclase. Granules and small undeformed plates of hornblende are also developed.

The petrography and texture of 413 indicate the observed depletion of Ba, Rb, K and Sr is probably the result of the upper amphibolite facies metamorphism and associated fluid interaction at ca.1100 Ma. The findings are consistent with documented elemental mobility in mafic dykes during amphibolite facies metamorphism (Weaver & Tarney, 1981). As a consequence, the reduction in K_2O will increase the primary silica saturation calculated in the CIPW norm and hence 413 projects towards the Qtz apex of the Oliv-Qtz-(Jd+CaTs) diagram (Fig. 5.3) compared with the trend defined by other subgroup I samples.

5.2.5 COMPARISON OF ORTHOPYROXENE PHENOCRYST CHARACTERISTICS BETWEEN SUBGROUPS

Chemistry

Orthopyroxene phenocryst analyses from each subgroup discussed above are plotted in the Mg-rich end of the pyroxene quadrilateral shown in Fig. 5.12. The orthopyroxene phenocrysts from each subgroup have overlapping ranges in Fe/Mg, but are distinct in terms of their CaO contents (% Wo). The most calcic orthopyroxenes are found in subgroup I, and with decreasing CaO are followed by subgroup II and subgroup III.

Because these liquids are not saturated in two pyroxenes, the Wo content of the orthopyroxenes will also be controlled by the CaO content of the coexisting liquid. This relation is reflected in the normative Di/Di+Hyp ratios of the subgroups, where the average value for this ratio is the greatest in subgroup I (average = 0.37), followed by subgroup II (0.32) and subgroup III (0.25).

The overlapping Fe/Mg but distinctly different Wo contents of the orthopyroxene phenocrysts from each subgroup, clearly indicates that the three subgroups cannot be related simply via the fractionation of the observed phenocryst phases.

Crystal Morphology

A characteristic common to the orthopyroxenes of each subgroup is a patchy extinction pattern when the crystals are viewed normal to (010) (Fig. 5.10C) which is suggestive of the cross-hatched extinction in microcline. Sharply bounded, straight lamellae which have a higher birefringence than the orthopyroxene host, traverse the zones of patchy extinction parallel to (100). Detailed microprobe analyses across the lamellae recorded only orthopyroxene suggesting they are twin planes or low Ca-pyroxene polymorphs (Coe and Kirby, 1975) but not exsolutions. Cross fractures perpendicular to crystal margins are common, some fractures are curved (Figs 5.4B and 5.4C). These fracture patterns are similar to clinoenstatite in Cape Vogel boninites illustrated by Dallwitz et al. (1966), but the orthopyroxene phenocrysts in the Vestfold Hills examples are too calcic to be clinoenstatite or clinobronzite. The phenocryst morphology may instead be related to quenching, as the fractures and patchy extinction are poorly developed (though present) in the orthopyroxenes of the relatively slowly cooled norites.

5.3 P-T ESTIMATES

The quench textured chilled margin samples of the high-Mg suite do not contain equilibrium assemblages that permit estimation of the crystallization pressure or temperature. However, it is possible to estimate these parameters from the coarser grained intercumulus minerals of the norites.

Temperatures were calculated by applying the Wells (1977), Kretz (exchange only, 1982) and Lindsley (1983) thermometers to the orthopyroxene-calcic clinopyroxene pairs exsolved from intercumulus primary pigeonite (Fig. 5.11). A comparison of these methods was made in Section 1.1.3. Only the pyroxene data calculated based on 4.000 cations are presented here (Table 5.7), although the maximum difference in temperature using Fe^T in the calculations is only 20°C.

An essentially identical temperature of 1200°C was determined from each of the Wells, Kretz solvus, and Lindsley (cpx limb) thermometers. The Lindsley (opx limb) records a significantly lower temperature similar to the findings of Section 1.1.3. A temperature of 1200°C is a very reasonable, though perhaps a slightly high temperature estimate as the liquidus of the high-Mg sample 060 was located at ~1280°C at 7-8 kbar, and pigeonite precipitation from this composition would be anticipated ~30°C below the liquidus when comparison is made with the data of Duncan & Green (submitted). The calculated temperature is clearly magmatic, and emphasizes the fact that extensive subsolidus re-equilibration of the norite has not occurred. In contrast, the temperature and bulk pigeonite composition suggests quite rapid cooling in order to inhibit granular exsolution of augite as found in Skaergaard pigeonites (Lindsley & Anderson, 1983). This in turn implies a relatively cool crust at the time of emplacement.

Pressure was estimated following the method of Ellis (1980) (see Section 1.1.3). The CaTs molecule was calculated from the Fe-rich rim compositions of the intercumulus calcic clinopyroxene and exsolution lamellae of the pigeonite, and combined with the most Na-rich intercumulus plagioclase rim composition (Table 5.8). The resulting pressure of 7.6 kbar is in excellent accord with the pressure calculated from the groundmass assemblage of sample 060 (8 kbar, Table 1.4) and the emplacement pressure determined from the liquidus study of 060 (7-8 kbar, Section 1.3.1).

TABLE 5.7
TEMPERATURE ESTIMATES FROM THE HIGH-MG NORITE

	a_{en}^{cpx}	a_{en}^{opx}	X_{Mg}^{opx}	X_{Mg}^{cpx}	X_{Ca}^{cpx}	Wells	Kretz solv.	Lindsley cpx limb	Lindsley opx limb
65584 Pigeonite exsolution lamellae:						T^oC:			
	0.1738	0.3997	0.672	0.775	0.357	1199	1203		
	0.1613	0.3739	0.657	0.743	0.355	1186	1190		
Avg.	0.1676	0.3868	0.665	0.759	0.356	1193	1197	1200	900

a_{en} CALCULATED FOLLOWING WOOD & BANNO (1973). X_{Mg} = MG/(MG+FE). X_{Ca} = CA/(CA+MG+FE).

TABLE 5.8
PRESSURE ESTIMATES FROM THE HIGH-MG NORITE

	X_{CaTs}	X_{Ab}		T^oC	P (kbar)
65584	0.0148	0.765	Wells	1193	7.6
	0.0369	0.708	Kretz (solv)	1197	7.6
	0.0328		Lindsley		
	0.0049		(cpx limb)	1200	7.6
	0.0097		Lindsley		
	0.0388		(opx limb)	900	9.2
Avg.	0.0230	0.737			

CaTs CALCULATED FOLLOWING KUSHIRO (1962).
X_{Ab} = NA/(NA+CA).

5.4 RELATIVE AGE RELATIONSHIPS OF THE SUBGROUPS

In the introduction to this chapter, the high-Mg suite was shown to be divisible into three chemically defined subgroups, each characterized by distinctive chilled margin textures and phenocryst compositions. The nature of the chemical differences between the orthopyroxene phenocrysts of each subgroup implies derivation from chemically distinct liquids. Thus, in order to evaluate the evolution of the source region(s) which gave rise to these distinctive liquid compositions, determining the relative age of the subgroups is essential.

Using the Rb/Sr method, the "absolute" age of the high-Mg suite was determined by Collerson & Sheraton (in press) to be 2424 $\pm$ 72 Ma. Data from the eleven samples grouped by these authors into the high-Mg suite produced a great deal of isotopic scatter and in order to define an isochron within acceptable statistical limits four analyses were excluded. The seven samples used in the isochron included five which chemically belong to the orthopyroxene phyric (Sr_N depleted) subdivision including samples from both subgroup III (Rb-rich) and subgroup II (Rb-poor), and two samples belonging to subgroup I. Two of the excluded samples have identical trace element patterns to subgroup II samples 229, 214 and 034 (Fig. 5.2; Collerson & Sheraton, in press; data in Sheraton, 1985).

Thus the "absolute" age of the high-Mg tholeiites reported by Collerson & Sheraton was determined on samples belonging to each of the chemical subgroups defined in this study and does not represent the emplacement age of a particular subgroup. The necessity to exclude samples in order to produce the isochron suggests refinements in the age could be made by considering individual subgroups defined in this study.

Because dykes of the high-Mg suite outcrop infrequently, dyke intersections which define the relative age of emplacement between members of the suite are uncommon. Thus, to generalize from the few documented crosscutting relationships, it is necessary to assume that each of the three subgroups was intruded as a separate, discrete event which did not overlap in time with the other subgroups.

The oldest subgroup based on dyke intersections is the olivine + orthopyroxene phyric subgroup I. Three separate dykes belonging to this subgroup were found to be cross cut by dykes belonging to both subgroups II and III. Unfortunately, no intersections were documented which relate the relative ages of subgroups II and III. However, circumstantial evidence

suggests that the quench textured subgroup III dykes are the youngest of the suite.

Standard field procedure while sampling the dykes was to estimate the dyke widths; Fig. 5.13 is a histogram of these estimates divided into the subgroups. Each of the three groupings contains eight samples (the width of three dykes was not estimated, and one dyke was sampled twice) and as the subgroups are based on chemical features there can be no field-introduced bias to the estimated widths. It is found that the average dyke width decreases in the order subgroup I, II, III. As the oldest subgroup based on cross cutting relationships has the widest average dyke width and is also the most primitive subgroup, the histogram is interpreted to reflect the evolution of a magma-induced stress field developed in the lower crust following the compressional tectonism of the ca.2500 Ma metamorphism. As the magmatic episode waned, dyke widths would be anticipated to narrow, and thus subgroup III dykes are thought to represent the youngest subgroup.

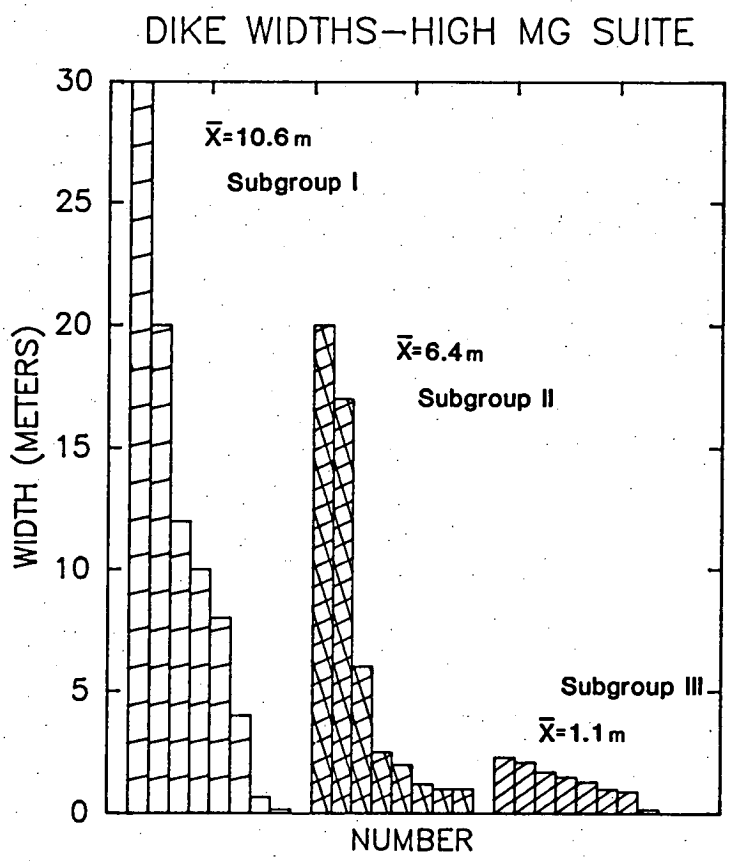

Figure 5.13
Histogram of field-estimated dyke widths divided to correspond to subgroup designations.

5.5 MAJOR AND TRACE ELEMENT GEOCHEMISTRY EMPHASIZING SOURCE CHARACTERISTICS

5.5.1 MAJOR ELEMENT CHARACTERIZATION

Major and trace element analyses and CIPW norms of the 30 samples comprising the high-Mg suite are tabulated in Appendix 2. Major element values have been normalized to 100% volatile-free with all Fe converted to FeO prior to the norm calculation; the recalculated analyses are used exclusively in the geochemical plots.

The high-Mg suite is in general characterized by relatively high SiO_2 (51-57%), MgO (7-14%) and low TiO_2 (<0.7%), and ranges from 7% normative olivine to 10% normative quartz. The high Mg#'s (~70) and Ni contents (>400 ppm) of the most mafic chilled margin compositions are within the range of values believed to be characteristic of liquids which could be in equilibrium with a peridotitic mantle composition.

Analyses of the high-Mg dykes are plotted on a Jensen cation diagram (Jensen, 1976) in Fig. 5.14, and are compared with other Mg-rich suites. The Vestfold Hills suite is generally similar to the komatiite-type fractionation trend defined on the Jensen diagram by increasing Al accompanied by only minor Fe enrichment, and contrasts sharply with the Fe-enrichment trend of tholeiite suites characterized by the Skaergaard Complex, and also displayed in the fractionation path of MORB glasses.

The variation in the major element compositions of the komatiites is controlled by the fractionation of the plagioclase-free assemblage olivine $\pm$ clinopyroxene (see for example Echeverria, 1980). In the Jensen diagram, the Cape Vogel, Troodos, Bushveld and Vestfold Hills compositions vary in Al versus Mg content with little variation in $(Fe^T + Ti)$, thus differing from komatiites and reflecting the relatively minor role of olivine and important roles of orthopyroxene $\pm$ clinopyroxene in controlling compositional variation.

The SiO_2-TiO_2-MgO relationships are shown in Fig. 5.15. At comparable levels of TiO_2 (Fig. 5.15A) the Munro komatiites are much more silica undersaturated than the Bushveld, Troodos and Cape Vogel suites, and display a marked increase in TiO_2 with fractionation. The low-Ca pyroxene dominant suites, which include the Vestfold Hills, contrast the komatiite fractionation trend in having generally constant TiO_2 over a somewhat narrower range and higher absolute content of SiO_2. The Vestfold Hills suite is significantly enriched in TiO_2 compared to the Cape Vogel, Bushveld and Troodos suites while having overlapping SiO_2 values.

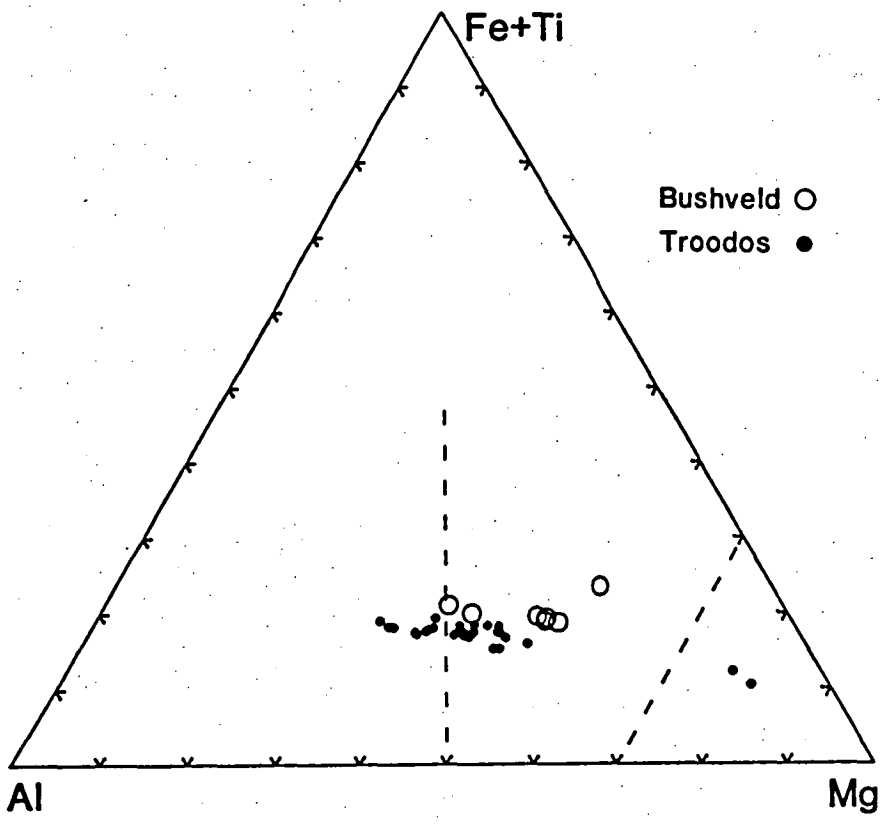
Fe+Ti
Bushveld ○
Troodos ●
Al
Mg

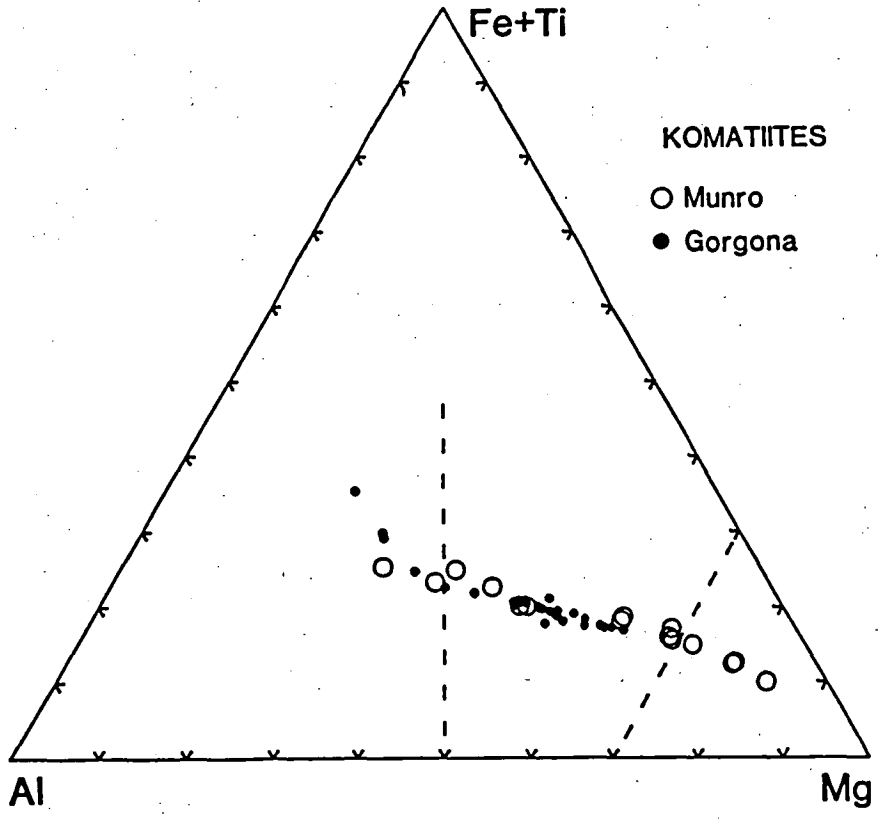
Fe+Ti
KOMATIITES
○ Munro
● Gorgona
Al
Mg

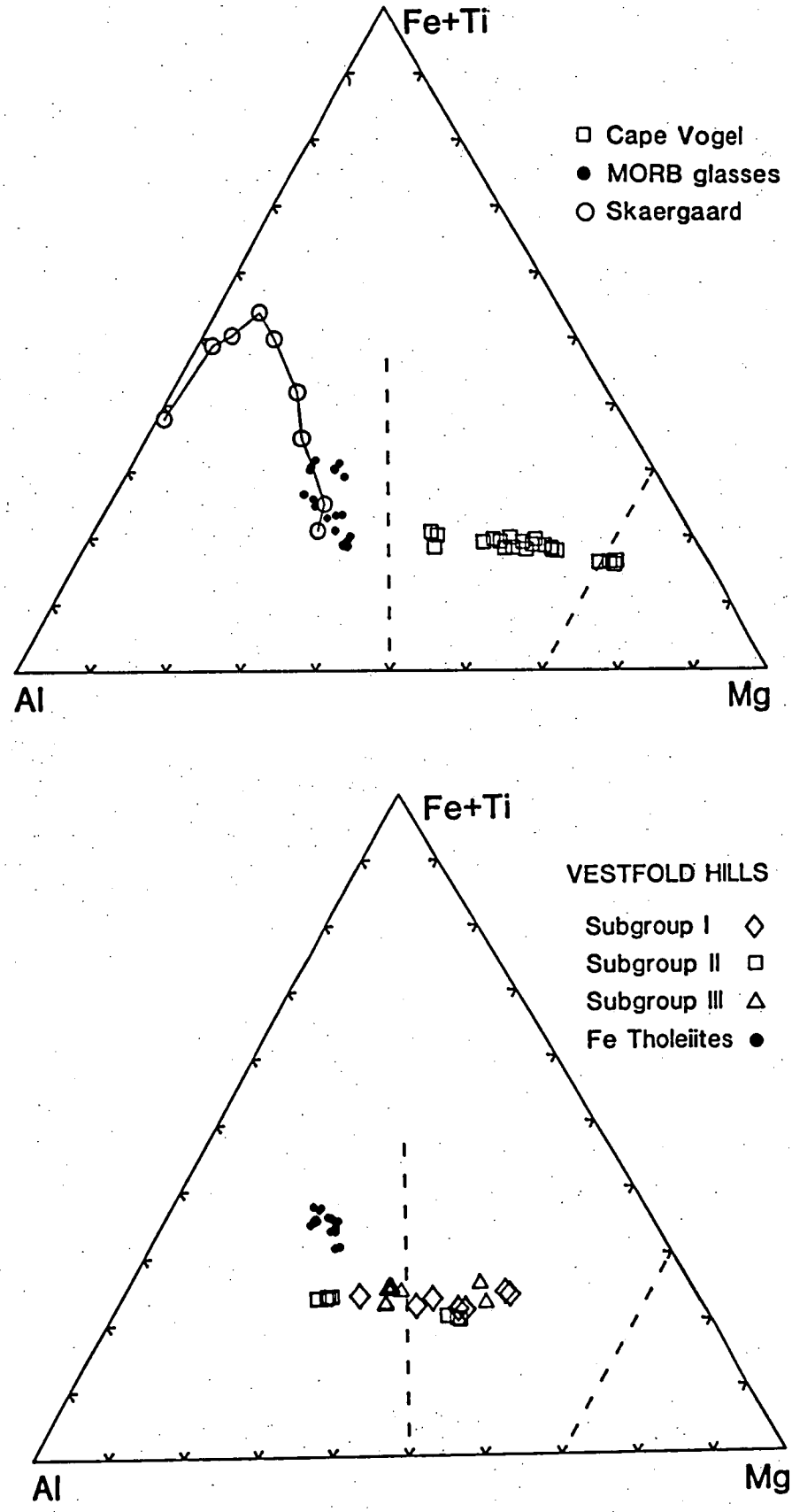

Figure 5.14

Comparison of the compositional trends in various Mg-rich suites on Jensen cation diagrams (Jensen, 1976). The boundaries from right to left are: ultramafic komatiite, basaltic komatiite and tholeiitic basalt (Jensen, 1976). Data from this study, Jensen (1976), Sharp & Hulbert (1985), Arndt et al. (1977), Frey et al (1980), Bryan & Moore (1977), Echeverria (1980), Cameron (1985) and Jenner (1981).

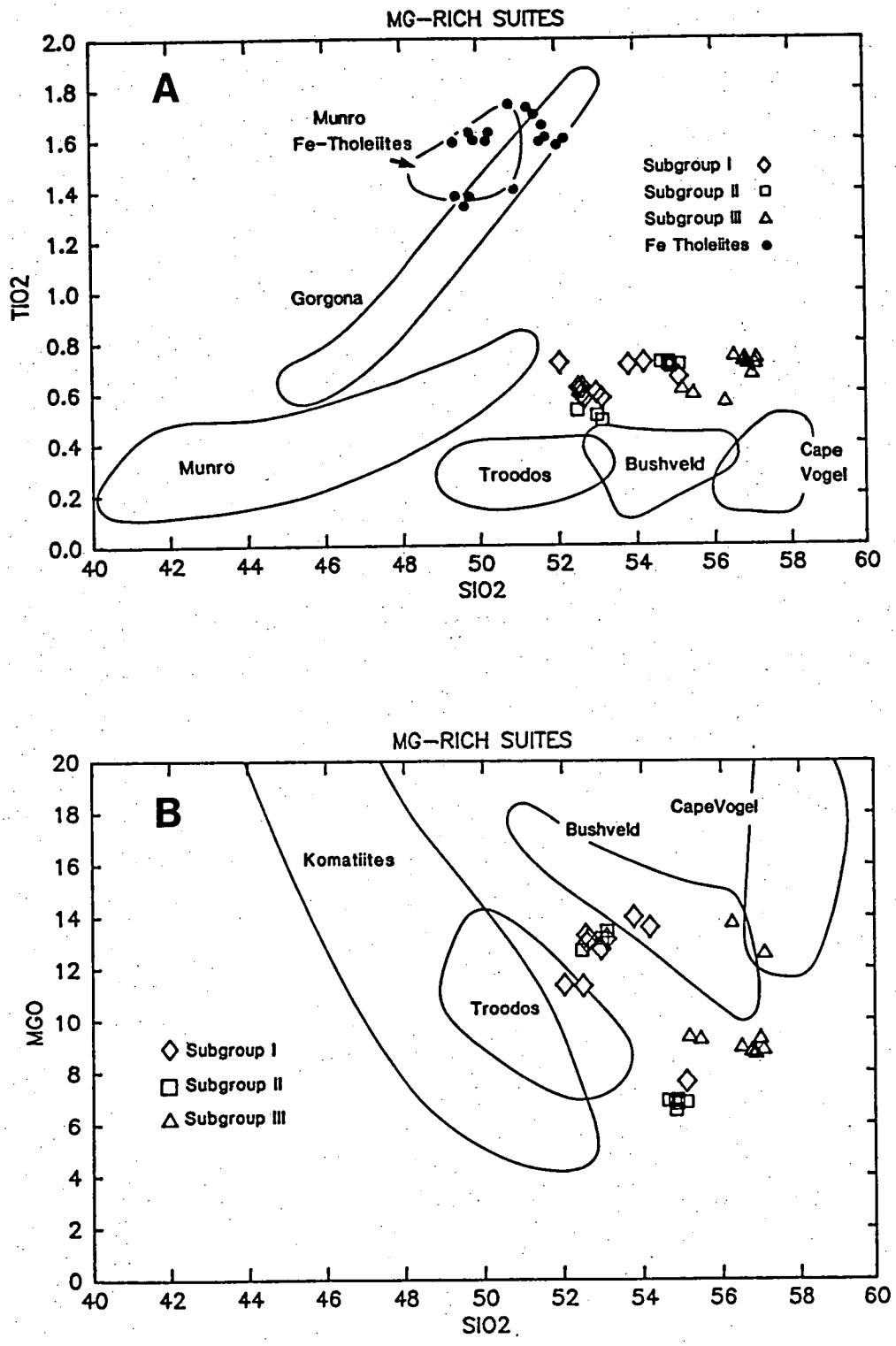

Figure 5.15

Comparison of TiO_2-SiO_2 (A) and MgO-SiO_2 (B) relationships of various Mg-rich suites including the Vestfold Hills ca.2420 Ma Fe-rich tholeiites and Munro Fe-rich tholeiites. Data sources as in Fig. 5.14.

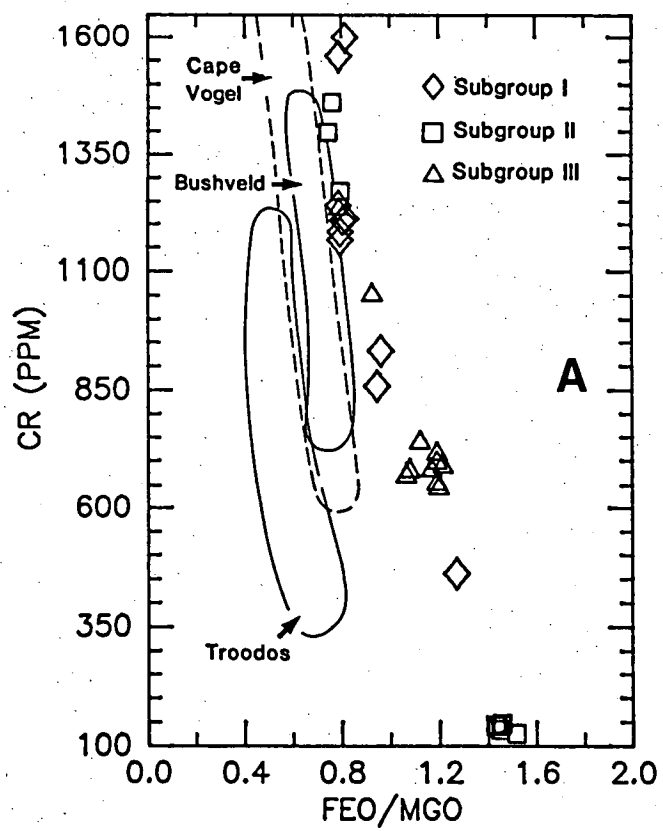

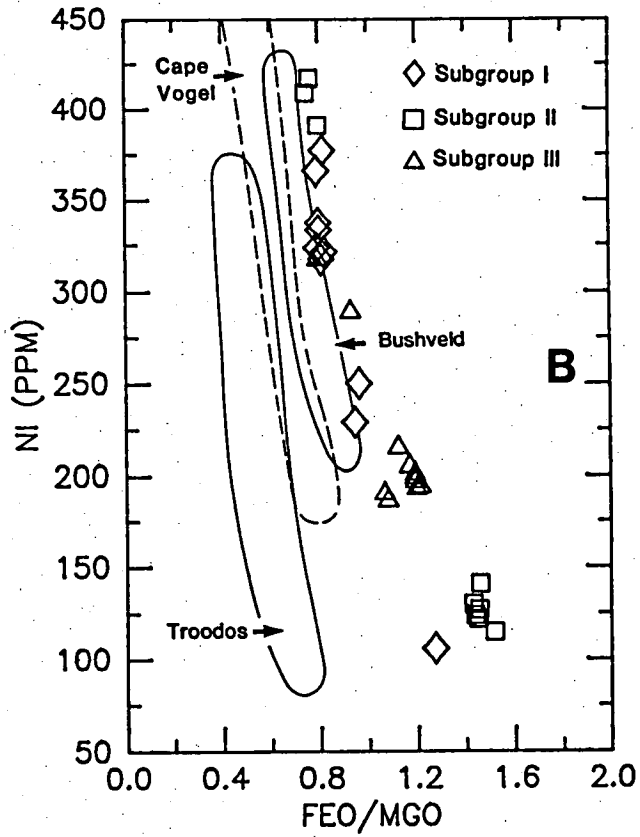

Figure 5.16
Comparison of Cr (A) and Ni (B) abundances with FeO/MgO variation between the Vestfold Hills high-Mg suite and the siliceous, magnesian suites of Fig. 5.15. Data sources as in Fig. 5.14.

Fig. 5.15B illustrates a general tendency for individual orthopyroxene-bearing suites to be more siliceous at a given MgO content in an order from the Troodos Upper Pillow Lavas to the SiO_2-rich Cape Vogel boninites, with the Vestfold Hills high-Mg suite falling between these extremes. The komatiites are the least siliceous, and range to much greater MgO (~30%).

The most mafic members of these high-SiO_2 suites are rich in Cr and Ni (Figs 5.16A and 5.16B) which decrease rapidly with fractionation. At a given level of Cr or Ni, the Vestfold Hills samples are Fe-rich while having comparable values of MgO with Troodos and some Cape Vogel samples.

In summary, the Vestfold Hills high-Mg suite shows some similarities with komatiites and their differentiates but the high SiO_2 and predominance of orthopyroxene more closely resembles the well-studied Troodos and Cape Vogel rocks. Although both of these suites evolved in an oceanic tectonic environment compared to the subcontinental source for the Vestfold Hills, the composition of their parental liquids were similarly governed by the composition of the source and the pressure and temperature of magma extraction. The high concentrations of compatible elements Cr and Ni, and the highly magnesian character of the proposed parental liquids to those suites (Troodos - Mg_{77}, Duncan & Green, 1980; Cape Vogel - Mg_{77-79}, Jenner, 1981) are believed to indicate their derivation from a refractory peridotite which had previously lost a basaltic melt fraction (Nesbitt & Sun, 1980). Incompatible trace elements are then expected to have low concentrations in these second stage melts, and in general this is the case. However, an enrichment event, via an incompatible element-rich fluid or melt fraction has complicated the multi-stage melting model in these localities (Hickey & Frey, 1982).

Bearing in mind the characteristics of these other suites, similar in many respects to the Vestfold Hills high-Mg tholeiites, the geochemistry of the high-Mg dykes will be examined, focussing on parameters which provide evidence for the geochemistry of the source and conditions of melt formation.

5.5.2 SUBGROUP I

The use of liquid compositions to evaluate source characteristics can be extended to a variety of elements if the liquid examined has not been extensively modified following its removal from the source. Subgroup I is the oldest of the high-Mg suite, and the most primitive with samples ranging in Mg# from 65-70 (FeO^T). In Fig. 5.17, various elemental ratios

of this subgroup are shown, normalized with respect to chondrite values (Nesbitt & Sun, 1980). Chondrite-normalized diagrams are thought to be a reasonable method to characterize the trace element ratios of the high-Mg suite as the composition of the mantle at ca.2420 Ma is expected to more closely resemble 'chondrite' in the proportions of many elements than present day earth, where subduction and melt extraction have significantly modified these abundances.

CaO-Al_2O_3-TiO_2

Inspection of Fig. 5.17 reveals that the ratios involving CaO-Al_2O_3-TiO_2 have essentially chondritic values indicating these elements behaved largely as incompatible elements during melting and subsequent fractionation. This contrasts with MORBs, where CaO/Al_2O_3 is generally chondritic, but CaO/TiO_2 and Al_2O_3/TiO_2 display a range of values that are less than chondrite (Sun & Nesbitt, 1978). In the latter case, the ratios reflect the incompatible nature of TiO_2, but more importantly, indicate that liquids were extracted from the mantle leaving varying proportions of a Ca-Al-bearing phase(s) in the residue (clinopyroxene $\pm$ garnet $\pm$ spinel $\pm$ plagioclase). In contrast, the Cape Vogel and Troodos suites have Al_2O_3/TiO_2 (33, 60 respectively) and CaO/TiO_2 (48, 20 respectively) greater than chondrite (20, 16.4 respectively; Nesbitt & Sun, 1980), which have been interpreted as indicating that the primary liquids to these suites were derived from melting of a source that had lost a large proportion of its basaltic components through a previous melting episode.

Reasons for the departure from chondritic CaO-TiO_2-Al_2O_3 relations in liquids inferred through geochemical arguments to be primary have been discussed widely and a number of explanations presented (Nesbitt & Sun, 1980; Arndt et al., 1977; Cawthorn & Strong, 1974). The chondritic nature of subgroup I with respect to CaO-TiO_2-Al_2O_3 eliminates many of these complexities and implies that the primary melt to this subgroup was derived from a source region that had not experienced a previous melting event. Furthermore, residual Ca-Al-rich phases are not indicated by the ratios, implying that these phases were eliminated through fairly high degrees of partial melting. The ratios also place a relative constraint on the depth of melting in that liquids which segregated at high pressure leaving an olivine + orthopyroxene residue are expected to have a CaO/Al_2O_3 ratio greater than chondrite due to the retention of aluminous orthopyroxene in the residue. The absence of this feature in subgroup I samples implies low pressure liquid extraction with a low Al-orthopyroxene residue.

It is noted however, that two samples, 067 and 209, do have high CaO/Al_2O_3 ratios, but have comparable trace element ratios with other samples. This difference may indicate these liquids were derived by a sequential melting process as discussed by Nesbitt et al. (1979).

Y-Ti

Yttrium shares many geochemical characteristics with the heavy rare earth elements (HREE) and behaves as a relatively compatible element up to moderate degrees of melting (~15-20%), at appropriate pressures, if garnet is retained in the residue. The chondritic Ti/Y ratio (Fig. 5.17) indicates that Y, and by inference the HREE, have acted as incompatible elements, implying that garnet has not been involved in the generation of the parental liquid to subgroup I, nor in any geochemical enrichment processes which may have determined the incompatible element contents of the source region.

V-Sc

These elements share similar geochemical characteristics but can be decoupled from one another by spinel (V-rich), garnet (Sc-rich) and to a lesser extent by pyroxene fractionation. Scandium is a moderately compatible element in clino- and orthopyroxene compared to V (K^{Sc} = 3.1, 1.1 respectively, K^{V} = 1.5, 0.3 respectively; Frey et al., 1978) and the relatively broad range of $(Ti/Sc)_N$ compared to $(Ti/V)_N$ (Fig. 5.17) suggests minor pyroxene fractionation has modified the relative concentrations of these elements, a conclusion consistent with the petrography of this subgroup.

Vanadium has a much greater partition coefficient for spinel/liquid than Sc and fractionation of chromite will result in a marked depletion in V. The somewhat greater than chondrite Ti/V suggests minor chromite fractionation has taken place. However, this must be balanced by the high Cr contents of the most primitive members of the subgroup (>1500 ppm) and the discussion in Section 5.2.1, where it was indicated that chromite played an insignificant role in the fractionation of Cr during the evolution of the liquid compositions. However, minor chromite fractionation from the parental liquid cannot be excluded, and the Ti/V ratio may be evidence for this process.

Ti-Zr-Nb

Titanium, Zr and Nb are high field strength elements which behave incompatibly when partial melting of mantle peridotite exceeds ~5%. As Ti/Y is in chondritic proportions the chemically similar Zr and Nb would also be expected to share this feature. However, Fig. 5.17 illustrates that Zr and Nb have relative concentrations in excess of what is anticipated from the enrichments of Ti and Y. The Ti/Zr ratios for subgroup I range from 67-56, considerably less than chondrite (110), and straddle the boundary suggested by Jenner (1981, Ti/Zr < 60) used to characterize high-Mg andesites generated at subduction zones. The low Ti/Zr in the Cape Vogel second stage melts is in part due to previous depletion in Ti, with subsequent enrichment in Zr, whereas the Vestfold Hills example is attributed entirely to Zr enrichment. The less than chondritic Zr/Nb ratio further displays the decoupling of these geochemically similar elements and indicates relative enrichment in the order Nb > Zr > Ti.

Low field strength elements

The low field strength elements Rb, K, Ba and Sr and the light REE La, are greatly enriched in subgroup I compared to primordial mantle (Fig. 5.1) and would indicate fairly low degrees of melting if they were considered independent of other geochemical features as discussed above. Instead, previous discussions indicate that enrichment of these elements was superimposed onto a "chondritic" source prior to melting. By considering various trace element ratios, relative enrichments are found to follow the order

$$Rb > Ba > K \geq La > Sr \geq Nb > Zr > \text{chondrite} = Y = Ti = Ca = Al > Sc \geq V.$$

Even though Nb has been enriched relative to other high field strength elements (Zr, Ti), it has not been enriched to the extent anticipated from elements of similar levels of incompatibility such as La or K (Fig. 5.1). Similarly, negative $(Nb)_N$ anomalies are commonly observed in island-arc volcanics and have been interpreted to reflect the retention of Fe,Ti oxides in the source of the metasomatic fluids (Saunders et al., 1980).

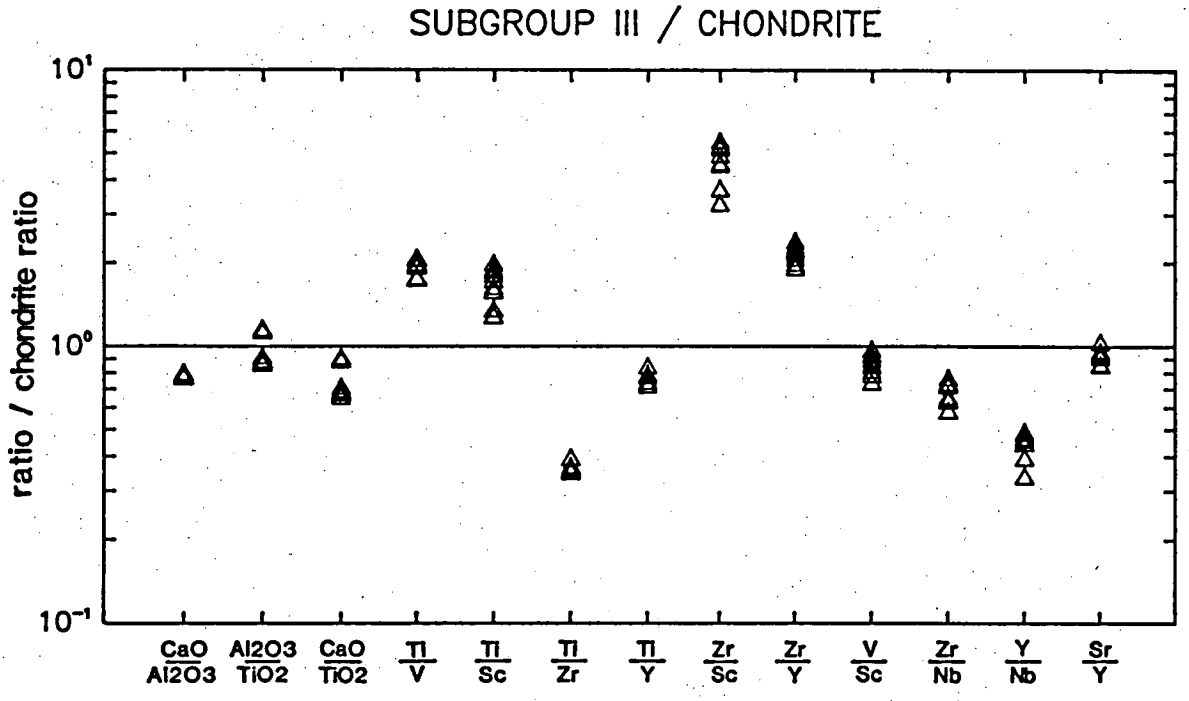

Figure 5.19
Various oxide and elemental ratios of subgroup III samples normalized with respect to chondritic abundances (Nesbitt & Sun, 1980).

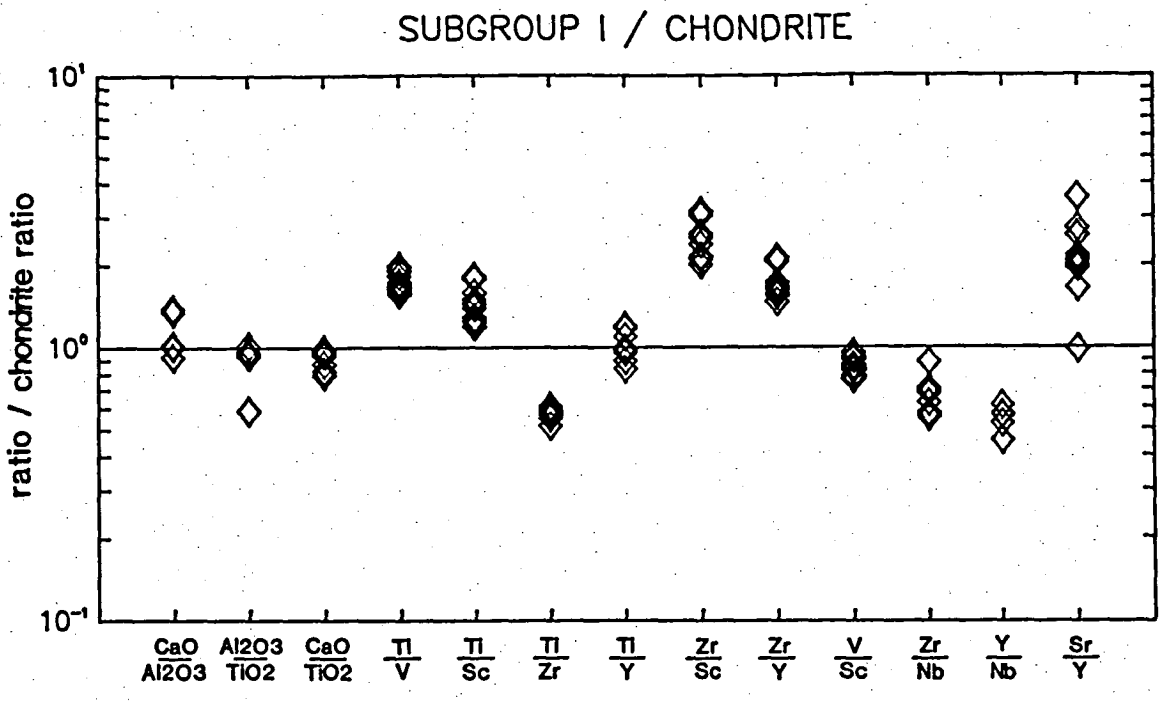

Figure 5.17
Various oxide and elemental ratios of subgroup I samples normalized with respect to chondritic abundances (Nesbitt & Sun, 1980).

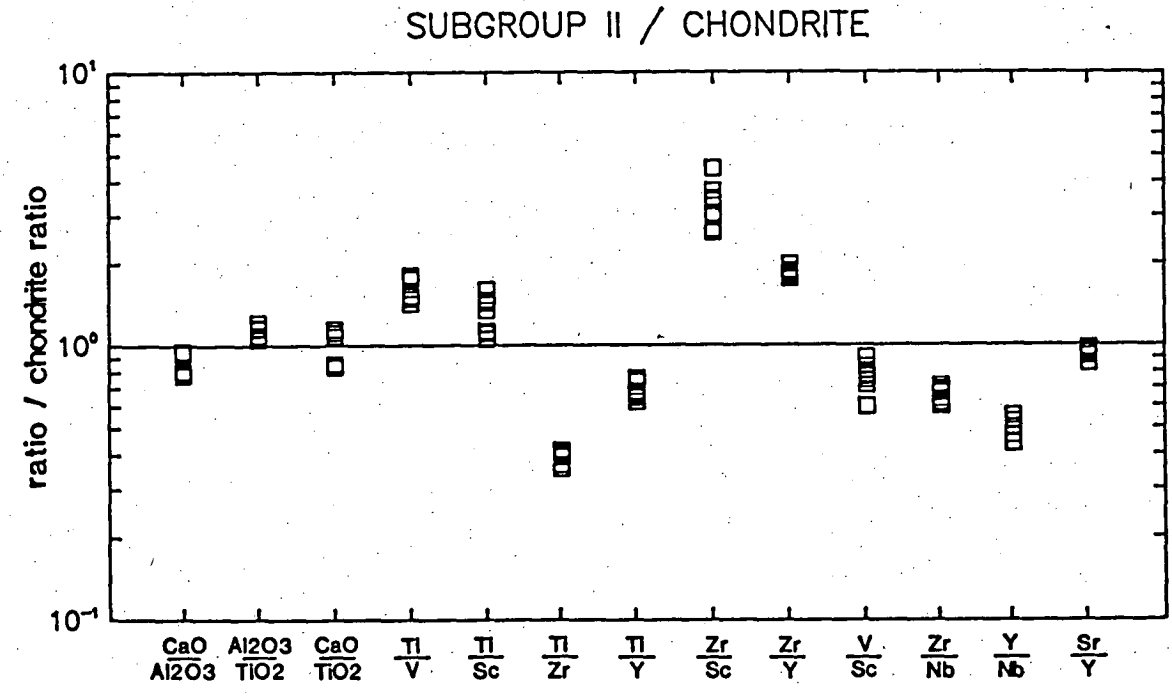

Figure 5.18
Various oxide and elemental ratios of subgroup II samples normalized with respect to chondritic abundances (Nesbitt & Sun, 1980).

5.5.3 SUBGROUP II

It was noted in the introduction to this chapter that subgroup II (and III) could not be related to subgroup I by crystal fractionation of olivine, orthopyroxene or clinopyroxene, as these phases cannot significantly fractionate Sr from a basaltic liquid and consequently cannot account for the relative $(Sr)_N$ depletion in subgroups II and III, and the absence of a $(Sr)_N$ anomaly in subgroup I.

As subgroups II and III are younger than subgroup I, the simplest model which might be considered based on the successively lower CaO contents of the orthopyroxene phenocrysts (I > II > III) and deduced relative ages is that they were derived by melting the subgroup I residue. If subgroup II was formed by partial melting the harzburgitic residue of subgroup I, then the model would predict subgroup II to be severely depleted in incompatible elements and consequently have high Al_2O_3/TiO_2 and CaO/TiO_2 ratios with less than chondritic CaO/Al_2O_3. Fig. 5.2 illustrates that subgroup II, however, is highly enriched in incompatible trace elements. As the chondritic source of subgroup I is inferred to have been enriched in incompatible elements prior to the melting event, it is possible that a second enrichment may have imposed a high incompatible element character, with the exception of Sr, to a refractory subgroup I residue. Thus the enriched nature of the incompatible elements in subgroup II does not preclude derivation from a clinopyroxene-poor harzburgitic source provided that a post-subgroup I enrichment process is postulated to prepare the residue as a subgroup II (or III) source.

Chondritic normalized ratios of subgroup II analyses are shown in Fig. 5.18. The olivine-bearing and most mafic samples of subgroup II do have a greater than chondrite Al_2O_3/TiO_2 ratio (23-24), as predicted if the source region had lost a previous melt fraction. However, the depletion in TiO_2 is only marginal compared to chondrite (Al_2O_3/TiO_2 = 20) and differs greatly from Troodos and Cape Vogel second-stage melts (~60 and ~33, respectively; Nesbitt & Sun, 1980). On this basis it is unlikely that subgroup II was derived from the harzburgitic residue of subgroup I, but an initial source depletion in TiO_2 followed by enrichment of incompatible elements which fortuitously resulted in a near-chondritic Al_2O_3/TiO_2 ratio cannot be excluded. However, the CaO/Al_2O_3 ratio of the olivine-bearing samples of subgroup II is chondritic, which makes derivation from a clinopyroxene (CaO) poor source unlikely. Furthermore, the chondritic CaO/Al_2O_3 not only indicates separate sources for subgroups I and II, but similarly indicates an extensive degree of melting and the absence of Ca-Al-rich phases in the residue of subgroup II.

A comparison of the olivine-bearing samples of subgroup II (034, 207, 214) with subgroup I sample 054A reveals that while these four samples have similar MgO contents (12.6-13.3%) the subgroup II samples are enriched in the compatible elements Cr and Ni (Fig. 5.16). Considering the chondritic CaO/Al_2O_3 and Sr/Y ratios of the subgroup II samples, the primary liquid to subgroup II probably experienced a greater degree of partial melting than the liquid parental to subgroup I. This implies however, that the subgroup II source had non-chondritic Ti abundances or the Ti concentration was modified following the formation of the primary melt.

5.5.4 SUBGROUP III

The most mafic sample of the orthopyroxene phyric subgroup III has relatively low Mg#, Cr and Ni (62.6, 670 ppm, 190 ppm respectively) compared to the Mg_{69-70} compositions of subgroups I and II. If the primary melt to subgroup III was derived from a separate chondritic sources as I and II, then the primitive characteristics of the source should retained in the $CaO-Al_2O_3-TiO_2$ ratios of subgroup III samples as long as orthopyroxene ($\pm$ olivine) was the only fractionating phase.

Selected chondrite normalized ratios are shown in Fig. 5.19. The CaO/Al_2O_3 ratio for all samples is essentially identical and is consistent with the fractionation of only orthopyroxene $\pm$ olivine from a primitive liquid. However, the absolute CaO/Al_2O_3 ratio (~0.62) is significantly below chondrite (0.82; Sun & Nesbitt, 1978) and implies either the subgroup III source was depleted in CaO relative to that of subgroups I and II, or the fractionation of a Ca-rich, Al-poor phase has modified the primary liquid composition.

Although subgroup III is depleted in $CaO > Al_2O_3$ compared to subgroup II and could then possibly represent further melting of the subgroup II source, subgroup III is enriched in $Zr \geq Nb > Ti$ compared to subgroup II but has equivalent Sr/Y. These features are inconsistent with derivation of subgroup III from the subgroup II residue unless the residue was enriched in incompatible elements prior to the formation of the subgroup III parental liquids.

When compared to subgroup I, subgroup III is depleted in $CaO > Al_2O_3$, Ti and Sr relative to Y, and is enriched in Zr > Nb. These features are also inconsistent with remelting the subgroup I residue without the prior introduction of incompatible elements.

The possibility that the less than chondritic CaO/Al_2O_3 is the result of fractionating a CaO-rich phase will be addressed in a later section.

As in subgroup I, the normalized trace element patterns of subgroups II and III have a negative $(Nb)_N$ anomaly (Figs 5.1 and 5.2) implying that the fluid or melt which introduced the incompatible elements to the subgroup II and III source(s) was at some stage buffered by a phase which could decouple Nb from other incompatable elements (Saunders et al., 1980). The feature which distinguishes the spiderplots of subgroups II and III from those of subgroup I is the existence of a negative $(Sr)_N$ anomaly in the former. The Sr/Y ratio is chondritic in both subgroups II and III, while the geochemically similar Nd and Ce are strongly enriched. By contrast, in island-arc petrogenesis in the modern earth, a negative $(Nb)_N$ anomaly is also characteristic but Nd, Ce and Sr all show coherent and similar behaviour - all are enriched (Perfit et al., 1980).

If the Nb depletion is due to the buffering effect of a residual phase in the source region of the metasomatic fluid or melt, then the absence of $(Sr)_N$ enrichment may also indicate Sr was withheld from entering the metasomatic component by a residual phase. Of the major rock-forming minerals only plagioclase is able to decouple Sr from other LIL elements such as Ba, Rb and K. If plagioclase has played a role in decoupling the compositions of the source region(s) of subgroups II and III, it implies very shallow levels of melt extraction (<12 kbar; Green & Hibberson, 1970b).

5.5.5 RARE EARTH ELEMENTS

Rare earth element (REE) concentrations in three high-Mg samples (one from each subgroup) where determined following the ion-exchange XRF procedure of Robinson et al. (1986). The chondrite normalized patterns (Leedy chondrite / 1.2; Masuda et al., 1973; Sun & Hanson, 1975) are shown in Fig. 5.20 and the data listed in Table 5.9. The three analysed samples have essentially parallel REE patterns characterized by flat HREE, and strongly enriched LREE. Considering the precision of the analytical method (1-4%), the concentration of several HREE in subgroup I sample 054A (Mg_{69}) and the subgroup II sample 214 (Mg_{70}) overlap, and are thus indistinguishable. But these samples contrast with one another by having small $(+Eu)_N$ and $(-Eu)_N$ anomalies respectively, and 214 has a greater $(Ce/Sm)_N$ than 054A (2.5 versus 1.8).

An important aspect of the HREE is their low concentrations relative to chondrite. As discussed previously, samples of subgroups I and II have geochemical characteristics implying large degrees of partial melting leaving an olivine + orthopyroxene residue. Due to the low mineral/melt K_D

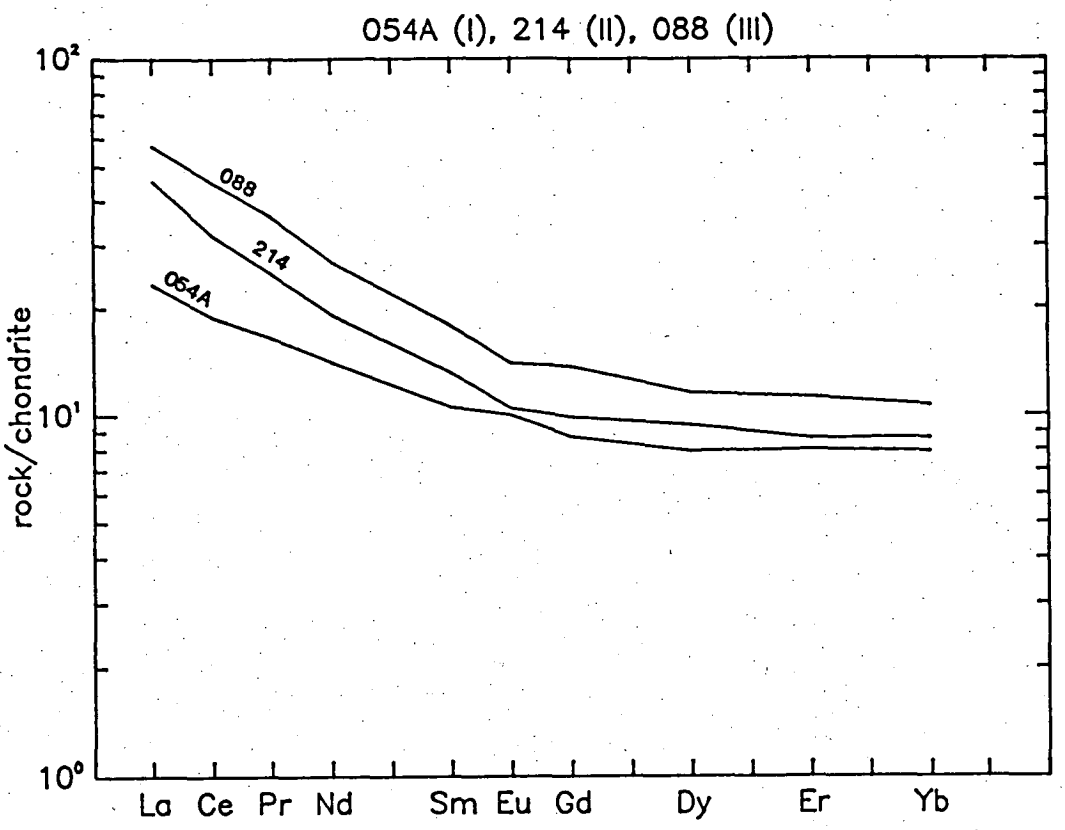

Figure 5.20
Chondrite normalized REE patterns (Leedy/1.2; Masuda et al., 1973; Sun & Hanson, 1975) of samples representing the three high-Mg subgroups.

TABLE 5.9
RARE EARTH ANALYSES* OF DYKES REPRESENTING SUBGROUPS I, II AND III

	La	Ce	Pr	Nd	Sm	Eu	Gd	Dy	Er	Yb	(Y)
054A I	7.35	15.33	1.90	8.42	2.02	0.73	2.25	2.57	1.78	1.64	15.7
214 II	14.4	2.60	2.87	11.43	2.53	0.75	2.55	3.04	1.82	1.79	16.6
088 III	18.1	36.6	4.15	16.1	3.43	1.01	3.54	2.75	2.39	2.21	23.1

* FOLLOWING THE METHOD OF ROBINSON ET AL. (1986), VALUES IN PPM.

for REE in these phases (Kay & Gast, 1973), the shape of the HREE pattern will be identical to that of the source, and its relative enrichment dependent on the degree of melting. The percentage of melting required to achieve the observed enrichment can be estimated from the batch melting expression of Shaw (1970):

$$\frac{C_L}{C_O} = \frac{1}{D(1-F) + F}$$

where C_O and C_L represent the concentration of an element in the original source and resulting liquid respectively, F is the fraction of liquid produced and D is the bulk mineral-melt distribution coefficient of the residue. For the case of residual olivine and orthopyroxene, $D \simeq 0$, thus

$$\frac{C_L}{C_O} \simeq \frac{1}{F}.$$

Studies of the abundances of REE in mantle-derived peridotites suggests the primordial mantle contains absolute REE concentrations 2-4X chondrite (Frey & Green, 1974). Ringwood (1979) suggests an enrichment of 2.2X and using a Yb concentration of 0.208 ppm, the calculation results in a minimum estimate for the degree of melting to derive 054A from a chondritic mantle as 28%. Aside from uncertainty in the estimates of mantle REE abundances, this is a minimum estimate due to the likelihood that 054A does not represent the composition of the primary liquid.

The nearly identical REE patterns of 088 and 214 suggest they were derived from a common parental liquid and differ in levels of REE enrichment due simply to the more fractionated composition of 088 (Mg_{60}). To test this possibility, increments of equilibrium orthopyroxene were added to 088 until the resulting composition was equivalent in Mg-value to 214 (70.5). Assuming Rayleigh fractionation, the proportion of added orthopyroxene was combined with the partition coefficients of Yb (Frey et al., 1978) to calculate the Yb concentration in a hypothetical parental liquid to 088. The calculation results in a value of 1.82 ppm Yb compared with 1.79 $\pm$ 0.07 ppm in 214. A similar calculation was performed considering olivine as the sole fractionating phase which gives 1.87 ppm Yb in an Mg_{70} liquid. These calculations indicate the source region of subgroup III primary liquids was not depleted in HREE, and was therefore no more refractory than the source region for 214.

5.6 CRYSTAL FRACTIONATION WITHIN THE HIGH-Mg DYKE SUITE

In the previous geochemical discussions of the three high-Mg subgroups, CaO-Al_2O_3-TiO_2 ratios of the most primitive samples in each subgroup were used to indicate source mineralogy both prior to and following extraction of the parental liquids. In Fig. 5.21, variations in CaO/TiO_2 and Al_2O_3/TiO_2 ratios of chilled margin samples are shown relative to the fractionation parameter Zr. In this section, the more evolved samples will be examined and their relationship to the Mg-rich compositions evaluated through least-squares mass balance calculations following the method of Reid et al. (1973).

5.6.1 SUBGROUP I

Excluding the anomalous low Al_2O_3 samples (Section 5.5.2), compositional variations in the olivine-bearing samples can be simply modelled through a varying proportion of orthopyroxene and minor olivine fractionation. Calculations also indicate that the composition of the olivine-free sample 069 can be obtained through the fractionation of these phases from the more magnesian sample 054A. However, the resulting least-squares composition (CaO/Al_2O_3 = 0.84) fails to reproduce the less than chondritic CaO/Al_2O_3 ratio of 069 (0.75).

Sample 069 contains phenocrysts of clinopyroxene with resorbed cores of orthopyroxene and pigeonite. Incorporation of these phases and compositions into the calculation results in an excellent statistical fit between the calculated and observed whole-rock analyses. The proportion of the extracted phases (~20% total) to derive 069 from 054A depends on the compositions used in the calculation but CaO/Al_2O_3 can only be balanced by including 6-10% fractionation of calcic clinopyroxene and the resorption of pigeonite. These results are in good agreement with the disequilibrium petrographic features of 069.

5.6.2 SUBGROUP II

In the previous geochemical discussions of subgroup II the three olivine-bearing samples were found to have chondritic CaO/Al_2O_3 and Sr/Y ratios implying derivation from a primitive undepleted source. Recalling that the majority of samples in this subgroup are olivine-free and orthopyroxene phyric, their derivation from the olivine-bearing samples is

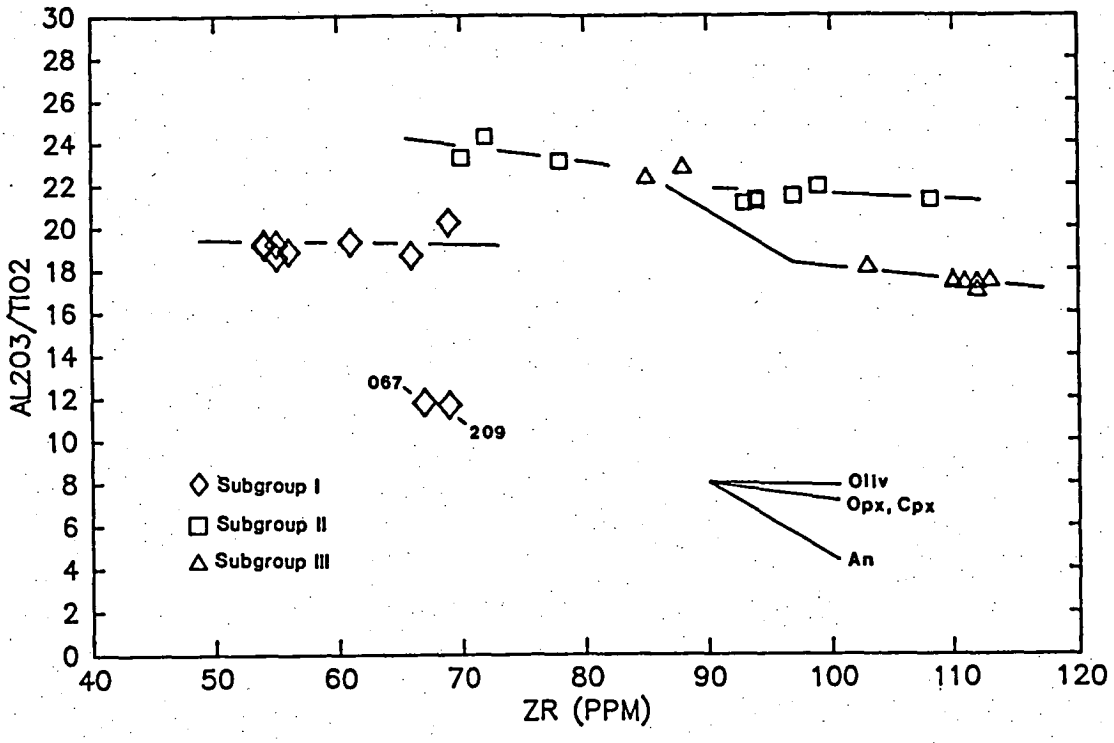

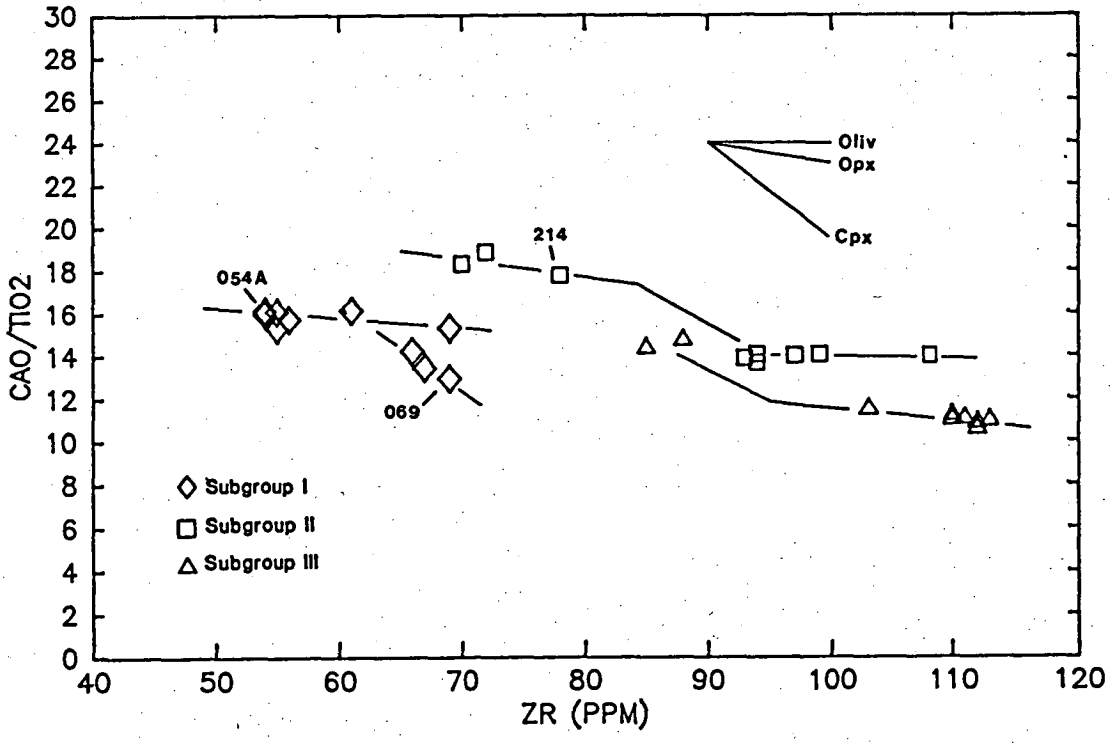

Figure 5.21

Variations in the ratios Al_2O_3/TiO_2 and CaO/TiO_2 in the three high-Mg subgroups with differentiation (increasing Zr). Vectors show changes in these ratios due to extraction of the indicated phases. Vector length equivalent to ~10% fractionation.

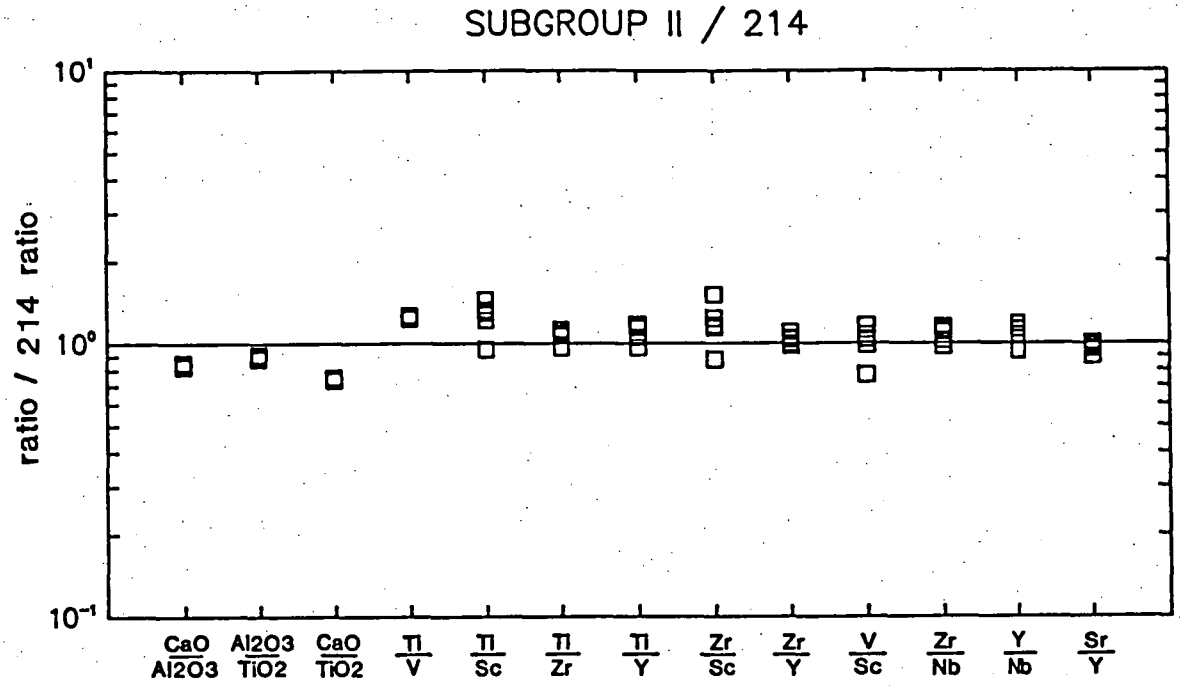

Figure 5.22
Various oxide and elemental ratios of subgroup II orthopyroxene phyric samples normalized to the olivine-orthopyroxene phyric subgroup II sample 214.

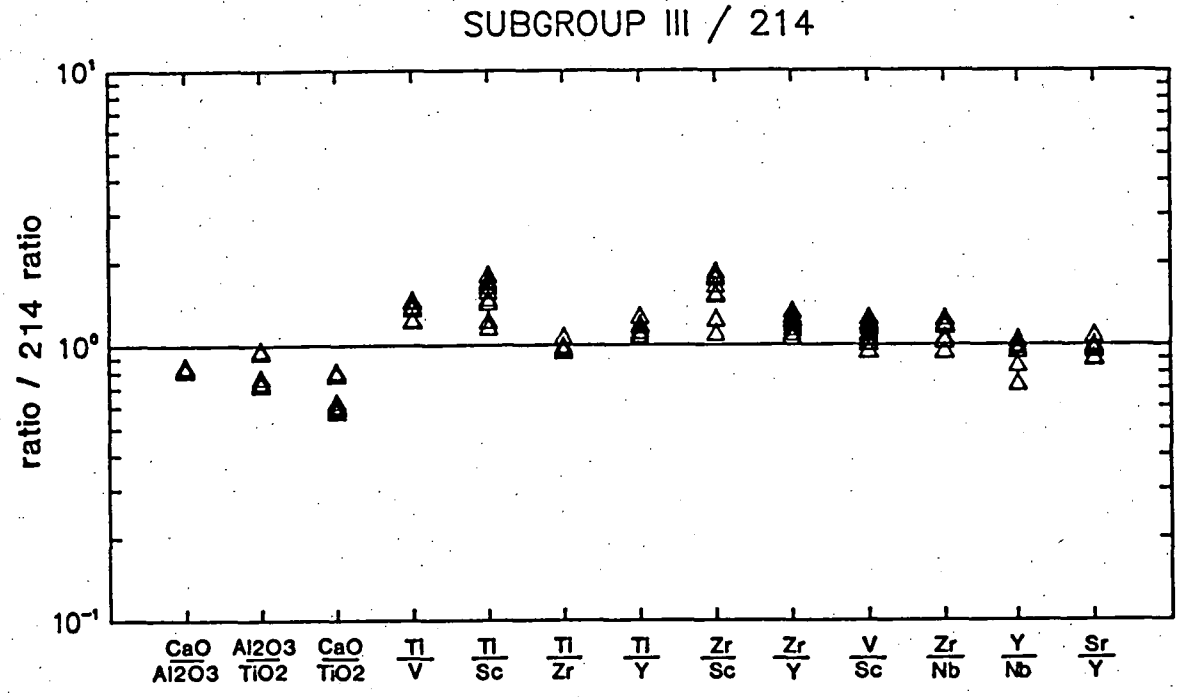

Figure 5.23
Various oxide and elemental ratios of subgroup III orthopyroxene phyric samples normalized to the olivine-orthopyroxene phyric subgroup II sample 214.

likely to be the result of olivine ± orthopyroxene fractionation. If this hypothesis is true, ratios involving $CaO-Al_2O_3-TiO_2$ should remain constant throughout the fractionation series. Fig. 5.21 shows that this has not occurred. To further evaluate this variation, elemental and oxide ratios of the olivine-free samples were normalized to the olivine-bearing sample 214 (Fig. 5.22). Ratios involving the incompatible elements Ti-Zr-Y-Nb-Sr have very similar values to those of 214 confirming a genetic relationship between the olivine-bearing and olivine-free samples (see also Fig. 5.12). As Sc is a compatible phase in pyroxenes, the wider range of Ti/Sc compared to Ti/V implies pyroxene fractionation was involved in the evolution of the olivine-free samples. The depletion in CaO and to a lesser extent Al_2O_3 implies fractionation of clinopyroxene.

To quantify these observations, mass balance calculations were used to model the relationship between the most magnesian olivine-free sample (234) and 214 (see Fig. 5.21). As clinopyroxene is not found as a phenocryst in any subgroup II samples, an analysis from 069 was used in the calculations. The test indicates that the major element composition of 234 can be derived from 214 by fractionating ~20% orthopyroxene and minor olivine with ~10% clinopyroxene. Calculations using wide variations in the Al_2O_3 and CaO contents of orthopyroxene do not result in statistically valid solutions nor reproduce the observed CaO/Al_2O_3 ratio of 234.

The variations in major element composition of the olivine-free subgroup II samples were also modelled and found to be controlled by <5% orthopyroxene fractionation. However these samples exhibit a wide range of Zr (Fig. 5.21) which requires the fractionation of ~15% orthopyroxene This is a significant difference and may indicate Zr, and perhaps other incompatible elements, were being enriched by an unrecognized process in excess of what is anticipated by crystal fractionation following extraction of the primary liquid from the source region.

5.6.3 SUBGROUP III

Subgroup III has been treated separately from subgroup II throughout the geochemical discussions because they define separate trends on the (Jd+CaTs)-Oliv-Qtz diagram (Fig. 5.3) and each group also has distinctive phenocryst compositions (Fig. 5.12). However, subgroups II and III do share similar patterns on spiderplots, differing only in the degree of relative elemental enrichment. This suggests a close relationship between the two subgroups which was also indicated in the REE patterns. A further comparison of subgroups II and III is shown in Fig. 5.23, where subgroup

III samples have been normalized to sample 214. The incompatible trace elements of subgroup III samples have identical ratios to 214, further illustrating the close relationship of these subgroups. The compatible elements, Sc, and V, are moderately depleted in subgroup III relative to 214, suggesting the possible derivation of subgroup III from a parental liquid common to subgroups II and III by pyroxene fractionation and the depletion in CaO implies this process involves clinopyroxene.

Fig. 5.21 shows that two subgroup III samples (025 and 072) have CaO/TiO_2 and Al_2O_3/TiO_2 ratios between those of 214 and other subgroup III samples. Calculations indicate that derivation of these two samples from 214 can be modelled by fractionating <10% olivine + orthopyroxene in roughly equal proportions if they are accompanied by ~10% clinopyroxene fractionation. Furthermore, the compositional variation in the more evolved subgroup III samples can be related by <6% orthopyroxene fractionation. However, modelling the compositional path between 025 or 072 and the evolved subgroup III samples using various compositions and combinations of olivine-orthopyroxene-clinopyroxene and pigeonite does not produce valid results. Only by including an unrealistic and highly calcic plagioclase composition ($>An_{90}$) does the calculation give an acceptable mathematical solution. The main effect of plagioclase is to reduce the Al_2O_3 content to within acceptable limits, implying more complicated relationship between samples 072, 025 and other subgroup III samples than suggested by the discriminants used to characterize this subgroup.

In summary, intra-suite chemical variations between the mafic olivine + orthopyroxene phyric subgroup I samples, and the relatively evolved calcic clinopyroxene-phyric sample 069, can be successfully modelled through the fractionation of the observed phenocryst phases. However, the chemical variation in subgroup II can only be reproduced by including calcic clinopyroxene in the calculation, for which there is no petrographic evidence. Furthermore, the most mafic subgroup III samples can only be equated with more fractionated subgroup III samples by including calcic clinopyroxene and a highly calcic plagioclase in the formulation. Neither of these phases appear as phenocrysts in the studied samples.

5.7 THE ROLE OF CRUSTAL CONTAMINATION

The role of crustal contamination in modifying the compositions of the high-Mg tholeiites is an important problem to address in view of their enriched incompatible element nature, which up to now has been considered a mantle characteristic. Contamination processes may take several forms such as assimilation of crustal blocks by a fractionating magma chamber, the movement of anatectic (minimum) melts into the mafic liquid, or the selective transfer of elements into the magma by a fluid phase whose composition is buffered by the mineralogy of the country rock.

The identification of crustal involvement as opposed to mantle heterogeneity in controlling trace element variation is often a very difficult process (Thompson et al., 1983) and is usually based on detailed isotopic studies. Thirlwall & Jones (1983) studied Pb-Sr-Nd isotopic systems in conjunction with major and trace elements to document the effect of crustal contamination in the Skye lavas. In this province, crustal contamination was extensive enough to convert mildly Ne-normative basalts to Hyp-normative compositions, but despite the detailed study, the process involved could not be identified and apparently included the three types listed above and as well as open-system crystal fractionation (O'Hara & Mathews, 1981). Even when isotopic studies are used to evaluate crustal contamination the interpretation may be equivocal. Kyle (1980) studied the extensive Jurassic Ferrar dolerites of the Trans Antarctic Mts and Tasmania which have a very high initial Sr isotopic ratio of 0.7089-0.7153, which would seem to be conclusive evidence for crustal contamination. However, Kyle considered the degree of contamination required to attain the high Sr values over the extensive area involved to be prohibitive, and instead favoured an unusual mantle composition. In contrast, Hoefs et al. (1980) also studied the Ferrar dolerites and considered the systematic variation in isotopic characteristics with major element chemistry as indicative of extensive crustal contamination, but could not identify the process responsible.

Sheraton & Black (1981) and Collerson & Sheraton (in press) have considered the role of crustal contamination in the evolution of the high-Mg suites of the Vestfold Hills and Enderby Land. These authors considered the low initial Sr of these suites (0.7019 $\pm$ 0.0011, 0.7020 $\pm$ 0.0008 respectively) as evidence that extensive incorporation of old crust was an unimportant process. Furthermore, nearly identical trace element ratios and enrichments are observed in the Enderby Land suites as in

subgroups II and III (compare Sheraton and Black (1981) Fig. 5 with Fig. 5.2 of this thesis) which, based on the arguments of Kyle (1980), are unlikely to be the result of large scale crustal contamination over such a large distance (Fig. I1.1) and is in greater accord with an enriched mantle.

A further observation which limits the extent of possible crustal contamination in the high-Mg dykes is the very regular and tight clustering of normalized elemental abundances displayed in Figs 5.1 and 5.2 with differentiation. Incorporation of assimilated crustal blocks into a magma consumes energy (heat) thus cooling and crystallizing the liquid. Therefore, more evolved compositions should be the most contaminated, a feature observed in the Skye basalts (Thirlwall & Jones, 1983) but absent in the high-Mg suites. Highly contaminated Mg-rich liquid compositions do occur in the Deccan and Karoo flood basalt provinces (Cox & Thompson, 1983), but these liquids have traversed thick continental crust and probably experienced contamination through a 'wallrock erosion' process (Huppert & Sparks, in press). The deep crustal emplacement of the high Mg suite suggests this process is unlikely to be a significant factor in the chemical evolution of the Vestfold Hills high Mg suite.

The observations outlined above are considered good evidence for the absence of large scale crustal assimilation as an important process in the evolution of the high-Mg suites in the Vestfold Hills and Enderby Land. However, identification of more subtle but none-the-less important styles of elemental enrichment such as selective contamination or open system crystal fractionation is beyond the scope of this study and requires an independent focus of its own. Even by applying various isotopic systems these processes, if operative, may not be identifiable (Thirlwall & Jones, 1983; Hoefs et al., 1980).

5.8 SUMMARY AND DISCUSSION OF SUBGROUP CHARACTERISTICS

The distinctive CaO concentration in the magnesian orthopyroxenes of each subgroup shows that the different "activities" of the diopside molecule, i.e. different major element compositions, were intrinsic to the parental liquids of each subgroup. This is further exemplified by the cognate pyroxenite nodule collected from a subgroup III dyke, which requires the low Di/Di+Hyp ratio of this subgroup to be a feature of an Mg_{75} liquid. Considering only these phenocryst characteristics, derivation of the primary liquids to each subgroup by removing batches of magma from a single source undergoing increasing degrees of partial melting could account for the variation in phenocryst compositions as well as the close chemical and physical relationship of the dykes. In this scenario, the first formed liquids derived from a more fertile mantle, would have the highest Di/Di+Hyp ratio, resulting in the most calcic liquidus orthopyroxene phenocrysts (subgroup I). As the clinopyroxene/orthopyroxene ratio of the residue decreases with increasing partial melting, extracted liquids will become progressively more refractory, culminating in the low Di/Di+Hyp subgroup III.

Additional evidence for this process includes higher Cr and Ni content of subgroup II samples than subgroup I at similar MgO contents, and the progressive depletion of Ti relative to Ca and Al from subgroups I to III. This proposed sequence of liquid extraction would also conform with the relative ages of the subgroups inferred from dyke widths (Section 5.4).

However, successive extraction of liquids from a single source is inconsistent with many other geochemical features of the subgroups. The chondritic CaO/Al_2O_3 ratios of subgroup I and the olivine-bearing samples of subgroup II rule out their derivation from a source retaining significant quantities of clinopyroxene if it is assumed that the source initially had a chondritic CaO/Al_2O_3 ratio. This chondritic ratio also precludes models which would rely on high pressure clinopyroxene fractionation to reduce the CaO content of a subgroup I partial melt in order to derive the intermediate CaO subgroup II. The high level of incompatible element enrichment (including LREE) found in each subgroup also excludes the development of liquids with varying Di/Di+Hyp ratios by an incremental batch melting process, as the progressive extraction of liquids should also result in continuing depletion of incompatible elements. More realistic melting models such as sequential (Arndt, 1977; Nesbitt et al., 1979) and dynamic melting (Langmuir et al., 1977) also fail

to account for the enriched incompatible trace element concentrations with the relative reductions in CaO.

The consistency of incompatible trace element ratios between the olivine-bearing and olivine-free subgroup II samples implies that they were derived from a common parental liquid. This is in agreement with the CaO contents of the orthopyroxene phenocrysts in these samples. The similarity in trace element ratios and patterns (including REE) of subgroup III compared to subgroup II samples also seem to require the same conclusion. However in this case the CaO contents of the orthopyroxene phenocrysts are distinctive, in addition to which subgroup III samples, while having a lower Fe/Mg than subgroup II have a higher enrichment of incompatible elements (compare Figs 5.2 and 5.16).

In Fig. 5.24 the high-Mg dyke compositions ($Fe_2O_3/FeO = 0.10$) are projected from Di onto the plane (Jd+CaTs)-Ol-Qtz of the basalt tetrahedron following Green (1970). A 7-8 kbar olivine-orthopyroxene cotectic is indicated based on the experimental study of 060 (Section 1.3.1, see also Section 2.2.1) and is shown to intersect a clinopyroxene phase volume dictated by the occurrence of clinopyroxene phenocrysts in the fractionated sample 069, which is also in agreement with the data of Duncan & Green (submitted).

The projected positions of subgroup II samples are consistent with this orientation of cotectic boundaries: the olivine-bearing samples plot along the 7-8 kbar olivine-orthopyroxene cotectic and the differentiated samples which can be modelled by olivine+orthopyroxene+clinopyroxene fractionation from the olivine-bearing samples, plot along the inferred orthopyroxene-clinopyroxene cotectic. Similarly, subgroup III samples trend parallel to the orthopyroxene-clinopyroxene cotectic.

As discussed previously, neither subgroup II nor subgroup III samples have clinopyroxene phenocrysts, suggesting that the trends may be the result of an interval of higher pressure fractional crystallization of clinopyroxene. This hypothesis has been invoked by Bence et al. (1979) to explain clinopyroxene-free MORBs that display clinopyroxene controlled major element variations. However primitive MORBs have much higher Di/Di+Hyp ratios than any sample in the high-Mg suite. For example, DSDP-3-18 ($Mg_{69.5}$, studied experimentally by Green et al., 1979) has a Di/Di+Hyp ratio of 0.70 compared with 0.39 and 0.26 for samples 054A and 214 respectively. This, and similar MORBs are able to precipitate near-liquidus calcic clinopyroxene with olivine at pressures $\geq$10 kbar.

Neither subgroup I sample 060 (Section 1.3.1) nor the inferred parental liquid to the Troodos upper pillow lavas studied by Duncan and

Green (submitted, Di/Di+Hyp = 0.31, Mg_{77}) have near-liquidus calcic clinopyroxene at any studied pressure (0-12 kbar). Within the experimentally studied pressure range, the first clinopyroxene to precipitate in both compositions is a pigeonite, even at pressures greater than liquidus olivine saturation. Calcic clinopyroxene saturation is not reached in the Troodos liquid until more than 100°C below the 10 kbar liquidus. Furthermore, the magnesian subgroup II and III orthopyroxenes are too subcalcic to be in equilibrium with a calcic clinopyroxene at temperatures above ~1100°C (10 kbar, Lindsley, 1983). Thus it is unlikely that high pressure clinopyroxene fractionation can be responsible for the observed trends in Fig. 5.21.

As clinopyroxene fractionation from olivine-bearing compositions has been found not to be a viable mechanism to produce the high quartz normative compositions of subgroup III or the olivine-free subgroup II samples, the possibility arises that these silica-enriched compositions could be derived from a primary liquid produced under hydrous melting conditions. Experimental studies by Green (1976b) and Jenner (1982) have shown that liquids produced from a peridotitic source under conditions of $P_{H2O} = P_{total} \lesssim 15$ kbar may be quartz normative. Applying these results to the subgroup II and III compositions suggests they may have been derived through the fractionation of orthopyroxene from a parental liquid formed through hydrous melting at 10-15 kbar. However, this model also lacks credibility as high pressure quenching of H_2O-rich liquids will produce amphibole-bearing assemblages, which are absent from all high-Mg dykes.

The deficiencies in any simple unifying model that tries to relate the geochemical characteristics of the subgroups as discussed above, becomes apparent when trace elements are included in the arguments. Major and some trace element features are consistent with a one or two source partial melting model with an olivine + orthopyroxene residue, but if it is assumed that the enriched incompatible element nature of the subgroups was also a source characteristic then these types of models breakdown.

Another possibility is that at least some of the incompatible element character was imparted to batches of liquid during transit to the continental crust through a "zone refining" or a "wall rock reaction" process (Harris, 1974; Green & Ringwood, 1967a). Although different in mechanism, both models predict mafic liquids will become enriched to a maximum of 1/D in elements which are incompatible in the wall rock. These will typically be LIL elements and LREE, but decoupling of these elements can be envisaged if the wall rock peridotite contains a small percentage of micas, amphiboles or other accessory phases.

If this open system process is considered to take place within the relatively shallow, high temperature mantle below the Moho, then a zone of plagioclase peridotite may exist. Since Sr is a compatible trace element in plagioclase it will be "withheld" from entering the magma, compared to Ce and Nd, possibly explaining the "$(Sr)_N$ depletion" in subgroups II and III. Clearly no simple mechanism can explain all of the features of the high-Mg dykes, and a combination of more complex models is required.

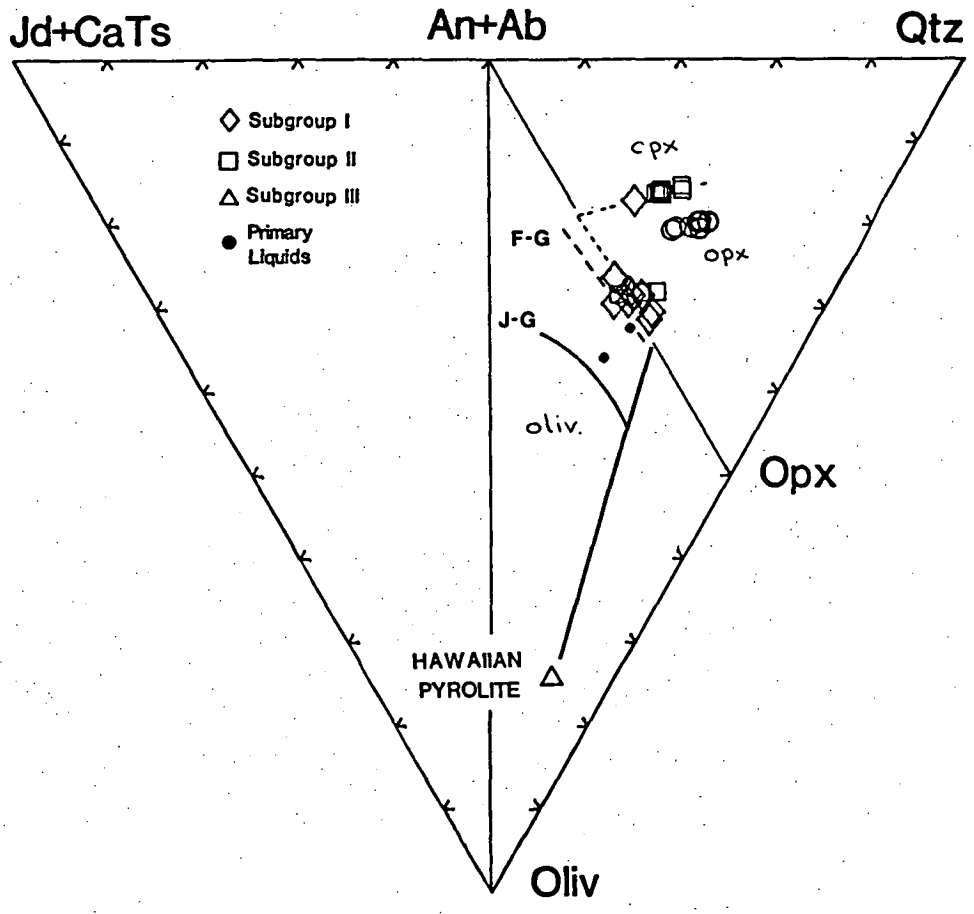

Figure 5.24

Compositions of the high-Mg dykes projected from Diop onto the plane (Jd+CaTs)-Oliv-Qtz following Green (1970) ($Fe_2O_3/FeO = 0.10$). Short dashed line is 7-8 kbar oliv $\pm$ opx $\mp$ cpx cotectics defined by experimental studies documented in Section 1.3.1, Chapter 2, and inferred from crystal fractionation relations in Section 5.6. Solid curve is Jaques & Green (1980) 10 kbar oliv-opx cotectic, long dashed line is Falloon & Green (in prep.) 10 kbar oliv-opx cotectic, both for Hawaiian pyrolite compositions. Solid dots represent endmember Mg_{75} parental liquid compositions to the high-Mg suite calculated by adding olivine or orthopyroxene to sample 054A (see text).

5.9 ESTIMATION OF THE DEPTH OF MELTING

One of the basic tenets to understanding the origin of basaltic liquids is the effect of pressure on the relative stabilities of olivine and orthopyroxene under mantle conditions. Kushiro (1965, 1968) demonstrated that decreasing pressure expands the stability field of olivine relative to orthopyroxene, such that liquids derived from low pressure melting of peridotite will be more silica-saturated than liquids derived at higher pressures (anhydrous). Assuming a modest Fe^{3+}/Fe^{2+} ratio of 0.10, the most undersaturated high-Mg tholeiite composition contains only 3.3% normative olivine (sample 054A, Mg_{71}) indicating the parental liquid to this suite must have been derived by melting at relatively low pressures. Quantitatively, the minimum pressure such a primary melt could be generated is ~8 kbar - the load pressure at the time of dyke emplacement in the lower crust (Sections 1.3.1 and 5.3). The following discussion attempts to restrict the upper boundary to the depth of magma segregation from residual peridotite.

The olivine-bearing samples 054A (subgroup I) and 214 (subgroup II) have Mg values, Ni and Cr contents consistent with their being unmodified melts from a mantle peridotite (Appendix 2). However these liquid compositions are saturated in olivine and orthopyroxene at 7-8 kbar, an unrealistic pressure for their genesis, implying they have evolved from more mafic liquids. The only evidence presently recognized for more primitive liquids in this suite is the Mg_{91} orthopyroxenes in the pyroxenite nodule (Section 5.2.4) which requires the existence of a ~Mg_{75} liquid ($K_D^{Fe/Mg}{}_{opx/liq}$ = 0.30, Jaques & Green, 1979). The most primitive subgroup III sample (the suite to which the pyroxenite nodule is cognate) is considerably evolved compared to a primitive liquid composition. Thus in order to reconstruct a possible primary liquid composition the olivine + orthopyroxene phyric sample 054A (Mg_{71}, Fe^{3+}/Fe^{2+} = 0.10) was used as a starting point because it is saturated in the phases thought to be residual to the melting process and has only experienced minor fractionation from the estimated Mg_{75} parental liquid composition. Because the proportions of olivine + orthopyroxene theoretically fractionated to derive 054A from a primary liquid are not known, endmember compositions were estimated by adding increments of equilibrium olivine or orthopyroxene (assuming 2% Al_2O_3, 2.5% CaO) to 054A. The resulting compositions are listed in Table 5.10 and plotted in Fig. 5.24.

The pressure at which the calculated liquid compositions could be derived from a primitive mantle peridotite leaving an olivine + orthopyroxene residue can be estimated by comparing these compositions with the peridotite melting experiments of Jaques & Green (1980, hereafter J-G) and the preliminary reversal data of the Jaques & Green results presently being studied by Falloon & Green (F-G).

The results of the study by J-G erroneously predicts olivine + orthopyroxene saturation for sample 060 and the parental composition of the Troodos Upper Pillow Lavas at 5 kbar, compared to the experimental determinations of co-saturation at 7-8 kbar for both compositions (Sections 1.3.1 and 2.1.1; also Duncan & Green, submitted). Furthermore the preliminary work of F-G has shown that the J-G 10 kbar oliv-opx cotectic is also too olivine normative, and presently places the 10 kbar oliv-opx cotectic slightly to the olivine normative side of the Plag-Hyp join (Fig. 5.24). The range of calculated Mg_{75} primitive liquids falls within these 10 kbar cotectic boundaries defined by J-G and F-G, with the more undersaturated "olivine-addition" compositions plotting near the estimated 15 kbar of F-G.

Liquid compositions, saturated in olivine + orthopyroxene, from two 10 kbar reversal experiments (1400°C and 1380°C; supplied by T. Falloon) are compared in Table 5.10 with the estimated parental liquid compositions of the high-Mg suite. Very good agreement exists between these compositions in all elements except TiO_2, CaO and FeO. The much higher TiO_2 and marginally enriched CaO in the glass compositions is probably due entirely to the very fertile Hawaiian pyrolite used in the experiments of F-G compared to the chondritic source demonstrated for the high-Mg suite. The higher FeO in the calculated composition could be due to several reasons, such as differences in pressure and temperature of melt generation, or simply that the source of the high-Mg suite was Fe-rich compared to the Hawaiian pyrolite. With regards to pressure and temperature, the liquid compositions reported by J-G display very little variation in absolute FeO contents over a wide range of temperatures at pressures $\gtrsim$5 kbar, while other oxides vary markedly. As there is in general a very good correspondence between the glass analyses and theoretical liquid composition in oxides other than FeO, it is considered that significant variations in P or T are unlikely to be responsible for the observed difference in concentration. Because of this observation, the high estimated FeO is believed to indicate the source for the high-Mg parental liquid had a greater absolute concentration of FeO (and lower MgO) than Hawaiian pyrolite ($Mg_{88.7}$). Similar inferences concerning the

absolute Fe content of the Archean mantle have been made by Glikson (1983) and Arndt et al. (1977).

It is concluded from the very close correspondence between the analyses presented in Table 5.10 that the parental liquid(s) to the high-Mg suite was derived by melting a primitive and comparatively Fe-rich peridotite at ~10 kbar, leaving an olivine + orthopyroxene residue. Assuming a chondritic source as suggested by the HREE pattern of 054A (Fig. 5.20), the degree of melting can also be estimated by following the method outlined in Section 5.5.5. Assuming a source with 2.2x chondrite (Ringwood, 1979) the degree of melting required to obtain 1.46-1.50 ppm Yb in the hypothetical primary liquid is ~31%.

The most important aspect of the estimated depth of melting is that is places an upper limit on the thickness of the crust (~35 km) in both Enderby Land and the Vestfold Hills at ca.2400 Ma. Considering the present exposure level in the Vestfold Hills records depths of 25-28 km and is presently underlain by ~30 km of crust (Kadmina et al., 1983), significant amounts of crustal addition via an underplating process have taken place since the melting event which formed the parental liquids to the high-Mg suite. Further aspects of this result have been discussed in Chapter 4.

TABLE 5.10
COMPARISON OF CALCULATED "ENDMEMBER" PRIMITIVE LIQUID COMPOSITIONS WITH EXPERIMENTAL 10 KBAR GLASS ANALYSES*

	054A + 8.7% OLIV	054A + 11.9% OPX	10 KBAR 1400°C FE CAPS.	10 KBAR 1380°C PT CAPS.
SIO2	51.67	53.04	52.29	51.44
TIO2	0.53	0.51	2.11	2.12
AL2O3	10.21	10.16	10.22	10.53
FE2O3	1.16	1.12	0.96	1.06
FEO	9.43	9.03	7.78	8.58
MNO	0.17	0.16	-	-
MGO	16.09	15.20	15.91	14.16
CAO	8.54	8.58	9.00	9.13
NA2O	1.72	1.67	1.43	1.75
K2O	0.47	0.46	0.41	0.37
P2O5	0.07	0.07	-	-
MG#	75.3	75.0	78.5	74.6

* GLASS ANALYSES FROM FALLOON & GREEN, IN PREP.

MG# = 100 MG/(MG+FE^{2+})

CHAPTER 5

GENESIS OF THE CA.2420 Ma DYKE SUITES

B. THE Fe-THOLEIITES

CHAPTER 5

GENESIS OF THE CA.2420 Ma DYKE SUITES

B. THE Fe-THOLEIITES

INTRODUCTION

The Fe-rich tholeiites described in this part of Chapter 5 have not been recognized by previous workers. The dykes comprising this suite were distinguished in the field during this study by distinctive small, rust-stained pits on otherwise greenish tinted weathering surfaces. On broken surfaces, a granular "salt and pepper" character due to the abundance of small Fe-oxides is common. The dykes also have a strong E-W component in their strike, thus differing from the broadly N-S orientation of the ca.1360 Ma dykes. Three of the sixteen dykes included in this suite (see also Fig. I2.1), lack the rust-stained pits on the weathering surface and have a steel blue-grey colour in outcrop. This dyke group is typified by ~0.5 cm scale plagioclase "megacrysts" (henceforth referred to as PM dykes). These three, and several greenish coloured dykes do not have the near-vertical dips typical of all other Vestfold Hills dykes, but display a moderate 60-70^{o} dip to the north or south.

The Fe-rich dykes have not been dated isotopically but their crosscutting inter-relationship with the dated high-Mg tholeiite dykes logically implies their emplacement at ca.2420 Ma (Collerson & Sheraton, in press). Whole-rock major and trace element analyses and CIPW norms of the dykes comprising this suite are listed in Appendix 2 (note: samples 078, 079, 080 are from the same structurally off-set dyke). The dykes are strongly differentiated, with Mg# ranging from 47-35. Silica saturation is variable (7% Oliv-3% Qtz; FeOt) and as anticipated the dykes have relatively low Cr (<200 ppm) and Ni (<100 ppm).

5.10 RELATIVE AGE RELATIONSHIPS BETWEEN THE Fe-RICH THOLEIITE AND HIGH-Mg THOLEIITE DYKE SUITES

It was considered in Part A of this chapter that the dykes of the high-Mg suite were emplaced during discrete events in the order subgroup I followed by II and III. Fig. 5.25 illustrates all the documented crosscutting relationships between dykes of the high-Mg and Fe-rich tholeiite suites with arrows joining samples collected from intersecting dykes and pointing to the younger of the two. The documented intersections illustrate a very complex intrusive relationship between the suites, as dykes which characterize the Fe-rich suite were emplaced both prior to, and following, intrusion of the high-Mg subgroups II and III. The emplacement relationships can be further characterized by considering the FeO/MgO versus TiO_2 relations of Fig. I2.1. The relatively older dykes, emplaced prior to subgroup II, have higher TiO_2 and FeO/MgO (abbreviated as HiTi) than the younger, low TiO_2 dykes, (LoTi) emplaced after subgroup II. The exception to this observation is the differentiated PM dykes which were emplaced following subgroup III. No intersections were recorded to relate the PM dykes with other dykes of the Fe-rich suite, but all are crosscut by ca.1360 Ma dykes. In strict terms, only the HiTi dykes have intersecting relationships which definitely places a ca.2420 Ma age on their emplacement. The PM and LoTi dykes could be considerably younger.

Assuming the simplest interpretation, that each of the dyke divisions illustrated in Fig. 5.25 was emplaced as a discrete event, then the dyke intersections are evidence for a cyclic process involving the production of primitive Mg-rich liquids followed by the emplacement of strongly fractionated Fe-rich dykes. The most obvious hypothesis to account for this relationship is a crystal fractionation mechanism, deriving the Fe-rich dykes from individual high-Mg subgroups. If the Mg- and Fe-rich suites are not related to one another, then multiple sources and independently fractionating magma chambers supplying Fe-rich and Mg-rich liquids to the lower crust are required. Other increasingly complex scenarios can be envisaged from the dyke intersections. None of these can be excluded as an explanation for the field observations until the intra-suite relationships of the Fe-rich dykes are considered.

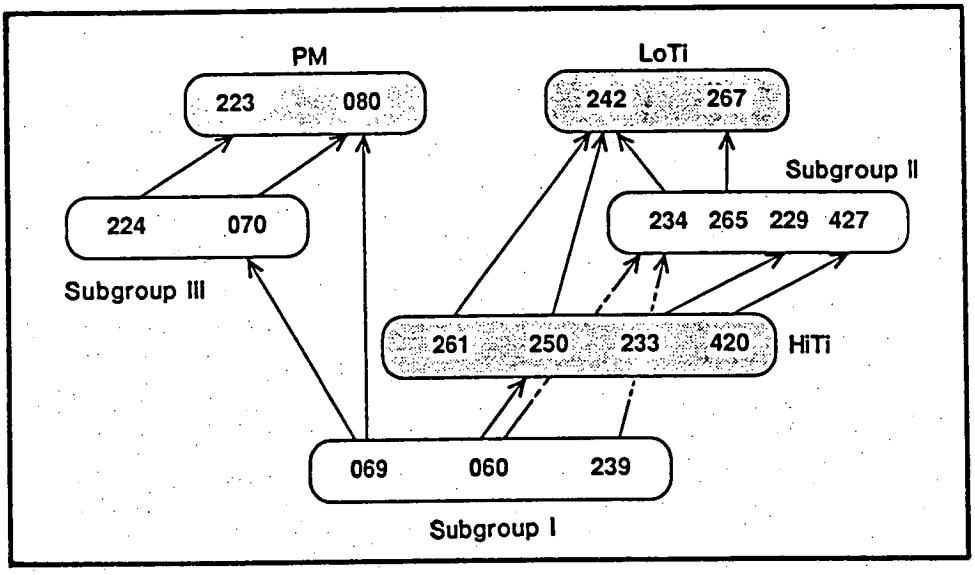

Figure 5.25
Field determined intersecting relationships between dykes of the ca.2420 Ma Fe-tholeiite (shaded) and high-Mg suites. Arrows connect sample numbers of cross-cutting dykes and point to the younger.

5.11 PETROGRAPHY AND CRYSTAL CHEMISTRY OF Fe-RICH THOLEIITES

Dyke intersections, used in conjunction with $FeO/MgO-TiO_2$ relationships, suggest that the emplacement of the dykes comprising the Fe-rich suite took place in two, and possibly three events. Dykes which characterize the LoTi and HiTi groups also have petrographically dissimilar phenocryst assemblages. Furthermore, the PM dykes are also petrographically distinctive. All studied samples of the Fe-rich suite display varying degrees of subsolidus hydration resulting in the development of secondary green amphibole + Fe-Ti oxides, through reaction between plagioclase and pyroxene, which is responsible for the greenish tint to the dyke colour in outcrop. The PM dykes have experienced the least amount of hydration.

HiTi dykes are petrographically indistinguishable from the much younger Group I Amundsen Dykes of Enderby Land (Sheraton & Black, 1981; see Fig. 2.6 of this thesis). Chilled margin samples of the HiTi dykes are composed of individual and intergrown orthopyroxene-clinopyroxene-plagioclase phenocrysts (~1-2 mm in length) in a dark, opaque and amphibole-rich, fine grained groundmass. Clinopyroxene invariably displays multiple twinning and complex intergrowths with other clinopyroxene phenocrysts. Reddish brown orthopyroxene is more commonly found as single crystals but does form aggregates with clinopyroxene and plagioclase and is evidence for co-precipitation of these phases. The orthopyroxenes have very narrow clinopyroxene quench rims and, particularly in sample 233, may display hour glass zoning patterns. Olivine does not occur in the HiTi samples, although very rare highly altered and irregularly shaped pale red inclusions can be found in orthopyroxene phenocrysts which may be evidence for an earlier precipitation of olivine and subsequent fractionation/resorption. The three most Fe-rich compositions (Fig. I2.1) were collected from the southwest corner of the Vestfold Hills and have been recrystallized to a garnet-bearing assemblage (Chapter 3). Opaque-filled relict orthopyroxene phenocrysts are preserved in these samples.

Selected analyses from the only extensively analysed sample, 244, are listed in Table 5.11 and plotted in Fig. 5.26. Plagioclase phenocrysts are ~An_{64}, with one large, optically zoned grain having a broad compositionally homogeneous ~An_{80} core with a narrow rim similar in chemistry to the plagioclase phenocrysts. An unusual feature of the orthopyroxene phenocrysts is their high calculated Fe^{3+} (up to 3.5%; based on 4.000 cations). Similarly, high Fe^{3+} is indicated in the Na-free clinopyroxene suggesting Fe^{3+} is coupled in a (Fe,Mg)-Tschermaks molecule. Subsolidus

secondary alteration resulting in high Fe^{3+} would be expected to readjust the CaO content of the pyroxenes to subsolidus equilibrium values, but this has not taken place, nor were exsolutions of Fe-Ti oxides observed during microprobe study of this sample, both suggesting that the high Fe^{3+} in the orthopyroxenes is a magmatic feature.

Liquidus temperatures were estimated using averaged Fe^{3+} and Fe^{T} based data from the coexisting orthopyroxene and clinopyroxene phenocrysts; the data and results are listed in Table 5.12. As in previous temperature determinations (see the discussions in Section 1.1.3), the Wells (1977), Kretz (solvus and exchange reactions; 1982) and the Lindsley (1983) graphical thermometer were applied.

Excellent agreement exists between the Wells, Lindsley (opx and cpx limbs) and Kretz (solvus) temperatures giving an average of ~1200°C. There is a negligible difference between temperatures calculated using Fe^{3+} or Fe^{T}. Temperatures calculated using the Kretz exchange reaction give similar results for Fe^{3+} and Fe^{T} determinations, but these temperatures are more than 300°C above the temperatures calculated using the other thermometers, and are clearly in error. Similar conclusions were reached in previous discussions of the Kretz exchange thermometer (Section 1.1.3). The preferred two-pyroxene temperatures of ~1200°C derived from the phenocryst assemblage of sample 244 is in very good agreement with the 1180°C, 8 kbar liquidus temperature (and phase assemblage) of the compositionally similar sample 206 studied experimentally in Section 1.3.2 of this thesis (see Fig. 1.13).

The LoTi dykes are olivine + clinopyroxene + plagioclase phyric, and lack orthopyroxene phenocrysts. The studied samples have a subophitic to moderately porphyritic texture. In the latter case, although single phenocrysts are common, equidimensional to slightly elongate clinopyroxenes do form radial glomerocrysts with plagioclase laths. Olivine is rare in all samples, and highly altered. Its irregular form and inclusion in pyroxene clots suggest olivine was in reaction with the liquid prior to quenching. The groundmass is composed of a mosaic of green amphibole enclosing plagioclase laths and Fe-oxides. One sample, 415, is recrystallized to a garnet-bearing assemblage (see Chapter 2).

Compositions of LoTi phenocrysts are plotted on Fig. 5.26, and listed in Table 5.11. The analyses of two small, relict olivines are Fe-rich (Mg_{65-67}) and cannot be in equilibrium with the 207 bulk rock composition ($Mg_{47.1}$; equilibrium olivine is Mg_{73}), and are probably "rim" compositions which crystallized from a differentiated, subliquidus composition. Compared to HiTi, LoTi clinopyroxenes are in general slightly more

magnesian and tend to be enriched in Al_2O_3. The calculated Fe^{3+} is more variable in the LoTi clinopyroxenes than in the HiTi analyses, though the LoTi analyses are also Na-free. Plagioclase phenocryst compositions are essentially identical between the two groups (An_{60-68}).

The PM dyke samples are mineralogically unique among the Fe-rich dyke suite in having phenocrysts of magnesian pigeonite (Mg_{72-74}). The pigeonite comprises < modal 5% of the samples examined and form euhedral, tabular single crystals or stellate clots with plagioclase phenocrysts. Plagioclase "megacrysts" are euhedral and simply twinned with complex optical zoning. Although the megacrysts are much larger than the matrix crystals they rarely exceed ~3 mm in length in the studied samples, and display some gradation in size to the plagioclase phenocrysts of the matrix (<1 mm). Very rare, mostly resorbed crystals of olivine can be found, but are usually completely altered.

Analyses of the PM phenocryst phases are also plotted on Fig. 5.26, and listed in Table 5.11. The most calcic plagioclase megacryst analysis is similar to the core composition of the large plagioclase crystal in the HiTi sample 244 (~An_{80}), but zoning in the PM megacryst is to more Na-rich compositions. Plagioclase phenocryst compositions are very similar between all three divisions of the Fe-rich suite. The magnesian pigeonite phenocrysts have narrow rims of Al_2O_3-rich Ca-clinopyroxene only marginally less calcic than the calcic clinopyroxene phenocrysts of the HiTi and LoTi dykes. Pyroxene analyses from the PM dykes also have 1-3% calculated Fe^{3+}.

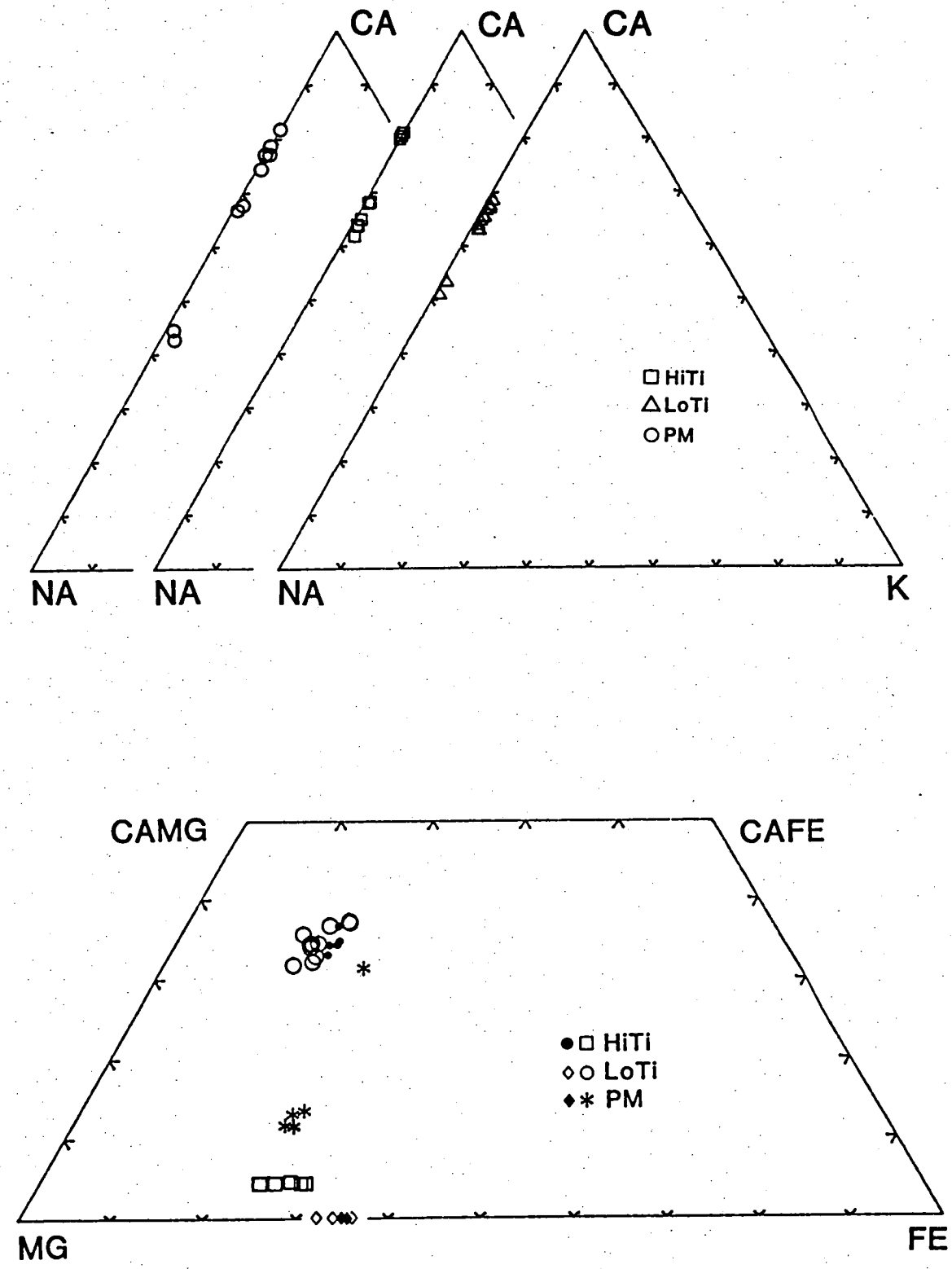

Figure 5.26
Comparison of plagioclase (upper Ca-Na-K diagram) and pyroxene phenocryst compositions between Fe-tholeiite groups. Olivine is also plotted in the lower quadrilateral.

TABLE 5.11
MINERAL ANALYSES[1] FROM ca.2420 Ma FE-RICH THOLEIITES.

PHASE	OPX	OPX	CPX**	CPX	PLAG	PLAG	OLIV	OLIV	PLAG
SUBGROUP	HITI	HITI	HITI	HITI	HITI	HITI	LOTI	LOTI	LOTI
SAMPLE	244	244	244	244	244	244	207	207	207
SIO2	53.38	51.43	51.68	51.74	49.03	52.17	36.4	36.44	52.42
TIO2			0.32	0.29					
AL2O3	1.32	2.07	2.44	2.44	32.46	30.23			29.77
FE2O3*	2.15	3.58	1.32	1.19					
FEO	15.31	17.72	10.55	10.82	0.57	0.74	30.44	29.23	0.62
MNO		0.22					0.23	0.33	
MGO	25.63	22.91	17.38	16.67			32.50	34.00	0.17
CAO	2.21	2.12	16.06	16.86	15.89	13.35	0.42		13.30
NA2O					2.05	3.40			3.51
K2O						0.12			0.20
SI	1.9422	1.9057	1.9156	1.9218	2.2422	2.3704	0.9883	0.9829	2.3823
TI			0.0089	0.0081					
AL	0.0566	0.0902	0.1067	0.1068	1.7495	1.6187			1.5945
FE3+	0.0589	0.0984	0.0368	0.0333					
FE2+	0.4658	0.5491	0.3269	0.3360	0.0217	0.0281	0.6909	0.6595	0.0237
MN		0.0069					0.0052	0.0075	
MG	1.3901	1.2655	0.9599	0.9231			1.3149	1.3672	0.0118
CA	0.0863	0.0842	0.6377	0.6709	0.7785	0.6499	0.0123		0.6475
NA					0.1819	0.2994			0.3094
K						0.0068			0.0116
TOTAL					4.9739##	4.9733	3.0117	3.0171	4.9808
MG#	74.7	69.7	74.6	73.3			65.5	67.5	
CA#	4.4	4.4	33.1	34.8	81.1	68.0			66.9
a_{en}	0.4830	0.3969	0.1864	0.1644					

PHASE	PLAG	CPX	CPX	OLIV	PIG	PIG	PLAG	PLAG	PLAG
SUBGROUP	LOTI	LOTI	LOTI	PM	PM	PM	PM	PM	PM
SAMPLE	207	207	207	080	080	080	079	079	080
SIO2	53.19	51.58	51.40	35.98	53.13	52.93	48.62	49.11	52.25
TIO2		0.36	0.37		0.32	0.18			
AL2O3	29.55	3.25	3.83		1.34	1.40	32.60	32.27	29.98
FE2O3*		1.28	0.27		0.97	1.55			
FEO	0.40	8.10	12.21	31.18	15.23	14.59	0.45	0.42	0.39
MNO				0.36	0.31	0.27			
MGO		17.83	17.35		22.96	22.62			0.31
CAO	12.64	17.26	14.56	0.16	5.74	6.46	16.32	15.83	13.36
NA2O	3.96						2.01	2.37	3.58
K2O	0.25								0.13
SI	2.4108	1.8972	1.9023	0.9812	1.9488	1.9435	2.2268	2.2466	2.3728
TI		0.0098	0.0103		0.0087	0.0049			
AL	1.5787	0.1407	0.1670		0.0581	0.0604	1.7593	1.7399	1.6048
FE3+		0.0354	0.0077		0.0267	0.0429			
FE2+	0.0152	0.2493	0.3780	0.7109	0.4670	0.4478	0.0172	0.0161	0.0147
MN				0.0084	0.0096	0.0085			
MG		0.9776	0.9572	1.3137	1.2554	1.2381			0.0211
CA	0.6139	0.6802	0.5775	0.0046	0.2255	0.2540	0.8007	0.7758	0.6501
NA	0.3476						0.1786	0.2098	0.3150
K	0.0147								0.0074
TOTAL	4.9809			3.0188			4.9827	4.9882	4.9859
MG#		79.7	71.7	64.9	72.9	73.4			
CA#	62.9	35.7	30.2		11.6	13.1	81.8	78.7	66.8
a_{en}									

MG# = 100MG/(MG+FE). CA# = 100CA/(CA+MG+FE) OR 100CA/(CA+NA+K).
NOTE, LOW TOTALS DUE TO SLIGHT ERROR IN SIO2 CALIBRATION AND DOES NOT AFFECT CA# (SEE SECTION 1.3.2).
* CALCULATED ON 4.000 CATIONS.
** INCLUDES 0.25% CR2O3 AND 0.0074 ATOMS CR.
a_{en} CALCULATED AFTER WOOD & BANNO (1973).

1 All elements listed were analysed for in end phase, blanks indicate concentration was below the detection limit.

TABLE 5.12
TEMPERATURE ESTIMATES ON THE PHENOCRYST ASSEMBLAGE OF 244 (HITI)

	a_{en}^{cpx}	a_{en}^{opx}	X_{Mg}^{opx}	X_{Mg}^{cpx}	X_{Ca}^{cpx}
FE3+	0.1655	0.4316	0.715	0.736	0.334
	0.1864	0.4255	0.703	0.746	0.331
	0.1441	0.4830	0.749	0.740	0.367
	0.1753	0.4516	0.732	0.747	0.343
	0.1644	0.3969	0.697	0.733	0.348
AV.	0.1672	0.4377	0.719	0.740	0.345
FE^T	0.1579	0.4151	0.688	0.710	0.336
	0.1804	0.4149	0.686	0.725	0.325
	0.1692	0.4679	0.726	0.725	0.358
	0.1589	0 4331	0.703	0.714	0.337
	0.1440	0.3771	0.662	0.717	0.342
AV.	0.1621	0.4216	0.693	0.718	0.340

	FE^{3+}	FE^T
WELLS	1194°C	1178°C
KRETZ (SOLV)	1206	1203
(EXCH)	1575	1534
LINDSLEY (CPX LIMB)	1150-1200	-
(OPX LIMB)	1200	-

a_{en} CALCULATED FOLLOWING WOOD & BANNO (1973)

X_{Mg} = MG/(MG+FE). X_{Ca} = CA/(CA+MG+FE).

5.12 WHOLE-ROCK GEOCHEMISTRY

5.12.1 MAJOR ELEMENTS

In order to investigate the possibility that "low pressure"* crystal fractionation was responsible for the chemical diversity found within the dykes of the Fe-rich suite, chemical variations were evaluated by using Pearce molecular norm diagrams (Pearce, 1968).

In this method, the mole proportions of major element oxides are normalized to a parameter not involved in the differentiation process. Unlike Harker diagrams, the oxides on the axes of a Pearce diagram are not a subset of an analysis which totals 100%, but instead the normalized molar ratios vary independently of one another, and reflect only the processes acting upon them. For example, on a Harker diagram of MgO versus SiO_2, MgO will increase through a fractionation sequence involving only plagioclase because the analyses are recast to 100%. In a Pearce diagram of molar MgO/TiO_2 versus molar SiO_2/TiO_2, MgO/TiO_2 will remain constant (slope = 0) because MgO (and TiO_2) are not removed by plagioclase fractionation, while SiO_2/TiO_2 will decrease. When a MgO-bearing phase is fractionated, the resulting slope on a Pearce diagram will be proportional to the molar composition of the fractionating phase.

Pearce diagrams displaying the chemical variation in the Fe-tholeiite suite are shown in Fig. 5.27. Yttrium was chosen as a normalizing component because garnet is the only common phase capable of fractionating Y to a significant extent from a basaltic melt composition (Pearce & Norry, 1979) and is restricted to pressures $\gtrsim$ 20 kbar. Furthermore, many of the studied samples have experienced subsolidus alteration, and as Y is generally considered immobile during this process (see Clough & Field, 1980), the analysed samples should retain igneous Y abundances. An important point to note when viewing these diagrams is that fractionation of silicates extracts SiO_2, while Y increases, thus molar SiO_2/Y will decrease during fractionation.

A linear, positive sloping trend is shown on the SiO_2/Y-Al_2O_3/Y diagram (Fig. 5.27A) joining samples of each group which is consistent with the groups forming a cogenetic suite. The inset vectors display the trends expected by fractionating the phases indicated, and the trend defined by

---

* Although these dykes were emplaced at 7-8 kbar, the term "low pressure" will be used to designate fractionation at pressures near emplacement conditions.

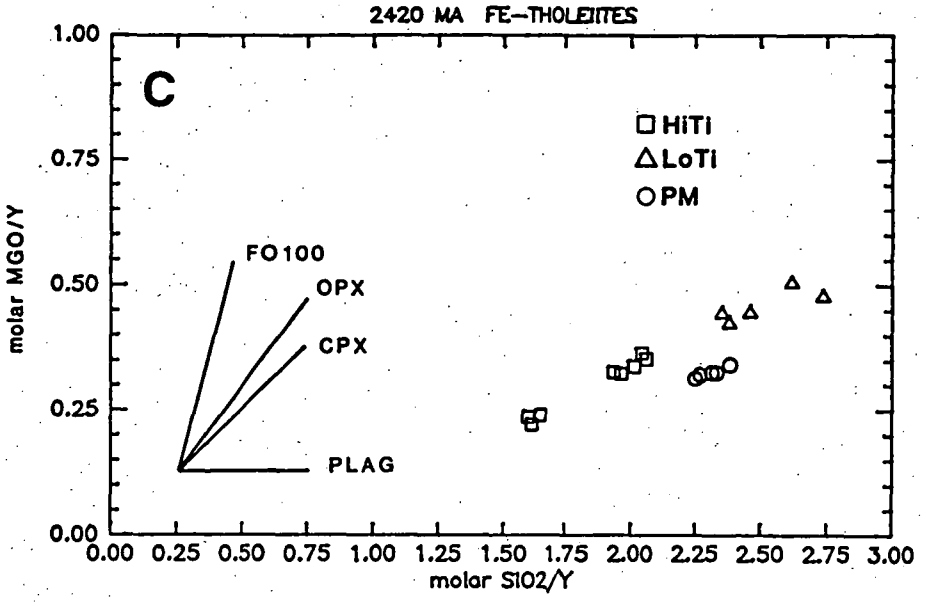
2420 MA FE-THOLEIITES
C
HiTi
LoTi
PM
FO100
OPX
CPX
PLAG
molar MGO/Y
molar SIO2/Y
1.00
0.75
0.50
0.25
0.00
0.00 0.25 0.50 0.75 1.00 1.25 1.50 1.75 2.00 2.25 2.50 2.75 3.00

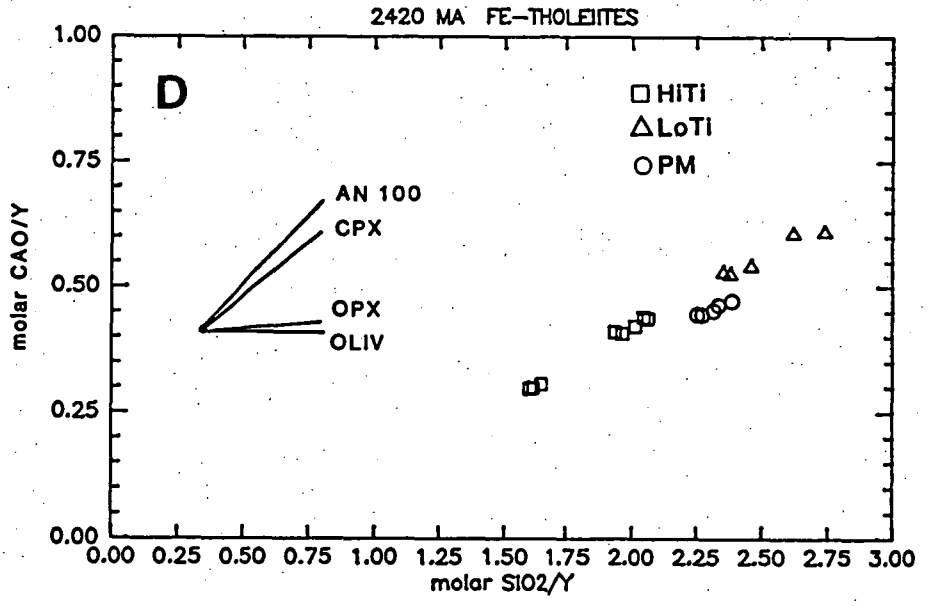
2420 MA FE-THOLEIITES
D
HiTi
LoTi
PM
AN 100
CPX
OPX
OLIV
molar CAO/Y
molar SIO2/Y
1.00
0.75
0.50
0.25
0.00
0.00 0.25 0.50 0.75 1.00 1.25 1.50 1.75 2.00 2.25 2.50 2.75 3.00

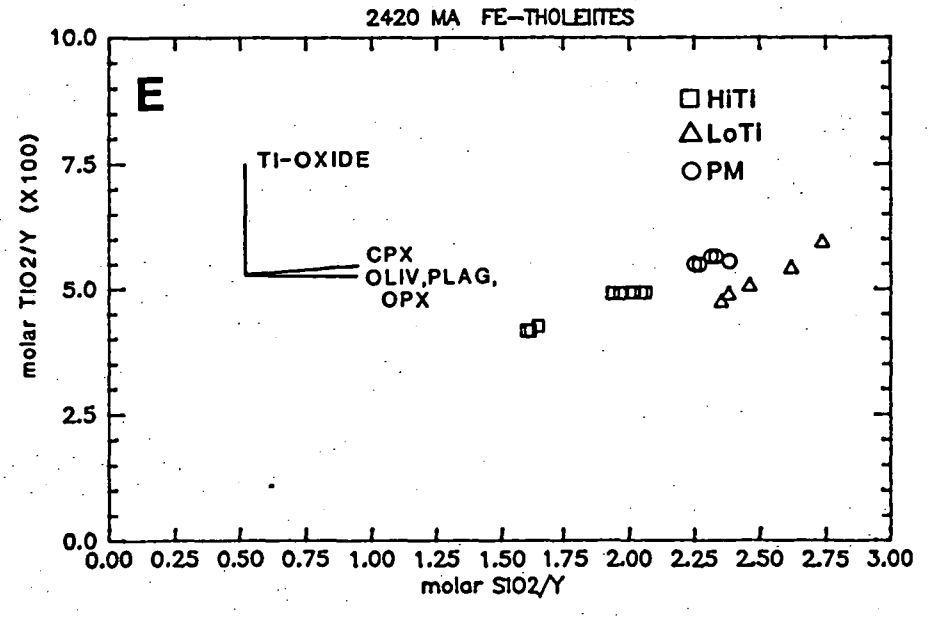
2420 MA FE-THOLEIITES
E
HiTi
LoTi
PM
TI-OXIDE
CPX
OLIV,PLAG,
OPX
molar TIO2/Y (X100)
molar SIO2/Y
10.0
7.5
5.0
2.5
0.0
0.00 0.25 0.50 0.75 1.00 1.25 1.50 1.75 2.00 2.25 2.50 2.75 3.00

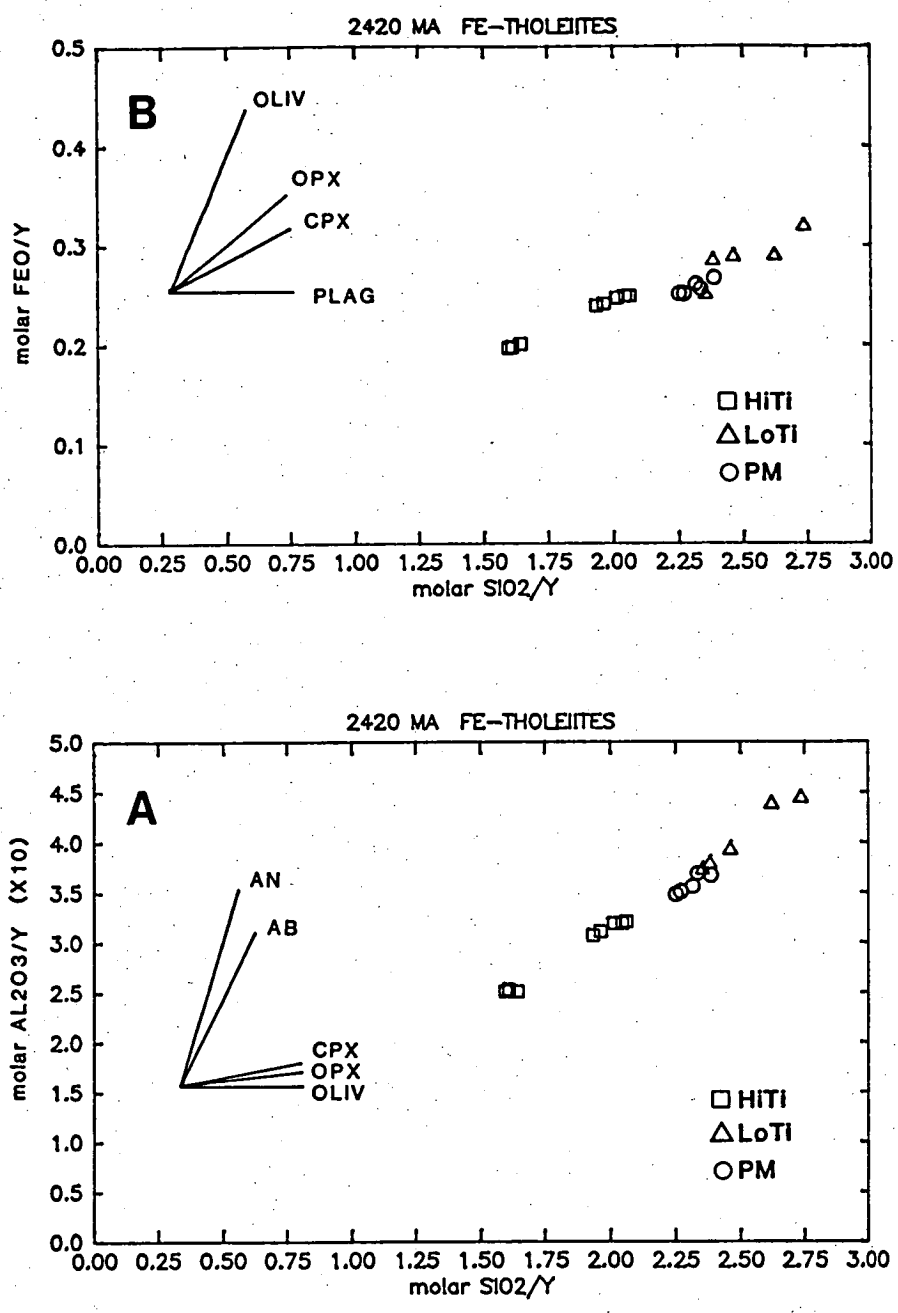

Figure 5.27 A-E

Pearce molecular ratio diagrams (Pearce, 1968) illustrating the major element chemical variation between groups of the Fe-tholeiite suite. Compositions used in vector inserts are: CPX - 35% Wo, 4% Al_2O_3, 0.4% TiO_2, Mg_{80}; OPX - 2% Al_2O_3, Mg_{75}; OLIV - Mg_{75}.

the chemical variation in the samples is consistent with fractionation of a plagioclase + pyroxene ± olivine assemblage. A modest change in slope is apparent between the LoTi and HiTi trends, compatible with orthopyroxene becoming a fractionating phase in the HiTi samples, compared to plagioclase + clinopyroxene ± olivine in the LoTi group. Similar observations and conclusions result from examining the $FeO/Y-SiO_2/Y$ diagram (Fig. 5.27B): the trends are consistent with the chemical variation of the samples being controlled by fractionation of the phenocryst phases as indicated by the vector inset.

However, a significant modification in the interpretation of the genetic relationship of the dykes is required by the trends shown in the diagrams involving MgO and CaO (Fig. 5.27C,D). At a given SiO_2/Y, the PM analyses are depleted in MgO and CaO relative to HiTi and LoTi. This difference cannot be accounted for by the fractionation of any silicate phase from the LoTi suite and implies the PM dykes were derived from a parental liquid separate from that of the LoTi samples. Furthermore, fractionation of the phenocryst phases in the PM dykes cannot produce HiTi compositions. Both the MgO/Y and CaO/Y diagrams are consistent with a low pressure crystal fractionation relationship between the LoTi and HiTi groups involving first clinopyroxene + plagioclase fractionation and joined by orthopyroxene in the HiTi dykes.

In a plot of $TiO_2/Y-SiO_2/Y$ (Fig. 5.27), two distinct slopes are developed in the trends of the analyses implying distinctive fractionating assemblages. The vector inset shows that the fractionation of TiO_2-free phases, such as plagioclase and olivine, will produce a slope of zero on this diagram. Microprobe analyses of clinopyroxene phenocrysts contain up to ~0.4% TiO_2, and a clinopyroxene vector with this concentration is shown. The fractionation of clinopyroxene + plagioclase can adequately explain the subhorizontal trends of the PM and HiTi groups, but the steep slope in the LoTi analyses implies the removal of a Ti-rich phase, in addition to plagioclase + clinopyroxene. Petrographically, the existence of magmatic ilmenite or titanomagnetite in the LoTi samples is equivocal due to extensive subsolidus hydration. If a magmatic Ti-rich phase did precipitate from the LoTi magma, and assuming for this discussion that the HiTi dykes are derived from parental magmas matching the LoTi dykes in chemical composition (Figs I2.1, 5.27A-D), then precipitation of the Ti-rich phase ceased at the onset of orthopyroxene crystallization. This is implied by the intersecting trends in the TiO_2/Y diagram. The TiO_2/Y trends also indicate that the three most fractionated HiTi samples (428, 433, 443; see also Fig. I2.1) apparently cannot be related to the more

"primitive" HiTi samples without the fractionating assemblage containing a Ti-rich phase. Such a phase is not seen in the chilled margin samples of the HiTi group.

The absence of a Ti-rich phase in the phenocryst assemblage of all tholeiitic dykes examined from the Vestfold Hills and Enderby Land makes the implied fractionation of a Ti-rich phase difficult to reconcile. Green & Parson (1986) found that the TiO_2 content of a liquid saturated in a Ti-rich phase was a function of the SiO_2 content of the liquid, as well as P, T and fO_2. Decreasing SiO_2 increases the amount of TiO_2necessary for Ti-rich phase saturation, as does increasing temperature. Increasing pressure, and to a lesser extent fO_2, have the opposite effects.

If the LoTi and HiTi TiO_2/Y trends are the result of ilmenite or titaniferous spinel extraction, then these liquid compositions must fall within the limits of the variables defined by Green & Parson (1986) for Ti-rich phase saturation. At 7.5 kbar, a liquid with 50% SiO_2 and at a relatively low temperature of 1050°C, must contain >3% TiO_2 in order to precipitate a Ti-rich phase. This compares with <2% TiO_2 found in the analysed ca.2420 Ma Fe-tholeiite dykes. At 20 kbar and equivalent T and SiO_2 contents, saturation in a Ti-rich phase is at ~2.7% TiO_2. Increasing temperature to realistic values (>1200°C) greatly increases the solubility of TiO_2 in a basaltic liquid. Thus, based on the study of Green & Parson, it is very unlikely that the TiO_2/Y trend displayed by the LoTi and HiTi analyses can be the result of fractionating a Ti-rich phase from these, or more primitive liquids. This implies processes more complex than closed-system crystal fractionation were affecting minor element concentrations during the magmatic evolution of these dykes.

In summary, variation in the proportions of the major elements (SiO_2, Al_2O_3, FeO, MgO, CaO) within and between the HiTi and LoTi groups can be explained by fractionation of the phenocryst assemblages, implying a genetic relationship between these groups. Variations in TiO_2 are not consistent with the petrographic characteristics and suggest the involvement of processes other than closed-system crystal fractionation. Emplacement of the evolved HiTi group prior to the more mafic LoTi group (Fig. 5.25) makes it difficult to envisage a strict parent-daughter relationship between these groups as suggested by the variations in major element chemistry. These observations suggest that the HiTi group was derived from liquids very similar in composition to the LoTi samples, but examples of more mafic compositions with a relative age consistent with that required to be parental to the HiTi group were not found.

The PM dykes cannot be related to either the LoTi or HiTi groups by fractionation of the observed phenocryst assemblages. However, these major element diagrams do not rule out the possibility that the PM dykes and the HiTi-LoTi dykes shared a similar primary liquid, but followed slightly different evolutionary paths involving, perhaps, variations in the extent of high pressure crystal fractionation. Examination of trace element abundances is required to evaluate this possibility, and to further assess the HiTi-LoTi relationship.

5.12.2 TRACE ELEMENTS

Incompatible element "spiderplots" normalized to primordial mantle abundances (Wood et al., 1979) are shown for each Fe-tholeiite group in Fig. 5.28. The chemical variation within each group results in distinctive and consistent patterns for most elements, although the LoTi samples 242 and 415 (Fig. 5.28A) show considerable scatter in high "D" elements. Petrographically, these two samples display extensive amphibolitization, and 415 is also garnet bearing. The depletion in the elements Rb > K $\geq$ Ba is similar to that observed in the high-Mg sample 413 (Section 5.2.4) and is typical of the relative incompatible element depletions during subsolidus fluid interaction with lower crustal mafic dykes (Weaver & Tarney, 1981). Sample 207 (Fig. 5.28A) is depleted in Nb, but enriched in Ba and K compared to other LoTi samples and will be discussed later.

The most prominent feature common to the spiderplots of dykes unaffected by extensive hydration is a large negative $(Sr)_N$ anomaly which, unlike the similar $(Sr)_N$ depletion in the high-Mg subgroups II and III, can be attributed in the Fe-tholeiites to fractionation of plagioclase phenocrysts. Also common to each Fe-tholeiite group is a negative $(Nb)_N$ anomaly. As the mineral/liquid distribution coefficient for Nb in Fe-Ti oxides is quite high ($D_{Nb}^{ilm/liq} \simeq 0.8$; Pearce & Norry, 1979) the depletion in Nb relative to K and La could indicate fractionation of ilmenite or titaniferous spinel which would also be consistent with the lack of Ti-enrichment during differentiation. But as discussed in the previous section, fractionation of a Ti-rich oxide phase from any parental liquid to these groups is untenable due to the very high concentration of TiO_2 (>4%) needed to saturate these liquids at the P and T under consideration.

Furthermore, the K/Nb ratio in the HiTi analyses is generally constant during differentiation, but should markedly increase if a Fe-Ti oxide was extracted. The relative Nb depletion in the HiTi dyke samples is thus considered to be a source characteristic. The effect of fractionation

Figure 5.28 A-C

Incompatible element 'spiderplots' of Fe-tholeiite groups. Note the LoTi sample 207, defined on the basis of FeO/MgO-TiO_2 relationships and phenocryst assemblage, is also plotted with the PM dykes (C).

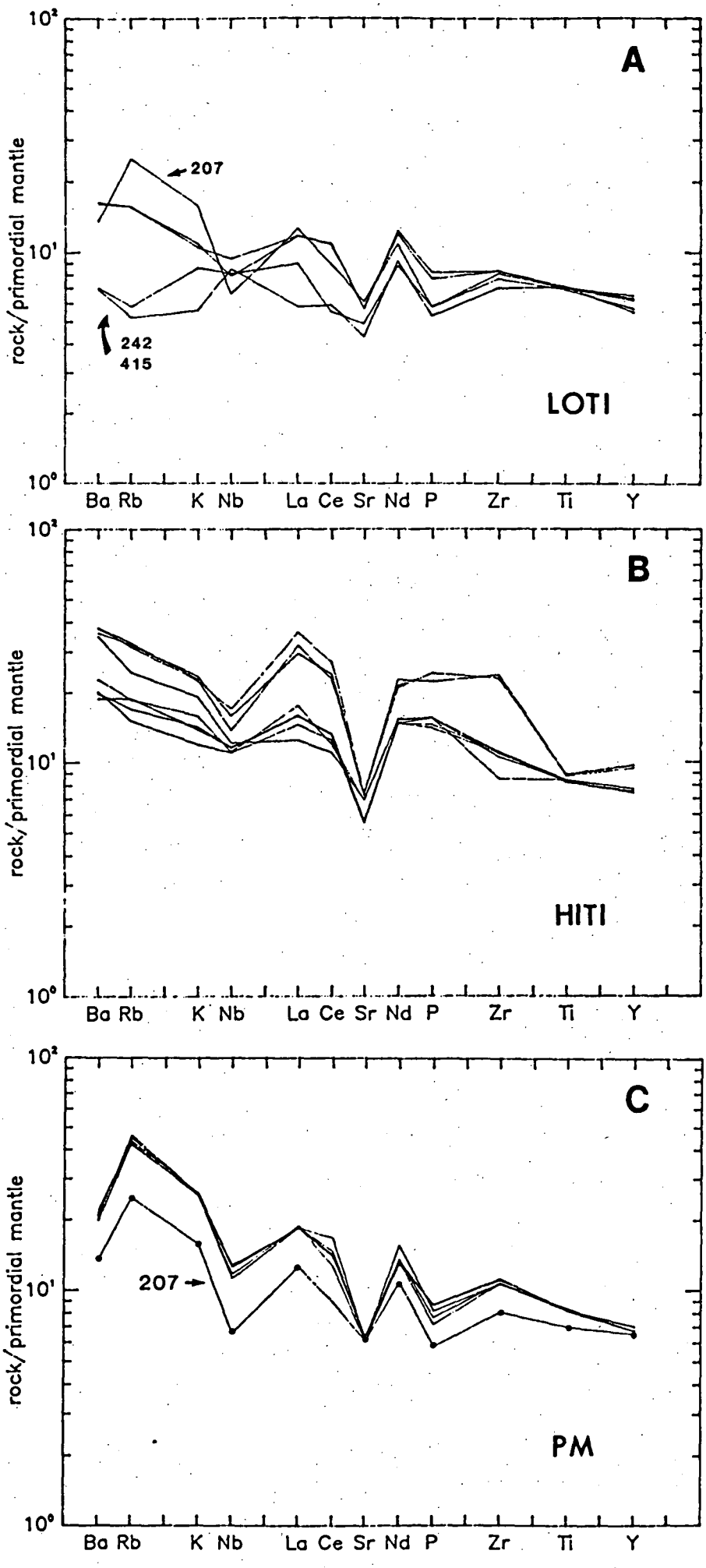
A
207
242
415
LOTI
rock/primordial mantle
Ba Rb K Nb La Ce Sr Nd P Zr Ti Y
B
HITI
C
207
PM

on K/Nb cannot be evaluated in the PM or LoTi dykes, but by inference based on the absence of Fe-Ti oxides in these samples, the $(Nb)_N$ anomaly is also considered a source characteristic.

The conclusion dictated by the major element variations (excluding TiO_2) is that the chemical trends in the HiTi samples are the result of fractionating the phenocryst assemblage of plagioclase + clinopyroxene + orthopyroxene. This conclusion is broadly substantiated by the parallel enrichment of incompatible elements in the HiTi spiderplots (Fig. 5.28B) particularly in the elements with D-values $\geq$ Nb. The normalized LREE and P patterns in the three evolved samples are similar to the more mafic samples, but these elements have been enriched beyond that expected by closed system crystal fractionation. By considering all the HiTi samples to be related by fractional crystallization, the change in $(La/Nd)_N$ and $(Ce/Nd)_N$ ratios from <1 to >1 indicates the LREE were enriched in the order La $\geq$ Ce > Nd. This relative enrichment is accompanied by a marked increase in Zr. The absence of Ti enrichment with respect to Y, as seen in the Pearce diagrams (Fig. 5.27E), is clearly evident on the spiderplots.

The major element variation depicted in the Pearce diagrams also suggested that LoTi-like compositions were parental to the dykes of the HiTi group through crystal fractionation. In Fig. 5.29A, spiderplots of LoTi samples (excluding the elements apparently affected by alteration in samples 415 and 242) are combined with the HiTi spiderplots. The LoTi samples have lower abundances of all elements compared to HiTi samples, and importantly, the relative abundances of these elements form parallel trends to the HiTi patterns. These features support a genetic relationship between the HiTi and LoTi groups. The only feature not readily explained by a fractional crystallization relationship is the marked enrichment of P from the most mafic LoTi sample, to the most mafic HiTi sample. This difference does not preclude a genetic relationship between the groups as the P/Y ratio progressively increases with fractionation (increasing Y) within the LoTi group. On a plot of P/Y versus Y (Fig. 5.30) the trend of increasing P/Y in the LoTi samples forms a straight line path to the HiTi P/Y values with the fractionated HiTi samples falling along a slightly lower slope indicating P was continuously added to the magmatic system during crystal fractionation.

The mechanism for P enrichment is not known, but is very unlikely to involve incorporation of lower crustal granitoids as the LIL elements show no evidence for enrichment outside of that predicted by crystal fractionation. The marked relative enrichment in P suggests selective contamination by an "apatite-rich" component. The accompanying enrichment

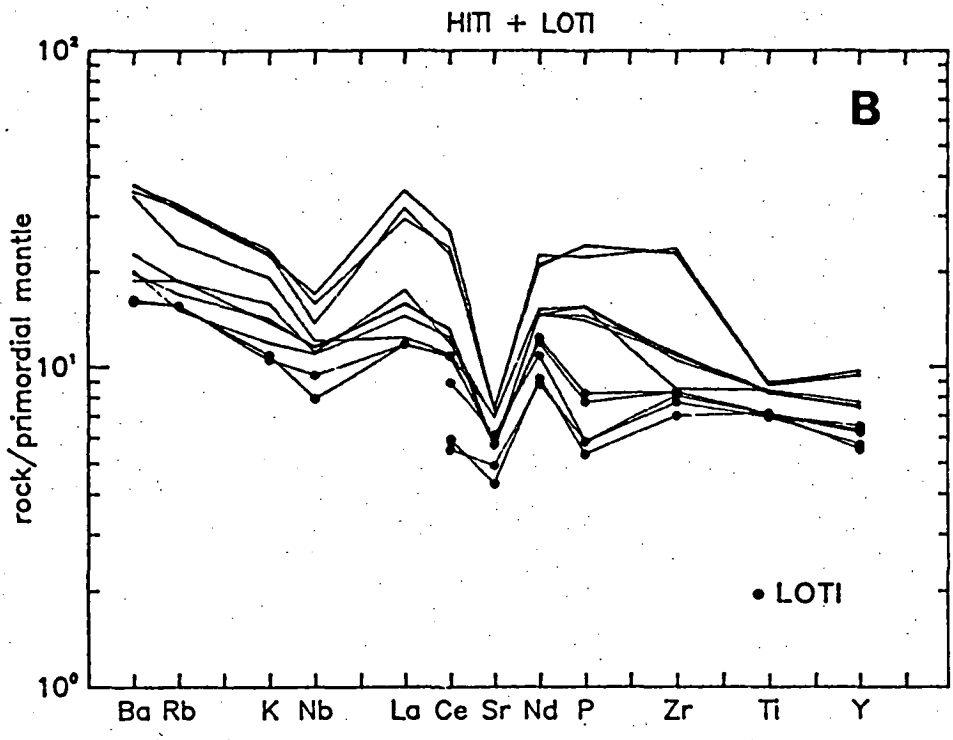

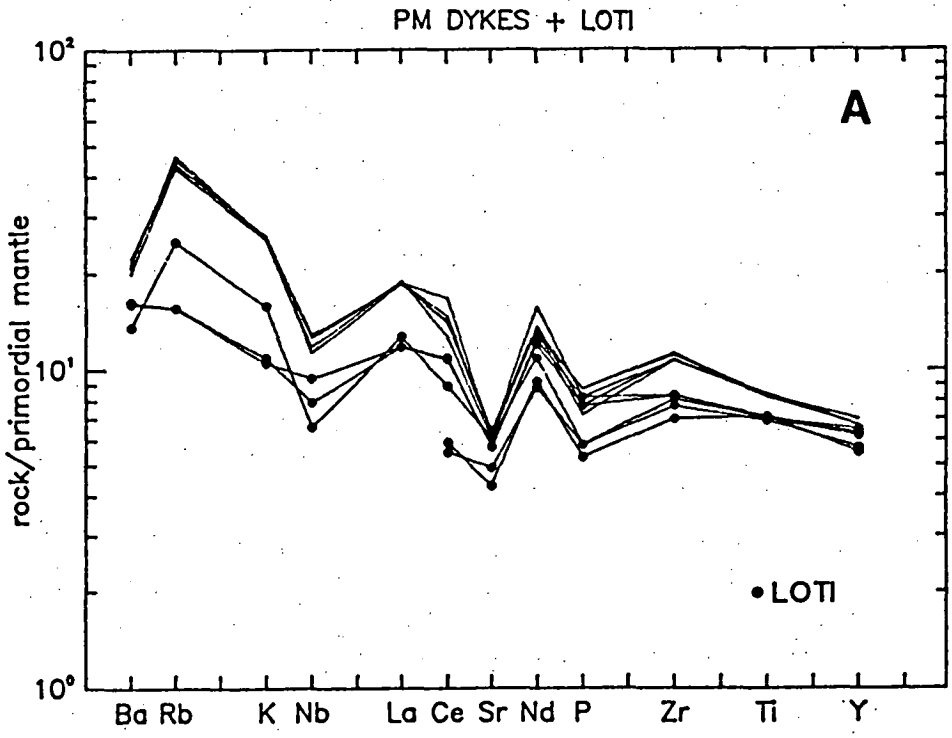

Figure 5.29
'Spiderplots' comparing the patterns and relative elemental enrichments between PM and LoTi compositions (A), and between HiTi and LoTi compositions (B).

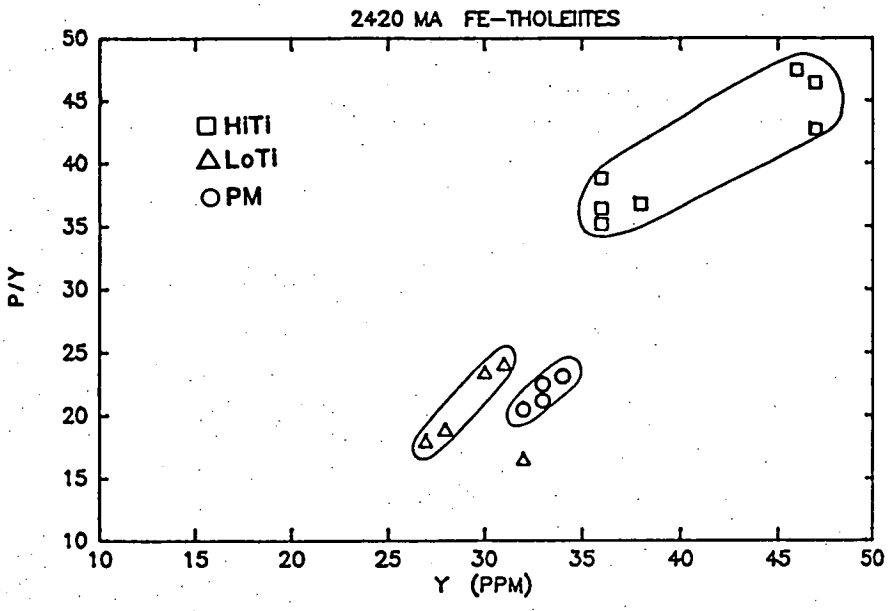

Figure 5.30
P/Y versus Y diagram illustrating the enrichment of P with differentiation within each Fe-tholeiite group. The uncircled LoTi analysis is from sample 207.

of LREE (La > Ce > Nd) indicates that if an apatite component was involved, other REE-rich species were also introduced as crystal/liquid K_D's for apatite are generally considered to favour the middle REE (Hansen, 1980). How such a process could also result in Zr-enrichment and Ti-depletion is even less clear.

The spiderplot of the PM dykes (Fig. 5.28C) differ markedly from the HiTi patterns in having a pronounced positive $(Rb)_N$ anomaly, and $(Rb/Ba)_N > 1$. On this basis, it is unlikely that these two groups shared a common parental liquid, a conclusion not inconsistent with the major element variations. However, the normalized trace element pattern of the LoTi sample 207 is nearly identical to that of the PM dykes (Fig. 5.28C), yet the major element variations clearly indicate 207 cannot be related to the PM dykes by "low pressure" fractional crystallization. This conclusion is not dependent on the normalizing parameter used in the Pearce diagrams (Y) as an identical interpretation is required from plots normalized to Ba. Compared with the spiderplots of relatively unaltered LoTi samples (271, 267), the PM dykes display only minor differences in relative and absolute enrichments of medium to low "D" elements (excluding P as discussed above) and including Nb and Ba (Fig. 5.29B). The similarity in patterns suggests that the marked enrichment of $(Rb > K)_N$ in the PM dykes may be the result of a "secondary" process superimposed upon primary liquid concentrations not unlike that found in the LoTi dykes.

Excluding the marked enrichment of $(Rb > K)_N$ in the PM dykes (and 207), and the P-Ti relationship, both of which may be the result of secondary processes, the spiderplots are inconclusive as far as distinguishing the three petrographically distinct groups, implying the parental liquids to these groups had very similar geochemical characteristics.

5.12.3 RARE EARTH ELEMENTS

Rare earth element (REE) analyses were determined in one sample from each of the LoTi, HiTi and PM groups and are shown normalized to chondrite abundances in Fig. 5.31; the data are listed in Table 5.13. The similarities in the three REE profiles do not contradict the conclusion, based on the spiderplots, that these three groups were derived from a compositionally similar, primitive liquid. The flat $[(Ce/Yb)_N = 1.1\text{-}1.4]$ generally unfractionated patterns displayed by all samples indicate that the primary liquid parental to these samples is unlikely to have been derived from a source which had previously lost a melt fraction. The

progressive increase in $(Ce/Yb)_N$ apparently reflects the enrichment process identified in the spiderplots; crystal fractionation of the phenocryst phases observed in the groups should result in an equivalent enrichment of all REE (except Eu), not just LREE.

The negative $(Eu)_N$ in 080 and 267 is consistent with the negative $(Sr)_N$ anomalies on the spiderplots, and is chemical evidence for plagioclase fractionation. However, the lack of a negative $(Eu)_N$ anomaly in 244 in contradictory to the petrography, major and trace element patterns of this sample, all of which imply that plagioclase fractionation played a major role in producing the chemical composition of the sample. This feature could develop by accumulating plagioclase (Eu-rich) into a liquid with a negative $(Eu)_N$ anomaly, such that the relative plagioclase/liquid proportions fortuitously produced a smooth REE profile. Calculations indicate ~30% plagioclase accumulation is necessary to produce the 244 pattern from a liquid having a Eu anomaly similar in extent to 267, but this cannot be supported petrographically. The other possibility (excluding that of analytical error) is that fO_2 conditions in the HiTi liquid were such that Eu existed in the trivalent state, and was then not partitioned into the fractionating plagioclase. The REE pattern of 244 indicates Eu has not been depleted relative to the other REE, even though significant plagioclase fractionation is indicated in the geochemical history of the HiTi group based on the spiderplots. Thus the presumed relatively high fO_2 conditions must have been a characteristic of the parental HiTi liquids since at least the onset of plagioclase precipitation and did not develop during differentiation. Such a significant difference in the intrinsic properties of the HiTi compared to the LoTi group would preclude derivation of the HiTi group from LoTi compositions.

The similarity in REE patterns, including the existence of a negative $(Eu)_N$ anomaly between samples 080 and 267 lends support to the suggestion, based on spiderplots, that the LoTi and PM dykes are closely related, and the $(Rb > K)_N$ enrichment in the PM dykes is the result of a secondary process and not a source characteristic.

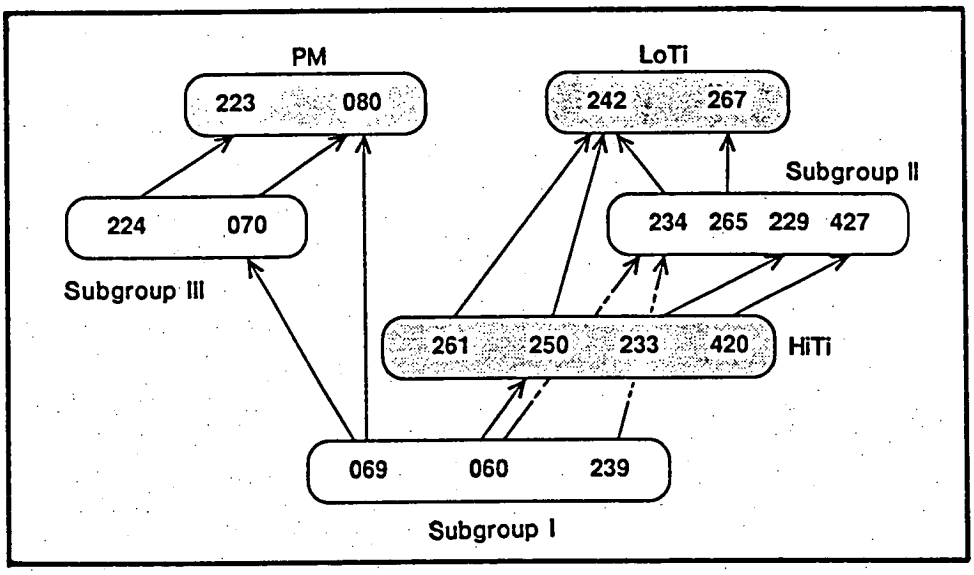

Figure 5.25
Field determined intersecting relationships between dykes of the ca.2420 Ma Fe-tholeiite (shaded) and high-Mg suites. Arrows connect sample numbers of cross-cutting dykes and point to the younger.

5.11 PETROGRAPHY AND CRYSTAL CHEMISTRY OF Fe-RICH THOLEIITES

Dyke intersections, used in conjunction with $FeO/MgO-TiO_2$ relationships, suggest that the emplacement of the dykes comprising the Fe-rich suite took place in two, and possibly three events. Dykes which characterize the LoTi and HiTi groups also have petrographically dissimilar phenocryst assemblages. Furthermore, the PM dykes are also petrographically distinctive. All studied samples of the Fe-rich suite display varying degrees of subsolidus hydration resulting in the development of secondary green amphibole + Fe-Ti oxides, through reaction between plagioclase and pyroxene, which is responsible for the greenish tint to the dyke colour in outcrop. The PM dykes have experienced the least amount of hydration.

HiTi dykes are petrographically indistinguishable from the much younger Group I Amundsen Dykes of Enderby Land (Sheraton & Black, 1981; see Fig. 2.6 of this thesis). Chilled margin samples of the HiTi dykes are composed of individual and intergrown orthopyroxene-clinopyroxene-plagioclase phenocrysts (~1-2 mm in length) in a dark, opaque and amphibole-rich, fine grained groundmass. Clinopyroxene invariably displays multiple twinning and complex intergrowths with other clinopyroxene phenocrysts. Reddish brown orthopyroxene is more commonly found as single crystals but does form aggregates with clinopyroxene and plagioclase and is evidence for co-precipitation of these phases. The orthopyroxenes have very narrow clinopyroxene quench rims and, particularly in sample 233, may display hour glass zoning patterns. Olivine does not occur in the HiTi samples, although very rare highly altered and irregularly shaped pale red inclusions can be found in orthopyroxene phenocrysts which may be evidence for an earlier precipitation of olivine and subsequent fractionation/resorption. The three most Fe-rich compositions (Fig. I2.1) were collected from the southwest corner of the Vestfold Hills and have been recrystallized to a garnet-bearing assemblage (Chapter 3). Opaque-filled relict orthopyroxene phenocrysts are preserved in these samples.

Selected analyses from the only extensively analysed sample, 244, are listed in Table 5.11 and plotted in Fig. 5.26. Plagioclase phenocrysts are $\sim An_{64}$, with one large, optically zoned grain having a broad compositionally homogeneous $\sim An_{80}$ core with a narrow rim similar in chemistry to the plagioclase phenocrysts. An unusual feature of the orthopyroxene phenocrysts is their high calculated Fe^{3+} (up to 3.5%; based on 4.000 cations). Similarly, high Fe^{3+} is indicated in the Na-free clinopyroxene suggesting Fe^{3+} is coupled in a (Fe,Mg)-Tschermaks molecule. Subsolidus

secondary alteration resulting in high Fe^{3+} would be expected to readjust the CaO content of the pyroxenes to subsolidus equilibrium values, but this has not taken place, nor were exsolutions of Fe-Ti oxides observed during microprobe study of this sample, both suggesting that the high Fe^{3+} in the orthopyroxenes is a magmatic feature.

Liquidus temperatures were estimated using averaged Fe^{3+} and Fe^{T} based data from the coexisting orthopyroxene and clinopyroxene phenocrysts; the data and results are listed in Table 5.12. As in previous temperature determinations (see the discussions in Section 1.1.3), the Wells (1977), Kretz (solvus and exchange reactions; 1982) and the Lindsley (1983) graphical thermometer were applied.

Excellent agreement exists between the Wells, Lindsley (opx and cpx limbs) and Kretz (solvus) temperatures giving an average of ~1200°C. There is a negligible difference between temperatures calculated using Fe^{3+} or Fe^{T}. Temperatures calculated using the Kretz exchange reaction give similar results for Fe^{3+} and Fe^{T} determinations, but these temperatures are more than 300°C above the temperatures calculated using the other thermometers, and are clearly in error. Similar conclusions were reached in previous discussions of the Kretz exchange thermometer (Section 1.1.3). The preferred two-pyroxene temperatures of ~1200°C derived from the phenocryst assemblage of sample 244 is in very good agreement with the 1180°C, 8 kbar liquidus temperature (and phase assemblage) of the compositionally similar sample 206 studied experimentally in Section 1.3.2 of this thesis (see Fig. 1.13).

The LoTi dykes are olivine + clinopyroxene + plagioclase phyric, and lack orthopyroxene phenocrysts. The studied samples have a subophitic to moderately porphyritic texture. In the latter case, although single phenocrysts are common, equidimensional to slightly elongate clinopyroxenes do form radial glomerocrysts with plagioclase laths. Olivine is rare in all samples, and highly altered. Its irregular form and inclusion in pyroxene clots suggest olivine was in reaction with the liquid prior to quenching. The groundmass is composed of a mosaic of green amphibole enclosing plagioclase laths and Fe-oxides. One sample, 415, is recrystallized to a garnet-bearing assemblage (see Chapter 2).

Compositions of LoTi phenocrysts are plotted on Fig. 5.26, and listed in Table 5.11. The analyses of two small, relict olivines are Fe-rich (Mg_{65-67}) and cannot be in equilibrium with the 207 bulk rock composition ($Mg_{47.1}$; equilibrium olivine is Mg_{73}), and are probably "rim" compositions which crystallized from a differentiated, subliquidus composition. Compared to HiTi, LoTi clinopyroxenes are in general slightly more

magnesian and tend to be enriched in Al_2O_3. The calculated Fe^{3+} is more variable in the LoTi clinopyroxenes than in the HiTi analyses, though the LoTi analyses are also Na-free. Plagioclase phenocryst compositions are essentially identical between the two groups (An_{60-68}).

The PM dyke samples are mineralogically unique among the Fe-rich dyke suite in having phenocrysts of magnesian pigeonite (Mg_{72-74}). The pigeonite comprises < modal 5% of the samples examined and form euhedral, tabular single crystals or stellate clots with plagioclase phenocrysts. Plagioclase "megacrysts" are euhedral and simply twinned with complex optical zoning. Although the megacrysts are much larger than the matrix crystals they rarely exceed ~3 mm in length in the studied samples, and display some gradation in size to the plagioclase phenocrysts of the matrix (<1 mm). Very rare, mostly resorbed crystals of olivine can be found, but are usually completely altered.

Analyses of the PM phenocryst phases are also plotted on Fig. 5.26, and listed in Table 5.11. The most calcic plagioclase megacryst analysis is similar to the core composition of the large plagioclase crystal in the HiTi sample 244 (~An_{80}), but zoning in the PM megacryst is to more Na-rich compositions. Plagioclase phenocryst compositions are very similar between all three divisions of the Fe-rich suite. The magnesian pigeonite phenocrysts have narrow rims of Al_2O_3-rich Ca-clinopyroxene only marginally less calcic than the calcic clinopyroxene phenocrysts of the HiTi and LoTi dykes. Pyroxene analyses from the PM dykes also have 1-3% calculated Fe^{3+}.

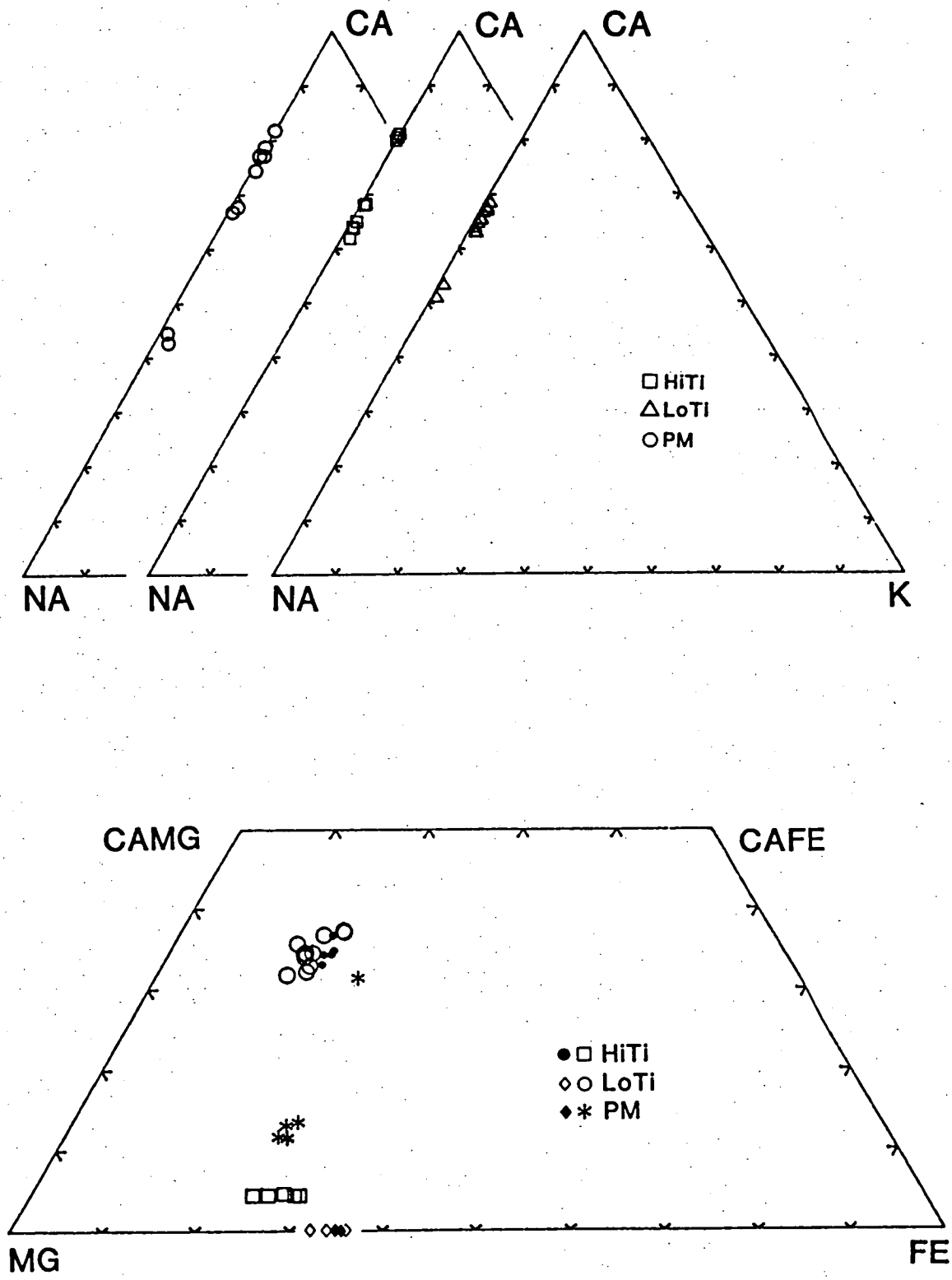

Figure 5.26
Comparison of plagioclase (upper Ca-Na-K diagram) and pyroxene phenocryst compositions between Fe-tholeiite groups. Olivine is also plotted in the lower quadrilateral.

TABLE 5.11
MINERAL ANALYSES[1] FROM ca.2420 Ma FE-RICH THOLEIITES.

PHASE	OPX	OPX	CPX**	CPX	PLAG	PLAG	OLIV	OLIV	PLAG
SUBGROUP	HITI	HITI	HITI	HITI	HITI	HITI	LOTI	LOTI	LOTI
SAMPLE	244	244	244	244	244	244	207	207	207
SIO2	53.38	51.43	51.68	51.74	49.03	52.17	36.4	36.44	52.42
TIO2			0.32	0.29					
AL2O3	1.32	2.07	2.44	2.44	32.46	30.23			29.77
FE2O3*	2.15	3.58	1.32	1.19					
FEO	15.31	17.72	10.55	10.82	0.57	0.74	30.44	29.23	0.62
MNO		0.22					0.23	0.33	
MGO	25.63	22.91	17.38	16.67			32.50	34.00	0.17
CAO	2.21	2.12	16.06	16.86	15.89	13.35	0.42		13.30
NA2O					2.05	3.40			3.51
K2O						0.12			0.20
SI	1.9422	1.9057	1.9156	1.9218	2.2422	2.3704	0.9883	0.9829	2.3823
TI			0.0089	0.0081					
AL	0.0566	0.0902	0.1067	0.1068	1.7495	1.6187			1.5945
FE3+	0.0589	0.0984	0.0368	0.0333					
FE2+	0.4658	0.5491	0.3269	0.3360	0.0217	0.0281	0.6909	0.6595	0.0237
MN		0.0069					0.0052	0.0075	
MG	1.3901	1.2655	0.9599	0.9231			1.3149	1.3672	0.0118
CA	0.0863	0.0842	0.6377	0.6709	0.7785	0.6499	0.0123		0.6475
NA					0.1819	0.2994			0.3094
K						0.0068			0.0116
TOTAL					4.9739##	4.9733	3.0117	3.0171	4.9808
MG#	74.7	69.7	74.6	73.3			65.5	67.5	
CA#	4.4	4.4	33.1	34.8	81.1	68.0			66.9
a_{en}	0.4830	0.3969	0.1864	0.1644					

PHASE	PLAG	CPX	CPX	OLIV	PIG	PIG	PLAG	PLAG	PLAG
SUBGROUP	LOTI	LOTI	LOTI	PM	PM	PM	PM	PM	PM
SAMPLE	207	207	207	080	080	080	079	079	080
SIO2	53.19	51.58	51.40	35.98	53.13	52.93	48.62	49.11	52.25
TIO2		0.36	0.37		0.32	0.18			
AL2O3	29.55	3.25	3.83		1.34	1.40	32.60	32.27	29.98
FE2O3*		1.28	0.27		0.97	1.55			
FEO	0.40	8.10	12.21	31.18	15.23	14.59	0.45	0.42	0.39
MNO				0.36	0.31	0.27			
MGO		17.83	17.35		22.96	22.62			0.31
CAO	12.64	17.26	14.56	0.16	5.74	6.46	16.32	15.83	13.36
NA2O	3.96						2.01	2.37	3.58
K2O	0.25								0.13
SI	2.4108	1.8972	1.9023	0.9812	1.9488	1.9435	2.2268	2.2466	2.3728
TI		0.0098	0.0103		0.0087	0.0049			
AL	1.5787	0.1407	0.1670		0.0581	0.0604	1.7593	1.7399	1.6048
FE3+		0.0354	0.0077		0.0267	0.0429			
FE2+	0.0152	0.2493	0.3780	0.7109	0.4670	0.4478	0.0172	0.0161	0.0147
MN				0.0084	0.0096	0.0085			
MG		0.9776	0.9572	1.3137	1.2554	1.2381			0.0211
CA	0.6139	0.6802	0.5775	0.0046	0.2255	0.2540	0.8007	0.7758	0.6501
NA	0.3476						0.1786	0.2098	0.3150
K	0.0147								0.0074
TOTAL	4.9809			3.0188			4.9827	4.9882	4.9859
MG#		79.7	71.7	64.9	72.9	73.4			
CA#	62.9	35.7	30.2		11.6	13.1	81.8	78.7	66.8
a_{en}									

MG# = 100MG/(MG+FE). CA# = 100CA/(CA+MG+FE) OR 100CA/(CA+NA+K).
NOTE, LOW TOTALS DUE TO SLIGHT ERROR IN SIO2 CALIBRATION AND DOES NOT AFFECT CA# (SEE SECTION 1.3.2).
* CALCULATED ON 4.000 CATIONS.
** INCLUDES 0.25% CR2O3 AND 0.0074 ATOMS CR.
a_{en} CALCULATED AFTER WOOD & BANNO (1973).

1 All elements listed were analysed for in end phase, blanks indicate concentration was below the detection limit.

TABLE 5.12
TEMPERATURE ESTIMATES ON THE PHENOCRYST ASSEMBLAGE OF 244 (HITI)

	a_{en}^{cpx}	a_{en}^{opx}	X_{Mg}^{opx}	X_{Mg}^{cpx}	X_{Ca}^{cpx}
FE3+	0.1655	0.4316	0.715	0.736	0.334
	0.1864	0.4255	0.703	0.746	0.331
	0.1441	0.4830	0.749	0.740	0.367
	0.1753	0.4516	0.732	0.747	0.343
	0.1644	0.3969	0.697	0.733	0.348
AV.	0.1672	0.4377	0.719	0.740	0.345
FE^T	0.1579	0.4151	0.688	0.710	0.336
	0.1804	0.4149	0.686	0.725	0.325
	0.1692	0.4679	0.726	0.725	0.358
	0.1589	0 4331	0.703	0.714	0.337
	0.1440	0.3771	0.662	0.717	0.342
AV.	0.1621	0.4216	0.693	0.718	0.340

	FE^{3+}	FE^T
WELLS	1194°C	1178°C
KRETZ (SOLV)	1206	1203
(EXCH)	1575	1534
LINDSLEY (CPX LIMB)	1150-1200	-
(OPX LIMB)	1200	-

a_{en} CALCULATED FOLLOWING WOOD & BANNO (1973)

X_{Mg} = MG/(MG+FE). X_{Ca} = CA/(CA+MG+FE).

5.12 WHOLE-ROCK GEOCHEMISTRY

5.12.1 MAJOR ELEMENTS

In order to investigate the possibility that "low pressure"* crystal fractionation was responsible for the chemical diversity found within the dykes of the Fe-rich suite, chemical variations were evaluated by using Pearce molecular norm diagrams (Pearce, 1968).

In this method, the mole proportions of major element oxides are normalized to a parameter not involved in the differentiation process. Unlike Harker diagrams, the oxides on the axes of a Pearce diagram are not a subset of an analysis which totals 100%, but instead the normalized molar ratios vary independently of one another, and reflect only the processes acting upon them. For example, on a Harker diagram of MgO versus SiO_2, MgO will increase through a fractionation sequence involving only plagioclase because the analyses are recast to 100%. In a Pearce diagram of molar MgO/TiO_2 versus molar SiO_2/TiO_2, MgO/TiO_2 will remain constant (slope = 0) because MgO (and TiO_2) are not removed by plagioclase fractionation, while SiO_2/TiO_2 will decrease. When a MgO-bearing phase is fractionated, the resulting slope on a Pearce diagram will be proportional to the molar composition of the fractionating phase.

Pearce diagrams displaying the chemical variation in the Fe-tholeiite suite are shown in Fig. 5.27. Yttrium was chosen as a normalizing component because garnet is the only common phase capable of fractionating Y to a significant extent from a basaltic melt composition (Pearce & Norry, 1979) and is restricted to pressures $\gtrsim$ 20 kbar. Furthermore, many of the studied samples have experienced subsolidus alteration, and as Y is generally considered immobile during this process (see Clough & Field, 1980), the analysed samples should retain igneous Y abundances. An important point to note when viewing these diagrams is that fractionation of silicates extracts SiO_2, while Y increases, thus molar SiO_2/Y will decrease during fractionation.

A linear, positive sloping trend is shown on the SiO_2/Y-Al_2O_3/Y diagram (Fig. 5.27A) joining samples of each group which is consistent with the groups forming a cogenetic suite. The inset vectors display the trends expected by fractionating the phases indicated, and the trend defined by

---

* Although these dykes were emplaced at 7-8 kbar, the term "low pressure" will be used to designate fractionation at pressures near emplacement conditions.

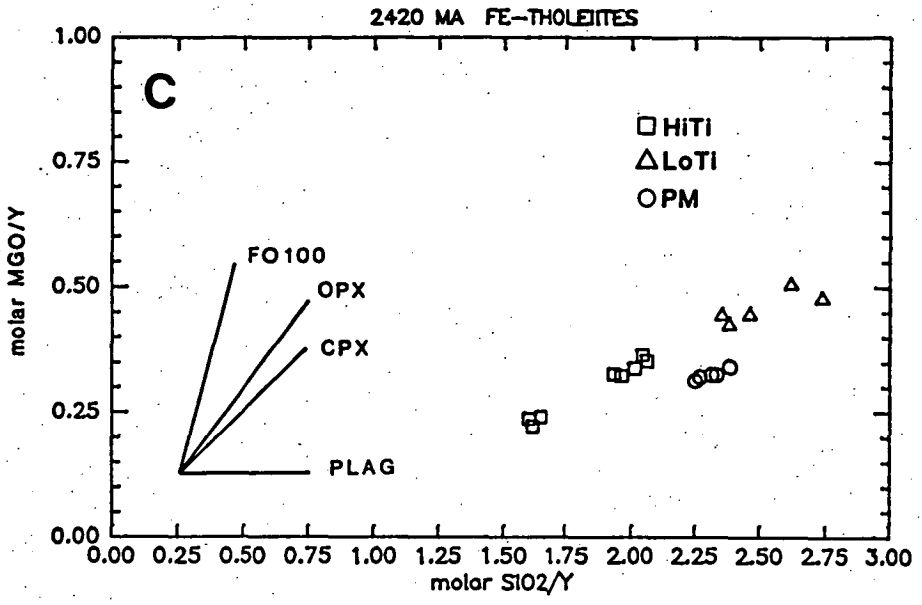
2420 MA FE-THOLEIITES
C
HiTi
LoTi
PM
FO100
OPX
CPX
PLAG
molar MGO/Y
molar SIO2/Y
1.00
0.75
0.50
0.25
0.00
0.00 0.25 0.50 0.75 1.00 1.25 1.50 1.75 2.00 2.25 2.50 2.75 3.00

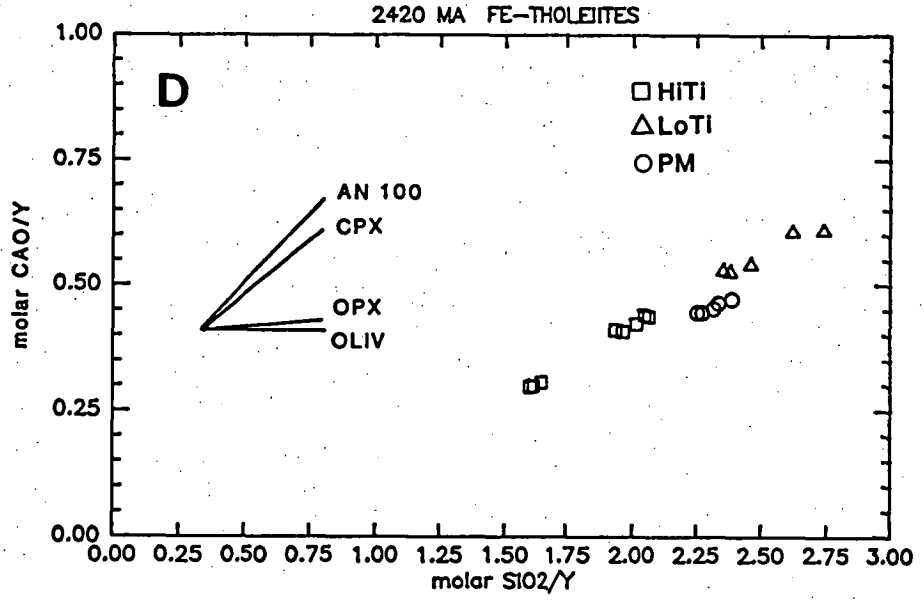
2420 MA FE-THOLEIITES
D
HiTi
LoTi
PM
AN 100
CPX
OPX
OLIV
molar CAO/Y
molar SIO2/Y
1.00
0.75
0.50
0.25
0.00
0.00 0.25 0.50 0.75 1.00 1.25 1.50 1.75 2.00 2.25 2.50 2.75 3.00

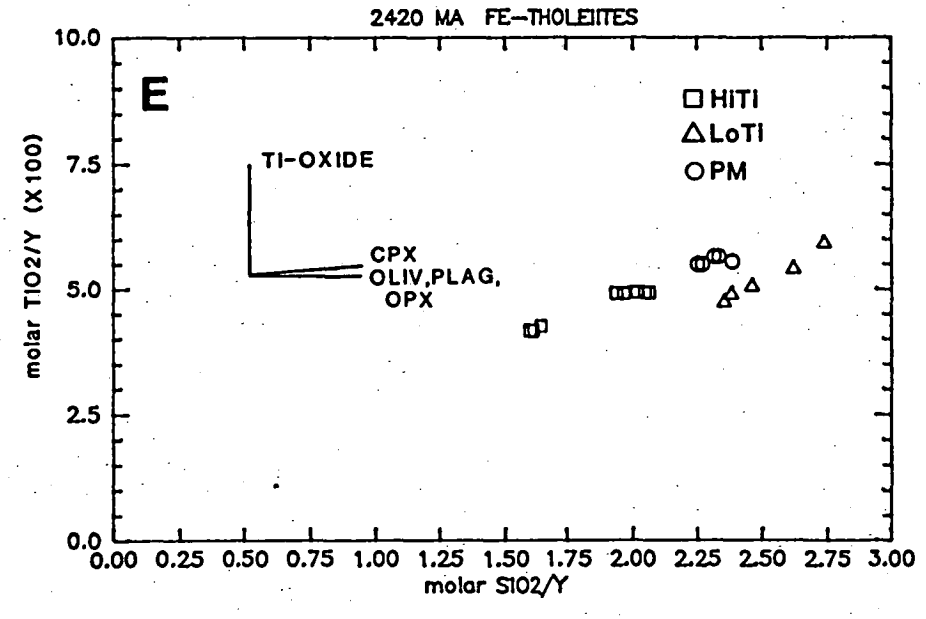
2420 MA FE-THOLEIITES
E
HiTi
LoTi
PM
TI-OXIDE
CPX
OLIV,PLAG,
OPX
molar TIO2/Y (X100)
molar SIO2/Y
10.0
7.5
5.0
2.5
0.0
0.00 0.25 0.50 0.75 1.00 1.25 1.50 1.75 2.00 2.25 2.50 2.75 3.00

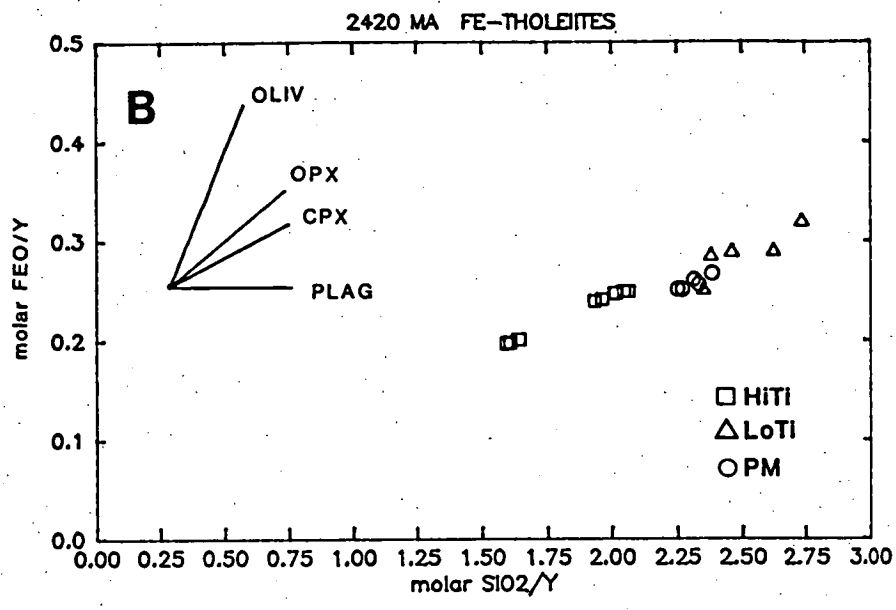

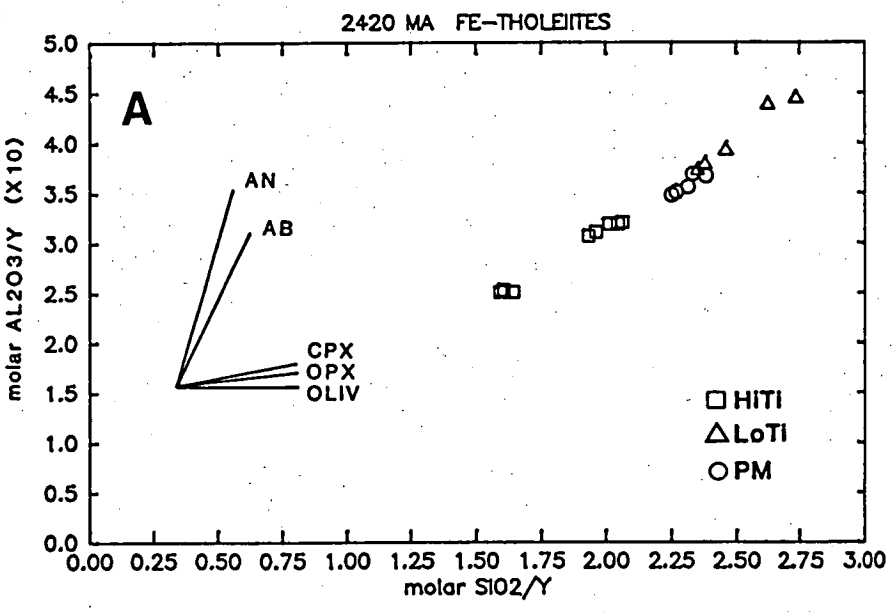

Figure 5.27 A-E

Pearce molecular ratio diagrams (Pearce, 1968) illustrating the major element chemical variation between groups of the Fe-tholeiite suite. Compositions used in vector inserts are: CPX - 35% Wo, 4% Al2O3, 0.4% TiO2, Mg_{80}; OPX - 2% Al2O3, Mg_{75}; OLIV - Mg_{75}.

the chemical variation in the samples is consistent with fractionation of a plagioclase + pyroxene ± olivine assemblage. A modest change in slope is apparent between the LoTi and HiTi trends, compatible with orthopyroxene becoming a fractionating phase in the HiTi samples, compared to plagioclase + clinopyroxene ± olivine in the LoTi group. Similar observations and conclusions result from examining the FeO/Y-SiO_2/Y diagram (Fig. 5.27B): the trends are consistent with the chemical variation of the samples being controlled by fractionation of the phenocryst phases as indicated by the vector inset.

However, a significant modification in the interpretation of the genetic relationship of the dykes is required by the trends shown in the diagrams involving MgO and CaO (Fig. 5.27C,D). At a given SiO_2/Y, the PM analyses are depleted in MgO and CaO relative to HiTi and LoTi. This difference cannot be accounted for by the fractionation of any silicate phase from the LoTi suite and implies the PM dykes were derived from a parental liquid separate from that of the LoTi samples. Furthermore, fractionation of the phenocryst phases in the PM dykes cannot produce HiTi compositions. Both the MgO/Y and CaO/Y diagrams are consistent with a low pressure crystal fractionation relationship between the LoTi and HiTi groups involving first clinopyroxene + plagioclase fractionation and joined by orthopyroxene in the HiTi dykes.

In a plot of TiO_2/Y-SiO_2/Y (Fig. 5.27), two distinct slopes are developed in the trends of the analyses implying distinctive fractionating assemblages. The vector inset shows that the fractionation of TiO_2-free phases, such as plagioclase and olivine, will produce a slope of zero on this diagram. Microprobe analyses of clinopyroxene phenocrysts contain up to ~0.4% TiO_2, and a clinopyroxene vector with this concentration is shown. The fractionation of clinopyroxene + plagioclase can adequately explain the subhorizontal trends of the PM and HiTi groups, but the steep slope in the LoTi analyses implies the removal of a Ti-rich phase, in addition to plagioclase + clinopyroxene. Petrographically, the existence of magmatic ilmenite or titanomagnetite in the LoTi samples is equivocal due to extensive subsolidus hydration. If a magmatic Ti-rich phase did precipitate from the LoTi magma, and assuming for this discussion that the HiTi dykes are derived from parental magmas matching the LoTi dykes in chemical composition (Figs I2.1, 5.27A-D), then precipitation of the Ti-rich phase ceased at the onset of orthopyroxene crystallization. This is implied by the intersecting trends in the TiO_2/Y diagram. The TiO_2/Y trends also indicate that the three most fractionated HiTi samples (428, 433, 443; see also Fig. I2.1) apparently cannot be related to the more

"primitive" HiTi samples without the fractionating assemblage containing a Ti-rich phase. Such a phase is not seen in the chilled margin samples of the HiTi group.

The absence of a Ti-rich phase in the phenocryst assemblage of all tholeiitic dykes examined from the Vestfold Hills and Enderby Land makes the implied fractionation of a Ti-rich phase difficult to reconcile. Green & Parson (1986) found that the TiO_2 content of a liquid saturated in a Ti-rich phase was a function of the SiO_2 content of the liquid, as well as P, T and fO_2. Decreasing SiO_2 increases the amount of TiO_2necessary for Ti-rich phase saturation, as does increasing temperature. Increasing pressure, and to a lesser extent fO_2, have the opposite effects.

If the LoTi and HiTi TiO_2/Y trends are the result of ilmenite or titaniferous spinel extraction, then these liquid compositions must fall within the limits of the variables defined by Green & Parson (1986) for Ti-rich phase saturation. At 7.5 kbar, a liquid with 50% SiO_2 and at a relatively low temperature of 1050°C, must contain >3% TiO_2 in order to precipitate a Ti-rich phase. This compares with <2% TiO_2 found in the analysed ca.2420 Ma Fe-tholeiite dykes. At 20 kbar and equivalent T and SiO_2 contents, saturation in a Ti-rich phase is at ~2.7% TiO_2. Increasing temperature to realistic values (>1200°C) greatly increases the solubility of TiO_2 in a basaltic liquid. Thus, based on the study of Green & Parson, it is very unlikely that the TiO_2/Y trend displayed by the LoTi and HiTi analyses can be the result of fractionating a Ti-rich phase from these, or more primitive liquids. This implies processes more complex than closed-system crystal fractionation were affecting minor element concentrations during the magmatic evolution of these dykes.

In summary, variation in the proportions of the major elements (SiO_2, Al_2O_3, FeO, MgO, CaO) within and between the HiTi and LoTi groups can be explained by fractionation of the phenocryst assemblages, implying a genetic relationship between these groups. Variations in TiO_2 are not consistent with the petrographic characteristics and suggest the involvement of processes other than closed-system crystal fractionation. Emplacement of the evolved HiTi group prior to the more mafic LoTi group (Fig. 5.25) makes it difficult to envisage a strict parent-daughter relationship between these groups as suggested by the variations in major element chemistry. These observations suggest that the HiTi group was derived from liquids very similar in composition to the LoTi samples, but examples of more mafic compositions with a relative age consistent with that required to be parental to the HiTi group were not found.

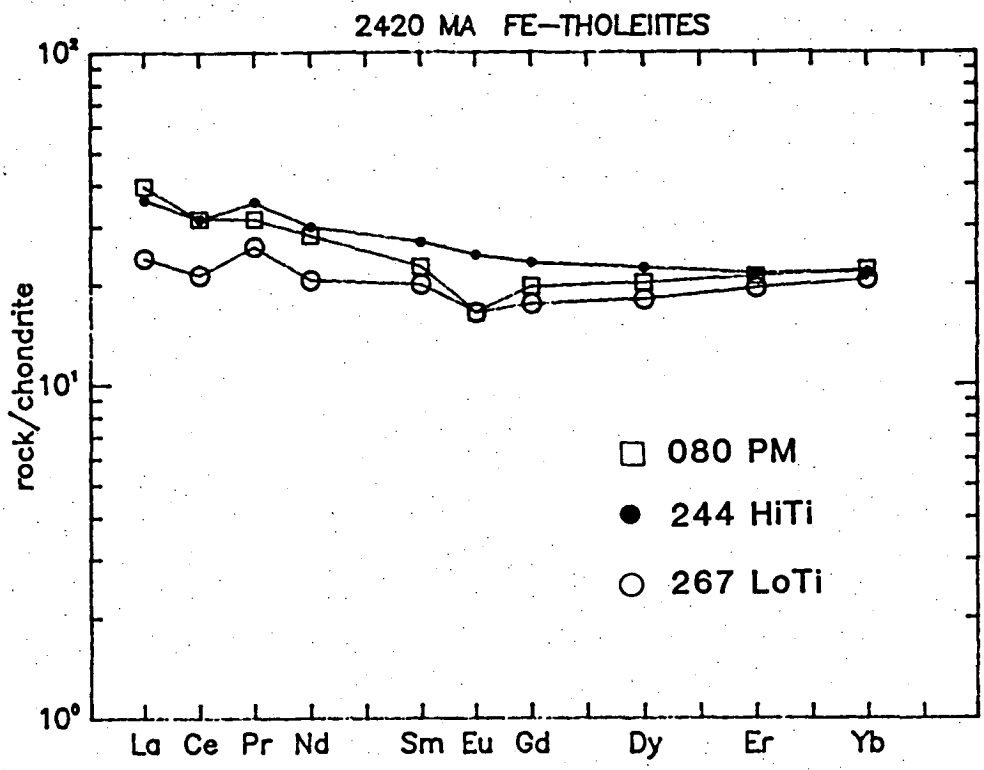

Figure 5.31
REE patterns of a selected sample from each of the three Fe-tholeiite groups.

TABLE 5.13
RARE EARTH ANALYSES* OF DYKES REPRESENTING HITI, LOTI AND PM GROUPS.

	LA	CE	PR	ND	SM	EU	GD	DY	ER	YB	(Y)
HITI											
244	11.35	25.6	4.07	17.8	5.15	1.77	6.01	7.27	4.59	4.53	42.3
LOTI											
267	7.56	17.34	2.99	12.29	3.84	1.19	4.53	5.85	4.15	4.31	39.6
PM											
080	12.46	25.65	3.62	16.74	4.34	1.19	5.11	6.57	4.5	4.61	39.4

* FOLLOWING THE METHOD OF ROBINSON ET AL. (1986), VALUES IN PPM.

5.13 SUMMARY OF THE GEOCHEMICAL CHARACTERISTICS OF THE Fe-RICH THOLEIITE SUITE

Major element variations between the HiTi and LoTi samples display trends consistent with a fractional crystallization relationship between the groups, in the sense of a parent-daughter lineage. This conclusion is supported by trace element spiderplots, although open system fractionation is required by the relative enrichments in P, LREE, Zr and depletion in TiO_2. The relative age relationships of these two groups do, however, make it difficult to consider these groups as a parent-daughter sequence. However, it seems highly coincident that primitive HiTi and evolved LoTi dykes with the appropriate intersecting relationships were not found such that the chemical variations in these groups overlapped on Pearce diagrams, which would indicate separate lineages from compositionally similar primary liquids. The REE patterns representing the LoTi and HiTi groups support the field evidence and the separate liquid model, but the absence of a negative $(Eu)_N$ in the HiTi group should be confirmed by further analysis.

The major element variations in the PM dykes cannot be related to either the HiTi or LoTi compositions by fractional crystallization of the observed phenocryst assemblages. However, incompatible element patterns, with the exception of K and Rb, parallel the more mafic LoTi patterns suggesting a common parental liquid. The similarities in minor elements including REE, but differences in major element geochemistry between the HiTi-LoTi and PM compositions, then suggests that the PM dykes followed a P-T differentiation path distinct from that of the HiTi and LoTi groups. The possibility that the prominent $(Rb > K)_N$ spike in the PM dykes was superimposed onto a LoTi-type trace element pattern by an open-system process is supported by a LoTi sample, defined on the basis of petrography and major element geochemistry, with a $(Rb > K)_N$ spike.

As discussed in Section 5.1, one of the features used to distinguish olivine-free, high-Mg subgroups II and III samples from subgroup I is the existence of a pronounced $(Rb)_N$ anomaly and a $(Rb/Ba)_N$ ratio >1 in the later subgroups (Figs 5.1 and 5.2). The incompatible element enrichments in the high-Mg dykes are considered, in part, to be due to a wall rock contamination process, and as the high-Mg primitive liquids were inferred to have been generated at ~10 kbar, the relative enrichment in $(Rb > K)_N$ must reflect a process operative in at least the uppermost portions of the subcontinental mantle. The fact that the PM dykes (and LoTi sample 207) display a similar enrichment style to subgroups II and III, apparently superimposed upon an incompatible element pattern not unlike that of mafic

LoTi compositions, suggests the PM dykes were affected by this process at shallow mantle levels, while the absence of the $(Rb)_N$ spike in the HiTi and most LoTi samples may indicate this process did not occur at higher pressure. A further and complementary inference from this discussion is that the distinctive major element composition of the PM samples, as opposed to HiTi and LoTi groups, may be the result of differentiation of the parental PM liquid at ~10 kbar, whereas HiTi and LoTi compositions fractionated at a somewhat greater pressure.

5.15 SUMMARY OF AND INFERENCES FROM THE HIGH-Mg AND Fe-RICH THOLEIITE ASSOCIATION IN THE VESTFOLD HILLS

Geochemical and petrographical divisions of the Fe-rich and high-Mg suites, used in conjunction with detailed documentation of dyke intersections suggest emplacement of these dykes took place in three, apparently alternating, Mg-rich to Fe-rich cycles. Because of this intimate spatial association, the question then arises as to the genetic relationship between these distinctive suites.

The simplest model that will relate the emplacement of Fe-rich dykes with Mg-rich precursors is one involving a crystal fractionation process. Such a model has been successfully applied to explain komatiite-Fe-tholeiite cycles associated with the Proterozoic Cape Smith fold belt of Northern Quebec (Francis & Hynes, 1979). However, as inferred in Section 5.12.2, based on the difference in style of trace element enrichment between the Fe-rich and high-Mg suites, this is an unlikely relationship for the Vestfold Hills association. This conclusion is firmly substantiated by examining the SiO_2-TiO_2 variation diagrams shown in Fig. 5.15A. This diagram illustrates that the Fe-rich suite is less siliceous than the high-Mg suite, making impossible their highly evolved composition through fractionating any realistic phase from the high-Mg suite. Furthermore, the Fe-rich suite has a lower abundance of incompatible elements than the high-Mg tholeiites (Figs 5.1, 5.2 and 5.28) also proving the relationship is not one of simple crystal fractionation.

The framework around which a model to satisfy the field relationships is built must contain the following features:

1) Major and trace element characteristics of LoTi and HiTi Fe-tholeiite indicate these groups are products of crystal fractionation of observed phenocryst phases, and for many elements can be interpreted as products from a common parental magma type. However, complexities in Ti, P and Zr abundances are not resolved by this simple relationship and some type of open system behaviour involving these elements is required. Field observations are unequivocal in recording the emplacement of the evolved HiTi group prior to intrusion of the more mafic LoTi dykes.
2) The Fe-rich suite is highly evolved and thus many of its primary chemical characteristics have been modified. However, the HREE patterns of samples from each of the three groups, and the unfractionated $(Ce/Yb)_N$ of the most mafic LoTi sample indicates that the primary liquid to the Fe-tholeiite suite was derived from a primitive source which had not experienced a previous melting event.

3) Liquids parental to the high-Mg suite have experienced extensive incompatible element enrichment. In spite of this process, mafic compositions have preserved some chemical characteristics of the primary magmas. Subgroup I samples have chondritic $CaO-Al_2O_3-TiO_2$ ratios, as well as chondritic Ti/Y. The olivine-bearing samples of subgroup II similarly have chondritic CaO/Al_2O_3 and Sr/Y but are depleted in Ti. All three subgroups have flat, unfractionated HREE patterns. These characteristics indicate derivation from a primitive source which had not experienced a previous melting event.

It is clear from this summary that the Fe-rich and high-Mg suites cannot be related through a single source model, as both suites were derived from liquids extracted from sources unmodified by previous partial melting episodes. Thus, appealling to models whereby each cycle reflects polybaric or incremental melt extraction processes from individual diapirs is inapplicable in this terrain (Arth et al., 1977; Arndt, 1977; Francis et al., 1981). The data instead require at least three separate primitive sources to have been involved in generating the ca.2420 Ma association. Both subgroups I and II high-Mg tholeiites may, as indicated by their chondritic characteristics, represent melts extracted from separate primitive diapirs. The origin of subgroup III is less clear, but is likely to be related to subgroup II. Depending on which characteristics are emphasized in the HiTi-LoTi relationship (major & trace elements versus REE) at least one other primitive source is required to generate the dyke compositions in the Fe-rich suite.

By combining the geochemical features characterizing the high-Mg and Fe-rich suites with detailed field relationships, many more questions were exposed than were answered. Subsequently, a variety of cartoon-type models can be envisaged to integrate the data presented in this chapter. One interesting aspect, however, is that of the Fe-rich, Mg-rich association itself; a common characteristic of Archean greenstone belts (see Arth et al., 1977; Arndt, 1982; Glikson, 1983). Comparison of the Vestfold Hills dyke compositions with greenstone belt examples is shown in Fig. 5.32, and the Fe-tholeiite suite is specifically compared to Fe-rich compositions from Munro township in Figs 5.14 and 5.15. Although peridotitic dykes have not been found in the Vestfold Hills, the high-Mg and Fe-rich tholeiites are identical on these diagrams with compositions reported from a variety of greenstone belts.

The origin and tectonic setting of Archean greenstone belts is a strongly debated topic (see Glikson, 1982; Windley, 1977) and beyond the

scope of this comparison. However, one of the issues is whether or not greenstone belts are relics of a primordial basic crust, or are products of an ensialic extensional process. The evidence from the Vestfold Hills clearly shows that greenstone belt volcanic compositions can be produced beneath a sialic crust ~35 km thick, providing evidence for the latter model. However, based on the theoretical study of heat transfer from magmas traversing continental crust (Huppert & Sparks, in prep.) all the ca.2420 Ma dykes (with the possible exception of the ring dyke) will freeze prior to reaching the surface due to their narrow widths. Thus, although magma compositions comparable to those in greenstone belts can be produced in a subcontinental setting, eruption may only be possible when the liquids traverse thin continental (<<35 km) or oceanic crust, unless the width of the feeder dykes are substantially increased from that found in the Vestfold Hills.

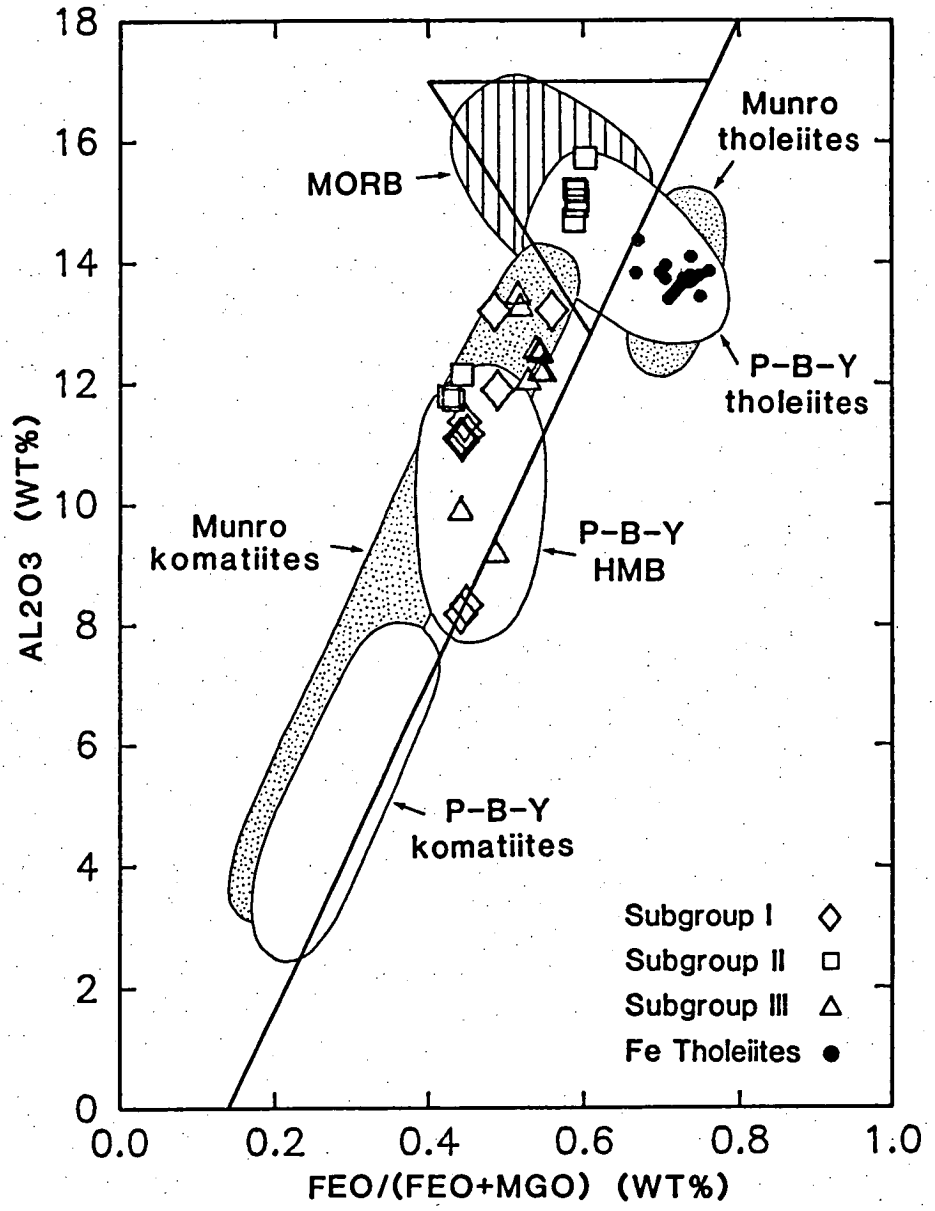

Figure 5.32

Comparison of Archean Mg-rich and Fe-rich greenstone belt associations, with Vestfold Hills dyke compositions.

Diagram boundaries (komatiites, transitional compositions, tholeiites) from Nesbitt et al. (1979). Munro data from Arndt et al. (1977). MORB as in Fig. 5.14.
P-B-Y (Pilbara, Barberton, Yilgarn) from Glikson (1983).
HMB = High-Mg basalt.

CHAPTER 6

PETROLOGY AND GEOCHEMISTRY OF THE CA.1360 MA THOLEIITES

CHAPTER 6

PETROLOGY AND GEOCHEMISTRY OF THE CA.1360 MA THOLEIITES

INTRODUCTION

Emplacement of the most voluminous Proterozoic dyke suite in the Vestfold Hills is dated at 1362 ± 108 Ma (Collerson & Sheraton, in press). All of these dykes, sampled in this study, have near-vertical dips and a prominent N-S component in their strike orientation. Dyke widths are variable, but are commonly 5-15 m, with a prominent, weather-resistant chilled margin up to to 15-20 cm wide. The coarser grained dyke centres are very susceptible to mechanical weathering processes and are commonly honey-combed and friable. Narrow, and therefore fine grained dykes as well as the chilled margins of wider dykes have a steel blue-grey colour in outcrop; the latter dykes have brownish-grey coarse grained interiors.

The very broad range in FeO/MgO of the dykes composing the ca.1360 Ma suite is shown in Fig. I2.1. Mg-values range from 57 to 33, over which FeO^T increases from 12 to 18%, while SiO_2 ranges by ~5%, highlighting the tholeiitic, iron-enrichment trend of the suite. Silica saturation is variable, ranging from 26% normative olivine to 1.3% normative quartz (FeO^T), with no readily apparent tendency to correlate with FeO/MgO (Fig. 6.4). Plagioclase + clinopyroxene ± olivine are phenocryst phases with very rare orthopyroxene (Fig. 6.4).

Also outcropping in the Vestfold Hills is an uncommon, but extensive suite of narrow (<1 m) alkaline dykes. These are primitive, olivine ± clinopyroxene-bearing dykes (Mg-value up to 74) often with accessory mica phenocrysts and carbonate ocelli. These dykes also have a general N-S orientation, and are readily weathered; often the only evidence for the existence of an alkaline dyke is a narrow rubble-filled straight trench within more weather-resistant gneisses.

Prior to this study, the alkaline dykes were correlated with those outcropping in the Prince Charles Mountains (Sheraton, 1983), and considered to be associated with the fragmentation of Gondwanaland during the Mesozoic (Collerson & Sheraton, 1986). However, field work undertaken for this thesis has revealed three localities where alkaline dykes are crosscut by ca.1360 Ma tholeiites, logically indicating their emplacement during the Proterozoic.

This chapter will discuss the ca.1360 Ma tholeiite suite only. Whole rock major and trace element analyses of the alkaline dykes are reported in Appendix 2, but will not be discussed.

6.1 INTERSECTING RELATIONSHIPS WITHIN THE THEOLIITE SUITE

The main objective in detailing the intrusive relationship between dykes sampled for this thesis was to relate the chemical evolution of an individual suite with time. This approach revealed quite complicated relationships and igneous processes within, and between the several groups of the ca.2420 Ma suite (see Chapter 5). The ca.1360 Ma tholeiites will also be viewed by first integrating broad geochemical characteristics with field determined, intrusive relationships.

A general view of the chemical trend in the ca.1360 Ma tholeiites is shown in Fig. 6.1. The trend suggests the chemical variation within the suite may be the result of a simple fractionation process producing an increase in the moderately incompatible element, Ti, during differentiation (increasing FeO/MgO). Fig. 6.1 shows that the chemical trend of increasing TiO_2 and FeO/MgO is defined by clusters of analyses, with each cluster separated by a small gap in FeO/MgO. This observation is emphasized in a histogram (Fig. 6.2) where a geometric function has been used to obtain a geologically meaningless FeO/MgO value for each sample by projecting the actual FeO/MgO in X-Y space to the x-axis (TiO_2 = 0) along a line perpendicular to the fractionation trend. The resulting histogram of the calculated FeO/MgO shows several distinct sample clusters.* For the purpose of this and following discussion, these clusters, and samples which plot between them, are labelled as groups 1-9. For the sake of categorizing the chemical analyses in Appendix 2, two samples which do not readily fall in groups 1-9 are classed as group 10. One possible hypothesis to explain the clustering of analyses is that the clusters represent pulses of liquid extracted sequentially from a single fractionating magma body. Assuming, then, that each group was emplaced during a single event, the intrusive relationships are considered.

All documented intersecting relations involving dykes of group 5, for example, are shown in Fig. 6.3A. Dykes with crosscutting relationships are joined by an arrow which points to the younger dyke. The figure illustrates that intersecting relationships have been observed where group 5 dykes crosscut not only dykes with more primitive compositions

---

* It should be noted here that each analysis used in Fig. 6.2 is from a separate dyke.

(groups 2, 3) as anticipated, but also dykes with more evolved compositions (group 8). Furthermore, other dykes, defined on the basis of TiO_2-FeO/MgO into groups 2, 3 and 8, were emplaced after group 5, which is interpreted as indicating the simultaneous emplacement of groups 2, 3, 5, and 8. Based on these relationships, at least four separate magma bodies seem to be required to explain the temporally related, yet compositionally distinct dyke groups associated with group 5 intersections. Similar observations and conclusions result from examining other groups in an equivalent manner. A further example is shown in Fig. 6.3B, where group 8 dykes are shown to have been emplaced contemporaneously (i.e. pre-date and post-date) with more mafic group 5 and group 7 dykes, but pre-date evolved group 9 compositions. Thus, the general trend of increasing TiO_2 with differentiation (Fig. 6.1) within the suite cannot be explained by a simple fractionation process acting on a single batch of magma. Instead, the integrated field and geochemical evidence apparently requires multiple, independently evolving magma bodies.

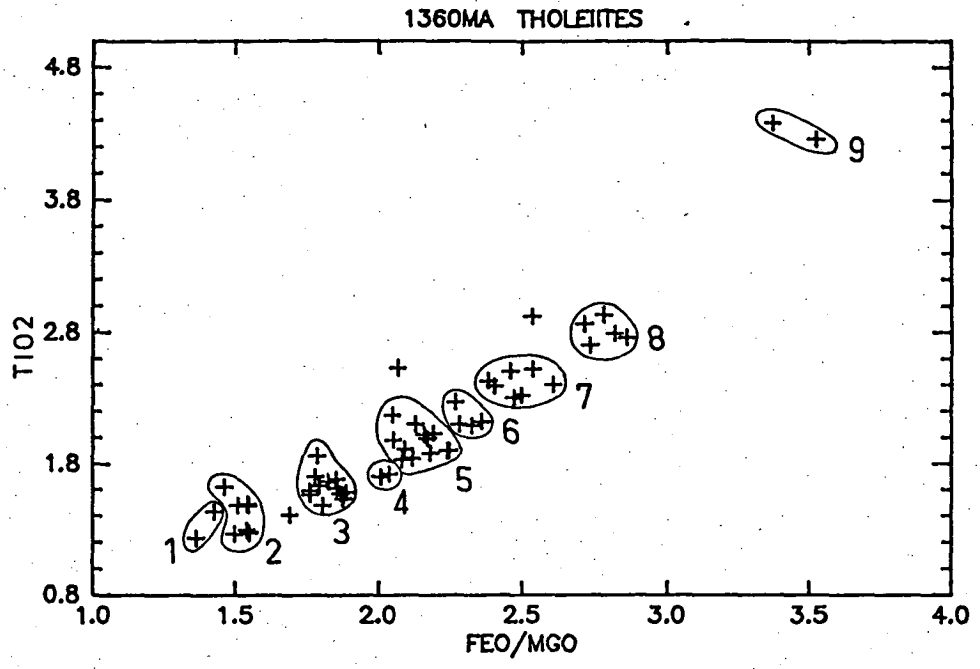

Figure 6.1
FeO/MgO-TiO_2 relationships of the ca.1360 Ma dykes. Numbers correspond to group designations of the circled analyses. (WT%)

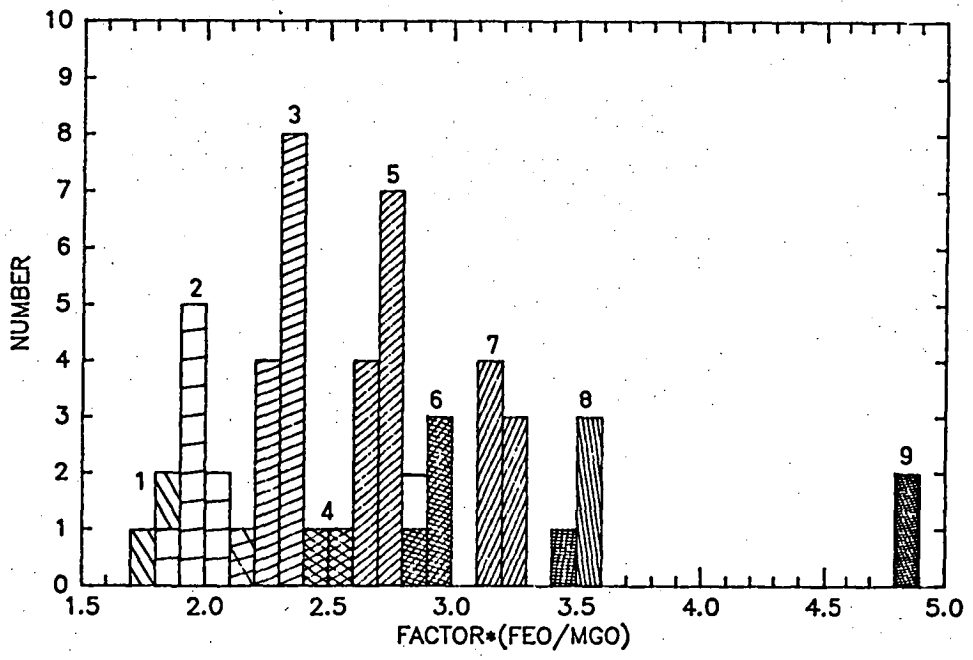

Figure 6.2
Histogram illustrating the clustering of analyses based on FeO/MgO groups of Fig. 6.1 (above). "Factor" refers to a geometric expression used to project the analyses of Fig. 6.1 to a FeO/MgO value where TiO_2 = 0. (WT%)

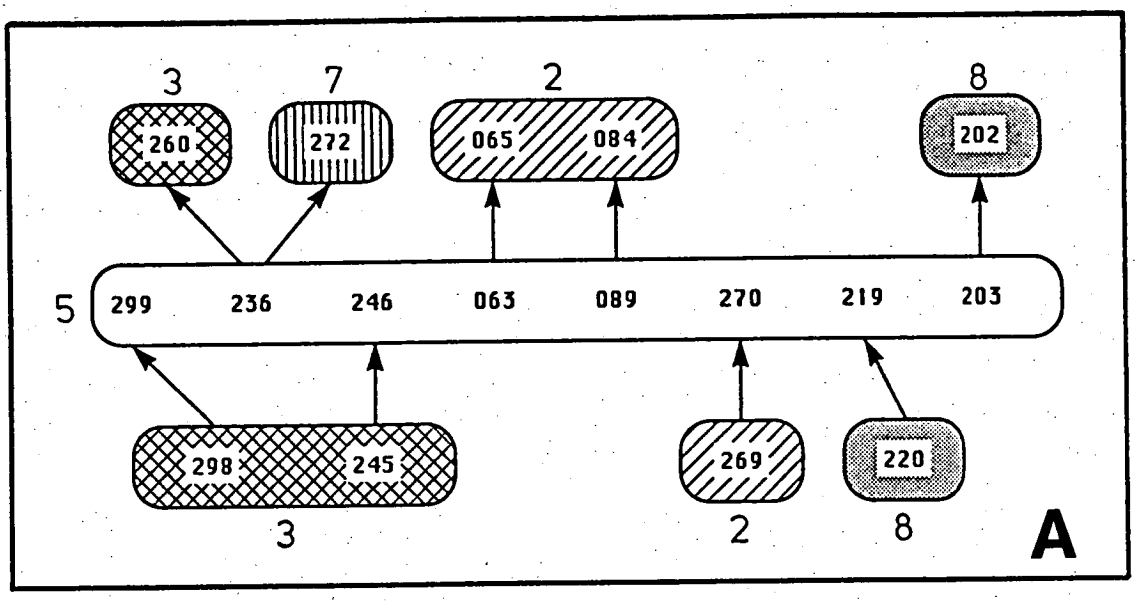

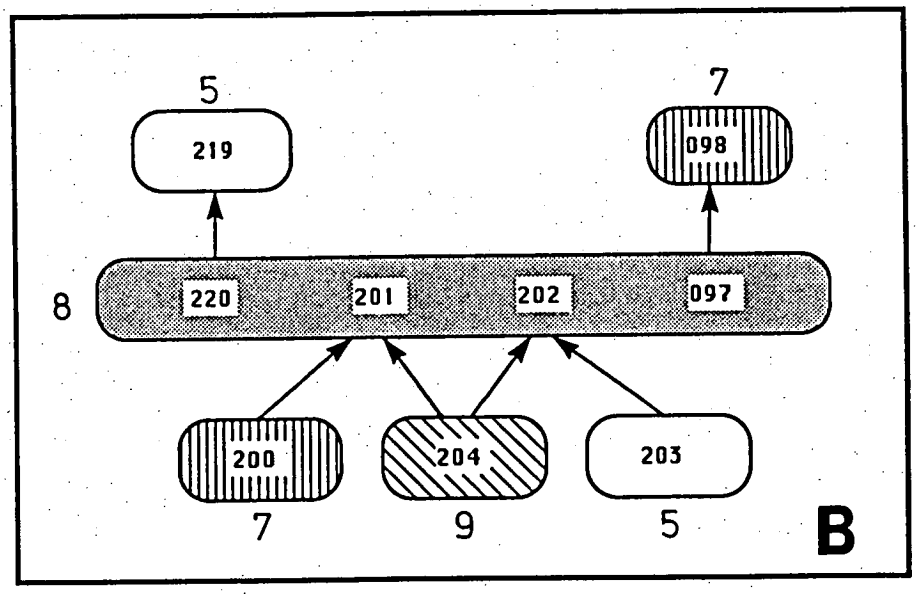

Figure 6.3

Summary of field determined crosscutting relationships involving dykes of group 5 (A) and group 8 (B). Arrows join sample numbers of intersecting dykes and point to the younger. Patterns correspond to individual groups and are consistent between figures.

6.2 PETROGRAPHY AND CRYSTAL CHEMISTRY OF THE THOLEIITE DYKES

6.2.1 PETROGRAPHY

It was shown in the previous section that the differentiation trend of the ca.1360 Ma tholeiites (Fig. 6.2) was defined by clusters of analyses with similar FeO/MgO ratios. Furthermore, it was noted in the introduction to this chapter that despite the very broad range of Mg-values in the analysed samples, silica saturation does not correlate with the degree of differentiation, a feature also noted by Collerson & Sheraton (in press). In Fig. 6.4, the extent of silica saturation (normative olivine or quartz; FeO^T) is plotted against the geometrically determined FeO/MgO ratio of each sample. It is found that the analyses of each group (Figs 6.1, 6.2) span a range of silica saturation from olivine normative to near-saturated or slightly quartz normative compositions. The diagram displays a chaotic arrangement of analyses if the group boundaries are ignored, and a single fractionation sequence assumed. Contoured onto Fig. 6.4 is a petrographic summary illustrated by boundaries marking the appearance of plagioclase, clinopyroxene and disappearance of olivine, in the phenocryst assemblage

It has already been shown from the crosscutting relationships, that samples comprising this suite are not simply related, although there is no textural evidence for the divisions as found in the ca.2420 Ma suites (Chapter 5). Plagioclase phenocrysts are found in all samples studied. The most primitive chilled margin samples of group 2(15-17% normative olivine) carry euhedral microphenocrysts of olivine, with serriate-textured, felted plagioclase. Many of the plagioclase crystals are hollow, and it is considered that these liquid compositions have only just reached plagioclase saturation prior to quenching. The most primitive group 1 sample (18.5% normative olivine) in contrast, has subhedral plagioclase phenocryst laths up to 2 mm in length.

As shown in Fig. 6.4, the phenocryst assemblage of the tholeiitic suite is dominated by clinopyroxene and plagioclase. In chilled margin samples, plagioclase + clinopyroxene form single crystals as well as glomeroporphyritic clots, in an opaque-rich groundmass, and grade to subophitic textures towards the centre of the dykes. In olivine-bearing samples, all three phases may be intergrown, signifying their co-precipitation.

The "clinopyroxene-in" boundary is drawn through samples of groups 2, 3 and 9, and sample 299. Excluding group 2 (see above), these chilled margin samples have euhedral olivine and plagioclase laths, with <1% of the

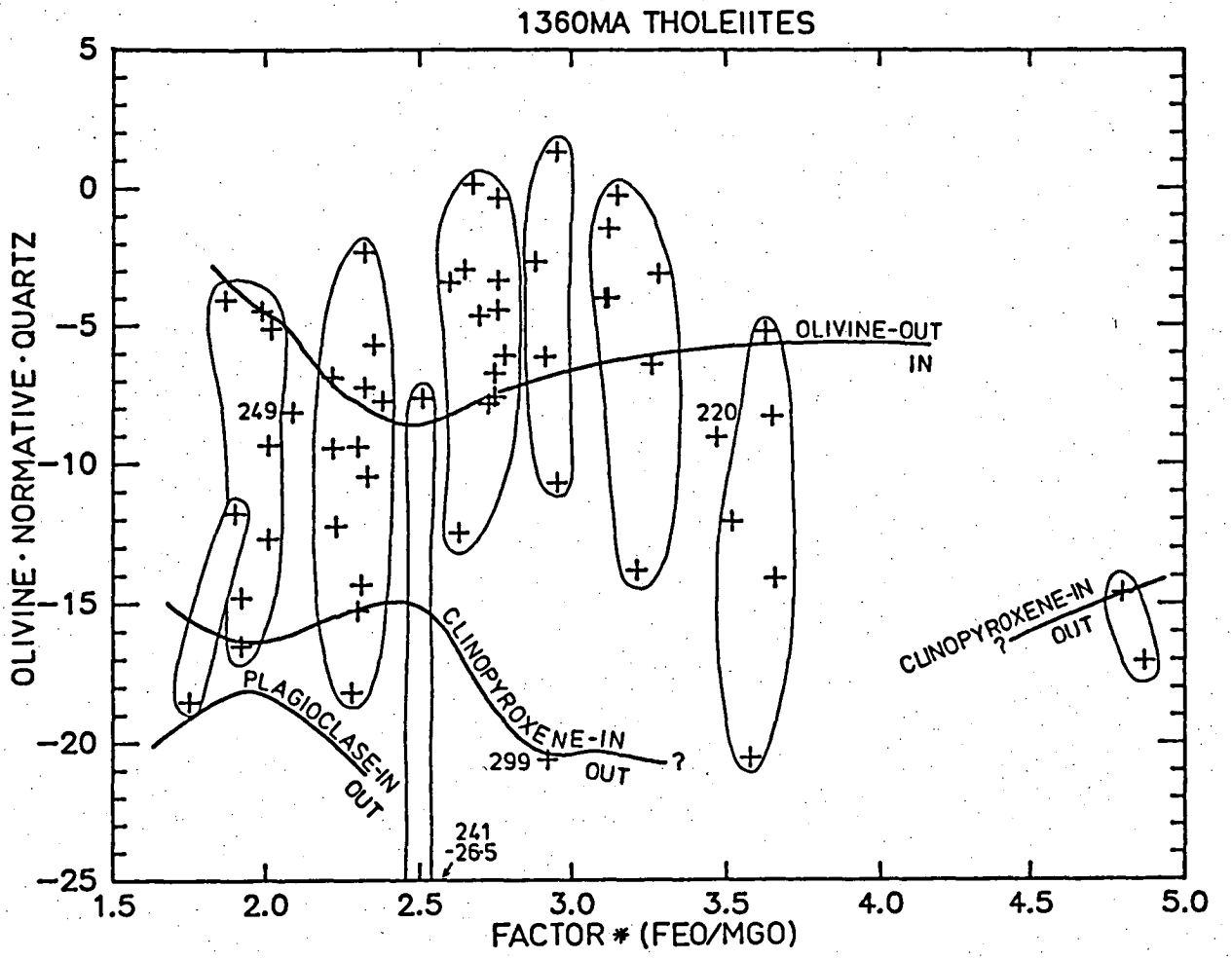

Figure 6.4

Analyses of samples defining FeO/MgO based groups (Figs 6.1 and 6.2) plotted with respect to silica saturation. Quartz normative compositions have positive values, olivine normative compositions have negative values. Contours summarize the petrographic features of chilled margin samples. The clinopyroxene boundary is not continuous as the most mafic group 8 sample is recrystallized, and consequently the phenocryst assemblage is unclear.

phenocryst assemblage composed of anhedral clinopyroxene. Sample 400 (group 1) is the only chilled margin not containing clinopyroxene phenocrysts.

Pyroxene phenocrysts, when not intergrown with other phases, are in general, elliptical to euhedral, and commonly display a fine, detailed variety of sector zoning. When crystals are viewed normal to the b-axis, opposite sectors are found to be composed of numerous columnar sections radiating from the centre of the crystal and extending to the grain boundary. Extinction in each sector follows a fan-like pattern. In some examples, sectors with a base parallel to the c-axis are convex towards he liquid, extending past the crystal width defined by sector bases normal to the c-axis. Opposing sectors are compositionally distinct as described by Wass (1973) and Ferguson (1973); an example (sample 65011) is listed in Table 6.2. Low SiO_2 sectors have high Ti, (Al+Cr) and Ca, while high SiO_2 sectors have low Ti, (Al+Cr) and Ca. As Mg-values are essentially constant the substitution mechanism is clearly dominated by the $CaTiAl_2O_6$ molecule. Compositionally, these colourless sector-zoned pyroxenes are much less extreme in their chemical variation than the Ti-augites studied by Wass (1973) and Ferguson (1973), though in absolute terms, TiO_2 may reach 1.5% and Al_2O_3 > 7% in the Vestfold Hills examples.

Sector zoning is believed to be the result of rapid crystallization relative to ionic diffusion in the liquid (Wass, 1973) such that the crystallographic growth direction plays an important role in controlling whether or not Si, or Al-rich substitutions are incorporated. This view is supported in the present study by the absence of sector zoning in slowly cooled, subophitic textured samples. Yagi & Onuma (1967; quoted in Wass, 1973, and Ferguson, 1973) have shown that incorporation of $CaTiAl_2O_6$ molecule is enhanced at low pressure. This is consistent with the relatively low emplacement pressure inferred for this suite (4-5 kbar; Chapter 1) and with the absence of sector zoned pyroxenes in the chilled margins of the ca.2420 Ma Fe-tholeiite emplaced at 7-8 kbar (Chapter 5).

The olivine-out boundary is somewhat speculative in that some samples contain only a few, highly altered and irregularly shaped olivine fragments. These olivines are considered xenocrysts in the sense that they are believed not to have crystallized from liquid composition of the bulk rock, but are relict from higher temperature conditions. Only rarely are olivine phenocrysts unaffected by at least partial oxidation to magnetite-orthopyroxene symplectites. In some examples (samples 400 and 292) well developed fibrous amphibole coronas have formed between adjacent olivine and plagioclase. A narrow, fibrous inner shelf of magnetite-free

orthopyroxene is commonly visible next to the olivine, with the wider amphibole shell, sometimes peppered with fine spinel, contacting the plagioclase. As orthopyroxene is a stable phase in both corona and symplectite, and is magnetite-free in the corona, these two textures must not be coincident in their formation as it is unlikely for an amphibole + orthopyroxene corona to develop along a secondary orthopyroxene + magnetite + plagioclase boundary. Thus the oxidation and replacement of olivine by orthopyroxene + magnetite symplectites must post-date the formation of the corona.

6.2.2 CRYSTAL CHEMISTRY

Phenocryst compositions are plotted in Figs 6.5 and 6.6, and the data listed in Tables 6.1 and 6.2. Microprobe studies of this suite have focussed primarily on porphyritic chilled margin samples in general, and did not attempt to define phenocryst characteristics of each FeO/MgO group. Samples from groups 2, 3 and 7 were the most extensively studied; group 2 and group 3 due to many chilled margins with relatively fresh olivine, and group 7 sample 206 was examined in detail as it was chosen for experimental studies (Chapeter 1).

The compositional trends in the plagioclase phenocrysts (Fig. 6.5A) are as expected from a suite of rocks derived from a single magmatic series. Plagioclase compositions are the most calcic in groups 2 and 3 (An_{86-87}) and become increasingly sodic and potassic to group 8 ($\sim An_{62}$). All plagioclase crystals examined display varying degrees of chemical zoning, but in each case the zoning was normal, i.e. Ca-rich cores to more Na-rich rims. Plagioclase "xenocrysts" identified by mottled, resorbed cores, are often reversely zoned. These crystals can be cognate, high pressure phases (see Section 1.3.2) and not the result of magma mixing, a process often invoked to explain similar textures (Tsuchiyama, 1985).

The fractionation trend defined by the pyroxenes is one of a more rapid decrease in CaO with a relatively slight increase in FeO, compared to the Skaergaard clinopyroxene trend (Fig. 6.5C). However, in the latter case, the clinopyroxenes are in equilibrium with orthopyroxene, and define one limb of the pyroxene solvus. Orthopyroxene phenocrysts do not co-exist with clinopyroxene in the ca.1360 Ma tholeiite suite (except in sample 207, see Chapter 1) and thus the clinopyroxenes are not confined to pyroxene solvus, Ca-Mg-Fe compositions.

Pyroxene compositions (Table 6.2) become, in general, more Fe-rich and Ca-poor from groups 2-8, as anticipated (Fig. 6.5B). Detailed core-rim analyses from groups 2 and 3, however, cover most of the chemical range

observed within the entire suite (note, pyroxenes from group 9 were not analysed, but should be quite Fe-rich).

Two differing fractionation trends are suggested from the analyses of groups 2 and 3 compared to 5-8 (Fig. 6.5B). Overall, groups 2 and 3 clinopyroxenes decrease in FeO and CaO while clinopyroxenes in groups 5-8 show a narrow, almost constant, range of FeO/MgO over a broad range of CaO, resulting in a near-vertical trend in the pyroxene quadrilateral. Similarly, Al_2O_3 has a broad range of values over a narrow FeO/MgO in groups 5-8 (Fig. 6.6) while groups 2 and 3 display a moderate negative correlation between these components. The coupling of variable CaO and Al_2O_3 with constant FeO/MgO in groups 5-8 indicates $CaTi_2AlO_6$ and/or $CaAl_2SiO_6$ substitutions, as discussed above. Pyroxenes in groups 2 and 3 are also sector zoned (see Table 6.2, sample 65011) and the spread in Cao on Fig. 6.5C is probably due to this feature. The contrasting trends are believed due only to the lack of extensive analysis of samples in groups 5-8; four samples were analysed in each of groups 2 and 3, two samples in groups 5 and 7, and one in groups 6 and 8).

Olivine compositions are also plotted in Fig. 6.5B, and listed in table 6.2. The analyses span a wide range of compositions from Mg_{81} to Mg_{36}. The Fe-rich compositions are from olivine rims in the subophitic, group 4 sample 241. Due to the generally altered nature of the olivines, extensive analyses from individual samples could not be made, and thus crystal/liquid evaluation was not possible.

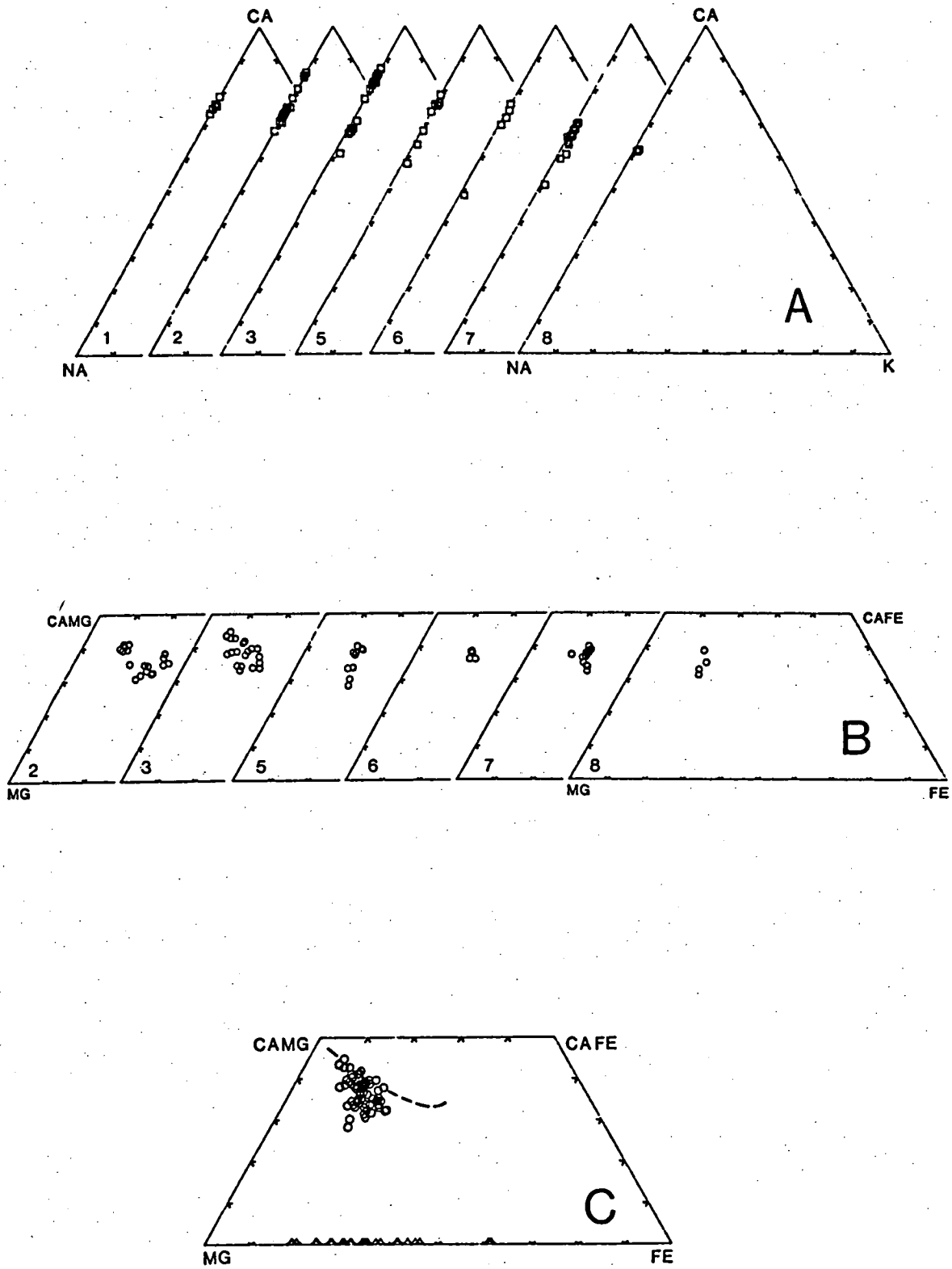

Figure 6.5

Phenocryst compositions plotted according to FeO/MgO group designation (Figs 6.1 and 6.2); plagioclase (A), clinopyroxene (B) and olivine (C) triangles. All clinopyroxene phenocryst analyses are shown in C, and compared to the clinopyroxene compositional trend of Skaergaard (dashed line).

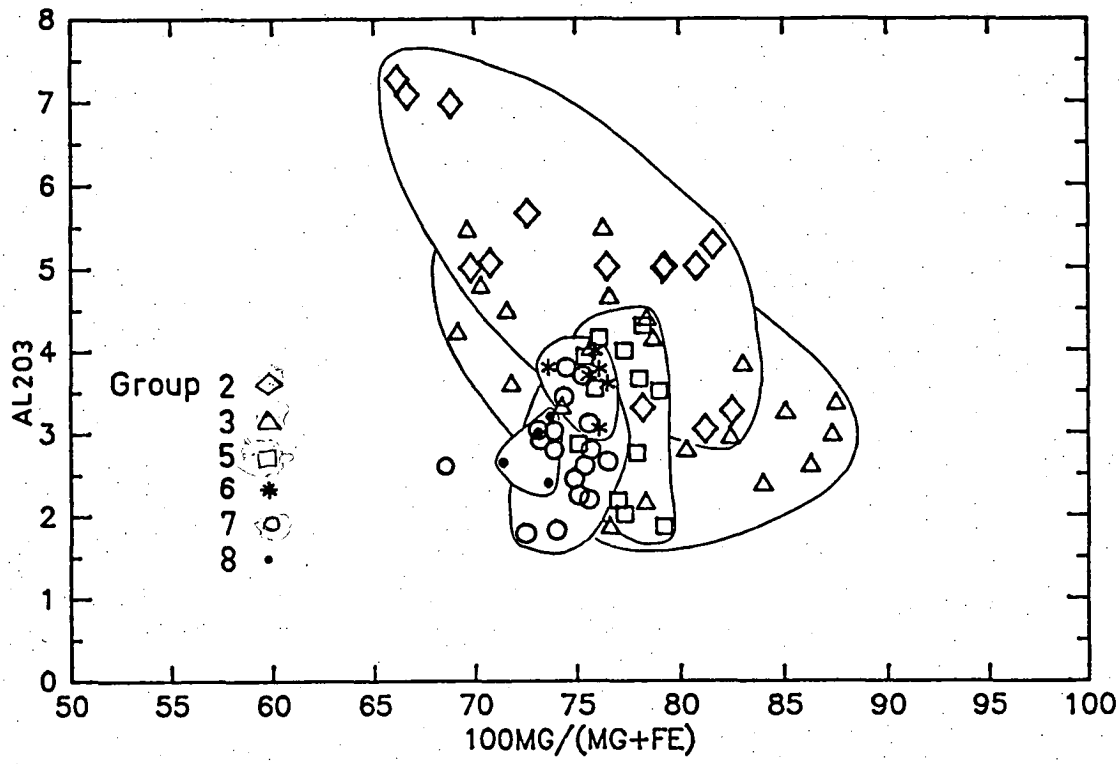

Figure 6.6

Al_2O_3 contents of group defined clinopyroxene phenocrysts plotted versus 100 Mg/(Mg+Fe). See text for discussion.

6.3 WHOLE ROCK GEOCHEMISTRY

6.3.1 MAJOR ELEMENTS

Some major element geochemical features of the ca.1360 Ma tholeiites have been introduced in previous sections. FeO/MgO-TiO_2 relationships (Fig. 6.1) define a continuous trend of increasing TiO_2 with differentiation, suggesting the dyke suite may be the result of fractionation from a single primitive liquid. However, this simple explanation cannot be substantiated considering the erratic variation in silica saturation with respect to the degree of differentiation (increasing FeO/MgO; Fig. 6.4). Furthermore, the FeO/MgO-TiO_2 trend was found to be composed of clusters of individual analyses having comparable FeO/MgO ratios. Dyke intersections, relating individual clusters, are clear in illustrating that the chemical variation within the suite cannot be one of simple crystal fractionation from a single primitive liquid.

In this section, Pearce molecular ratio diagrams (Pearce, 1968; see Section 5.12.1) are used to examine the major element geochemistry of the tholeiite suite (Appendix 2) with respect to the groups defined in Fig. 6.1 and 6.2. Yttrium is used as a normalizing component, as it is considered to be an incompatible element during crystal fractionation processes that do not include garnet (Pearce & Norry, 1979). In order to simplify the resulting figures, groups 4, 6 and 10 (a total of eight samples) have been excluded. With three exceptions (Samples 269, 298, 299) the analyses which define the clusters of Fig. 6.1 remain as coherent groups in the variation diagrams.

As shown in Fig. 6.7A, the groups define a smooth, curved trend on a plot of MgO/Y versus SiO_2/Y, concave towards the MgO/Y axis. With respect to the vector inset, the curve can be interpreted as defining a simple magmatic evolutionary path where the more mafic samples (high SiO_2/Y; group 1) define an olivine controlled fractionation trend. With progressive evolution of the liquid composition, the precipitating assemblage becomes increasingly dominated by the phases clinopyroxene + plagioclase, resulting in the continuous change of slope on the Pearce diagram.

Similarly, the groups also define a continuous curved trend on the Al_2O_3/Y variation diagram (Fig. 6.7B), where plagioclase dominated control on the extraction of Al_2O_3 from mafic compositions is clearly indicated. The curvature may be due to not only a change in composition of the precipitating plagioclase, but also the inclusion of an increasing

TABLE 6.1
PLAGIOCLASE ANALYSES FROM THE ca.1360 Ma THOLEIITES.

SAMPLE	65400	65255	65084	65256	65256	65035	65247	65098X	65018	65202
GROUP	1	2	2	3	3	5	5	6	7**	8
SIO2	49.45	47.87	50.95	47.21	52.26	49.60	51.45	51.44	53.21	53.34
AL2O3	32.68	33.06	31.13	33.41	30.40	32.24	30.33	30.81	29.51	29.62
FEO		0.31	0.40	0.32	0.26	0.42	0.48	0.60	0.54	0.52
MGO			0.22	0.18			0.18			
CAO	15.56	17.21	14.28	17.47	13.42	15.00	13.95	13.78	12.71	12.29
NA2O	2.31	1.54	3.02	1.41	3.52	2.49	3.45	3.24	3.90	4.01
K2O					0.14	0.13	0.16	0.12	0.13	0.22
SI	2.2530	2.1959	2.3181	2.1691	2.3705	2.2659	2.3441	2.3402	2.4116	2.4155
AL	1.7550	1.7876	1.6696	1.8094	1.6253	1.7360	1.6287	1.6521	1.5760	1.5805
FE		0.0121	0.0151	0.0124	0.0098	0.0159	0.0182	0.0230	0.0206	0.0199
MG			0.0146	0.0126			0.0123			
CA	0.7593	0.8461	0.6963	0.8599	0.6523	0.7342	0.6809	0.6719	0.6169	0.5961
NA	0.2041	0.1373	0.2665	0.1256	0.3098	0.2204	0.3049	0.2856	0.3429	0.3518
K					0.0079	0.0076	0.0095	0.0072	0.0074	0.0127
TOTAL	4.9714*	4.9789	4.9803	4.9889	4.9756	0.9800	4.9986	4.9800	4.9754	4.9764
CA#	78.8	86.0	72.3	87.3	67.2	76.3	68.4	69.6	63.8	62.1

CA# = CA/(CA+NA+K)

** SEE ALSO TABLE 1.2 FOR PLAGIOCLASE ANALYSES FROM SAMPLE 65206 (GROUP 7).

* LOW TOTALS DUE TO SLIGHT ERROR IN SIO2 CALIBRATION BUT DOES NOT AFFECT CA# (SEE SECTION 1.3.2).

TABLE 6.2
CLINOPYROXENE AND OLIVINE ANALYSES FROM THE ca.1360 Ma THOLEIITES##.

SAMPLE	65255	65255	65074	65011**	65011	65011	65011	65247	65247	65202	65202	65400	65255	65241
GROUP	2	2	2	3	3	3	3	5	5	8	8	1	2	4
PHASE	CPX	CPX	CPX	CPX	CPX	CPX	CPX	CPX	CPX	CPX	CPX	OLIV	OLIV	OLIV
SIO2	49.74	52.19	51.73	50.26	50.71	52.97	52.47	50.42	52.15	51.25	50.74	36.90	38.85	32.94
TIO2	0.74	0.38	0.22	0.98	0.92	0.32	0.36	0.77	0.43	0.51	0.78			
AL2O3	5.28	3.30	2.86	4.37	4.12	1.84	2.14	4.30	1.86	2.39	3.19			
CR2O3	0.91	0.58	0.33	0.47	0.42		0.29	0.85	0.34	0.19	0.34			
FE2O3*	1.31			0.75	0.40		0.66	0.57	1.59	1.66	0.93			
FEO	6.53	9.19	12.71	7.68	7.70	9.80	8.95	7.96	8.69	10.87	9.91	26.62	17.63	48.85
MNO										0.29		0.37		0.77
MGO	16.22	18.51	15.54	15.61	15.95	17.98	18.16	16.00	18.56	17.02	15.54	35.96	43.52	17.29
CAO	19.29	15.85	16.61	19.88	19.78	17.04	16.97	19.13	16.38	15.81	18.55	0.15		0.14
SI	1.8335	1.9124	1.9300	1.8601	1.8729	1.9498	1.9303	1.8646	1.9207	1.9071	1.8899	0.9830	0.9878	0.9884
TI	0.0205	0.0105	0.0062	0.0272	0.0256	0.0104	0.0099	0.0213	0.0119	0.0144	0.0219			
AL	0.2292	0.1425	0.1256	0.1908	0.1795	0.0796	0.0925	0.1875	0.0808	0.1047	0.1401			
CR	0.0265	0.0168	0.0097	0.0137	0.0124		0.0085	0.0247	0.0098	0.0057	0.0101			
FE3+	0.0362			0.0209	0.0110		0.0184	0.0160	0.0442	0.0466	0.0262			
FE2+	0.2012	0.2818	0.3966	0.2376	0.2379	0.3017	0.2754	0.2461	0.2676	0.3381	0.3087	0.5931	0.3750	1.2256
MN										0.0091		0.0083		0.0197
MG	0.8910	1.0111	0.8641	0.8612	0.8780	0.9866	0.9963	0.8819	1.0189	0.9440	0.8628	1.4283	1.6494	0.7733
CA	0.7618	0.6222	0.6639	0.7885	0.7828	0.6719	0.6687	0.7579	0.6461	0.6302	0.7403	0.0043		0.0046
TOTAL		3.9973	3.9961									3.0087	3.0122	3.0116
MG#	81.6	78.2	68.5	78.4	78.7	76.6	78.3	78.2	79.2	73.2	73.7	70.7	81.5	38.7
CA#	41.1	32.5	34.5	41.8	41.2	34.3	34.5	40.2	33.4	33.0	38.7			

MG# = 100MG/(MG+FE). CA# = 100CA/(CA+MG+FE).
* BASED ON 4.000 CATIONS.
** THESE FOUR ANALYSES ARE FROM THE SAME CRYSTAL, BUT SEPARATE SECTORS.
SEE TABLE 1.2 FOR CLINOPYROXENE ANALYSES FROM SAMPLE 65206 (GROUP 7).

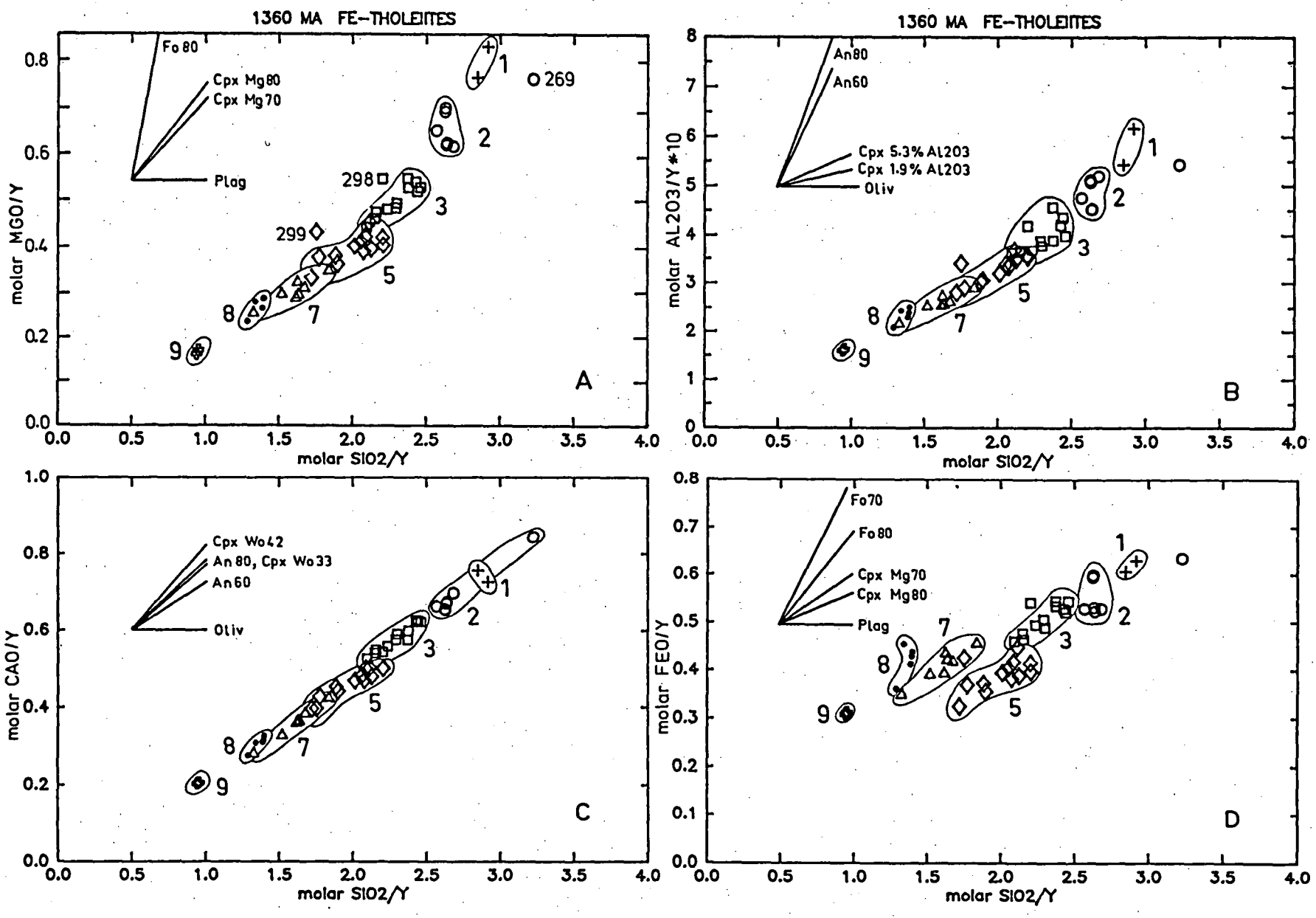
1360 MA FE-THOLEIITES
Fo80
Cpx Mg80
Cpx Mg70
Plag
269
298
299
molar MGO/Y
molar SIO2/Y
A
1360 MA FE-THOLEIITES
An80
An60
Cpx 5.3% Al203
Cpx 1.9% Al203
Oliv
molar AL203/Y*10
molar SIO2/Y
B
Cpx Wo42
An80, Cpx Wo33
An60
Oliv
molar CAO/Y
molar SIO2/Y
C
Fo70
Fo80
Cpx Mg70
Cpx Mg80
Plag
molar FEO/Y
molar SIO2/Y
D

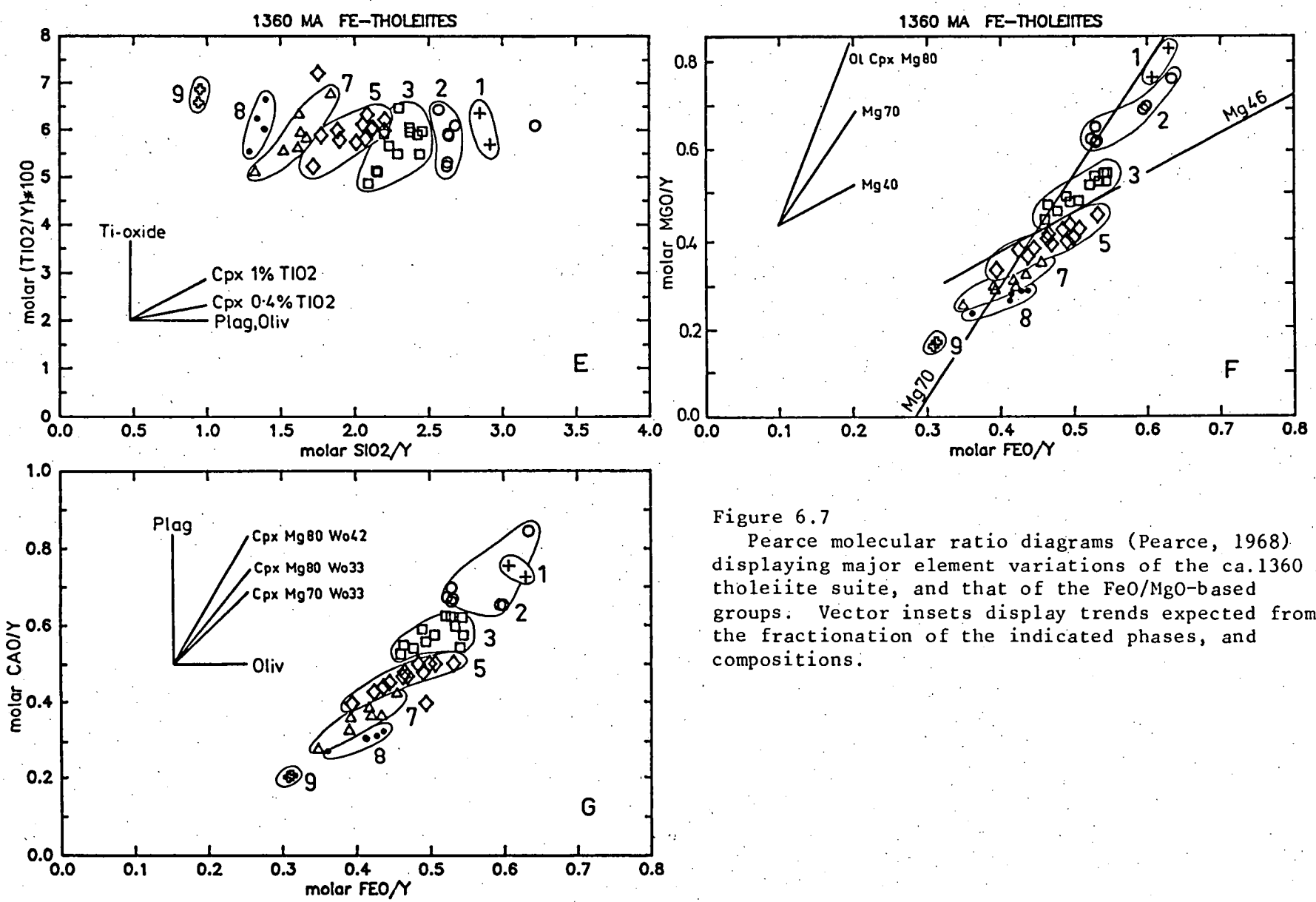

Figure 6.7
Pearce molecular ratio diagrams (Pearce, 1968) displaying major element variations of the ca.1360 Ma tholeiite suite, and that of the FeO/MgO-based groups. Vector insets display trends expected from the fractionation of the indicated phases, and compositions.

proportion of olivine or clinopyroxene in the fractionating assemblage. However, the MgO/Y variation diagram illustrates the progressive decrease of olivine involvement with differentiation. Thus, the curvature in the Al_2O_3/Y trend is due, in part, to the increasing importance of clinopyroxene fractionation through the magma series. In contrast, a straight differentiation path is shown on the CaO/Y-SiO_2/Y diagram (Fig. 6.7C). The vector inset shows, however, that CaO/SiO_2 ratio varies only slightly for a wide variety of clinopyroxene and plagioclase compositions, and the chemical variation in CaO is thus consistent with that of MgO/Y and Al_2O_3/Y.

The interpretation dictated by the geochemical variations in MgO-CaO-Al_2O_3/Y versus SiO_2/Y is complementary to the petrographic observations (see Fig. 6.4) for a crystallization sequence within the studied samples of oliv, oliv + plag, oliv + plag + cpx, plag + cpx. Without prior knowledge of the field relationships, the Pearce diagrams discussed thus far, could provide strong evidence indicating the ca.1360 Ma tholeiite suite comprised a single magmatic lineage related by fractionation of varying proportions of oliv-plag-cpx. However, the variation in FeO/Y and TiO_2/Y versus SiO_2/Y (Fig. 6.7D and 6.7E) do not support the MgO-CaO-Al_2O_3 based conclusions for a single differentiation process relating the chemical variation of the tholeiite suite. Groups 1, 2, 5 and perhaps 3 (Fig. 6.7D) could possibly be related through a fractionation mechanism involving the phenocryst phases. However, the average of each of groups 5, 7, 8 and 9 have a near-constant FeO/Y, with decreasing SiO_2/Y. Restated, these latter groups display a progressive enrichment in FeO with differentiation (decreasing SiO_2/Y). The vector inset shows that these groups can only be related at low pressures by extensive monomineralic fractionation of a FeO-free phase, such as plagioclase (i.e. Fe was incompatible). This implication cannot be supported by the petrography, nor the CaO/Y and Al_2O_3/Y variation diagrams. The FeO/Y variation **within** each Fe-enriched group with respect to SiO_2/Y is however, generally consistent with fractionation of the phenocryst assemblages.

Considering the tholeiite suite as a whole, the TiO_2/Y variation has a near-horizontal trend when plotted against SiO_2/Y (Fig. 6.7E, m = -0.14) suggesting that Ti acted essentially as an incompatible element for the differentiation process which relates the groups 1-9. Individual groups, in contrast, display a strong positive correlation between SiO_2 and TiO_2. The trends within groups require the extraction of TiO_2 in excess of the maximum upper limit possible assuming all clinopyroxene has ~1% TiO_2, and implies precipitation of a Ti-rich oxide. Similar features were found in

the ca.2320 Ma tholeiites (Section 5.12.1) where it was concluded, based on the absence of Ti-oxides in chilled margin samples and the Ti-rich phase solubility studies by Green & Parson (1986), that precipitation of a Ti-rich phase could not be responsible for the observed chemical features. An unspecified secondary process acting in conjunction with crystal fractionation was indicated. Similarly in the ca.1360 Ma tholeiites, the intra-group variation in TiO_2 cannot be accounted for by fractionation of a Ti-rich oxide as they are not found in chilled margin samples nor are these compositions sufficiently TiO_2-rich to be saturated in a Ti-rich phase. A presently unidentified mechanism is required to explain the intra-group variation in TiO_2.

In Fig. 6.7F and 6.7G the variation in MgO/Y and CaO/Y is examined with respect to FeO/Y. In both figures, the chemical variation in the tholeiite suite can be broadly related to fractionation of the phenocryst phases and their compositions. However, individual groups display differentiation paths that require separation of very Fe-rich olivine + clinopyroxene compositions. Furthermore, the curved MgO/Y-SiO_2/Y trend of Fig. 6.7A is poorly developed in Fig. 6.7F, though changes in Fe/Mg of separating phases during differentiation should be very evident on this diagram. The absence of a curved trend indicates that, if the tholeiite suite can be considered as a whole (based on SiO_2, MgO, CaO and Al_2O_3 variations) then differentiation involved a progressive increase in FeO, beyond that normally associated with crystal fractionation in tholeiitic magmas.

In summary, the chemical variation in the major elements SiO_2, Al_2O_3, MgO and CaO within the tholeiite suite is systematic, and complementary to the petrography. This suggests that a simple fractionation mechanism involving olivine, plagioclase and clinopyroxene controls the compositional range between groups but only broadly controls the chemical compositions within individual groups. In a major element sense, the data indicate that the multiple sources, apparently required by the field relationships, were compositionally indistinct. However, examination of FeO/Y with respect to differentiation (decreasing SiO_2/Y) indicates that at similar SiO_2 contents, Fe is progressively enriched in groups 7, 8 and 9 compared to other groups, **inconsistent** with simple differentiation models relating all the groups.

In the following section, trace element data is assessed in an attempt to reconcile these conflicting indications.

6.3.2 TRACE ELEMENTS

Variations in the concentrations of the major element oxides SiO_2, Al_2O_3, MgO and CaO, display trends consistent with the samples of the tholeiite suite forming a single magmatic series. Groups 7, 8 and 9, however, each have distinctive FeO/Y versus SiO_2/Y characteristics suggesting that they followed a somewhat different evolutionary path than the extrapolated trends of the more mafic compositions. In this section, the trace element abundances of the tholeiite suite are examined in order to further define the geochemistry of the suite and to characterize the FeO/MgO-defined groups.

Fig. 6.8 illustrates the incompatible element spiderplots of all samples, except for those in groups 4, 6 and 10. Because there is a continuous enrichment of incompatible elements, analyses from some adjacent FO/MgO groups overlap. For the sake of clarity, these groups are plotted separately. Two features of the spiderplots are readily apparent. First, the relative concentrations of incompatible elements (i.e. the shape of the patterns) remain generally constant throughout the suite, although there is a considerable amount of intra-group scatter in high D elements. Group 9 samples differ slightly in $(Rb/Ba)_N$ and have a moderate Zr enrichment. Also evident in group 9 is a minor K depletion, a feature not readily apparent in groups 5 and 3. Some analyses also have a marked $(Ce)_N$ depletion. The negative $(Sr)_N$ anomaly increases progressively through the differentiation sequence, consistent with petrographic evidence and CaO, Al_2O_3/Y-SiO_2 variations, requiring the extraction of plagioclase. Due to the large negative $(Ce)_N$ anomaly, the existence of a $(Sr)_N$ anomaly in group 1 is not readily discernible, but the $(Sr/Nd)_N$ ratio suggests no signifiant plagioclase fractionation occurred in liquids more mafic than chilled margin sample 400.

The second characteristic of the incompatible element patterns is that they are generally "flat". That is, there has been no major fractionation of large ion lithophile elements (LIL; Rb, Ba, K) from the high field strength elements (Zr, Ti, Y). This is significant in two respects. First, the tholeiite suite has been found to be composed of distinct groups based on FeO/MgO ratios. Each group varies over a broad range of silica-saturation and displays variations in TiO_2 which suggest occult fractionation of a TiO_2-rich phase. In view of the evolved nature of the suite and its relatively shallow emplacement level, crustal contamination may play a role in producing the unusual chemical features. Crustal granitoids are highly enriched in LIL elements compared to mafic liquids. Thus incorporation of crustal material will produce large

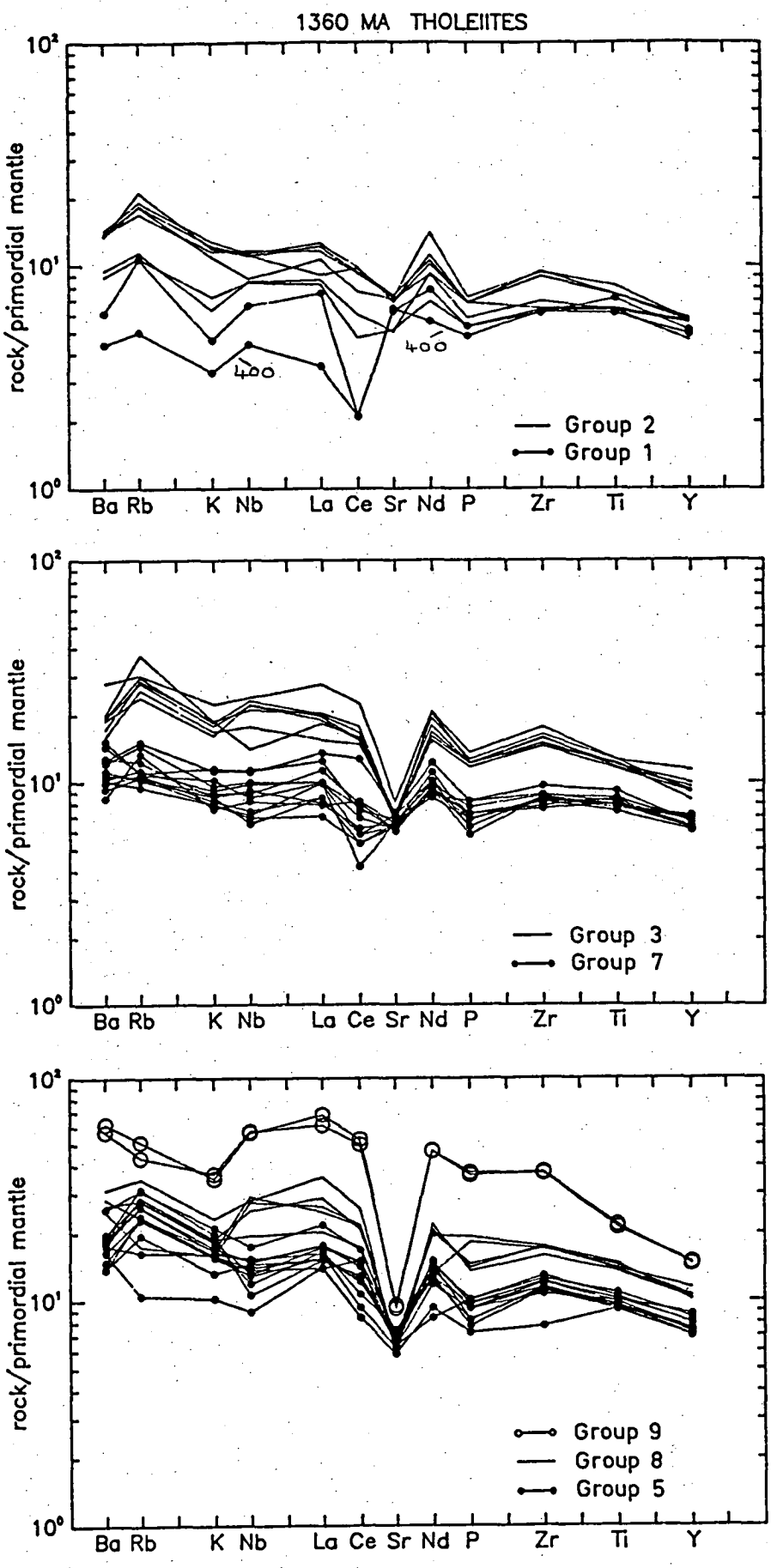

Figure 6.8
Incompatible element 'spiderplots' of the ca.1360 Ma tholeiites normalized to primordial mantle compositions (Wood et al., 1979) and divided into FeO/MgO-based groups.

enrichments of LIL elements, and high $(LIL/HFS)_N$ ratios. The unfractionated spiderplots strongly imply that crustal contamination played a very minor, if any, role in development of the chemical characteristics of the suite.

The other feature to note is that, with the exception of Sr and to a lesser extent Ti, the elements used on the spiderplot are incompatible in basaltic and mantle mineralogies at pressures less than that of garnet stability. The unfractionated patterns, relative to primordial mantle, indicate that the primary liquid to the tholeiite suite was derived from a source which had not experienced a previous melting event, or enrichment by a secondary process involving incompatible element-rich fluids.

Plots of selected trace elements are shown in Fig. 6.9, with FeO/MgO-based groups indicated (excluding 4, 6, 10). In each of the plots two contrasting styles of chemical variation are evident: that defined by assuming all samples of th suite are simply related, and intra-group chemical variations. Considering first, the suite as a whole, the following observations can be made with respect to differentiation (increasing Y or Zr). Of the elements plotted, only Ti displays a strong tendency to remain constant with respect to Y, Ti/Y is also chondritic. Zr/Y is broadly chondritic (Fig. 6.9B) but there is a tendency for Zr to increase from being slightly depleted with respect to chondrites in the mafic samples, to being strongly enriched in group 9. Similarly, Nb/Y increases with differentiation although Nb is enriched relative to Zr (Fig. 6.9D). Recalling the relative locations of these elements with respect to the spiderplots, the Nb-enrichment reflects the modest, overall enriched nature of the high D elements. With differentiation, the relative concentrations of Ti and Y remain constant, but slight enrichment occurs from Zr to Nb, but at a similar rate (Nb/Zr = constant). Although these enrichments are minor compared to those found in the ca.2420 Ma suites (Chapter 5) it can be deduced from these diagrams that the relative enrichment follows the order Nb > Zr > Ti = Y = chondrites, as found in the high-Mg, subgroup I compositions.

The variations in K with differentiation is not, however, consistent with that of Zr-Nb. It is shown in Fig. 6.9C that Nb increases with differentiation through the suite. The initial increase of K/Nb (Fig. 6.9E) indicates a progressive enrichment of K > Nb, a trend which is reversed midway through the differentiation sequence. The reversal cannot be the result of extracting an amphibole or mica and thus reducing the concentration of K. Conventional petrology would conclude that since the decrease in K cannot be related to the extraction of a phenocryst phase,

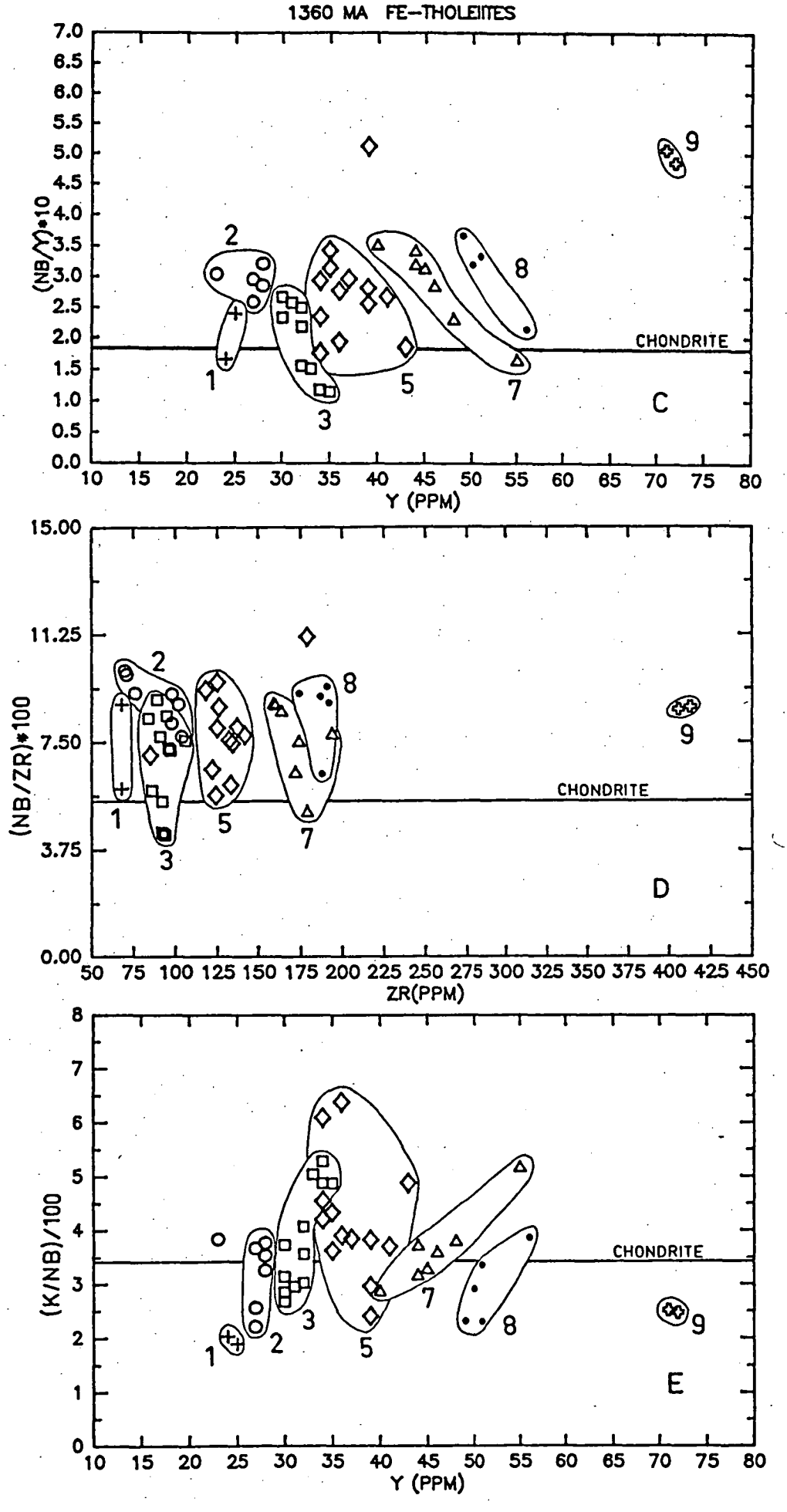
1360 MA FE-THOLEIITES
(NB/Y)*10
Y (PPM)
CHONDRITE
C
(NB/ZR)*100
ZR(PPM)
D
(K/NB)/100
E
1
2
3
5
7
8
9

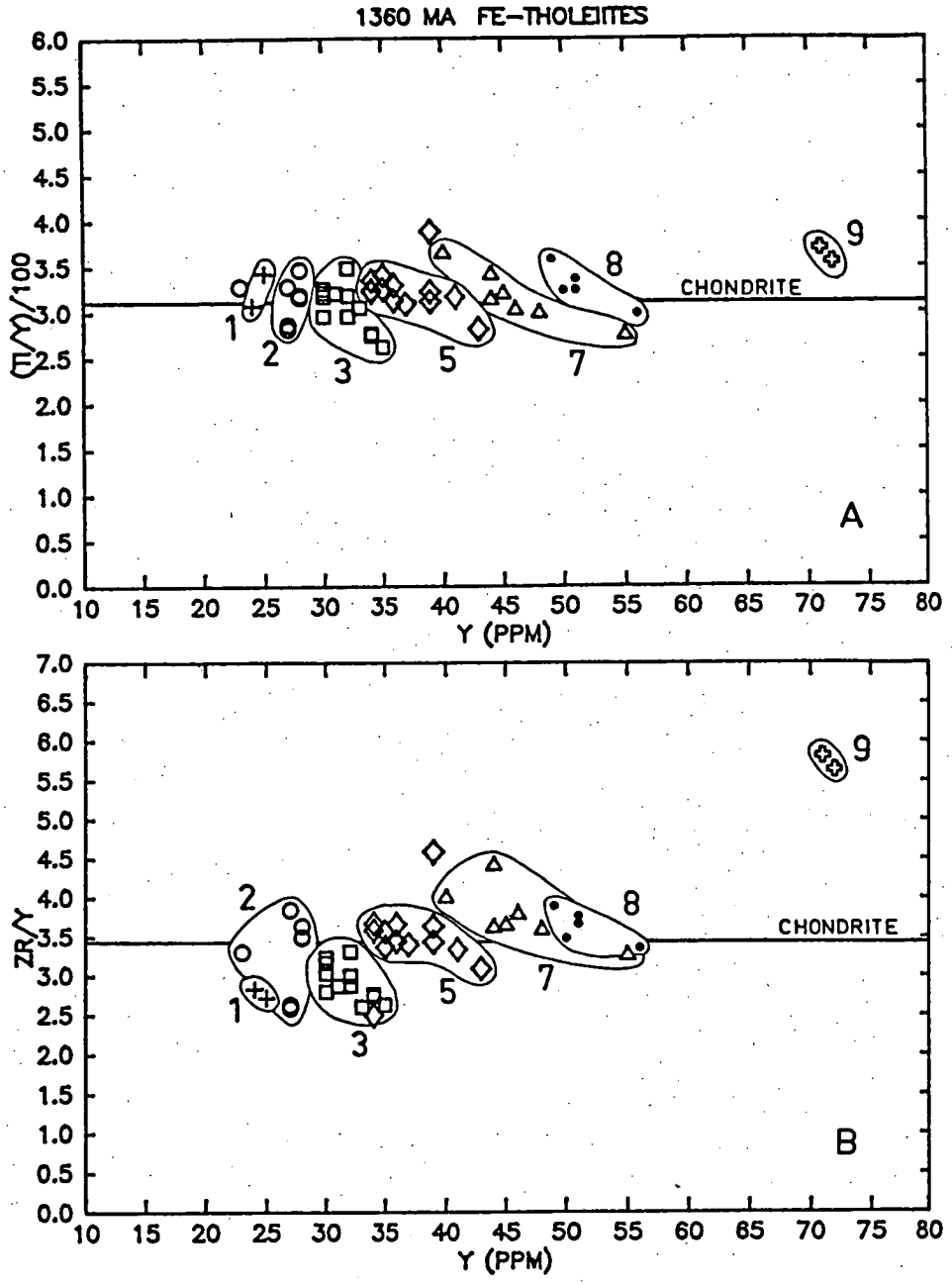

Figure 6.9
Selected trace element variations in the tholeiite suite, subdivided with respect to FeO/MgO-based groups.

groups 7, 8 and 9 cannot be related to groups 1-5. However, the geochemical features discussed previously, and below, indicate classical interpretations are inconsistent with much of the data. Hence, significant petrogenetic weight cannot be placed on the K/Nb ratio. Interestingly, the K/Nb trend parallels that of silica saturation shown in Fig. 6.4; silica saturation increases to a maximum in group 5, then decreases through group 9. The decrease in silica saturation is also unexplainable by any fractionation process.

In considering the geochemical variations within each group and their relative relationship, it is important first to recall that in each Pearce diagram (Fig. 6.7), the FeO/MgO-defined groups remained in sequential order throughout each of the major element variation diagrams. These relationships remain true when considering the trace element variations depicted in the plots of Fig. 6.9.

With reference to the diagrams in Fig. 6.9, the intra-group chemical variations are strongly oblique, to orthogonal, to the differentiation trend defined by the suite, as a whole. This accounts for the intra-group scatter on the spiderplots. The Ti/Y ratio of the tholeiite suite remains constant, and chondritic with differentiation (increasing Y). Yet the chemical variation within each group indicates a depletion in Ti with differentiation. Similarly, intra-group chemical variations show that Nb and Zr are also depleted with increasing Y. Separation of amphibole, or biotite + zircon could account for these depletions (Pearce & Nory, 1979), but this association is unattainable in these liquid compositions. Furthermore, Fig. 6.9D shows that for a given concentration of Zr, there is a broad range of Nb (see also Fig. 6.9E). This feature could represent sample inhomogeneity with respect to Fe-Ti oxides, but as discussed earlier, there is no petrographic evidence for this phase, nor is it likely that such a phase can precipitate from these liquid compositions at the P-T of interest.

One observation which may eventually be a key to understanding the process(es) involved in the generation of the geochemical features described above, is the "en echelon" geochemical trend defined by the groups. This feature is especially evident in Fig. 6.9A, B, C. Beginning with group 3, a differentiation process results in decreasing concentrations of Zr, Ti and Nb. However, the most mafic compositions of the more evolved group 5 do not have the low Zr, Ti and Nb of the most differentiated group 3 samples, but instead begin at high levels of Zr, Nb and Ti. These elements then decrease in abundance with increasing Y through group 5, and are again enriched in the low Y samples of group 7.

Moreover, the Y contents of the most mafic samples of, for example group 5, overlap with the Y content of the most evolved group 3 samples. Thus there is also evidence for a "cyclical" process operating during the differentiation of these liquids, in addition to a broad overall trend of crystal fractionation.

6.3.3 RARE EARTH ELEMENTS

Rare earth element (REE) patterns of one sample from five tholeiite groups are shown in Fig. 6.10, and the data listed in Table 6.3. A readily apparent feature of each sample except 097 (group 8) is a flat, unfractionated chondrite-normalized profile (normalizing values from Masuda et al., 1973). It was inferred from the spiderplots that the source region(s) of the tholeiite suite had a primitive character, and had not been enriched with incompatible elements by a secondary process. This conclusion is strongly supported by the flat REE profiles, which also indicate the mantle source region had not experienced a previous melting episode.

Except for sample 097, none of the analyses have negative $(Eu)_N$ anomalies. In the case of group 1 sample 400, the absence of a $(Eu)_N$ anomaly can be interpreted as indicating that plagioclase fractionation did not take place in the parental liquids to sample 400, as the spiderplot of this sample does not conain a significant negative $(Sr)_N$ anomaly. However, the analysed samples comprising groups 2, 3 and 7 have large negative $(Sr)_N$ anomalies, as well as defining major element differentiation trends requiring plagioclase fractionation (Figs 6.7A, 6.7B and 6.7C). A similar feature was observed in sample 244 of the ca.2320 Ma Fe-tholeiites (Fig. 5.31). In the latter example, plagioclase accumulation, analytical error and fO_2 were considered as possible causes for the anomaly-free pattern. In the case of the multiple analyses of the ca.1360 Ma tholeiites, analytical error seems unlikely, and plagioclase accumulation can not be supported petrographically. Thus the absence of a $(Eu)_N$ in these plagioclase-phyric samples may indicate that Eu existed predominantly in the trivalent state, and was thus excluded from incorporation into the precipitating plagioclase.

It is significant then, that group 8 sample 097, does display a negative $(Eu)_N$ anomaly, in addition to a generally concave upwards REE pattern compared to less differentiated examples. Since closed-system crystal fractionation of basaltic compositions results in progressively oxidized derivative liquids (Mathez, 1984), the development of a $(Eu)_N$ anomaly in more evolved compositions is unlikely if the parental liquid

already has a fO_2 which favous Eu^{3+}. This contrasting behaviour of Eu between groups 8 and 1, 2, 3 and 7, as well as the disk shaped versus flat patterns, are intrinsic features which may preclude a direct chemical relationship between groups.

A characteristic common to the REE patterns of groups 1-8 is a negative $(Ce)_N$ anomaly. The anomaly is also apparent in the spiderplots, and is therefore not an analytical artefact of the REE extraction method (Robinson et al., 1986). Submarine basalts are commonly depleted in Ce, due to secondary alteration (oxidation) and fluid transport of Ce^{4+} (A. Crawford, pers. comm., 1986). It is tempting then to equate the absence of a negative $(Eu)_N$, possibly due to relatively oxidizing conditions, and the existence of a negative $(Ce)_N$ anomaly. It should be emphasized that secondary alteration and fluid interaction (as in ocean floor examples) is not being advocated in the tholeiite dykes, as it is unsupported by the petrography. Instead, the intrinsic fO_2 may have been such as to create high Ce^{4+}/Ce^{3+} ratios, such that Ce^{4+} may have been extracted by precipitating phases.

Although the REE patterns of samples from groups 1-7 are broadly similar, they differ slightly in shape. Samples representing groups 1 and 3 have a $(Nd/Yb)_N$ of 0.9 and 1.0 respectively, while groups 2 and 7 have ratios of 1.2 and 1.5. These differences result in the REE pattern of sample 065 (group 2) crossing the patterns of groups 1 and 3. Without a more extensive data base it is not clear how significant these differences are. If the patterns are representative of each group, then crossing, yet unfractionated, patterns require the primary liquids to groups 2 and 7 to be derived from a modestly LREE-enriched source region compared to groups 1 and 3.

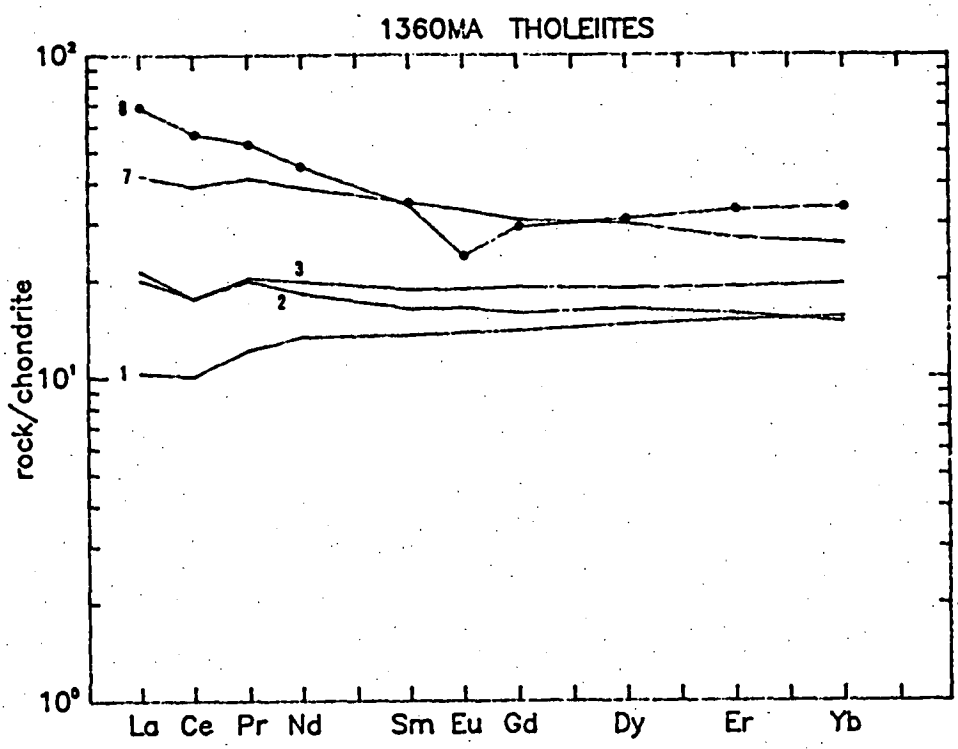

Figure 6.10

Chondrite normalized (Masuda et al., 1973) analyses of representative samples from selected FeO/MgO-based groups. Numbers correspond to group designations of Fig. 6.1. Data and sample numbers listed in Table 6.3 (below).

TABLE 6.3
RARE EARTH ELEMENT ANALYSES* OF REPRESENTATIVE SAMPLES FROM SELECTED CA.1360 MA THOLEIITE GROUPS.

	LA	CE	PR	ND	SM	EU	GD	DY	ER	YB	(Y)
GROUP I											
65400	3.24	8.15	1.39	7.95	2.58	0.99	3.6	4.72	3.19	3.2	28.9
GROUP 2											
65084	6.72	14.17	2.28	10.8	3.11	1.18	4.08	5.28	3.34	3.08	31.8
GROUP 3											
65256	6.3	14.23	2.33	11.79	3.57	1.35	4.92	6.12	4.05	4.05	36.0
GROUP 7											
65206	13.2	31.7	4.75	23.0	6.64	2.37	7.93	9.67	5.72	5.40	48.3
GROUP 8											
65097	21.71	46.2	6.1	26.7	6.49	1.70	7.55	10.03	7.01	6.99	61.7

* FOLLOWING THE METHOD OF ROBINSON ET AL. (1986), VALUES IN PPM.

6.4 SUMMARY AND DISCUSSION

Evaluation of major element concentrations using Pearce diagrams has shown that the "large scale" chemical characteristics of the suite, i.e. variation in the major element oxides SiO_2, Al_2O_3, MgO and CaO, can be simply accounted for by fractionation of the phenocryst assemblages. Furthermore, the progressive enrichment, and general shape of the incompatible element spiderplots are also consistent with a crystal fractionation dominated model. Superimposed upon these general features is a consistent clustering of analyses into nine geochemical groupings in which the chemical variation can only broadly be associated with fractionation of the phenocryst phases. The ordering of the groups, however, does not relate to a simple monotonic time sequence nor does it correlate with a spatial separation within the Vestfold Hills area.

With regards to the large scale geochemical patterns, there are features that cannot be readily explained by crystal fractionation of the phenocryst phases. Groups 7, 8 and 9 cannot be related to one another, nor to more mafic compositions based on FeO variations. Furthermore, the REE pattern of group 8 sample 097 is sufficiently different from groups 1, 2, 3 and 7, as to apparently require a separate source. The REE patterns of groups 1 and 3 differ slightly in slope from groups 2 and 7, possibly indicating two separate sources with slightly different REE enrichments. As only one sample was analysed from each of these groups, a wider data base is clearly required to firmly establish the significance of these observations.

Despite the field evidence and somewhat subtle geochemical signatures that may indicate multiple sources for some FeO/MgO-defined groups, it is dificult to envisage how four sources (based on crosscutting relationships of group 5; Fig. 6.3) or two or three sources based on REE, could produce liquids which have followed independent fractionation paths, possibly involving varying stages of polybaric crystal fractionation, such that the liquids from each source have fortuitously arrived at a particular FeO/MgO ratio having trace element abundances that could be confused with those defining a single magmatic suite. Even considering multiple source models, the following observations are not fully explained:

1. the origin of the FeO/MgO clusters, and their relatively even spacing as evidenced on Fig. 6.2;
2. the wide range of silica saturation within a cluster of analyses with only a minor range in FeO/MgO; and

3. the intra-group trace element characteristics (particularly Ti, Nb, Y, Zr, Sr, Eu) which cannot be explained by the fractionation of observed phenocryst phases, yet the trace elements as a whole are consistent with a crystal fractionation model for the suite.

The cyclical nature of the trace element variations as shown in Figs 6.9A, 6.9B and 6.9C, may be the evidence pointing to magma chamber processes as a major factor in controlling the trace element abundances and relative variations within the groups. Such processes have not been examined in any detail during this study, but cyclical elemental patterns have been described by O'Hara (1977) and Langmuir (1980). These authors have modelled the role of a periodically refilled magma chamber in which injection of new magma, mixing, crystallization and melt extraction are but a few of the factors which can influence the major and trace element compositions of derivative liquids. The ca.1360 Ma tholeiites have evolved compositions, and were emplaced in a tectonically stable crust at load pressures of 4-5 kbar. Thus the existence of a long-lived, fractionating magma body within the crust is not an unreasonable assumption, and may well be a major factor in producing the unusual chemical characteristics of the ca.1360 Ma tholeiites.

Chapter 7

SUMMARY

Mafic dyke swarms are common features of Precambrian shields of all continents. With the exception of palaeomagnetic studies, however, most mafic dyke swarms have been overlooked as a source of information concerning geological history of the shields. Mafic dykes have their origin in the upper mantle and freeze under the P-T regime of the crust. Interpretation of information recorded in the chilled margin geochemistry (mantle signature with or without crustal interaction) and mineral chemistry including phenocryst/liquid pairs (crustal conditions of crystallization), if used in conjunction with emplacement ages, can produce valuable information concerning the evolution of the crust and mantle.

Dyke suites record events between or post-dating major metamorphic and deformation events affecting shields and thus may provide additional P-T-t points on the crustal evolution, e.g. post-metamorphic uplift or subsidence. The East Antarctic Shield, and particularly the Vestfold Hills, is extremely well suited for this role as multiple episodes of dyke emplacement occurred over a ~1200 Ma period, and took place in the time interval between two well documented metamorphic events.

In Part A of this thesis, the uplift history of the East Antarctic Shield was evaluated over a time period of ~2000 Ma by studying the phenocryst assemblages of dykes emplaced at ca.2420 Ma., and ca.1360 Ma, in conjunction with metamorphic events at ca.3100 Ma, 2500 Ma and 1000 Ma. This project consisted of exploiting the dependency of liquidus phase assemblages and compositions on pressure and temperature. Thus by experimentally reproducing the natural phenocryst compositions and assemblages found in selected dyke chilled margins, the load pressure at the time of dyke emplacement was estimated.

The experimental studies indicate the load pressure during emplacement of the ca.2420 Ma dykes was 7-8 kbar but decreased to 4-5 kbar prior to emplacement of the ca.1360 Ma dykes. These results are in excellent agreement with estimated emplacement pressures determined independently on the solidus minerals of the dykes using geobarometric methods (8 kbar, 5 kbar respectively)

Extrapolating the results of the experimental study on Vestfold Hills dyke samples to compositionally similar dykes in the Napier Complex, it was found that both terrains existed at similar crustal levels at ca.2420 Ma (24-28 km). However, the ca.1190 Ma dykes of the Napier Complex are

inferred to have been emplaced at ~8 kbar (~28 km) while the ca.1360 Ma dykes were emplaced in the Vestfold Hills at crustal depths of 14-18 km.

Metamorphic and geochronological studies in the Napier Complex have estimated metamorphic pressures at 8-10 kbar during the ca.3100 Ma metamorphism, and 3-5 kbar at ca.1000 Ma. Thus the estimated emplacement pressure of mafic dykes, used in conjunction with the metamorphic history, indicates the Napier Complex remained at deep crustal levels for ~2000 Ma. Such long periods of crustal stability, continuing to the present time, occur in the tectonically stable shield areas of Canada and South Africa. By inference then, the Napier Complex was probably part of a stable continental mass well away from active continental margins during the early and middle Proterozoic. Although the ca.1360 Ma dykes were emplaced in the Vestfold Hills at significantly lower pressures than the ca.2420 Ma dykes, the uplift rate between these events is very slow (~1 cm/1000 a), and implies that the Vestfold Hills were also part of the same stable crustal segment as the Napier Complex, but that this area had undergone uplift prior to 1360 Ma in contrast to the Enderby Land region which remained at deep crustal levels at least until 1190 Ma.

Further crustal history is recorded in the metamorphic assemblages which developed in some Vestfold Hills dykes during the ca.1000 Ma metamorphism. Petrographic studies have shown that the secondary amphibole developed in these dykes has undergone a prograde dehydration reaction in which garnet and clinopyroxene were products. Geobarometric studies found that these assemblages record pressures of ~6.4 kbar, implying that the earlier hydration of the original igneous assemblage had taken place at pressures <6.4 kbar. These petrographic and geobarometric features are consistent with the experimental study which indicated the Vestfold Hills terrain was at 4-5 kbar at ca.1360 Ma, partial hydration then occurred, followed by localized prograde metamorphism under increasing P,T conditions (to 6.4 kbar) at ~1100 Ma.

It is concluded from this summary of Part 1 that a significant amount of information concerning crustal evolution may be obtained by studying phenocryst stability reactions of mafic dykes. The results of this study were found to be entirely consistent with independent pressure estimates for dyke emplacement based on geobarometric methods, and thus there should be no problems in confidently applying this approach to mafic dykes that do not contain suitable phases for geobarometric calculations.

Considering the wide distribution of mafic dyke swarms, application of this approach may become an important tool to further understand crustal conditions.

In Part 2 of this thesis, geochemical characteristics of mafic dykes sampled from the Vestfold Hills were examined in order to obtain information concerning the geochemical evolution of each suite, as well as to deduce characteristics of the mantle source regions. The earliest dykes were emplaced in the Vestfold Hills at ca.2420 Ma, and are composed of high-Mg and Fe-rich tholeiite suites. Each of these suites is divisible into subgroups based on petrographic, and whole-rock geochemical features. Two of the high-Mg subgroups have near-primary compositions and contain evidence for being derived from a primitive, chondritic source, i.e. a source which had not been depleted in a basaltic component by a previous melting event. Contradictory evidence exists concerning the origin of the third group: its incompatible trace element patterns suggest very close affinities to subgroup II, yet it is depleted with respect to CaO-TiO_2-Al_2O_3, suggesting derivation from a source which had previously lost a "basaltic" component.

Part of the contradiction in determining the genetic relationship of subgroup III is that all high-Mg subgroups are highly enriched with incompatible trace elements. This has been shown not to be the result of "bulk" crustal assimilation. Furthermore, mass balance calculations applied to model differentiation sequences requires the removal of phases, and phase compositions which cannot be substantiated petrographically. The nature of the incompatible element pattern of subgroups II and III (large relative depletion in Sr) suggests residual plagioclase, or plagioclase fractionation. However, these implications cannot be substantiated considering the high degree of melting required to obtain the major element geochemical features of the high-Mg suite. Furthermore, plagioclase is never a phenocryst phase. It is considered that the plagioclase signature, as well as enrichment in **some** trace elements is part of a selective contamination process in which trace elements, that are incompatible at high degrees of melting, are decoupled, or buffered by minor phases in the wall-rock. Thus, an "open system" model of chemical volution is evident in these Mg-rich compositions.

A highly refractory pyroxenite nodule which is believed to be cognate to subgroup III, provides evidence for the existence of a Mg_{75} parental liquid. The composition of the primary suite was estimated by adding olivine, or orthopyroxene to the most Mg-rich chilled margin composition (Mg_{70}), until the proposed primary composition was reached. The resulting composition compares extremely well to melts produced at ~10 kbar in experimental partial melting studies of model mantle compositions. Such

low pressures are consistent with the existence of a plagioclase-bearing lherzolite, as suggested by the trace element patterns.

Dyke intersections indicate that the subgroups of the high-Mg and Fe-rich suites were emplaced cyclically, with Fe-rich groups following Mg-rich. Although the subgroups of the ca.2420 Ma suite are highly differentiated, REE patterns and some trace element characteristics indicate that their parental liquid(s) was derived from a source which had not experienced a previous melting event. These features preclude crystal fractionation, or polybaric partial melting models as a means to relate these two suites, and indicate melt segregation took place from multiple diapirs, each with a primitive mantle composition.

Incompatible trace element variations in the Fe-rich groups also indicate "open system" magmatic processes. One suite has a trace element signature identical to that observed in the high-Mg dykes, and suggests at least some differentiation of this Fe-rich composition took place at shallow mantle levels (~10 kbar). The other two Fe-rich groups display a second enrichment pattern which may imply that the variable enrichment styles are reflecting processes operating in various pressure regimes of the mantle.

The compositions of the Fe-rich and high-Mg suites compare extremely well with Archean greenstone belt sequences, and the high-Mg dyke compositions also invite comparisons with major Archean-Proterozoic intrusive complexes such as the Bushveld and Stillwater.

The volumetrically largest suite of dykes (Fe-tholeiite) was emplaced in the Vestfold Hills at ca.1360 Ma. Although these compositions do not approach primary liquids, REE patterns and the generally [illegible]onated nature of the incompatible elements indicate [illegible]ental liquid to this suite was also derived from a primitive unfractionated source.

Archean-Proterozoic

Major and trace element variations can, in most cases, be related by a crystal fractionation mechanism. However, it was found that the differentiation trends are composed of distinct, coherent groups of analyses. Within each group, differentiation trends of most major elements are compatible with fractionation of the phenocryst assemblages, but trace element variations define trends which cannot be related to the precipitation of possible phenocryst compositions.

The inability of crystal fractionation models to account for the unusual nature of the trace element variation in the tholeiites also suggests "open system" differentiation processes were operating during evolution of the ca.1360 Ma suite. However, the pattern of trace element variation differs in the ca.1360 Ma tholeiite suite compared to the pattern

observed in the ca.2420 Ma suite. In the latter examples, the elements affected by the process continued to enrich throughout differentiation. For the case of the ca.1360 Ma tholeiites, enrichment is cyclical. That is, within an individual group, selected trace element concentrations increase with differentiation. But the most mafic composition of the adjacent evolved group begins a cycle at equally low concentrations as the more mafic group.

Clearly, all discussions of "open system" fractionation models are speculative. For the ca.2420 Ma suites, the method of enrichment was thought to be that of a wall-rock reaction process, while the trace element variation in the ca.1360 Ma tholeiite suite was thought to reflect cyclical magma chamber processes. However, a number of other models, or combination of models may also be applicable. Isotopic evaluation of subgroups within each suite may aid in further understanding the processes involved.

APPENDICES

page

APPENDIX 1

Appendix 1 contains averaged microprobe analyses and CIPW norms of glass compositions from the experimental liquidus study of samples 65060 and 65206 (Chapter 1). The analyses are first arranged according to experimental study, and then by run number. Co-existing phases and further run details are listed in Table 1.8.

APPENDIX 2

Appendix 2 lists major and trace element analyses and CIPW norms (calculated based on FeO^T) of dykes collected for this study from the Vestfold Hills. The analyses are arranged according to suite, and then sample number. Subgroup designations, where indicated, are defined in the pertinent chapter.

	AT169	AT170	AT171	AT173	AT175	AT176	AT183	T1593	T1594	T1595
65060										
SIO2	52.30	53.93	52.98	51.77	56.48	64.44	54.32	52.81	51.79	52.92
TIO2	0.58	0.65	0.59	0.60	0.82	1.57	0.64	0.53	0.57	0.55
AL2O3	11.74	13.21	12.48	11.87	14.42	13.53	13.81	11.76	11.70	12.02
FE2O3	0.00	0.00	0.00	0.00	0.00	0.00	0.00	0.00	0.00	0.00
FEO	11.42	10.52	11.01	11.91	10.19	8.03	10.22	11.09	12.28	11.37
MNO	0.00	0.00	0.00	0.00	0.00	0.00	0.00	0.00	0.00	0.00
MGO	11.41	7.99	10.07	11.42	5.17	2.40	7.06	11.46	11.34	10.60
CAO	10.08	11.29	10.49	9.95	9.60	5.42	11.34	10.06	9.98	10.31
NA2O	1.92	1.80	1.74	1.94	2.43	2.29	1.94	1.73	1.76	1.66
K2O	0.55	0.62	0.65	0.55	0.90	2.32	0.67	0.56	0.58	0.57
P2O5	0.00	0.00	0.00	0.00	0.00	0.00	0.00	0.00	0.00	0.00
TOTAL	100.00	100.00	100.00	100.00	100.00	100.00	100.00	100.00	100.00	100.00
MG#	64.0	57.5	62.0	63.1	47.5	34.8	55.2	64.8	62.2	62.4
WT% CIPW NORMATIVE MINERALS										
QTZ		3.13	0.12		7.44	23.04	3.89			0.01
OR	3.25	3.66	3.84	3.25	5.32	13.71	3.96	3.31	3.43	3.37
AB	16.25	15.23	14.71	16.43	20.56	19.38	16.43	14.64	14.89	14.05
AN	21.79	26.13	24.32	22.04	25.78	19.79	26.99	22.67	22.31	23.67
LC										
NE										
CPX	23.08	24.64	22.72	22.36	18.25	6.02	24.22	22.25	22.30	22.53
DI	14.30	13.70	13.62	13.64	8.39	2.17	12.90	13.95	13.38	13.58
HD	8.77	10.94	9.10	8.72	9.86	3.85	11.32	8.30	8.92	8.95
OPX	27.46	25.97	33.16	25.06	21.09	15.08	23.28	33.35	27.98	35.32
EN	16.12	13.55	18.77	14.45	8.98	4.97	11.60	19.82	15.85	20.11
FS	11.35	12.42	14.40	10.61	12.11	10.11	11.68	13.53	12.13	15.21
OL	7.06			9.72				2.77	7.99	
FO	3.98			5.37				1.58	4.34	
FA	3.09			4.34				1.19	3.66	
MT										
IL	1.10	1.23	1.12	1.14	1.56	2.98	1.22	1.01	1.08	1.04
AP										

	T1596	T1598	T1600	T1601	T1602	T1604	T1643	T1649	T1650	T1720
65060										
SIO2	52.06	52.06	52.15	53.04	53.12	52.86	53.09	53.33	53.05	54.21
TIO2	0.63	0.60	0.58	0.57	0.58	0.67	0.59	0.57	0.57	0.59
AL2O3	13.24	12.34	11.98	12.60	11.87	14.07	12.05	12.10	12.10	12.94
FE2O3	0.00	0.00	0.00	0.00	0.00	0.00	0.00	0.00	0.00	0.00
FEO	11.96	11.94	12.13	10.37	10.36	10.47	9.96	9.71	10.02	10.20
MNO	0.00	0.00	0.00	0.00	0.00	0.00	0.00	0.00	0.00	0.00
MGO	8.92	10.26	10.69	10.59	11.60	8.45	11.72	11.79	11.66	8.49
CAO	10.61	10.36	10.24	10.52	10.27	10.81	10.33	10.28	10.31	11.11
NA2O	1.94	1.83	1.67	1.73	1.65	2.01	1.69	1.68	1.73	1.83
K2O	0.64	0.61	0.54	0.58	0.55	0.67	0.57	0.54	0.56	0.64
P2O5	0.00	0.00	0.00	0.00	0.00	0.00	0.00	0.00	0.00	0.00
TOTAL	100.00	100.00	100.00	100.00	100.00	100.00	100.00	100.00	100.00	100.00
MG#	57.1	60.5	61.1	64.5	66.6	59.0	67.7	68.4	67.5	59.8
WT% CIPW NORMATIVE MINERALS										
QTZ				0.06		0.26		0.06		3.02
OR	3.78	3.60	3.19	3.43	3.25	3.96	3.37	3.19	3.31	3.78
AB	16.42	15.48	14.14	14.64	13.96	17.00	14.30	14.21	14.64	15.49
AN	25.53	23.65	23.61	24.90	23.36	27.39	23.61	23.88	23.60	25.19
LC										
NE										
CPX	22.38	22.80	22.35	22.30	22.49	21.59	22.48	22.04	22.43	24.60
DI	12.29	13.30	13.17	13.96	14.56	12.34	14.82	14.68	14.72	14.21
HD	10.09	9.49	9.18	8.34	7.93	9.25	7.66	7.36	7.71	10.39
OPX	26.80	27.96	31.86	33.57	35.38	28.52	33.90	35.53	33.21	26.79
EN	13.80	15.37	17.69	19.91	21.77	15.32	21.28	22.56	20.74	14.57
FS	13.00	12.59	14.16	13.66	13.61	13.19	12.62	12.97	12.47	12.22
OL	3.88	5.36	3.75		0.45		1.21		1.73	
FO	1.90	2.82	1.99		0.27		0.73		1.04	
FA	1.98	2.54	1.76		0.18		0.48		0.69	
MT										
IL	1.20	1.14	1.10	1.08	1.10	1.27	1.12	1.08	1.08	1.12
AP										

	T1669	T1689	T1690	T1693	T1694	T1699	T1730	T1734	T1845
65206									
SIO2	49.88	50.37	50.14	49.47	49.68	49.10	50.62	50.67	50.39
TIO2	2.34	2.28	2.38	2.19	2.48	2.21	2.61	2.77	3.13
AL2O3	13.54	13.87	14.04	13.64	13.54	13.61	12.62	12.41	11.68
FE2O3	0.00	0.00	0.00	0.00	0.00	0.00	0.00	0.00	0.00
FEO	16.04	14.44	14.70	16.03	15.83	16.33	16.30	16.60	17.37
MNO	0.00	0.00	0.00	0.00	0.00	0.00	0.00	0.00	0.00
MGO	5.65	6.38	5.98	6.33	5.67	6.45	5.22	4.87	4.69
CAO	10.04	10.13	10.17	9.79	10.04	9.81	10.03	9.99	10.00
NA2O	1.99	1.91	1.96	1.95	2.03	1.89	1.91	1.91	1.87
K2O	0.50	0.44	0.49	0.44	0.51	0.46	0.50	0.57	0.60
P2O5	0.00	0.17	0.13	0.15	0.22	0.15	0.19	0.21	0.27
TOTAL	100.00	100.00	100.00	100.00	100.00	100.00	100.00	100.00	100.00
MG#	38.6	44.1	42.0	41.3	39.0	41.3	36.3	34.3	32.5
WT% CIPW NORMATIVE MINERALS									
QTZ		1.03	0.66				2.41	2.80	3.02
OR	2.96	2.60	2.90	2.60	3.01	2.72	2.95	3.37	3.55
AB	16.84	16.17	16.59	16.50	17.18	15.99	16.16	16.16	15.83
AN	26.54	27.98	28.07	27.17	26.33	27.29	24.38	23.61	21.71
LC									
NE									
CPX	19.65	17.73	18.09	17.18	18.59	17.15	20.42	20.86	22.23
DI	7.60	7.89	7.70	7.08	7.32	7.06	7.52	7.29	7.43
HD	12.05	9.84	10.39	10.10	11.27	10.09	12.90	13.57	14.80
OPX	29.00	29.76	28.87	29.40	29.54	28.02	28.27	27.44	27.10
EN	10.29	12.24	11.33	11.15	10.67	10.62	9.52	8.75	8.24
FS	18.71	17.52	17.54	18.25	18.87	17.40	18.75	18.69	18.85
OL	0.56			2.63	0.13	4.28			
FO	0.19			0.94	0.04	1.52			
FA	0.37			1.69	0.08	2.75			
MT									
IL	4.45	4.33	4.52	4.16	4.71	4.20	4.96	5.26	5.95
AP		0.40	0.31	0.36	0.52	0.36	0.45	0.50	0.64

	AT178	AT179	AT180	AT181	AT182	T1660	T1662	T1664	T1665	T1668
65206										
SIO2	50.75	49.92	49.50	50.18	49.57	47.33	49.36	48.89	48.42	49.71
TIO2	2.75	2.36	2.25	3.48	2.26	3.12	2.21	2.18	2.28	2.27
AL2O3	12.29	13.57	13.80	11.97	13.82	13.16	13.88	13.60	13.50	13.80
FE2O3	0.00	0.00	0.00	0.00	0.00	0.00	0.00	0.00	0.00	0.00
FEO	16.29	15.60	15.49	18.02	15.57	19.32	16.15	16.53	16.92	15.24
MNO	0.00	0.00	0.00	0.00	0.00	0.00	0.00	0.00	0.00	0.00
MGO	5.00	5.80	6.40	4.01	6.37	4.62	5.95	6.45	6.49	6.38
CAO	10.19	10.09	9.99	9.64	9.95	9.57	9.95	9.87	9.86	10.05
NA2O	2.00	2.08	2.07	1.81	2.03	2.04	1.99	1.95	1.95	2.01
K2O	0.47	0.48	0.45	0.72	0.44	0.60	0.47	0.45	0.42	0.45
P2O5	0.25	0.11	0.06	0.17	0.00	0.25	0.04	0.08	0.16	0.10
TOTAL	100.00	100.00	100.00	100.00	100.00	100.00	100.00	100.00	100.00	100.00
MG#	35.4	39.9	42.4	28.4	42.2	29.9	39.6	41.0	40.6	42.7
WT% CIPW NORMATIVE MINERAIS										
QTZ	2.73			3.53						
OR	2.78	2.84	2.66	4.25	2.60	3.55	2.78	2.66	2.48	2.66
AB	16.94	17.60	17.51	15.32	17.17	17.26	16.84	16.50	16.50	17.01
AN	23.17	26.27	27.03	22.41	27.29	24.98	27.55	27.03	26.84	27.30
LC										
NE										
CPX	21.82	19.43	18.58	20.77	18.53	17.81	18.17	18.02	17.70	18.38
DI	7.86	7.79	7.90	6.14	7.83	5.40	7.18	7.35	7.16	7.89
HD	13.96	11.63	10.68	14.64	10.69	12.41	10.98	10.67	10.54	10.49
OPX	26.74	28.34	25.35	26.70	26.35	21.28	26.58	24.79	23.61	27.84
EN	8.80	10.44	9.94	7.14	10.27	5.86	9.65	9.30	8.78	11.03
FS	17.94	17.89	15.41	19.56	16.08	15.43	16.93	15.49	14.83	16.81
OL		0.79	4.44		3.76	8.61	3.79	6.67	8.15	2.27
FO		0.27	1.64		1.38	2.20	1.29	2.35	2.85	0.85
FA		0.51	2.80		2.38	6.40	2.50	4.32	5.30	1.42
MT										
IL	5.23	4.48	4.27	6.61	4.29	5.93	4.20	4.14	4.33	4.31
AP	0.59	0.26	0.14	0.40		0.59	0.09	0.19	0.38	0.24

APPENDIX 2

ANALYTICAL METHODS

Material selected for analysis was prepared by sectioning the sample into 1-1.5 cm cubes using a diamond-studded trim saw. Cube faces were ground on a tungsten carbide lap wheel to remove any traces of metal from the saw blade. The chips were then cleansed in an ultrasonic bath and air dried. Approximately 200 gm of sample material were pulverized to approximately -325 mesh in a tungsten carbide swing mill, and alloquats of this material used in major and trace element analyses.

Major element analyses, including Na, were determined on a Phillips DW1410 vaccuum spectrograph on fused glass disks following the methods of Norrish & Hutton (1969), and Norrish & Chappell (1967). Both international and "in house" standards were used in calibration, and were re-analysed after approximately every nine samples to monitor machine drift. Peak and background positions for Na were counted twice on each sample, at the beginning and end of each sample sequence, and the results averaged. Duplicate fusion disks of each of the 144 samples were analysed and averaged; 79% of all analyses fell between 99-100.5%, and 92% of the averaged analyses (original + duplicate) fell in this range. These totals include values for H_2O^+ and LOI, the weight loss after heating to 110°C and 1000°C respectively, also determined in duplicate.

Trace elements were analysed in pellets of boric acid using ~4 gm of sample, no binding agent was included. Standardization was on "in house" and international standards. Counting precision and XRF run details are given in the following table.

MAJOR ELEMENT PRECISION

	COUNTING PRECISION	TYPICAL PRECISION OF "IN HOUSE" STANDARD: TASBAS	TASBAS
SIO2	0.07	0.25	44.56
TIO2	0.01	0.02	2.31
AL2O3	0.04	0.12	14.14
FE2O3	0.02	0.06	12.05
MNO	0.004	0.004	0.17
MGO	0.05	0.15	8.16
CAO	0.02	0.06	7.81
NA2O	0.11	0.21	5.43
K2O	0.01	0.04	1.86
P2O5	0.01	0.02	0.97

INSTRUMENTAL CONDITIONS FOR TRACE ELEMENT ANALYSIS
ROUTINE XRF AUTOMATED ANALYSIS

ELEMENT (LINE)	TUBE	CRYSTAL*	COLLIMATOR	VACUUM	DETECTION LIMIT (PPM)	PRECISION
SC(Kα)	CR	200	C	YES	1	10±1,30±1
V (Kα)	AU	220	F	YES	3	30±2,100±1
CR(Kα)	AU	200	F	YES	2	10±2,400±4
NI(Kα)	AU	200	F	YES	1	3±0.5,20±0.5, 200±2
RB(Kα)	RH	220	F			10±1,70±1, 170±2
SR(Kα)	RH	220	F		1 1	10±1,200±2, 500±5
Y (Kα)	RH	220	F		1.5	10±2,20±1, 100±2
ZR(Kα)	RH	220	F		1	100±2,250±4, 500±10
NB(Kα)	RH	220	F		1	10±0.5,20±1
BA(Lα)	CR	200	F	YES	3	500±5,1200±5
LA(Lα)	AU	220	C	YES	2.5	20±1,40±2, 100±2
CE(Lβ)	AU	220	C	YES	5	30±2,80±3, 150±1
ND(Lα)	AU	220	C	YES	3	15±1,30±2, 50±2

X-RAY TUBE IS OPERATED AT 60 kV EXCEPT FOR BA, SC, LA, CE, ND WHERE 50 kV 50 mA IS USED.
DETECTION LIMITS ARE FOR 3σ (99%) CONFIDENCE LEVELS.

* PLANES IN LiF CRYSTAL.

number	65025	65027	65034	65053	65054A	65057	65060	65062	65067	65069
subgroup	III	III	II	I	I	I	I	I	I	I
(major elements: wt %)										
SiO2	54.48	56.40	52.29	52.16	52.17	51.75	52.10	52.71	52.55	54.45
TiO2	0.60	0.74	0.50	0.59	0.57	0.61	0.62	0.58	0.69	0.65
Al2O3	13.43	12.53	11.72	11.16	11.04	11.36	11.89	11.10	8.18	13.20
Fe2O3	10.88	11.56	10.99	11.45	11.54	11.48	12.00	11.55	12.00	10.62
FeO	0.0	0.0	0.0	0.0	0.0	0.0	0.0	0.0	0.0	0.0
MnO	0.17	0.16	0.18	0.18	0.18	0.19	0.18	0.13	0.19	0.16
MgO	9.19	8.89	12.96	12.53	13.00	12.76	11.22	13.02	13.66	7.52
CaO	8.63	7.79	9.21	9.29	9.24	9.32	9.93	9.29	9.32	9.99
Na2O	1.37	1.52	1.27	1.60	1.86	1.45	1.78	1.40	1.52	2.22
K2O	0.99	1.26	0.59	0.57	0.51	0.49	0.60	0.56	0.69	0.95
P2O5	0.07	0.10	0.05	0.08	0.08	0.08	0.10	0.07	0.10	0.10
LOI	0.01	-0.21	0.0	0.05	-0.19	0.93	-0.60	-0.44	0.93	-0.12
H2O-	0.08	0.10	0.13	0.01	0.17	0.16	0.09	0.02	0.17	0.14
total	99.90	100.84	99.89	99.67	100.17	100.58	99.91	99.99	100.00	99.88
(trace elements: ppm)										
Zr	85	112	70	56	55	55	61	54	67	69
Sr	98	110	89	166	146	161	176	170	197	272
Nb	7	8	6	5	5	4	5	4	5	4
Y	18	22	16	13	15	14	15	14	13	13
Rb	48	65	18	23	20	22	23	20	28	39
Ba	219	288	208	224	196	230	254	224	261	311
V	210	217	206	221	219	226	221	208	223	229
Ni	190	205	417	321	333	317	250	337	366	106
Cr	669	681	1461	1212	1183	1208	933	1165	1559	462
La	15	22	17	7	8	9	9	8	11	12
Ce	29	39	25	14	13	15	16	15	17	20
Nd	14	19	10	8	7	9	9	8	10	13
Sc	37	29	37	37	36	37	33	32	30	32
Mg#	62.6	60.37	70.02	68.43	69.05	68.77	64.94	69.07	69.28	58.38
WT% CIPW NORMATIVE MINERALS										
QTZ	6.12	7.91	0.18							3.51
OR	5.93	7.46	3.53	3.42	3.04	2.94	3.57	3.33	4.17	5.68
AB	11.74	12.89	10.89	13.75	15.89	12.48	15.18	11.94	13.17	19.01
AN	27.93	23.70	24.87	21.92	20.47	23.43	22.86	22.52	13.78	23.53
LC										
NE										
CPX	12.28	11.82	17.13	19.81	20.55	18.74	21.35	19.06	26.71	21.41
DI	7.40	6.89	11.60	13.12	13.73	12.48	13.38	12.76	17.95	12.03
HD	4.87	4.93	5.53	6.69	6.82	6.26	7.98	6.30	8.75	9.38
OPX	34.68	34.58	42.30	37.50	31.89	38.94	31.81	41.78	38.63	25.36
EN	19.76	19.00	27.34	23.65	20.32	24.71	18.89	26.67	24.77	13.39
FS	14.93	15.59	14.96	13.85	11.58	14.23	12.93	15.10	13.86	11.98
OL				2.27	6.86	2.10	3.79	0.10	1.96	
FO				1.38	4.22	1.28	2.16	0.06	1.22	
FA				0.89	2.65	0.81	1.63	0.04	0.75	
MT										
IL	1.15	1.41	0.96	1.14	1.09	1.18	1.19	1.11	1.34	1.25
AP	0.17	0.24	0.12	0.19	0.19	0.19	0.24	0.17	0.24	0.24

number	65070	65072	65088	65090	65209	65214	65215	65224	65229	65234
subgroup	III	III	III	III	I	II	III	III	II	II
(major elements: wt %)										
SiO2	56.30	54.60	56.44	55.96	53.67	52.59	56.04	56.55	52.04	54.14
TiO2	0.71	0.58	0.70	0.72	0.71	0.49	0.70	0.66	0.53	0.71
Al2O3	12.45	13.23	12.16	12.47	8.33	11.78	12.15	12.01	12.14	15.20
Fe2O3	11.40	10.88	11.52	11.47	12.19	11.03	11.51	11.42	11.15	10.88
FeO	0.0	0.0	0.0	0.0	0.0	0.0	0.0	0.0	0.0	0.0
MnO	0.16	0.17	0.16	0.17	0.18	0.18	0.16	0.16	0.18	0.18
MgO	8.61	9.07	8.70	8.62	13.45	13.29	8.52	9.16	12.57	6.82
CaO	7.83	8.55	7.74	7.79	9.23	9.14	7.82	7.63	9.34	9.75
Na2O	1.31	1.40	1.21	1.06	1.65	0.96	1.42	1.42	1.59	1.44
K2O	1.29	0.97	1.30	1.30	0.75	0.59	1.26	1.24	0.66	0.95
P2O5	0.10	0.09	0.11	0.10	0.09	0.06	0.09	0.10	0.06	0.09
LOI	-0.42	-0.05	-0.22	-0.50	-0.26	-0.10	0.08	-0.40	-0.58	-0.57
H2O-	0.07	0.04	0.01	0.09	0.06	0.03	0.05	0.04	0.24	0.23
total	99.81	99.53	99.83	99.25	100.05	100.04	99.80	99.99	99.92	99.82
(trace elements: ppm)										
Zr	110	88	111	112	69	72	110	103	78	94
Sr	106	99	104	106	209	90	107	114	98	110
Nb	8	7	8	10	5	6	9	7	6	8
Y	20	18	21	19	13	16	20	19	17	20
Rb	67	51	67	65	31	18	66	62	21	43
Ba	267	219	277	281	174	222	261	312	244	244
V	213	205	218	215	218	206	208	211	209	238
Ni	199	186	201	193	377	409	194	215	391	124
Cr	697	679	715	643	1600	1397	689	739	1271	142
La	18	15	19	22	9	15	20	18	17	19
Ce	32	31	37	38	17	27	34	35	26	34
Nd	16	13	17	18	10	12	18	17	11	16
Sc	30	34	35	30	31	34	32	32	36	38
Mg#	59.9	62.28	59.93	59.82	68.61	70.47	59.45	61.37	69.07	55.39
WT% CIPW NORMATIVE MINERALS										
QTZ	9.32	6.57	9.99	10.19		1.52	8.88	8.78		6.94
OR	7.70	5.82	7.77	7.80	4.48	3.52	7.56	7.39	3.93	5.67
AB	11.20	12.03	10.35	9.11	14.10	8.21	12.20	12.11	13.57	12.30
AN	24.52	27.38	24.18	25.81	13.24	26.35	23.41	22.92	24.25	32.51
LC										
NE										
CPX	11.55	12.39	11.45	10.49	26.34	15.45	12.66	11.97	17.95	13.01
DI	6.68	7.43	6.62	6.05	17.54	10.53	7.25	7.08	11.99	6.92
HD	4.87	4.96	4.83	4.44	8.80	4.92	5.40	4.89	5.96	6.09
OPX	34.10	34.46	34.65	34.97	39.63	43.86	33.73	35.33	34.48	27.99
EN	18.56	19.51	18.85	18.99	25.15	28.55	18.18	19.72	21.95	13.94
FS	15.54	14.96	15.80	15.98	14.48	15.30	15.55	15.61	12.53	14.06
OL					0.64				4.65	
FO					0.39				2.86	
FA					0.25				1.80	
MT										
IL	1.36	1.12	1.34	1.39	1.36	0.94	1.35	1.26	1.02	1.36
AP	0.24	0.22	0.26	0.24	0.22	0.14	0.22	0.24	0.14	0.22

number	65239	65265	65279	65281	65302	65410	65412	65413	65427	65584
subgroup	I	II	II	II	III	III	II	I	II	III
(major elements: wt %)										
SiO2	51.68	54.30	54.68	54.85	56.10	56.53	54.64	50.99	54.54	55.44
TiO2	0.58	0.69	0.72	0.71	0.72	0.72	0.71	0.71	0.71	0.55
Al2O3	11.09	14.68	15.72	15.16	9.16	12.50	15.02	13.19	14.92	9.86
Fe2O3	11.45	10.87	10.94	10.95	12.70	11.54	10.88	11.70	10.95	11.91
FeO	0.0	0.0	0.0	0.0	0.0	0.0	0.0	0.0	0.0	0.0
MnO	0.18	0.17	0.17	0.17	0.20	0.16	0.17	0.18	0.17	0.15
MgO	13.04	6.84	6.49	6.78	12.31	8.71	6.72	11.12	6.80	13.52
CaO	9.27	9.73	10.09	9.89	5.80	7.84	9.89	10.03	9.80	6.11
Na2O	1.48	1.74	1.01	1.11	1.26	1.43	1.59	1.07	1.64	1.14
K2O	0.56	0.87	0.88	0.90	1.18	1.20	0.91	0.10	0.93	0.95
P2O5	0.08	0.10	0.09	0.10	0.09	0.10	0.09	0.07	0.10	0.08
LOI	0.24	0.01	-0.72	-0.71	-0.23	-0.50	-0.68	0.70	-0.59	-0.14
H2O-	0.27	0.09	0.09	0.0	0.10	0.15	0.17	0.05	0.08	0.28
total	99.92	100.09	100.16	99.91	99.39	100.38	100.11	99.91	100.05	99.85
(trace elements: ppm)										
Zr	54	94	99	97	106	113	108	66	93	85
Sr	160	112	111	111	90	109	129	93	113	92
Nb	5	8	8	7	7	8	8	5	7	5
Y	13	20	20	22	19	20	24	16	20	16
Rb	21	42	44	43	61	68	48	3	45	49
Ba	227	249	242	234	351	286	48	95	245	239
V	226	237	245	241	219	213	239	237	239	194
Ni	323	130	115	127	289	197	141	229	122	317
Cr	1241	143	126	144	1051	653	146	859	134	1233
La	6	16	17	17	12	22	18	8	18	23
Ce	11	32	30	29	41	36	29	12	32	35
Nd	9	16	16	15	16	17	15	9	14	11
Sc	38	51	41	37	33	31	34	37	38	30
Mg#	69.3	55.48	54.02	55.09	65.75	59.92	55.02	65.31	55.16	69.22
WT% CIPW NORMATIVE MINERALS										
QTZ		6.22	9.55	9.30	7.33	8.92	6.93	2.10	6.52	5.89
OR	3.37	5.20	5.22	5.34	7.10	7.12	5.40	0.60	5.53	5.70
AB	12.75	14.89	8.57	9.44	10.85	12.15	13.52	9.24	13.95	9.79
AN	22.35	30.01	35.87	33.89	16.14	24.25	31.31	31.53	30.77	19.27
LC										
NE										
CPX	19.43	15.01	11.40	12.22	10.24	11.64	14.40	15.34	14.45	8.91
DI	13.03	8.00	5.92	6.47	6.51	6.73	7.62	9.70	7.66	5.97
HD	6.39	7.01	5.48	5.75	3.73	4.91	6.79	5.64	6.79	2.94
OPX	36.98	27.11	27.81	28.23	46.72	34.30	26.87	39.64	27.19	49.18
EN	23.66	13.52	13.47	13.97	28.19	18.67	13.29	23.77	13.48	31.42
FS	13.32	13.59	14.33	14.25	18.53	15.63	13.58	15.87	13.71	17.76
OL	3.81									
FO	2.35									
FA	1.46									
MT										
IL	1.12	1.33	1.37	1.35	1.39	1.37	1.35	1.38	1.36	1.06
AP	0.19	0.24	0.21	0.24	0.22	0.24	0.21	0.17	0.24	0.19

number	65078	65079	65080	65094	65207	65223	65233	65242	65244	65248
subgroup	PM	PM	PM	PM	LOTI	PM	HITI	LOTI	HITI	HITI
(major elements: wt %)										
SiO2	52.10	51.62	51.70	52.03	50.91	51.64	49.84	50.02	49.63	49.05
TiO2	1.64	1.62	1.64	1.64	1.39	1.66	1.63	1.40	1.65	1.62
Al2O3	13.65	13.43	13.51	13.95	13.67	13.48	13.19	13.72	13.36	13.12
Fe2O3	15.40	15.38	15.32	15.22	14.32	15.47	16.17	15.56	16.23	15.99
FeO	0.0	0.0	0.0	0.0	0.0	0.0	0.0	0.0	0.0	0.0
MnO	0.23	0.23	0.22	0.23	0.22	0.24	0.23	0.25	0.23	0.24
MgO	4.95	4.97	4.82	4.86	6.44	4.88	5.96	5.86	5.61	5.53
CaO	9.55	9.52	9.51	9.67	10.64	9.42	9.96	10.39	9.80	9.60
Na2O	2.13	2.15	2.15	2.07	2.16	2.29	2.44	2.53	2.61	2.16
K2O	0.77	0.76	0.77	0.78	0.48	0.76	0.42	0.17	0.41	0.56
P2O5	0.18	0.15	0.18	0.16	0.12	0.17	0.30	0.11	0.31	0.31
LOI	-0.81	-0.69	-0.63	-0.39	-0.54	-0.66	-0.35	0.45	-0.01	1.22
H2O-	0.13	0.10	0.09	0.07	0.06	0.15	0.22	0.25	0.17	0.31
total	99.92	99.24	99.28	100.29	99.87	99.50	100.01	100.71	100.00	99.71
(trace elements: ppm)										
Zr	124	117	122	118	89	118	122	77	121	115
Sr	147	141	144	145	141	144	128	99	130	158
Nb	9	9	9	10	4	9	9	7	9	9
Y	34	32	34	33	32	33	36	27	38	36
kb	40	37	39	38	22	36	15	5	16	21
Ba	158	151	162	168	103	167	150	52	142	263
V	350	350	342	343	352	360	383	413	389	374
Ni	22	23	21	24	44	21	90	69	87	84
Cr	28	25	26	27	83	26	128	123	105	105
La	13	13	13	13	9	13	11	4	11	9
Ce	27	24	28	27	17	32	25	11	25	21
Nd	17	17	17	18	14	20	19	12	19	20
Sc	45	45	43	44	48	43	42	50	38	43
Mg#	38.9	39.03	38.39	38.74	47.11	38.46	42.20	42.73	40.64	40.65
WT% CIPW NORMATIVE MINERALS										
QTZ	0.18	2.96	3.32	3.52	0.11	2.49				
OR	10.45	4.57	4.63	4.65	2.87	4.56	2.52	1.02	2.47	3.43
Ab	18.01	18.51	18.51	17.68	18.48	19.68	20.96	21.75	22.49	18.93
AN	22.45	25.18	25.37	26.71	26.48	24.64	24.16	25.98	23.96	25.32
LC										
NE										
CPX	20.05	18.48	18.12	17.45	21.81	18.34	20.20	21.57	19.80	18.46
DI	7.61	7.03	6.79	6.60	10.00	6.88	8.30	8.90	7.83	7.30
HD	12.44	11.45	11.33	10.85	11.82	11.47	11.90	12.67	11.97	11.16
OPX	25.32	26.81	26.45	26.46	27.30	26.68	24.24	22.40	21.98	29.78
EN	8.40	9.34	9.07	9.16	11.58	9.16	9.16	8.50	7.98	10.81
FS	16.52	17.47	17.38	17.30	15.72	17.52	15.08	13.90	14.00	18.97
OL							4.07	4.31	5.38	0.15
FO							1.45	1.54	1.83	0.05
FA							2.62	2.77	3.54	0.10
MT										
IL	3.11	3.13	3.17	3.14	2.67	3.20	3.14	2.70	3.19	3.19
AP	0.43	0.36	0.43	0.38	0.29	0.41	0.72	0.26	0.75	0.76

number	65250	65261	65267	65271	65415	65428	65433	65443
subgroup	HITI	HITI	LOTI	LOTI	LOTI	HITI	HITI	HITI
(major elements: wt %)								
SiO2	50.35	50.26	49.96	49.81	49.58	50.72	51.10	51.13
TiO2	1.66	1.62	1.39	1.37	1.35	1.74	1.72	1.76
Al2O3	13.57	13.28	13.45	13.48	14.07	13.57	13.24	13.66
Fe2O3	16.47	16.11	15.86	15.51	14.48	16.65	16.61	16.77
FeO	0.0	0.0	0.0	0.0	0.0	0.0	0.0	0.0
MnO	0.23	0.24	0.23	0.23	0.23	0.25	0.23	0.22
M_gO	5.55	5.76	5.96	6.03	6.42	5.02	4.99	4.71
CaO	9.75	9.93	10.27	10.21	10.73	8.80	8.87	8.85
Na2O	2.14	2.22	2.01	1.97	2.21	2.25	2.34	2.02
K2O	0.48	0.36	0.31	0.32	0.26	0.70	0.68	0.67
P2O5	0.32	0.29	0.17	0.16	0.12	0.45	0.49	0.49
LOI	-0.17	-0.04	0.03	0.22	-0.29	-0.21	-0.65	-0.48
H2O-	0.13	0.08	0.01	0.17	0.05	0.04	0.06	0.20
total	100.48	100.11	99.65	99.48	99.21	99.98	99.68	100.00
(trace elements: ppm)								
Zr	93	120	91	91	85	260	252	251
Sr	160	127	131	131	113	166	168	170
Nb	8	8	7	6	7	11	10	12
Y	38	36	31	30	28	47	46	47
Rb	16	13	13	13	5	28	28	27
Ba	172	152	122	123	53	272	285	286
V	382	384	395	382	361	295	286	284
Ni	79	93	85	89	92	86	75	90
Cr	95	117	117	122	170	111	102	87
La	12	10	8	8	6	21	23	26
Ce	23	24	21	21	10	45	43	51
Nd	20	19	16	16	11	29	27	27
Sc	38	39	40	40	41	37	39	39
Mg#	40.0	41.46	42.67	43.51	46.76	37.39	37.31	35.75
WT% CIPW NORMATIVE MINERALS								
QTZ	0.85	0.61	0.58	0.78		1.90	2.16	3.91
OR	2.87	2.16	1.87	1.94	1.57	4.20	4.08	4.02
AB	18.32	19.08	17.35	17.09	19.08	19.33	20.08	17.34
AN	26.30	25.60	27.30	27.68	28.27	25.24	23.95	26.60
LC								
NE								
CPX	17.30	18.95	19.80	19.48	21.12	13.63	14.76	12.46
DI	6.74	7.64	8.16	8.19	9.58	4.96	5.36	4.34
HD	10.57	11.31	11.65	11.29	11.54	8.67	9.40	8.12
OPX	30.41	29.77	29.99	29.98	23.44	31.26	30.50	31.13
EN	10.86	11.03	11.37	11.61	9.84	10.40	10.12	9.89
FS	19.55	18.74	18.62	18.38	13.61	20.87	20.37	21.24
OL					3.61			
FO					1.43			
FA					2.18			
MT								
IL	3.19	3.13	2.69	2.67	2.62	3.36	3.31	3.39
AP	0.77	0.70	0.41	0.39	0.29	1.08	1.18	1.18

number	65002	65003	65006	65011	65015	65018	65035	65063	65065	65071
group	8	8	3	3	7	7	5	5	2	2
(major elements: wt %)										
SiO2	45.82	45.67	47.71	49.05	48.80	49.53	49.41	49.77	47.88	49.01
TiO2	2.84	2.89	1.62	1.84	2.25	2.39	1.87	1.87	1.60	1.47
Al2O3	14.15	13.93	15.60	13.66	12.94	13.16	13.75	13.53	15.07	14.29
Fe2O3	18.82	18.97	14.58	13.87	16.15	16.94	15.13	14.95	13.10	13.14
FeO	0.0	0.0	0.0	0.0	0.0	0.0	0.0	0.0	0.0	0.0
MnO	0.27	0.27	0.22	0.23	0.26	0.27	0.23	0.24	0.20	0.21
MgO	6.23	6.13	7.32	6.99	5.88	5.84	6.05	6.00	8.06	7.66
CaO	9.79	9.89	10.78	11.74	10.41	10.26	10.39	10.56	11.53	11.63
Na2O	2.35	1.87	2.41	2.18	2.18	2.17	2.14	2.08	1.93	1.77
K2O	0.48	0.50	0.32	0.35	0.53	0.56	0.63	0.55	0.35	0.36
P2O5	0.38	0.40	0.17	0.17	0.24	0.25	0.20	0.17	0.15	0.14
LOI	-0.59	-0.96	-0.50	-0.07	-0.74	-0.85	-0.59	-0.46	-0.43	-0.48
H2O-	0.11	0.14	0.25	0.05	0.05	0.04	0.14	0.15	0.12	0.16
total	100.65	99.70	100.48	100.06	98.95	100.56	99.35	99.41	99.56	99.36
(trace elements: ppm)										
Zr	187	191	97	106	159	164	125	125	102	98
Sr	151	152	157	165	154	157	154	165	163	156
Nb	17	18	7	8	14	14	12	10	9	8
Y	51	49	30	32	44	45	35	34	28	28
Rb	15	20	13	10	24	26	27	24	15	16
Ba	188	214	97	109	146	148	193	143	105	103
V	357	360	289	395	412	430	351	368	293	317
Ni	79	80	94	71	46	46	43	42	117	84
Cr	104	106	175	220	92	72	167	109	317	306
La	19	18	9	10	13	14	16	12	8	6
Ce	41	41	14	24	29	32	32	28	18	18
Nd	28	25	11	16	20	21	19	19	18	14
Sc	44	42	47	55	52	52	50	49	44	48
Mg#	39.6	39.03	49.86	49.96	41.90	40.58	44.20	44.29	54.93	53.59
WTX CIPW NORMATIVE MINERALS										
QTZ										
Or	2.84	3.01	1.89	2.07	3.19	3.31	3.78	3.31	2.13	2.19
AB	20.06	16.08	20.56	18.70	18.79	18.45	18.45	17.94	16.59	15.23
AN	26.86	28.49	31.02	26.81	24.46	24.58	26.50	26.41	31.86	30.47
LC										
NE										
CPX	16.50	15.67	18.11	25.88	22.41	20.91	20.65	21.64	20.82	22.56
DI	6.57	6.16	8.86	12.83	9.35	8.47	9.02	9.47	11.31	11.89
HD	9.93	9.51	9.25	13.05	13.05	12.44	11.63	12.17	9.51	10.68
OPX	6.89	16.12	6.73	14.87	22.22	24.48	23.17	26.32	12.48	21.25
EN	2.52	5.82	3.06	6.86	8.54	9.11	9.34	10.63	6.35	10.46
FS	4.37	10.30	3.67	8.01	13.68	15.37	13.83	15.69	6.13	10.78
OL	20.55	14.11	18.19	7.74	4.00	3.12	3.37	0.37	12.69	5.13
FO	7.06	4.78	7.84	3.38	1.45	1.09	1.28	0.14	6.15	2.40
FA	13.48	9.33	10.35	4.35	2.56	2.03	2.09	0.23	6.54	2.73
MT										
IL	5.43	5.56	3.10	3.53	4.37	4.56	3.61	3.61	3.08	2.83
AP	0.90	0.97	0.40	0.40	0.57	0.59	0.47	0.40	0.36	0.33

number	65074	65081	65084	65085	65089	65097	65098X	65098	65200	65201
group	2	5	2	2	5	8	6	7	7	8
(major elements: wt %)										
SiO2	49.53	49.75	47.48	47.03	49.41	47.19	48.52	48.25	48.98	46.31
TiO2	1.47	1.85	1.28	1.25	1.88	2.72	2.25	2.47	2.39	2.66
Al2O3	14.44	13.58	15.59	15.58	13.36	13.28	13.36	13.34	13.11	13.48
Fe2O3	13.06	14.93	14.37	14.17	15.11	18.65	16.23	16.87	16.11	18.92
FeO	0.0	0.0	0.0	0.0	0.0	0.0	0.0	0.0	0.0	0.0
MnO	0.22	0.23	0.22	0.22	0.25	0.23	0.25	0.26	0.27	0.28
MgO	7.78	6.15	8.40	8.23	6.49	5.86	6.43	5.98	6.08	6.23
CaO	11.79	10.51	11.01	10.93	10.72	9.82	10.60	9.49	10.50	9.73
Na2O	1.74	2.35	1.80	1.90	1.80	1.84	2.42	2.27	2.00	1.82
K2O	0.39	0.54	0.19	0.22	0.51	0.69	0.37	0.56	0.48	0.56
P2O5	0.14	0.17	0.14	0.11	0.19	0.29	0.19	0.26	0.25	0.28
LOI	-0.49	-0.33	-0.70	-0.07	-0.53	-0.65	-0.44	-0.52	-0.51	-0.51
H2O-	0.14	0.05	0.17	0.10	0.20	0.01	0.10	0.12	0.06	0.11
total	100.21	99.78	99.95	99.67	99.39	99.93	100.28	99.35	99.72	99.87
(trace elements: ppm)										
Zr	98	124	71	70	126	192	127	179	160	174
Sr	155	169	115	117	150	134	148	153	165	135
Nb	9	7	7	7	11	17	6	9	14	16
Y	28	36	27	27	37	51	44	55	40	50
Rb	17	24	10	9	23	30	15	25	21	24
Ba	109	150	72	67	142	235	97	130	143	200
V	318	383	285	281	388	368	445	417	408	356
Ni	82	41	137	138	63	44	81	87	61	67
Cr	340	102	180	183	141	131	138	78	106	135
La	9	12	6	6	13	25	8	13	14	20
Ce	19	20	11	9	28	49	17	30	29	40
Nd	13	16	12	9	18	27	18	25	23	28
Sc	51	46	45	44	51	50	51	49	51	46
Mg#	54.1	44.93	53.66	53.50	45.97	38.36	43.97	41.25	42.78	39.48
WTX CIPW NORMATIVE MINERALS										
QTZ					0.13					
OR	2.30	3.25	1.12	1.30	3.07	4.14	2.19	3.37	2.90	3.37
AB	14.81	20.14	15.40	16.33	15.49	15.74	20.65	19.55	17.18	15.66
AN	30.70	25.30	34.22	33.97	27.36	26.29	24.79	25.06	25.73	27.40
LC										
NE										
CPX	22.62	22.18	16.60	17.02	21.39	17.88	22.71	17.83	21.37	16.73
DI	12.03	9.84	8.65	8.85	9.71	6.89	9.96	7.37	9.16	6.59
HD	10.58	12.33	7.95	8.18	11.68	10.99	12.75	10.46	12.21	10.14
OPX	21.96	20.51	15.09	12.18	28.48	21.73	14.20	22.36	26.16	18.98
EN	10.93	8.41	7.35	5.91	11.97	7.68	5.75	8.50	10.34	6.86
FS	11.03	12.10	7.74	6.27	16.51	14.05	8.45	13.86	15.81	12.12
OL	4.47	4.65	14.79	16.52		8.30	10.70	6.42	1.46	12.08
FO	2.12	1.80	6.84	7.61		2.75	4.08	2.30	0.55	4.10
FA	2.36	2.85	7.95	8.90		5.55	6.61	4.13	0.92	7.98
MT										
IL	2.81	3.57	2.45	2.41	3.63	5.24	4.31	4.79	4.62	5.13
AP	0.33	0.40	0.33	0.26	0.45	0.69	0.45	0.64	0.59	0.66

number	65202	65203	65204	65205	65206	65219	65220	65236	65240	65241
group	8	6	9	6	7	5	10	5	5	4
(major elements: wt %)										
SiO2	48.15	48.94	45.25	48.92	48.58	48.81	47.96	49.88	48.00	46.18
TiO2	2.76	2.07	4.34	2.06	2.36	2.06	2.88	1.80	1.82	1.68
Al2O3	13.23	13.10	13.10	13.04	13.69	13.32	12.91	13.71	14.19	15.43
Fe2O3	17.95	16.26	19.71	16.21	16.57	15.30	16.68	14.57	16.05	16.67
FeO	0.0	0.0	0.0	0.0	0.0	0.0	0.0	0.0	0.0	0.0
MnO	0.28	0.26	0.30	0.25	0.26	0.25	0.28	0.23	0.25	0.24
MgO	5.73	6.40	5.26	6.27	6.20	6.46	5.92	6.29	6.81	7.47
CaO	9.62	10.79	9.12	10.64	9.73	10.94	10.32	10.58	10.63	10.12
Na2O	2.11	1.86	2.17	2.21	2.07	2.06	2.35	2.23	2.20	2.55
K2O	0.56	0.42	1.10	0.40	0.50	0.39	0.59	0.59	0.31	0.18
P2O5	0.30	0.20	0.75	0.20	0.25	0.21	0.29	0.16	0.15	0.13
LOI	-0.55	-0.69	-0.69	-0.52	-0.44	-0.33	-0.55	-0.46	-0.40	-0.52
H2O-	0.10	0.08	0.06	0.09	0.08	0.09	0.08	0.15	0.08	0.08
total	100.24	99.69	100.47	99.77	99.85	99.56	99.71	99.73	100.09	100.21
(trace elements: ppm)										
Zr	188	130	413	129	172	142	171	122	85	88
Sr	156	132	211	131	153	157	211	157	133	149
Nb	12	10	36	8	11	11	14	8	6	2
Y	56	41	71	45	48	39	40	34	34	37
Rb	25	18	37	16	22	17	21	27	9	5
Ba	132	128	431	118	120	105	197	145	123	34
V	419	396	410	405	388	402	453	366	353	284
Ni	73	63	52	64	86	77	47	49	68	100
Cr	57	189	75	192	85	153	158	125	178	160
La	14	11	43	11	11	11	15	11	10	5
Ce	33	23	95	32	28	24	23	25	16	5
Nd	26	18	60	20	22	19	19	17	12	11
Sc	50	50	46	48	49	51	55	48	49	38
Mg#	38.7	43.81	34.58	43.38	42.57	45.54	41.28	46.09	45.66	47.02
WT% CIPW NORMATIVE MINERALS										
QTZ										
Or	3.37	2.54	6.56	2.42	3.01	2.36	3.55	3.55	1.83	1.06
AB	18.03	15.99	18.53	18.95	17.77	17.77	20.22	19.12	18.87	21.83
AN	25.27	26.48	22.96	24.83	26.97	26.37	23.27	26.04	28.26	30.43
LC										
NE										
CPX	17.76	22.21	14.99	22.98	17.10	22.99	22.53	21.86	20.21	16.23
DI	6.92	9.63	5.50	9.86	7.27	10.40	9.47	9.95	9.05	7.45
HD	10.83	12.58	9.49	13.12	9.83	12.58	13.06	11.91	11.16	8.79
OPX	24.36	25.66	12.25	20.23	25.99	21.57	15.16	22.14	14.49	0.39
EN	8.71	10.26	4.11	8.00	10.19	9.03	5.87	9.33	6.00	0.16
FS	15.65	15.39	8.14	12.22	15.81	12.54	9.29	12.81	8.49	0.22
OL	5.22	2.67	14.63	6.14	4.02	4.45	9.05	3.43	12.49	26.52
FO	1.75	1.01	4.60	2.29	1.48	1.76	3.30	1.37	4.88	10.64
FA	3.47	1.66	10.03	3.85	2.54	2.69	5.75	2.07	7.61	15.88
MT										
IL	5.30	3.99	8.32	3.97	4.54	3.99	5.55	3.48	3.49	3.23
AP	0.71	0.47	1.80	0.47	0.59	0.50	0.69	0.38	0.36	0.31

number	65245	65246	65247	65249	65255	65256	65257	65258	65260	65269
group	3	5	5	10	2	3	3	3	3	2
(major elements: wt %)										
SiO2	48.16	49.32	48.41	48.67	48.28	48.75	48.92	49.09	49.14	49.66
TiO2	1.56	1.95	2.14	1.38	1.46	1.46	1.56	1.52	1.57	1.25
Al2O3	14.15	13.77	13.46	14.56	15.87	14.78	14.06	14.41	14.11	14.20
Fe2O3	13.92	14.84	15.39	13.39	12.66	13.85	14.44	14.32	14.42	12.98
FeO	0.0	0.0	0.0	0.0	0.0	0.0	0.0	0.0	0.0	0.0
MnO	0.21	0.24	0.25	0.22	0.20	0.23	0.23	0.23	0.22	0.21
MgO	7.11	6.51	6.76	7.12	7.37	6.89	6.95	6.86	6.87	7.80
CaO	11.54	10.76	10.88	11.89	11.71	11.66	11.47	11.50	11.50	12.15
Na2O	2.25	2.03	2.06	2.04	1.88	1.98	2.58	2.25	2.36	1.69
K2O	0.27	0.47	0.49	0.19	0.36	0.23	0.24	0.24	0.25	0.33
P2O5	0.13	0.19	0.21	0.12	0.14	0.14	0.13	0.14	0.14	0.12
LOI	-0.04	-0.33	-0.36	-0.42	-0.37	-0.46	-0.77	-0.83	-0.73	-0.36
H2O-	0.30	0.16	0.11	0.20	0.16	0.11	0.32	0.36	0.39	0.0
total	99.56	99.91	99.80	99.36	99.72	99.62	100.13	100.09	100.24	100.03
(trace elements: ppm)										
Zr	95	132	137	81	104	91	94	92	92	76
Sr	141	148	145	148	167	149	150	153	145	161
Nb	8	10	11	6	8	7	4	4	5	7
Y	30	36	41	29	27	30	34	35	32	23
Rb	10	21	22	10	18	12	9	8	9	16
Ba	79	104	139	58	102	64	70	76	75	106
V	352	365	391	341	264	331	370	367	379	323
Ni	85	72	68	80	90	85	80	78	76	75
Cr	205	181	260	231	290	208	208	202	204	245
La	7	11	12	5	9	6	5	7	6	8
Ce	13	24	27	14	18	16	10	8	11	15
Nd	12	18	19	12	14	14	13	11	12	12
Sc	52	49	53	49	39	49	49	50	51	45
Mg#	50.3	46.49	46.53	51.30	53.56	49.63	48.81	48.69	48.55	54.34
WTZ CIPW NORMATIVE MINERALS										
QTZ										
OR	1.65	2.84	2.96	1.12	2.13	1.36	1.42	1.42	1.48	1.95
AB	19.46	17.43	17.69	17.60	16.16	17.01	22.00	19.21	20.14	14.47
AN	28.28	27.46	26.42	30.55	34.27	31.20	26.31	28.78	27.41	30.45
LC										
NE										
CPX	24.43	21.25	22.54	23.86	19.63	22.13	25.21	23.23	24.37	24.49
DI	12.07	9.80	10.45	11.96	10.35	10.74	12.04	11.06	11.59	12.98
HD	12.36	11.45	12.09	11.89	9.28	11.39	13.16	12.17	12.78	11.51
OPX	10.59	23.86	17.93	15.79	15.33	18.28	7.44	14.74	12.81	21.87
EN	4.87	10.19	7.70	7.37	7.56	8.24	3.30	6.52	5.66	10.84
FS	5.72	13.66	10.23	8.41	7.77	10.03	4.14	8.23	7.15	11.03
OL	12.26	2.96	7.85	8.14	9.34	6.87	14.33	9.38	10.46	4.09
FO	5.34	1.20	3.19	3.60	4.38	2.94	6.01	3.92	4.37	1.93
FA	6.92	1.77	4.67	4.53	4.96	3.94	8.32	5.46	6.09	2.16
MT										
IL	3.02	3.76	4.12	2.66	2.81	2.81	2.98	2.91	3.00	2.39
AP	0.31	0.45	0.50	0.28	0.33	0.33	0.31	0.33	0.33	0.28

number	65270	65272	65273	65283	65292	65298	65299	65400	65406	65418
group	5	7	3	6	1	3	5	1	4	9
(major elements: wt %)										
SiO2	49.40	49.42	49.14	50.77	47.47	47.07	45.87	46.60	48.89	44.77
TiO2	2.00	2.28	1.55	2.10	1.41	1.68	2.51	1.21	1.68	4.17
Al2O3	13.70	13.17	14.24	13.69	15.38	15.19	15.09	16.73	14.59	12.90
Fe2O3	15.05	15.95	14.05	14.98	13.46	15.38	17.19	13.37	13.57	19.49
FeO	0.0	0.0	0.0	0.0	0.0	0.0	0.0	0.0	0.0	0.0
MnO	0.23	0.25	0.21	0.23	0.22	0.24	0.25	0.21	0.21	0.27
MgO	6.26	5.74	7.17	5.71	8.48	7.76	7.47	8.82	5.99	4.98
CaO	10.61	10.22	11.66	9.69	11.76	10.82	9.70	10.83	11.44	8.97
Na2O	2.41	2.12	2.19	2.18	1.61	1.89	2.05	1.87	2.39	2.42
K2O	0.47	0.56	0.26	0.77	0.14	0.26	0.59	0.10	0.38	1.04
P2O5	0.20	0.25	0.12	0.26	0.11	0.16	0.32	0.10	0.16	0.75
LOI	-0.81	-0.59	-0.56	-0.76	-0.45	-0.54	-0.56	-0.24	-0.24	-0.71
H2O-	0.32	0.23	0.33	0.35	0.14	0.19	0.19	0.15	0.19	0.08
total	99.84	99.60	100.36	99.97	99.73	100.10	100.67	99.75	99.25	99.13
(trace elements: ppm)										
Zr	133	174	93	150	68	96	179	68	111	406
Sr	151	150	146	208	144	150	182	147	170	219
Nb	8	13	4	12	6	7	20	4	9	35
Y	43	46	34	36	25	32	39	24	30	72
Rb	20	32	9	30	9	11	26	4	12	44
Ba	113	153	85	237	46	97	208	33	50	468
V	389	420	371	401	319	304	284	240	342	398
Ni	75	58	84	30	158	90	118	137	63	41
Cr	172	158	211	116	198	165	134	177	196	68
La	11	15	6	20	5	6	20	3	9	48
Ce	23	34	10	42	4	12	32	4	16	100
Nd	19	26	12	26	10	13	22	7	12	60
Sc	47	46	48	46	46	45	37	38	30	34
Mg#	45.2	41.62	50.27	43.02	55.51	49.98	46.26	56.65	46.65	33.60
WT% CIPW NORMATIVE MINERALS										
QTZ				1.30						
OR	2.84	3.37	1.54	4.61	0.83	1.54	3.49	0.59	2.30	6.26
AB	20.65	18.28	18.70	18.62	13.79	16.16	17.43	16.08	20.64	20.90
AN	25.45	25.16	28.49	25.62	34.79	32.57	30.46	37.52	28.55	21.77
LC										
NE										
CPX	22.20	20.81	24.17	17.88	19.53	17.19	13.30	13.50	23.68	15.84
DI	9.96	8.66	11.93	7.67	10.62	8.43	6.16	7.45	10.92	5.63
HD	12.24	12.15	12.25	10.21	8.90	8.76	7.13	6.05	12.76	10.22
OPX	17.82	27.11	14.39	27.34	16.31	13.66	9.14	11.21	13.54	8.27
EN	7.39	10.39	6.61	10.82	8.32	6.23	3.93	5.80	5.78	2.68
FS	10.43	16.72	7.78	16.52	8.00	7.43	5.21	5.41	7.75	5.59
OL	6.74	0.28	9.46		11.78	15.27	20.63	18.53	7.64	17.06
FO	2.64	0.10	4.12		5.72	6.60	8.37	9.14	3.08	5.18
FA	4.10	0.18	5.35		6.06	8.68	12.26	9.39	4.56	11.88
MT										
IL	3.84	4.41	2.96	4.03	2.72	3.23	4.81	2.34	3.27	8.09
AP	0.47	0.59	0.28	0.62	0.26	0.38	0.76	0.24	0.38	1.82

number	65419	65421	65429	65431	65439	65445
group	3	3	3	5	7	5
(major elements: wt %)						
SiO2	49.50	49.28	49.22	47.45	47.66	49.04
TiO2	1.65	1.59	1.66	1.91	2.47	1.99
Al2O3	13.77	13.54	13.75	13.09	13.59	13.45
Fe2O3	14.79	14.51	14.46	15.33	16.92	15.00
FeO	0.0	0.0	0.0	0.0	0.0	0.0
MnO	0.24	0.22	0.23	0.23	0.24	0.24
MgO	7.29	7.02	7.02	6.34	6.19	6.16
CaO	11.63	11.62	11.45	10.62	9.95	10.65
Na2O	1.66	2.14	2.02	2.04	2.40	2.35
K2O	0.29	0.27	0.31	0.47	0.67	0.46
P2O5	0.15	0.15	0.15	0.18	0.28	0.20
LOI	-0.92	-0.62	-0.76	1.69	-0.80	0.01
H2O-	0.01	0.17	0.29	0.16	0.06	0.10
total	100.06	99.89	99.80	99.51	99.63	99.65
(trace elements: ppm)						
Zr	89	84	86	118	194	134
Sr	137	140	163	143	187	161
Nb	8	7	5	11	15	10
Y	31	30	33	35	44	39
Rb	13	9	9	14	26	20
Ba	92	82	115	133	211	125
V	352	342	380	356	356	375
Ni	88	76	47	64	55	65
Cr	315	288	316	244	141	159
La	7	8	7	12	20	10
Ce	15	15	11	18	43	29
Nd	12	12	13	15	27	16
Sc	52	43	52	56	44	49
Mg#	49.4	48.94	49.02	45.03	42.02	44.86
WT% CIPW NORMATIVE MINERALS						
QTZ						
Or	1.71	1.60	1.83	2.90	4.02	2.78
AB	14.13	18.28	17.26	17.94	20.57	20.31
AN	29.41	26.86	27.89	26.20	24.66	25.28
LC						
NE						
CPX	22.99	25.38	23.86	22.92	19.76	22.86
DI	11.14	12.18	11.49	10.20	8.32	10.17
HD	11.84	13.20	12.37	12.72	11.44	12.68
OPX	25.93	17.23	19.90	18.23	11.75	18.36
EN	11.68	7.68	8.90	7.50	4.56	7.55
FS	14.25	9.55	10.99	10.73	7.19	10.80
OL	2.32	7.24	5.71	7.59	13.83	6.10
FO	0.99	3.06	2.42	2.95	5.05	2.37
FA	1.33	4.19	3.29	4.64	8.78	3.73
MT						
IL	3.15	3.06	3.19	3.78	4.75	3.86
AP	0.36	0.36	0.36	0.45	0.66	0.47

number	65026	65030	65031	65040	65041	65043	65047	65051	65083	65087
(major elements: wt %)										
SiO2	39.13	51.20	51.08	37.57	48.25	44.71	42.18	43.79	38.87	43.07
TiO2	3.40	1.81	1.72	4.66	2.05	2.95	4.29	2.68	3.73	3.50
Al2O3	7.43	12.42	11.61	6.33	10.59	7.45	6.79	6.99	7.53	8.67
Fe2O3	15.37	12.42	12.46	15.01	12.92	13.61	15.99	14.10	14.03	14.93
FeO	0.0	0.0	0.0	0.0	0.0	0.0	0.0	0.0	0.0	0.0
MnO	0.21	0.14	0.15	0.18	0.16	0.17	0.17	0.19	0.16	0.17
MgO	16.09	8.65	10.45	14.30	11.52	14.94	13.57	16.75	15.35	11.56
CaO	9.51	9.54	9.02	10.54	9.48	9.44	9.11	9.36	9.71	8.90
Na2O	0.59	2.17	2.12	1.63	1.91	1.48	1.26	1.19	1.91	2.20
K2O	2.83	0.91	0.90	3.05	1.20	2.07	2.64	1.74	2.73	3.08
P2O5	0.78	0.31	0.29	0.88	0.24	0.53	0.89	0.62	0.66	0.88
LOI	3.88	0.48	0.21	4.82	1.11	1.77	1.48	1.35	3.91	3.07
H2O-	0.17	0.26	0.07	0.14	0.18	0.14	0.27	0.30	0.86	0.18
total	99.39	100.31	100.08	99.11	99.61	99.26	98.64	99.06	99.45	100.21
(trace elements: ppm)										
Zr	329	103	92	317	136	269	418	251	319	398
Sr	946	428	392	701	360	668	896	813	665	1221
Nb	100	24	22	71	33	45	66	55	81	66
Y	26	23	23	24	18	30	30	25	24	32
Rb	91	28	25	101	42	55	72	51	85	82
Ba	1423	585	537	1451	612	1179	1308	964	1299	1347
V	261	206	204	313	207	242	271	224	278	231
Ni	594	286	374	490	388	623	579	737	619	429
Cr	744	298	463	711	518	819	503	753	840	417
La	91	32	43	52	23	50	66	64	73	94
Ce	179	57	61	126	49	113	153	128	143	199
Nd	82	31	30	68	26	57	83	66	65	95
Sc	19	23	21	22	22	23	21	21	25	17
Mg#	67.5	57.97	62.42	65.36	63.85	68.50	62.70	70.18	68.43	60.53
WTZ CIPW NORMATIVE MINERALS										
QTZ										
OR		5.47	5.40		7.31	12.74	16.37	10.71		19.07
AB		18.68	18.20		16.66	8.70	3.98	7.50		2.46
AN	9.88	21.83	19.79	1.02	17.29	7.89	5.33	8.95	4.19	4.91
LC	13.98			15.25					13.56	
NE	2.88			8.06		2.35	3.91	1.62	9.39	9.23
CPX	26.50	19.93	19.37	26.94	24.10	30.16	29.27	28.43	27.30	28.84
DI	18.42	11.59	12.08	18.89	15.51	21.25	19.43	20.29	19.57	18.24
HD	8.08	8.34	7.29	8.05	8.59	8.92	9.84	8.14	7.72	10.60
OPX		28.95	27.88		12.38					
EN		15.86	16.47		7.57					
FS		13.09	11.40		4.81					
OL	37.24	0.91	5.36	32.03	17.67	31.03	30.42	35.98	33.53	26.39
FO	23.96	0.48	3.04	20.81	10.39	20.27	18.55	23.87	22.37	15.21
FA	13.28	0.43	2.32	11.22	7.28	10.76	11.88	12.11	11.16	11.18
MT										
IL	6.88	3.50	3.31	9.55	4.01	5.84	8.55	5.30	7.60	6.96
AP	1.97	0.75	0.70	2.25	0.59	1.31	2.21	1.53	1.68	2.18

number	65092	65095	65096B	65213	65216	65217A	65225	65226	65243	65274
(major elements: wt %)										
SiO2	46.62	42.69	40.18	38.68	43.84	47.46	40.94	46.61	44.21	41.21
TiO2	2.50	2.89	3.68	5.06	3.77	2.42	3.08	3.62	2.40	3.38
Al2O3	10.52	8.69	5.86	8.06	10.20	11.65	7.30	10.85	7.18	8.15
Fe2O3	13.32	13.61	14.37	15.20	14.72	12.91	14.91	13.45	13.82	14.74
FeO	0.0	0.0	0.0	0.0	0.0	0.0	0.0	0.0	0.0	0.0
MnO	0.17	0.19	0.17	0.19	0.18	0.17	0.18	0.16	0.17	0.17
MgO	10.93	13.54	20.83	10.64	9.40	7.99	16.45	8.39	17.07	13.30
CaO	9.53	10.54	7.90	10.41	9.41	8.68	9.27	7.95	8.88	10.89
Na2O	2.14	2.15	0.80	1.95	2.59	2.20	1.87	2.51	1.95	2.08
K2O	1.58	2.27	2.48	3.77	3.19	1.67	2.08	3.41	1.49	2.36
P2O5	0.63	0.51	0.48	0.85	1.18	0.54	0.44	0.81	0.41	1.05
LOI	1.95	1.79	3.13	4.47	1.20	4.49	3.59	1.77	1.70	2.14
H2O-	0.11	0.33	0.26	0.33	0.07	0.04	0.14	0.16	0.36	0.35
total	100.00	99.20	100.14	99.61	99.75	100.22	100.25	99.69	99.64	99.82
(trace elements: ppm)										
Zr	193	222	269	500	544	263	239	463	167	299
Sr	819	704	621	1107	1395	690	612	1163	559	1151
Nb	48	84	54	92	94	50	63	67	42	77
Y	28	23	19	34	39	24	21	32	21	32
Rb	48	93	70	103	82	49	69	85	45	78
Ba	1119	1264	1264	1242	1632	887	929	1370	982	2176
V	213	250	240	304	217	186	251	199	229	251
Ni	372	444	918	305	290	233	643	272	781	492
Cr	432	944	889	562	256	264	702	260	705	521
La	71	68	42	81	130	52	47	86	41	99
Ce	143	129	91	171	260	113	94	182	81	207
Nd	68	52	49	92	118	53	49	91	44	100
Sc	21	23	23	22	20	20	21	15	20	21
Mg#	61.9	66.34	74.17	58.10	55.85	55.07	68.61	55.27	70.99	64.12
WT% CIPW NORMATIVE MINERALS										
QTZ										
OR	9.67	9.03	2.18		19.43	10.45	3.25	20.90	9.15	4.70
AB	18.75				4.60	19.72		15.20	8.01	
AN	14.94	7.69	5.32	2.26	6.99	17.99	5.66	8.58	6.69	6.19
LC		3.91	10.35	18.73			7.59			7.72
NE		10.30	3.85	9.58	9.75		9.02	3.70	4.95	9.95
CPX	24.28	35.25	26.07	31.54	27.23	19.69	32.12	22.04	29.32	34.97
DI	15.35	24.04	20.03	20.19	16.16	11.11	22.58	13.04	21.05	23.28
HD	8.93	11.22	6.04	11.35	11.08	8.58	9.54	8.99	8.27	11.68
OPX	1.11					14.57				
EN	0.67					7.72				
FS	0.45					6.85				
OL	24.82	26.85	43.72	22.85	21.78	11.38	35.12	20.50	36.14	27.23
FO	14.30	16.88	31.64	13.35	11.67	5.75	22.88	10.95	24.14	16.66
FA	10.53	9.96	12.08	9.50	10.12	5.62	12.23	9.55	12.00	10.57
MT										
IL	4.92	5.73	7.33	10.30	7.38	4.87	6.16	7.13	4.74	6.70
AP	1.54	1.26	1.19	2.16	2.88	1.36	1.10	1.99	1.01	2.59

number	65275	65287	65288	65293	65295	65296	65297	65407	65411	65423	65438
(major elements: wt %)											
SiO2	41.77	44.86	44.66	45.85	45.73	43.41	45.94	48.45	45.73	44.91	43.52
TiO2	3.92	3.39	3.25	2.46	2.53	2.98	3.31	2.23	2.33	3.00	4.83
Al2O3	9.99	8.32	7.90	9.68	9.51	8.68	10.52	11.29	9.26	10.14	8.54
Fe2O3	14.37	14.09	14.13	13.39	13.15	13.64	14.15	11.78	13.57	14.29	15.80
FeO	0.0	0.0	0.0	0.0	0.0	0.0	0.0	0.0	0.0	0.0	0.0
MnO	0.19	0.17	0.18	0.17	0.18	0.18	0.18	0.14	0.17	0.17	0.16
MgO	7.77	13.25	14.08	11.56	13.05	13.79	9.80	9.56	12.70	11.44	11.75
CaO	12.57	8.72	8.37	9.62	9.33	9.92	8.59	9.63	9.60	10.37	8.69
Na2O	2.59	1.77	1.64	2.18	1.50	1.45	2.31	2.35	2.07	1.86	1.69
K2O	2.94	2.54	2.56	1.29	2.70	3.33	2.69	1.17	1.33	1.94	2.48
P2O5	1.25	0.82	0.76	0.57	0.68	0.81	0.86	0.35	0.57	0.43	0.53
LOI	1.88	1.43	2.62	3.08	0.50	1.06	1.23	1.55	2.51	0.93	1.25
H2O-	0.10	0.27	0.15	0.01	0.25	0.17	0.03	0.59	0.02	0.06	0.38
total	99.34	99.63	100.30	99.86	99.11	99.42	99.61	99.09	99.86	99.54	99.62
(trace elements: ppm)											
Zr	387	430	407	176	274	347	532	120	176	222	289
Sr	1672	924	920	782	925	1064	1158	725	747	608	752
Nb	105	110	107	43	60	75	81	39	42	63	74
Y	45	28	29	28	26	29	35	20	26	23	28
Rb	98	95	91	43	85	106	69	40	41	65	66
Ba	2618	1683	1569	1071	1675	2116	1048	656	1041	1019	1159
V	305	194	186	220	462	224	204	222	212	253	289
Ni	135	555	619	432	549	404	352	345	498	363	485
Cr	373	520	508	470	212	631	345	418	494	446	452
La	152	111	108	64	65	80	103	42	69	54	48
Ce	309	208	200	130	138	167	197	80	126	100	103
Nd	139	87	88	63	68	80	95	38	65	49	56
Sc	23	18	17	19	21	18	17	15	21	24	17
Mg#	51.7	65.07	66.37	63.10	66.28	66.69	57.84	61.65	64.96	61.33	59.6
WT% CIPW NORMATIVE MINERALS											
QTZ											
OR	5.48	15.55	15.74	7.99	16.44	12.97	16.40	7.22	8.19	11.80	15.20
AB		10.55	10.11	18.85	8.81		14.85	20.76	16.67	8.55	9.16
AN	7.25	7.52	6.90	13.43	11.58	7.58	10.72	17.54	12.55	13.99	8.71
LC	9.91					5.76					
NE	12.38	2.69	2.34	0.26	2.31	6.86	2.88		0.86	4.15	3.08
CPX	40.62	25.77	25.24	26.64	25.60	30.62	22.49	24.46	27.01	29.46	26.42
DI	22.65	17.47	17.35	17.12	17.31	21.05	13.62	15.42	17.77	18.65	17.07
HD	17.96	8.30	7.89	9.52	8.29	9.58	8.87	9.05	9.24	10.81	9.36
OPX								11.47			
EN								6.85			
FS								4.62			
OL	13.58	29.27	31.40	26.54	28.67	28.40	24.11	13.26	28.73	25.14	26.64
FO	6.78	18.29	19.94	15.58	17.85	18.02	13.22	7.61	17.33	14.50	15.73
FA	6.80	10.99	11.47	10.96	10.82	10.38	10.89	5.65	11.40	10.64	10.91
MT											
IL	7.76	6.67	6.42	4.90	4.95	5.85	6.49	4.42	4.61	5.87	9.52
AP	3.09	2.01	1.87	1.41	1.66	1.98	2.10	0.87	1.41	1.05	1.30

number	65004	65008	65012	65208	65222	65420	65422	65441
(major elements: wt %)								
SiO2	49.82	48.44	47.91	47.78	46.39	49.05	49.99	50.65
TiO2	1.99	2.87	2.46	2.29	2.52	3.17	3.23	2.94
Al2O3	12.47	12.15	12.27	12.16	12.39	11.89	12.08	12.65
Fe2O3	17.93	17.63	19.14	18.51	19.30	18.19	18.32	15.99
FeO	0.0	0.0	0.0	0.0	0.0	0.0	0.0	0.0
MnO	0.27	0.28	0.27	0.28	0.28	0.26	0.26	0.21
MgO	5.24	4.05	5.30	5.69	5.96	3.91	4.01	3.65
CaO	9.76	8.03	10.20	10.19	10.49	8.42	8.49	7.86
Na2O	2.22	2.35	2.12	1.97	1.74	2.33	2.34	2.92
K2O	0.54	1.42	0.20	0.20	0.30	1.19	1.22	1.47
P2O5	0.20	0.57	0.20	0.21	0.20	0.47	0.49	0.51
LOI	-0.92	1.30	-0.29	-0.25	0.11	-0.27	-0.81	0.67
H2O-	0.28	0.28	0.05	0.06	0.09	0.03	0.12	0.19
total	99.80	99.37	99.83	99.09	99.77	98.64	99.74	99.71
(trace elements: ppm)								
Zr	111	233	97	139	109	326	315	269
Sr	138	308	110	113	165	145	144	161
Nb	9	21	9	8	8	20	22	19
Y	42	40	35	43	35	70	69	61
Rb	22	40	5	9	6	60	62	77
Ba	165	642	34	53	53	350	320	317
V	437	395	592	541	603	363	355	358
Ni	22	32	77	79	83	20	23	21
Cr	82	23	81	123	134	34	36	25
La	8	38	4	8	6	34	34	30
Ce	15	76	12	17	7	73	69	65
Nd	12	40	10	18	12	43	40	39
Sc	56	32	46	44	51	43	48	42
Mg#	36.7	31.27	35.42	37.85	37.95	29.86	30.24	31.14
WT% CIPW NORMATIVE MINERALS								
QTZ		0.19				1.28	1.70	1.24
OR	3.24	8.74	1.20	1.21	1.82	7.25	7.31	8.93
AB	19.04	20.71	18.28	17.11	15.08	20.31	20.08	25.41
AN	22.78	19.17	23.81	24.38	25.72	19.03	19.12	17.55
LC								
NE								
CPX	21.17	15.71	22.40	22.08	22.18	17.79	17.36	16.28
DI	7.59	4.99	7.86	8.24	8.35	5.45	5.40	5.25
HD	13.59	10.72	14.55	13.84	13.83	12.34	11.96	11.04
OPX	28.79	28.42	24.30	26.84	20.68	27.00	27.04	23.61
EN	9.42	8.19	7.78	9.17	7.13	7.51	7.63	6.92
FS	19.37	20.23	16.52	17.67	13.56	19.50	19.41	16.70
OL	0.67		4.76	3.41	9.13			
FO	0.21		1.43	1.09	2.95			
FA	0.47		3.34	2.32	6.18			
MT								
IL	3.83	5.68	4.76	4.46	4.90	6.20	6.22	5.74
AP	0.48	1.41	0.48	0.51	0.49	1.15	1.18	1.24

REFERENCES

Arndt, N.T., 1976: Melting relations of ultramafic lavas (komatiites) at 1 atm and high pressure. Rep. Geophys. Lab., Carnegie Inst. Yrbk 75: 555-562.

Arndt, N.T., 1977: Ultrabasic magmas and high degree melting of the mantle. Contrib. Mineral. Petrol. 64: 205-221.

Arndt, N.T., Naldrett, A.J. & Pyke, D.R., 1977: Komatiitic and iron-rich tholeiitic lavas of Munro township, Ontario: trace element evidence. J. Petrol. 18: 319-369.

Arndt, N.T. & Nesbitt, R.W., 1982: Geochemistry of Munro Township basalts. In Arndt, N.T. & Nisbet, E.G. (Ed.): KOMATIITES. George Allen & Unwin, London: 309-329.

Arth, J.G., Arndt, N.T. & Naldrett, A.J., 1977: Genesis of Archean komatiites - trace element evidence from Munro Township. Geology 5: 590-594.

Basaltic Volcanism Study Project, 1981: BASALTIC VOLCANISM ON THE TERRESTRIAL PLANETS. Pergamon Press Inc., New York: 1286 pp.

Bence, A.E., Bayliss, D.M., Bender, J.F. & Grove, T.L., 1979: Controls on the major and minor element chemistry of mid-ocean ridge basalts and glasses. In Talwani, M., Harrison, C.H. & Hayes, D.E. (Eds): DEEP DRILLING RESULTS IN THE ATLANTIC OCEAN: OCEAN CRUST. American Geophysics Union, Washington, D.C.: 331-371.

Bird, P., 1979: Continental delamination and the Colorado Plateau. J. Geophys. Res. 84: 7561-7571.

Black, L.P. & James, P.R., 1983: Geological history of the Archean Napier Complex of Enderby Land. In Oliver, R.L., James, P.R. & Jago, J.B., (Eds): ANTARCTIC EARTH SCIENCE. Australian Academy of Science: 11-15.

Black, L.P., James, P.R. & Harley, S.L., 1983a: Geochronology and geological evolution of metamorphic rocks in the Field Islands area, East Antarctica. J. Metamorphic. Geol. 1: 277-303.

Black, L.P., James, P.R. & Harley, S.L., 1983b: The geochronology, structure and metamorphism of early Archean rocks at Fyfe Hills, Enderby Land, Antarctica. Precamb. Res. 21: 197-222.

Bohlen, S.R. & Essene, E.J., 1980: Evaluation of coexisting garnet-biotite, garnet-clinopyroxene, and other Mg-Fe exchange thermometers in Adirondack granulites: summary. Geol. Soc. Am. Bull. 91(1): 107-109.

Bohlen, S.R., Wall, V.J. & Boettcher, A.L., 1983: Experimental investigation and application of garnet granulite equilibria. Contrib. Mineral. Petrol. 83: 52-61.

Bryan, W.B. & Moore, J.G., 1977: Compositional variations of young basalts in the Mid-Atlantic Ridge rift valley near lat. 36°49'N. Geol. Soc. Am. Bull. 88: 556-570.

Buddington, A.F., 1963: Isograds and the role of H_2O in metamorphic facies of orthogneisses of Northwest Adirondacks, New York. Geol. Soc. Am. Bull. 74: 1155-1182.

Buddington, A.F., 1965: The origin of three garnet isograds in Adirondack gneisses. Mineral. Mag. 34: 71-81.

Cameron, W.E., 1985: Petrology and origin of primitive lavas from the Troodos ophiolite, Cyprus. Contrib. Mineral. Petrol. 89: 239-255.

Cameron, W.E. Nisbet, E.G. & Dietrich, V.J., 1979: Boninites, komatiites and ophiolitic basalts. Nature 280: 550-553.

Cawthorn, R.G. & Davis, G., 1983: Experimental data at 3 kbars pressure on parental magma to the Bushveld Complex. Cont. Mineral. Petrol. 83: 128-135.

Cawthorn, R.G. & Strong, D.F., 1974: The petrogenesis of komatiites and related rocks as evidence for a layered upper mantle. Earth Planet. Sci. Lett. 23: 369-375.

Clough, W.L. & Field, D., 1980: Chemical variation in metabasites from a Proterozoic amphibolite-granulite transition zone, South Norway. Contrib. Mineral. Petrol. 73: 277-286.

Coe, R.S. & Kirby, S.H., 1975: The orthoenstatite to clinoenstatite transformation by shearing and reversion by annealing: mechanism and potential applications. Contrib. Mineral. Petrol. 52: 29-55.

Collerson, K.D. & Sheraton, J.W., 1986: Bedrock geology and crustal evolutio of the Vestfold Hills. In Pickard, J. (Ed.): ANTARCTIC OASIS. Academic Press, New York: 21-62.

Collerson, K.D. & Sheraton, J.W. (in press): Age and geochemical characteristics of a mafic dyke swarm in the Archean Vestfold Block, Antarctica: Inferences about Proterozoic dyke emplacement in Gondwanaland. J. Petrol.

Collerson, K.D., Reid, E., Millar, D. & McCulloch, M.T., 1983a: Lithological and Sr-Nd isotopic relationships in the Vestfold Block: Implications for Archean and Proterozoic crustal evolution in the East Antarctic. In Oliver, R.L., James, P.R. & Jago, J.B. (Eds): ANTARCTIC EARTH SCIENCE. Australian Academy of Science: 77-84.

Collerson, K.D., Sheraton, J.W & Arriens, P.A., 1983b: Granulite facies metamorphic conditions during the Archean evolution and late Proterozoic reworking of the Vestfold Block, Eastern Antarctica. 6th Aust. Geol. Conv. Canberra (Abst.): 53-54.

Cox, K.G. & Jamieson, B.G., 1974: The olivine-rich lavas of Nuanetsi: a study of polybaric magmatic evolution. J. Petrol. 15: 269-301.

Dahl, P.S., 1980: The thermal-compositional dependence of Fe^{2+}-Mg distribution between coexisting garnet and pyroxene: applications to geothermometry. A. Mineral. 65: 852-866.

Dallwitz, W.B., Green, D.H. & Thompson, J.E., 1966: Clinoenstatite in a volcanic rock from the Cape Vogel area, Papua. J. Petrol. 7: 375-403.

De Paolo, D.J. Manton, W.I., Grew, E.S. & Halpern, M., 1982: Sm-Nd, Rb-Sr and U-Th-Pb systematics of granulite facies rocks from Fyfe Hills, Enderby Land, Antarctica. Nature 298: 614-618.

Dick, H.J.B. & Bullen, T., 1984: Chromian spinel as a petrogenetic indicator in abyssal and Alpine-type peridotites and spacially associated lavas. Contrib. Mineral. Petrol. 86: 54-76.

Drake, M.J., 1975: Plagioclase-melt equilibria. Geochim. Cosmochim Acta 40: 457-465.

Duncan, R.A. & Green, D.H., 1980: Role of multistage melting in the formation of oceanic crust. Geology 8: 22-26.

Dungan, M.A., Long, P.E. & Rhodes, J.M., 1978: The petrology and geochemistry of basalts from site 396, legs 45 and 46 of the deep sea drilling project. Initial Reports of the Deep Sea Drilling Project 45: 461-472.

Echeverria, L.M., 1980: Tertiary or Mesozoic komatiites from Gorgona Island Colombia: field relations and geochemistry. Contrib. Mineral. Petrol. 73: 253-266.

Ellis, D.J., 1980: Osumilite-sapphirine-quartz granulites from Enderby Land, Antarctica: P-T conditions of metamorphism, implications for garnet-cordierite equilibria and the evolution of the deep crust. Contrib. Mineral. Petrol. 74: 201-210.

Ellis, D.J., 1983: The Napier and Rayner complexes of Enderby Land, Antarctica - contrasting styles of metamorphism and tectonism. In Oliver, R.L., James, P.R. & Jago, J.B. (Eds): ANTARCTIC EARTH SCIENCE. Australian Academy of Science: 20-24.

Ellis, D.J. & Green, D.H., 1979: An experimental study of the effect of Ca upon garnet-clinopyroxene Fe-Mg exchange equilibria. Contrib. Mineral. Petrol. 71: 13-22.

Ellis, D.J. & Green, D.H., 1985: Garnet forming reactions in mafic granulites from Enderby Land, Antarctica - Implications for geothermometry and geobarometry. J. Petrol. 26: 633-662.

Ellis, D.J., Sheraton, J.W., England, R.N. & Dallwitz, W.B., 1980: Osumilite-sapphirine-quartz granulites from Enderby Land, Antarctica - Mineral assemblages and reactions. Contrib. Mineral. Petrol. 72: 123-143.

England, P.C. & Richardson, S.W., 1977: The influence of erosion upon mineral facies of rocks from different metamorphic environments. Geol. Soc. Lond. J. 134: 201-213.

Essene, E.J., 1982: Geologic thermometry and barometry. In Ferry, J.M. (Ed.): REVIEWS IN MINERALOGY. Mineral. Soc. Am. 10: 153:206.

Faure, G., Bowman, J.R., Elliot, D.H. & Jones, L.M., 1974: Strontium isotopic compositions and petrogenesis of the Kirkpatrick Basalt, Queen Alexandra Range, Antarctica. Contrib. Mineral. Petrol. 48: 153-169.

Ferguson, A.K., 1973: On hour-glass sector zoning in clinopyroxene. Min. Mag. 39: 321-325.

Ferry, J.M. & Burt, D.M., 1982: Characterization of metamorphic fluid compositions through mineral equilibria. In Ferry, J.M. (Ed.): REVIEWS IN MINERALOGY. Mineral. Soc. Am. 10: 207-262.

Finnerty, A.A. & Boyd, F.R., 1984: Evaluation of thermobarometers for garnet peridotites. Geochem. Cosmochim Acta 48: 15-27.

Foster, M.E & Hudleston, P.J., 1986: "Fracture cleavage" in the Duluth Complex, northeastern Minnesota. Geol. Soc. Am. Bull. 97: 85-96.

Francis, D.M. & Hynes, A.J., 1979: Komatiite-derived tholeiites in the Proterozoic of New Quebec. Earth Planet. Sci. Lett. 44: 473-481.

Francis, D.M., Hynes, A.J. Ludden, J.N. & Bedard, J., 1981: Crystal fractionation and partial melting in the petrogenesis of a Proterozoic high-MgO volcanic suite, Ungava, Quebec. Contrib. Mineral. Petrol. 78: 27-36.

Freer, R., 1981: Diffusion in silicate minerals and glasses: a data digest an guide to the literature. Contrib. Mineral. Petrol. 76: 440-456.

Frey, F.A. & Green, D.H., 1974: The mineralogy, geochemistry and origin of lherzolite inclusions in Victorian basanites. Geochim. Cosmochim. Acta 38: 1023-1059.

Frey, F.A., Green, D.H. & Roy, S.D., 1978: Integrated models of basalt petroenesis: a study of quartz tholeiites to olivine melilitites from south eastern Australia utilizing geochemical and experimental petrological data. J. Petrol. 19: 463-513.

Frey, F.A., Bryan, W.B. & Thompson, G., 1974: Atlantic ocean floor: Geochemistry and petrology of basalts from Legs 2 and 3 of the Deep Sea Drilling Project. J. Geophys. Res. 79: 5507-5527.

Frey, F.A., Dickey, J.S., Thompson, G., Bryan, W.B. & Davies, H.L., 1980: Evidence for heterogeneous primary MORB and mantle sources, NW Indian Ocean. Contrib. Mineral. Petrol. 74: 387-402.

Fujii, T. & Kushiro, I., 1977: Melting relations and viscosity of an abyssal tholeiite. Rep. Geophys. Lab. Carnegie Inst. Yrbk 76: 461-465.

Ganguly, J., 1979: Garnet and clinopyroxene solid solutions and geothermomery based on Fe-Mg distribution coefficients. Geochim. Cosmochim. Acta 43: 1021-1029.

Gansser, A., 1979: The Himalayas - A fascinating geological challenge. Episodes 4: 17-20.

Ghent, E.D., Stout, M.Z & Raeside, R.P., 1983: Plagioclase-clinopyroxene-garnet-quartz equilibria and the geobarometry and geothermometry of garnet amphibolites from Mica Creek, British Columbia. Can. J. Earth Sci. 20: 699-706.

Glassley, W.E. & Sørensen, K., 1980: Constant P_s-T amphibolite to granulite facies transition in Agto (West Greenland) metadolerites: Implications and applications. J. Petrol. 21: 69-105.

Glikson, A.Y., 1982: The early Precambrian crust with reference to the Indian Shield: an essay. J. Geol. Soc. India 23: 581-603.

Glikson, A.Y., 1983: Geochemistry of Archaean tholeiitic basalt and high-Mg to peridotite komatiite suites, with petrogenetic implications. Geol. Soc. India Memoir 4: 183-219.

Goodwin, A.M., 1981: Precambrian perspectives. Science 213: 55-61.

Green, D.H., 1970: The origin of basaltic and nephelinitic magmas. Trans. Leicester Lit. Philos. Soc. 64: 28-54.

Green, D.H., 1975: Genesis of Archean peridotitic magmas and constraints on Archean geothermal gradients and tectonics. Geology 3: 15-18.

Green, D.H., 1976a: Orthopyroxene in the lunar interior and constraints on early lunar differentiation. Lunar Science 7th, 1. Lunar Science Inst., Houston, Texas: 336-338.

Green, D.H., 1976b: Experimental testing of "equilibrium" partial melting of peridotite under water-saturated, high pressure conditions. Can. Mineral. 14: 225-268.

Green, D.H., 1981: Petrogenesis of Archean ultramafic magmas and implications for Archean tectonics. In Kröner, A., PRECAMBRIAN PLATE TECTONICS. Elsevier: 469-489.

Green, D.H. & Hibberson, W., 1970a: Experimental duplication of conditions of precipitation of high-pressure phenocrysts in a basaltic magma. Phys. Earth Planet. Interiors 3: 247-254.

Green, D.H. & Hibberson, W., 1970b: Instability of plagioclase in peridotite at high pressure. Lithos 3: 209-221.

Green, D.H., Hibberson, W.O. & Jaques, A.L., 1979: Petrogenesis of mid-ocean ridge basalts. In McElhinny, M.W. (Ed.): THE EARTH: ITS ORIGIN, STRUCTURE AND EVOLUTION. (A volume in honour of J.C. Jaeger and A.L. Hales.) Academic Press, London.

Green, D.H. & Ringwood, A.E., 1967a: The genesis of basaltic magmas. Contrib. Mineral. Petrol. 15: 103-190.

Green, D.H. & Ringwood, A.E., 1967b: An experimental investigation of the gabbro to eclogite transformation and its petrological applications. Geochim. Cosmochim Acta 31: 767-833.

Green, D.H. & Ringwood, A.E., 1972: A comparison of recent experimental data on the gabbro-garnet granulite-eclogite transition. J. Geol. 80: 277-288.

Green, D.H., Ringwood, A.E., Hibberson, W.O. & Ware, N.G., 1975: Experimental petrology of Apollo 17 MARE basalts. Proc. Lunar Sci. Conf. 6th: 871-893.

Green, T.H & Pearson, N.J., 1986: Ti-rich accessory phase saturation in hydrous mafic-felsic compositions at high P,T. Chem. Geol. 54: 185-201.

Grew, E.S., 1980: Sapphirine + quartz association from Archaean rocks in Enderby Land, Antarctica. Am. Mineral. 65: 821-836.

Grew, E.S., 1978: Precambrian basement at Molodezhnaya Station, East Antarctica. Geol. Soc. Am. Bull. 89: 801-813.

Grew, E.S., 1981: Granulite-facies metamorphism at Molodezhnaya Station, East Antarctica. J. Petrol. 22: 297-336.

Griffin, B.J., 1979: Enwegy dispersive analysis system calibration and operation with TAS-SUEDS, an advanced interactive data-reduction package. Department of Geology Publication 343, University of Tasmania.

Griffin, W.L., Wass, S.Y. & Hollis, J.D., 1984: Ultramafic xenoliths from Bullenmerri and Gnotuk Maars, Victoria, Australia: Petrology of a subcontinental crust-mantle transition. J. Petrol. 25: 53-87.

Grove, T.L. & Bence, A.E., 1977: Experimental study of pyroxene-liquid interaction in quartz-normative basalt 15597. Proc. Lunar Sci. Conf. 8th: 1549-1579.

Grove, T.L. & Bryan, W.B., 1983: Fractionation of pyroxene-phyric MORB at low pressure: An experimental study. Contrib. Mineral. Petrol. 84: 293-309.

Hanson, G.N., 1980: Rare earth elements in petrogenetic studies of igneous systems. Ann. Rev. Earth Planet. Sci. 8: 371-406.

Hargroves, R.B., 1981: Precambrian tectonic style: A liberal uniformitarian interpretation. In Kröner, A. (Ed.): PRECAMBRIAN PLATE TECTONICS: 21-56.

Harley, S.L., 1983: Regional geobarometry-geothermometry and metamorphic evolution of Enderby Land, Antarctica. In Oliver, R.L., James, P.R. & Jago, J.B. (Eds): ANTARCTIC EARTH SCIENCE. Australian Academy of Science: 25-30.

Harley, S.L., 1985a: Paragenetic and mineral-chemical relationships in orthoamphibole-bearing gneisses from Enderby Land, East Antarctica: A record of Proterozoic uplift. J. Metamorphic Geol. 3: 179-200.

Harley, S.L., 1985b: Garnet-orthopyroxene-bearing granulites from Enderby Land, Antarctica: Metamorphic pressure-temperature-time evolution of the Archean Napier Complex. J. Petrol. 26: 819-856.

Harris, P.G., 1974: Origin of alkaline magmas as a result of anatexis. In Sørenson, H. (Ed.): THE ALKALINE ROCKS: 427-434.

Hatton, C.J. & Von Gruenewaldt, G., 1985: Chromite from the Swartkop chrome mine - an estimate of the effects of subsolidus reequilibration. Econ. Geol. 80: 911-924.

Hensen, B.J., 1971: Theoretical phase relations involving cordierite and garnet in the system MgO-FeO-Al_2O_3-SiO_2. Contrib. Mineral. Petrol. 33: 191-214.

Hensen, B.J., 1976: The stability of pyrope-grossular garnet with excess silica. Contrib. Mineral. Petrol. 55: 279-292.

Hensen, B.J. & Essene, E.J., 1971: Stability of pyrope-quartz in the system MgO-Al_2O_3-SiO_2. Contrib. Mineral. Petrol. 30: 72-83.

Herzberg, C.T., Fyfe, W.S. & Carr, M.J., 1983: Density contraints on the formation of the continental Moho and crust. Contrib. Mineral. Petrol. 84: 1-5.

Hickey, R.L. & Frey, F.A., 1982: Geochemical characteristics of boninite series volcanics: Implications for their source. Geochem. Cosmochim. Acta 46: 2099-2115.

Hill, R. & Roedder, P., 1974: The crystallization of spinel from basaltic liquid as a function of oxygen fugacity. J. Geol. 82: 709-729.

Hoefs, J., Faure, G. & Elliot, D.H., 1980: Correlation of ^{18}O and initial $^{87}Sr/^{86}Sr$ ratios in Kirkpatrick basalt on Mt Falla, Transantarctic Mountains. Contrib. Mineal. Petrol. 75: 199-203.

Hollister, L.S., 1982: Metamorphic evidence for rapid (2 mm/yr) uplift of a portion of the Central Gneiss Complex, Coast Mountains, B.C. Can. Mineral. 20: 319-332.

Huppert, H.E. & Sparks, R.S.J., in prep.: Cooling and contamination of mafic and ultramafic magmas during ascent through continental crust.

Irvine, T.N., 1967: Chromium spinel as a petrogenetic indicator, Part 2. Petrologic applications. Can. J. Earth Sci. 4: 71-103.

Irvine, T.N., 1976: Chromite crystallization in the join Mg_2SiO_4-$CaMgSi_2O_6$-$CaAl_2Si_2O_8$-$MgCr_2O_4$-SiO_2. Carnegie Inst. Wash. Yearbk 76: 465-472.

Irvine, T.N., 1977: Origin of chromitite layers in the Muskox Intrusion and other stratiform intrusions: a new interpretation. Geology 5: 273-277.

Irving, A.J., 1978: A review of experimental studies of crystal/liquid trace element partitioning. Geochim. Cosmochim. Acta 42: 743-770.

James, P.R. & Black, L.P., 1981: A review of the structural evolution and gochronology of the Archean Napier Complex of Enderby Land, Australian Antarctic Territory. Spec. Pub. Geol. Soc. Aust. 7: 71-83.

James, P.R. & Tingey, R.J., 1983: The Precambrian geological evolution of the East Antarctic metamorphic shield - a review. In Oliver, R.L., James, P.R. & Jago, J.B. (Eds): ANTARCTIC EARTH SCIENCE. Australian Academy of Science: 5-10.

Jaques, A.L. & Green, D.H., 1979: Determination of liquid compositions in high pressure melting of peridotite. Am. Mineral. 64: 1312-1321.

Jaques, A.L. & Green, D.H., 1980: Anhydrous melting of peridotite at 0-15 kb pressure and the genesis of tholeiitic basalts. Contrib. Mineral. Petrol. 73: 287-310.

Jenner, G.A., 1981: Geochemistry of high-Mg andesites from Cape Vogel, PNG. Chem. Geol. 33: 307-332.

Jenner, G.A., 1982: PETROGENESIS OF HIGH-Mg ANDESITES. Unpublished Ph.D. thesis, University of Tasmania: 205 pp.

Jensen, L.S., 1976: A new cation plot for classifying subalkalic volcanic rocks. Ontario Div. Mines Misc. Pap. No.66.

Johnson, C.A., Bohlen, S.R. & Essene, E.J., 1983: An evaluation of garnet-clinopyroxene geothermometry in granulites. Contrib. Mineral. Petrol. 84: 191-198.

Kadmina, I.N., Kurinin, R.G., Masolov, V.N. & Grikurov, G.E., 1983: Antarctic crustal structure from geophysical evidence: a review. In Oliver, R.L., James, P.R. & Jago, J.B. (Eds): ANTARCTIC EARTH SCIENCE: 498-502.

Kay, R.W. & Gast, P.W., 1973: The rare earth content and origin of alkali-rich basalts. J. Geol. 81: 653-682.

Kirkpatrick, J.R., 1981: Kinetics of crystallization of igneous rocks. In Ribbe, P.H. (Ed.): REVIEWS IN MINERALOGY. Mineral. Soc. Am. 8: 321-398.

Kretz, R., 1982: Transfer and exchange equilibria in a portion of the pyroxene quadrilateral as deduced from natural and experimental data. Geochim. Cosmochim. Acta 46: 411-421.

Kröner, A., 1985: Evolution of the Archean continental crust. Ann. Rev. Earth Planet. Sci. 13: 49-74.

Kuehner, S.M., 1987: Mafic dikes of the East Antarctic Shield: A note on the Vestfold Hills and the Mawson Coast occurrences. Geol. Assoc. Canada Spec. Pap., in press.

Kushiro, I., 1962: Clinopyroxene solid solutions, Pt 1. The CaTs component. Jap. Jour. Geol. Geogr. 33: 213-220.

Kushiro, I., 1965: The liquidus relations in the system forsterite-$CaAl_2SiO_6$-silica and forsterite-nepheline-silica at high pressures. Carnegie Inst. Wash. Yearbk 64: 103-108.

Kushiro, I., 1968: Compositions of magmas formed by partial zone melting of the earth's upper mantle. Jour. Geophys. Res. 73: 619-634.

Kushiro, I., 1975: On the nature of silicate melt and its significance in magma genesis: Regularities in the shift of the liquidus boundaries involving olivine, pyroxene, and silica minerals. Am. J. Sci. 275: 411-431.

Kyle, P.R., 1980: Development of heterogeneities in the subcontinental mante: evidence from the Ferrar Group, Antarctica. Contrib. Mineral. Petrol. 73: 89-104.

Langmuir, C.H., 1980: A major and trace element approach to basalts. Unpublished Ph.D. thesis, State University of New York at Stoney Brook: 330 pp.

Langmuir, C.H., Bender, J.F., Bence, A.E. & Hanson, G.N., 1977: Petrogenesis of basalts from the Famous area: Mid-Atlantic Ridge. Earth Planet. Sci. Lett. 36: 133-156.

Lindsley, D.H., 1983: Pyroxene thermometry. Am. Mineral. 68: 477-493.

Lindsley, D.H. & Anderson, D.J., 1983: A two pyroxene thermometer. Proc. 13th Lunar and Planetary Science Conf., Part 2. J. Geophys. Res. 88: A887-A906.

Mathez, E.A., 1984: Influence of degassing on oxidation states of basaltic magmas. Nature 310: 371-375.

Masuda, A., Nakamura, N. & Tanaka, T., 1973: Fine structures of mutually normalized rare-earth patterns of chondrites. Geochim. Cosmochim. Acta 37: 239-248.

Matsui, Y. & Nishazawa, O., 1974: Iron (II)-magnesium exchange equilibrium between olivine and calcium-free pyroxene and a temperature range 800^{o} to 1300^{o}C. Bull. Soc. Mineral. Crystallogr. 97: 122-130.

Maurel, C. & Maurel, P., 1984: Etude experimentale de la distribution du fer ferreux et du mangesium entre spinelle chromifere et bain silicate basique. Bull. Mineral. 107: 767-776.

McCulloch, M.T. & Cameron, W.E., 1983: Nd-Sr isotopic study of primitive lavas from the Troodos ophiolite, Cyprus: evidence for a subduction-related setting. Geology 11: 727-731.

McKenzie, D., 1984: A possible mechanism for epeirogene uplift. Nature 307: 616-618.

Merrill, R.B. & Wyllie, P.J., 1973: Iron absórption by platinum capsules in high pressure rock melting experiments. Am. Mineral. 58: 16-20.

Mori, T. & Green, D.H., 1978: Laboratory duplication of phase equilibria obseved in natural garnet lherzolites. J. Geol. 86: 83-97.

Nehru, C.E. & Wyllie, P.J., 1975: Compositions of glasses from St Paul's peridotite partially melted at 20 kilobars. J. Geol. 83: 455-471.

Nesbitt, R.W. & Sun, S-S., 1980: Geochemical features of some Archean and post-Archean high-magnesian-low-alkali liquids. Phil. Trans. R. Soc. London A 297: 365-381.

Nesbitt, R.W., Sun, S-S. & Purvis, A.C., 1979: Komatiites: Geochemistry and genesis. Can. Mineral. 17: 165-186.

Newton, R.C. & Perkins, D., 1982: Thermodynamic calibration of geobarometers based on the assemblages garnet-plagioclase-orthopyroxene (clinopyroxene)-quartz. Am. Mineral. 67: 203-222.

Newton, R.C. & Hanson, E.C., 1983: The origin of Proterozoic and late Archean charnokites - evidence from field relations and experimental petrology. Geol. Soc. America Mem. 161: 167-178.

Nickel, K.G. & Brey, G., 1984: Subsolidus orthopyroxene-clinopyroxene systematics in the system CaO-MgO-SiO_2 to 60 kb: A re-evaluation of the regular solution model. Contrib. Mineral Petrol 87: 35-42.

Norrish, K. & Hutton, J.T., 1969: An accurate X-ray spectrographic method for the analysis of a wide range of geologic samples. Geochim. Cosmochim. Acta 33: 431-451.

Norrish, K. & Chappell, B.W., 1977: X-ray fluorescence spectrometry. In Zussman, J. (Ed.): PHYSICAL METHODS IN DETERMINATIVE MINERALOGY. Second edition. Academic Press, London: 254-272.

O'Donnell, T.H. & Presnall, D.C., 1980: Chemical variations of the glass and mineral phases in basalts dredged from 25°-30°N along the Mid-Atlantic Ridge. Am. J. Sci. 280A: 845-868.

O'Hara, M.J. & Humphries, D.J., 1977: Problems of iron gain and loss during experimentation on natural rocks: The experimental crystallization of five lunar basalts at low pressures. Phil. Trans. R. Soc. Lond. A286: 313-330.

O'Hara, M.J. & Mathews, R.E., 1981: Geochemical evolution in an advancing, periodically replenished, periodically tapped, continuously fractionating magma chamber. J. Geol. Soc. London 138: 237-277.

Ollier, C.D., 1981: TECTONICS AND LANDFORMS. Longman, London: 324 pp.

Ozawa, K., 1983: Evaluation of olivine-spinel geothermometry as an indicator of thermal history for peridotites. Contrib. Mineral. Petrol. 82: 52-65.

Padgham, W.A., 1981: Archaean crustal evolution - a glimpse from the Slave Province. Spec. Publ. Geol. Soc. Aust. 7: 99-110.

Papike, J.J., Cameron, K.L. & Baldwin, K., 1974: Amphiboles and pyroxenes: Characterization of other than quadrilateral components and estimates of ferric iron from microprobe data. (Abstract) Geol. Soc. Am. Abstracts with Programs 6: 1053-1054.

Pearce, J.A. & Norry, M.J., 1979: Petrogenetic implications of Ti, Zr, Y and Nb variations in volcanic rocks. Contrib. Mineral. Petrol. 69: 33-47.

Pearce, T.H., 1968: A contribution to the theory of variation diagrams. Contrib. Mineral. Petrol. 19: 142-157.

Perfit, M.R., Gust, D.A., Bence, A.E., Arculus, R.J. & Taylor, S.R., 1980: Chemical characteristics of island-arc basalts: Implications for mantle sources. Chem. Geol. 30: 227-256.

Poldervaart, A. & Hess, H.H., 1951: Pyroxenes in the crystallization of basaltic magmas. Jour. Geol. 59: 472-489.

Raheim, A., & Green, D.H., 1974: Experimental determination of the temperature and pressure dependence of the Fe-Mg partition coefficient for coexisting clinopyroxene and garnet. Contrib. Mineral. Petrol. 48: 179-203.

Reed, S.J.B. & Ware, N.G., 1973: Quantitative electron microprobe analysis using lithium-drifted silicon detector. X-ray Spectrometry 2: 69-74.

Reed, S.J.B. & Ware, N.G., 1975: Quantitative electron microprobe analysis of silicates using energy dispersive X-ray spectrometry. J. Petrol 16: 499-519.

Reid, M.J., Gancarz, A.J. & Albee, A.L., 1973: Constrained least squares analysis of petrologic problems with an application to lunar sample 12040. Earth Planet. Sci. Lett 17: 433-445.

Rhodes, J.M., Blanchard, D.P., Dungan, M.A., Rodgers, K.V. & Brannon, J.C., 1978: Chemistry of Leg 45 basalts. Initial Reports of the Deep Sea Drilling Project 45: 447-459.

Richardson, S.H., Gurney, J.J., Erland, A.J. & Harris, J.W., 1984: Origin of diamonds in old enriched mantle. Nature 310: 198-202.

Ridley, W.I., Rhodes, J.M., Reid, A.M., Jakes, P., Shih, C. & Bass, M.N., 1974: Basalts from Leg 6 of the Deep Sea Drilling Project. J. Petrol. 15: 140-159.

Ringwood, A.E., 1979: ORIGIN OF THE EARTH AND MOON. Springer-Verlag, New York: 295 pp.

Robinson, P., Higgins, N.C. & Jenner, G.A., 1986: Determination of rare-earth elements, yttrium and scandium in rocks by an ion exchange X-ray fluorescence technique. Chem. Geol. 55:

Roeder, P.L., Cambell, I.H. & Jamieson, H.E., 1979: A re-evaluation of the olivine-spinel geothermometer. Contrib. Mineral. Petrol. 68: 325-334.

Ryburn, R.J., Raheim, A. & Green, D.H., 1975: Determination of the P,T paths of natural eclogites during metamorphism - record of subduction. Lithos 9: 161-164.

Sandiford, M., 1985: The metamorphic evolution of granulites at Fyfe Hills; implications for Archean crustal thickness in Enderby Land, Antarctica. J. Metamorphic Geol. 3: 155-178.

Sandiford, M. & Wilson, C.J.L., 1983: The geology of the Fyfe Hills-Khmara Bay region, Enderby Land. In Oliver, R.L., James, P.R. & Jago, J.B., (Eds): ANTARCTIC EARTH SCIENCE. Australian Academy of Science: 16-19.

Saunders, A.D., Tarney, J. & Weaver, S.D., 1980: Transverse geochemical variations across the Antarctic Peninsula: Implications for the genesis of calc-alkaline magmas. Earth Planet. Sci. Lett. 46: 344-360.

Saxena, S.K., 1979: Garnet-clinopyroxene geothermometer. Contrib. Mineral. Petrol. 70: 229-235.

Schreiber, H.D. & Haskin, L.A., 1976: Chromium in basalts: Experimental determination of redox states and partitioning among synthetic silicate phases. Proc. Lunar Sci. Conf. 7th: 1221-1259.

Shackleton, R.M., 1970: On the origin of some African granites. Geol. Assoc. (Lond.) Proc. 81: 549-559.

Sharma, K.K., Bal, K.D., Parshad, R., Lal, N. & Nagpaul, K.K., 1980: Paleo-uplift and cooling rates from various orogenic belts of India, as revealed by radiometric ages. Tectonophysics 70: 135-158.

Sharpe, M.R., 1984: Petrography, classification and chronology of mafic sill intrusions beneath the Eastern Bushveld Complex. Geol. Surv. South Africa Bull. 77: 40 pp.

Sharpe, M.R. & Hulbert, L.J., 1985: Ultramafic sills beneath the Eastern Busheld Complex: Mobilized suspensions of early lower zone cumulates in a parental magma with boninitic affinities. Econ. Geol. 80: 849-871.

Shaw, D.M., 1970: Trace element fractionation during anatexis. Geochem. Cosmochim. Acta 42: 933-943.

Sheraton, J.W., 1981: Chemical analyses of rocks from East Antarctica. B.M.R. Aust. Jour. Geol. Geophys. Rec. 1981/14.

Sheraton, J.W., 1985: Chemical analyses of rocks from East Antarctica: Part2. BMR Jour. Aust. Geol. Geophys. Rec. 1985/12: 124 pp.

Sheraton, J.W. & Black L.P., 1981: Geochemistry and geochronology of Proterozoic tholeiite dykes of East Antarctica: Evidence for mantle metasomatism. Contrib. Mineral. Petrol 78: 305-317.

Sheraton, J.W. & Black, L.P., 1983: Geochemistry of Precambrian gneiss: Relevance for the evolution of the East Antarctic Shield. Lithos 16: 273-196.

Sheraton, J.W., Black, L.P. & McCulloch, M.T., 1984: Regional geochemical and isotopic characteristics of high grade metamorphics of the Prydz Bay area: The extent of Proterozoic reworking of Archean continental crust in East Antarctica. Precambrian Res. 26: 169-198.

Sheraton, J.W. & Collerson, K.D., 1983: Archean and Proterozoic geological relationships in the Vestfold Hills-Prydz Bay area, Antarctica. B.M.R. Aust. Jour. Geol. Geophys. 8: 119-128.

Sheraton, J.W. & Collerson, K.D., 1984: Geochemical evolution of Archaean granulite-facies gneiss in the Vestfold Block and comparisons with other Archaean gneiss complexes in the East Antarctic Shield. Contrib. Mineral. Petrol. 87: 51-64.

Sheraton, J.W., Offe, L.A. Tingey, R.J. & Ellis, D.J., 1980: Enderby Land, Antarctica - an unusual Precambrian high-grade metamorphic terrain. J. Geol. Soc. Aust. 27: 1-18.

Sheraton, J.W., Thompson, J.W. & Collerson, K.D., 1987: Mafic dyke swarms of Antarctica. Geol. Assoc. Can., in press.

Sigurdsson, H. & Schilling, J.G., 1976: Spinels in Mid-Atlantic Ridge basals: chemistry and occurrence. Earth Planet. Sci. Lett. 29: 7-20.

Stephenson, N.C.N., 1984: Two-pyroxene thermometry of Precambrian granulites from Cape Riche, Albany-Fraser Province, Western Australia. J. Meamorphic Geol. 2: 297-314.

Stern, C.R. & Wyllie, P.J., 1975: Effect of iron absorption by noble-metal capsules on phase boundaries in rock-melting experiments at 30 kilobars. Am. Mineral. 60: 681-689.

Stolper, E. & Walker, D., 1980: Melt density and the average composition of basalt. Contrib. Mineral. Petrol. 74: 7-12.

Sun, S-S. & Hanson, G.N., 1975: Origin of Ross Island basanitoids and limitations upon the heterogeneity of mantle sources for alkali basalts and nephelinites. Contrib. Mineral. petrol. 52: 77-106.

Sun, S-S. & Nesbitt, R.W., 1978: Geochemical regularities and genetic significance of ophiolitic basalts. Geology 6: 689-693.

Takahashi, E. & Scarfe, C.M., 1985: Melting of peridotite to 14 GPa and the gnesis of komatiite. Nature 315: 566-568.

Taylor, W.R., 1985: The role of C-O-H fluids in upper mantle processes: A theoretical, experimental and spectroscopic study. Unpubl. Ph.D. thesis, University of Tasmania: 358 pp.

Thirlwell, M.F. & Jones, N.W., 1983: Isotope geochemistry and contamination mechanics of Tertiary lavas from Skye, Northwest Scotland. In Hawkesworth, C.J. & Norry, M.J. (Eds): CONTINENTAL BASALTS AND MANTLE XENOLITHS. Shiva Publ. Ltd, U.K.: 186-208.

Thompson, A.B., 1984: Geothermal gradients through time. In Holland, A.D. & Trendall, A.F. (Eds): PATTERNS OF CHANGE IN EARTH EVOLUTION. Springer-Verlag: 345-355.

Thompson, R.N., 1974: Some high-pressure pyroxenes. Mineral. Mag. 39: 768-787.

Thompson, R.N., 1975: Primary basalts and magma genesis. II. Snake River Plain, Idaho, U.S.A. Contrib. Mineral. Petrol 52: 317-341.

Thompson, R.N., Morrison, M.A., Dickin, A.P. & Hendry, G.L., 1983: Continental flood basalts ... Arachnids rule OK? In Hawkesworth, C.J. & Norry, M.J. (Eds): CONTINENTAL BASALTS AND MANTLE XENOLITHS. Shiva Publishing Limited, Nantwich, U.K.: 158-185.

Tingey, R.J. 1982: The geologic evolution of the Prince Charles Mountains - An Antarctic Archean cratonic block. In Craddock, C. (Ed.): ANTARCTIC GEOSCIENCE. Univ. of Wisconsin Press: 455-464.

Tingey, R.J., 1985: Uplift in Antarctica. Z. Geomorph. N.F., Suppl.-Bd.54: 85-99.

Tsuchiyama, A., 1985: Dissolution kinetics of plagioclase in the melt of the system diopside-albite-anorthite, and origin of dusty plagioclase in andesites. Contrib. Mineral. Petrol. 89: 1-16.

Viljoen, M.J., Viljoen, R.P. & Pearton, T.N., 1982: The nature and distribution of Archean komatiitic volcanics in South Africa. In Arndt, N.T. & Nisbet, E.G. (Eds): KOMATIITES. George Allen & Unwin, London: 53-79.

Wager, L.R., Brown, G.M. & Wadsworth, W.J., 1960: Types of igneous cumulates. J. Petrol. 1: 73-85.

Wass, S.Y., 1973: The origin and petrogenetic significance of hour-glass zoning in titaniferous clinopyroxenes. Min. Mag. 39: 133-144.

Weaver, B.L. & Tarney, J., 1981: Chemical changes during dyke metamorphism in high-grade basement terrains. Nature 289: 47-49.

Wellman, P. & Tingey, R.J., 1982: A gravity survey of Enderby Land and Kemp Land, Antarctica. In Craddock, C. (Ed.): ANTARCTIC GEOSCIENCE. Univ. of Wisconsin Press: 937-940.

Wellman, P. & Williams, J.W., 1982: Extent of Archean and late Proterozoic rocks under the ice cap of Princess Elizabeth Land, Antarctica, inferred from geophysics. B.M.R. Aust. Jour. Geol. Geophys. 7:213-218.

Wells, P.R.A., 1977: Pyroxene thermometry in simple and complex systems. Contrib. Mineral. Petrol 62: 129-139.

Wells, P.R.A., 1981: Accretion of continental crust: thermal and geochemical consequences. Phil. Trans. R. Soc. Lond. A301: 347-357.

Whitney, P.R., 1978: The significance of garnet "isograds" in granulite facies rocks of the Adirondacks. In Metamorphism in the Canadian Shield. Geol. Surv. Canada Pap. 78-10: 357-366.

Williams, I.S., Compston, W., Black, L.P., Irleand, T.R. & Foster, J.J., 1984: Unsupported radiogenic Pb in zircon: A cause of anomalously high Pb-Pb, U-Pb, Th-Pb ages. Contrib. Mineral. Petrol. 88: 322-327.

Wintsch, R.P., 1985: The possible effects of deformation on chemical processes in metamorphic fault zones. In Thompson A.B. & Rubie, D.C. (Eds): METAMORPHIC REACTIONS - KINETICS, TEXTURES AND DEFORMATION.

Wood, B.J. & Banno, S., 1973: Garnet-orthopyroxene and orthopyroxene-clinopyroxene relationships in simple and complex systems. Contrib. Mineral. Petrol. 42: 109-124.

Wood, D.A., Joron, J-L., Treuil, M., Norry, M.J. & Tarney, J., 1979: Elemental and Sr isotope variations in basic lavas from Iceland and the surrounding ocean floor: The nature of mantle source inhomogeneities. Contrib. Mineral. Petrol. 70: 319-339.

Yagi, K. & Onuma, K., 1967: The system $CaMgSi_2O_6$-$CaTiAl_2O_6$ and its bearing on the titanaugites. Hokkaido Univ. Fac. Sci. Jour. 13: 467-483.

Zeitler, P.K., 1985: Cooling history of the NW Himalaya, Pakistan. Tectonics 4: 127-151.